An Excitation Function of Particle Production at the AGS

by

James Colville Dunlop

B.S., Yale University(1994)

Submitted to the Department of Physics
in partial fulfillment of the requirements for the degree of

Doctor of Philosophy

at the

MASSACHUSETTS INSTITUTE OF TECHNOLOGY

June 1999

Author .....
Department of Physics
May 23, 1999

Certified by .....
Craig A. Ogilvie
Professor of Physics
Thesis Supervisor

Accepted by .....
Thomas J. Greytak
Professor, Associate Department Head for Education

An Excitation Function of Particle Production at the AGS

by

James Colville Dunlop

Submitted to the Department of Physics
on May 23, 1999, in partial fulfillment of the
requirements for the degree of
Doctor of Philosophy

Abstract

Measurements of π^+, K^+, K^-, and p production from $Au - Au$ reactions have been made by experiments $E866$ and $E917$ at the Brookhaven National Laboratory Alternating Gradient Synchrotron. The measurements have been made as a function of beam energy, at kinetic beam energies in the laboratory of 2 and 4 $A \cdot GeV$, by experiment $E866$, and of 6 and 8 $A \cdot GeV$, by experiment $E917$. The data has been divided into event classes, based on the total multiplicity in an event. The particles were measured in an angular range from 14 to 57°. Within a range of rapidity $|Y - Y_{nn}| < 0.25 Y_{nn}$, and within the upper 339 mb in total multiplicity, the yields of all produced particles increase as the beam energy increases. The yields of K^- increase more rapidly with beam energy than those of the K^+, and those of the K^+ increase more rapidly with beam energy than those of the π^+. The $\langle m_\perp - m_0 \rangle$ of the particles also increase as the beam energy increases, but not as rapidly as the yields.

The ratio of the yields, K^+/π^+, within this range of rapidity increases steadily from 3% at 2 $A \cdot GeV$ to 20% at 10.8 $A \cdot GeV$. The K^+/π^+ in $Au - Au$ collisions is larger than that in $p-p$ collisions at the same beam energy, and the amount by which it is larger decreases with increasing beam energy.

The K^-/K^+ ratio within this range of rapidity, in the upper 339 mb of total multiplicity, increases steadily from 8% at 4 $A \cdot GeV$ to 19% at 10.8 $A \cdot GeV$. The K^-/K^+ ratio is constant as a function of centrality at all beam energies and rapidities measured. It is not constant with rapidity. The production of kaons therefore shows a clear consistency across all beam energies in the range measured in this thesis. Hadronic models cannot reproduce the dN/dY of K^+ at all beam energies at this stage of their development.

At an equal distance from the $p - p$ production threshold, the K^- yield is lower by a factor of 5 than than the K^+ yield. This stands in contrast to the value of 1.0±0.4 measured by the $KaoS$ collaboration in $Ni - Ni$ collisions at a $\sqrt{s} - \sqrt{s_{th}}$ of -0.24 $A \cdot GeV$[B+97], but is consistent with the general trend in $p - p$ collisions.

Thesis Supervisor: Craig A. Ogilvie
Title: Professor of Physics

Contents

List of Figures

List of Tables

Chapter 1

Introduction

1.1 Overview

Heavy ion collisions are highly complex. In any given collision, a few hundred particles interact strongly in an unbounded volume, producing a slew of particles in an abundant soup of rescattering, absorption, and resonance formation. The results of these processes stream to the detectors of a given experiment, from which it is the experimentalist's job to extract meaningful results.

The question naturally comes up as to why such complicated systems are studied. The energies to which nuclei have been accelerated sit strongly in the regime of soft hadronic physics, and it is known that soft hadronic physics is difficult to understand at a basic level. Therefore, one would think that increasing the number of such interactions would only serve to make the problem more complicated. However, as in condensed-matter physics, as the system becomes larger its understanding can often become simpler, rather than more complicated.

A concept that is useful is that of the "degrees of freedom" of a system. Much of condensed-matter physics is devoted to the search for a relevant set of variables with which to describe a system. The variables are chosen so as to transform the description from one in which the couplings between individual particles are strong into one one in which the effects of the interactions are folded into the variables themselves, leaving only residual corrections. The set of these variables is usually called the set of

relevant degrees of freedom of the system. In the limit that the residual interactions can be ignored, and in the static thermodynamic limit, the system can be completely described in terms of its degrees of freedom.

1.2 Quark-Gluon Plasma

So the question then becomes, "What are the relevant degrees of freedom in a heavy-ion collision?" At the limit of very high energies, an intuitive guess would define them as the individual quarks and gluons, because of the asymptotic freedom of the fundamental theory of strong interactions, QCD. This guess is borne out by many studies using Lattice QCD[DeT96]. Such studies assume static equilibrium, at zero baryon density, and so the relevant energetic quantity is the energy density or, related to this, the temperature of the system. At high energy densities, the studies show that an interacting gas of quarks and gluons has a high entropy density, while at lower energy densities it has a low entropy density. Since the entropy density is related to the number of degrees of freedom of a system, this change has been interpreted as a change from a system in which the quarks and gluons are highly correlated, as they are when bound into hadrons, to one in which they are relatively free. This argument is further bolstered by the asymptotic value seen for the entropy density, which matches that expected for an ideal gas of quarks and gluons. Such a gas is called a "Quark-Gluon Plasma". The term plasma is used to provide an analogy to an ordinary plasma, in which electrons are no longer bound within atoms.

The transition between these two regions is seen to be relatively abrupt, and lies at a transition temperature of $\sim$140-160 MeV in the latest sets of calculations. The location of this transition point makes sense in terms of the size of a typical hadron ($\sim$1 fm), which adds further support to the argument that the transition is between a system made up of hadrons and a system made up of relatively free quarks and gluons. The sharpness of the transition leads to the proposal that there is a phase transition between the two regions, in the strict thermodynamic sense. The order of this phase transition, and even the question as to whether it is actually a phase

transition in the strict sense of the word, is a constant source of debate.

At lower energies, the picture is not quite as clear. The argument for a transition rests on the baryon density of the system, which is expected to be large, perhaps near its maximum, in the range of energies available at the AGS. For technical reasons, finite baryon density cannot be included into lattice calculations. However, intuitively, one would think that as the baryon density increases, the probability of overlap will also increase, leading to a to a state in which there is essentially no normal space available. Recent theoretical work in this regime of density [ARW98] has led to a proposal of another state, in which normal hadrons no longer exist, but there remain large correlations between the quarks.

1.3 Masses in the Medium

A related set of ideas focuses on the effective masses of particles in the dense medium created in these collisions. This set of ideas spans the boundary between the extreme change in the relevant degrees of freedom expected in the quark-gluon plasma and those in the regime of normal hadronic matter. Within such frameworks, borrowing again from condensed-matter physics, "quasiparticles", closely related to the usual hadrons, are introduced, the properties of which incorporate a complex mix of effects. This set of ideas has explored a great deal, both at the higher energies of the SPS at CERN (158 $A \cdot GeV$) and at the lower energies of the SIS at GSI (approximately 1 $A \cdot GeV$).

There are actually two sets of ideas. The first is perhaps more fundamental, since it treats all hadrons as quasiparticles moving through the QCD vacuum. The ground state of QCD, the vacuum, is a complicated object, due to the strong self-coupling of the carriers of the force, the gluons. In some theoretical frameworks the properties of hadrons are to a great degree determined by the properties of this vacuum. It has been proposed that the presence of a large number of particles, or regions of high baryon or energy density, will modify the vacuum, which will in turn modify the properties of the particles lying within the modified vacuum. Therefore, in a heavy

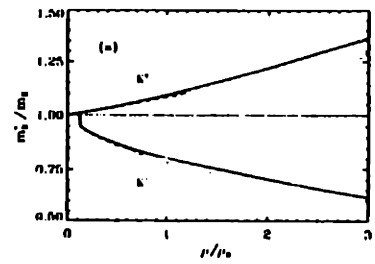

Figure 1-1: An example of calculations made predicting medium effects on the kaons. Shown in the figure are the effective masses of kaons in one calculation including nuclear potentials. The vertical axis shows the effective mass divided by the free mass, where the effective massis defined as the value of the dispersion relation at zero momentum. The horizontal axis shows the baryon density, divided by that in normal nuclear matter. The plot is from[WW97].

ion collision, in which regions of high baryon or energy density are produced, one might expect that a modification of particle properties may occur.

On a more familiar level in the context of nuclear physics, there has been some recent theoretical and experimental work on the effects that nuclear potentials may have on mesons, with particular attention paid to kaons. Studies of various interaction lengths and kaonic atoms indicate that kaons feel opposite potentials in the nuclear medium, with an attractive potential for the K^- and a weaker repulsive potential for the K^+. Using mean field arguments, at infinite time scales and for systems of infinite extent, the effects of these potentials can be incorporated into effective masses of the kaons.[WW97] Not surprisingly, the divergent potentials lead to opposite effects on the kaon mases, with the K^- mass dropping in the medium and the K^+ mass rising.

Figure 1-1 shows one such calculation. The figure shows the effective mass for the K^+ and K^-, defined as the dispersion relation of the particle at zero momentum, as a function of the baryon density of the system. Note the large size of the effect at relatively small baryon densities. While other calculations produce somewhat different levels for the effect, due to the existence of a rather strong resonance between K^- and nucleons, the basic picture of a divergence between the properties of kaons in the medium is common across all calculations.

Experimentally, changes in the mass of particles can be explored in two ways. The first way is somewhat obvious: if one wants to find a mass shift, one should look at a

mass. Some particles, such as the ρ, have decay channels to leptons. Such channels have the nice property that, to an excellent level of approximation, the products of the decay do not suffer from final state interactions. Therefore, by looking at the invariant mass of the products, one can see directly the mass of the particle as it was at the point of decay. No experiment at the AGS can measure dileptons, so this avenue is closed. There are dilepton experiments both at the Bevalac (approximately 1 $A{\cdot}GeV$) and at the SPS.

The ϕ has a dominant decay to $\phi \rightarrow K^+K^-$, the measurement of which is a large focus of experiment $E917$. This measurement suffers from both the strong interaction of the decay products with the medium and the large decay length of the ϕ, relative to a nuclear size, but remains potentially sensitive.

There is, however, another way to search for shifts in mass. Particle production in nuclear collisions at energies near or below the $p-p$ threshold is sensitive to the threshold location. Mass shifts can adjust the position of this threshold, resulting in large changes in the production probability, if one assumes that the shift, which strictly only applies to the dispersion relation in an infinite medium, applies to the process of production. This is necessarily an indirect method to search for a shift, and the interpretation is rather model-dependent.

There are hints of this effect experimentally, although the results still do not constitute a proof. The yields of K^- were measured in $Ni-Ni$ collisions, at beam energies below the $p-p$ threshold, by the $KaoS$ experiment at the SIS accelerator at GSI. The yields of K^+ were also measured, at an energy an equal value below the K^+ threshold. The two measurements were therefore said to be measured at "equivalent" energies. The ratio between the two yields is strikingly large[B+97], approximately unity. Figure 1-2 shows the data measured, as a function of the kinetic energy of the kaons, along with two models for the collision. One model includes the effects of shifting masses, with parameters describing the effect adjusted to the data, and the other model includes no mass shift [LLB97]. The underlying cascade code is the same in both cases. The difference between the two models is also large, a factor of 5 at low $m_\perp$, and the model with the mass shifts reproduces the data. This leads to the

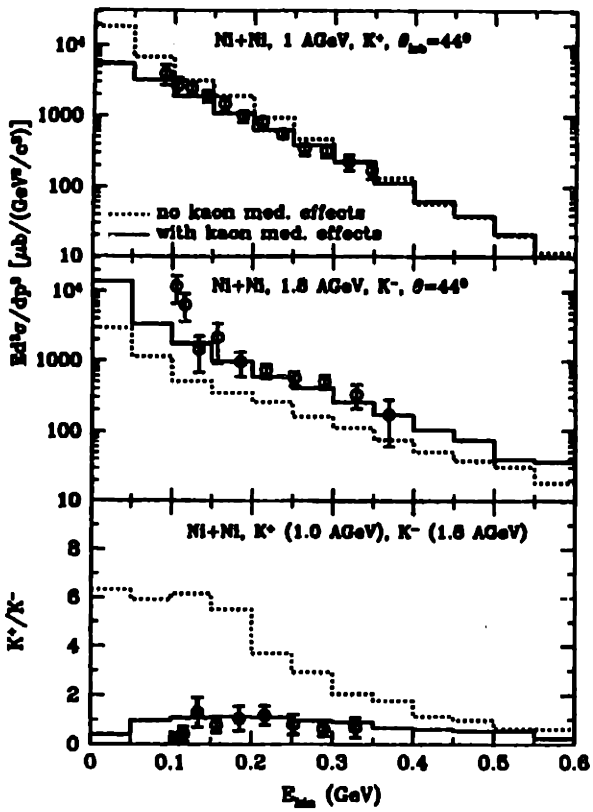

Figure 1-2: The data on K^- and K^+ production in $Ni-Ni$ collisions at GSI energies, along with models including and not including mass shifts of the kaons. The data is from[B+97], and the models from [LLB97]. The figure is from [LLB97].

claim that mass shifts are necessary to describe the data.

Such a claim is necessarily model-dependent. At the higher energies of the AGS and the SPS, kaon production is known to be enhanced in nuclear collisions as compared to $p-p$ collisions, as will be described in the next section, but the mechanisms for this enhancement are still poorly understood. There is no value from $p-p$ collisions with which to compare the GSI results, since by definition the yields of K^+ and K^- are zero below threshold. The lack of understanding of the mechanisms for enhancement is due to the complicated nature of the environment, which leads to a range of effects in the models, none of which can be clearly singled out as the leading cause. The model, with kaon mass shifts, describes the data in one situation. There are, however, some rather large effects in the cascade portion of the model that need to be constrained, such as the absorption of the K^-. It is, therefore, difficult to conclude from the description under one set of conditions that mass shifts are necessary.

1.4 The AGS

The program at the AGS has run for many years, but few hard conclusions have been made from the data measured at these beam energies.

The highest beam energy achievable at the AGS, 10.8 $A \cdot GeV$, is thought to lie in the strong "stopping" region. That is to say, in this region of energies, a large fraction of the energy of the incoming nucleons is deposited in the primary region of particle production, the "participant zone". There is some evidence for this effect in the proton rapidity distributions [A+98a], in that these distributions show a large pileup at mid-rapidity. This pileup stands in contrast to the gap at mid-rapidity seen in $p-p$ collisions.

Kaon production is enhanced at AGS energies relative to that in $p-p$ collisions. One number that shows this enhancement is the ratio of the yields of the K^+ to that of the π^+, which has a value of 0.19 ± 0.01 [O+98] in central $Au-Au$ collisions at 10.8 $A GeV$. It is also enhanced in the lighter systems studied, at slightly higher beam energies of 14.6 $A GeV$. This value should be contrasted with a value of approximately

0.04 in $p - p$ collisions of this energy.

The ratio includes two effects, since both an enhancement of kaon production and a suppression of pion production will lead to a large ratio. Therefore, the dependence of the K^+ production alone on system size, or, somewhat equivalently, on measured quantities related to the impact parameter between the two Au nuclei in $Au - Au$ collisions, may help to determine which of these effects is at work. Figure 1-3 shows the dependence of the total yields of kaons at 10.8 $A \cdot GeV$ on the number of projectile nucleons that participated in the reaction, N_{pp}, with the leading linear behavior removed by a division of the yields by N_{pp}. N_{pp} is determined from the energy measured by a calorimeter at zero degrees. The figure clearly shows that the level rises nonlinearly with the number of participants measured in this way. The pions [A+99b] show a more complicated dependence on N_{pp}, as shown in figure 1-4.

The production of K^- at 10.8 $A \cdot GeV$ is rather similar to that of the K^+. This is shown most clearly by the ratio of the total yields as a function of N_{pp}, shown in figure 1-5. The constancy of this ratio, despite the large and nonlinear rise of the yields of both particles, is a bit of a puzzle, as will be discussed in chapter 7.

The gross characteristics of kaon production at 10.8 $A \cdot GeV$, along with the dependence on the centrality of the collision, are relatively well reproduced by at least one model of these collisions, RQMD. [SSG89],[Ahl97] This model is of the cascade type, and includes both a large set of hadronic cross-sections, some of which are unmeasured, and some further enhanced cross-sections at higher energies due to strings. The production and rescattering of resonances, such as the Δ, has been shown to be critical in reproducing the data for the lighter systems. [G+95b] The cross-sections between a Δ and a nucleon, say, are not measured, and so must be assumed. The reproduction of the data by the model, over a broad range of impact parameters, leads to the suggestion that the collisions are well understood at this beam energy, but it is difficult to pin down which of the many included effects cause the model to reproduce the data. It is also not clear how much tuning of the model's parameters has been necessary to reproduce the data at this one beam energy.

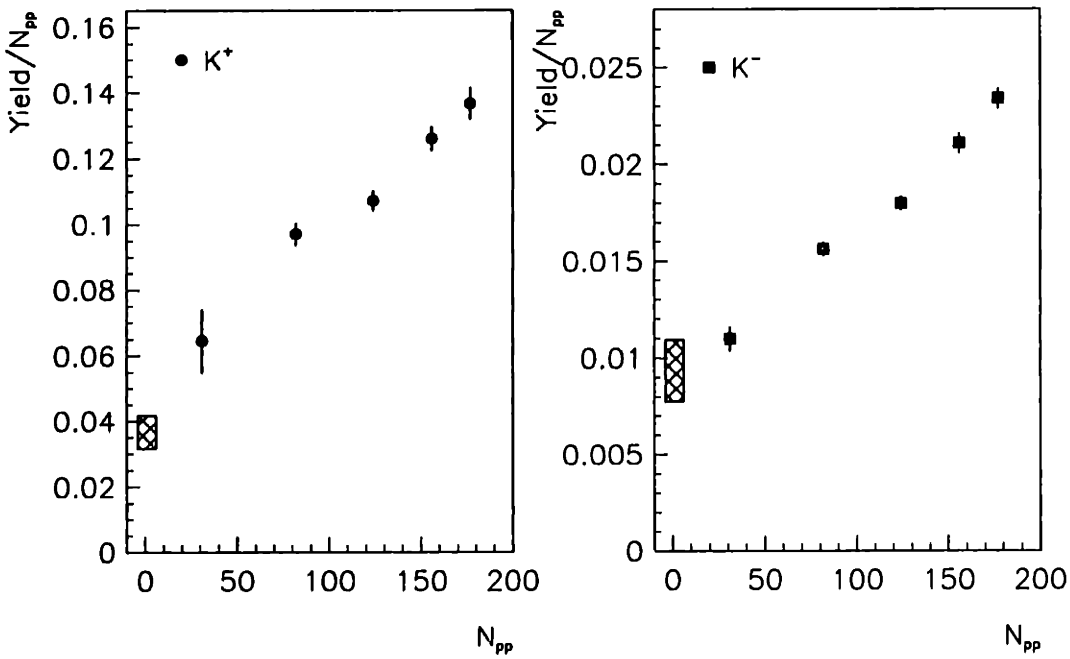

Figure 1-3: The total yield of kaons, per projectile participant, as a function of the number of projectile participants. The number of projectile participants, N_{pp}, is estimated by the energy measured in a cone of 1.5° about the beam axis. The total yields are from a Gaussian fit to the dN/dY distributions, which are in turn from an exponential fit to the differential invariant yields in $m_\perp$. The figure is from [A+99a].

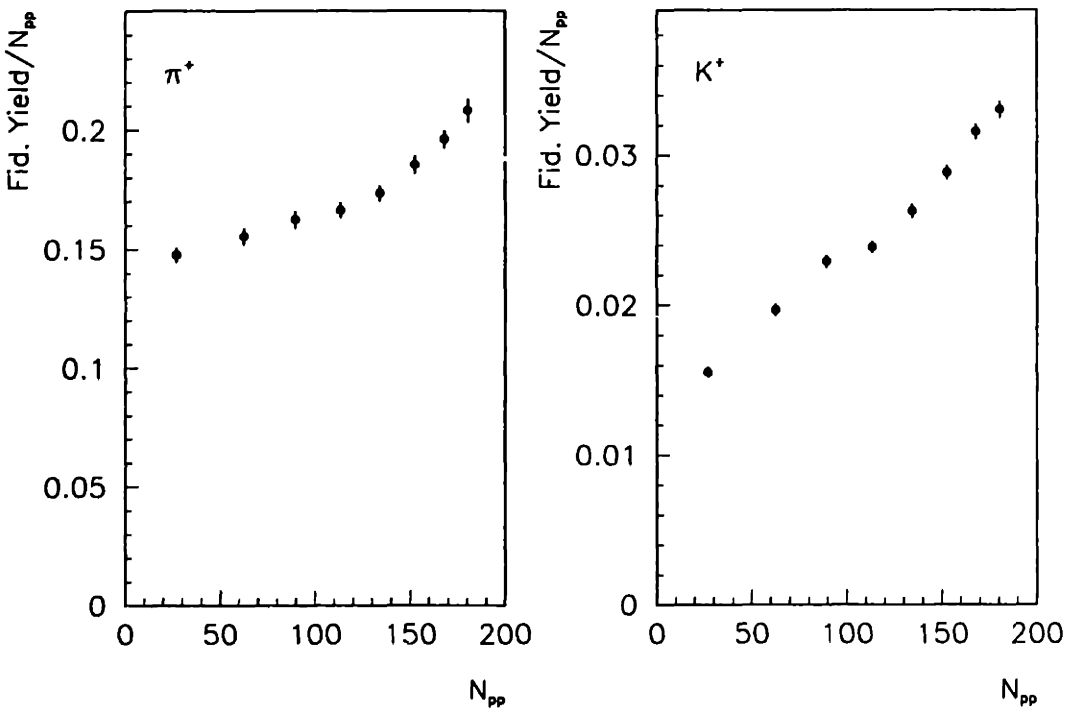

Figure 1-4: The fiducial yields of kaons and pions, in the restricted range $0.6 < Y < 1.3$, per projectile participant, as a function of the number of projectile participants. Y denotes the rapidity, and the number of projectile participants, N_{pp}, is estimated by the energy measured in a cone of 1.5° about the beam axis. The dN/dY are derived from fits to the differential invariant yields in $m_\perp$. The figure is from[A+99b].

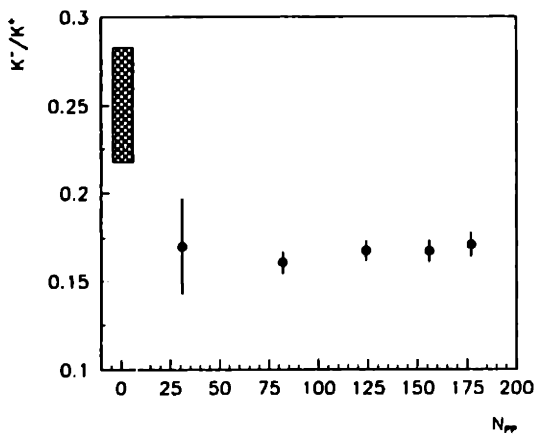

Figure 1-5: The ratio of the total yields, K^-/K^+, as a function of N_{pp}, from $Au-Au$ collisions at 10.8 $A{\cdot}GeV$. The figure is from [A+99a]

1.5 Goals of the Thesis

Particle production in heavy-ion collisions at the highest energies of the AGS, with $\sqrt{s}$ of approximately 5 $A{\cdot}GeV$, has been exhaustively measured. Production has also been measured extensively at the SPS, at the higher $\sqrt{s}$ of 17 $A{\cdot}GeV$, and at the Bevalac and GSI, at $\sqrt{s}$ values of approximately 2.5 $A{\cdot}GeV$. These three sets of beam energies are very different. At GSI energies, particle production is a rare process, so that the dominant particles in the collision zone are the baryons from the initial state. At the highest energies of the AGS, the number of pions in the final state is approximately equal to the number of protons, so that the collision zone consists of a complex mix of baryons and produced particles. At SPS energies, mesons are dominant, with the protons accounting for only approximately 10% of the particles in the final state.

Within the framework of hadronic models, estimates of the density of the colliding matter range from from approximately 8 times normal nuclear matter density at beam energies of 10 $A{\cdot}GeV$[LK95] to approximately 2 times nuclear matter density at beam energies of 2 $A{\cdot}GeV$[SG86, BG88, C+90, SJWR]. While these are model-dependent

estimates, they serve as indications of the possible range achievable in these collisions. At the upper end of this range of densities, it may be possible to create regions of the collision zone in which the relevant degrees of freedom are not those of normal nuclear matter, and in which a baryon-rich QGP may be formed. The appearance or disappearance of such regions, due to changes in the baryon density, may potentially be observable as correlated changes in the properties of particle production as the beam energy decreases.

Therefore, the region between these three energies is fertile ground for further study. In the complex systems created in heavy-ion collisions, it is very difficult to make conclusions based on a measurement at a single point. By measuring particle production at energies previously unexplored, $E866$ and $E917$ hoped to find direct evidence for changes in the degrees of freedom of the system in the evolution of its properties. Failing this, the large data set obtained by these measurements serves to constrain the understanding of collisions at either end of the energy spectrum.

Chapter 2

Description of the Experiment

Experiments $E866$ and $E917$ are the continuation of a string of experiments at the AGS, beginning in 1987 with experiment $E802$. The data presented in this thesis was taken at the end of the final run period of experiment $E866$, in January 1996, and at the beginning of the first (and only) run period of $E917$, in November 1996. The experiments consist of four groups of detector subsystems, each with a specific measurement purpose. The following is a description of the detector subsystems, along with the triggering and data acquisition systems.

2.1 Definitions

2.1.1 Electronic readout

There are two main types of readout in the experiment, the acronyms for which will be scattered throughout this chapter. The first is a Time-to-Digital Converter (TDC). This converts the difference between the edges of two times into an integer, which is then stored. The TDC's in the experiment are of varying levels of complexity and resolution. The second is the Analog-to-Digital Converter (ADC), which integrates the charge of a signal pulse within a certain gate in time and returns an integer corresponding to that time. These are also of varying levels of complexity, resolution, and linearity of response, and handle abnormal pulse shapes in different ways. These

always have a "pedestal", which is an arbitrary offset placed onto the measured charge in order to assure that small signals fall into the linear region of response. This pedestal must be subtracted from the recorded numbers before the charge can be obtained.

2.1.2 Coordinate Systems

Since the Henry Higgins spectrometer (section 2.9) rotates about the nominal target position (section 2.4.2), when discussing the positions of various detectors it becomes important to define the coordinate systems. There are three coordinate systems used in the experiment, each having its own particular use. These coordinate systems are described in table 2.1. The planes at $Z = 0$ of the three coordinate systems intersect only along the line $X = Z = 0$. Usually the SPEC coordinate system will be used for systems on the spectrometer platform and the BEAM coordinate system for those not.

BEAM	$+z$ is defined along the beam axis, pointing from the AGS ring through the target. $+y$ points upwards vertically against gravity. $+x \propto y \times y$, and so points to the left of the target, looking along $+z$. The Henry Higgins spectrometer is at $+x$. $x = y = z = 0$ sits at the nominal target position.
SPEC	$+z$ is defined to be the direction perpendicular to the front faces of the chambers, pointing from the target through the magnet. $+y$ points upwards vertically against gravity. $+x \propto y \times z$, and so points along the front faces of the chambers, in the direction away from the beam line. $x = y = z = 0$ sits at the nominal target position.
MAGN	The magnet is angled with respect to the chambers, but the spectrometer angle, θ_{HH}, is defined in terms of the magnet. The MAGN coordinate system describes a system rotated in the xz plane to θ_{HH}. It is rotated from the SPEC coordinate system by -7.4° in the xz plane about the nominal target position.

Table 2.1: Definition of the coordinate systems used in this thesis

2.2 The AGS

The Alternating Gradient Synchrotron (AGS) at Brookhaven National Laboratory (BNL) has a long and venerable history. It was first commisioned in the 1960's. Needless to say, much has changed since then, but the accelerator has remained relevant.

2.2.1 History

The AGS was originally a proton accelerator, and still serves in this capacity. However, in the early 1980's it was realized that the construction of a transfer line between an existing Tandem van de Graff accelerator and the AGS ring would allow for the acceleration of ions, rather than protons. After this transfer line was completed, first O and then Si beams were accelerated. Experiment $E802$ was one of the first set of experiments to measure collisions between these beams and a large range of targets.

For a few years, Si remained the heaviest nucleus that could be accelerated. During this time, $E802$ evolved into $E859$, with the addition of a second-level trigger and various upgrades to its detector systems. In the early 1990's, an upgrade was made to the Booster portion of the AGS that allowed Au beams to be accelerated, with the first Au beam delivered to the experiments in 1992. $E859$ became $E866$ to measure results from these new beams.

For a few more years, the AGS delivered Au beams of a "fixed" momentum to the experiments. In January 1996, however, the AGS began a program to deliver lower energy beams, providing beams of kinetic energy 2 and 4 A·GeV. Throughout this thesis this run period will be referred to as the "1995 $E866$" run period, since it followed two months of running in November and December of 1995. This served as the final run period of $E866$.

It was known at the time that there were plans for the AGS to deliver 6 and 8 $A \cdot GeV$ beams the following November. Experiment $E917$ was formed from a portion of $E866$, combined with a set of new collaborators, partially to finish the job of measuring these low energy beams. With a string of upgrades, $E917$'s purpose was

also to increase the sensitivity of the measurements of the rarer processes at the high energy, the beam of which was delivered in December 1996 and January 1997. This period of data taking will be referred to as the "$E917$ (1996)" run period.

2.2.2 The Acceleration Process

The beam is accelerated in three stages. First, in the Tandem van de Graaf facility, a number of Au ions are boiled off of a source and accelerated in a static electric field to an energy of approximately 6 $A{\cdot}MeV$. The ions in the beams emerging from this stage are partially stripped of their electrons. These beams are then transferred to the AGS booster, which further accelerates the beams to approximately 1 A·GeV. The ions in the beams are then stripped to a charge state of 77. The last two electrons of the Au atom, $Z = 79$, are difficult to remove, and so no attempt is made to do so. The resulting beams are sent into the AGS, which then accelerates the beams to the final beam energy. Particles from the AGS are extracted down the beam lines in small packets called "spills", one of which lasts $\sim 1\ s$ and contains approximately $50 - 800K$ particles. These spills occur approximately every $4 - 6\ s$,

The exact numbers for the length, repetition rate, and quantity of beam in a given spill depend on the extraction parameters used, and were consciously varied for the different run periods of the experiment. In particular, for the $E917$ run the ratio of spill length to total time was maximized to improve the performance of the DAQ (see section 2.12). Also, due to the lowered rates of production at the lower energies, the experiment petitioned the safety board to increase the beam rate allowed for both sets of low-energy runs. Therefore, for portions of the run period that needed it, the rate of beam particles presented to the experiment was the highest in the string of experiments, at maximum approximately 800K/spill, as compared to approximately 100K/spill during the 1994 run period.

Name	P $(A{\cdot}GeV/c)$	E_{kin} $(A{\cdot}GeV)$	$\sqrt{s}\,(A{\cdot}GeV)$	Y_{NN}^{lab}	year
2 $A{\cdot}GeV$	2.783	2.004	2.683	0.9075	1995 (second)
4 $A{\cdot}GeV$	4.883	4.040	3.315	1.180	1995 (first)
6 $A{\cdot}GeV$	6.841	5.973	3.820	1.346	1996 (first)
8 $A{\cdot}GeV$	8.859	7.977	4.281	1.474	1996 (second)
10.8 $A{\cdot}GeV$	11.67	10.78	4.85	1.61	1994

Table 2.2: The energies of the beams used in this thesis. For comparison, the parameters for the 1994 high-energy beam are also listed. Y_{NN} denotes the rapidity of the center of mass between the target and the beam. $\sqrt{s}$ denotes the total energy per nucleon available in the center of mass. The "year" column denotes the data-taking period during which the beam was presented, along with its place in the sequence of two energies per year. All quantities are derived from the beam momentum measured in the AGS ring, using $m_{nucleon} = 0.931131\ GeV/c^2$.

2.2.3 A Note on Energies

The maximum momentum to which the AGS can accelerate a proton is 30 GeV/c. However, the accelerator only acts on the charge of the nucleus, and so for nuclei a penalty in momentum is payed. This loss is proportional to the Z/A of the nucleus accelerated. The result is a maximum beam momentum of 14.6 $A{\cdot}GeV/c$ (14.6 GeV per nucleon) for Si beams, and 11.7 $A{\cdot}GeV/c$ for Au beams. Due to various problems and changes in the accelerating systems, the beam momentum reached in 1992 for the Au beams was 11.45 $A{\cdot}GeV/c$, that in 1993 was 11.06 $A{\cdot}GeV/c$, and those in 1994-1996 were 11.7 $A{\cdot}GeV/c$.

The minimum energy is set by stability requirements. The transverse emittance of the beam that the AGS can present is set by the parameters of the various injection stages, and so is a fixed quantity regardless of the final energy of the beam. As the energy of the beam decreases, the relative effect of this emittance increases, with the end effect that the AGS cannot produce a useable beam of Au ions at momenta much below 2.7 $A{\cdot}GeV/c$. For special run periods, paid for by NASA and used in biological experiments, the AGS accelerated Fe beams of 1 $A{\cdot}GeV$. $E866$ and $E917$ did not take data from these runs.

Various parameters of the beams used in this thesis are listed in table 2.2.

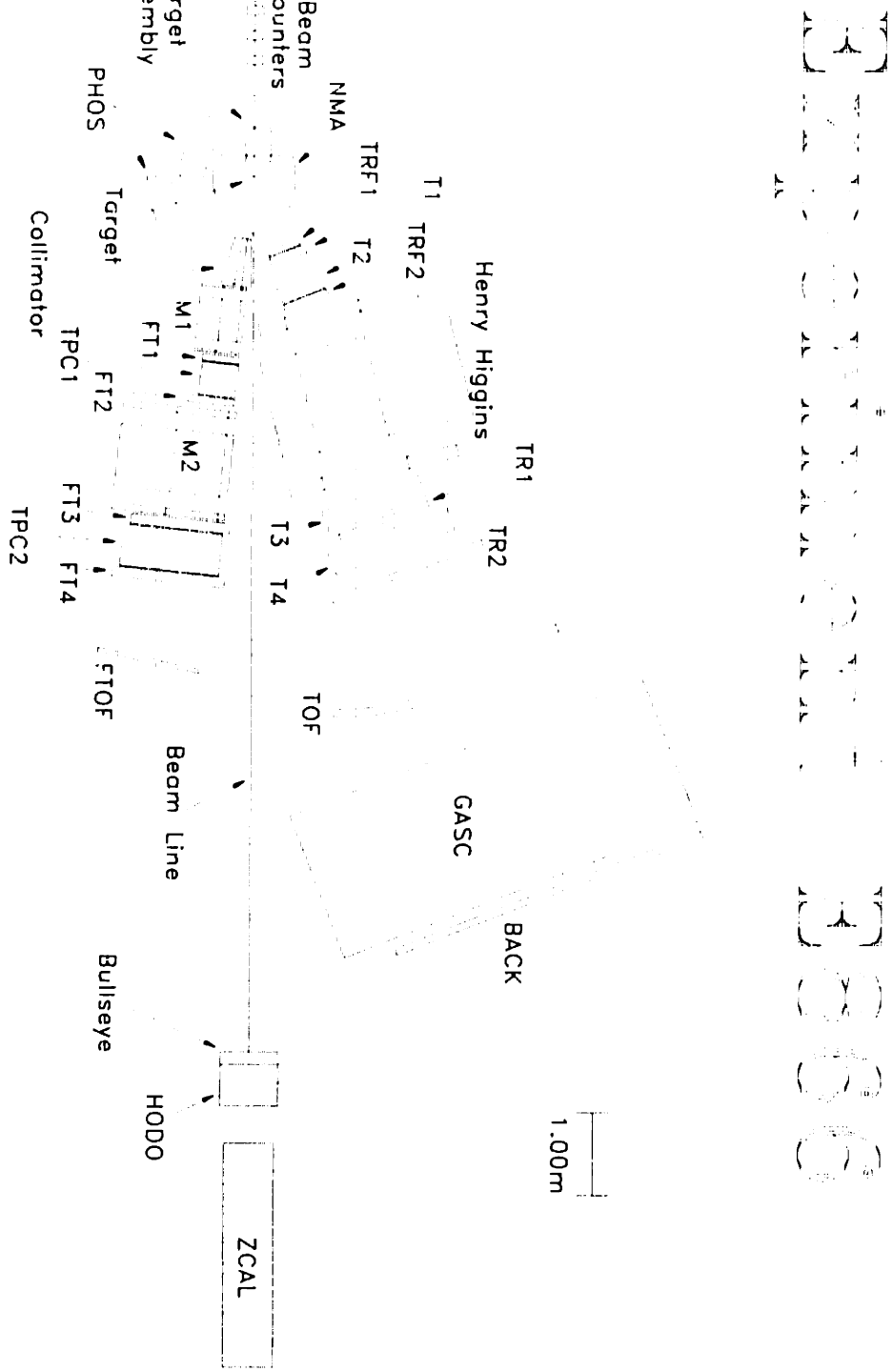

Figure 2-1: The *E*866 experiment. This is a plan view of the experiment, with all detector systems highlighted. *E*917 is very similar, with the addition of the two BVER stages upstream of the target and the replacement of TR1 with TR1MIT. The Henry Higgins Spectrometer is at 14°, and the Forward Spectrometer at 8°. The figure is from [Ahl97].

Section	z_{min} (in)	z_{max} (in)	$Wall\ Thickness$ (in)	ID_{min} (in)	ID_{max} (in)
1	0	4	0.080	1.94	1.94
2	4	21	0.020	1.94	1.94
3	21	37	0.040	1.94	1.94
4	37	60	0.040	1.94	2.2
5	60	80	0.050	2.2	Cont.
6	80	100	0.070	Cont.	Cont.
7	100	120	0.085	Cont.	5.94
8	120	125	0.100	5.94	5.94

Table 2.3: Dimensions of the first stage of the $E866$ beam pipe. Listed are the minimum and maximum edges along z_{BEAM}, the wall thickness, and the inner diameter (ID) at each of these edges. The notation "Cont." refers to the fact that the taper is continuous for sections 5-7. The scale is in inches, and the aspect ratio is 30:1 in $x_{beam} : z_{beam}$. The 1.18° line is also shown.

2.3 Experimental Layout

As noted before, the experiment sits on the B1 beam line. Figure 2-1 shows the basic layout of the detectors. Throughout the description of these detectors the terms "upstream" and "downstream" will be used. These terms refer to directions along the nominal beam axis, with "upstream" pointing towards the AGS ring from the target and "downstream" pointing from the AGS ring towards the target.

2.4 Control of the Beam

2.4.1 Beam Pipe

It is undesirable to allow the beam to pass through air on its way from the target to the ZCAL, which defines the farthest extent of the experiment. The probability of showers in air from the highly charged beam is large, which would have both health-related consequences and would produce an unacceptable level of background in the detectors. Therefore a pipe, held under vacuum, is used to contain the beam in the forward direction.

The beam pipe was redesigned for $E866$. It is designed both to hold a reasonable vacuum (~ 1 $mbar$) and to minimize the amount of material that a particle passes

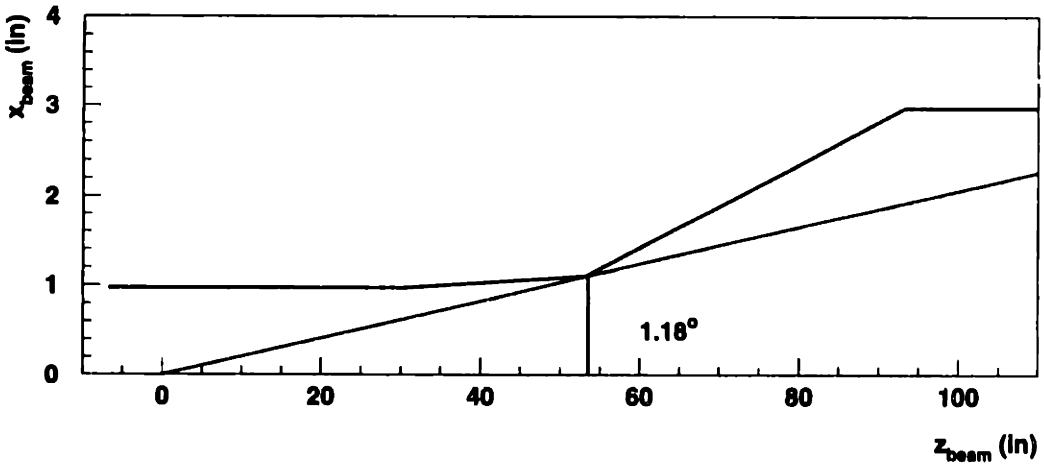

Figure 2-2: Profile of the beam pipe, with x_{spec} chosen as the transverse direction. Note that the scale is in inches, and that the aspect ratio is 30:1 in $x_{beam} : z_{beam}$. The 1.18° line is also shown.

through on its way to the detectors. It is made of four stages, only the first of which was new for $E866$.

The first stage consists of a carbon-fiber composite of density 1.54 gm/cm^3. It extends upstream from the nominal target position to the face of the target assembly, detailed in section 2.4.2. The wall thickness and diameter vary along the pipe (see table 2.3 for dimensions and figure 2-2 for the transverse profile).

The entire stage is continuous: that is to say, it is molded to this shape rather than formed from separate sections. The minimum opening angle from the nominal target position occurs at the start of the fifth section, and is approximately 1.18°.

The next three stages of the beam pipe consist of three aluminum cylinders of staggered diameter. Their dimensions are the same as for $E859$, and will not be described in this thesis.

The beam pipe was one of the limiting factors in the low-energy runs. As discussed in sections 2.6.3 and 2.6.4, the differing kinematics at the lower energies had some implications for the detectors at the far end of the experiment. These effects could have been removed by placing the detectors closer to the target. However, such

a change would have required a change in the beam pipe's design, which was not feasible.

The assembly attaching the exit window to the beam pipe is not circularly symmetric. This asymmetry is a leading explanation for effects seen the Hodoscope, described in section 2.6.4.

2.4.2 Target Assembly

The experiment has the capability to change targets rapidly. These targets sit in a vacuum, though, so it is a simple undertaking to design a mechanism to allow this transfer. In addition, the target assembly needs to be as spare as possible to decrease backgrounds from interactions between the beam and the assembly itself. Therefore for *E*866 a new target assembly was built.

The target assembly is described in detail in [Ahl97], so I will only briefly discuss it. A target is glued onto the end of one of six carbon-fiber cylinders, of radius 1.5 cm, length 33 cm, and wall thickness 0.024 in. These six tubes sit within an enclosing cylinder of diameter 30 cm and length 40 cm. The front edge of this cylinder sits 18 cm upstream of the nominal target position. The target-holding tubes are arranged as in a revolver, with one aligned along the nominal beam axis. The entire assembly can rotate so as to place a given tube along the beam axis. To place the target "in position", the tube that sits along the beam axis is extended by 18 cm so as to place the end of the tube at the nominal target position.

Only three of the tubes, or "target positions", are used in the data presented in this thesis. In two of these (positions "1" and "6"), the tube holds a *Au* target, of thickness 975 mg/cm^2 and 1961 mg/cm^2 respectively. The target at position 6 was new for the 1995 run period. Since the interaction rate measured by the Bull's Eye for these targets is approximately 1.5% and approximately 3%, respectively, these are also termed the "1.5%" and "3%" targets. The third position (position "2") holds no target, and so is termed the "MT" target.Data taken using this target position is extremely important in order to subtract the backgrounds from interactions between the *Au* beam and materials not in the target. Under this design, the only difference

between the configuration with a target in place and that with an MT target is the presence of the target material itself, and so data taken with the MT target in position gives a direct measurement of these backgrounds.

In addition, for $E917$ two special targets (the 3-HOLE and CROSS targets) were put into place in an attempt to calibrate the BVER's geometry. These were less than successful, and so will not be included in the discussion.

2.4.3 Shielding Blocks

A set of concrete blocks sit between the beam pipe and the spectrometer. These serve to shield the spectrometer from background produced by showering, both in the imperfect vacuum inside the beam pipe and in the beam pipe material itself. In addition, in $E866$ there is showering from the Forward Spectrometer, placed on the other side of the beam pipe from the Henry Higgins spectrometer. Because of this additional showering, the Forward Spectrometer was placed at its most backward setting (24°) for the 2 and 4 $A{\cdot}GeV$ run period presented in this thesis.

The shielding blocks, combined with the redesigned beam pipe, limit the range in the most forward direction to which the Henry Higgins can rotate to 14°. This is in contrast to the 5° setting available in $E859$.

2.5 Devices for the Measurement of the Beam

Before one can measure the effect of an interaction of a Au beam particle with a Au particle in the target, one must know about the Au beam itself. Hence experiments $E802$ through $E917$ have had a set of detectors placed upstream of the target (towards the AGS ring from the target) to measure various properties of the beam. There are four detector stations upstream of the target for this purpose. The specific detectors planced into the stations have changed considerably over the 10 years that the different experiments have spanned. Rather than repeat 10 years of history, I will only describe the detector systems that were actually in place for the data on which this thesis is based.

2.5.1 BTOT

Detector Description

The BTOT serves three related purposes in the experiment. Given the relatively low rates of beam particles, at most approximately 800K beam particles per spill, it is possible to detect each beam particle individually. The BTOT is used to do this. In addition, the BTOT provides a quality check on the beam particles that it observes, by measuring the charge of the particle, and provides a start time to the rest of the experiment, by measuring the time at which the beam particle passes.

The BTOT is a piece of quartz, 2 in high x 3 in wide x 200 μm thick. It is placed 2 m upstream (towards the AGS ring) of the target, with its narrow dimension oriented parallel to the direction of the incoming beam, and its longest dimension oriented horizontally. Two phototubes are placed horizontally on the ends of the quartz, coupled to the quartz by "cookies" of transparent gel, to record the Čerenkov signal[1] of a passing beam particle.

Detector Application

The signals from the BTOT's phototubes are used in multiple places throughout the experiment. First, the signals from the two tubes are discriminated and passed into the LVL0 trigger logic, described in section 2.11.1, where a coincidence between the two signals and those from other detectors is formed. In this discrimination, a lower bound is placed on the size of the signal from the BTOT tubes. The threshold is placed at approximately 3-4 σ below the main peak of the beam.

The difference in time between these discriminated signals and the start time produced by the LVL0 logic is recorded into the data stream. In principle, since the start time is determined by a coincidence of the two BTOT signals, it should be an exact copy (perhaps with some delay) of one of the BTOT signals. The above time differences are recorded to check that this is true, and to measure the level of jitter

[1]Since a large portion of our detectors use Čerenkov radiation as their basic mechanism, I refer the reader at this point to [Jac75],ceren.

that is produced by the LVL0 trigger system, The distribution for one of the tubes is always seen to be a sharp spike to within the 50 *ps* counting resolution of the TDC, except in cases in which two beam particles pass within the timing gates of the experiment.

More importantly, a copy of these discriminated signals is sent into the TOF electronics. The TOF electronics are triggered on the LVL1 trigger rather than a LVL0 trigger. The additional overhead of the LVL1 trigger introduces a significant jitter, on the order of 100 *ps*, which would increase the width of the measured TOF distributions to an unacceptable level were there no way to remove it. However, by measuring the start time under the same trigger conditions as the TOF time, the effect of this jitter can to a large extent be removed. The integrated pulse height of each signal is also recorded for later use in offline charge cuts.

Detector Effects

For portions of the *E*917 run period, the duplicates of the signals read out through the TOF electronics were not recorded correctly. These portions of the run period have been removed from the analysis.

The charge resolution of the BTOT varies somewhat across the four beam energies, as described in section 5.6.2, but is never greater than 4%. The timing resolution is difficult to measure, since the start time, against which one measures the time of the signal, is intrinsically tied to the time of the signal from one of the tubes. Lab tests showed the BTOT to have approximately 40-60 *ps* resolution.

2.5.2 The Hole Counter

The aptly named Hole Counter (HOLE) is a detector consisting of a 2 in high x 3 in wide x 0.125 in deep piece of scintillator, with a circular hole 1 cm in diameter cut from its center. The center of this hole is placed along the nominal beam axis. As with the BTOT, the long dimension of the scintillator is oriented horizontally transverse the beam axis. The HOLE is located 50 cm downstream (towards the target from

the AGS ring) of the BTOT. As with the BTOT, it is read out by phototubes placed horizontally on either side.

A signal from the HOLE indicates the presence of beam halo, either from particles associated with the beam or from a bad beam tune. Such a halo can have undesirable effects on the data. Therefore, online an upper threshold is placed on the sum of the signals from the two phototubes in order to cut out such events. The signal from each tube is read separately into the data stream to allow for tighter offline cuts. It is impossible to calibrate the signals from this detector, since there is no reference point on which to calibrate. Accordingly, it is impossible to measure a resolution.

2.5.3 BVER

Detector Description

The BVER (Beam VERtexing system) is a new detector system installed for *E*917. It was designed and built by a collaboration of members from Argonne National Laboratory (ANL) and the University of Illinois at Chicago (UIC), and represented their initial contribution to the experiment. The purpose of this detector system is to track of the trajectory of the incoming beam. It was installed in the two detector stations left empty for experiment *E*866.

The BVER consists of four planes of square scintillating optical fibers, each of which is 200 μm on a side. One end of each fiber is fed to an array of stations placed above a multi-anode phototube. There is one such phototube per fiber plane. The four planes are arranged into two crossed pairs, one along the vertical and one along the horizontal. One such crossed pair is placed 1.72 m upstream of the target, while the other sits at 5.84 m.

Each phototube has a square grid of sensitive elements on its front face, and so in principle can measure the signals from individual fibers. However, each element is not read out separately. Instead, along each edge of the grid the signal from a line of elements is summed and read out as a whole. Since the energy deposited by a true beam particle is many orders of magnitude higher than that from other particles

that might pass through the detector, such as δ electrons moving with the beam, this arrangement allows for single-fiber identification of the beam particle. This is done by crossing the two sets of signals, and finding the position of the maximum.

For further details, see [B+98].

Detector Effects

The energy deposition from a *Au* beam in a scintillating fiber is rather large. Therefore it was realized at the design stage of the detector that an allowance would need to be made for radiation damage to the fibers. Each plane is accordingly made many times longer than the length of the crossing region, and the planes initially placed such that the crossing region occurs at the end of the fibers farthest from the readout. Once the signals from the plane have decreased, such that the loss in efficiency of a plane reaches approximately 7%, the fiber plane is moved along the long direction of the fibers so that the crossing region passes through undamaged portions of the fiber. Under this arrangement, the majority of the light will pass through undamaged regions of the fiber on its trip to the phototube. There were approximately 10 such separate positions along a given plane, although the differing shape of the beam profile across the planes led this to be more or less for a given plane. The fibers needed to be moved approximately twice per week. Given that there were 12 weeks to the run, each plane was completely replaced once during the *E*917 run period.

When the BVER was first put into place, it was found that the divergence of the beam in the vertical direction was larger (approximately 10 mrad) than had been expected. This had two consequences: a small portion of the beam (approximately 3-5%, depending on the beam tune) missed the upstream vertical plane, and the focus of the beam on the downstream vertical plane was tighter than had been expected. This last effect caused rapid radiation damage in the downstream plane, since the beam essentially always hit a single fiber. For this reason the beam in *E*917 was defocused slightly, with the effect that the size of the beam spot on the target increased in the vertical direction, to approximately 0.25 mm. This width remains small compared to the $\sim$ 2 mm projection resolution of the tracking in the spectrometer for high

momentum particles, but is large compared to the projection resolution of the BVER.

One further consequence from the addition of the BVER is that, in $E917$, the background from interactions not occurring in the target increased dramatically. The total thickness of the BVER assembly is such that the expected probability of interaction of the Au beam in these detectors was approximately 1.5%. This is approximately equal to the sum total of the backgrounds that existed for $E866$. Therefore, the BVER caused these backgrounds to increase by a factor of 2. The final background rate, approximately 3%, is on the same order as the interaction rate in the target. However, the material of the BVER is primarily plastic, and so has a much lower A than that of the Au target. As explained in section 5.6, this difference is used in numerous ways to account for this background.

The overall efficiency of the detector system was essentially 100% for the majority of the run, with local decreases to approximately 90% just before a plane move. These numbers ignore the approximately 5% effect from particles missing the upstream vertical plane. This inefficiency is not a problem for normalization. The efficiency of the detector is not correlated with the occurrence of an interaction, so one can cut events in which the BVER does not register a hit on all planes from both the numerator and denominator without affecting the results. The position resolution obtained was essentially that of a single-fiber.

2.6 Devices for Global Event Characterization

The experiment has a set of devices for "global" event characterization. These measure gross properties of the collisions on an event by event basis, rather than discussed properties on an event-averaged basis.

2.6.1 Bull's Eye

Detector Description

The Bull's Eye detector provides the information necessary to state that an interaction has occured in the target. The physical process that it uses to provide this information is the charge dependence of Čerenkov radiation, applied to the fragments of the beam that continue in the forward direction.

The detector consists of a circular piece of radiation-hard quartz with thickness 300 μm and diameter 20 cm. The quartz was replaced at the beginning of the 1995 data run, due to observed radiation damage in the lower-quality sample used in 1994. No need was seen to replace it before the $E917$ run period. The quartz is located at zero degrees, in direct line of sight of the beam, at a position 10.6 m downstream of the target. Hence it subtends a cone of angular width 9.4 *mrad.* The active element sits at the front of an octagonal enclosure of radius 66 cm and depth along the beam direction of 10 cm. This enclosure is light-tight and lined with aluminized mylar to reflect the light output back into the enclosure. Phototubes sit at openings on the eight sides of the octagon, and hence are coupled to the radiator through the intermediary of the enclosure. The phototubes are inclined towards the target at an angle of 15° with respect to the plane perpendicular to the line of the beam. The phototubes are surrounded by cylinders of μ-metal to provide shielding against stray magnetic fields. The entire apparatus is enclosed in a light-tight box. Dry nitrogen is fed through this box to reduce atmospheric effects.

The signals from the eight phototubes are gain-matched on the amplitude of the beam peak. These signals are then summed together and passed to the trigger for further processing. The summed signal is also fed into the data stream, along with the individual signals from the tubes, for offline analysis.

For further details, see [DMC98].

Detector Application

Since Čerenkov radiation scales as the Z^2 of the particle producing the radiation, the Bull's Eye measures $\sum Z^2$ of the forward-going fragments. This statement assumes that there are no saturation effects, either in the light collection efficiency or in the signal produced by the phototube. Such effects decrease the power-law coefficient from 2 to some number α. Such a sum is very sensitive to any fragmentation of the beam nucleus. To take an extreme and unlikely example, if the original Au nucleus were to fragment into 2 equally charged nuclei, and these nuclei were both to pass within the acceptance of the Bull's Eye, the signal would decrease by a factor of 2.

In a real interaction between Au nuclei, the probability of a less extreme version of such fragmentation, or of the transfer of charge to angles outside of the acceptance of the Bull's Eye, is quite large. Hence we use a decrease in the total signal seen in the Bull's Eye as a signal to decide whether an interaction has occurred. With the cuts used in the offline analysis, as discussed in section 5.6.6, this process has a cross-section of approximately 5.4 mb, or approximately 80% of the total interaction cross-section to which the Bull's Eye is potentially sensitive.

Since the probability of the Au beam interacting in the target is only approximately 4%, it is not possible to allow the trigger signal from all beam particles through to the later trigger logic. Such a high rate of triggers would swamp the apparatus. As described in section 2.11.1, another trigger is created placing a threshold on the summed signal from the Bull's Eye. The majority of events are selected from this sample of triggers. Therefore, the performance of the Bull's Eye is critical to the quality of the data that is recorded.

Detector Effects

Unfortunately, there were three unforeseen effects on the signals from the Bull's Eye. The μ-metal shields cannot shield against magnetic fields of all orientations. Since the phototubes cover eight separate orientations transverse to the beam line, any stray magnetic fields can affect these phototubes in different ways. During the low-energy

run period such fields existed. Our neighboring (and competing) experiment E895 used the MPS magnet, which is a C-shaped magnet with a large hole in the iron on the side towards our experiment. Stray fields on the order of a few gauss from this magnet produced a noticeable and tube-dependent effect on the output signal from the phototubes. The signal from the tubes showed a clear difference between periods when the MPS magnet was turned on and when the MPS magnet was turned off. Because of this effect, during both the 1995 and 1996 run periods we placed the trigger threshold at an artificially high level, increasing the rate of events with amplitude less than the threshold. This removed the dependence of our data on the run schedule of our competitors, but came at the cost of creating a less restrictive trigger.

There are wide variations in the pedestals of the ADC readout of the detector. This effect is attributed to 60 Hz pickup noise in the signal lines that run from the detector. In order to correct for this effect, a second set of signal lines was run, parallel to the first. The signal from this second set of lines was delayed by 200 ns, so that the actual signal from the detector did not fall within the ADC gate. This delayed readout, which in principle gives a measure of the noise level event by event, was recorded into the data stream, and was subtracted from the recorded signal in the offline analysis. The same method was used in 1996, but during that run the effect of the noise was not as pronounced.

There are events in which one of the eight tubes produces an anomalously large signal. This is thought to be due to a direct hit by a particle onto the face of the phototube. Such a hit would naturally give a large signal, since the source of the signal from such a hit would be far closer to the phototube's avalanche chain than the quartz radiator. In the offline analysis, such signals were subtracted from the event by event sum.

These three effects are corrected in the offline analysis. However, they could not be corrected in the online trigger, and so affected the events that were recorded. The most serious of these is the third effect, since it can cause large increases in the summed signal, and is in principle correlated with the multiplicity at angles away

from the beamline. Therefore it cannot be completely removed by an offline cut on the calibrated Bull's Eye signal.

The resolution of the detector before offline calibrations is approximately 3% of the signal, as measured by the width of the beam peak. After the offline calibrations the resolution on the summed signal is approximately 1.5%, with that of the direct sum of the signals (the "HARDSUM") slightly better than that of the sum of the ADC readouts of the individual tubes (the "SOFTSUM"). Given that the total dynamic range of the signal in the Bull's Eye is, ignoring saturation effects, $1 : 79^2$, or $1 : 6241$, this resolution does not allow us to detect individual charge changes.

2.6.2 NMA

Detector Description

In 1994 a New Multiplicity Array (NMA) was installed for $E866$. The purpose of this detector was to measure a large portion of the total number of produced particles on an event by event basis, and so characterize the violence of the collisions.

The detector consists of 346 Lucite modules coupled to phototubes for readout. The physical process used for detection is Čerenkov radiation by particles passing through the Lucite modules. The signal from the radiation is recorded in an ADC, from which the particle count is determined. This produces the number of particles capable of producing Čerenkov radiation that passed through the module. The resolution of each module is sufficient to resolve the single particle peak, but for multiple hits on a given module more complicated methods must be used, as detailed in section 3.2.3.

Each module consists of a 5 cm thick piece of UVT Lucite, transparent to ultraviolet radiation, with an index of refraction $n = 1.5$. The module is wrapped in white Teflon tape for reflection, followed by a layer of black electrical tape to make it light-tight. The wrapping produces an insensitive region of 0.050 in between modules. A small hole is drilled into the back of each module to which an LED is attached for testing purposes.

Phototubes of two types are mounted with optical glue directly onto the back face of each module. The modules in the forward 4 "rings", where "ring" is defined below, use Hamamatsu Hybrid Assembly H3165-01, which consists of of shrink-wrapped package of an R647-01 tube, a base, and a μ-magnetic shield. This assembly has a diameter of 14.3 mm. The modules in the backward rings use Hamamatsu tube R268, with a base and shielding assembly designed specifically for this detector. This phototube has a diameter of 28 mm. Given that neither phototube completely covers the back face of a module, the design depends on reflection at the back face for light collection.

Lead sheets of thickness 1.7 mm are attached to the front of each module. The thickness was chosen to produce a probability of 1/4 for conversion of photons into an e^+ e^- pair. The decay $\pi^0 \rightarrow 2\ \gamma$ produces two photons, each of which can be converted into two charged particles in the conversion processs $\gamma \rightarrow e^+\ e^-$. Hence, on average, for every π^0 produced in the collision one charged particle will be detected in the NMA. The preceding statement ignores the conversion of photons in the target, the probability of which has an angular dependence due to the target's severely foreshortened shape.

The modules are machined to cover rectangular regions in (η, ϕ), or equivalently in (θ, ϕ). Hence they have a trapezoidal shape in the direction along ϕ, with straight edges that are not parallel. In the direction along θ, the edges are curved. The front and back faces along r are flat.

There are 14 "rings" of common η, with varying acceptance in ϕ across the rings. The distance between a module and the target is common within a ring, but is not the same across rings. The choice of ϕ acceptance for each ring was determined by the necessity that the other detectors in the experiment have an unobstructed view of the target. Table 2.4 details the coverage of the various rings. Note that the detector is symmetric about the xz plane, but not about the yz plane, with larger gaps on the side away from the Henry Higgins spectrometer.

Due to financial limitations, the high voltage placed on every phototube is not controllable tube by tube. Instead, the high voltage lines are split and fed to two

Ring	η_{min}	η_{max}	$\cos\theta_{min}$	$\cos\theta_{max}$	$\Delta(\cos\theta)$	ϕ_{min}^{top}	ϕ_{max}^{top}	$\Delta\phi(rad)$	$\Delta\Omega(sr)$
1	2.4	2.8	0.984	0.993	0.009	70	130	2.09	0.019
2	2.1	2.4	0.970	0.984	0.013	52.5	142.5	3.14	0.042
3	1.9	2.1	0.952	0.970	0.019	36	156	4.19	0.078
4	1.6	1.9	0.922	0.952	0.030	30	160	4.54	0.136
5	1.4	1.6	0.885	0.922	0.036	30	160	4.54	0.165
6	1.2	1.4	0.834	0.885	0.052	20	150	4.54	0.235
7	1.0	1.2	0.762	0.834	0.072	20	150	4.54	0.327
8	0.8	1.0	0.664	0.762	0.098	10	150	4.89	0.477
9	0.6	0.8	0.537	0.664	0.127	10	150	4.89	0.621
10	0.4	0.6	0.380	0.537	0.157	10	150	4.89	0.768
11	0.2	0.4	0.197	0.380	0.183	0	150	5.24	0.956
12	0.0	0.2	0.000	0.197	0.197	0	150	5.24	1.033
13	-0.2	0.0	-0.197	0.000	0.197	0	150	5.24	1.033
14	-0.4	-0.2	-0.380	-0.197	0.183	0	150	5.24	0.956
								Sum	6.85
								per 4π	0.54

Table 2.4: The acceptance of the New Multiplicity array in η and ϕ, divided into the 14 rings as described in the text of section 2.6.2. The detector is symmetric about the xz plane, so the ϕ range given is for the top half only. Also calculated is the total solid angle subtended by the array.

phototubes at once. This means that the finest level of control possible over the gains of the phototubes is at a granularity of two. It is therefore not possible to create an online trigger based on the NMA, since it is not possible to match the gains of the tubes at the required precision. Also, the smaller forward phototubes have a strongly nonlinear response, which would make their use in a trigger problematic.

Detector Application

As mentioned above, there exists a β threshold below which a module will not register a signal. A lower limit to this threshold is given by $\beta = 1/n$, where n is the index of refraction of the material. In the case of an NMA module, this lower limit is $\beta = 0.67$. However, near the threshold for light production the strength of the signal grows markedly with the β of the particle. The signal strength has additional dependences on the wavelength of the light emitted and on the angle with respect to the emitting particle, and is proportional to the total length of sensitive material

through which the particle passes. The sum total of these effects, combined with the specific configuration of the NMA modules, causes the threshold for an observable signal to move up to $\beta \approx 0.8$.[2]

Even with a β threshold of 0.8, there is still a significant contamination of protons in the quantity measured by the NMA. Fast protons from these collisions will give a signal, and will accordingly be included into the multiplicity sum. Estimates during the design phase of the detector indicated that, at the highest energy of the AGS, at $\theta = 15^{\circ}$ the modules would be sensitive to 95% of the protons from these collisions, while at $\theta = 45^{\circ}$ only about 50% of the protons would produce a detectable signal.[3] These numbers will obviously change as the beam energy decreases, and depend on the distributions of particles that are produced in the collisions.

The proton contamination is therefore not removed to quote a total pion multiplicity. Instead, an "NMA multiplicity", $Mult_{NMA}$, is quoted, which corresponds directly to the quantity measured. Related to this, the quantity quoted is not corrected for acceptance, as discussed in section 5.6.7.

Detector Effects

For unknown reasons, the light output of the modules has decreased over time. This led to increases in the high voltage applied to the phototubes in two steps, once at the start of the 1995 run period and once before the $E917$ run period in 1996. Coupled with the lower occupancy at the lower energies, this effect led to a revised calibration procedure for the 1995 and 1996 data runs, as described in section 3.2.3.

2.6.3 ZCAL

Detector Description

The zero-degree calorimeter (ZCAL) measures the energy in a small cone at forward angles, and therefore measures the amount of energy that was not scattered from the

[2]This number results from a full Monte Carlo study at the design stage of the detector.

[3]These numbers come from particle distributions output by ARC, a cascade model, not from those measured.

initial direction of the beam. This is an arguably more direct measurement of the impact parameter between the beam and target nuclei than the measurement made by the NMA. The ZCAL was modeled after the hadronic calorimeter of experiment WA80 at CERN, with iron substituted for uranium as the passive element.

The calorimeter consists of 138 layers of scintillator, 60 cm wide x 60 cm high x 0.4 mm thick, alternating with 138 layers of iron, 1 cm thick and of the same transverse dimension. The assembly is centered on the beam line, with the front face at 11.7 m from the target. The readout is segmented among 16 phototubes. These are arranged to record the signals from the front and back halves separately, and within these halves to read separately along the four sides of the square. Therefore, for each front-to-back half of the calorimeter, two phototubes read from a given side.

The calorimeter has been in place since $E802$. However, due to severe radiation damage to the scintillating elements it has been rebuilt twice, once between the 1992 and 1993 run periods of $E866$ and once between the 1995 run period of $E866$ and the 1996 run period of $E917$. Over the span of the $E917$ running period the resolution worsened by a factor of approximately 2 due to radiation damage.

For further details, I refer the reader to [B+89].

Detector Effects

The ZCAL is not used for the data presented in this thesis, due to some effects as the beam energy decreases.

As the beam energy decreases, the kinematics "open up" in the forward direction. To take an illustrative example, if one considers a nucleon with a p_t kick on the order of a Fermi momentum, say 250 MeV/c, the angle that this nucleon will make with respect to the beam axis is approximately 1.2° at the full kinetic beam energy of 10.8 $A{\cdot}GeV$ but approximately 5.2° at the lowest kinetic beam energy of 2 A·GeV. Note that the minimum angular width of the beam pipe is also approximately 1.2°. Given that the extreme corners of the ZCAL sit at 1.5°, and given that the resolution of the ZCAL will suffer if the hadronic shower from the incoming beam particle is not fully contained, one would expect the resolution to suffer as the energy is lowered.

As the energy of the incoming beam particle decreases, the longitudinal extent of the shower will decrease, leading to a change in the balance between the energy deposited in the back and front of the calorimeter. This affects the resolution in two ways. First, in order to maximize the quality of the resolution, the measured energy in the ZCAL is formed from a weighted sum of the energies measured in the front and back. If the ratio of energy deposition between the front and back half of the detector changes, the weighting parameters can possibly change. There are difficulties in determining the parameters for Au beams. Second, the radiation damage in the front half of the ZCAL is greater than that in the back half of the ZCAL, and the level of this difference becomes larger as the overall level of radiation damage increases. Therefore if a larger fraction of the total energy is deposited in the front half, the resolution will suffer accordingly.

The 2 and 4 $A{\cdot}GeV$ run periods came at the end of the 1995 $E866$ run period, during which the radiation damage to the detector was at the highest level over all of the $E802$ run periods. At the end of the 10.8 $A{\cdot}GeV$ run period that immediately preceded the 4 $A{\cdot}GeV$ run period, the resolution was worse by a factor of approximately 3 than in the 1993 run period, before which the detector had been rebuilt.

The measured energy distributions in the 2 and 4 $A{\cdot}GeV$ data show clearly the net effect on the ZCAL response. The beam peak at 2 $A{\cdot}GeV$ reaches zero energy at the 2σ level, and the response at 4 $A{\cdot}GeV$ is not much better. Based on this experience, during the 6 $A{\cdot}GeV$ run the rebuilt ZCAL was rolled out of the beam line and replaced by a large concrete block. While the ZCAL was in place for the 8 $A{\cdot}GeV$ data, and shows a relatively good response, it will not be used in this analysis for reasons of consistency.

2.6.4 Hodoscope

Detector Description

The hodoscope is designed to measure the centroid of the charge distribution of the beam fragments, and so measure the reaction plane through the deflection of the

beam in the forward direction.

In $E866$, the hodoscope consisted of two planes of 39 scintillator slats, each 40 cm high x 1 cm wide x 1 cm deep. The slats in the plane closest to the target are oriented with the long side along the vertical, while those of the second plane are oriented with the long side along the horizontal. Each plane is centered along the beam axis. This placement causes some number of slats in the center of the array to be directly hit by the beam. This leads to a host of problems, many of which are resolved in the $E917$ analysis. The detector is placed directly behind the Bull's Eye. Each slat has a phototube on both ends for readout. The signal from each of these tubes passes into both an ADC, for charge measurement, and a TDC, for time measurement.

The hodoscope was rebuilt for $E917$. The middle four slats in each plane were replaced due to radiation damage, and all slats were rewrapped to improve their light tightness. In addition, some of the phototubes, which showed a poor coupling, were reattached to their associated slats. The rewrapping of the slats led to the introduction of an extra gap between them, which in turn led to a decrease in the number of slats per plane by 1, to a total of 38.

Detector Effects

For the same kinematic reasons that affect the ZCAL, the hodoscope is not used in this analysis for 2 and 4 A·GeV. The radiation damage of the middle 4 slats is also quite severe during these runs, and this, coupled with the high beam rate, makes its analysis problematic. The hodoscope is in principle usable at 8 A·GeV, but, as with the ZCAL, for consistency it is not used in this thesis.

2.7 The Phoswich Array

The Phoswich Array (PHOS) is of interest to this thesis mainly due to the rather stringent constraints that it placed on the design of the NMA. The PHOS consists of an array of 100 modules of the usual phoswich type, consisting of a thin layer of fast scintillator, followed by a thick layer of slow scintillater, followed by a phototube

for readout of the combined signal. The modules are reminiscent of a phototube sandwich, hence the name "pho-s-wich". The array's coverage in θ extends from 37.5° to 147°. In terms of vertical coverage, the array is divided into two sections. The modules of the first, with $\theta < 90°$, are placed 100 cm from the target and cover ±10 cm in the vertical direction. The modules of the second, with $\theta > 90°$, are placed 60.5 cm from the target and cover ±7 cm in the vertical direction. This coverage, combined with the need for the PHOS to have an unobstructed view of the target, determined the size of a large portion of the gaps in the NMA. The array is on the opposite side of the beam line from the Henry Higgins spectrometer, so the gaps in the NMA coverage are larger on the side away from the spectrometer.

The array is able to separately identify the momentum and angle of protons, deuterons, and nuclei of higher mass in the region of very backward rapidity. The PHOS was not active during the 2 and 4 $A \cdot GeV$ runs, but was resurrected for the $E917$ run. Data from the PHOS is not used in this thesis. For further discussion, see [A+98b].

2.8 The Forward Spectrometer

The largest upgrade between experiments $E859$ and $E866$ came in the commision-ing of the Forward Spectrometer. As the name suggests, this detector system is a spectrometer meant to track and identify particals in the very forward region. It can rotate to cover a range of angles in the forward direction, from $\theta = 6 - 24°$. It has a smaller aperture than the Henry Higgins spectrometer, has TPC's in addition to drift chambers for improved track recognition, and has an additional sweeper mag-net between the first tracking station and the target. Hence it is better equipped to cope with the extreme particle densities at small angles than the Henry Higgins spectrometer.

While the Forward Spectrometer took a large quantity of data at 2 and 4 A·GeV, it was removed before the $E917$ run. Therefore I will not use data from it in this thesis, and refer the reader to numerous theses and papers that describe the detector,

and its analysis, in more detail [Shi94, Sak97, A+99a].

2.9 The Henry Higgins Spectrometer

The "Henry Higgins" spectrometer has been in place since experiment $E802$[A+90]. As with the global detectors, it has undergone some upgrades over time. By experiment $E866$ nothing remained of the original front half of the apparatus, and the back half of the apparatus had some significant modifications. Therefore, as with the global detectors, only the detectors that were in place for the data presented in this thesis will be described.

2.9.1 Henry Higgins Magnet

The magnet comes from the Cambridge Electron Accelerator Facility, and is dubbed the "Henry Higgins" magnet after the character of that name. $E802$ found this name compelling, and so the name was extended to describe the entire spectrometer.

The magnet is a dipole, of maximum field strength 1 T. For the data presented in this thesis, it was run solely at a field strength of 2 kG. It is mounted 2.84 m from the target on a platform that can rotate in the xz plane about the nominal target position. The detectors of the spectrometer are also mounted on this platform. If we use as a reference point the inner edge of the magnet's aperture on the side towards the beam, the platform can rotate from 14° to 44°.

The magnet is angled by 7.4° in the xz plane with respect to the axis of this platform, and therefore with respect to the chambers that surround it. It has a rectangular aperture 84 cm wide x 42 cm high x 240 cm deep.

The dominant component of the field points in the vertical direction. Using the convention standard at the AGS, at the "A" polarity this field points down in the negative y direction, and so bends positive particles away from the beam line. The opposite polarity is termed the "B" polarity. When a signed field quantity is used, the "A" polarity corresponds to a negative field.

The magnet is surrounded by field clamps to create a sharp cutoff in the field. Section 4.6 describes the level of success these clamps attain.

2.9.2 Time of Flight Wall

The Time of Flight (TOF) wall is designed to measure just that: the time of flight that a particle takes in traveling from the target to the wall. This time is used for particle identification purposes, since the velocity of a particle is uniquely determined by its mass and momentum. Hence a knowledge of the distance of flight and momentum of the particle (determined by the tracking) and the time of flight (determined by the TOF wall) allows one to uniquely identify the particle.

Detector Description

The Time of Flight (TOF) wall, consists of a set of 78 cm x 1.6 cm x 1.6 cm plastic scintillator slats, 160 in all, mounted with the long side along the vertical in an approximate arc roughly 660 cm from the target. The arc has a radius of curvature of 2.4 m, and so is designed to have as be centered at the midpoint of the magnet. The slats are read out by phototubes mounted onto light guides that protrude at an angle from the top and bottom faces of the slats. The slats are arranged into ten straight-line panels of 16 slats each. These panels are mounted at an angle to one another in the xz plane, the combined turn of which generates the arc. Figure 2.9.2 shows this geometry. Due to space restrictions at the boundary between the panels, in each panel the slat furthest from the beam line is twice as wide as the others.

The signal from each tube is read out in three places. One set of these signals is discriminated on the floor, rediscriminated after traveling to the recording apparatus, and fed into a high-resolution TDC, which has a channel by channel clock of approximately 50 *ps*. Note that no facility exists in the hardware to measure this clock, with implications to be discussed later. The discriminated signal is also sent into a high-speed FERET system for use in the LVL2 trigger. This system also has a clock of 50 *ps*. In addition, a set of the signals is sent into an ADC for charge measurement.

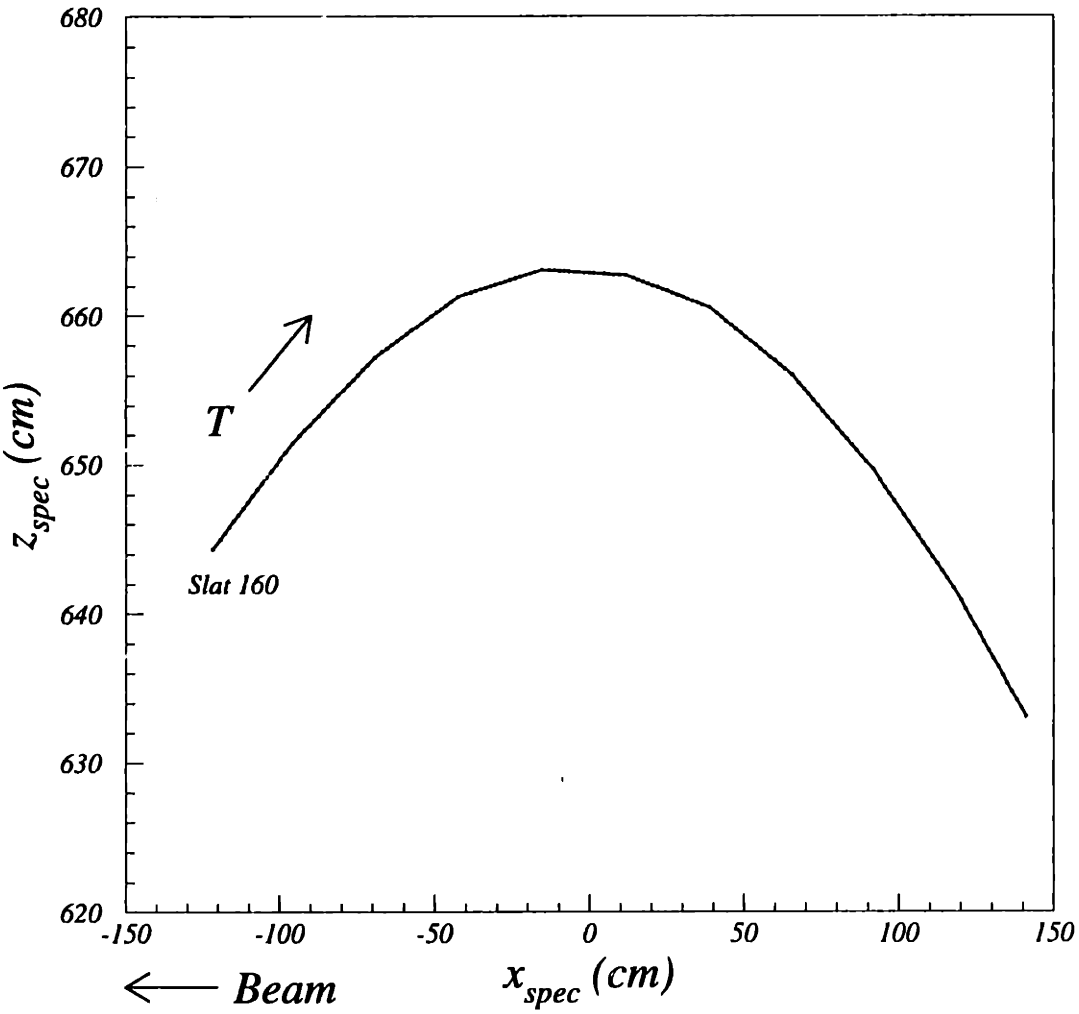

Figure 2-3: TOF wall configuration. The position of the TOF wall in the SPEC coordinate system. Each point represents the center of a slat. Note that the aspect ratio is 5:1 in x_{spec} : z_{spec}. The position of the points is after geometry adjustment.

The numbering scheme of the TOF slats is opposite to that of the chambers, with high-numbered slats closest to the beam line (at smallest x_{spec}). That the lowest-numbered panel (containing slats 1-16) was not active for $E866$ or $E917$.

The TOF wall was reconditioned before the $E917$ run, with the coupling between the phototubes and slats checked, and some tubes replaced with spares from the lowest panel.

Detector Effects

The resolution of the TOF wall has degraded over time. For the data presented in this thesis, it is no worse than 130 ps. The measurement of the times at the top and bottom of the slat allows one to reconstruct the y position of the hit along the slat. The resolution of this determination is approximately 1.5 cm.

For some unknown reason, the timing resolution of the TOF wall is significantly better during the 6 and 8 $A{\cdot}GeV$ run period than during the high-energy run period that immediately followed.

The readout chain is quite fragile, and this leads to degraded signals from some of the slats. Given the importance of the TOF wall to the analysis, these slats are cut from the analysis, as described in section 5.4.

2.9.3 The Gas Čerenkov Complex

The Gas Čerenkov Complex (GASC) is designed to extend the particle identification capabilities of the spectrometer by using the presence of Čerenkov radiation to place a threshold on the speed of the particle.

It consists of 4 rows of 10 cells filled with Freon-12. These are equipped with a spherical mirror and phototube to gather the light produced by Čerenkov radiation in the Freon-12. The assembly of cells is surrounded by an aluminum tank, both to keep the gas at 3 atm pressure and to isolate the cells from external influences. The cells come in two sizes: those in the top and bottom rows are 23 cm x 28 cm x 72 cm deep, while those in the middle two rows are 23 cm x 28 cm x 101 cm deep.

The GASC was turned off for the 1995 2 and 4 $A{\cdot}GeV$ run period, although it was turned back on for the $E917$ run. It is not used in this analysis.

2.9.4 The Back Counter

The Back Counter (BACK) is designed to be used in tandem with the GASC to remove a number of undesirable effects. Because of the length of the GASC and the thickness of its aluminum walls, there is a significant probability that a particle will not pass completely through the radiating elements. The signal that the GASC records in such a case will be modified. This modification can affect the use of the GASC in a complicated way, and so the Back Counter is used to verify that a track has passed completely through to the back of the GASC.

The BACK sits directly in back of the GASC. It consists of 64 vertical streamer tubes. At the center of each tube is an anode wire, and along the outside of the tube sits a line of 24 square copper pads 6 cm to a side. The tubes are filled with an ionizing gas. The pads pick up the signal from ionization inside the tube, and so produce a three-dimensional measurement of the point at which a charged particle has passed.

The Back Counter showed numerous problems during the 1995 $E866$ run period, and was turned off for the 2 and 4 $A{\cdot}GeV$ portion of the run. It remained off for the 6 and 8 $A{\cdot}GeV$ portion of the $E917$ run period, and was removed from the spectrometer platform after the 8 $A{\cdot}GeV$ portion. It is therefore not present in this analysis, and is not used. Without a Back Counter, the analysis of the GASC, already difficult, is made extremely problematic.

2.10 Tracking Chambers

There are five distinct sets of tracking chambers surrounding the magnet. These were built at 4 institutions, and installed at various stages in the string of experiments. The set of drift chambers T2-T4 were built by MIT, originally for $E802$. With some replacements, these chambers survived through to the $E917$ run period. TR1MIT,

used solely as a multiwire proportional chamber, was also built by MIT, as a hardware project for my graduate studies. It served as a replacement for TR1, and was installed for $E917$. T1, a drift chamber, was built by LLNL, and was installed for $E866$. The TRFs, which are multiwire proportional chambers used as drift chambers, were built by Columbia, and also installed for $E866$. TR1 and TR2, mutiwire proportional chambers, were taken from the MPS experiment for use in $E859$. During the $E917$ run period, responsibility for the maintenance of all chamber systems fell to MIT. For a complete list of the materials used, as they contribute to the total interaction thickness of the spectrometer, I refer the reader to [Hei99].

2.10.1 Basic Principles

It is easiest to begin with the basic physical process on which drift and/or multiwire proportional chambers are based. Consider a charged particle incident on a volume of gas. If the gas has a low ionization threshold, the particle will lose energy in the gas through ionization. If the gas is held at a potential, the charge separated by this ionization will drift apart in a predictable way. One can then register a signal from the passage of the charged particle through the volume of the gas by measuring the charge collected on the systems that produce the potential.

Such a process would produce a very small signal were there no amplification. However, if one uses wires to produce the potential, a large field gradient will be introduced around these wires. If the wires are of a small enough diameter, and if the potential at which the wires are held is high enough, the acceleration of the charge in the gradient will be enough to cause further ionization in the gas surrounding the wires. Hence the charge produced by the original ionization will cause a cascade of charge around the wire, the signal from which will be at a measureable level.

One can easily manufacture an array of duplicate cells, each of which can be held at a potential and has at its center a sensitive wire, the "sense" wire. If these cells are isolated, such that the original ionization does not cross cell boundaries, the position of the charged particle can be isolated to a given cell. Such an array of cells is called a multiwire proportional chamber.

More information can be gleaned from the ionization process. It is possible to shape the fields of a cell such that they are essentially uniform except in the immediate vicinity of the wires. In such a field, due to the interactions of the charge with the gas, the drift velocity of the charge will be uniform across a large fraction of the cell. Hence, by measuring the time between the assumed passage of the ionizing particle and the registering of the signal, one can measure the distance between the original ionization point and the sense wire. An array of cells of this type is called a drift chamber.

A signal in a cell does not isolate the position of the ionization center in the direction along the sense wire. The signal therefore determines only two of the three dimensions that describe the ionization point, to a resolution determined by the size of the cell.

By placing a set of such detectors in an array, with varying orientations of the sense wires, one can reconstruct the full trajectory of a particle. This is what is known as a "projective" geometry. In our experiment, we use four orientations of the sense wires: X, which measures along x_{spec}, Y, which measures along y_{SPEC}, and U and V, which measure along an axis at 30° from x_{spec}, one in each direction. By requiring a consistent set of hits in some fraction of these planes, we reconstruct the track. Figure 2-4 shows this in action. Since the planes cannot be placed on top of one another, and so sit at a different z_{spec}, it is not possible to simply cross the lines measured and obtain one space point, as the planes sit at different points along the trajectory of the track. The figure is a bit of a simplification in that regard.

In a drift chamber the resolution of the measurement can be improved, but only to within an additional ambiguity. By measuring the drift time, one measures only the distance between the ionization center and the sense wire, not the direction of this difference. Therefore the measurement isolates the ionization point only to within a circle about the sense wire. Since the cells used in the drift chambers of this experiment are wider than they are deep, this additional ambiguity is termed the "Left-Right" ambiguity.

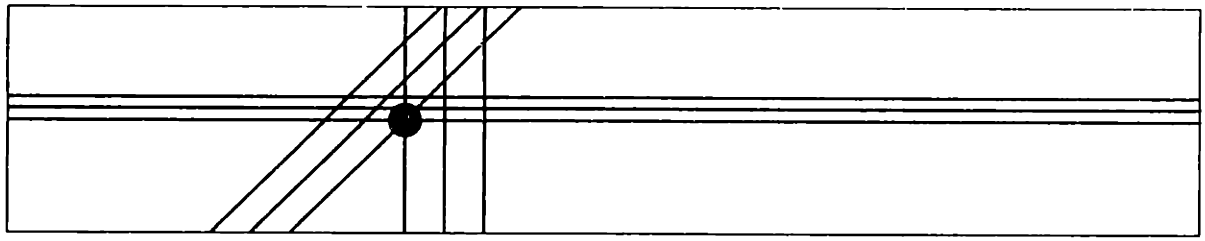

Figure 2-4: A schematic of projective geometry. The two outer lines in each direction are the lines of constant drift distance perpendicular to z_{spec}, while the center line shows the wire position. The figure assumes that the track is incident along z_{spec}, so that the different z position of the planes does not matter. Also, one of the wires is assumed not to have fired.

2.10.2 T2-T4

Basic Design

T2-T4 are drift chambers in the fullest sense of the word. They consist of arrays of rectangular cells, arranged into planes with four orientations perpendicular to z_{spec}. These planes are grouped into "modules" of a common orientation, which are then placed back-to-back to create a "chamber". There are three of these chambers, termed T2-T4, with T2 placed between the target and the magnet and T3 and T4 placed behind the magnet. Each chamber has its own unique set of planes and modules, as shown table 2.5.

While the construction details of these chambers have been described extensively elsewhere [Col92, Cia94], and the chambers were completed before my time in the experiment, some of these details will be repeated here, both because TR1MIT (section 2.10.3) was designed along the same lines and because the contrast between their design and that of the other chambers of the experiment led to many of the decisions made in the reconstruction algorithms.

All fields in a given cell are generated by parallel wires. Figure 2-5 shows a schematic of the cells. At the center of a cell is the "sense" wire, which consists of a

Chamber	Planes	View	Orientation	Wires	Spacing (cm)	Stagger (cm)
T1	1-2, 9	X	0°	40	0.635	0, 0.318, 0
	3-4, 10	Y	-90°	20	0.635	0, 0.318, 0
	5-6	U	-30°	40	0.635	0, 0.318
	7-8	V	30°	40	0.635	0, 0.318
T2	1-3	X	0°	28, 27, 27	1.4	0, 0.7, 0.7
	4-6	Y	-90°	13, 13, 14	1.4	0, 0, 0.7
	7-9	U	-30°	28	1.4	0, 0.7, 0.7
	10-12	V	30°	28	1.4	0, 0, 0.7
T3	1-2	U	-30°	36	3.22	0, 0
	3-5	X	0°	36	3.06	0, 0.075, 0
	6-8	Y	-90°	36	1.40	0, 0.7, 0
	9-10	V	30°	36	3.22	0, 0
	11-13	X	0°	36	3.06	0, 0.075, 0
T4	1-3	Y	-90°	16	3.44	0, 0.075, 0
	4-5	U	-30°	44	3.30	0, 0
	6-8	X	0°	40	3.50	0, 0.075 0
	9-11	Y	-90°	40	1.40	0, 0.7, 0.7
	12-13	V	30°	44	3.30	0, 0

Table 2.5: Vital statistics of T1-T4. The orientation angle is defined in the SPEC coordinate system such that 0° points in the positive y direction and -90° points in the positive x direction. This is only an approximate number. The stagger listed is with respect to the center of the cell.

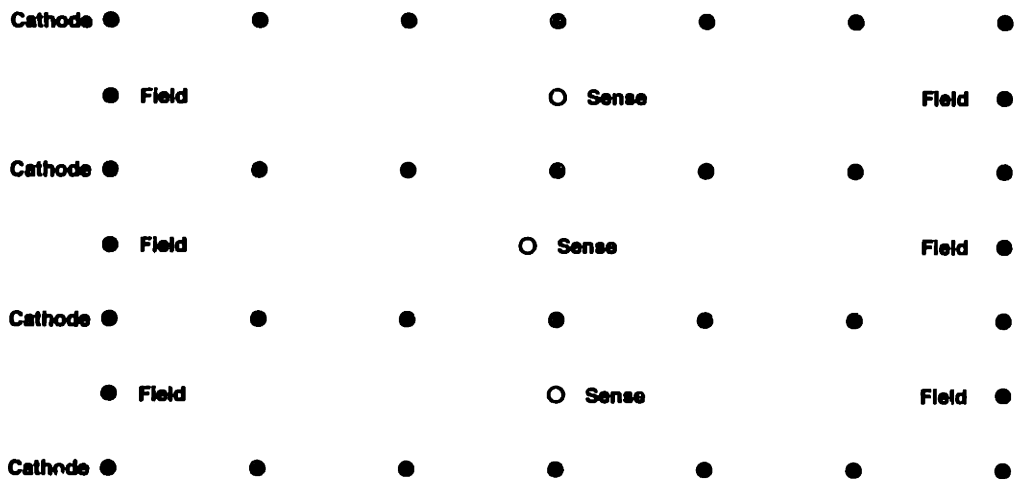

Figure 2-5: A schematic representation of cells in T2-T4. A module with three planes is shown. The direction of duplication is along the horizontal, and the figure portrays a cross-section in a plane perpendicular to the wire orientation. The relative dimensions are different across the chambers, and the diameters of the wires are not to scale.

30 μm diameter gold-plated tungsten wire held at a potential. On either side of the sense wire, along the direction of duplication of the cells, sit the "field" wires. Each field wire is 100 μm in diameter, and is made of a copper-beryllium alloy. The field wires are held at a potential of opposite sign to that of the sense wire, and are shared between neighboring cells within a plane. Offset by 7 mm along z_{spec} from the sense wires are 14 "cathode" wires per cell, 7 on either side. The cathode wires are held at varying voltages along the cell to shape the field. They are shared by adjacent cells, both along z_{spec} within a module and along the direction of duplication within a plane.

In a cell of a given module, the sense wires can be in one of two positions with respect to the field wires. That is to say, the sense wires are "staggered". This is done to help resolve the left-right ambiguity noted previously. Besides the basic dimensions of the cells in all of the chambers, table 2.5 lists the amount of this stagger. Note that the U and V planes of T3 and T4 have no stagger.

The last plane of T3 is also strung with high-resistance wires, designed to allow

for the determination of the ionization position along the wire. This can in principle be done by recording the difference in pulse height at either end. The resolution of this determination was found to be poor when this system was first installed for $E859$, with the leading explanation the properties of the FASTBUS ADC's used for readout. Accordingly, in $E917$ the readout was replaced by a set of CAMAC ADC's. Problems in the signal cables were never resolved, so the detector is not used in this thesis.

Despite the fact that a cell consists of 17 wires (14 cathode, 1 sense, and 2 field), due to the sharing of the wires across cells not all voltages can be adjusted independently. The cells in different modules have differing dimensions, and the stagger of the sense wires is not common across all cells in a given module. The field configurations will be different for cells of different stagger. For these reasons the potentials placed on the wires are controlled to the maximal level possible, both by a multichannel LeCroy high voltage crate, for most of the cathode and field wires, and for the other wires by individual high-voltage modules to allow finer control and monitoring.

Construction

Partially because of this need for fine control, and partially for other reasons, the wires in T2-T4 are strung in a somewhat unusual way. The method is modeled after one first developed at SLAC. Instead of being wound as a group onto the chamber frame, each wire is individually strung. Holes for each wire are drilled into a G10 frame. There is one such frame per module. The wires are threaded through this frame, set to a given tension (30 g for the sense wires, 100 g for the field and cathode wires), and held at this tension by a spring and associated assembly as shown in [Cia94]. The signal and high-voltage leads are soldered directly to a cap at the end of each wire.

The G10 frame is placed into an aluminum frame. The chambers are then sealed with a ring of silicone rubber (GE 118 RTV), and the front faces covered by a 1 *mil* aluminized mylar sheet. This sheet is glued to the aluminum with silver paint for grounding, and so provides both electrical isolation and defines the gas volume of the module.

The design allows for the required control of the high voltage. It also minimizes the effects of bend of the G10 frame on the tension of the wires. The wires place a rather strong pressure on the frame that holds them, causing the frame to deflect inwards. This bend is a constant problem in the production of chambers through the winding method, and can lead to cracked leads at the most extreme and a reduced ability to hold voltage at the least extreme. Since the tension in the MIT method is set wire by wire, the bend can be caught and corrected for as the chamber is strung. For this reason, we string the chambers from the outside edges towards the middle.

The gas used in T2-T4 is 50-50 Argon-Ethane, which has a saturated drift velocity of 50 $\mu m/ns$, and is available in pre-mixed bottles. It flows through a bubbler, containing research-grade ethanol chilled to 0° C, to increase the lifetime of the chambers. The modules of T3 and T4 are isolated individually by the mylar windows. Therefore the flow of the gas to these chambers is controlled on a module by module basis by pin valves placed between the alcohol bubbler and the chambers. The gas output from the modules is controlled and monitored using silicone-oil bubblers. T2 is isolated by windows into two sets of modules, one set of the X and Y modules and other set of the U and V. Therefore the control of the flow of gas to this chamber is split among these two sets. Unfortunately, the AGS in winter is not the most friendly environment for gas systems, with drastic variations in temperature and pressure the norm.

The electronic readout of these chambers is discussed in [Col92]. Of greatest note here is that the combination of readout characteristics and cell configuration allows for a two-hit separation at 2 mm. Therefore the effective segmentation of the chambers is quite a bit higher than it might appear at first glance.

The precision attained by these chambers is ~ 150 μm, although the accuracy of the knowledge of their positioning limits this somewhat.

I refer the reader to [Col92, Cia94] for further details.

Detector Effects

The method does have a few problems. The first is that the accuracy of the wire placement is completely determined by the accuracy of the machining of the holes.

The effect of this is illustrated at its most extreme by the U and V planes in T2. In these two planes, a line of holes was missed in the machining of the frames [Cia94]. The error was not discovered until the chambers were fully strung and in place on the spectrometer platform, and leads to a dependence of the wire orientation on the wire number along the chamber. Obviously, this causes a host of problems in the tracking software. On a less extreme level, for all of the chambers the position of the wires, as seen by the tracking code, is adjusted on a wire by wire basis. See section 3.3.3 for more details.

The second problem is related to the method's strength. Since the high voltage leads must be individually soldered to the end of each wire, there is a natural limit to the segmentation that the process allows. As the segmentation becomes finer, the isolation of the high voltage between neighboring wires becomes increasingly more difficult, with the end result that arcs between adjacent leads become more probable. This problem was especially noticeable on the highly segmented T4.5Y module, and led us to run this chamber at a slightly decreased voltage during the 1995 low energy run.

During the calibration phase of the chambers for the 1995 data set, it was discovered that a large fraction (approximately 50% in the worst cases) of hits on T1 and T2 had unphysical times. That is to say, the time recorded would map to a distance much larger than the size of a cell. The rate of such unphysical hits was uniform with time within a given run. The number of unphysical hits in an event showed no correlation to the number of hits with physical timing, or to the ratio $GoodT1/\left(GoodT3+T4\right)$, where "Good TX" is the number of hits with physical times on chamber X. The same held true for T2. Therefore it was assumed that the hits were due to problems in the TDC electronics. One possible explanation is that for some channels the TDC was not being cleared properly between events, so that the hits of the previous event were being duplicated, with the recorded times shifted by the difference in time between the events. However, this was never completely proven.

The event sample in which this effect was found was not cut on FOLLOW (section 2.11.1), and so included events in which two beam particles hit the target within

the timing windows of the electronics. However, the lack of such hits on T3 and T4 in the same events rules this out as a full explanation.

Such hits are rejected from all analysis. The level of hits with unphysical times in the 1996 data set is lower, $\sim$ 5%, and follows the rate of both FOLLOW's and such hits on T3 and T4. We cut events with the FOLLOW bit set in the analysis.

In the commissioning phase of the *E*917 run, the controller board for the FASTBUS crate that contains the TDC's for T1, T2, and the TRFs (see section 2.12) failed completely, and was replaced.

2.10.3 TR1MIT

TR1MIT was built for *E*917 as a replacement for TR1, described below. It's construction was a hardware project in the course of my graduate studies. Since TR1 was not designed specifically for the experiment, but was recycled from the MPS, its acceptance was mismatched to those of the the other chambers behind the magnet. It was originally thought that TR1 could be placed between the magnet and T3, where its acceptance would be better matched, but the frame would not fit in the space available. Therefore with the simple replacement of a single plane a dramatic effect could be made on the total acceptance of the spectrometer.

Basic Design

TR1MIT was designed along the lines of T2-T4 and strung in the same way. However, its design requirements were somewhat different. It needed to act as a multiwire proportional chamber, rather than as a drift chamber, needed to be read out through the existing LVL2 electronics, and required a relatively high segmentation.

It consists of a single plane of 192 square cells, each of which is 0.66 cm to a side, as shown in figure 2-6. The wires are aligned along the vertical, so that the cells are duplicated along x_{spec}. The active area along y_{SPEC} is 54 cm. This is also approximately the distance over which the wires are under tension. The chamber is placed at a distance of 445 cm from the target, near the previous position of TR1.

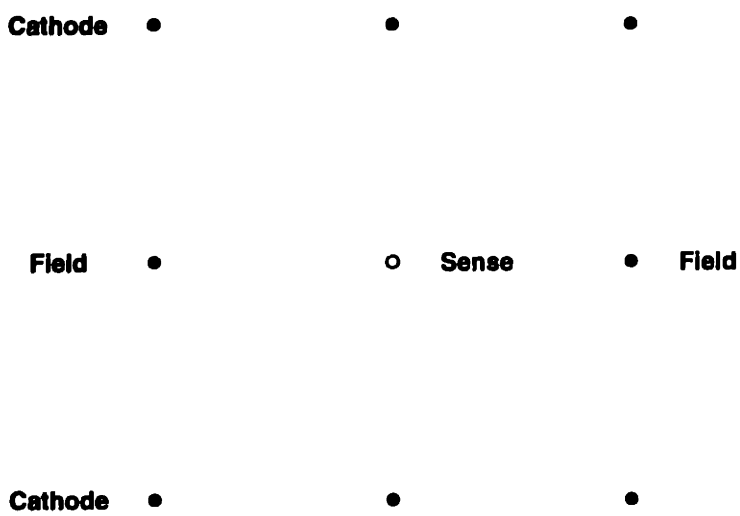

Figure 2-6: A schematic representation of cells in TR1MIT. The direction of duplication is along the horizontal, and the figure shows a cross-section in a plane perpendicular to the wire orientation. The relative dimensions are different across the chambers, and that the diameters of the wires are not to scale.

At the center of each cell is a sense wire, of the same type as those of T2-T4. On either side of this sense wire is a field wire, for isolation. There are 6 cathode wires per cell, three on either side along z_{spec}. The field wires and the cathode wires parallel to them are shared across neighboring cells. As with T2-T4, there are windows of aluminized mylar, placed at a distance of 2.14 cm from the center of the main plane. At each end of the plane sit an extra set of ground wires to terminate the field.

While the design allowed for some individual control over the field and cathode wires, during the experiment all were held at the same voltage. The detailed shape of the field configurations matter far less for TR1MIT than for T2-T4, since the drift time is not read out, and so such an extra level of control was not necessary. The sense wires were run at a separate voltage.

Detector Effects

One problem did show itself during the run. As described in section 2.11.3, the LVL2 system required the readout to be made through a LeCroy 2735 PCOS Preamplifier/Discriminator card. This card has an amplification factor of approximately 3 less than the MIT preamplifiers. Therefore, to obtain a good efficiency we needed to run the chamber at a very high voltage, corresponding to a field strength of 3550 V/cm. This led to some sparking problems.

We also decreased the level of the threshold on the PCOS card from 10 V to 4 V. From $E859$ onwards, the thresholds had been placed at their maximum on TR1 and TR2, since it was observed that the noise levels on these chambers were quite large. In the design of TR1MIT a few simple shielding efforts were made, and close attention paid to the grounding of the chamber. The net effect of this was to decrease the noise level so that a decrease in the threshold level was allowed.

The final efficiency of the chamber was relatively high, greater than 95%.

TR1MIT used the same gas system as T2-T4.

2.10.4 T1

The T1 that was in place for $E802$ and $E859$ showed rather poor performance. Therefore a replacement was built for $E866$. This replacement is of a somewhat simpler design than T2-T4, but has a higher segmentation. It is strung in a winding machine, and has 0.25 *mil* aluminum foils rather than wires as the cathode planes. The sense wires are 30 μm diameter Tungsten. Like T2-T4 it has field wires for isolation between the cells. The field wires are 75 diameter Tungsten. The lack of fine-grained voltage control leads to a slightly higher nonlinearity in the mapping of drift time to distance than that seen in T2-T4. However, the level of this nonlinearity is easily corrected for by the calibration procedure developed for the other chambers.

The electronics for this chamber are mostly separate from those of T2-T4, and their design, combined with the size of an individual cell, preclude any double hit capability in this chamber.

T1 used the same gas system as T2-T4.

2.10.5 TRFs

The TRFs were designed and built at Columbia for installation into $E866$. The original design criteria for these chambers was dramatically different than that for T2-T4: they were to serve as multiwire proportional chambers of high segmentation.

They were needed to aid in pattern recognition in the high multiplicity environment produced by the Au beam. However, they were instrumented with timing readout, and subsequently evolved to be used as drift chambers.

Basic Design

The TRFs consist of eight highly segmented planes divided between two modules, each of which has one plane each of a given view. They were wound in a winding machine, use foils for the cathode plane, and do not have field wires. The separation between the planes of a given chamber along z_{spec} is 4 mm. For the run periods of this thesis, TRF1 sits between T1 and the target and TRF2 sits between T2 and

Chamber	Plane	View	Orientation	Wires	Spacing
TRF1	1	X	0°	128	2.0 mm
	2	V	30°	144	2.0 mm
	3	Y	-90°	64	2.0 mm
	4	U	-30°	144	2.0 mm
TRF2	1	X	0°	160	2.4 mm
	2	V	30°	192	2.4 mm
	3	Y	-90°	96	2.4 mm
	4	U	-30°	192	2.4 mm

Table 2.6: Vital statistics of the TRFs. The orientation angle is defined in the SPEC coordinate system such that 0° points in the positive y direction and -90° points in the positive x direction

the magnet. I refer the reader to [Wan96] for greater detail on the construction of these chambers. Note that the relative position of T2 and TRF2 was different for the running period of that thesis.

Detector Effects

The lack of field wires leads to a somewhat complicated analysis procedure, due to the lack of isolation between neighboring cells. In addition, the geometry of the cells, combined with a lack of fine control over the voltages, causes a strongly nonlinear association between drift time and drift distance. This nonlinearity must be calibrated away if the chambers are to be used as drift chambers. The analysis procedure used to do this is described in section 3.3.2.

The resolution attained from this procedure varies slightly from chamber to chamber, and run condition to run condition, but is never more than 300 μm. The nonlinearity seems to be a strong function of time, so that the calibration is done on a very fine scale. In addition, in 1995 it showed some odd dependencies.

There is no simple mechanism to resolve the left-right ambiguity in these chambers. However, in special cases, the deficiency in isolation between neighboring cells is used as an advantage help in the resolution of the ambiguity.

The electronic readout of these chambers is an interesting design: in order to save on electronics cost, the signals from four wires are combined into one signal, with the

signals separated by a 100 *ns* on-board delay. In order to make this separation, the signals are required to fall within a 80 *ns* gate. This gate is tight, given the drift times in the chambers and the time taken by slow particles to reach the chambers from the target. Also, due to the timing needs of the readout, the electronics must be triggered directly on a LVL0 signal. This means that one must be very careful to time the electronics correctly in order to obtain useable results.

Due to the geometry of the cells, the signals from the chambers are quite small. Therefore the thresholds for discrimination must be carefully tuned so as to remain sensitive to all signals but not to introduce noise. The electronics latch on for 80 ns after a hit is detected, and so are completely insensitive to the time of any subsequent hit. Therefore, any noise early in the gate will cause the timing information of a real hit to be lost. For reasons discussed below, in order to increase the sensitivity to low pulse heights we decreased the threshold from 5 V to 3.5 V for the *E*917 run. While this change did increase the noise level, it was not observed to negatively impact the efficiency for detection.

The gas used in the TRFs is Argon-Isobutane, of a mix that varied from 60-40 to 80-20 across the runs. These gases must be mixed by the gas system before being introduced into the chambers. The mixture is bubbled through a chilled bubbler containing dimethoxymethane. The mixing, combined with some instabilities in the system, makes the gas system of the TRFs difficult to control.

During the 1995 *E*866 run period, some combination of these effects and a rather low voltage setting caused the chambers to be highly inefficient, with the inefficiencies on one of the chambers reaching the 25% level. To account for these effects, substantial modifications were necessary to the tracking algorithm. This inefficiency was discovered during the commisioning period of the *E*917 run, and was fixed by a combination of increasing the voltages on the chambers, decreasing the thresholds of the electronics, and monitoring the gas system intently. See section 4.4 for further details.

2.10.6 Trigger Chambers

The trigger chambers TR1 and TR2 were recycled from the MPS experiment[E+83, EK80, Etk79] for use in $E859$. No attempt was made to use these for their original purpose, as drift chambers. They were instead used as multiwire proportional chambers, both for the LVL2 trigger and to aid pattern recognition behind the magnet. TR1 was only used in 1995, but TR2 was used in both run period periods.

The sense wires are vertical, with inter-wire spacing of 0.25 in and diameter 1 *mil*. The cathode and field wires are 3 *mil* stainless steel. The cells are 0.25 in deep. TR1 has 160 cells, and is placed at 442 cm from the target. TR2 has 256 cells, and sits at $z_{spec} = 509$ cm. The chamber gas used is 70-30 Argon-Isobutane, bubbled through a dimethoxymethane bubbler.

2.11 Triggering

The signals from all of the detectors must be collected and recorded for later analysis. At most 4% of the possible events are of interest, and in many cases far fewer. Since the rate at which data can be recorded is lower than the rate of events that occurs, a fast selection mechanism must be produced to select only those events that are of interest. This selection method is termed "triggering".

There are three "levels" of triggers in the experiment, numbered 0-2 in increasing level of selectivity. These add to the experiment's lexicon of four-letter words the terms LVL0, LVL1, and LVL2. Associated with each event in the data stream are three "trigger words", with trigger word 2 corresponding roughly to LVL0, trigger word 1 directly to LVL1, and trigger word 3 to LVL2. These trigger words are simple integers, which have a bit set to true if a given trigger is satisfied.

Before launching into the discussion of the various trigger systems, one term will be defined, the "scaledown". It is desirable to have a sample of triggers that is unbiased, but also that has been winnowed so as not to dominate the data stream. Therefore in this experiment there are a set of places where a trigger is "scaled-down". This means that a count is kept of triggers that have been set true, and only one out of

every N trigger in a series is kept. The number N is referred to as the "scaledown". This is only the simplest method of scaling down triggers: one could, in principle, randomize the sample from which one chooses the triggers, so that on average only one out of every N triggers is chosen. This method is used in other experiments, but is not used here. The reason for such a complicated method is that a bias can be placed on the sample, if the counting is begun at a fixed place for every run through the possible triggers. To correct for such a bias would require a knowledge of the initial parameters of the count. This knowledge does not exist for the set of scaledowns used in this experiment, and so any possible bias is ignored. That is to say, we assume always that the mean number of real triggers, given a scaledown N and measured number of triggers X, is simply NX. The above biases could place the actual mean anywhere between $NX - N/2$ and $NX + N/2$, exclusively.

2.11.1 LVL0

The LVL0 trigger is the Ur-signal of the experiment. It serves as the basis for the later triggers, and is used in various detector systems as the signal to begin digitizing.

There are two types of triggers that can form a LVL0, the BEAM and the INT. On a logic level, the BEAM is defined from a coincidence of signals from the BTOT and the HOLE counter as:

$$\mathrm{BEAM} = \overline{\mathrm{PRE}} \wedge \mathrm{BTOT}_1 \wedge \mathrm{BTOT}_2 \wedge \overline{\mathrm{HOLE}} \tag{2.1}$$

where logic notation is used, so that $\overline{\mathrm{HOLE}}$ means that the signal from the HOLE counter is below a given threshold, and $\wedge$ means that both signals must be present. The PRE in equation 2.1 refers to one of the two signals that are used to reject pileup. The first, PRE, is set true for a fixed time after a valid BEAM trigger, and therefore signals that a beam particle has "PREceded" the given trigger within the gate. Triggers with PRE set are therefore immediately cut from the data stream. The gate used in $E866$ was 500 ns, while for the $E917$ run it was reduced to 300 ns. In addition, if a valid BEAM trigger is followed by a possible trigger rejected only due

to PRE, the trigger is recorded, but has a special bit, the FOLLOW bit, set in trigger word 2 for rejection offline. Note that there is a window, of $O(10$ ns), around every BEAM trigger during which it is impossible to set the PRE or FOLLOW. Therefore if two BEAM triggers occur at a time difference smaller than this, neither will be cut. During the low energy runs, the fraction of events taken for which FOLLOW was set ranged from $\sim 5 - 10\%$, depending on the year and the rate of beam particles.

As discussed in section 2.6.1, the rate of BEAM triggers is far too high for the apparatus to handle. Therefore, the INT trigger is formed for later use:

$$\text{INT} = \text{BEAM} \wedge \overline{\text{BE}} \tag{2.2}$$

where BE refers to the analog sum of the eight phototubes of the Bull's Eye. For LVL0, the BEAM triggers are scaled down to form the BEAM/n triggers, while the INT triggers are passed through unmodified.

For a portion of the beginning of the 6 A· GeV run, a further scaledown on the INT triggers was placed immediately before the data aquisition system, and so was reflected in trigger word 2. For a while, there was concern that this INT scaledown had been placed at the same point in the chain as the BEAM scaledown, which would have caused a loss of events. Various ratios of triggers effectively ruled out such a concern.

The final trigger, the LVL0, is used as the effective start signal for digitization of many of the electronics. This digitization takes some time, during which the experiment is effectively "dead" to incoming signals. Therefore it is desirable to have a trigger that is only true when the experiment can effectively digitize. The signal that the experiment is dead in this way is generated by the Trigger Supervisor, described below, and is termed TSBUSY. Therefore, the final definition for the LVL0 trigger is:

$$\text{LVL0} = (\text{BEAM/n} \vee \text{INT}) \wedge \overline{\text{TSBUSY}} \tag{2.3}$$

where, following logic notation, $\vee$ denotes an OR.

2.11.2 LVL1

While the INT trigger of the LVL0 system provides some restrictions on the possible set of events to be recorded, it is of interest to create a more restrictive set of triggers. This is where the LVL1 triggering system steps in.

At the center of this system is the Trigger Supervisor, which consists of a set of custom-designed programmable VME modules. It collects and coordinates a set of triggers in order to make the final decision to record the event. For each trigger signal, there is one module that collects the signal and scales it down by a programmable factor. There are 16 such modules, each of which can be programmed to be enabled or disabled in the final decision. For a given event, if an individual trigger is satisfied, if the trigger also satisfies the scaledown, and if the module to which the trigger is attached is enabled, the Trigger Supervisor will signal that the event should be recorded.

Note that this is an inclusive process: events for which multiple triggers are satisfied will always be recorded, with all bits set in trigger word 1 that correspond to the triggers that were satisfied. However, there is an exclusive component: as discussed in section 2.11.3, the LVL2 system can generate a signal that an event is to be rejected. Therefore, each trigger module has an additional input from the LVL2 system, the "VETO", which can be programmed to be "enabled" or "overridden", i.e. disabled, on a module by module basis. If the VETO is enabled, and if a signal comes from the LVL2 system that the event is to be rejected, the trigger module sends a signal to the main supervisor that the trigger is to be rejected. This mechanism allows certain triggers to ignore the decision of the LVL2 system.

The actual timing of the LVL1 trigger, especially with the addition of the VETO ability, is quite complicated. I refer the reader to [Ahl97] for details.

While an assortment of triggers have been used in the past, only four were used in the data presented in this thesis. These are BEAM, INT, SPEC1, and SPEC1 Veto Override.

BEAM

The LVL1 BEAM trigger is the scaled-down LVL0 BEAM/n trigger, with a further scaledown placed upon it by the LVL1 system. Therefore the BEAM triggers have two scaledowns applied to them before they pass into the data stream. It sits at bit 1 (counting from 1) in trigger word 1.

INT

For most of this data, the INT trigger is the unscaled LVL0 INT trigger, with a scaledown placed upon it by the LVL1 system. However, as noted in 2.11.1 above, for a portion of the 6 $A{\cdot}GeV$ run, the INT trigger had an additional scaledown placed directly before the input to the Trigger Supervisor module, but after being included into the LVL0. Therefore for this data there are also two scaledowns, while for most of the data there is only one. The trigger sits at bit 2 (counting from 1) in trigger word 1.

SPEC1

This trigger unfortunately has many definitions. First, there are portions of the data for which the LVL2 was not enabled, called "SPEC" runs. For these runs, no LVL2 VETO was enabled on this trigger. For runs for which the LVL2 was enabled, it was enabled on this trigger. Therefore the meaning of the trigger depends on whether the LVL2 was activated. This information is not directly recorded into the data stream.

Second, the presence of the trigger is supposed to mean that at least one valid particle entered the spectrometer, hence the name "SPECtrometer 1".

For the 1995 data run, this was specifically interpreted as:

$$\mathrm{SPEC1}_{1995} = \mathrm{TOF1} \wedge \mathrm{TR1} \wedge \mathrm{LVL0} \tag{2.4}$$

where TOF1 means that at least one signal was registered above threshold on the TOF, and TR1 means at least one signal was registered on TR1. Neither of these definitions correspond directly to what is stored for the hits on the detector, but are

generated separately.

For the *E*917 run period (and for portions of the 1995 high-energy run, not included in this thesis), the electronics necessary to create the TR1 signal showed some problems. Therefore, to avoid any possible bias, the trigger was relaxed to:

$$\mathrm{SPEC1}_{1996} = \mathrm{TOF1} \wedge \mathrm{LVL0} \tag{2.5}$$

Since this definition lacks the extra coincidence of TR1, and since the TOF wall is rather noisy, the change in definition caused the selectiveness of the SPEC1 trigger to decrease by a factor of approximately 2.

The SPEC1 trigger is not scaled-down in the data used in this thesis, and sits at bit 5 (counting from 1) in trigger word 1. It is sometimes also referred to as SPC1, or as SPEC.

SPEC1 VETO OVERRIDE

This is a copy of the SPEC1 trigger, fed into another trigger module. The LVL2 VETO is never enabled on this module, and the module is always programmed with a scaledown. The trigger is only enabled when the LVL2 trigger as a whole is enabled, and serves to produce a sample of unbiased SPEC1 triggers, taken under the same run period conditions as the SPEC1 VETO-ENABLED triggers. The ability to do this was new in the 1994 data set. It is crucial to be able to compare unbiased data to LVL2-enhanced data. By taking the unbiased data under the same set of run period conditions as the enhanced data, many systematics in such a comparison are removed.

In addition, for some of the run period conditions in the low-energy data, there was a very low rate of events that satisfied the LVL2 trigger, despite the increased target thickness and beam rate. Therefore, in order not to waste the recording bandwidth of the experiment, we loosened the scaledown on these triggers to get a large sample of unbiased events.

This trigger sits at bit 10(counting from 1) in trigger word 1, and is sometimes referred to as S1VO.

Trigger Mix

The scaledowns were typically adjusted so that the mixture of triggers (the "trigger mix") was 75-10-10-5 SPC1-S1VO-INT-BEAM when the LVL2 trigger was enabled and 85-10-5 SPC1-INT-BEAM when the LVL2 trigger was disabled.

In addition, for an unknown reason, for much of the 1995 2 and 4 $A \cdot GeV$ run period, a further bit, the FSPEC bit, was set to be true in every event.

2.11.3 LVL2

Trigger Description

The LVL2 trigger was commisioned for $E859$, and is descibed in [Cia94]. The modifications to the trigger for $E866$ are discussed in [Ahl97]. With a few exceptions noted below, the trigger remained unmodified for the 1995 and 1996 data periods. The trigger was designed to enhance certain types of events in the data stream, and was designed to minimize biases in this enhancement rather than for extreme selectivity.

It consists of a set of large lookup tables that mimic online tracking and PID. It is implemented in a complicated set of CAMAC modules and signal cables. The tracking done is extremely simple and is only done in the x_{spec} direction.

Hits on TR1 and TR2 are recorded through the LeCroy PCOS system. Hits and times on the TOF wall are recorded through a fast-readout FERET system. Combinations between the hits on the TOF wall and those on TR1 are made, and the lookup tables consulted to find the projection onto TR2 of the straight line that joins the hits. If a TR2 hit is found within a programmable search width about this projection, a "track" is said to have been found. For PID purposes, a momentum is read from the lookup tables for this track. This momentum is produced by assuming that the track originates from the target. The TOF of the slat associated with the track is then combined with the momentum of the track, and another lookup is performed to see if the momentum and TOF are within allowed windows for PID. If this is satisfied, a complete track of a given PID has been found, and this information is sent to the final stage of the trigger. The trigger can be programmed to require

one or two such tracks, the parameters of which can be different, and also to ignore tracks which either share the same TOF hit or have hits on neighboring slats. This last set of requirement is known as "cluster-busting". In the end, if the trigger has looped through all TR1-TOF combinations without finding what it requires, it will send a VETO to the Trigger Supervisor.

The timing resolution obtained in this system is poorer than that of the full TOF readout system, approximately 250 *ps*, and has a shorter total range. The momentum resolution is also somewhat poorer than that of the full spectrometer, since the hits are only determined to within the size of a cell on TR1 and TR2. However, since there is a significant contribution to the momentum resolution from multiple scattering, which does not depend on the position resolution, this is not as significant a difference as might seem at first glance. A far greater difference in the tracking quality is the existence of duplicate tracks, since the tracks are only formed in one dimension. Such tracks decrease the selectivity of the trigger but do not produce biases. This statement is not completely true in the case of full cluster-busting.

Modifications and Calibrations

The trigger must make its decision within a certain time window, the length of which was increased for the 1995 run period. If by this time the trigger has not looped through the entire set of TR1-TOF combinations, no VETO will be sent and the event will be digitized.

The programming and hardware needed to be extended and modified slightly for *E*917 because of TR1MIT. The size of a cell in TR1MIT is slightly larger than that of TR1, and there are 32 more wires.

In addition, at the start of every data taking period (and at a few intervals within these periods) the FERETs needed to be calibrated. The slat by slat timing offsets on the TOF wall are removed in the trigger system by programming the FERET with a set of pedestals. Since the FERET system basically replaces a TDC with a separate ADC and readout, online pedestal subtraction is equivalent to time subtracton. The pedestals are determined once, slat by slat, at the start of the data-taking period,

Beam Energy	Table Name	Pids allowed	θ_{HH}	$B_{HH}(kG)$
2 $A{\cdot}GeV$	K^+/K^-	K^+ or K^-	34,39	2A
	K^+	K^+	19-29	2A
4 $A{\cdot}GeV$	$K^+/K^-/\overline{p}$	K^+ or K^- or $\overline{p}$	14-44	2B
6 $A{\cdot}GeV$	$K^+/K^-/\overline{p}$	K^+ or K^- or $\overline{p}$	14-44	2B
8 $A{\cdot}GeV$	$K^+/K^-/\overline{p}$	K^+ or K^- or $\overline{p}$	14-44	2A
	$K^-/\overline{p}$	K^- or $\overline{p}$	14-44	2B

Table 2.7: The LVL2 tables used for this thesis. The LVL2 tables used for this thesis are listed, along with the angles of θ_{HH}, and the fields (in kG) for which they were applied. All tables were satisfied by at the minimum one track, which could be of any of the types listed.

using full offline reconstruction and PID of the tracks. This process is repeated later as necessary. The subtraction allows one to adjust the timing to within 50 ps. In addition, the timing is monitored closely online, based on LVL2 "tracking". The difference between the TOF measured and that predicted, assuming the pion mass, for tracks of momentum > 1 GeV/c is gathered run by run, and a global shift placed on all pedestals if the peak of this distribution shifts by more than 100 ps. Unlike the full TOF calibration procedure, discussed in section 3.4, the clocks of the FERET's are not adjusted slat by slat.

For the data presented in this thesis, the pedestals were determined once per energy period, each of which lasted approximately two weeks.

The lookup tables used in this thesis were also generated once per energy period, and are listed in table 2.7. All tables used a relatively loose set of criteria to provide a margin of safety. The total range of ΔTOF allowed was ± 1 ns, and, for the 6 and 8 $A{\cdot}GeV$ run periods, the search window on TR2 was increased to ± 2 wires from ± 1 wire. No cluster-busting was enabled. Also programmed, but not used in this thesis, were some tables requiring two tracks to be found, regardless of PID, either with no selection on sign or with both tracks required to be negative.

Due to the decreased multiplicity at the lower energies, the LVL2 trigger outperformed expectations by a factor of approximately 2.

The decision that the LVL2 has made is recorded in trigger word 3, discussed in table 2.8. This is very useful for analyzing events for which the LVL2 decision was

Bit	Name	Meaning
1	ROF-ROF	All combinations of TR1 and TOF analyzed
2	Veto	The trigger decided to VETO the event
3	No Start	No combinations of TR1 and TOF existed

Table 2.8: Definitions in trigger word 3. The definition of each bit stored in trigger word 3, where the bit count starts from 1.

ignored.

2.12 The Data Acquisition System

The construction of a successful Data Acquisition System (DAQ) is an art, the description of which lies beyond the possible scope of this thesis. I will make a few notes, but refer the reader to the theses [Yao97] and [Ahl97] which describe the data acquisition systems of $E917$ and $E866$ in more detail.

There was an upgrade to the DAQ between the 1994 and 1995 run, which caused an increase in the throughput of a factor of approximately 2. There was a second upgrade for $E917$, which caused an increase by another factor of approximately 2, and made the entire system far more reliable. The upgrades, combined with the decreased size of a given event at the low energy, led to, at its greatest, an approximately 6-fold increase in the data-taking rate during the low-energy runs as compared to that taken in 1994. The maximum number of events recorded per spill was seen to be, oddly enough, 917[4].

The digitization of the readout of the experiment is done in a set of LeCroy FASTBUS crates, 6 in all, combined with an assorted set of LeCroy CAMAC crates for a few of the specialized subsystems(TOF,LVL2,BEAM). The TDCs for T1, T2, and the TRFs are contained in one such crate, those for T3 and T4 in another such crate, and the TDCs and ADCs for the other detectors in two others. The Forward Spectrometer has two additional crates. The total digitization time in the FASTBUS crates is approximately 500 μs, and in the CAMAC modules approximately 150 μs.

[4]This number was not hard-coded into the DAQ software, though we checked.

The digitized results are sent over fiber links to modules in one of two VME crates. The link from a CAMAC crate is connected directly to a VME module called an SBE, based on a 68020 Motorola CPU, while that from a FASTBUS crate is connected to a memory unit called a FIFO. The collection of FIFOs in a given VME crate is controlled by a single SBE, one per crate. There are two modules called TADPOLEs, one per crate, which are based on Motorola 68040 CPUs. These collect and organize the output from the SBEs and, in the case of the 1995 run period, directly translate a portion of the output from raw FASTBUS data into banks organized by detector system. In the 1995 configuration, the TADPOLEs then transfer the data directly to TTi 8510 8mm tape drives, of the EXABYTE type, which write the data to tape for later analysis. In the 1996 configuration, the responsibility for translating and recording the data stream is offloaded to a dedicated SGI workstation, linked directly to the VME crates through a BIT3 interface.

The upgrades for 1995 were as follows. A second VME crate was added to the system. A second tape drive was also added, and the data interleaved in succession between the two tape drives, such that events #1,3,etc. were written to one tape, and events #2,4,etc. were written to the other. A threshold on the size of the event was placed, above which the event would not be translated. This led to the requirement to translate the data offline in the analysis passes, a task that ended up being more complicated than it should have been. In addition, the introduction of the second tape drive led to some reliability problems, and this, combined with the need to use new tapes whenever the DAQ "crashed", led to a rather large amount of wasted space on the output tapes.

For the *E*917 run period, many of these reliability problems, and the I/O bottleneck caused by the tape drives, were removed by writing the data directly to disk and copying the data to tape afterwards. Also, the offloading of the task of translation to a more powerful CPU, combined with the freeing up of memory in the TADPOLEs that this offloading allowed, resulted in a faster system. With the new DAQ the amount of data that could be taken per spill scaled completely with the spill length, so we petitioned the AGS for long spills. This petition was successful during the 6

and 8 *A·GeV* run period, but was not as successful during the high-energy run period.

The sum total of raw data taken during the low-energy runs is on the order of 100 Million events, and takes up a few terabytes.

Chapter 3

Collaboration Analysis *I*: Calibration

Calibration of the raw data is necessary to obtain final results. I will only discuss calibrations that impact the data of this thesis. There are approximately 1 Million separate calibration constants used in this data set, each of which has the potential to affect a portion of the data. The methods used to determine their values must therefore be robust and well-founded.

Much of the discussion of this chapter serves as a repository for the techniques developed to derive these constants. It will therefore be rather detailed. Due to the size of the data set, and the total number of configurations for which the constants needed to be derived, many of the procedures for their derivation needed to be modified. These modifications were made in order to increase the stability of the results across configurations. The need for such modifications is a general problem with large data sets, and is becoming more problematic as the size of data sets increases.

3.1 Division of the data

A "run" is an arbitrary division based on time: that is to say, each "run" contains X number of events written to tape in succession, where X is generally ~200,000. It should therefore be noted that every run has a specific set of conditions associated

with it. Some of these are under direct (and planned) experimental control: the angle of the spectrometer, θ_{HH}, the field of the spectrometer magnet, B_{HH}, the target position, and the beam energy. Others are not under direct control (and are unplanned), but are discovered later in the analysis. These tend to be a combination of slow drifts, which must be parametrized as a function of run or recalibrated on a fine scale, and discrete shifts, which must be dealt with in distinct blocks of runs. Table 6.1 lists the important quantities that must be dealt with on a run-by-run basis.

The term "run" is also used in the experiment to denote an entire data-taking period. This causes confusion. To avoid this confusion, I will always use modifiers when I mean a chunk of time as a whole, such as "running period", "data-taking run", etc.

Three major passes through the data are made. The raw data is stored as YBOS data banks, in an analysis framework taken from CDF a decade ago. The three major passes are called PASS0, PASS12, and PASS3. PASS0 produces no YBOS output, and is used to produce calibration constants and check the performance of the detectors. PASS12 produces YBOS output, and is used for most calibrations and for reconstruction of the tracks. It tends to double or triple the total size of the data that it outputs. PASS3 is used for calibrations that need a third pass, and is also used to create final calibrations for the TOF wall. It also produces a greatly reduced column-wise ntuple (CWN) (in the framework of the CERN libraries) to allow for final analysis. Due to the large number of calibration constants, the constants are stored in a relational database (DEC RDB), indexed by run number and calibration type.

As a final definiton, the term "clean beam", as used below, is formed from the two triggers INT and BEAM, by requiring the BEAM bit to be set in trigger word 1 (section 2.11.2) and no INT bit to be set in trigger word 2(section 2.11.1). The term comes from the fact that the INT bit in trigger word 2 will always be set if the Bull's Eye is below threshold, even if the event count within the scaledowns caused the LVL1 trigger to take the event as an unbiased BEAM event. Therefore the cut on trigger word 2 is used to remove the $\sim$ 6% of unbiased BEAM events for which the Bull's

Eye is below threshold. Note that, for the 6 $A{\cdot}GeV$ runs noted in section 2.11.1 for which the INT trigger was scaled-down before entering into the Trigger Supervisor, this mechanism is not effective. In addition, the FOLLOW bit (section 2.11.1) is required not to be set. This definition of clean beam is not as restrictive as our final set of "good event" cuts, detailed in 5.6.2.

3.2 Calibration of the Global Detectors

3.2.1 Charge on the BTOT (Z_{BTOT})

The ADC readout of the BTOT needs to be calibrated to allow for a consistent measurement of the charge of the beam. This calibration is done run-by-run, and places the sum of the ADC readout of the two phototubes, ADC_{BTOT_1} and ADC_{BTOT_2}, at a value of 79. The calibration constants are formed at the PASS0 stage. The mean of the distribution of ADC values, taken only within a predetermined window, is formed for values from clean beam events. The pedestals of the ADCs are determined from "Pedestal" runs, in which a pulser is used to trigger digitization, and the beam is not allowed to reach the target. At the PASS12 stage, the pedestals are subtracted from the ADCs, and the resulting values muliplied by a factor to place their sum, Z_{BTOT}, at the correct value. Note that the gains of the tubes have already been roughly calibrated for the online cuts, and the ADC values do not vary greatly year-to-year. The accuracy attained by this procedure, as determined from run-by-run fluctuations in the mean, is approximatel 0.4 units of charge, or 0.2σ.

3.2.2 The Bull's Eye ($BE_{HARDSUM}$)

As discussed in section 2.6.1, there are some complications in the analysis of the Bull's Eye. The calibration is done run-by-run. The peaks of the 9 ADC values (one for each phototube, and one for their analog sum, the HARDSUM) are formed from clean beam events. The delayed readout and direct hits are subtracted event-by-event from the values that go into these peaks. The peaks are fit to Gaussians, and

calibration constants produced. These constants place the peaks of the individual at a value of 100 for the individual phototubes and 800 for the HARDSUM. The accuracy attained by this procedure, as determined from run-by-run fluctuations in the mean, is approximately 6 units, or $\frac{1}{2}\sigma$.

3.2.3 The NMA Multiplicity ($Mult_{NMA}$)

The operating characteristics of the NMA during the 1995 and 1996 running period required the calibration procedure to be changed from that described in [Ahl97], as mentioned in section 2.6.2. For that analysis, the calibration constants had been derived in PASS0. Unfortunately, the problem in the 1995 and 1996 data sets was not discovered until after PASS0, and the information necessary to calibrate had been lost. Therefore, the information was resurrected in PASS12, and the final, calibrated $Mult_{NMA}$ created in PASS3.

I will describe the original calibration method, and then present the modifications. Both methods were developed by James Chang at the University of California at Riverside(UCR).

Calibration

The smaller tubes at the front of the detector have a somewhat nonlinear response, due to their small size. The back tubes show a smaller level of nonlinearity.

Therefore the tubes are calibrated to second order. The pedestal, single-particle peak, and two-particle peaks are found, and the ADC value transformed into a hit value by the equation:

$$\frac{(2x_1 - x_0 - x_2)\,ADC^2 + [(x_2^2 - x_0^2) - 2\,(x_1^2 - x_0^2)]\,ADC + x_0\,[2x_1\,(x_1 - x_0) - x_2\,(x_2 - x_0)]}{(x_1 - x_0)\,(x_2 - x_0)\,(x_2 - x_1)} \tag{3.1}$$

where x_0 is the ADC value determined for the pedestal peak, x_1 is that for the single-particle peak, and x_2 is that for the two-particle peak.

One needs to be able to find these three constants in a robust way. The original method to do this was:

- Histogram the hit distributions module-by-module for BEAM events, or, if the sample of BEAM events is not sufficient, for peripheral events as determined by the ZCAL. Call this the "PEDESTAL" histogram.
- From the PEDESTAL histogram, determine the pedestal position by finding the ADC value that corresponds to the maximum number of hits.
- Also from this histogram, determine the width of the pedestal from the ADC value that corresponds to a 20% decrease in the number of hits from the peak.
- Move to a histogram containing all hits on a given module from all events. Call this the "ALL" histogram.
- Find the ADC point with the lowest value between the mean of the previously determined pedestal and the next maximum in hits at positive ADC values. Call this the "low point".
- Fit an exponential in the region between 0 and the low point.
- Subtract this exponential vertically from the ALL histogram. That is to say, at every point in the histogram, the number of counts is decreased by a number given by the exponential.
- Find the rough location of the one particle-peak in this subtracted histogram. This is done by averaging neighboring bins and searching for a maximum.
- Fit the subtracted histogram to a Gaussian in a window around the rough peak.
- Subtract this Gaussian from the histogram.
- Use the same method to find the two-particle peak on the doubly-subtracted ALL histogram.

Quality checks existed in this procedure to guard against instabilities. These

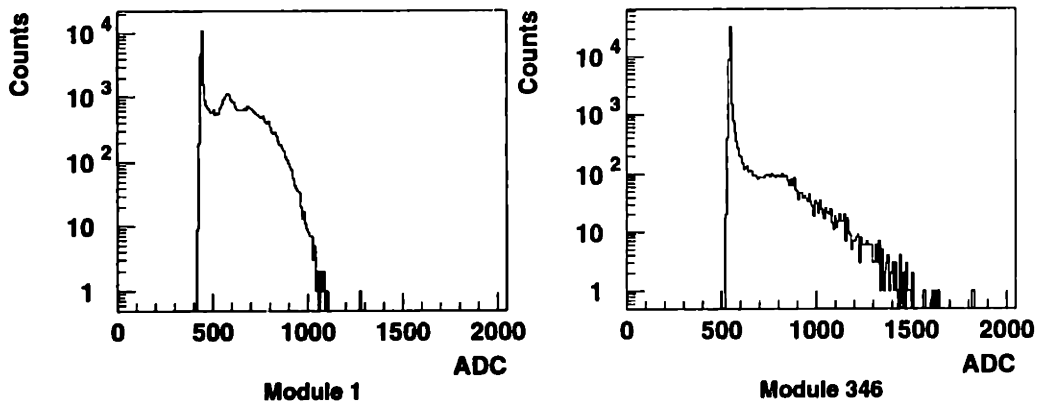

Figure 3-1: NMA module ADC distributions.

would call a module "BAD" if not passed, and the "BAD" modules would be removed from the multiplicity sum. In 1994, ~20 modules out of the total of 346 were designated "BAD". In the 1995 and 1996 data sets, the procedure resulted in ~50 "BAD" modules, with the number reaching as high as 100 in some cases. Since this would lead to a substantial correction for dead modules, it needed to be fixed.

The problem lay in the fitting of the two-particle peak. Figure 3-1 shows one of the worst-case distributions, along with one for which the peak finding worked relatively well. The two-particle peak is not very prominent in the "BAD" distribution. The dead modules tended to be clustered in backwards rings, which were known to be less nonlinear, and yet the reason given for these modules to be "BAD" was that the tubes were determined to be too nonlinear. The calibration procedure was fitting based on statistical fluctuations, and the resulting positions of the two-particle peak were falling far outside of the allowed values.

However, the position of the single-particle peak was relatively robust, and so a minimal modification was made to the procedure. Runs were combined in order to increase the statistics of the two-particle peak. It was noticed that the level of nonlinearity, measured by the ratio between the positions of the single and two-

particle peak, did not change strongly as a function of run within the run block. This ratio was therefore used to form a starting point for the fit of the two-particle peak run-by-run, which was further restricted to a limited range. The width of the peak from this fit was checked and, if the width was below a threshold, the fit was kept. Otherwise the starting point was used. I defer the discussion of the results of the new calibration procedure to section 5.6.7, in which the results as they apply directly to the data are discussed quantitatively.

Weighting

A weighting scheme is used on the NMA. This weighting scheme "bootstraps" the multiplicity distribution, based on the total multiplicity of an event, the resolution of the detector, and some parameters determined by the data.

Since the data analysis depends on the weighting scheme, I will summarize it here. For a given event, the so-called Real total multiplicity is obtained by summing the hits on all good modules, with these hits treated as Real numbers. A lower threshold of 0.5 is placed on the number that a given module can contribute to this sum, so if a module records, say, a multiplicity of 0.3, it is not added to the sum. As a function of this Real multiplicity, for every ring of the NMA there are a set of parameters that describe the probability of a particle to pass through the module. These parameters are determined from a linear fit to the data. The parameters are the means of two Poisson distributions, one of the number of charged particles that pass through the module, μ_{ch}, and the other of the number of γ's that convert in the lead at the front of a module, μ_γ. From these two parameters one can form the total probability for n hits:

$$B(n) = \sum_{i=0}^{\frac{n}{2}} P(2i, \mu_{ch}) P(n/2 - i, \mu_\gamma), \ n \text{ even} \tag{3.2}$$

$$= \sum_{i=0}^{\frac{n-1}{2}} P(2i+1, \mu_{ch}) P((n-1)/2 - i, \mu_\gamma), \ n \text{ odd} \tag{3.3}$$

where $P(n, \mu)$ is the Poisson probability to see n hits, given a mean μ. The various

factors of 2 come from the fact that the converted γ will give a signal of 2, one from the e^+ and one from the e^-. The calibrated hits are then summed into a "Weighted" sum, which includes the effect of detector resolution, to produce a total multiplicity. The weighting function used is:

$$W(h) = \frac{\sum_{n=0}^{\infty} nS(h,n)}{\sum_{n=0}^{\infty} S(h,n)} \tag{3.4}$$

$$S(h,n) = \frac{B(n)}{\sqrt{2\pi n\sigma_1^2}} exp\left(-\frac{(h-n)^2}{2n\sigma_1^2}\right) \tag{3.5}$$

where h is the Real hit number recorded by a module, and σ_1 is the width of the single-particle peak. Given perfect knowledge of μ_{ch} and μ_{gam}, this quantity gives the best predictor for the multiplicity.

μ_{ch} and μ_γ are derived ring-by-ring by linear fits to the mean number of hits in a module vs the Real multiplicity.

Note the presence of an ∞ in equation 3.4. Since a computer can't sum to ∞, the code actually iterates until the sum converges. This iteration can cause some effects in the final output for certain sets of parameters.

Also, one important note: the quantity used for a given module is integerized in the Weighted scheme in the region between 0 and 1. That is to say, if the module records a calibrated value of 0.49, the module will not be included in the sum, but if the module records a value of 0.51, it will be included in the sum, and will be included as a 1. In the Real scheme, the module with value 0.49 is also excluded, but that with value 0.51 is included with value 0.51.

For reference, at one point in the development, the actual meaning of the methods stored changed slightly. The revised meanings are listed in table 3.1.

Method Number	Calibration Method	Multiplicity Method	Unused Correction	Gap Correction
1	Mixed	Weighted	Y	N
2	Linear	Real	Y	N
3	Linear	Real	N	N
4	Mixed	Weighted	N	N
5	Mixed	Weighted	Y	Y
6	Non-Linear	Real	N	N
7	Non-Linear	Real	Y	N
8	Non-Linear	Real	Y	Y
9	Mixed	Real	N	N
10	Mixed	Real	Y	N
11	Mixed	Real	Y	Y
12	Non-Linear	Weighted	N	N
13	Non-Linear	Weighted	Y	N
14	Non-Linear	Weighted	Y	Y

Table 3.1: The NMA Multiplicity Methods as stored in 1995 and 1996. This table is patterned after that in [Ahl97]. It details the various method numbers and their meanings. All methods use all tubes. "Mixed" is a historical term, and in the final data is equivalent to "Non-Linear". Method 13 is the default method.

3.3 Chamber Calibrations

3.3.1 T1-T4 Timing

T1-T4 need to have the mapping of drift time to distance calibrated. The procedure to do so has not changed for many years.

Tracks are reconstructed using the previous set of calibrations, and the "signed" residuals formed between the tracks and the hits found. The signed residuals are defined as the distance between the tracks and an associated hit, multiplied by a sign corresponding to the direction between the hit and the track. This is done plane-by-plane, and the residuals fit to a third-order polynomial. The reconstruction is then redone, using the new calibrations, and wire-by-wire timing offsets fit. The process is iterated until the calibrations converge, usually twice, and sometimes needs intervention to prevent the fit parameters from wandering. The detection of such wander has evolved into an art.

An informed binary search is made through the data to find places where the

calibration needs to be performed. The timing process is performed for multiple runs, selected to span different running conditions, and the differences checked between the runs. The calibrations are quite stable with time, and for the data presented in this thesis only needed to be performed once per experiment, once for the 6 and 8 $A{\cdot}GeV$ running and once for the 2 and 4 $A{\cdot}GeV$ running. The high-energy $E917$ running period was somewhat longer than that for the low energies, and had a period where the timing shifted. Therefore there were 5 separate timing calibrations applied to this set of data.

The level of accuracy with which the calibration can be made is $\sim 10 - 30 \mu m$, as evidenced by the mean of the signed residuals after calibrations. T1 represents the upper edge of this range, along with the cells on the edges of some of the U and V planes. These cells are quite a bit shorter than the other cells in the chambers, and so the control of their fields is more difficult. As mentioned in 2.10.4, the level of nonlinearity is slightly higher in T1 than in the MIT chambers, and so is a bit more difficult to correct.

The spurious hits in the 1995 data set, as mentioned in 2.10.2, were discovered in this set of calibrations, and are not used in the determination of the constants.

3.3.2 TRF timing

As stated in 2.10.5, the TRFs have no field wires, and use foils instead of wires as their cathode planes. This, combined with the geometry of the cells, leads to a large level of nonlinearity in the mapping of drift time to distance. In addition, this nonlinearity has a time dependence, with the end result that the TRFs are calibrated run-by-run.

Calibration

The method for the calibration of the TRFs is detailed in [Wan96], so I will only state its basic principles here. Given that the cells of the TRFs are small, it is a good approximation that the distribution of hits along the cell is uniform. Therefore the distribution of distances along the cell should be uniform. However, the distribution

of times is not uniform. It is well-fit by a Gamma distribution:

$$dN/dt = C\left(\frac{t-t_0}{\tau}\right)^{\alpha} exp\left(-\frac{t-t_0}{\tau}\right) \tag{3.6}$$

where C,t_0 and τ are fit parameters. Using these parameters and the assumption that the true distance distribution is uniform between $(0, L)$, where L is the maximum drift distance, the measured distribution is inverted to obtain:

$$x = L\frac{\int_0^L \frac{dN}{dt}dt}{\int_0^\infty \frac{dN}{dt}dt} \tag{3.7}$$

The integrals are analytic, and routines exist to obtain their values.

Clustering

The reconstruction algorithm does not use the raw hits of the TRFs. Instead, a cluster analysis is done on the raw hits, and the tracking performed on the results of this analysis.

First, with the fit parameters obtained in the timing calibrations, two cuts are formed. These are the "LATE1" and "LATE2" cuts, formed so that 0.5% or 5%, respectively, of the fitted distribution falls beyond the cut in drift time. These cuts are placed on the times of the real hits. The actual number of hits satisfying these cuts can be significantly greater than is indicated by their nominal fractions. In a study performed on 1995 data [Mou98], ~5% of the hits satisfied the "LATE1" cut and ~20% of the hits satisfied the "LATE2" cut.

These cuts have implications for the clustering algorithm, a brief description of which follows.

- No hits on adjacent wires.
  - Hits not LATE1 are kept, position as in equation 3.7.
  - LATE1 hits are called BAD, and rejected.

- Two neighboring wires have hits.
  - Neither hit LATE2. Two clusters kept, position as in equation 3.7.
  - One hit LATE2. The LATE2 hit is rejected. The LR ambiguity is resolved for the other hit, in favor of the side of the rejected hit.
  - Both hits LATE2. One cluster created, with position at midpoint between the wires.
- Three or more neighboring wires have hits. All clusters formed have additional uncertainties given to them for the purpose of the tracking algorithm.
  - One cluster is formed at their midpoint.
  - Each hit not LATE1 forms an additional cluster at the wire position of the hit.
  - The additional cluster at the wire position of a LATE1 hit is called BAD, and rejected.

Therefore the clustering algorithm rejects some hits based on timing considerations, and, in the case of two neighboring hits, can do so for the 20% of hits that fall within LATE2. For most of the clusters containing more than one wire, the resolution of the cluster, stored for the purposes of the tracking algorithm, is increased to some multiple of the wire spacing to account for this. For the 1993 data, BAD hits were not ignored by the tracking algorithm. The CPU needs of the algorithm skyrocketed with this inclusion, and so for 1994-1996 BAD hits were rejected.

Further Concerns

The timing of the TRFs showed some unexpected dependencies on total multiplicity in the plane during the 1995 run [Mou98]. These did not seem to exist during the 1994 or 1996 runs. It is not known whether the dependencies are related to the efficiency problems. For the data of this thesis, no cuts were placed on the multiplicity of hits in the derivation of the calibrations.

Results

The residuals on the TRFs between fully reconstructed tracks and the positions of the hits range in width from ~150 μm at their best to ~300 μm at their worst. Signed residuals cannot be used to measure the quality of the timing calibrations, because a strong correlation exists between the allowed range of the signed residual and the allowed set of times. This correlation can be ignored in T1-T4 since the cells are larger.

3.3.3 Geometry

In order to accurately reconstruct tracks, the positions of the wires must be known. Therefore a set of procedures to adjust the positions of the chambers and the wires within them has arisen over the years [Ste90]. The procedure is designed to minimize the sensitivity to fitting effects. It uses straight-line tracks from "Zero Field" runs, runs taken with the Henry Higgins magnet off, to align the chambers and wires. These are combined with higher statistics data from both field polarities, both to reach portions of the chambers that are shadowed by the magnet and to minimize a few other effects. The alignment is always done by minimizing the residuals between a reconstructed track and the hits on the chambers.

The accuracy of this procedure is ~50 μm, although it should be noted that the procedure has a few degeneracies. The geometry was adjusted slightly for the 1995 data set, and again for the 1996 data set. In both cases the same shift was applied for all angles of the spectrometer, and involved shifting as a whole the relative positions of the chambers behind the magnet against those in front of the magnet.

The geometry of TR1MIT also needed to be tuned at the start of the $E917$ run, but the requirements for this are much less stringent. This was done at the installation stage of the detector, after first beam, again by looking at residuals from tracking. It did not change subsequently.

For the analysis of this thesis, the geometry of the TOF wall was tuned angle-by-angle, once for the 1995 data set and once for the 1996 data set. This is detailed in

section 4.8.

3.3.4 TR1, TR2, TR1MIT

Since these are multiwire proportional chambers, they do not need to be calibrated. In addition, since their resolution is significantly poorer, their geometry was not retuned after the data run. TR1 and TR2 have had the same geometry for years.

3.4 TOF Calibration

The TOF is one of the most sensitive pieces of equipment in the experiment. The requirements on its calibration are strict, so the procedures used are necessarily rather advanced.

The TOF wall is used in three ways in the analysis.

The first way is as the only detector in the experiment (as used in this analysis) that can measure a full 3-dimensional space-point. As detailed in 4.3, the Y-position measured on the TOF wall is used as a seed to start the reconstruction behind the magnet.

The TOF wall's primary purpose, though, is given by its name. It must measure the time of flight (TOF) of a particle, and it must do this both precisely and accurately. This serves two purposes: as described in 4.3, a "transit-time" correction is applied to the hits on the chambers behind the magnet, based on the TOF of the associated hit on the TOF wall. Therefore, the TOF calibrations affect the quality of the tracking, although only at the level of $\sim$1 ns.

Most importantly, though, the TOF is used to determine the particle's identity, as described in 4.8.

The basic method used for calibration is similar to that used in the geometry: form a residual between an expected and found value, and adjust the constants until the two match. The residual is defined in terms of $TOF_{expected}$, which can be formed from a mass hypothesis, the measured momentum of the track, and the measured

path length of the track, as:

$$TOF_{expected} = \frac{L}{c}\frac{\sqrt{p^2 + m^2}}{p} \tag{3.8}$$

where p is the momentum of the track, L is the path length taken by the track to the TOF wall, c is the speed of light (taken to be 27.98 cm/ns), and m is the mass from the mass hypothesis. The residual, Δ_{TOF} is defined as:

$$\Delta_{TOF} = TOF_{found} - TOF_{expected} \tag{3.9}$$

where TOF_{found} is the TOF measured by equation A.10 below.

The required accuracy of the procedure is $\sim \pm 20$ ps in TOF, and $\sim \pm 1$ cm in Y. This level of accuracy is obtained by the procedure, although to satisfy the requirements for the $E917$ data a modification needed to be made, as described in appendix A. The need for the modification was not found until the analysis of the $E917$ data. To a lesser extent, the problem also affects the $E866$ data at 2 and 4 $A{\cdot}GeV$, but, for reasons described in appendix A, only for a certain portion of the TOF wall. Therefore in the analysis of the 2 and 4 $A{\cdot}GeV$data, a fiducial cut is placed so that all measured tracks lie within the portion of the TOF wall covered by protons. The cuts are, specifically, $40 < Slat < 132$ for positively charged particles and $40 < Slat < 120$ for negative particles. As described in section 5.4, the cuts are made based on the known geometry of the TOF wall, and are applied to all tracks, within the framework of the acceptance calculation.

The results of the various calibration procedures are quite good, well within the requirements. The average resolution across the TOF wall is less than $130ps$ for all running periods, as described in 5.5.

For further details about the calibration procedure, see appendix A.

Chapter 4

Collaboration Analysis *II*: Reconstruction and Particle Identification

The task of reconstructing a particle trajectory from a collection of lines measured at various points in z is daunting. A set of complicated algorithms for this purpose has therefore developed over the years in the $E802$ string of experiments. The algorithms used in this thesis are for the most part based on the work of F. Wang [Wan96] for $E866$, and of P. Rothschild [Rot94] for $E859$, but have had some significant modifications for the 2 and 4 $A \cdot GeV$data due to specific problems in the detector systems. From this work, a few modifications were made in the algorithm used by $E917$ in order to produce more accurate results. Much of the modification work was performed by M. Moulson[Mou98] at Columbia.

Because of these modifications, this chapter, as the previous chapter, is meant to serve as a repository of information.

4.1 Overview

The Henry Higgins spectrometer (figure 2-1) has a natural division into two parts, one in front of the magnet, towards the target, and one behind the magnet, towards the

TOF wall. There are no magnetic fields in these two sections, so particle trajectories are straight. Hence all reconstruction algorithms in the $E802$ string of experiments have had two stages corresponding to this division. The terms "front" and "back" refer to these two stages. In $E866$, the construction of the TRF's allowed these algorithms to completely split, such that reconstruction in front proceeded independently from that in back. This meant that a third algorithm needed to be produced, in order to match the front tracks with the back tracks. This algorithm is called, oddly enough, MATCH.

There is a fourth stage, which is not strictly a reconstruction stage, but which will be discussed in this chapter, since it is associated with the tracking. This is the particle-identification stage, which produces from a track, the momentum of which has been measured by the magnet, and the TOF wall, which measures the time the particle takes in its trajectory, the identity of the particle. This is termed the "PID" stage, which stands for "Particle IDentification". The algorithm used for this is called PICD.

There are a few stringent and mutually exclusive requirements for algorithms of this type. First, the algorithm must be robust. That is to say, it must not find spurious particles, the effects of which on the results can be very difficult to disentangle. Second, the algorithm must be accurate. This means that it does not introduce into the results inaccuracies additional to those produced by effects in the detectors. Third, the algorithm must be efficient. That is to say, it must find the most tracks possible, or at least, when it does not find a track, lose the track in a predictable way.

Successful algorithms balance these requirements, but can never satisfy them all. Much of the discussion of the success of the algorithms is relegated to chapter 5.

4.2 Definitions

One term that will come up frequently is that of a "road". A road consists of a line, formed between two hits acting as a seed, combined with two parameters. These parameters are a search width about the line, within which one collects hits, and a

cutoff, which determines whether the hits on the road are kept and passed to the next stage of the algorithm. In varying ways, our algorithms are all based on this construct.

Another important concept is that of filtering. Every tracking algorithm has a set of filtering stages, in which tracks are called duplicates, based on some set of criteria, and the choice of which duplicate to keep is made based on some other set of criteria. I will call the first set of criteria the "duplicate criteria", and the second set of criteria the "rejection criteria". Most of the modifications made in this analysis were made to the rejection criteria, after a careful rethinking of their effects by M. Moulson at Columbia.

Throughout this chapter I will be referring to particle "momenta". These are not strictly momenta. The spectrometer does not measure momentum and charge separately, since a magnetic field does not act on these separately. Instead, it acts on p/Z, where Z is the charge of the particle. This quantity is termed "rigidity". However, since this analysis is interested in particles with $\mathrm{abs}(Z) = 1$, I will use the two terms interchangeably. I will, however, place a sign on the momentum in some places, corresponding to the sign of the particle's charge, but in other places use an unsigned momentum. Note that this has implications for particles of higher charge, since multiple scattering is used in many places to determine cuts and is proportional to Z^2.

4.3 Reconstruction in Back: A34

4.3.1 History

The algorithm used in this thesis for reconstruction behind the magnet is termed "A34". The term is a bit cryptic, but comes from a severe shortening of the name of the fuller algorithm "AUSCON", from which it was recycled from $E859$ for $E866$.[1] The "34" comes from the fact that it performs reconstruction using T3 and T4.

[1]The "AUS" in "AUSCON" stands for "Australian", since the author of the algorithm, Peter Rothschild, was from Australia.

The algorithm has had some minor modifications, once for $E866$ by M. Baker, and once for this data set by G. Heintzelman. The modifications by M. Baker removed some dependencies on the ordering of the tracks, which are not randomized. The modifications by G. Heintzelman, which are new for this analysis, removed further ordering dependencies in the filtering, and updated certain places to correctly include the high segmentation Y plane on T4, which was new for $E866$.

The results of these modifications were minimal, on the order of 1 track in 100,000.

4.3.2 Description

The algorithm uses the three detectors in back, TR1, TR2, and the TOF, which are of high segmentation but low resolution, as seeds for pattern recognition. It then uses the higher accuracy but lower segmentation drift chambers to restrict the tracks so found, and to determine the track parameters.

The first stage of the algorithm is exclusively in the $x_{spec} - z_{spec}$ plane (section 2.1.2). First, it forms roads from all combinations between hits on TR1 or TR2 and the TOF wall. These roads collect hits on the T3 and T4 X planes, and have one set of parameters, a search width and a cutoff in the number of hits collected for a road to be valid. If the road is valid, the algorithm forms further roads, with another cutoff and search width, from all combinations of hits collected on the outermost X planes on T3 and T4. If the hits along these roads are above the cutoff, an "X track" has been found, the parameters of which are then determined by a straight-line fit to the hits and pushed onto a list of found tracks. It performs the same set of steps for hits on the next outermost planes on T3 and T4 that have not already been associated with a track.

Then the algorithm moves to the $y_{spec} - z_{spec}$ plane. For every X track, it forms a road between the target Y position (which has been determined run-by-run previously, as will be described in section 4.7.1) and the TOF hit associated with the X track. The same procedure as in the X case is used to find valid "Y" tracks.

Every X-Y combination so found is then verified on the U and V planes, using the following procedure. A road is formed from the X-Y combination, projected into

the U and V directions, and the hits on the U and V planes collected. Again, if the number of hits so collected is above a cutoff, a full 3-dimensional track is formed, but in this case a further cutoff is made on the total number of hits found. A full 3-dimensional fit is performed to all (X,Y,U,V) hits so collected, and the track pushed onto the stack of all found tracks.

Once all tracks have been found, they are filtered. The duplicate criterion is simply the number of shared hits, and the rejection criterion a modified χ^2 of the final fit. The χ^2 is modified, in that, rather than decrease the number of degrees of freedom for missing hits, the missing hits are assumed to be at the edge of the search width and added into the χ^2.

4.3.3 General Results

The algorithm performs well in the environment behind the magnet. The multiplicities behind the magnet are low for the most part, and so various of the simple steps made in the formation of tracks, as compared to TRFCK (section 4.5.2) or the even more advanced TRFCK95 (section 4.5.5) do not seem to have a large effect.

However, there are known or suspected sources of background in the back tracking. These include shower from the edges of the magnet aperture and showers from the shielding blocks mentioned in section 2.4.3, which are quite close to the spectrometer at 14 degrees.

In addition, the projection to the target is not well determined by the tracking in back, because of the need to project through the magnet. This target projection is needed in many parts of the analysis. Therefore the experiment was designed from the beginning to do tracking in front of the magnet.

4.4 TRF efficiencies

As mentioned in section 2.10.5, the TRF's were inefficient in 1995. The inefficiency was found to have a dependence on β, and was largest at high β. This dependence is to be expected from an energy loss effect, since the energy loss, and therefore the mean

pulse height of the signal in the chamber, increases as β decreases. The inefficiency in $E917$ data was consistent with 0 to the level of this procedure.

In order to handle this problem, significant changes were made in 1995 to the tracking algorithms in front of the magnet.

4.5 Tracking in front: A12, TRFCK, TRFCK95

4.5.1 A12

A12 is the front portion of "AUSCON". It is used primarily in this thesis as a cross-check, both of TRF efficiencies and of TRFCK95, since it does not include some of the more advanced procedures of TRFCK and TRFCK95.

The algorithm as originally written is basically the same as A34. However, since no high-segmentation detectors existed in front in $E859$, the initial roads are formed by projecting the tracks from A34 through the magnet to the target. Hits are collected about these roads, and tracks formed in the same order as in A34: first X tracks, then Y tracks, and finally verification on U and V.

Four aspects of this procedure are notable. First, simple cutoffs on the number of found hits are be ineffective, due to the segmentation in front of the magnet. Therefore, at each stage, tracks are cut by reprojecting through the magnet, and requiring that the found tracks match those from A34. The projection is done rather empirically, based on fits to data, rather than from any prior knowledge about the configuration of the magnet. The cuts determining a valid match were derived from projections of tracks onto the front planes of T3 and the back planes of T2, performed for the $E859$ configuration of chambers. This procedure is not the same as the one used in MATCH (section 4.6), and is less well-founded. It is also tighter at low momentum. However, the is absolutely necessary to avoid an exponential increase in the number of tracks found, at least in the configuration used in this analysis.

Second, in its original configuration, filters were placed at each stage. One of the filters required that a single track in back produce a single track in front, therefore

using track parameters from early stages to remove sets of hits from consideration at later stages of the algorithm. At early stages the tracks are constrained less fully than the final tracks, so these cuts were removed.

Third, as described in section 4.5.2, TRFCK contains a complicated refitting procedure, in which hits far from the track are removed and the track parameters refit. This is to avoid problems in the determination of track parameters from the inclusion of spurious hits. No such mechanism exists in A12.

Fourth, the parameters of the algorithm had not been retuned since $E859$. Since T1 was replaced for $E866$, and since the position of T2 had changed in 1994, such a retuning was necessary.

Therefore, in order to make the efficiency determination robust, the following changes were made. Most of these changes were made by G. Heintzelman.

First, the requirement that a single track in back produce a single track in front was dropped. This required a number of changes to the implementation of the algorithm.

Second, the final filtering algorithm was changed to reflect the increased pressure put upon it from the first change. The duplicate criteria were adjusted by the addition of a cut on "shared chambers". For a given chamber, T1 or T2, a view (X,Y,U or V) is considered shared if the number of hits shared on that view is ≥ 2. If the number of shared views on a chamber is ≥ 2, the chamber is considered shared. If both T1 and T2 are shared, the two tracks are considered duplicates.

Also, the algorithm to find duplicates was modified. In high-occupancy environments, there is a significant possibility of a "percolation" effect. Take three tracks, tracks 1-3. There is a possibility that track 1 is found to be a duplicate of track 2, based on one set of hits, track 2 is found to be a duplicate of track 3, based on a disjoint set of hits, and so track 1 is not a duplicate of track 3. The decision as to which tracks to keep in such a situation becomes complicated. A12 was modified to use a "killed"-"killer" algorithm, in which multiple loops through the data are made to find tracks that are "killed" by the duplicate and rejection criteria, with the end result that no track that is killed can kill another track. This is a rather loose algorithm, but the decision was made to allow MATCH (section 4.6) rather than A12 decide

among the candidates. The rejection criteria in A12 consists of the same modified χ^2 used in A34, performed only among the front hits, while the MATCH criteria use information from both the front and back portions of the spectrometer.

Third, the parameters were retuned. The residuals between tracks found and the hits associated with the tracks were formed for each stage of the algorithm. These residuals have a double-Gaussian shape, as shown in figure 4-1. The widths of the inner Gaussians from fits to the residuals show some dependency on plane, and there is some reason to believe that at least some of the tails are due to multiple-scattering. There is also a combinatoric effect, which can produce a background under the peak. Therefore, for each view on each chamber the search widths were separately set to 5 times the σ of the inner Gaussians. In addition, the AUSCON matching criteria were loosened, to decrease the effects of cutting with two different methods on the matching between front and back.

No attempt was made to add a refitting procedure to the algorithm.

The end result of these changes increased the number of front tracks found by A12 rather significantly. However, for data from the 1994 data set, the total number of matched full tracks was found to be quite similar to the number found by the collaboration-standard AUFCK (section 4.7). The TRF's were efficient in 1994. There are, however, discrepancies at low momentum tracks. For further discussion see section 4.7.

4.5.2 TRFCK

4.5.3 Overview

As used in this thesis, TRFCK (the name of which comes from its use of the TRF's) is nearly the same as the algorithm described in [Wan96], with the retuned parameters and small fixes described in [Ahl97]. It was further modified by M. Moulson for this data set. It is used for the 1996 data set at 6 $A{\cdot}GeV$ and 8 $A{\cdot}GeV$, since for this data set the TRF's were found to be efficient. Very minimal differences were found between the results of TRFCK and TRFCK95 (section 4.5.5) in 1996. This statement

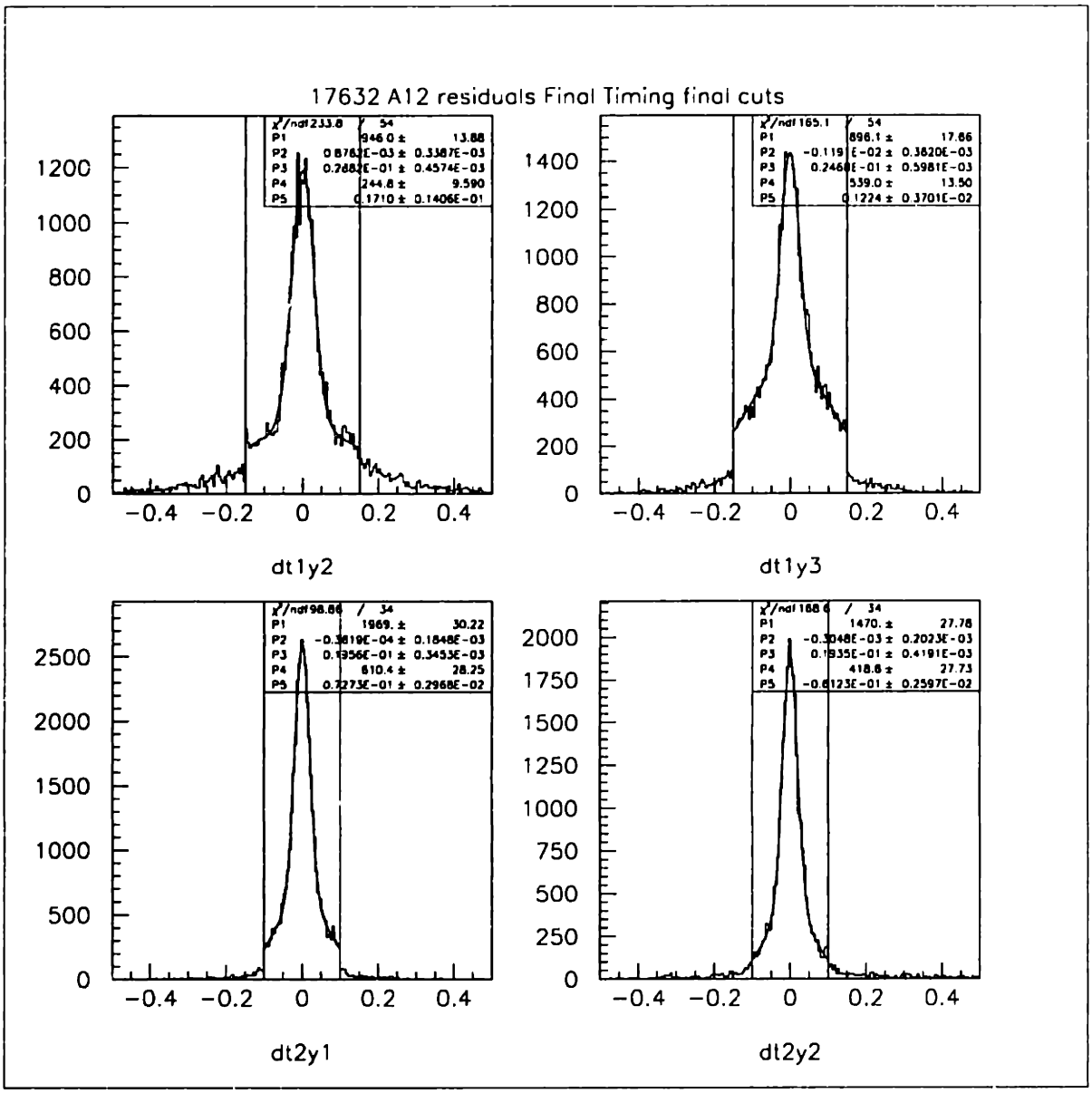

Figure 4-1: The residual of the hits from tracks in Y at the track collection stage. The terms 'dtXyY' refer to residuals on chamber X, plane Y. The cuts are indicated by the lines. The first planes on each chamber are not shown, since no search is ever performed on these tracks.

is not true for the 1995 data set. This, combined with the fact that the CPU needs of TRFCK95 are ~2 times larger than those of TRFCK, led to the decision to use TRFCK in 1996, rather than TRFCK95.

The Algorithm

The algorithm starts with the TRF's, since they provide points of high segmentation in front of the magnet. The quantities used for the TRF's are the clusters described in section 3.3.2. For each view (X,Y,U,V), roads are formed using the hits on the TRF's, along which hits are collected in the drift chambers T1 and T2. The parameters of the tracks formed along the road are fit using these hits, with an iterative rejection process used to reject hits far from the fitted track. This process consists of using the track parameters to reform the road, recollecting the hits along this road, and fitting. The tracks for a given view are filtered, and the resulting tracks pushed onto a stack of "1-D" tracks.

The machining error in the UV planes of T2 (section 2.10.2) plays havoc with this process. The angle of the wires in these planes is not the same as that on T1 or the TRF's, and is dependent on the position of the hit along the chamber. Therefore, the search widths in U and V are widened, taking into account the dependencies of the angles. The end result is that the number of 1-D tracks found in the U and V directions is ~4 times larger than that in the X and Y directions, with larger discrepancies as the multiplicity increases.

The number of 1-D tracks found is large, on the order of a few hundred at the extreme. To give a feel for relative sizes, the maximum number of real tracks found in an event is ~10, and the probability for this is extremely low. The high number is due to random combinatorics.

Therefore, the 1-D tracks are collected and matched to form "2-D" tracks. This is where TRFCK95 and TRFCK diverge. TRFCK divides the 1-D tracks into two types, those in X and Y, and those in U and V. It forms XY combinations separately from UV combinations, and verifies each combination by both the presence of a third 1-D track and hits on chambers in the other view. That is to say, if an XY combination

is verified by a 1-D track in U, then the 2-D track formed by this combination is projected onto the V chambers, and hits gathered along these projections. If there are enough such hits, a full 3-dimensional fit is made to all hits. The parameters of the resulting track are used to form a 3-dimensional road, projected onto all chambers. Along this road hits are gathered, from which the 3-dimensional track is refit. Again, this process is iterated a few times, and, if the final track contains enough hits, the resulting track pushed onto a stack of "2-D" tracks. A final filtering of this collection of tracks is then performed.

Left-Right Ambiguity

As mentioned in section 2.10.5, the TRF's do not have a mechanism for resolving the left-right ambiguity except in special cases. Since the segmentation of the drift chambers is lower than that of the TRF's, the stagger in these chambers does not help this situation as much as might be hoped. A doubling of tracks leads to a combinatoric effect much larger than a factor of 2, and so at various stages of the algorithm, attempts to resolve the left-right ambiguity are made. However, if simply applied, this would imply that track parameters determined at an early stage would affect the position of hits used at a later stage. Due to the effects of this, at various stages of the algorithm the left-right determination is erased, with the exception of two-hit clusters for which the ambiguity has been resolved by the cluster characteristics.

Also, as noted in section 3.3.2, clusters of different types have their resolutions increased for the purposes of the tracking algorithm. A similar procedure is used in cases in which two 2-D tracks share the same TRF hit, but pass on opposite sides of the wire.

4.5.4 Changes for $E917$

The filtering of both the 1-D tracks and the 2-D tracks changed for the 1996 data set. The filtering was one of the major improvements for TRFCK95, and has a few effects (section 4.5.5). One of these was an improvement in speed.

After some studies of various distributions of shared hits, all criteria were modified for TRFCK95. The duplicate criteria for TRFCK remained as it had been, for consistency with 1994 data, but there was a clear case against the original rejection criteria.

The terms "left" and "right" are used in this scheme to refer to combinations of chambers, T1+TRF1 called "left" and T2+TRF2 called "right". Two tracks are called duplicates in the following cases.

- The number of total shared hits are above a cutoff, or
- The number of left and right hits shared are summed separately, as are the number of left and right views shared, where a view is shared if the two tracks share one or more hit on a view. If the number of left and right hits shared is greater than a cutoff, and if the number of left and right views shared is above a cutoff.

The rejection criteria were modified. First, if two tracks are duplicates, the track with a greater number of hits is kept. If the two tracks have the same number of hits, the track with the greater number of TRF hits is kept. If, further, the two tracks have the same number of TRF hits, the track with the higher probability of χ^2 is kept. If the two tracks have the same probability of χ^2, the track parameters are tested to see if the track is an exact duplicate. If so, one is arbitrarily deleted. If none of these tests are passed, both tracks are kept.

Finally, the rejection algorithm used is a "mark and delete" one, in which a pass through the tracks is made and all duplicates between all tracks marked, irregardless of whether the tracks are themselves duplicates. One of the duplicates marked in this way is then deleted, based on the rejection criteria. This is in contrast to the method used in A12.

Results

The effects of the changes to the filtering are largest on close tracks. The total fraction of tracks that are close in both x and y is small, and so the changes do not significantly

impact the single particle distributions studied in this thesis. They are, however, somewhat critical for HBT and resonance studies, which led to the decision to make the changes. In terms of the single particle distributions, the inefficiencies in this region are taken into account by the insertion method, as described in (section 5.3). The values of the inefficiency are obtained separately, and applied separately, for the specific tracking algorithm used at each beam energy.

4.5.5 TRFCK95

History

TRFCK uses the TRF's at a fundamental level. In 1995, the TRF's were inefficient. Therefore, it was expected that the collaboration's standard reconstruction algorithm, AUFCK, would suffer. A rewrite of TRFCK was performed to decrease its sensitivity to the inefficiencies. The work was done by M. Moulson, but will not be discussed in his thesis. Therefore it will be discussed here.

Principles

The basic reasoning behind TRFCK95 is simple. TRFCK requires that 7 TRF hits be registered along a track. One could think of relaxing this to 6, using increased requirements on the drift chamber hits to make up the difference, but then if the hits were lost on different views the algorithm would still lose the track. The algorithm requires three 1-D tracks, which are seeded by TRF hits, and so the TRF hit requirements are not on a simple sum. Therefore, the combination of 1-D tracks into front tracks needed to be modified.

The algorithm uses TRFCK's 1-dimensional tracking, unchanged, but in the creation of full three-dimensional tracks allows combinations consisting of only two 1-D tracks to be valid. It then uses hits, rather than tracks, on the other chambers to account for the reduced selectivity. The combinatorics and specific configuration of the inefficiencies are such as to reduce a large effect to the order of a few percent.

However, the implementation was not so simple. TRFCK treats the views asym-

metrically. Only combinations of X and Y, or U and V, are allowed, with the UV combination decreased in importance. In order to gain back the efficiency, all 6 combinations of views needed to be considered: XY, XV, XY, YU, YV, UV. Since the number of 1-D tracks in the U and V views is larger than that in the X and Y views, the combinatorics increase greatly. This puts greater stress on the filtering algorithms, the changes to which are described in section 4.5.2.

View Combination

The actual algorithm used for combination is far too complicated to go into here. Suffice it to say that it is cleaner than that of TRFCK, and treats the 6 view combinations in a nearly uniform way.

The views are not treated completely uniformly. In the case of duplicate combinations, it weights the combinations based on the angle between the views. The full track parameters determined from a crossing between X and U, say, are less well-constrained than those from a crossing of X and Y, since the angle between X and U is only 30^o, while that between X and Y is 90^o. In selecting whether to use an XY match or an XU match, all other things being equal, the algorithm will prefer to use the XY match. If three or more combinations of 1-D tracks are found to form a valid track, the algorithm proceeds much as TRFCK.

Other than the combination stage, it is very similar to TRFCK, with the same type of refit stages. This means that all information about the actual views used to gather hits is thrown away in the final fitting stage. The final fitting stage performs the fits on a collection of hits, and does not directly depend on the methods used to collect the hits.

Filtering

The duplicate criteria are based on shared hits, and are different between TRFCK95 and TRFCK. The requirements consist of the following, each of which can cause two tracks to be called duplicates if the number calculated is above a threshold.

- TRF hits, with shared hits counted by chamber.
- Number of drift chamber views shared, where a view is determined to be shared if the number of hits shared on a given view (X,Y,U,V) is above a cutoff
- Number of views shared in the "left" and "right" portions of the front tracking, where "left" refers to the combination T1+TRF1, and "right" refers to T2+TRF2.
- Number of total views shared, where a total view is shared if the number of shared hits on the view, counted across all chambers, is above a cutoff.

As with the modified TRFCK, the rejection algorithm is a "mark and delete" one, although for historical reasons it is implemented somewhat differently from the one used in TRFCK. The two implementations are equivalent, but the one used in TRFCK95 is slightly less memory-intensive.

4.5.6 Results

The results from TRFCK95 are good, and so it is used as the final tracking algorithm of this thesis for the 1995 data set (2 and 4 $A{\cdot}GeV$). The results will be discussed in section 4.7.

4.6 Matching between the Front and Back: MATCH

4.6.1 Overview

MATCH was developed by F. Wang at Columbia, and is described in [Wan96]. For a further discussion of the implications of this algorithm to the acceptance calculation,

and to the momentum determination in the magnet, I refer the reader to [Ahl97]. The MATCH algorithm has been used unchanged in every $E866$ analysis, and in the analysis of this thesis.

4.6.2 Implementation

The purpose of the algorithm is to match front tracks to back tracks, and from this determine the momentum of the particle measured by the track. We call such a matched set of tracks a "full track".

The algorithm depends on three parameters for its selectivity. The three parameters have as their basis an effective-edge approximation to the field of the Henry Higgins magnet, adjusted based on approximations to the actual field shape. For each combination of front and back track, residuals are formed in the parameters, and combinations cut based on a momentum-dependent width.

Multiple combinations are not allowed for a given front track or back track. That is to say, a single front track can only match to a single back track, and vice-versa. When, for a given back track, say, the combination with two front tracks falls within the cuts, one combination will be rejected. The rejection criterion is the sum in quadrature of the three residuals, with a relative weighting described in equation 4.4 below. All combinations within the cuts are kept in the data stream, with rejected duplicates marked bad.

The momentum determined by the algorithm is also adjusted based on the modified field shape. The level of adjustment is $\sim 1\%$ at its maximum, and produces a mean shift of $\sim 0.5\%$. These numbers are for the 1993 $E866$ data set, for which the algorithm was developed.[Wan96]

The widths of the residuals have a momentum dependence that is well-motivated from multiple-scattering arguments, but have parameters that were fit from the 1993 data set. They were not refit for the 1995 or 1996 data set, but were checked in the process of tuning AUSMATCH (section 4.7), and seem to describe the data relatively well at low multiplicity. The data required the parameters for AUSMATCH to be slightly larger than those for AUFCK. This check was previous to the algorithmic

changes in TRFCK and TRFCK95.

Multiple-scattering is not simply a function of p, but of βp. Therefore the cuts applied are also dependent on β. Rather than use the TOF wall to determine β, the particle's mass, determined by the PICD algorithm (section 4.8), is used to calculate βp, and the matching reperformed with mass-dependent cuts. The cuts for the data presented in this thesis remained at the 4σ level, as used in [Ahl97], rather than at the 3σ level, as used in [Wan96]. The maximum mass used in this scheme is that of the proton, so the cuts placed on deuterons and higher mass nuclei are tighter than 4σ.

The acceptance calculation, described in section 5.4, accounts for these adjustments in an empirical way, but is less sensitive to their effects.

4.6.3 Description of the parameters

Assume, for a moment, that the field of the Henry Higgins magnet is very simple. Assume that there exists in a box of a given size in the magnet coordinate system $(x_{magn}, y_{magn}, z_{magn})$(section 2.1.2), a uniform magnetic field along the y_{magn} direction. Call the strength of this field B. The geometry of a particle's trajectory in such a field is also simple.

There are two relations from this geometry. The first determines the momentum in the $x_{magn} - z_{magn}$ plane. This momentum, p_{xz}, is related to the radius of curvature of the track in this plane by:

$$R = \frac{p_{xz}c}{qB} \tag{4.1}$$

where c is the speed of light, q is the charge of the particle, and B is the strength of the field. From the geometry of the problem, this works out to a relation between p_{xz}, the length of the magnetic field L, along z_{magn}, and the angles between the particle's incoming and outgoing trajectories and a line perpendicular to the face of the magnetic field, θ_{in} and θ_{out}. This relation is given by:

$$p_{xz} = \frac{qB}{c}\frac{L}{\sin(\theta_{in}) - \sin(\theta_{out})} \tag{4.2}$$

Therefore, in this approximation, one can completely determine the momentum vector from the parameters of the front track, which give θ, ϕ, and θ_{in}, and those of the back track, which give θ_{out}. The θ and ϕ are necessary to convert p_{xz}, a projection into the xz plane, into a full momentum vector.

The second relation is an identity strictly satisfied, in this approximation. It is therefore useful in restricting possible matches between front tracks and back tracks. We cannot simply form all combinations of front and back tracks and determine the momentum of the combination from equation 4.2. That would lead to false combinations. However, in the $x-z$ plane the relation:

$$\alpha_{in} + \alpha_{out} = 0 \equiv \Delta\alpha \tag{4.3}$$

is always satisfied, where α_{in} and α_{out} are the angles between the front and back track segments, respectively, and the chord joining the projections of the track segments onto the front and back faces of the magnet. This constraint produces one parameter, called, confusingly, $\Delta\alpha$, which is expected to be zero for a field of perfect cutoff, and in the absence of multiple scattering between the front and back of the spectrometer.

The second and third parameters are determined in the vertical direction, along y_{magn}. In the effective edge approximation, dy/ds, where s is the direction along the path of the particle, is the same before and after the magnet. Therefore the quantity $\Delta dy/ds$ should be zero. Also, Δy_{mid}, which is the difference in y of the projection to the midpoint of the magnet, should be approximately zero, given the aspect ratio of the experiment.

The rejection criteria for duplicates is determined by a weighted sum in quadrature of these residuals:

$$RC = \sqrt{\left(\frac{\Delta\alpha}{\sigma_{\Delta\alpha}}\right)^2 + \frac{1}{2}\left(\left(\frac{\Delta dy/ds}{\sigma_{\Delta dy/ds}}\right)^2 + \left(\frac{\Delta y_{mid}}{\sigma_{\Delta y_{mid}}}\right)^2\right)} \tag{4.4}$$

However, the magnet's edge is only approximately sharp. To correct for systematic shifts seen in the residuals, the algorithm models the magnetic field with a linear

rise at both edges of the field. The magnet is also allowed to shift in z_{spec} from the surveyed postion. This shift was changed between the 1993 and 1994 analyses, but no change was made between the 1994 and the 1995 or 1996 analyses. The width of this linear region is constant across x_{magn}. In the $y_{magn} - z_{magn}$ plane, the linear region ranges from 0 at the top and bottom of the magnet to a maximum at the center of the magnet. This dependency of the length of the rise on y implies that the pathlength of a particle in the field depends on the y position of the particle at the faces of the magnets.

Shifts are then applied to the momentum that has been measured, based on the vertical focusing approximation and the lengths of these regions. The shifts modify equation 4.2 to:

$$p_{xz} = \frac{\frac{q}{c}BL_0}{\sin\theta_{in} - \sin\theta_{out}}\left(1 + \frac{\Delta L}{L_0} + \frac{\Delta L_H}{L_0} - \frac{\Delta L_V}{L_0}\sin\theta_{out}\right) \tag{4.5}$$

where L_0 is the length of the region of uniform field, and ΔL is a correction for the y dependence of field width. ΔL_H and ΔL_V are determined from the differences between the track parameters in in front and back as:

$$\Delta L_V = \frac{dy}{ds}\Delta\left(y\tan\theta\right) \tag{4.6}$$

$$\Delta L_H = \Delta\left(y\frac{dy}{dz}\right) \tag{4.7}$$

The momentum determined by equation 4.5 is then associated with tracks for which the adjusted $\Delta\alpha$, Δy_{mid}, and $\Delta dy/ds$ are within 4σ of the cuts.

The path length of the particle from the target to the TOF wall is also produced by MATCH. This is for the most part constant, but has some adjustments on the order of ~ 2 *cm* out of 660 *cm* for the particles of lower momentum.

Algorithm	Match	Front	Back	Method Word	Used
AUFCK95	REMATCH	TRFCK95	A34	$0x20482$	2 and 4 $A{\cdot}GeV$
AUFCK	REMATCH	TRFCK	A34	$0x20282$	6 and 8 $A{\cdot}GeV$
AUSMATCH	REMATCH	A12	A34	$0x20182$	diagnostic
AUFCK95	MATCH	TRFCK95	A34	$0x10482$	intermediate stage
AUFCK	MATCH	TRFCK	A34	$0x10282$	intermediate stage
AUSMATCH	MATCH	A12	A34	$0x10182$	intermediate stage

Table 4.1: Full tracking algorithms. The various tracking algorithms stored at different points in the data stream are listed. The method word is written in hexadecimal notation in order to make clear the way in which it is formed. The first two algorithms are the ones used in this thesis.

4.7 Final tracks:

AUSMATCH, AUFCK, and AUFCK95

The results of the algorithms in front of the magnet, those behind the magnet, and match itself, are combined to form a full particle trajectory, to which a momentum is associated.

AUSMATCH is formed by combining A12 tracks in front with A34 tracks in back using MATCH. It is therefore "AUSCON+MATCH". AUFCK is formed from TRFCK in front, A34 in back, and MATCH. AUFCK95 is formed from TRFCK95 in front, A34 in back, and MATCH. For these three algorithms, there are two types, those which are simply matched assuming the proton mass, and those for which the cuts and selection are adjusted based on the particle mass returned from the PICD algorithm. The second method of matching, based on mass, is termed "REMATCH". For this thesis, AUFCK95 is used for the 2 and 4 $A{\cdot}GeV$ data, and AUFCK for the 6 and 8 $A{\cdot}GeV$ data. Table 4.1 lists these, along with the "method word" stored in the datastream to identify the track.

A comparison between AUFCK95 and AUSMATCH for a 1995 data run for which the TRF's were inefficient is shown in figure 4-2. AUSMATCH does not use the TRF's. The algorithms show some discrepancies at low momentum, but the general trend is very similar, with AUFCK95 finding more tracks finding significantly more tracks at very low momentum. This stands in contrast to the situation with AUFCK

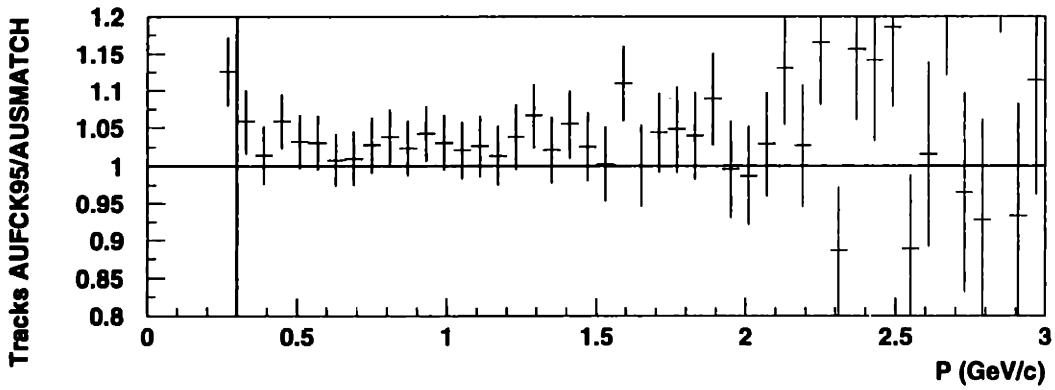

Figure 4-2: Comparison of good status tracks produced by AUFCK95 and AUSMATCH. The figure shows the ratio of good status tracks in AUFCK95 to that in AUSMATCH, for a typical 1995 run, run 17551. The vertical line shows the low-momentum cut used due to *Monte Carlo* studies. No tracks are used below this line.

in 1995, in which the effects of the TRF inefficiencies caused AUFCK to find fewer tracks than AUSMATCH. The discrepancies are to be expected from the effect of the AUSCON matching cuts, but would be corrected in the efficiency analysis (chapter 5). AUFCK95 was found to perform better than AUSMATCH, in terms of hits per track, at the higher multiplicities of the forward angle settings. It was therefore preferred.

4.7.1 Target Position

At the beginning of PASS12, 10,000 events are reconstructed with the target position set to zero, tracks from these events reconstructed, and the target position at $Z = 0$ fit in both x and y. The results are stored in the database. Unfortunately, the target position is stored in different coordinate systems for different algorithms. TRFCK and its derivatives store the target position in the BEAM coordinate system, at $z_{BEAM} = 0$. This is more correct than A12 and its derivatives, which store the target position at $z_{spec} = 0$, with x_{target} in the SPEC coordinate system. A12 uses this

information in its initial projection, and all tracking algorithms place a loose cut of ± 2 cm on the difference between the projection of the front track and the position of the target. Note that this cut is made in the BEAM coordinate system by AUFCK and AUFCK95, at $z_{beam} = 0$, but in the SPEC coordinate system, at z_{spec}=0, for AUSMATCH. The cuts in AUFCK and AUFCK95 are more correct.

4.8 Particle Identification: PICD

4.8.1 Overview

The strength of the experiment comes in its particle identification capabilities. Combined with an accurate momentum determination, the time resolution of the TOF wall is such to allow a unique identification of particles over a wide range of momenta. The criteria used for this identification are simple: the TOF must fall within 3σ of the one expected from a mass hypothesis. As described in section 5.5, the presence of backgrounds does lead to selected use of slightly tighter cuts in momentum in this analysis. There is one additional cut, which will be described later, based on E_{loss} in the TOF wall.

The algorithm as used in this analysis is mostly unchanged from $E859$ [Cia94], although some improvements were made in the association of a track to the TOF wall. These changes were made by M. Moulson [Mou98], and required some shifts in the geometry of the TOF wall. A34 was rerun with these shifts. For $E866$ F. Wang added the REMATCH stage, and adjusted the parameters describing the momentum resolution [Wan96].

For the rarer particles, there are some backgrounds inside the 3σ cut, both from the tails of the less rare particles and, at a greatly decreased level, from some apparently random background. Section 5.5 details these as they apply to this analysis.

4.8.2 Algorithm

The decision is made in the space $1/\beta$ *vs* p. It is not done in mass, for a simple reason. $1/\beta$ is directly proportional to the measured TOF_{found} (equation A.10). This means that a constant offset in TOF_{found} will lead to a constant offset in $1/\beta$. At high momentum, where σ_{TOF} is basically a constant, the ratio of this offset to the cuts applied will also remain constant, so any systematic inefficiency caused by such an offset will be independent of momentum. Another reason for cutting in $1/\beta$ rather than mass is is that the equation reconstructing a mass from TOF_{found}, the momentum measured, and the path length introduces asymmetries into the measured mass distribution.

For a given mass hypothesis and measured momentum, the expected $1/\beta_{expected}$ is given by:

$$\frac{1}{\beta_{expected}} = \frac{\sqrt{p^2+m^2}}{p} \tag{4.8}$$

Meanwhile, from the TOF_{found}, measured by the TOF wall, and the path length to the TOF wall, measured by the tracking, one gets:

$$\frac{1}{\beta_{found}} = \frac{c}{L} TOF_{found} \tag{4.9}$$

If everything is calibrated properly these two quantities should be equal, ignoring resolution. The calibrations of the TOF wall (section 3.4) calibrate directly on these quantities. The resolution on the residual between equations 4.9 and 4.8 has two components, added in quadrature:

$$\sigma_{\Delta(\frac{1}{\beta})} = \sqrt{\left(\frac{c}{L_{ref}}\sigma_{TOF}\right)^2 + \left(\frac{m^2}{pE}\frac{\sigma_p}{p}\right)^2} \tag{4.10}$$

where the first comes from the timing resolution of the TOF wall, and the second from the momentum resolution of the spectrometer. L_{ref} is taken to be a constant for the purposes of resolution determination only. This second resolution is momentum-

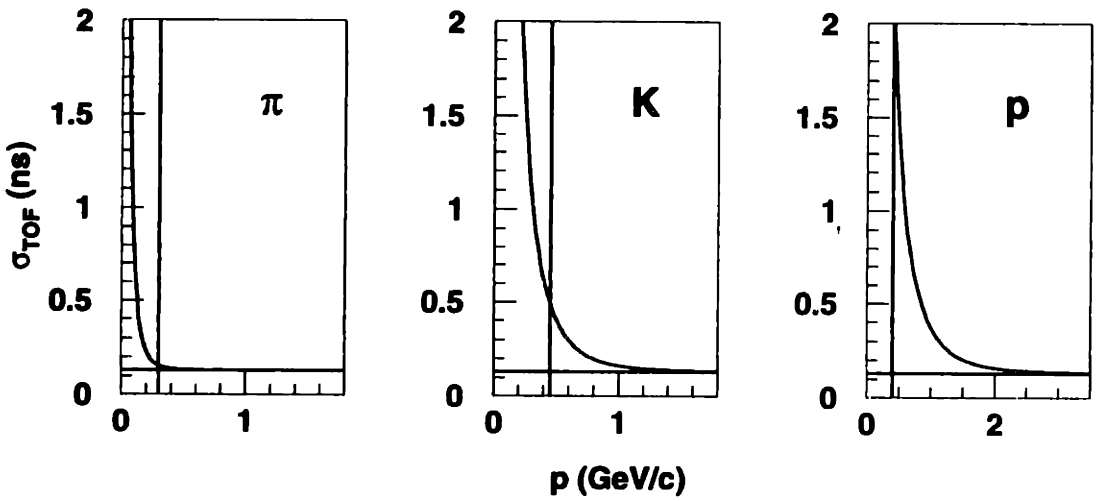

Figure 4-3: The three panels show the TOF resolution used in PICD for this thesis, for π, K, p, along with the 130 ps line along the horizontal. The vertical lines show the momenta below which the particles are not included into the presented data. These low momentum cuts result from other criteria than TOF resolution.

dependent, due to multiple scattering and the effects of finite chamber resolution.

$$\frac{\sigma_p}{p} = \sqrt{C_{sp}^2 p^2 + \left(\frac{C_{ms}}{\beta}\right)^2} \tag{4.11}$$

where C_{sp} and C_{ms} are independent of p and β, but are assumed to depend linearly on the strength of the magnetic field, B_{HH}. Figure 4-3 shows the resolution (in TOF, rather than $1/\beta$) for the 2 kG field used in this thesis. The parameters are listed in table 4.3. Equations 4.8 and 4.10 are then used to form cuts in $1/\beta$ vs p space. If $1/\beta_{found}$ and p associated with a track is within these cuts, the track is uniquely identified. Above momenta where the cuts overlap, tracks are not identified.

Table 4.2 details the momenta at which this occurs for this analysis. Kaon contamination is allowed into the identified protons, and electron contamination is allowed into the pions. This is unlike the analyses in [Ahl97] and [Wan96], in which the GASC was used to reject electrons.

Figure 4-4 shows the cuts, figure 4-5 shows the data, and figure 4-6 shows the data

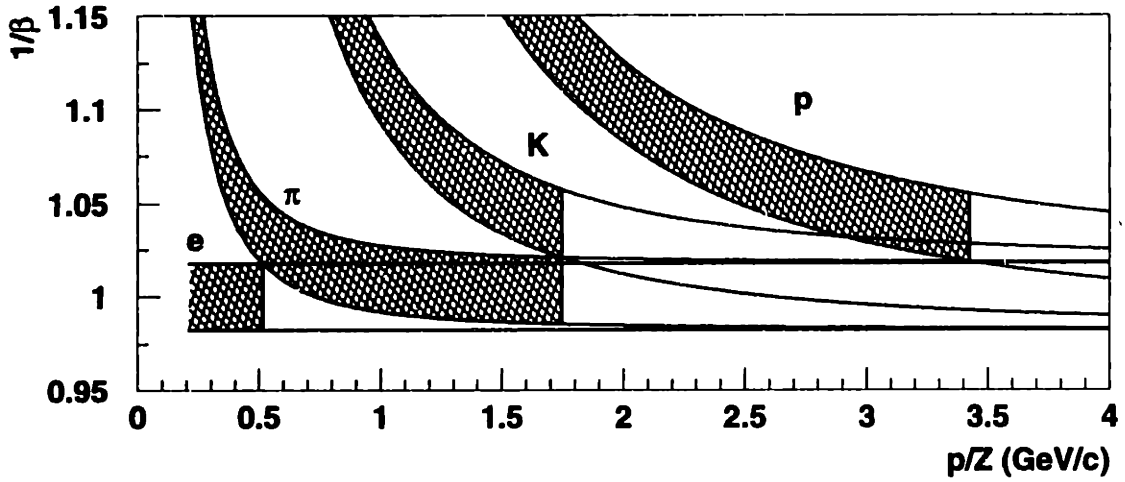

Figure 4-4: The cuts used in $1/\beta$ *vs* p space. The shaded regions are those allowed by the cuts. Only the cuts for p, π, and K are shown.

with the cuts outlined. For this analysis the high-momentum threshold used is more restrictive for the kaons, because of backgrounds (section 5.5). The low-momentum threshold is also determined by different criteria, either from efficiencies(section 5.2) or from backgrounds.

Since 2-dimensional plots can be misleading, mass distributions are shown in in figure 4-7 to give a feel for the relative level of background. Section 5.5 contains a more detailed discussion of the backgrounds.

There is one further cut. There is a large amount of noise on the TOF wall, approximately equal to the number of hits associated with full tracks. This noise comes from the discriminator thresholds, which are consciously placed low to minimize slewing effects(section 3.4). It also comes from background behind the magnet. Times measured by the TOF wall will be odd for hits due to noise, and there is a possibility that such hits will be associated with a track due to combinatorics.

Luckily, there is a simple handle on these occurrences, in that the pulse height on the slat will be low. Therefore a lower bound is placed on the recorded E_{loss} (equation A.3). The actual quantity on which the cut is placed has some slight

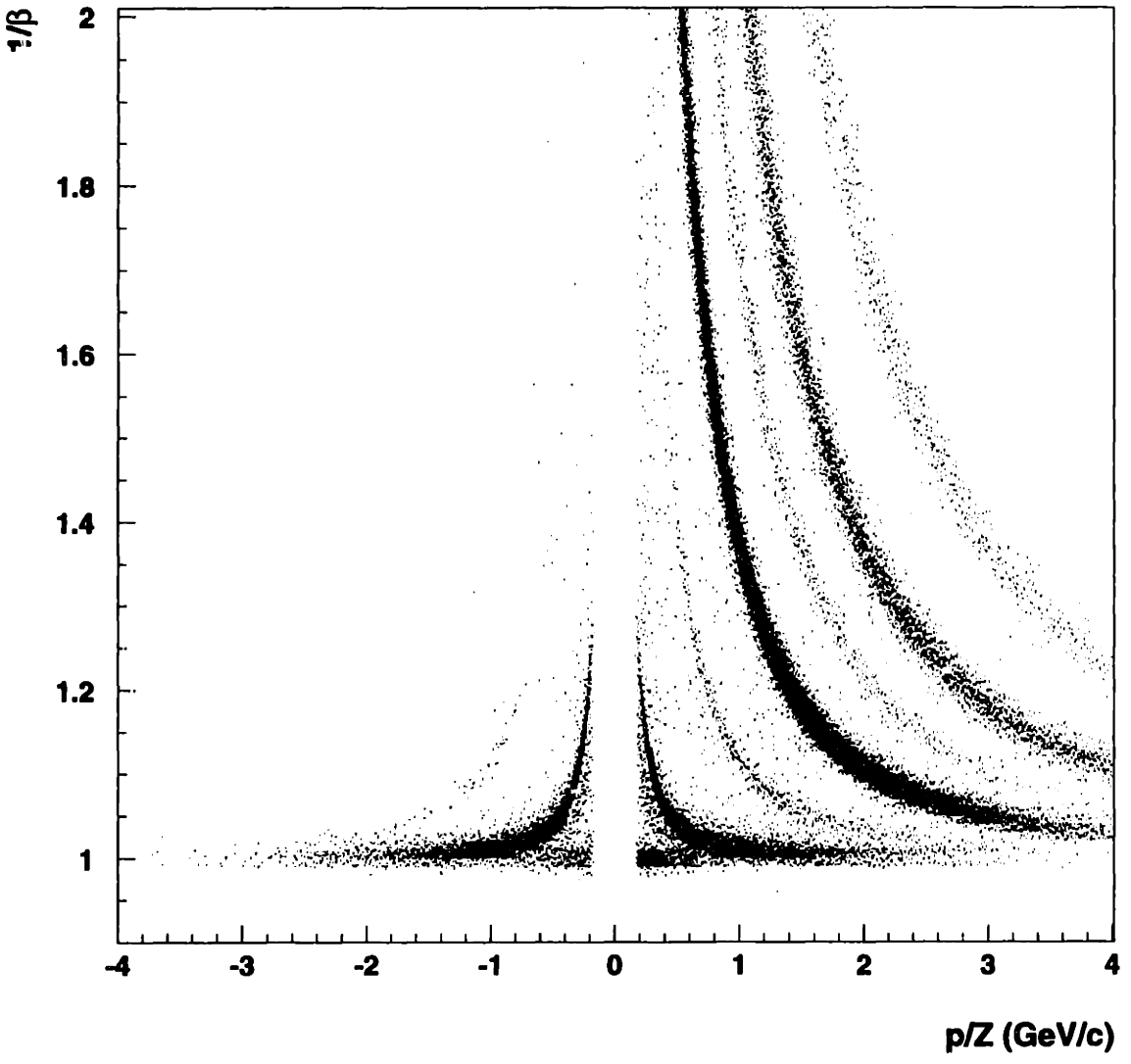

Figure 4-5: The data in $1/\beta vs\ p$ space is shown. The data is from a 24^0 4 $A \cdot GeV$ non-lvl2 run (run 17602), on which all quality cuts have been made.

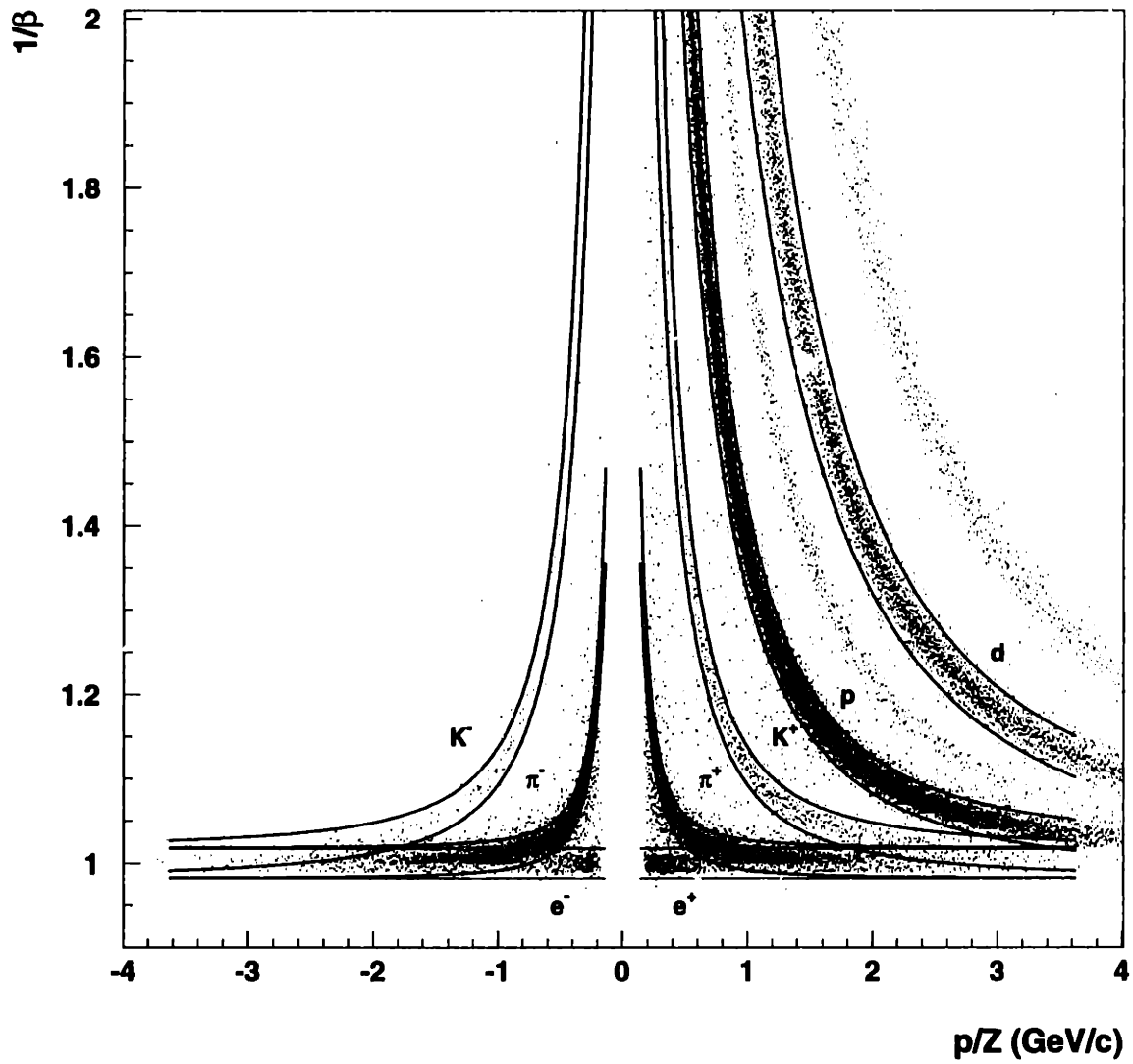

Figure 4-6: The data in $1/\beta$ vs p space is shown, along with the cuts in the algorithm. The cuts, as plotted here, assume the reference path length of 660 cm, but the data uses the path length from the tracking. Only cuts for e, π, K, p, and d are shown, but one can see faint lines for ^3He and ^3H. The data is from a 24^0 4 $A{\cdot}GeV$ non-lvl2 run (run 17602), on which all quality cuts have been made.

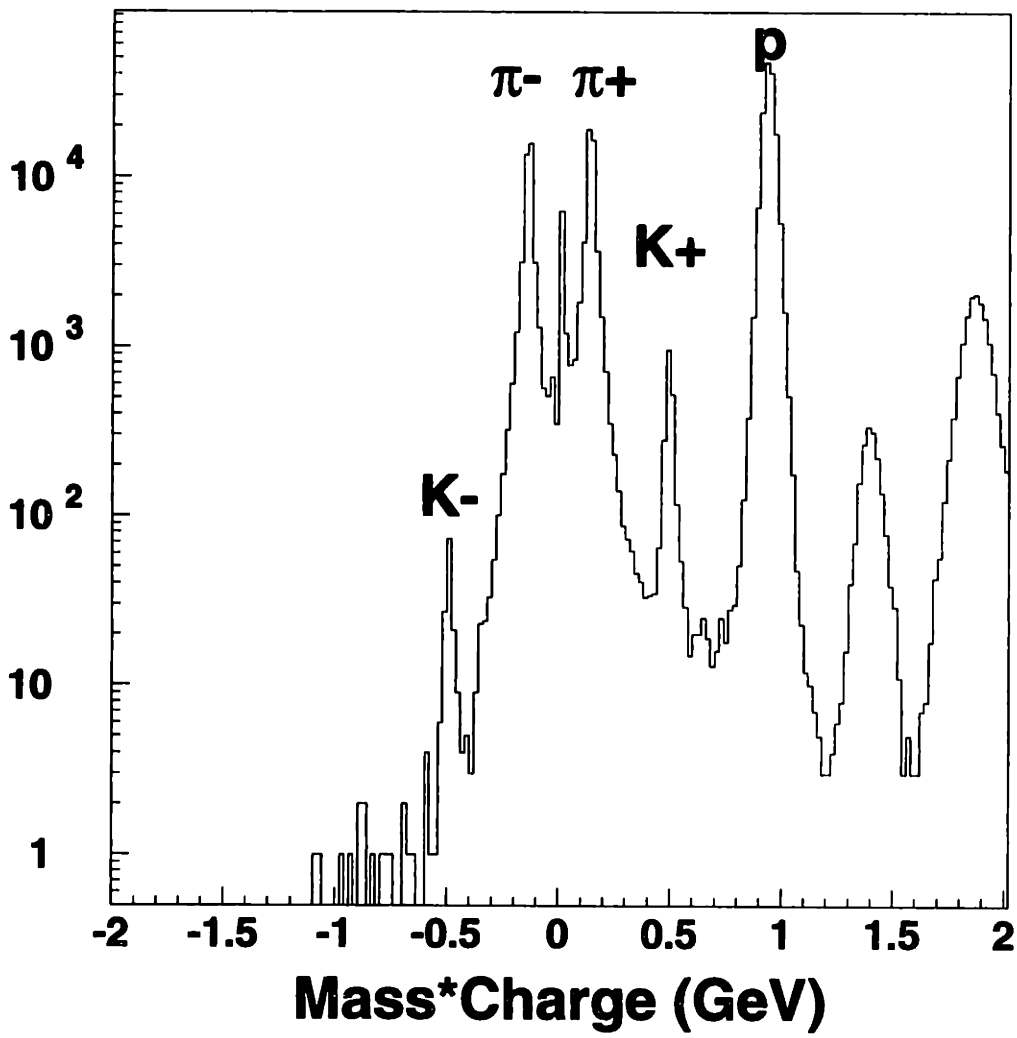

Figure 4-7: The mass of particles in the spectrometer, as unfolded from a combination of TOF measurement and tracking. The data is from a 24^0 4 $A \cdot GeV$ non-lvl2 run (run 17602), and only includes tracks as included into the K yields of this analysis. There is an error in the figure label, which should read *mass/charge*.

Particle	Momentum Cut (GeV)	Reason	Contamination (GeV)	Reason
e	0.5244	$e-\pi$ separation		
π	1.7446	$\pi-K$ separation	0.5244-1.7446	e
K	1.7446	$\pi-K$ separation		
p	3.4238	$\pi-p$ separation	2.9038-3.4248	K

Table 4.2: Momentum cuts as determined by the PICD algorithm. Particles of the given type are identified only below the momentum cuts listed by the PICD algorithm. There is negligible contamination allowed in some regions.

modifications described in section 4.8.4. This cut is made as a function of TOF, to allow for the $1/\beta$ dependence of E_{loss}, and is rather loose. The parameters are shown in table 4.3, and consist of three points describing a line in E_{loss} below which the association is not made. Because of Landau tails in the E_{loss} spectrum, no upper bound is placed on E_{loss}. Also, no attempt is made to separate deuterons from α's. A faint band can be seen from ^3He.

There are some more complicated procedures in the algorithm to allow for the use of the GASC and the BACK counters (section 2.9.3), but these were not used in this analysis, and so will not be described here.

4.8.3 Parameters

There are three parameters describing the resolution, C_{sp}, C_{ms}, and σ_{TOF}. Not all can be derived from the data, since C_{ms} dominates at low momentum and σ_{TOF} dominates at high momentum. The values for C_{sp} and C_{ms} were derived for the 1993 data set by F. Wang [Wan96] from *Monte Carlo* studies. As mentioned in section 5.2 and [Hei99], the *Monte Carlo* used for these studies had some incorrect parameters. The values were found to describe the data relatively well, and so were kept. The value used for σ_{TOF} remained at 130 ps, as used in [Ahl97], for this analysis, to account for possible slat-by-slat differences in resolution.

4.8.4 TOF-track association

In order to identify a particle, a track must be associated with a hit on the TOF wall. Since there is $\sim 2\ m$ of air between the back edge of T4 and the TOF wall, this

association is not as simple as it may seem, due to multiple scattering. The association was changed by M. Moulson for this analysis, and the parameters describing it derived from the data. The resulting set of routines is termed "TOF_VERIFY", and are described here as part of the collaboration record.

The association used in the past analyses was simple, the cuts used wide, and the rejection criteria for duplicate associations not completely correct.

The TOF wall had been assumed to be an arc. As mentioned in section 2.9.2, the TOF wall is not strictly an arc, but consists of 10 straight-line sections. Therefore, for this analysis, the geometry of the TOF wall was parametrized in terms of these sections. The mechanism existed to do so, and consists of 10 numbers, each describing the position of the "fat" double width slats at the end of each section. This mechanism needed to be placed into the algorithm. This geometry is shown in figure 4-8, repeated here. The direction T corresponds to the distance along the wall. The mapping between T and $x_{spec} - z_{spec}$ has discrete jumps at the edges of the sections.

After modifying the parametrization of the geometry of the TOF wall, it was found that the geometry parameters adjusted by F. Wang in 1993 [Wan96] did not describe the data. Offsets as large as a few *cm* were found. Therefore, the geometry was tuned on residuals between tracks and TOF hits, associated with the new method described below, with results as shown in figure 4-9. The precision of the tuning procedure was not as great as we had expected, but the dispersion is significantly smaller that the widths used to associate a track with a TOF hit. The geometry was adjusted separately for each angle setting and year, corresponding to each set of geometry parameters for the chambers (section 3.3.3).

The description of the response function along the TOF wall was changed. A schematic of the modified function is shown in figure 4-10. The probability distribution for firing a TOF slat is a simple square pulse in T, the direction along the wall, such that if a particle falls within the edges of the TOF slat the slat will fire, but if the particle falls outside these edges the slat will not fire. That is to say, it is described by:

$$\Delta T_{raw}(T) = \frac{1}{2}\left(\Theta\left(T + T_{slat}\right) + \Theta\left(T - T_{slat}\right)\right) \tag{4.12}$$

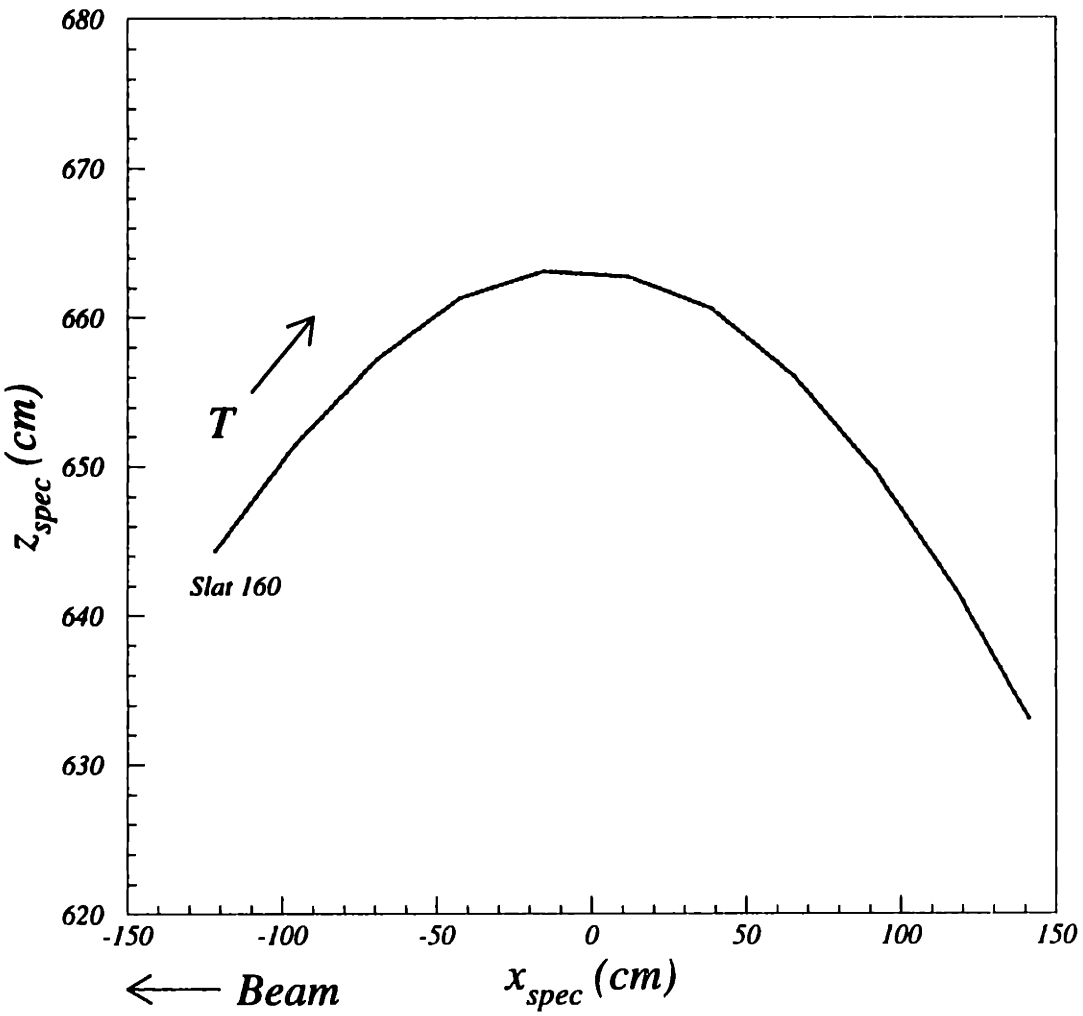

Figure 4-8: TOF wall configuration. The position of the TOF wall in the SPEC coordinate system. Each point represents the center of a slat. The aspect ratio is 5:1 in x_{spec} : z_{spec}. The position of the points is after geometry adjustment.

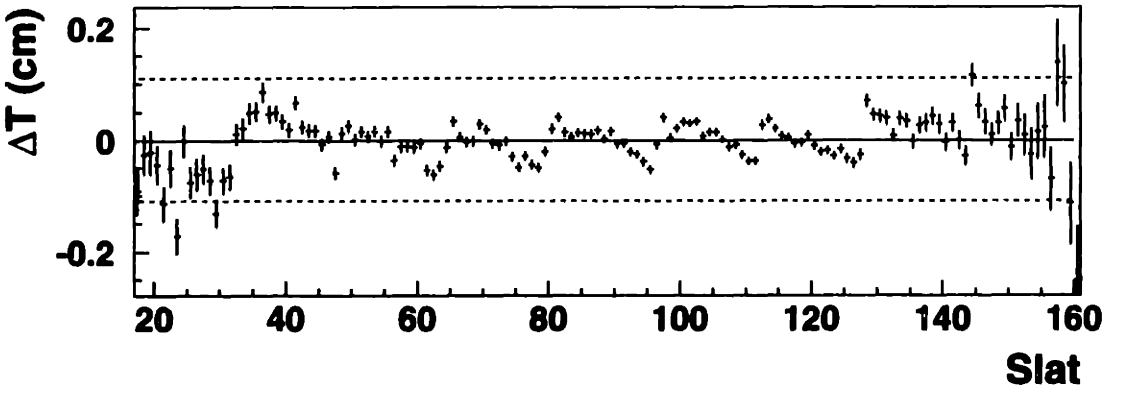

Figure 4-9: TOF geometry after adjustment. The data is from a set of 4 $A{\cdot}GeV$ 19^o runs, and shows the mean of the residuals in T between a track and the center of the TOF slat, after adjustment of the geometry. The line comes at the 1σ level at high momentum. Search widths are at 4σ.

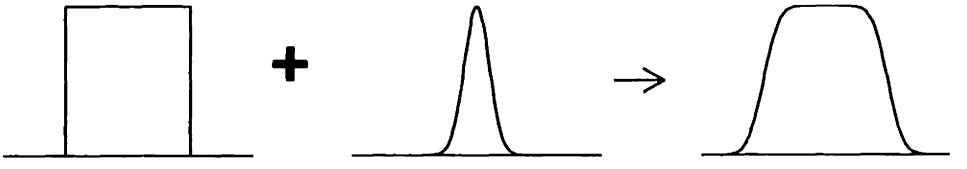

Figure 4-10: A schematic drawing of the effect of projecting, with finite resolution, onto a TOF slat. A square pulse is convolved with a Gaussian of finite width, giving the resulting curve.

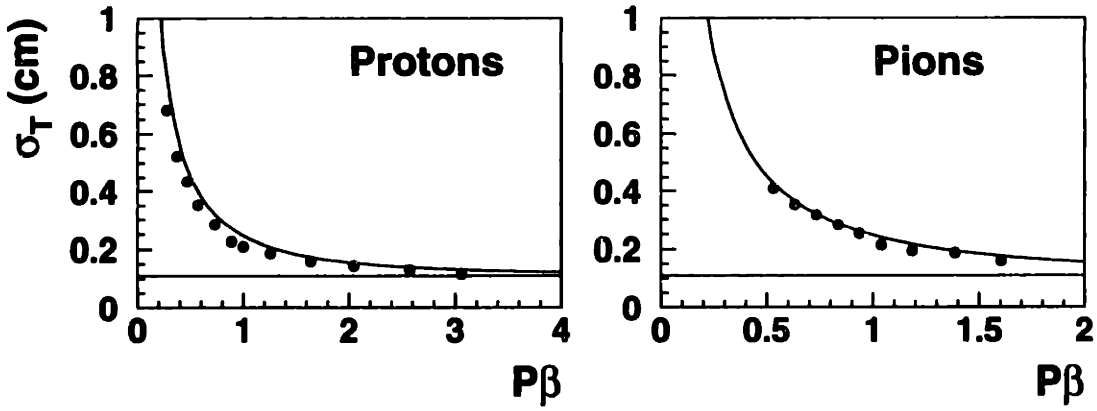

Figure 4-11: σ_T from residual fits. The data is from a set of 4 $A \cdot GeV$ 19^o runs. The data from which the parameters are extracted are shown in figure 4-12. σ_T is defined in equation 4.13. The line is from the parameters used in the analysis, using equation 4.15. βp is in units of GeV.

where T_{slat} describes the half-width of the slat along T, and $\Theta(x)$ is the Heaviside step function, 0 for $x < 0$ and 1 for $x > 0$. This is complicated by multiple-scattering, which has a Gaussian shape, the width of which is dependent on βp. Convolving these, one gets:

$$\Delta T_T = \int_{-T_{slat}}^{T_{slat}} \exp\left(-\frac{(T-u)^2}{2\sigma_T}\right) du \tag{4.13}$$

$$= A\left[\mathrm{erf}\left(\frac{T_{slat}-T}{\sqrt{2}\sigma_T}\right) - \mathrm{erf}\left(\frac{T_{slat}+T}{\sqrt{2}\sigma_T}\right)\right] \tag{4.14}$$

where A is an arbitrary factor, σ_T is the width of the Gaussian due to multiple scattering, and erf is the error function, which is readily available. For large σ_T, the Gaussian will dominate, while for small σ_T, the square pulse will dominate.

Unfortunately, the situation is such that both extremes occur in the data. Figure 4-12 shows the residual in ΔT betweeen a projected track and the center of the associated slat, along with fits to the distributions. These distributions are averaged across the TOF wall and omit double-width slats. The σ_T of the fits *vs* momentum is shown in figure 4-11 for pions and protons separately. It shows the expected dependence on momentum from multiple-scattering, and is further fit to an expression

of the form:

$$\sigma_T = \sqrt{C_{Tsp}^2 + \left(\frac{C_{Tms}}{\beta p}\right)^2} \tag{4.15}$$

where C_{Tsp} and C_{Tms} are parameters of the fit. These are not simply related to the parameters describing the momentum resolution, since for the most part they depend only on multiple scattering between the last chamber of T4 and the TOF wall, not the scattering through the entire spectrometer. Also, these parameters have no dependence on the magnetic field, B_{HH}. The parameters were found not to be completely consistent between the pions and protons, perhaps due to misalignments in the geometry, and so the maximum between the two sets was used for both parameters. Table 4.3 lists the parameters as used. The residuals in Δy_{spec} are dominated by the resolution of the TOF wall itself and so show no dependence on momentum.

The algorithm for associating the track with the TOF slat uses this information. First, the track is projected to the TOF wall, both in T and y_{spec} space. Hits on the TOF wall are collected about this projection, within search widths in both T and y_{spec}. The search widths are determined as multiples of the resolutions. If the edge in T of any slat with a TOF hit falls within the search width in T, and if the y position of the hit falls within the search width in y, the TOF hit is pushed onto a stack of duplicates. The previous algorithm ignored the y information.

Then comes the filtering stage. For each TOF hit in this set of duplicates, β is determined from TOF_{found}, and σ_T recalculated. The duplicates are then filtered, with the rejection criterion:

$$RC = P\left(T_{proj}\,;\, T_{slat}^{min}, T_{slat}^{max}, \sigma_T\right) P\left(\Delta y\,;\, \sigma_y\right) \tag{4.16}$$

where $P(X;Y)$ denotes a probability for X given parameters Y, T_{proj} denotes the projected position of the track along T, T_{slat}^{min} and T_{slat}^{max} denote the edges of the slat in T, and Δy denotes the residual between the y position measured by the TOF wall, y_{found}, and the projected y position of the track,y_{proj}. The slat with the greatest RC is kept. Figure 4-13 shows a schematic of these probabilities. $P\left(\Delta y\right)$ is the upper tail probability to measure y_{found}, assuming perfect resolution in y_{proj}. $P\left(T_{proj}\right)$ is

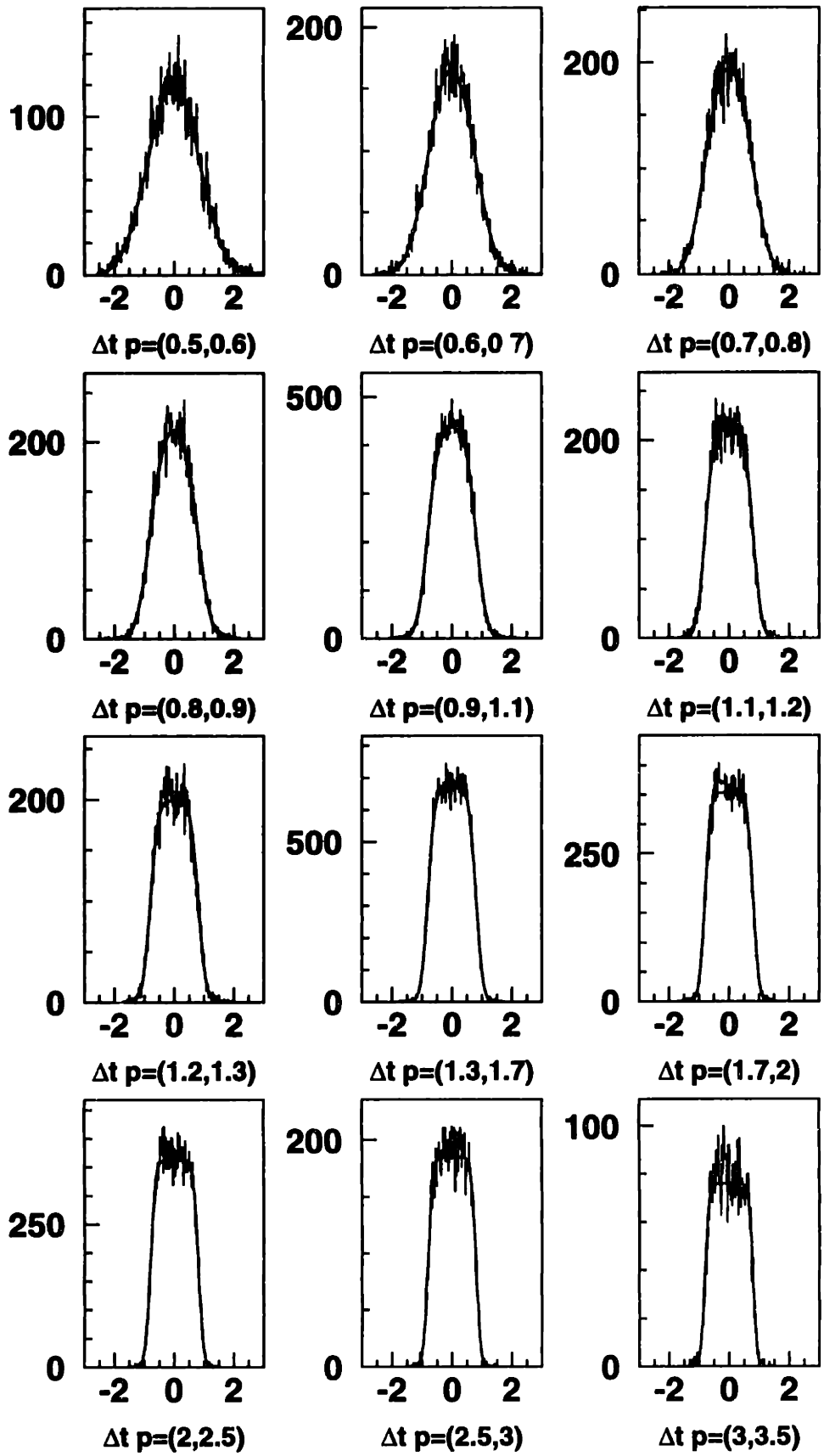

Figure 4-12: Residual in ΔT for protons. The data is from a set of 4 $A{\cdot}GeV$ 19^o runs, and is binned in momentum. ΔT is defined in the text of section 4.8.4, and has units of *cm*. The fits are to equation 4.15.

Figure 4-13: A schematic drawing of the rejection criteria used in TOF_VERIFY. In T, the probability is the double-hatched region, the overlap of a Gaussian of the track projection with a region of fixed length. In y, the probability is the upper-tail probability of the Gaussian of the TOF hit y, given the track projection. The relative scales in the figure are not realistic.

the probability for the track to hit the TOF slat, given the finite resolution of the projection and assuming perfect geometry. They are given by:

$$P(\Delta y) = 1 - \mathrm{erf}\left(\frac{\mathrm{abs}(\Delta y)}{\sqrt{2}\sigma_y}\right) \tag{4.17}$$

$$P(T_{proj}) = \frac{1}{\sigma_T\sqrt{2\pi}} \int_{T_{proj}-T_{max}}^{T_{proj}-T_{min}} \exp\left(-\frac{u^2}{2\sigma_T^2}\right) du \tag{4.18}$$

where T_{min} and T_{max} are the lower and upper edges of the slat in T.

Finally, for the purposes of the charge cut described in section 4.8.2, the measured E_{loss} on a slat is summed across slats in the original duplicate pool. This is to account for cases in which a track crosses slat boundaries, and so deposits its energy across the slats that it crosses. The E_{loss} of a duplicate is only added to the sum if there is only one A34 track pointing to the duplicate, if there is another duplicate immediately adjacent, and if the difference in time between the adjacent duplicates is within 3 σ_{TOF}. The same type of summing was done in the previous procedure, but there were no adjacency requirements, the collection of duplicates was done regardless of y information, and the track requirement was made on full target-pointing tracks rather than back tracks. A34 finds a relatively large number of tracks that either do not match front tracks or do not point to the target. A large fraction of these are thought to be real tracks that originate from other sources rather than spurious "ghosts", as

Parameter	Value	Units	Where applied
σ_{TOF}	0.130	ns	$1/\beta$ vs p
C_{ms}	0.018	1	$1/\beta$ vs p
C_{sp}	0.003	GeV^{-1}	$1/\beta$ vs p
L_{ref}	660	cm	$1/\beta$ vs p
x_1^Z	28	ns	charge cut
y_1^Z	0	$Yasuos/ns$	charge cut
x_2^Z	45	ns	charge cut
y_2^Z	150	$Yasuos/ns$	charge cut
$x3^Z$	60	ns	charge cut
y_3^Z	320	$Yasuos/ns$	charge cut
C_{Tms}	0.22	$cm\ GeV$	TOF_VERIFY
C_{Tsp}	0.11	cm	TOF_VERIFY
σ_y	1.4	cm	TOF_VERIFY
SW_T	4	# of σ	TOF_VERIFY
SW_Y	4	# of σ	TOF_VERIFY

Table 4.3: Parameters used in PICD. The unit $Yasuos$ is a collaboration-specific energy unit, which places the E_{loss} in the TOF wall of a minimum-ionizing at 100. The momentum resolution parameters are for the 2 kG field. For other fields, multiply by $B_{HH}\ (kG)/2$. See equations 4.10, 4.15, 4.11.

can be seen by their presence in empty target events of low multiplicity(section 5.6).

Various quantities related to the number of tracks associated with a given slat and the number of slats associated with a given track are stored in the data stream. The meanings of these changed slightly, but are not used in this analysis, and so will not be described.

The effect of these changes was small, but the modifications were well motivated by the physical parameters of the TOF wall.

The TOF-track association in A34 and MATCH was not modified.

Chapter 5

Corrections

5.1 Overview

Corrections have been applied to the data output from the reconstruction algorithms. These corrections are of four types: those for single track effects, those for occupancy effects, those for backgrounds in particle identification, and those for acceptance. The four quantities are obtained by different methods, either directly from analysis of the data or through modeling of the spectrometer.

These corrections have been obtained separately for the two tracking algorithms used in this thesis, AUFCK and AUFCK95, and applied separately to the appropriate set of data.

Also described in this chapter will be the quantities used for normalization of the yields. These are obtained separately by beam energy, and the stability of these quantities within a given running period has been investigated.

Just as in the determination of calibrations, it is good practice to derive the corrections from the data as much as possible. However, one must always be careful not to allow fitting instabilities to cause unphysical effects.

At various places in the analysis, cuts are placed on the data in order to ensure that the corrections are not large. These cuts are determined so as not to introduce bias into the measurement, but to limit the range over which high-quality results are determined. As such, they are never based on quantities, such as the multiplicity

in the spectrometer, that can affect the results of the analysis in complicated and biased ways, but on relatively simple variables such as the momentum and angle of the particles measured.

5.1.1 A Note on the Errors on Efficiencies

The errors on efficiencies are actually not completely trivial to obtain. Every efficiency is found by forming the ratio:

$$\epsilon = \frac{Found}{Thrown} \tag{5.1}$$

where *Thrown* is the number of particles of a given type thrown through the algorithm for efficiency determination, and *Found* is the number of particles found as a result of the algorithm. For very small inefficiencies, simple binomial errors, under the Gaussian approximation, will give the wrong errors. An extreme case comes when $Found = Thrown$, in which case $\epsilon = 1$ and the error as 0. This cause serious problems when trying to find the dependency of ϵ on a parameter, e.g. the momentum. In the extreme case described above, the results of fitting $\epsilon(p)$ with a χ^2 fit, which assumes Gaussian errors, will be extremely biased towards the single point with zero error. Therefore for this analysis a Bayesian method was used for the errors, the derivation of which is described in [Hei99]. This is still not strictly correct, since the distribution of possible measurements is not guaranteed to be Gaussian or even symmetric. Despite this, the method seems to be relatively robust.

The error used is:

$$\sigma_{Bayesian} = \frac{n+1}{N+2}\left(\frac{n+2}{N+3} - \frac{n+1}{N+2}\right) \tag{5.2}$$

where N is equivalent to *Thrown* in equation 5.1 and n is equivalent to *Found*.

5.2 Single Track Effects

There are three types of single track effects: those due to multiple scattering in the materials from the target through to the end of the spectrometer, those due to

hadronic interactions in these materials, and those due to decays. These cannot be derived directly from the data, and so need to be modeled.

The methods used here are based strongly on work described in [Hei99],[Wan96], and[Ahl97]. The corrections used for the 1996 data set (6 and 8 $A{\cdot}GeV$) were derived by G. Heintzelman. For the 1995 data set (2 and 4 $A \cdot GeV$) the corrections were performed separately, using AUFCK95, the tracking algorithm for that data set. The methods used were nearly the same.

Monte Carlo methods were used for these studies, using the standard package GEANT. In order to give correct results, GEANT needs correct input. It was found that the input describing the detectors was not correct. Some detectors had not been updated since $E859$, and some detectors had been installed with incorrect parameters. As [Hei99] has an extensive discussion of the modifications made because of this, they will not be discussed here. I do note, though, that the correct $E866$ beam pipe was also installed into the *Monte Carlo* for both analyses, and that for 1995 the correct TR1 parameters, rather than those for TR1MIT, were used.

5.2.1 Technique

The method used to derive the corrections is simple. No attempt is made to model the actual distributions of the particles as they enter the spectrometer. Because of this, the corrections are not parametrized as a function of quantities that could affect this distribution, such as the beam energy or spectrometer angle, but only in terms of the tracking algorithm and parameters that affect the strength of the physical effect in the *MonteCarlo*. These are the momentum of the particle and its type, π^+, π^-, K^+, K^-, and p. The only physical effect that depends on the sign of the particle is that of hadronic interactions, and so for the other effects only the positive particle is used.

The target is not included directly into the method, but its thickness is used in the correction for hadronic interactions, as described below. This inclusion introduces an angular dependence to the correction, which derives from the cylindrical shape of the target.

Physical Process	Particles used
None	$\pi^+, \pi^-, K^+, K^-, p$
Multiple Scattering	π^+, K^+, p
Decays	π^+, K^+
Hadronic Interactions	$\pi^+, \pi^-, K^+, K^-, p$
All	$\pi^+, \pi^-, K^+, K^-, p$

Table 5.1: A list of the various combinations of GEANT processes used in deriving the corrections.

For each particle type, tracks are generated, in a distribution flat in momentum and θ. Call these particles the "thrown" particles. The thrown particles are then required to pass through the acceptance of the spectrometer, placed at a nominal angle and field polarity. The particles resulting from this requirement are further passed, one at a time, through the full GEANT calculation, which models a large range of physical processes. These processes can be included separately. Hits are created from the modeled response of the detectors of the spectrometer, and the hits passed through into the full reconstruction chain, one particle per event. Then, the ratio of the number of tracks found to the number of tracks thrown is determined, which gives a direct measure of the inefficiencies.

One must be careful to use the correct acceptance in this method to avoid including tracks that pass through the aluminum frame of TR1, which falls within the acceptance of the other detectors behind the magnet. Therefore, for this analysis, tracks were required to fall within the acceptance, calculated as described in section 5.4.

Table 5.1 lists the physical processes that can be "turned on and off" in the procedure. That is to say, one can tell GEANT that this process does not exist, and GEANT will not calculate it. The corrections are assumed to factorize, and this assumption was checked for the 1995 data set. The energy loss of particles in the spectrometer cannot be turned off, because this process is responsible for the production of hits.

5.2.2 Hadronic Correction

The correction for hadronic scattering is first derived. This is in principle achievable by simply counting up the materials in the spectrometer and applying known momentum-dependent cross-sections, since in a hadronic interaction it is almost certain that the particle will be lost. In practice this is difficult, and GEANT has all of these cross-sections in its internals.

There are two things of note here. First, in order not to double count the corrections, the loss of tracks due to the finite resolution of the chambers was derived. This efficiency was measured by running GEANT with no processes but E_{loss} and the resolution of the chambers turned on. The efficiency was parametrized linearly with p. The parameters should not depend on particle type, except in that E_{loss} depends on β rather than p. In this study, the fit parameters for separate particle types were found to be consistent, so the form was forced to be the same for all particle types:

$$\epsilon_{resolution} = 0.978 - 2.6 \times 10^{-}3\, p \tag{5.3}$$

Figure 5-1 shows the results, with the common fit line.

Then, the hadronic efficiency was obtained by turning on the hadronic interactions in GEANT. The efficiency found is a combination of that due to resolution and that due to hadronic effects. It is fit to the following form:

$$\epsilon_{hadronic} = H_0 \left(1 + \frac{H_1}{p^{H_2}}\right) \epsilon_{resolution} \tag{5.4}$$

Figure 5-2 shows the results, and table 5.2 the parameters obtained.

The inclusion of the target into the hadronic correction is done in an extremely simple way, but was done incorrectly in the past. The cross-sections are assumed to scale as $\sigma_A = \sigma_N A^{2/3}$, where σ_N is the cross-section for a single nucleon, and σ_A is the cross-section for a nucleus of mass number A. This is rather reasonable, given that they have not been measured for all of the materials of the spectrometer in this momentum regime, and that the processes are hadronic. The past analyses

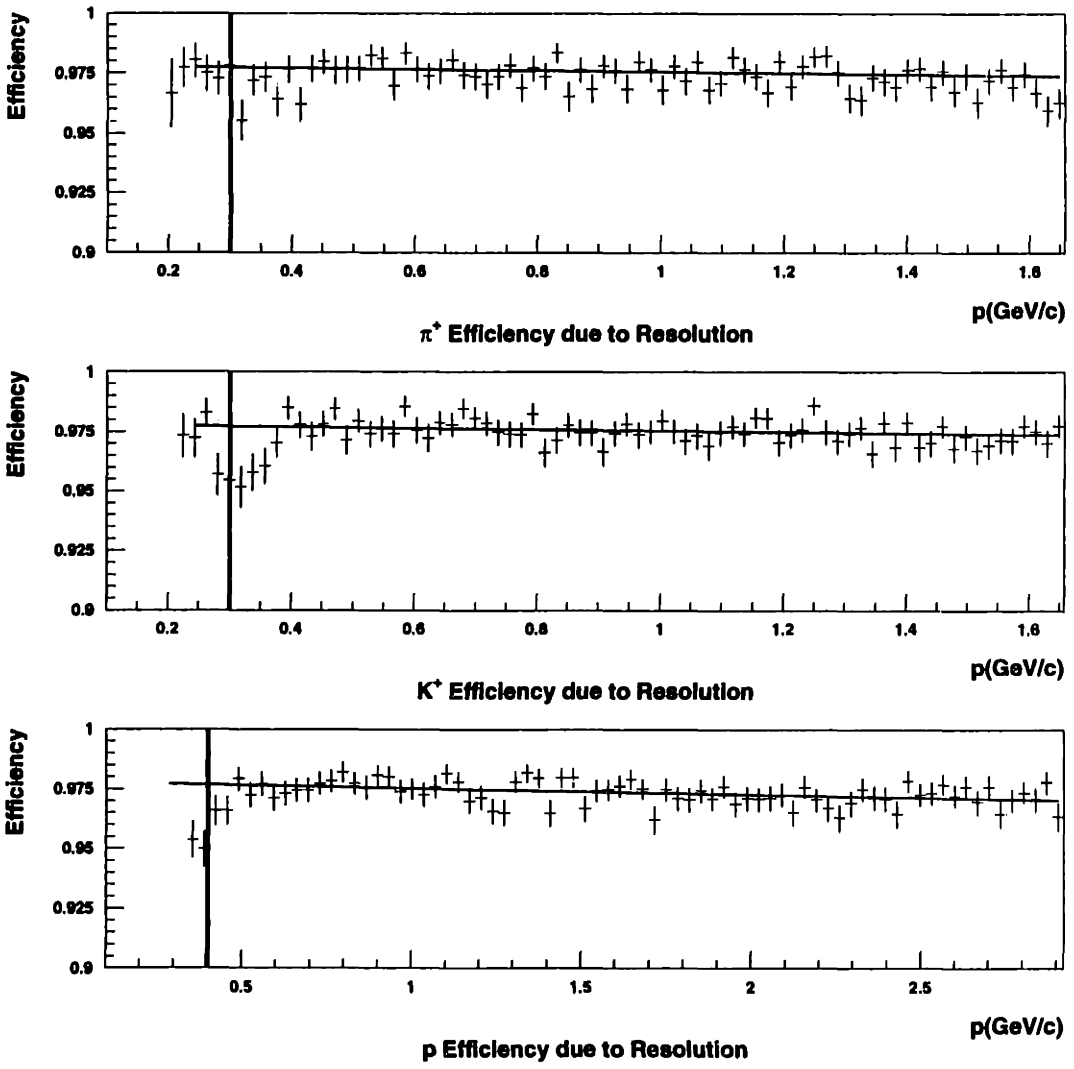

Figure 5-1: The efficiency as a function of momentum with no physical processes except for E_{loss} and detector resolution. The efficiencies were determined from GEANT studies for AUFCK95. The vertical lines indicate the cuts placed at low momentum in this analysis.

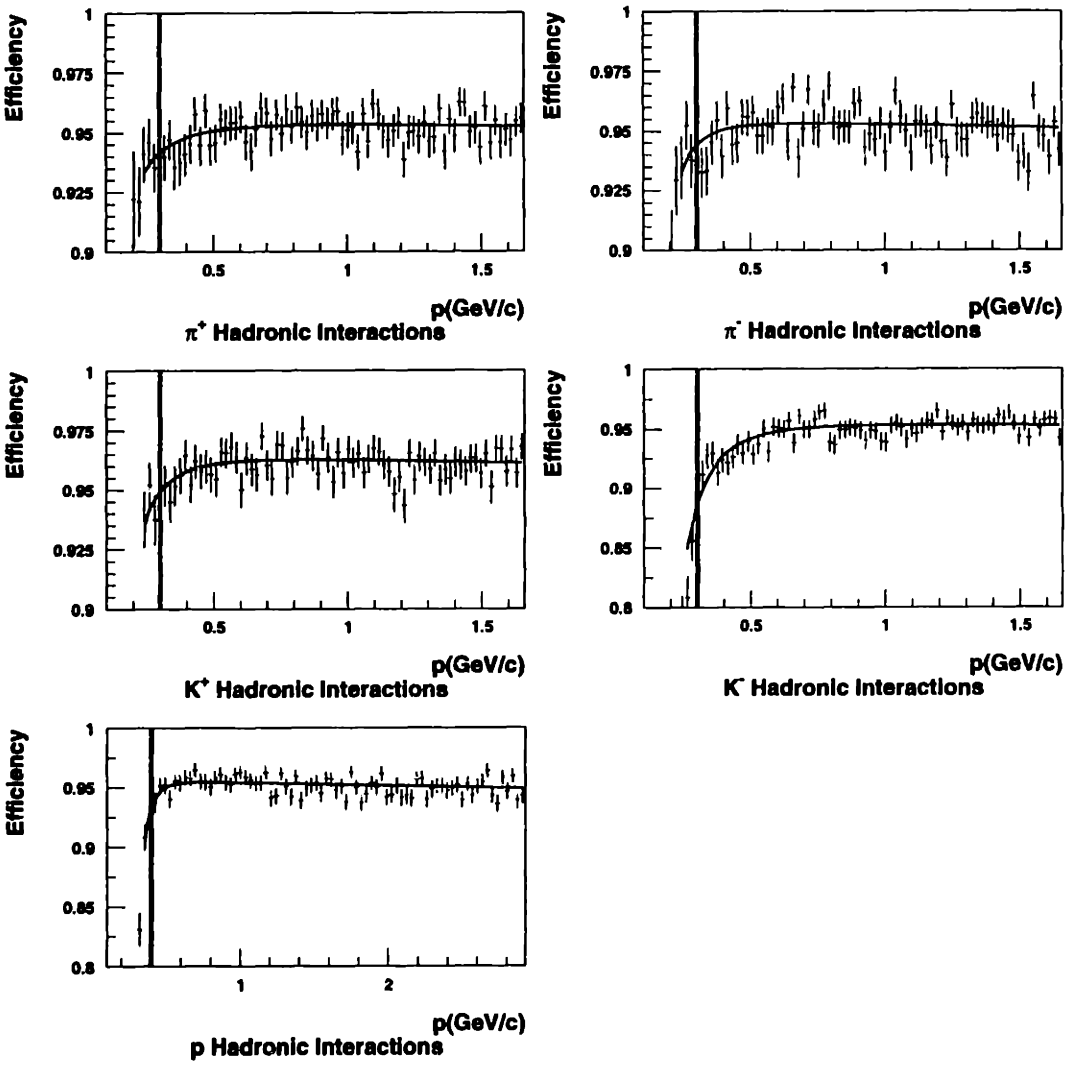

Figure 5-2: The efficiency as a function of momentum due to hadronic interactions, as determined by GEANT for AUFCK95. The vertical lines indicate the cuts placed at low momentum in this analysis.

Year	PID	H_0	H_1	H_2
1995	π^+	0.02131	0.05912	2.075
1995	π^-	0.02300	0.007523	3.443
1995	K^+	0.01267	0.03677	2.9379
1995	K^-	0.02107	0.07890	3.124
1995	p	0.02196	0.01759	6.995
1996	π^+	0.0206	0.0573	2.21
1996	π^-	0.026	0.0051	4.02
1996	K^+	0.0101	0.281	1.11
1996	K^-	0.0232	0.033	3.73
1996	p	0.0205	0.0166	4.65

Table 5.2: Table of fit parameters for 1995 and 1996 hadronic correction. The parameters are as given in equation 5.4.

([Wan96],[Ahl97]) assumed that they scaled as A. Under the $A^{2/3}$ assumption, all of the known material of the spectrometer is added and weighted appropriately, as described in [Hei99], and the hadronic correction, as obtained from GEANT, multiplied by an appropriate, angle-dependent number:

$$\epsilon_{hadronic}^{applied} = \epsilon_{hadronic}^{GEANT}\left(1 + \frac{t_{targ}}{2\cos\theta}\frac{A_{targ}^{-1/3}}{t_{spec}}\frac{\langle A_{spec}\rangle}{\left\langle A_{spec}^{2/3}\right\rangle}\right) \tag{5.5}$$

where t_{spec} and t_{targ} are the total thickness of the spectrometer and target, in g/cm^2, and $\langle\rangle$ denotes a mean, weighted by the amount of material of a given A in the spectrometer. The angular dependence comes from the cylindrical shape of the target, assuming that the particle exits from the target's front face.

5.2.3 Multiple Scattering

The physical process of multiple scattering was turned on, and the efficiencies derived. This was done for π^+, K^+, and p. The results are shown in figure 5-3, and are fit to a functional form. The functional form is the one used in [Ahl97] for the 4 kG field, since the 2 kG parametrization used there was not sufficient to describe the data.The

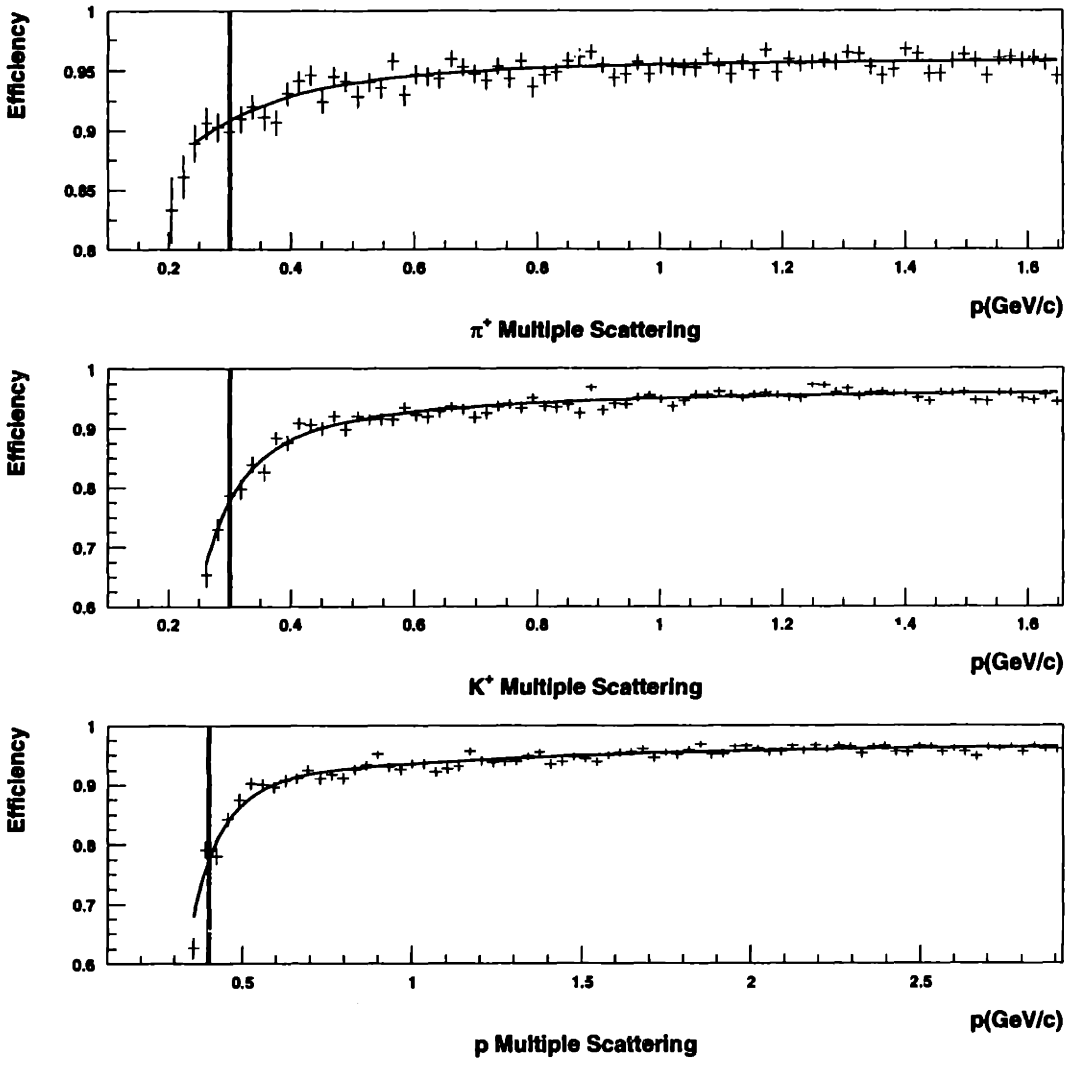

Figure 5-3: The efficiency as a function of momentum due to multiple scattering as determined by GEANT for AUFCK95. The vertical lines indicate the cuts placed at low momentum in this analysis.

Year	PID	M_0	M_1	M_2	M_3
1995	π	0.8213	-9.562×10^{-4}	-0.1689	0.04494
1995	K	0.9443	4.298×10^{-3}	-0.02235	0.541
1995	p	0.9421	4.402×10^{-3}	-0.02849	1.597
1996	π	0.9685	3.366×10^{-3}	0	0
1996	K	0.9679	4.722×10^{-3}	0	0
1996	p	0.9632	5.167×10^{-3}	0	0

Table 5.3: Table of fit parameters for 1995 and 1996 multiple scattering correction. The parameters are as given in equation 5.6.

functional form used is:

$$\epsilon_{ms} = M_0 \left(1 - \frac{M_1}{\beta p^2}\right) \left(1 + M_2 \exp\left(-\frac{M_3}{\beta^2 p^2}\right)\right) \tag{5.6}$$

and the parameters found are given in 5.3. This functional form with $M2 = M3 = 0$ was satisfactory for the 1996 data set.

5.2.4 Decay Correction

The decay correction is a source of much confusion. It is large, especially for the kaons, but it is also extremely well known.

The dominant correction is the analytic one,

$$\epsilon_{decay}^{raw} = \exp\left(-\frac{L}{\beta\gamma c\tau}\right) \tag{5.7}$$

where τ is the lifetime of the particle, and L is the total pathlength of the particle. The uncertainty in this efficiency is negligible, despite its large absolute effect on the data.

However, there is a finite possibility to reconstruct a particle despite its decay. For kaons this is easy to understand, since, if the kaon decays into a charged particle between T4 and the TOF wall, there is a possibility that the TOF-to-track association algorithm will not be sensitive to the kink in the trajectory that occurs at the point of decay. The TOF wall will in this case measure a time relatively close to that of the kaon. The daughter particle will only have traveled a small distance, and so the kaon

Year	PID	D_0	D_1
1995	π	0.1800	0.1969
1995	K	0.0005786	0.05912
1996	π	0.217	0.236
1996	K	0.0002	0.0676

Table 5.4: Table of fit parameters describing the probability to reconstruct decayed particles for the 1995 and 1996 data sets. The parameters are as given in equation 5.9.

will be fully reconstructed and identified. Therefore, as in [Wan96], a cut is made on decays past $z_K = 480$ cm, and the reconstruction probability obtained only for such particles. From this, ϵ^{raw}_{decay} becomes modified to:

$$\epsilon_{decay} = \epsilon^{raw}_{decay} + P_{recon}\left(exp\left(\frac{z_{TOF} - z_K}{\beta\gamma c\tau} / \left(\frac{dz}{ds}\right)_{back}\right) - 1\right) \tag{5.8}$$

where z_{TOF} is the z_{spec} of the TOF slat hit, dz/ds is the slope of the back track, and $\beta\gamma$ is calculated from the momentum. The functional form used for P_{recon} was the same used by L. Ahle[Ahl97],

$$P_{recon} = D_0 + D_1 p \tag{5.9}$$

For the pions, a similar thing is done, except with $z_\pi = 400$ cm. The cut in z for the pions is made partially to subtract out muons from the pion decay. These muons have a rather large probability to be reconstructed completely as pions, since the muon mass is very close to that of the pion. The parameters found from the *Monte Carlo* study for the 1995 and 1996 data sets are listed in table 5.4, and the fits in figure 5-4.

5.2.5 Combined cuts

All processes were turned on, including decay, and the product of the efficiencies used checked against the results. Figure 5-5 shows the comparison of the parametrized efficiencies to the ones produced by all three processes. There is generally good consistency. However, the pions were not required to decay only after $z_{spec} = 400$

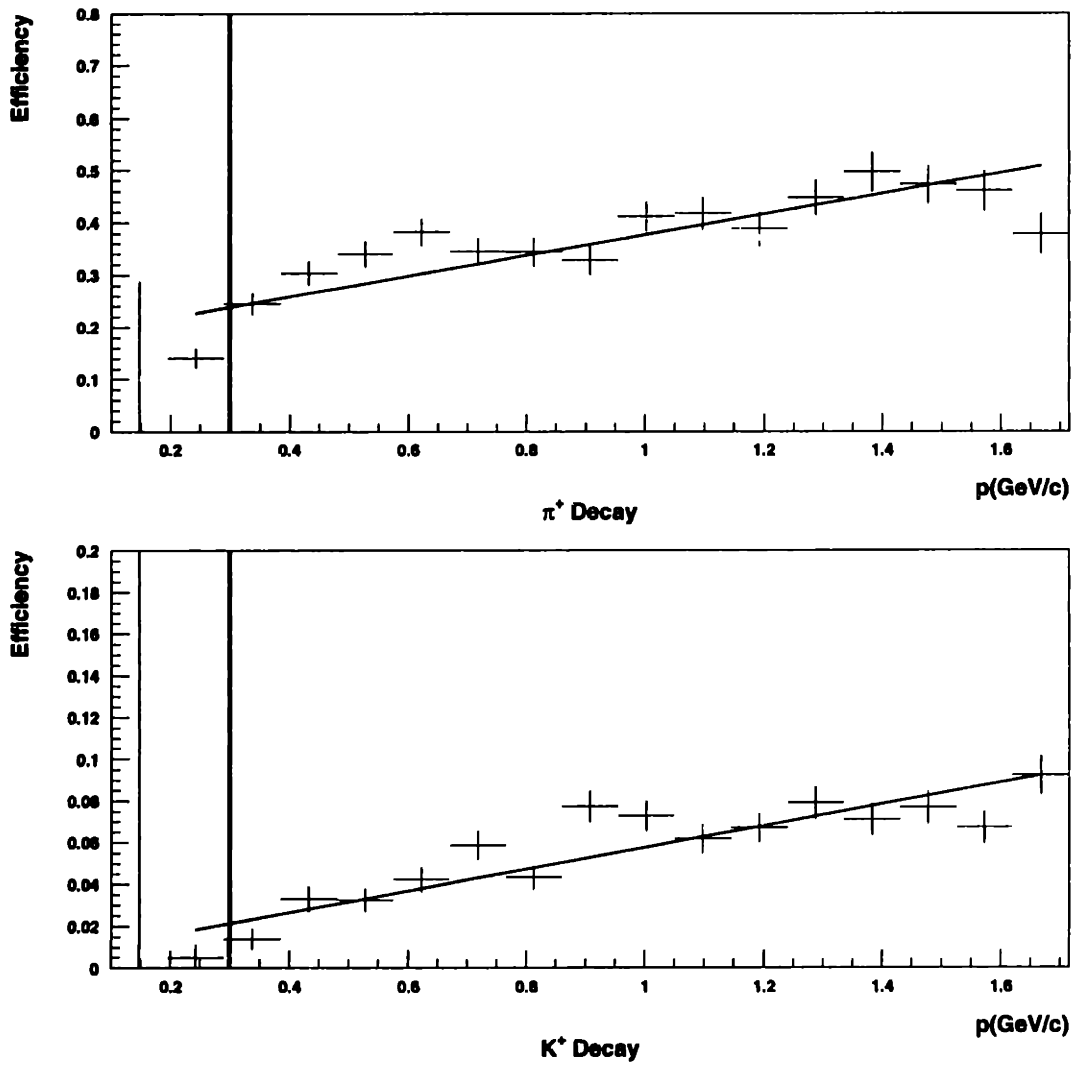

Figure 5-4: The probability to reconstruct decayed π and K, as determined by GEANT for AUFCK95. The cuts on decay position that enter into these plots are described in the text of section 5.2.4. The vertical lines indicate the cuts placed at low momentum in this analysis.

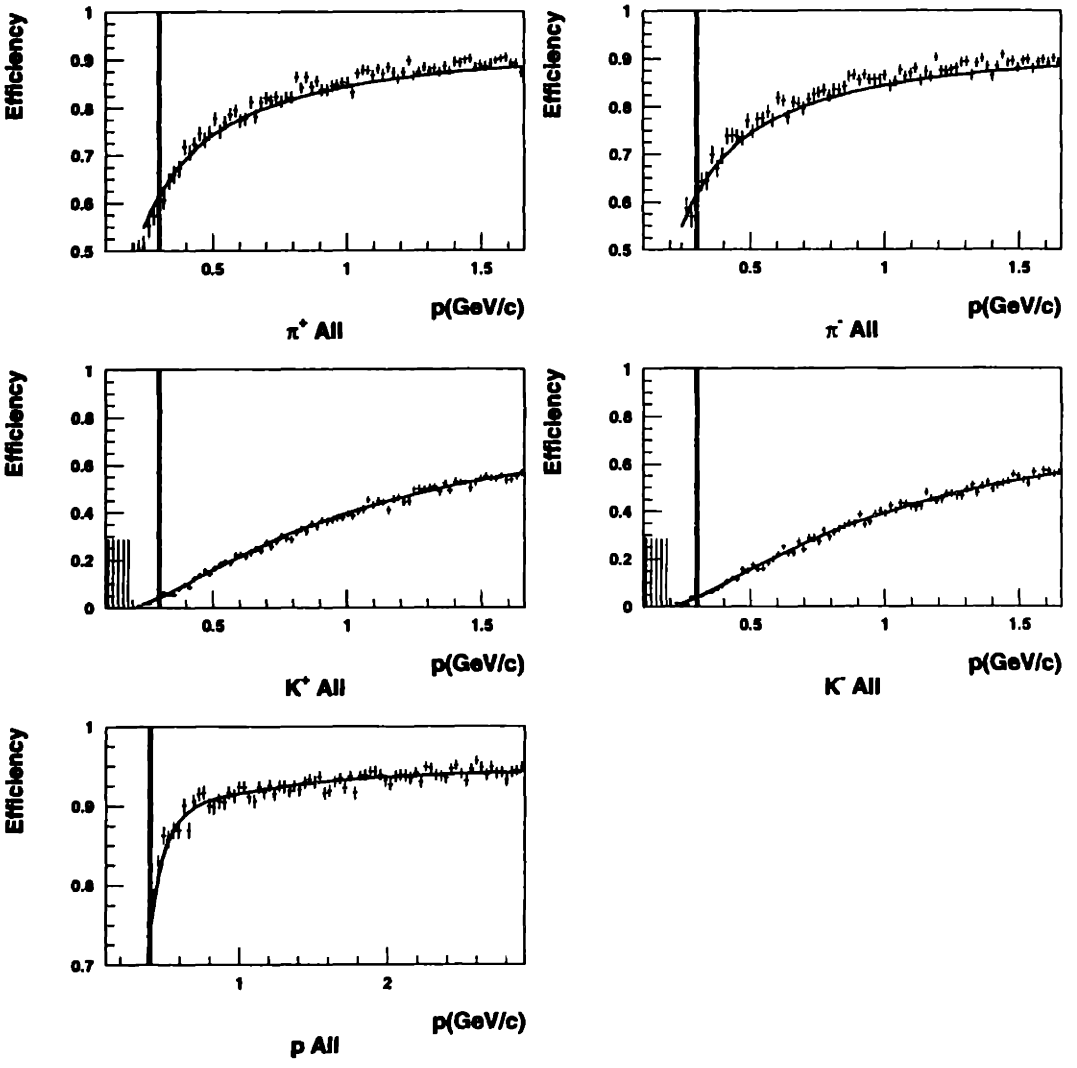

Figure 5-5: Combined efficiencies as determined by GEANT for AUFCK95. The lines show the total efficiency used in the corrections. The vertical lines indicate the cuts placed at low momentum in this analysis.

cm. Since the efficiencies attempt to remove the muons reconstructed as pions from decays before z_{spec} = 400 cm, there is a slight discrepancy seen between the results with all processes turned on and the correction.

5.2.6 A comparison between the years

There are some differences between the parameters of the 1995 data set and the 1996 data set. However, there are also differences in the algorithms between the years. The cuts in AUFCK95 were tuned rather tightly, in order to cut down on combinatoric problems. Since the multiple scattering correction is basically a measure of the tightness of the cuts, relative to the low-momentum widening of the actual distributions, it makes sense that the corrections are different. The cuts were not modified in AUFCK as run in 1996 from the values used in 1994. The existence of TR1, which is somewhat thicker than TR1MIT, will also play a role overall in the corrections.

5.2.7 Uncertainties

Cuts at low momentum are placed on the data in order to keep the corrections from becoming too large, and therefore too uncertain. All tracks identified with the given particle type with momentum below the cut values are not included. These cuts were placed at the momentum at which the efficiencies drop to approximately the 70% level. For the kaons and pions, this occurs at 0.3 GeV, while for the protons the cut was set at 0.4 GeV. The systematic uncertainty of these corrections is therefore estimated to be approximately 2%, with perhaps a bit more at the very lower edge in momentum.

5.3 Occupancy Effects

The method used for obtaining the effects on the tracking algorithms due to high occupancy was developed by L. Ahle, and is described in [Ahl97]. The method uses

the data itself to determine the corrections. Events with clean tracks are collected from the data and inserted into an unbiased sample of events. These combined events are reconstructed, and the efficiencies determined from the fraction of the clean tracks that are reconstructed in the merged events. The method therefore avoids problems in modeling the distribution of hits at high occupancy by using the data itself to create these distributions.

The results of the method consist of a large set of parameters, each of which is applied to separate portions of the data. Due to the large number of such parameters in the data set of this thesis, the space of these parameters was explored to find regularities.

No cuts are placed on the data based on these corrections, since the corrections show complicated dependencies on the conditions within the spectrometer. The variables used, with the exception of the momentum of the particle, do not directly map to measured quantities, and therefore cuts on these variables could introduce biases.

5.3.1 Method

The method is as follows. First, one finds events with one "clean" track, which satisfies a set of criteria for cleanliness. These are gathered from the data, and are called "inserted" events. Another sample of unbiased events is collected. These are selected from the data with basically no cuts, although in this analysis events were required to satisfy the SPEC1 trigger and the set of beam quality cuts, to ensure that they matched exactly the data used in the final analysis. These are called the "original" events. Then, the hits of the two types of events are merged to form the "merged" event. The merging is done using models of detector response, most critical for T2-T4 (due to their double hit capability) and the TOF wall. The merging method is described in [Ahl97], and I will not describe it here. Information is kept about the tracks in both the original and the inserted events. The merged events are then reconstructed, and the information is used to find if the clean track has been lost.

The criteria for the selection of clean tracks are simple, but very selective at high occupancy. They were carefully considered so as not to introduce biases, and to

ensure that the background in the clean event would not affect the reconstruction in the merged event. The criteria did not change for this analysis, but I will repeat them here for clarity.

First, every clean event can only have one fully matched reconstructed track, which must also have good status. The difference between these two definitions is the target-pointing and the sharing of front and back segments described in section 4.6. Second, the track needs to be inside the TR1 acceptance, because of the effects of the TR1 frame. Then, the track is projected onto the drift chamber planes. The number of hits in a search width of ± 5 mm about the projection are counted. If there are more than 2 such hits on any one plane, the event is cut. If the total number of such hits in a given module is greater than $2N_{planes} - 1$, where N_{planes} is the number of planes in a module, the event is cut. If there are more than 26 such hits on T1 or T2, or more than 30 such hits on T3 or T4, or more than 54 total such hits, the event is cut. Finally, if there are more than 300 total hits in the event, the event is cut.

These criteria can be very selective, leading only $\sim$0.5% of the events to be selected as clean in the most extreme cases. This causes difficulties in the method, since it depends on the existence of high statistics for stability of its parametrizations. Therefore, for this analysis, a single clean event is merged into multiple original events. The reasoning behind this is simple: the reasons for losing a track depend on the properties of the original event, not in detail on the properties of the event that is inserted. To the level that they do depend on such properties, the method is incorrect. The results of the method done in both ways were checked against one another, at one configuration, and were identical to within error bars.

The derived inefficiencies are then binned in a large number of ways, all of which show a dependency. The first set of these bins are separated by the beam energy, E_{beam}, the angle setting of the spectrometer, θ_{HH} and the polarity of the field. This set of quantities will be called a configuration throughout this section. Further division is made on the properties of the clean track. The sign of the clean track's charge is selected on, and the projection of the track onto T2 is binned into 8 bins. This projection basically measures the $x_{spec} - z_{spec}$ projection of the track's angle.

Then, for each such subset of the data, the dependency of the efficiency on two quantities are fit: the momentum of the clean track, and a quantity which describes the original event, the weighted hit sum (WHS). This is defined as:

$$WHS = \sum_{i=1}^{chamber} \sum_{j=1}^{view} h_{ij}/w_{ij} \tag{5.10}$$

where the first sum is a sum over the drift chambers and the TRFs, 6 in all, the second sum is a sum over the views, (X,Y,U,V), h_{ij} is the total number of hits on a given view on a given chamber, and w_{ij} is the total number of wires in that view. It is basically an average occupancy, and has a value of 24 when every wire in the experiment has a hit. It is possible for the quantity to range beyond 24 due to the double-hit capability of the chambers.

These distribution in WHS and momentum are then fit separately for each spectrometer configuration and for each T2X projection and track charge. The parameters resulting from the fit are stored, and a correction applied to the data that assumes that the contribution to the inefficiency factorizes between momentum and WHS. The factorization is simplified by the assumption (well borne out by the data) that the inefficiency shows a linear dependency on momentum. The dependency on WHS is fit to a quadratic polynomial. In other words,

$$I_{mom} = C^{p}_{off} + C^{p}_{lin}\, p \tag{5.11}$$

$$I_{WHS} = C^{WHS}_{off} + C^{WHS}_{lin}\, WHS + C^{WHS}_{quad}\, WHS^2 \tag{5.12}$$

where I_X is an inefficiency directly dependent on X, and the various C_X are "constants" determined for each configuration .

These two are then combined to give the total inefficiency:

$$I_{insertion} = I_{WHS}(WHS)\frac{I_{mom}(p_{trck})}{I_{mom}(p_{ave})} \tag{5.13}$$

where, in order to keep the factorization from overcounting, p_{ave} is the average momentum of the tracks in the sample over which the WHS was fit. The average momentum

of the clean tracks can be significantly different from that in of the original tracks. For this analysis, the momenta allowed into the sample were required to be within the range PID'd, $< 1.75\ GeV$ for negatives, and $< 3.5\ GeV$ for positives, and $> 0.3\ GeV$ for all tracks. This was to avoid some nonlinearities seen in the efficiencies at low and high momentum, and is the same set of cuts used in the creation of cross-sections.

5.3.2 Application to this analysis

It was found in the initial study [Ahl97] that the constants in equations 5.12 and 5.11 were not global, but needed to be adjusted as a function of spectrometer angle. It follows from this that the parameters do not completely describe the complicated effects of the environment. No attempt was made to find more global variables. The variables used showed only small dependences on the conditions, giving at maximum 10% deviations. These effects were large enough to cause the efficiencies to be derived separately for each beam energy, but small enough not to cause a reinvestigation of the immense parameter space available.

One modification was made to the method. In L. Ahle's analysis, the tracks used were gathered at the PASS12 stage. They therefore had not been through the REMATCH stage of reconstruction, and so the MATCH cuts had been made based on momentum alone, rather than βp. This was changed for this analysis, so that the tracks used in the efficiencies shown here are the same set of tracks in the final analysis.

Now, if one counts up all of the possible bins that one needs to make in the data from this method, one ends up with a staggering amount. There are $\sim$7 angle settings per beam energy, 4 beam energies, 2 polarity settings of the magnet, two signs of particle charge, and 8 bins in T2X, which leads to 896 configurations. There are 6 correction parameters per bin, so this works out to 5376 correction parameters that need to be determined, each robustly. In addition, not all configurations are equal. There are some configurations with extremely low statistics, but which nevertheless are desirable to include.

Therefore some simplifications were made, and a search was performed for patterns

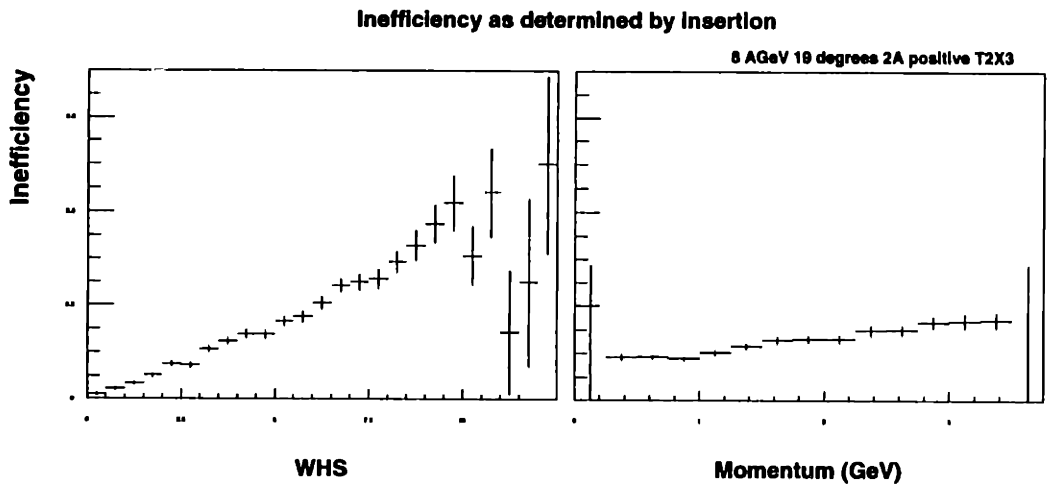

Figure 5-6: A typical inefficiency as a function of WHS and momentum. The range of WHS varies significantly across the data set.

in the parameters in order to constrain their behavior.

Figure 5-6 shows the inefficiency as a function of WHS for one configuration. This inefficiency intersects at the origin, which was found to be relatively common for all configurations. Therefore 896 parameters could be removed by requiring the polynomial fit to intersect the origin.

Figure 5-7 shows the inefficiency as a function of WHS for a configuration, for different combinations of the polarity of the field and sign of the charge. For the most part, the inefficiencies are similar across bend angles, defined as the multiple of the sign of the charged particle and the polarity of the field. L. Ahle used this combined variable, rather than the sign and polarity separately. However, at the extremes there is an $\sim$5% difference between the two settings. For the analysis of this thesis, the parameters were determined independently in sign and polarity for the 2 and 8 $A{\cdot}GeV$ data, but in terms of the bend angle for the 4 and $6A{\cdot}GeV$ data.

After these constraints, the parameter space was searched for trends, both to see if it was possible to interpolate between configurations and to see if the fitting could be made more robust. Figure 5-8 shows one of the results of this search, for one set

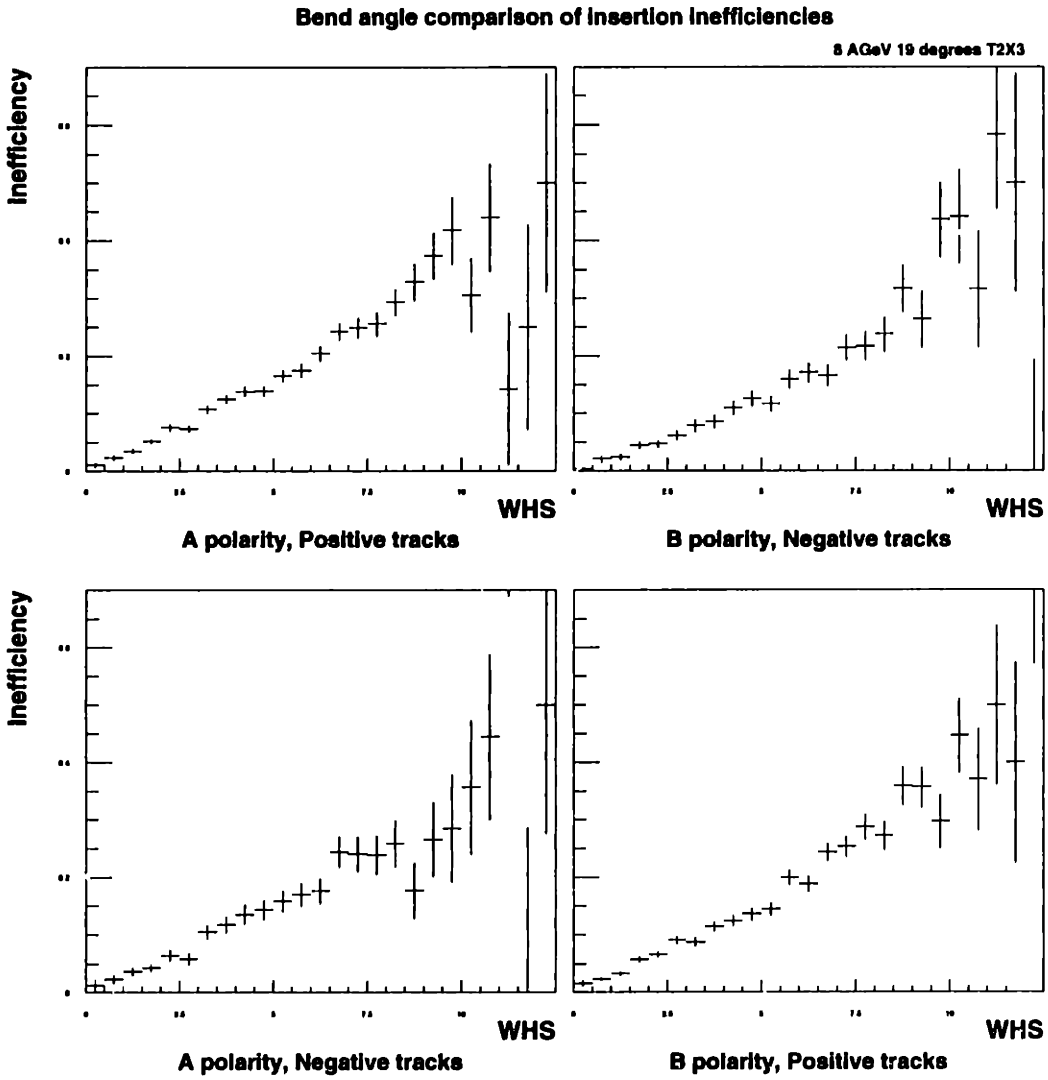

Figure 5-7: A comparison of inefficiencies for particles at the same configuration, with the exception of the sign of the charge of the particle and the polarity of the field. The data are at $8A{\cdot}GeV$, $\theta_{HH} = 19^{\circ}$, $-10 < T2X_{proj} < -5$cm.

of configurations. First, the WHS space was explored, in the two parameters C_{quad}^{WHS} and C_{lin}^{WHS} of equation 5.12. The left column of the figure shows the results of an independent fit for each angle setting of the spectrometer, within this set of configurations. The χ^2 per degree of freedom of each fits was good, but the parameters showed a level of correlated jitter across the settings, indicating that they were not independently constrained by the data. The parameter C_{quad}^{WHS} was by far the smallest, and showed the most regular behavior with θ_{HH}. This parameter was therefore constrained to lie on a line as a function of $\sin\theta_{HH}$, which seemed to describe the parameter's dependence relatively well, with a good χ^2 per degree of freedom. Then, for each angle setting, the value of C_{quad}^{WHS} was calculated based on this line, and the inefficiency as a function of WHS, $I(WHS)$, was refit, allowing only C_{lin}^{WHS} to vary. The results of this refit were used as the correction parameters. The results from this procedure were good, as shown by the bottom two panels of 5-8.

Given the regularity of C_{quad}^{WHS} and C_{lin}^{WHS} with θ_{HH}, the parameters used at some angle settings were formed from a linear interpolation between values measured at neighboring angle settings. At 2 $AGeV$, the values of C_{quad}^{WHS} and C_{lin}^{WHS} for θ_{HH} of 24° and 34° were formed in this way, while at the other energies this was done for the angle settings 29° and 39°. While the parameters describing the momentum dependence of the inefficiency (equation 5.11) showed no simple linearity on $\sin\theta_{HH}$, as seen in figure 5-9, the clear trends still permitted an interpolation between configurations.

5.3.3 Uncertainties

The uncertainties of the procedure are a bit hard to estimate. As in [Ahl97] one can check the parametrizations. By applying the parametrized efficiencies to the merged sample, track-by-track, one can check if the ratio of efficiency-corrected found tracks to inserted tracks is unity. Figure 5-10 shows the results of such an analyis, as applied to a typical configuration. The efficiencies described in section 5.3.2 parametrize the data well, although at the edges of WHS and p there are deviations on the order of 5-10%. This is not as trivial a check as it may seem, since if the factorization hypothesis is not valid the parameters will not apply correctly across the full distribution of WHS

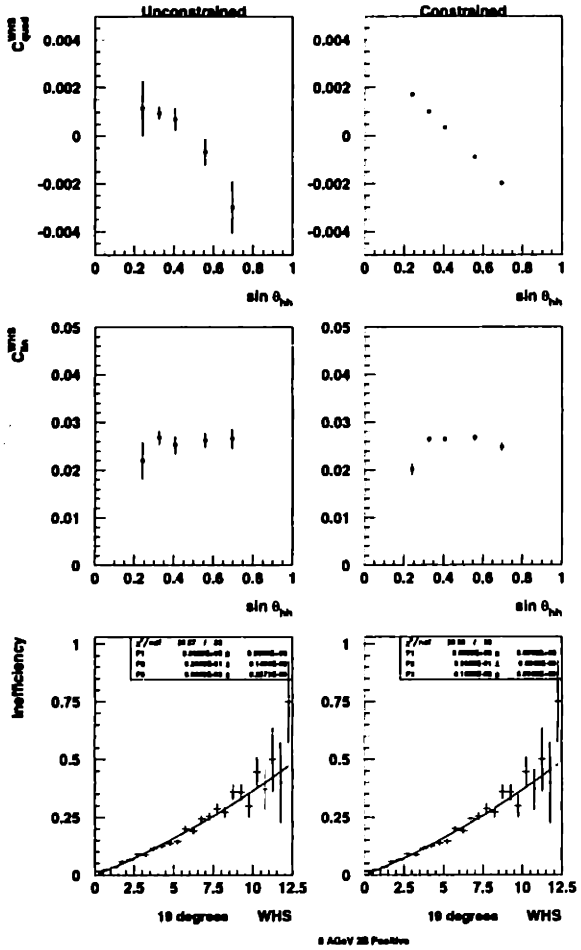

Figure 5-8: The paramaters C_{quad}^{WHS} and C_{lin}^{WHS} are plotted as a function of the spectrometer angle, $\sin\theta_{HH}$ in the top two panels. On the left are the results with an unconstrained fit, while on the right are the results after C_{quad}^{WHS} has been constrained, as described in the text of section 5.3.2. The bottom two plots show the results of the fits for the 19 degree angle setting. The data are at $8A{\cdot}GeV$, B polarity, positive tracks, $-10 < T2X_{proj} < -5$cm.

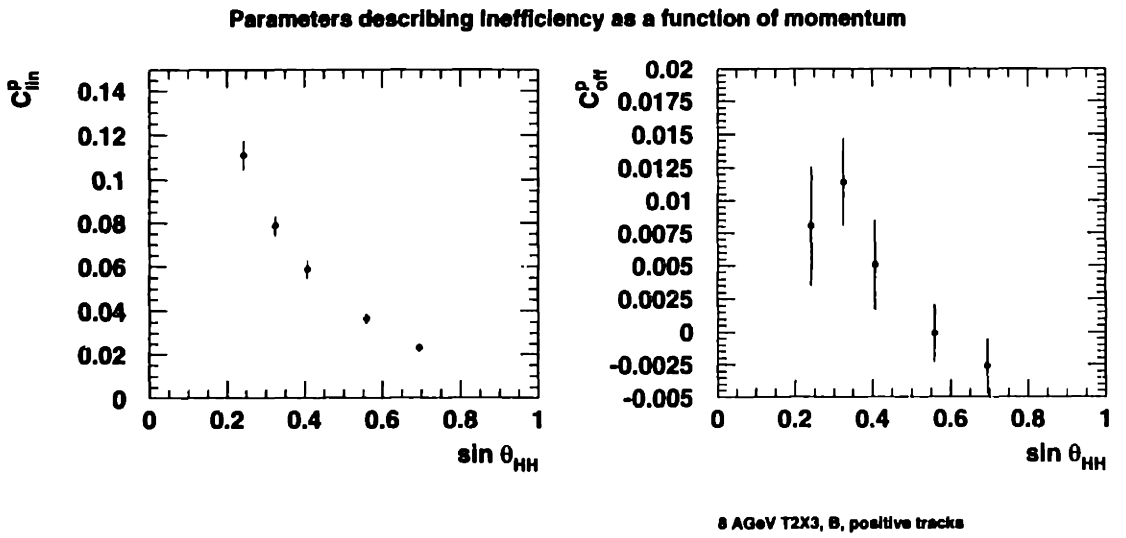

Figure 5-9: C^p_{off} and C^{MOM}_{quad} as a function of $\sin\theta_{HH}$ The parameters shown are at $8A{\cdot}GeV$, for B polarity, positive tracks, $-10 < T2X < -5$cm.

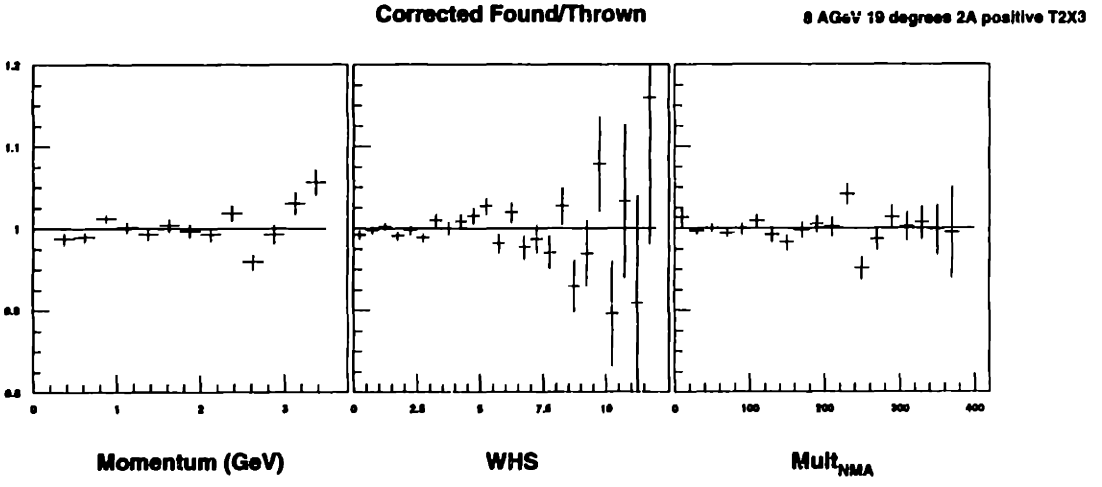

Figure 5-10: Typical Corrected Found/Thrown as a function of WHS, p, and the independent variable $Mult_{NMA}$ after applying the efficiency correction determined by the insertion method. The data are from a specific configuration at $8A{\cdot}GeV$ (19° 2A, positive tracks, T2X bin 3).

and p. The same quantity is also plotted in this figure for an independent variable, $Mult_{NMA}$. For each value of $Mult_{NMA}$, there is a broad range of WHS and p values in the spectrometer. Again, the corrections seem to work well, with some small deviations at edge values of $Mult_{NMA}$.

The systematic errors of this procedure are therefore estimated to be 5-10% at the extremes of momentum and WHS.

5.4 Single Particle Acceptance

The single particle acceptance code has a long history. It was originally written for $E802$ by C. Parsons [Par92] and was modified by D. Morrison [Mor94]. I then took over to place it within the new CWN-based analysis framework created for $E866$ by V. Cianciolo, and made a few minor modifications. L. Ahle modified it further [Ahl97] to account for the corrections made to the momentum in MATCH.

The philosophy behind the code is to use the known chamber geometries to determine the geometrical acceptance. Multiple scattering is not handled. Hence we implicitly assume that the level of scattering out of the acceptance is equal to that of scattering into the acceptance. This is valid since a fiducial cut, smaller than the active chamber region, is made on all chambers. Therefore the acceptance calculation is completely analytic, and has no probabilistic component.

There are two relevant facts about the spectrometer. The first is that the chambers have rectangular faces, not wedges of constant ϕ acceptance such as in the NMA. Further, the distribution in ϕ of the incoming impact parameter vector is uniform. Therefore, the distribution along ϕ of the outgoing particles is uniform. We use this to simplify the vertical case, which is the dominant case. In the xz plane, we divide our measurements into Y and $m_\perp$, defined in section 6.1.4, which, modulo ϕ, map directly onto positions in the xz plane. Therefore it makes sense to divide the problem into two parts: that along the vertical, y_{spec}, and that along the horizontal, x_{spec}. The dominant correction then comes in the vertical direction, by measuring the fraction of the uniform ϕ distribution that the spectrometer covers, while the edges in $(y, m_\perp)$

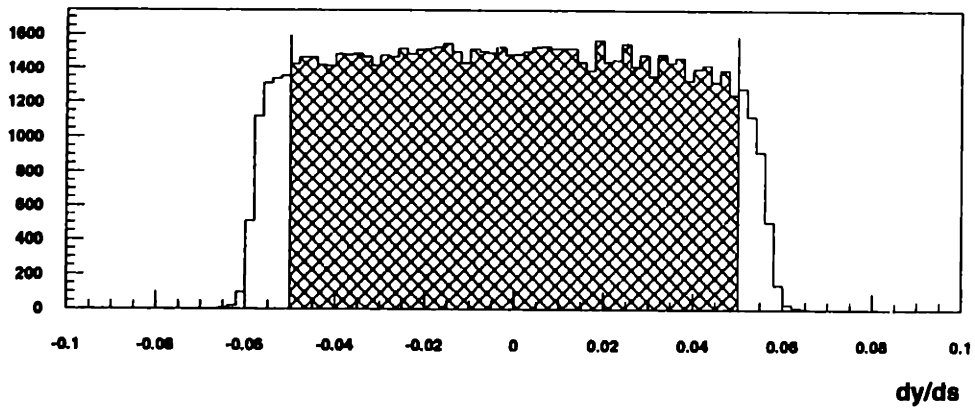

Figure 5-11: The distribution of dy/ds from a sample of good-status tracks. The cuts are shown by the lines, and the shaded region is kept. The data is from run 17602, a 24° $4A{\cdot}GeV$ run.

are calculated in the xz plane.

Beginning with the ϕ component, the spectrometer basically has a fixed range in dy/ds, defined as $\sin\theta \sin\phi$. This makes sense, given that the shape of the faces of the chambers is rectangular. However, there are some effects from vertical focusing in the magnet which lead to tails to this distribution, as described in [Wan96]. Rather than correct for these, in this analysis, as in that of [Ahl97] a hard fiducial cut is placed at the innermost edge of these effects, such that $|dy/ds| < 0.05$. Figure 5-11 shows the distribution in the data, along with the cut.

The edges of the chambers in the xz plane are then used. First, the innermost edges in x_{spec} are found across all X planes in a given chamber. These innermost x_{spec} values are then associated with the z_{spec} of the last plane of the chamber, to create one set of edges for a given chamber. The edges are then artificially decreased inwards by 0.5 cm in front of the magnet and by 1.0 cm in back.

Each such edge maps to a line in terms of two angles in the xz plane. These are θ_{xz}^{front}, the angle of the track in front of the magnet, and θ_{xz}^{bend}, the difference between the angle of the track behind the magnet with that in front. The front chambers map

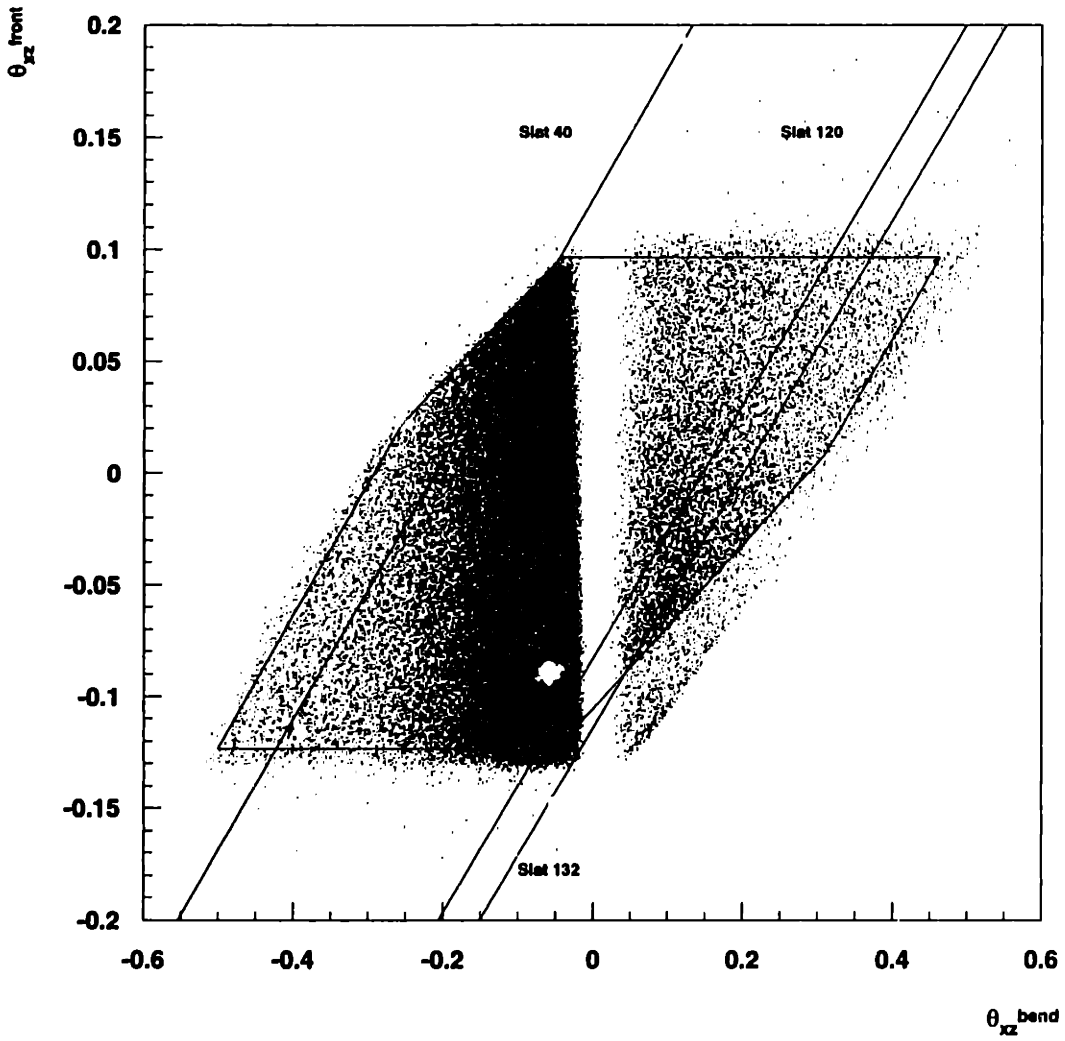

Figure 5-12: The chamber boundaries applied in θ_{xz}^{front} vs θ_{xz}^{bend}, along with data in this space. The data are from run 17602, a 1995 run, so the edge from the frame of TR1 can be clearly seen at the bottom right.

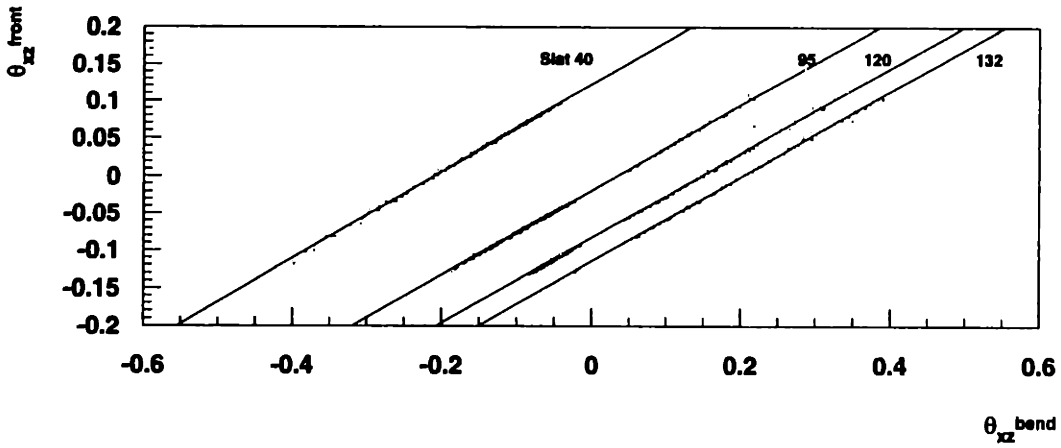

Figure 5-13: The lines describing the centers of a few TOF slats, along with data selected to point to these slats. The axes are the same as those used in in figure 5-12. At 2 and $4A{\cdot}GeV$, all tracks that hit slats less than or equal to 40, all positive tracks that hit slats greater than or equal to 132, and all negative tracks that hit slats greater than or equal to 120 are removed.

to horizontal lines, and the back chambers to lines along the diagonal. The lines that exclusively determine the acceptance are shown in figure 5-12, along with the data in this space. As described in [Mor94], the edges of the chambers in θ_{xz}^{front} shift as the target position changes in x. No modification to the acceptance is made for changes in the y position of the target.

There are TOF slats that have problems, either in hardware or in their calibrations. Such slats need to be removed from the analysis, and are removed in one of two ways. In the first, slats on the edges of the TOF wall are removed directly from the acceptance boundaries. A 1 cm fiducial cut is applied to the boundaries from such edge slats. The fiducial cut on TOF slats accepted, made at 2 and 4 $A{\cdot}GeV$(section 3.4), is applied at this point. Figure 5-13 shows the lines describing a few TOF slats, along with the positions in the acceptance space of tracks that point to these slats. The figure indicates that the position of the slats is well parametrized within the acceptance code.

From the boundaries, an average xz acceptance, $acc\,(\theta_{xz}, tof)$, is calculated for each bin in rapidity and transverse mass, $(Y, m_\perp)$ (defined in section 6.1.4). Each bin is divided into an 11x11 grid. For every $(y, m_\perp)$ point on this grid, θ_{xz}^{front} and θ_{xz}^{bend} are calculated by assuming that the particle lies in the xz plane at $y = 0$. For each of these test particles, the total range in ϕ allowed, $\Delta\phi$, is calculated, using either the relation $|dy/ds| < 0.05$ or one calculated from the minimum and maximum θ_{xz} given by the chamber boundaries. TOF slats on the inner portion of the TOF wall are removed at this stage. The ϕ range occluded by a slat is cut from $\Delta\phi$, and the fraction of $\Delta\phi$ that has been cut is returned. In order to account for multiple scattering, this correction is given a finite width in slat space, such that a weighted portion of the neighboring slats are also removed. Within a given $(Y, m_\perp)$ bin, a weighted average is made of the fractions returned for the set of test particles, with weights taking account of the effects on the edges of the bin. The average fraction over the bin is then used as a correction to the data, bin by bin in $(y, m_\perp)$.

Further, the fraction $\Delta\phi$ is applied to the data on a particle-by-particle basis. The application of both of these corrections to the data will be described in more detail in section 6.

5.4.1 Uncertainties

The errors in the determination of $acc(\theta_{xz}, TOF)$ are estimated to be approximately 5% of the correction. A cut is applied to the data, such that the total correction applied to the data from $acc(\theta_{xz}, tof)$ is never above 30%, and therefore this error is small. Uncertainties in the empirical bend-angle reconstruction add another source of error, potentially larger, since for certain ranges of (p, θ, ϕ) this determination enters into the much larger $\Delta\phi$ correction.

5.5 Backgrounds in Particle Identification

Backgrounds in particle identification have not previously been considered in the analysis of kaons. However, as the beam energy decreases, the ratio of kaons to other

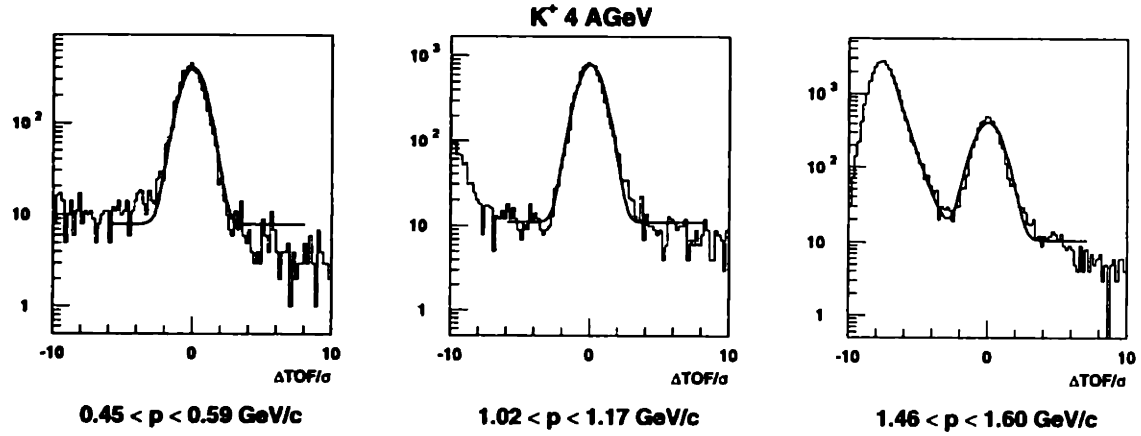

Figure 5-14: The distribution of $(\Delta TOF)/\sigma_{TOF}$ for kaons. The distributions include all of the K^+ at $4A{\cdot}GeV K^+$, and the fit is as described in the text of section 5.5.

particles decreases. This leads the kaons to become a somewhat "rare" particle, though not to the level of the antiprotons.

Therefore, background levels were investigated, using the methods developed by G. Heintzelman for the analysis of antiprotons, and described in [Hei99]. The backgrounds were found to be significant in restricted regions of momentum. At high momenta, the tails of the pion distributions overlap with the 3σ cuts at a significant level, and at low momenta a flat background becomes significant.

In this analysis the momentum range over which kaons are measured is restricted to those in which the backgrounds can be determined.

The basic method is as follows. First, a distribution of $\Delta TOF/\sigma_{TOF}$ is formed over a wide range, out to ± 10. The definitions of these quantities are similar to those of $\Delta 1/\beta$ and $\sigma_{1/\beta}$ in PICD (section 4.8), except that the path length enters into the expected quantity rather than the measured quantity. A kaon mass hypothesis is taken. For different bins in momentum, a separate $\Delta TOF/\sigma TOF$ distribution is formed. For each of these bins, the fraction of the total number of tracks that is due to the signal, the signal fraction, is determined directly from a fit to the distribution. The functional form used is the sum of an exponential, a Gaussian, and a flat component. Figure 5-14 shows one such distribution along with the fit, and figure 5-15 shows the

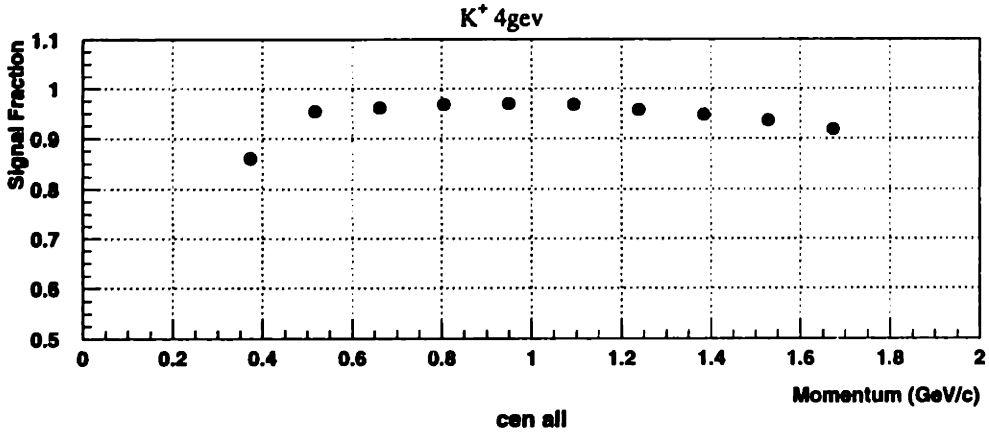

Figure 5-15: The signal fraction, as determined from the fits, as a function of momentum. The data are for K^+ at $4A{\cdot}GeV$, integrated over all configurations. the fit is as described in the text of section 5.5.

momentum dependence of the signal fraction for the entire sample of K^+ at $4A{\cdot}GeV$. For momenta below 1.17 GeV for the K^+ and 1.31 GeV for the $K-$ the exponential portion of the fit is removed. These momenta correspond roughly to the lower edge in momentum below which the tails of the pion distributions do not affect the fits. Removing the exponential improved the stability of the fits. In order to make the fits match the data, the width of the peak needed to be artificially decreased to 85% of its assumed value. The value was calculated based on a 130 ps timing resolution, implying that the actual resolution, averaged over all TOF slats, is on the order of 110 ps. In order to produce stable fits, each ΔTOF distribution needs to contain on the order of a few hundred particles. The signal fraction is likely to depend on the momentum of the particle, p,the angle of the spectrometer, θ_{HH}, the energy of the beam, E_{beam}, and the NMA centrality class. Exploring these dependencies leads to lower statistics at each configuration.

For a given E_{beam} and p, the data was binned in three ways:

- In $Mult_{NMA}$, regardless of θ_{HH}

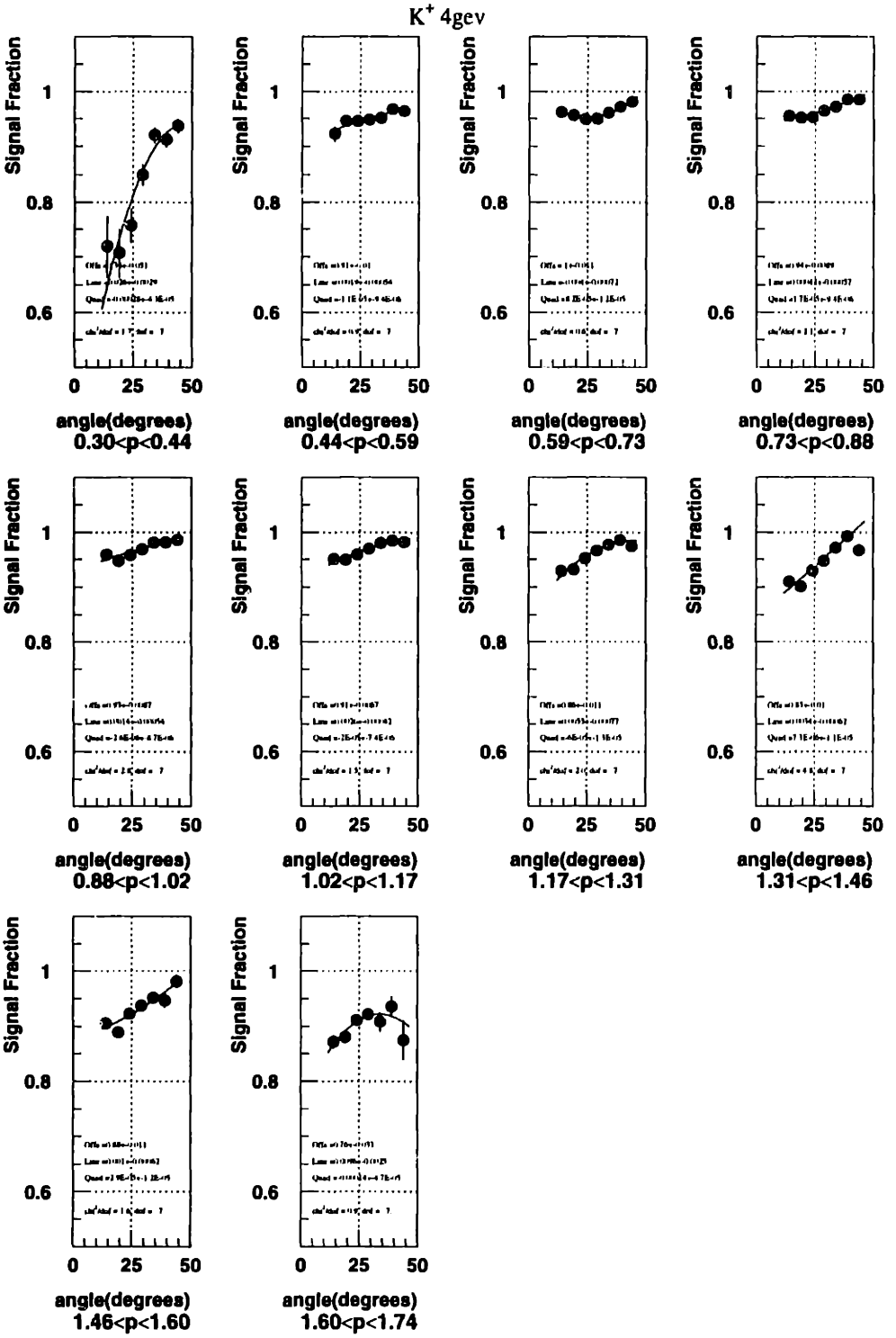

Figure 5-16: The signal fraction, as determined from fits to $\Delta_{TOF}/\sigma_{TOF}$, as a function of θ_{HH}, for 10 momentum bins. The data are for K^+ at $4A{\cdot}GeV$, and the fit is as described in the text of section 5.5.

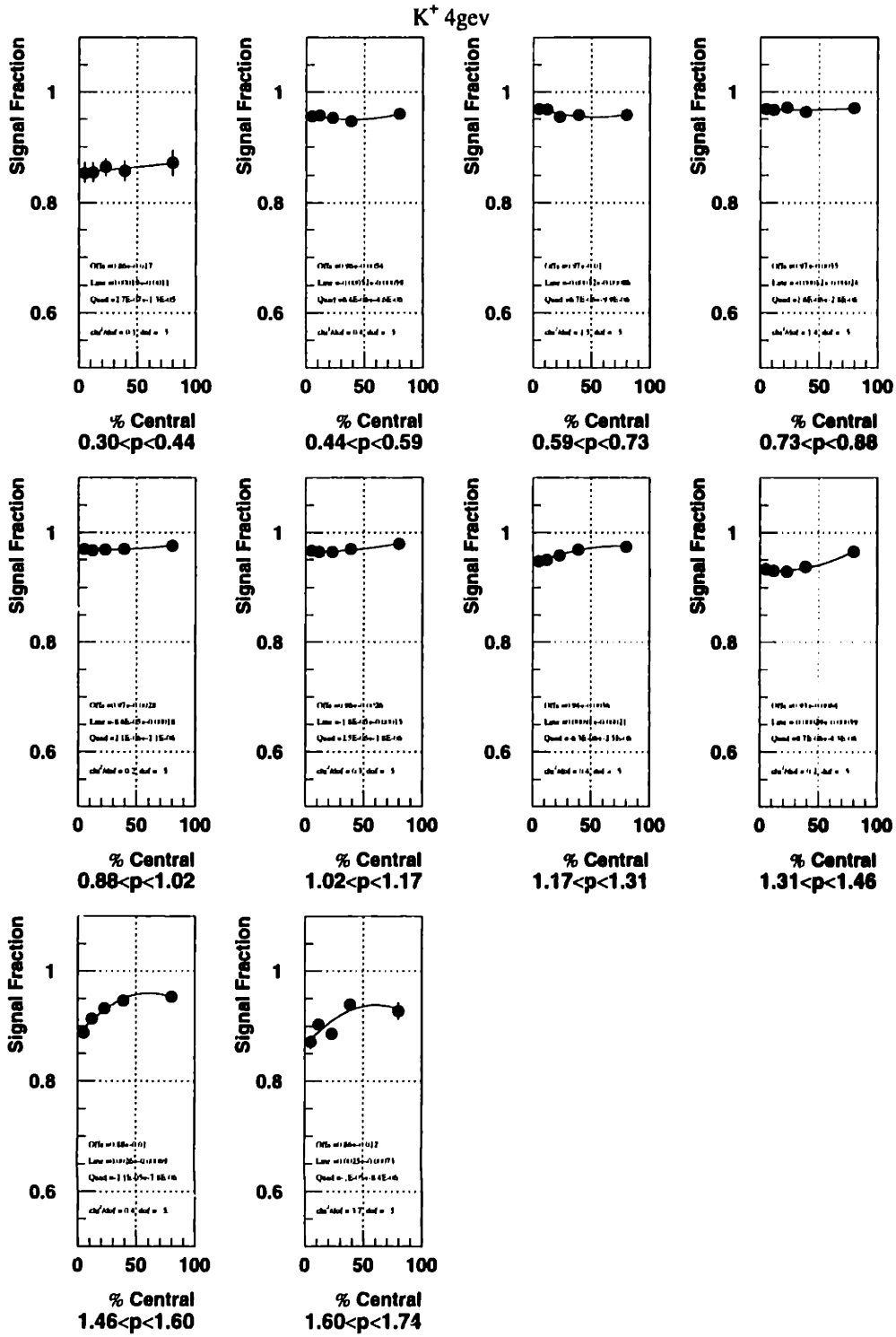

Figure 5-17: The signal fraction, as determined from fits to $\Delta_{TOF}/\sigma_{TOF}$, as a function of the NMA centrality class, for 10 momentum bins. The data are from 4, and the fit is as described in the text of section 5.5.

- In θ_{HH}, regardless of $Mult_{NMA}$
- Regardless of either $Mult_{NMA}$ or θ_{HH}

The results were then applied to the data using a factorization hypothesis, since the statistics did not allow for a determination in $Mult_{NMA}$ and θ_{HH} separately.

If we assume that the value of the signal fraction factorizes in $Mult_{NMA}$ and θ_{HH}, at each momentum p and beam energy E_{beam} it is given by:

$$SF(p, E_{beam}; \theta_{HH}, Mult_{NMA}) = \frac{SF(p; E_{beam}, \theta_{HH}) SF(p; E_{beam}, Mult_{NMA})}{SF(p; E_{beam})} \quad (5.14)$$

where $SF(X;Y)$ stands for the signal fraction as a function of X, given the set of cuts Y.

In order to remove some of the stability problems in the fits, a regularization approach similar to that used in the insertion method was taken. For a given momentum bin, the signal fraction was fit to a second-order polynomial as a function of θ_{HH} and centrality class. Figure 5-16 shows one such fit, for K^+ from the 4 $A{\cdot}GeV$ running. The signal fraction is binned in momentum and plotted as a function of θ_{HH}. The dependency is quite regular, but the dependency is also quite large for the lowest and highest bin in momentum. For completeness, the signal fraction as a function of centrality class is shown in figure 5-17. The signal fraction is then extracted from the second-order polynomial fuction for each configuration of θ_{HH} and centrality class. Figure 5-18 shows an example of the final correction results, again for K^+ at $4A{\cdot}GeV$.

The factorization hypothesis cannot be easily checked in the momentum regions in which the corrections become large. The level of change across angle settings in these regions is large, which most likely implies that the dependency in angle across the spectrometer is also large. Since the correction is not parametrized as a function of the angle within the spectrometer, the corrections may have a large degree of uncertainty in these momentum regions.

Therefore, in order to ensure that all data is of high quality, the momentum region over which the kaons are measured is restricted in this analysis. The location of the cut is common across all configurations, as with the cuts used in the PID algorithm

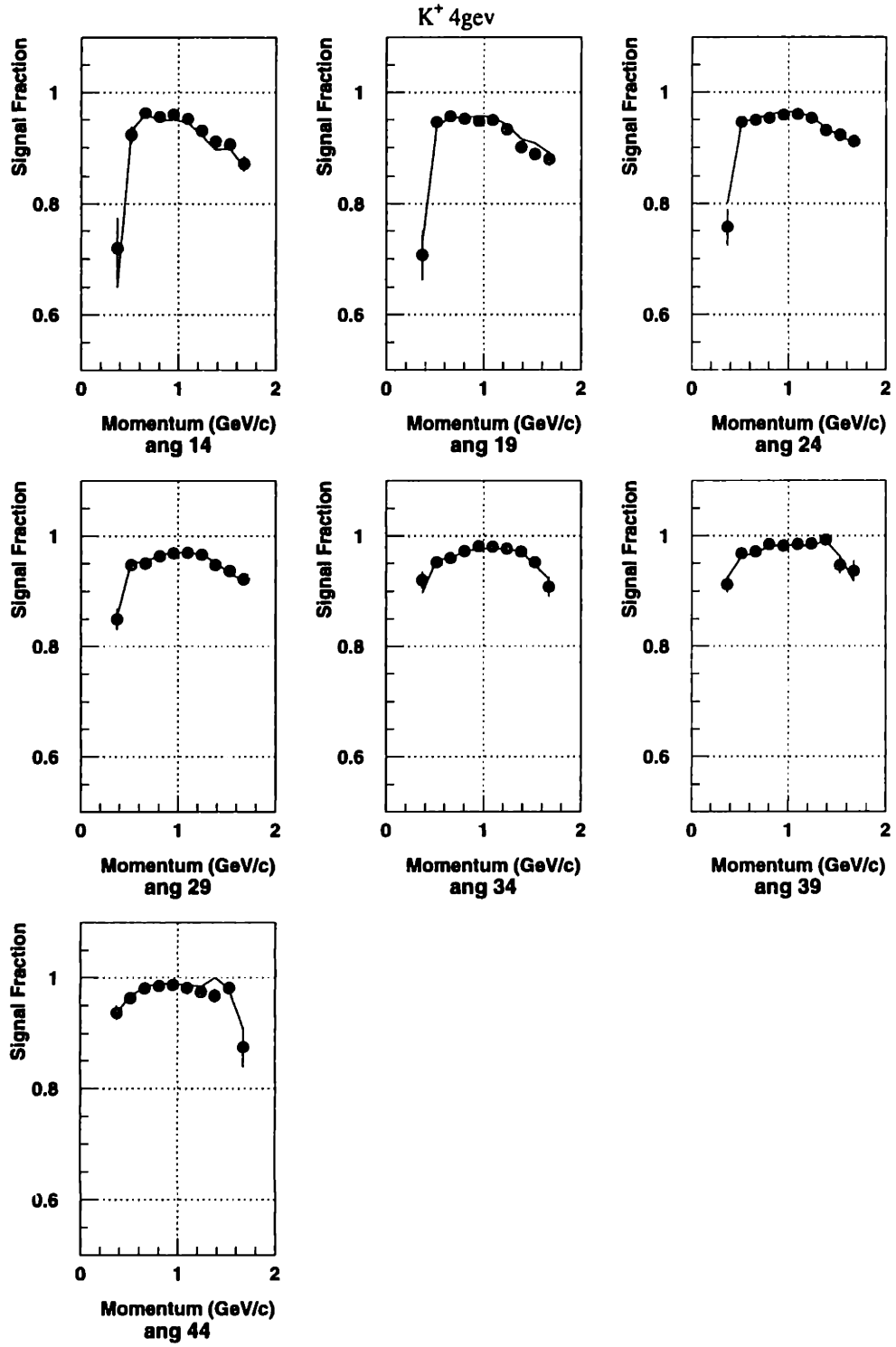

Figure 5-18: The signal fraction, as determined from fits to $\Delta_{TOF}/\sigma_{TOF}$, as a function of momentum, for the 7 angles of the spectrometer. The data are for K^+ at $4A{\cdot}GeV$. The line is the correction applied to the data. It has been regularized as described in the text of section 5.5.

and those determined from the *Monte Carlo* studies. To be precise, all kaons shown in this analysis have momenta less than $1.6A{\cdot}GeV$ and greater than $0.45A{\cdot}GeV$, the location of which was chosen so that the correction would not be more than 30%.

Given the coarse-grained nature of the parametrization, combined with both the need to use a factorization hypothesis and the level of the backgrounds, the uncertainties in this procedure are estimated to be approximately 5% at the extremes of momentum.

5.6 Normalization

5.6.1 Overview

In order to produce cross-sections, one needs to normalize the number of particles seen in the spectrometer to a quantity related to the number of interactions that have occurred. This normalization has some subtleties, due to the large empty target backgrounds of the experiment. These empty target backgrounds rarely produce a good-status track in the spectrometer, but need to be subtracted from the rate of interaction triggers.

In addition, to form yields given a cut in centrality, the cross-section within the centrality cut needs to be known.

5.6.2 Beam Quality Cuts

5.6.3 Overview

The interaction events have a significant empty target background in this experiment. This is especially the case in $E917$, with the addition of the BVER. There was also a high beam rate for the data presented in this thesis, and, as mentioned in 2.6.1, the online interaction trigger was loosened for the low-energy data. The combination of these factors leads to a significant number of interaction events that need to be cut in order to ensure that the events taken are of the highest quality, so as not to introduce

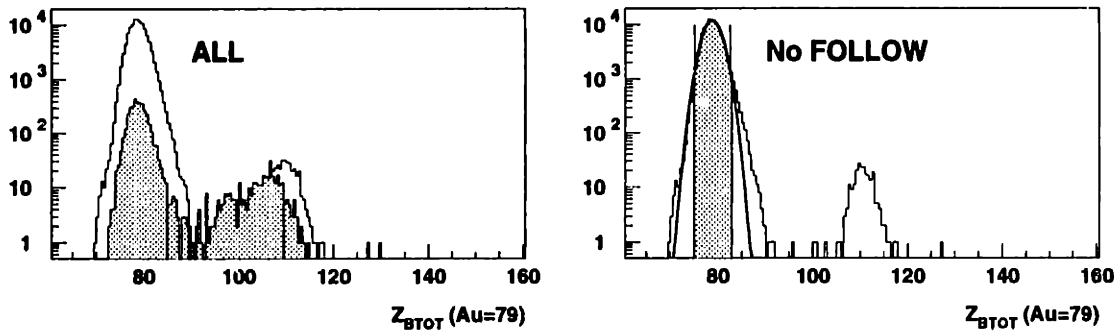

Figure 5-19: A typical Z_{BTOT} distribution. On the left, the unshaded histogram shows the distribution of charge in the BTOT for all events, while the shaded histograms shows that for FOLLOW events. The right histogram shows the distribution for events with no FOLLOW bit set, along with the cut value used. The data are from a 4 $A{\cdot}GeV$ run, run 17602.

errors into the measured cross-sections. Table 6.3 lists the cuts made.

The strategy is to cut in quantities that are correlated with the empty target background, ensuring that minimal biases are introduced. Residual background after these cuts is then subtracted from the normalization. Cuts are also made to ensure that the particles measured come from single collisions between Au nuclei, rather than between two or more such collisions that fall within the time window of a single normal event.

5.6.4 Description

The first set of cuts consists of a set of hardware cuts, made on FOLLOW and PRE, as described in 2.11.1. These are relatively simple cuts made to reduce pileup, in which two or more $Au-Au$ collisions fall within the timing windows of the experiment. The second set of cuts is made on the charge measured by the BTOT, Z_{BTOT}. Figure 5-19 shows a typical distribution of this type. Notice the tail at the high end of the main peak, and the secondary peak that is not completely cut by FOLLOW. This high tail is not a Landau tail, since the BTOT uses Čerenkov radiation rather than E_{loss} as its physical detection method. The width and center of the peaks are checked run-

E_{beam} $(A{\cdot}GeV)$	Mean Z	σ_Z	Low cut	High cut
4	78.90	1.89	75.12	82.68
2	78.84	2.4	74.04	83.64
6 & 8	78.6	2.6	73.4	83.8

Table 5.5: The cuts applied to Z_{BTOT} as a function of E_{beam}. The table is in chronological order as the data was taken. The 6 and 8 $A{\cdot}GeV$ data were found to be consistent with the high-energy data of $E917$, shown in [Hei99]. Note the slight worsening of resolution.

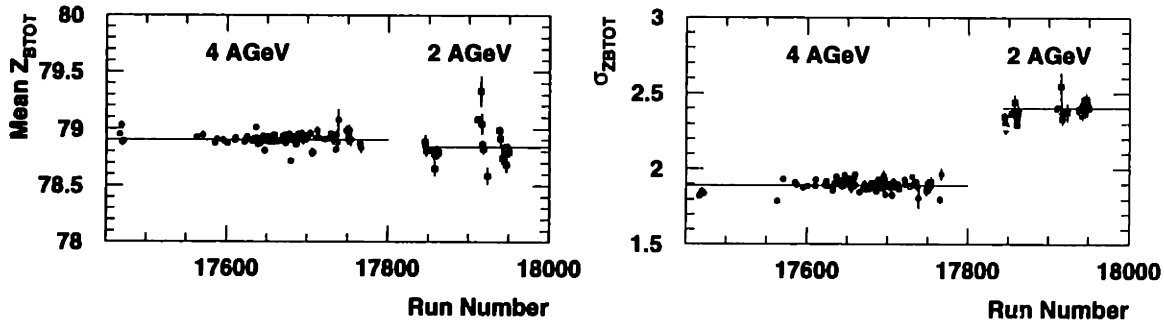

Figure 5-20: The mean and σ of a Gaussian fit to the peak in Z_{BTOT} vs run in the 2 and 4 $A{\cdot}GeV$ data.

by-run, and a strict 2σ cut is made on the charge distribution. The center and width of the peak were found to be relatively stable as a function of run, within a given E_{beam}, and so the mean and width of the distributions were fit as a function of run and applied beam energy by beam energy. The fits were performed on distributions cut on "clean beam", which required the BEAM trigger to be fired, $BE_{hardsum}$ to be above 650 (see section 5.6.6), and the FOLLOW bit not to be set. Table 5.5 lists the cuts applied, and figure 5-20 shows the data on which the cuts are based for 2 and 4 $A{\cdot}GeV$. The cuts needed for the 6 and 8 $A{\cdot}GeV$ data were found to be consistent with the high-energy data, the derivation of which is described in [Hei99].

The next cut is on the HOLE detector. As described in section 2.5.2, the HOLE detector is used to remove events in which there are either other particles associated with the beam, or in which a beam particle the scintillator outside the hole. It is impossible to calibrate the HOLE detector. Therefore, the assumption is made that clean beam events should, to first order, have no upstream interactions, and we can

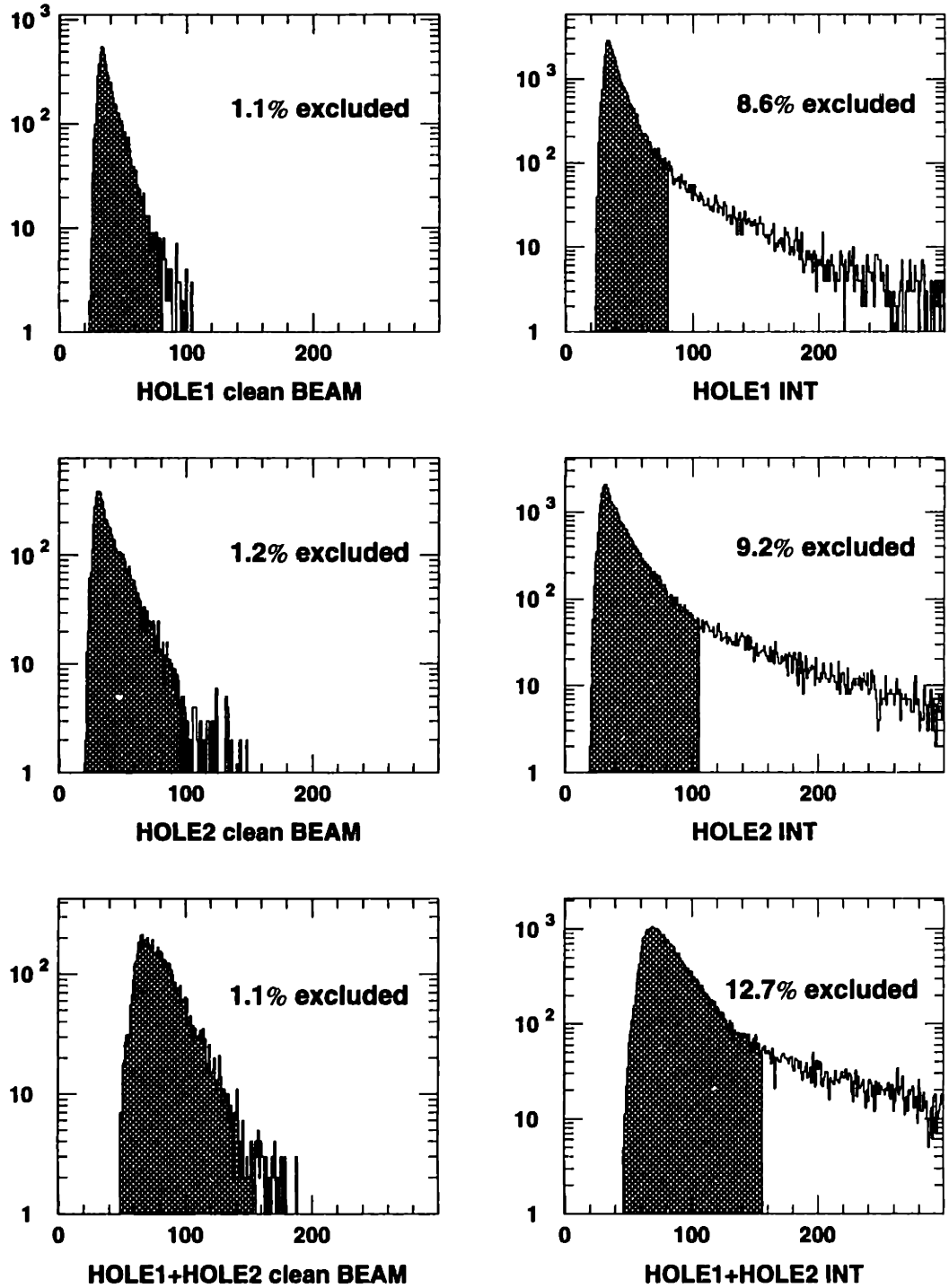

Figure 5-21: A typical set of HOLE distributions. The left panel is from clean BEAM events, and the right panel is from INT events. The shaded portion is kept by the cuts, and the fraction removed by the cuts indicated. The data are from run 30175, an early 6 $A{\cdot}GeV$ run.

E_{beam} (A·GeV)	HOLE1	HOLE2	HOLE3
4	32	45	77
2	28	39	68
6	80	105	155
8	80	48	111

Table 5.6: The cuts applied to HOLE as a function of run. The table is in chronological order as the data was taken. For a portion of the 6 A·GeV run HOLE2 was not active, so the last two cuts were not applied.

remove the last 1% of the tails of the clean beam distributions without introducing bias. There are three quantities on which the cut is made: HOLE1, corresponding to the ADC readout of one phototube, HOLE2, corresponding to the readout of the other tube, and HOLE1+HOLE2. For each of these quantities, the cut value is set at the value above which 1% of the clean beam events fall. Figure 5-21 shows these distributions, along with the cuts, for a typical run. Also plotted in that figure. are the distributions for INT events, where INT is defined in software as $BE_{hardsum} < 600$. A much larger fraction of interaction events than clean beam events are cut.

The cut values required by this criterion were then studied as a function of run. Figure 5-22 shows the values necessary for the four beam energies. There is a portion of the 6 A·GeV run period in which HOLE2 was not active, and so no cut is applied on HOLE2 or HOLE1+HOLE2 in these runs. There are some shifts in the values of the cuts that need to be used. This is to be expected, since the readouts are not calibrated. Table 5.6 lists the cuts applied.

A further cut is made on the NMA $\langle\eta\rangle$ distribution. A typical distribution of $\langle\eta\rangle$ vs $Mult_{NMA}$ is shown in figure 5-23 for both a run with the target in place and an empty target run. η is the pseudorapidity, and <> denotes a mean. The mean is taken over all Weighted hits on the NMA for the 6 and 8 A·GeV data, and over all Real hits on the NMA for the 2 and 4 A·GeV data, for reasons described in 5.6.7.

There is a secondary peak at low η, which is dominant in the empty target run. This is thought to be caused by the shower of particles from upstream interactions onto the backward modules. A similar effect was seen in $E802$[Par92] with the multiplicity detector in place for that experiment, the TMA. The tail of this secondary peak

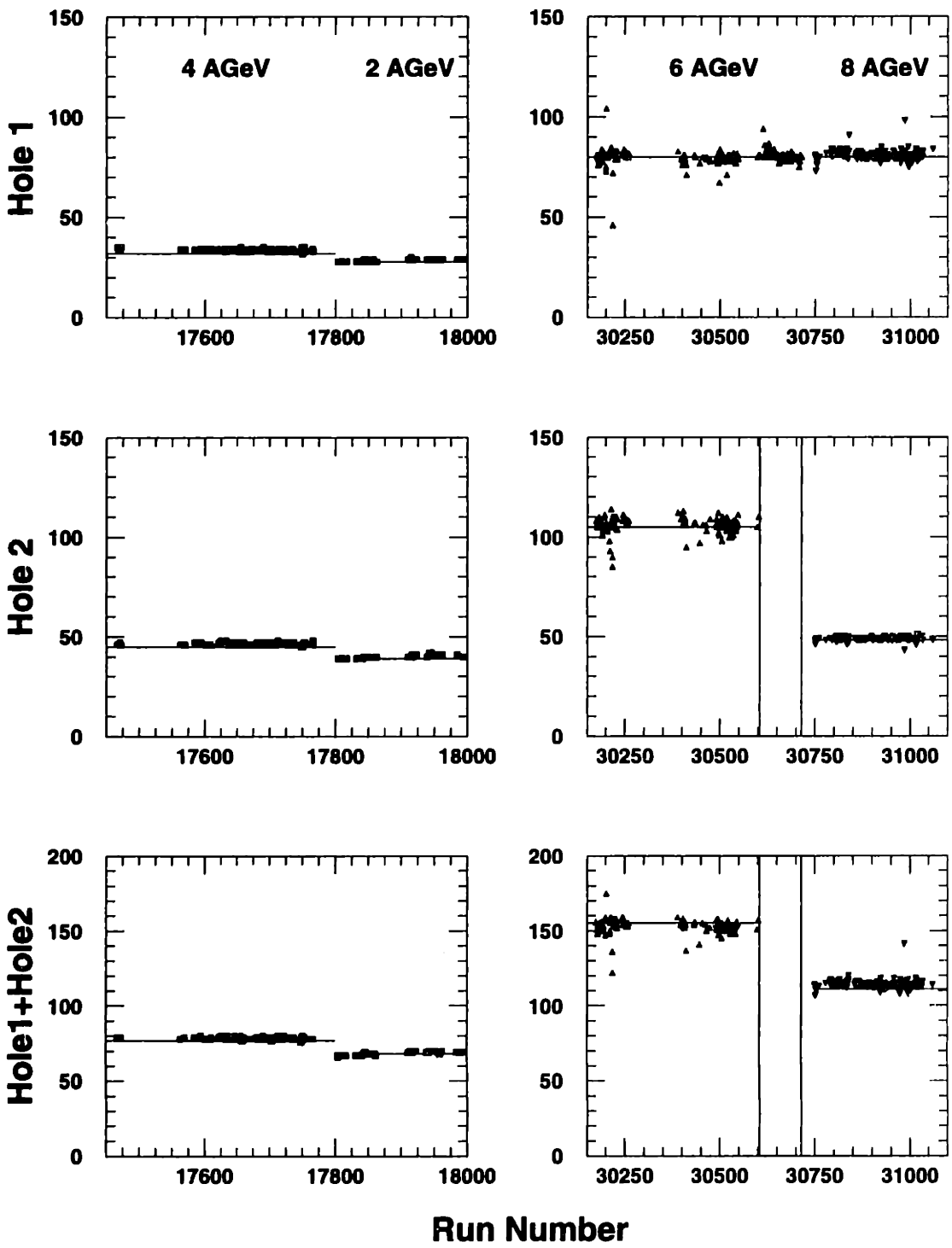

Figure 5-22: The cut values required for the three hole cuts, vs run, for all 4 beam energies. Note the area in the 6 $A \cdot GeV$ running where HOLE2 was not active.

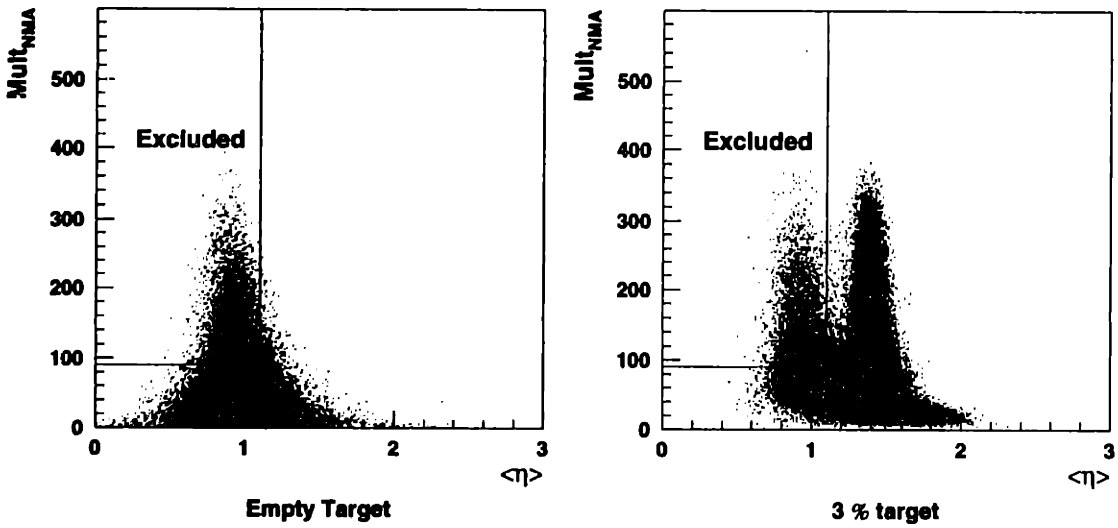

Figure 5-23: A typical NMA $\langle\eta\rangle$ vs $Mult_{NMA}$ distribution. The left panel show an empty target run, and the right panel shows a run with the target in place. The lines show the location of the cuts. The 3% target data is from run 30175, an early $6A{\cdot}GeV$ run, while the empty target data is from run 30184, taken a few hours later.

extends to high multiplicity, and has the potential to affect central events. In data where the ZCAL information is trustworthy, the hits in this secondary peak fall into a secondary band in the correlation between the ZCAL energy and $Mult_{NMA}$[Ahl97].

Therefore, events for which $\langle\eta\rangle < 1.1$ and $NMA_{mult} > 90$ are removed. The value 1.1 was chosen since it falls approximately at the minimum between the two secondary peaks, in areas in which the peaks are distinguishable, and 90 was chosen as the point below which the two peaks were indistinguishable. These criteria were stable for all E_{beam}.

There are two further binary cuts. The first requires all 4 planes of the BVER to be hit, and is therefore only applied in $E917$. As mentioned in section 2.5.3, the beam misses one of the upstream planes for certain tunes. This was considered undesirable, and so this occurrence was cut. The cut also includes any inefficiencies in the BVER. Since the beam moves around for different tunes, and since the BVER measures a full beam vector, any further cuts on the BVER require some careful examination of the data, run-by-run, that was not performed for this thesis.

At a very low level, approximately 0.05% at worst, the readout chain of the NMA (and all detectors in FBU0, including the ZCAL, the BVER, and the Hodoscope) fails. This failure is assumed to be uncorrelated with any physics of the event, but is cut in order to ensure that a central event is not called a peripheral event due to a zero in the NMA.

5.6.5 Results

The combined result of the beam quality cuts is rather large, especially in $E917$. The change between $E866$ and $E917$ is not surprising, given the change in in the overall level of the empty target contribution. This change is likely due to the addition of the BVER material.

Figure 5-24 shows a breakdown of the results of the cuts, cut type by cut type. The offline $BE_{hardsum}$ cut (see section 5.6.6) is applied to the data before the fractions are calculated. There is quite a bit of overlap between the various cuts, as can be seen by the difference between the Sole and Regardless panels.

Overall, in the 6 and 8 $A{\cdot}GeV$ periods, approximately $35-40\%$ of the interaction events are cut due to the combined beam quality cuts, although the fraction varies with running conditions. The fraction is smaller for the 2 and 4 $A{\cdot}GeV$ periods, around 10%. Figure 5-25 shows the total fraction of events cut for all four beam energies. Again, the $BE_{hardsum}$ cut has been applied before creating the fractions.

As should be expected, for empty target runs the fraction of interaction events cut is significantly larger. This fraction is approximately 20% at 2 and $4A{\cdot}GeV$, and approximately 60% at 6 and $8AGeV$, as opposed to the 10% and 40%, respectively, for events in which the target is in place. This indicates that the cuts are well correlated with interactions outside of the target material.

A study was made of the number of tracks found in empty target runs, after all beam quality cuts had been applied. While there were a significant number of tracks found, only 1 out of the sample of 100,000 was a good-status track. The rest were mostly tracks that did not pass the target cut. Because of the low rate, no attempt is made to subtract the cross-sections measured in empty target runs from those

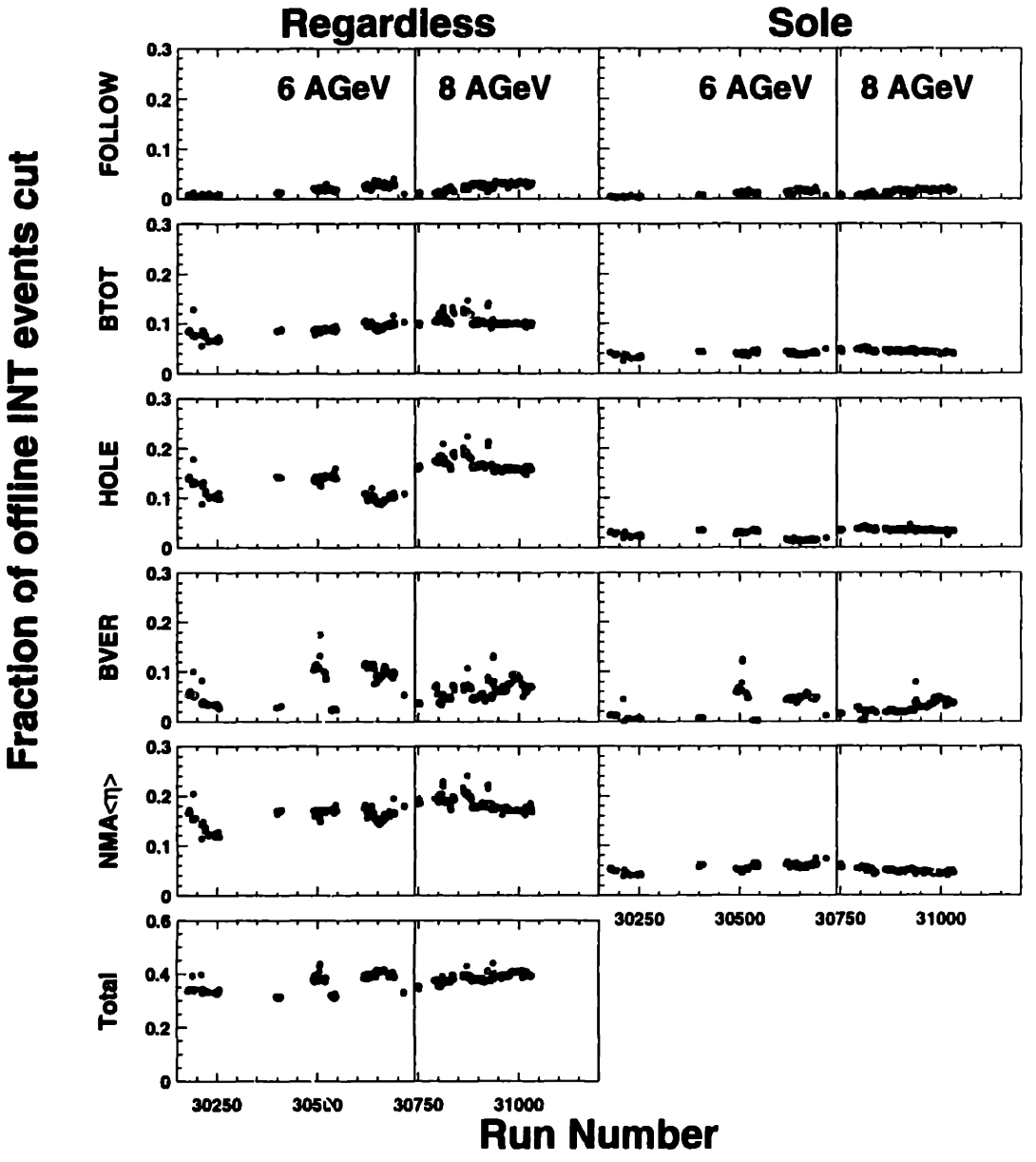

Figure 5-24: Breakdown of the individual contributions to the beam quality cuts. The figure shows the fraction of software INT triggers (section 5.6.6) cut by the individual cuts, as a function of run number, in the 6 and 8 $A \cdot GeV$ periods. The "Regardless" panel shows the fraction cut by the given cut, regardless of whether any other cut applies to that event. The "Sole" panel shows the fraction of software INT triggers that are cut solely due to the given cut.

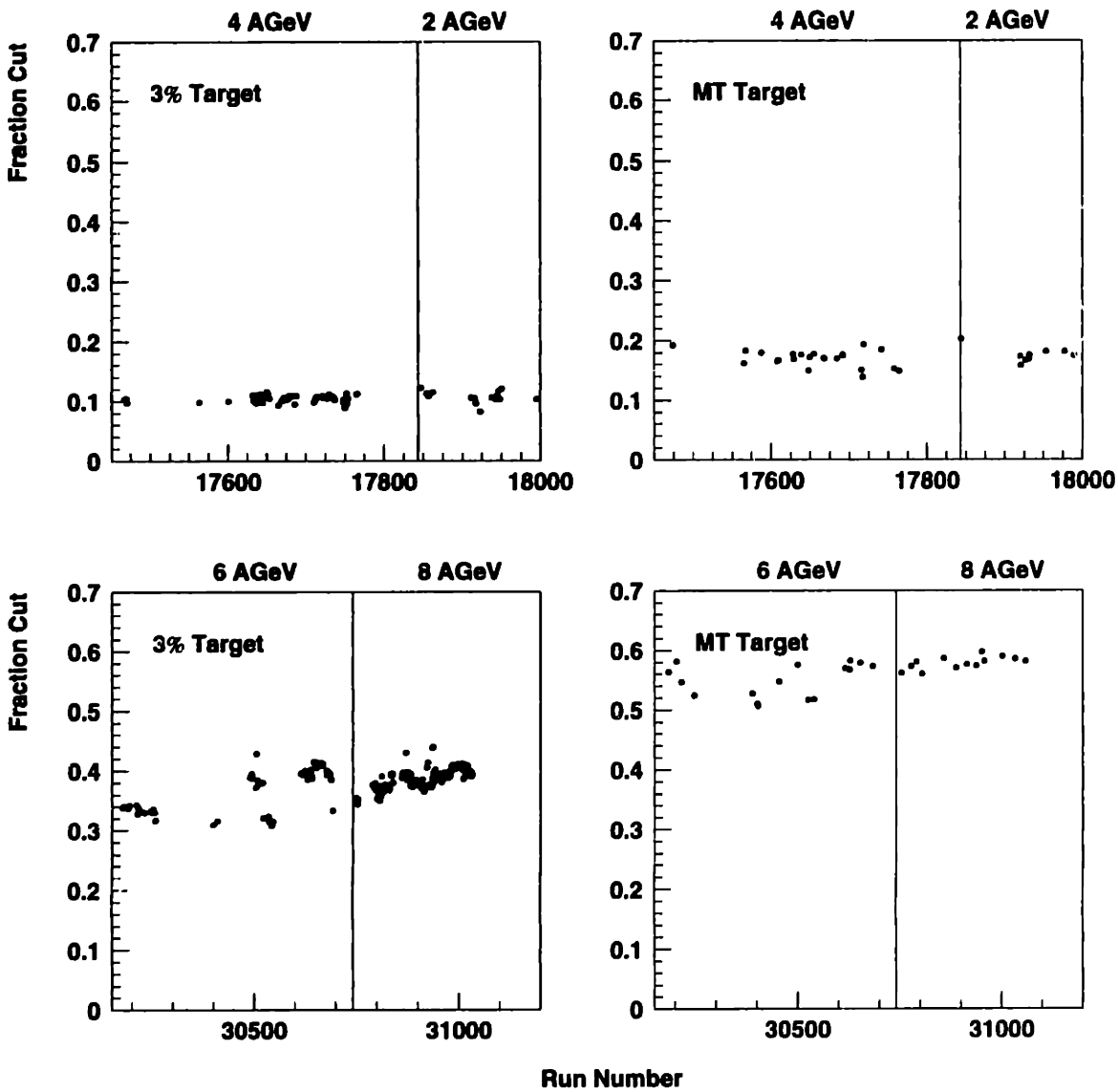

Figure 5-25: The total fraction of software INT events cut by the beam quality cuts for all four energies. The left set of figures shows the fraction cut for target-in events, while the right set of figures shows that for empty target events.

measured with the target in place.

5.6.6 Interaction Cross-Section

The inelastic cross-section, σ_{inel}, for collisions between two Au ions is not known at the beam energies of this analysis. This leads to problems in determining the event classes in centrality, since in principle these should be determined as fixed fractions of σ_{inel} across all beam energies. This lack of knowledge is further complicated by the interaction trigger, determined by the Bull's Eye (section 2.6.1), which is not sensitive to all of σ_{inel}.

As will be described in section 6.2.3, the interaction cross-section does not enter directly into the measured yields, but only into the determination of the event classes.

Figure 5-26 shows the total and elastic cross-sections in $p-p$ collisons in the energy range of this analysis. The inelastic cross-section is the difference between these two numbers, and changes by at most $\sim$5% over this energy range. It is not strictly required that σ_{inel} in Au collisions scale directly with the $p-p$ cross-section, but it most probably follows the same trend. There are some indications[G+95a] that the nuclear charge-changing cross-section is dependent on E_{beam}, but the exact values are not known between 1 and $10A\cdot GeV$.

The experiment uses the Bull's Eye as an interaction trigger, and so the performance of the Bull's Eye affects the portion of σ_{inel} measured. Figure 5-27 shows the distribution of the output from this detector, $BE_{hardsum}$, as measured at $8A\cdot GeV$. The peak corresponding to an unfragmented beam particle in this distribution is calibrated to lie at 800 at all E_{beam}. In order to remove effects from the online trigger threshold, a cut is placed on this calibrated value of $BE_{hardsum}$, which requires that $BE_{hardsum}$ be less than 600 for the event to be counted as a valid interaction. As shown by the figure, this cut only significantly affects the most peripheral centrality class, as determined by the NMA.

Figure 5-28 shows the cross-section measured in the Bull's Eye for each of the running periods, both for runs with the "3%" target and for runs with an empty target in place. These cross-sections include the cut on $BE_{hardsum}$, and have been divided by

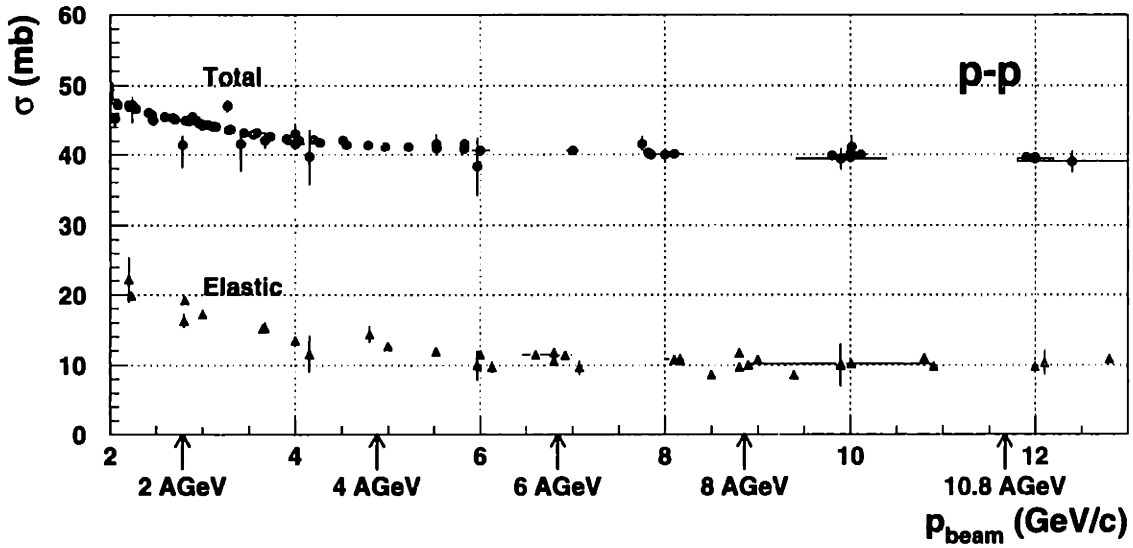

Figure 5-26: The total and elastic cross-sections for $p - p$ collisions. The inelastic cross-section is given by their difference. The location of the 5 energies used in this thesis are also indicated. The values shown are from [Gro98a].

a number constant across all E_{beam}, 6.78 b. This is the $Au - Au$ cross-section to which the Bull's Eye is potentially sensitive at an E_{beam} of 10.8 $A{\cdot}GeV$. The value of 6.78 b comes from an interpolation between the cross-sections measured for different nuclei in reference [G+95a], since the authors of that article did not measure the $Au - Au$ cross-section directly, and includes the cross-section for electromagnetic dissociation, to which the Bull's Eye is in principle sensitive. The cross-section translates into an interaction probablity of 4.07% for the "3%" Au target, of thickness 1961 mg/cm^2.

The empty target background is large, and is larger for the $E917$ run periods at 6 and 8 $A{\cdot}GeV$. Figure 5-29 shows the cross-section after the empty target background has been subtracted. The subtraction was done separately by run group, as will be described in section 5.6.7, and there are indications of some stability problems in the early $6A{\cdot}GeV$ run period. The cross-section selected by the interaction trigger shows a dependence on E_{beam}. The value measured at $8A{\cdot}GeV$, of approximately 5.4 b, is consistent with the selected interaction cross-section measured at 10.8 $A{\cdot}GeV$.

This dependence on E_{beam} is problematic. At 10.8 $A{\cdot}GeV$, the Bull's Eye is known not to be sensitive to the full cross-section The change in the measured cross-section

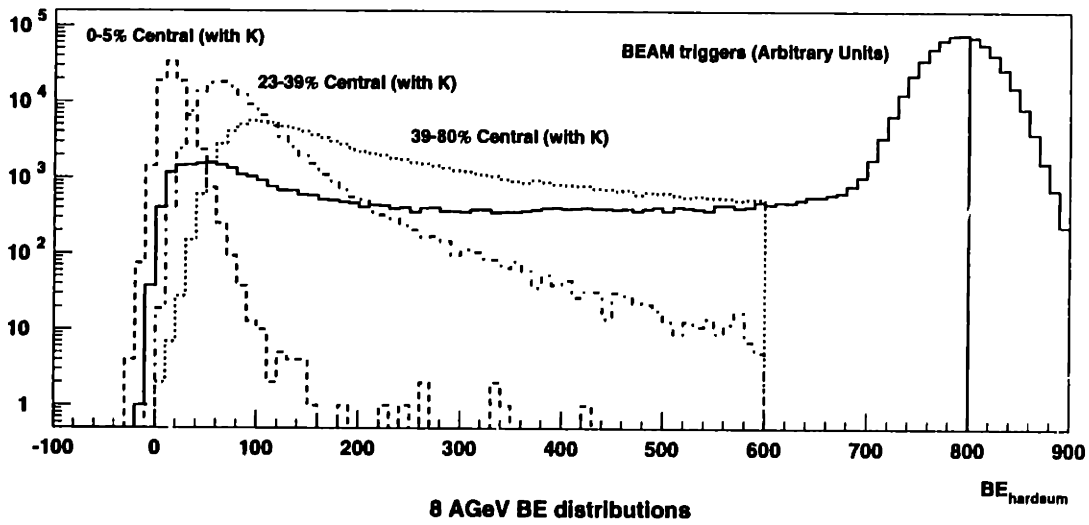

Figure 5-27: Distributions of $BE_{hardsum}$ at $8A \cdot GeV$. The four distributions are from BEAM events and events from the 0-5%, 23-39%, and 39-80% centrality class as determined by the NMA (see section 5.6.7). The peripheral edge of the 39-80% centrality class is defined by the Bull's Eye. The three samples selected on centrality have the further requirement that a K must be found in the event, and the distribution for BEAM triggers has an arbitrary normalization due to scaledowns. All beam quality cuts have been applied, along with the requirement $BE_{hardsum} < 600$ in the samples selected on centrality.

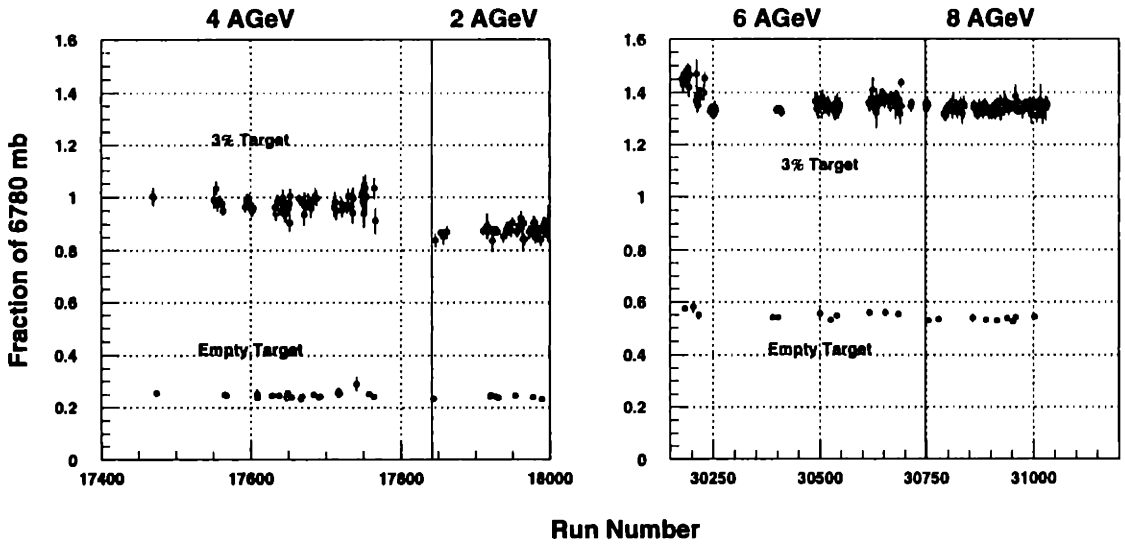

Figure 5-28: The cross-section measured in the Bull's Eye for runs with the "3%" target and the empty target. The cross-section includes values of $BE_{hardsum} < 600$ only, and all beam quality cuts have been applied. The cross-section has been divided by 6.78 b, and the boundaries between the four beam energies are shown.

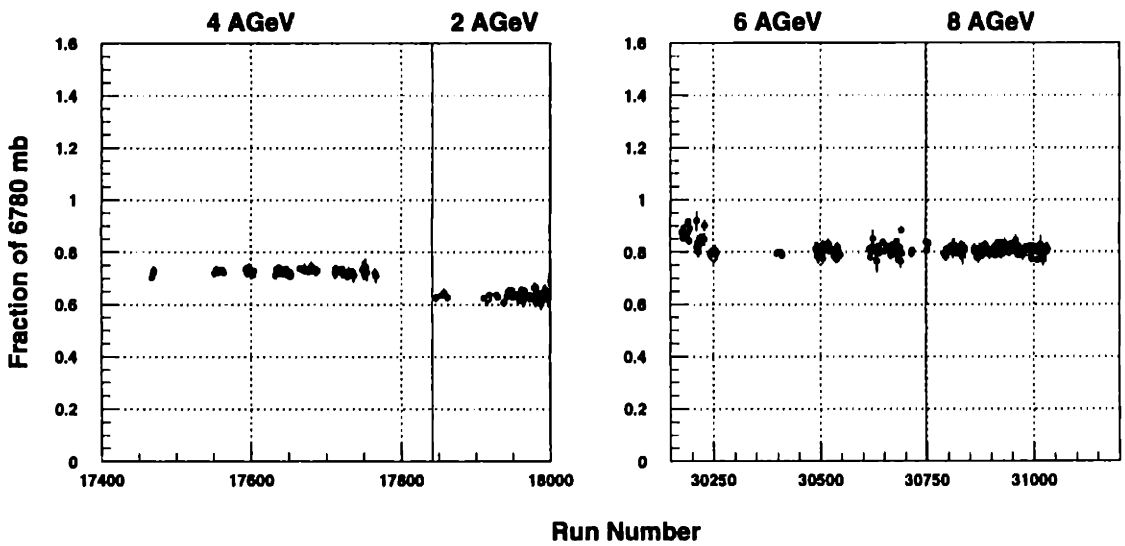

Figure 5-29: The cross-section measured in the Bull's Eye after empty target subtraction. The cross-section includes values of $BE_{hardsum} < 600$ only, and all beam quality cuts have been applied. The cross-section has been divided by 6.78 b, and the boundaries between the four beam energies are shown.

could be due either to a change in the fraction of σ_{inel} to which the Bull's Eye is sensitive or to a real change in σ_{inel}. At any one beam energy, the Bull's Eye measures $\sum Z^2$ (assuming no saturation). In a peripheral collision, $\sum Z^2$ can change due either to charge exchange or fragmentation. Because it is the $\sum Z^2$, one cannot simply state that the Bull's Eye threshold corresponds to a requirement that the charge of the projectile change by $\Delta Z > 10.6$, and so for comparisons with other experiments it is difficult to state precisely what reactions are measured in the peripheral bin.

In this analysis, common cross-sections are used across the beam energies for cuts in each centrality class. This choice makes comparisons using the most peripheral bin problematic, since it is impossible to make the cross-sections match for this bin. Related to this, the term "minimum bias" will not be used.

5.6.7 Centrality cuts

Cuts are placed on the data to select events of a given "centrality" class. The term centrality is used, rather than impact parameter, because no measurement method directly determines the impact parameter of the collision. The vagueness of the term reflects the vagueness of the concept. There are always problems comparing data between experiments because of this.

Within the *E*802 string of experiments, centrality has historically been measured using a combination of the ZCAL (section 2.6.3) and detectors that count the total multiplicity of an event. Since the ZCAL showed poor performance during the low energy running, the cuts in this thesis are made using the NMA exclusively.

The criterion used to determine the cuts is the cross-section contained within a certain window of NMA multiplicity. Figure 5-30 shows the distributions of the NMA at all energies, along with a schematic of the cuts applied. As expected, as the beam energy decreases, the multiplicity decreases. Since it is desirable to make cuts with common physical content across all beam energies, in this thesis the cuts are made to correspond, at least in principle, to a common overlap of the incoming nuclei. The closest one can come to this, with the NMA, is to require a common cross-section within the cuts at all beam energies. I refer the reader to section 5.6.6 for caveats.

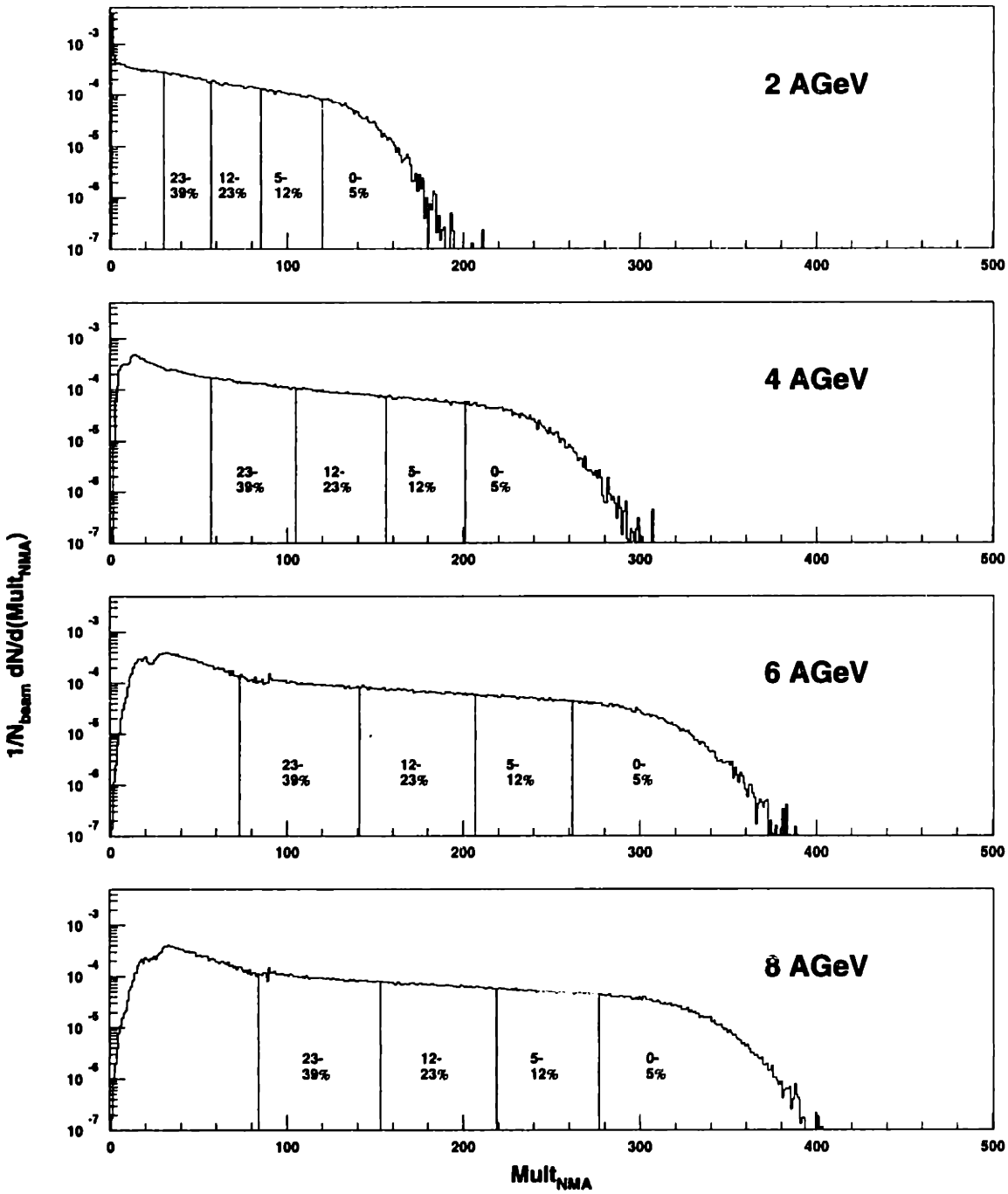

Figure 5-30: The distribution of $Mult_{NMA}$ for all beam energies. All beam quality cuts have been applied here, as with all of the figures in this section. The empty target contribution has been subtracted. The cuts shown are only schematic for the reasons discussed in the text of section 5.6.7.

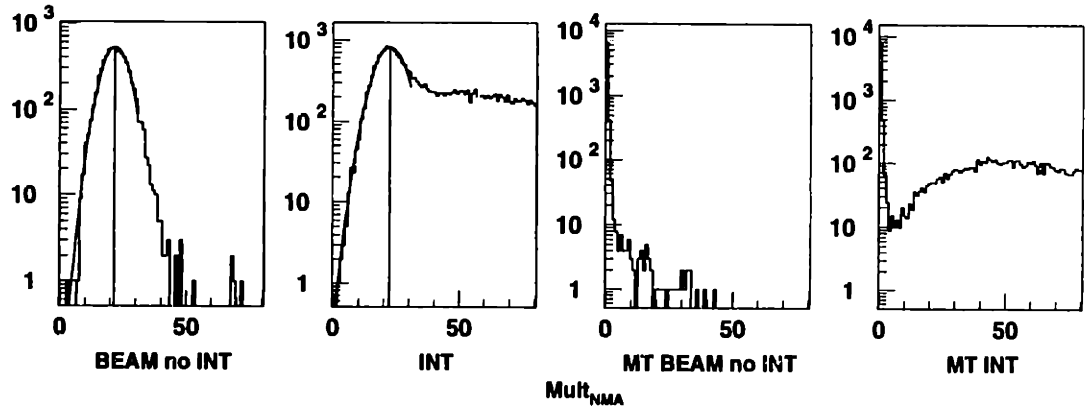

Figure 5-31: A comparison between the location of the low multiplicity peak in $Mult_{NMA}$ from empty and 3% target runs. All beam quality cuts have been applied. The left two plots show the target-in distributions, and the right two plots show the empty target distributions. Clean BEAM is defined as $BE_{hardsum} > 650$, and INT is defined as $BE_{hardsum} < 600$. The data are from runs 30175 for the 3% target and 30184 for the empty target. Both of these are early 6 $A{\cdot}GeV$ runs, separated by a few hours.

Empty target subtraction

The distributions of $Mult_{NMA}$ in the previous section have had the empty target background subtracted from them, as described below. There is a problem in this subtraction, though, in that the distributions with the target in place and those with an empty target have a different shape at low $Mult_{NMA}$, an example of which is shown in figure 5-31. The runs with the target in place have a peak at low $Mult_{NMA}$ that is systematically shifted from that in empty target events, presumably due to δ-electron production in the target.

For this thesis, as in [Ahl97], a correction is applied to the empty target distributions before the subtraction is performed. For clean beam events, in runs with the target in place, the peak at low $Mult_{NMA}$ is fit to a Gaussian, from which the mean and width are extracted. A random number is then selected from a distribution with the same mean and width, and added event-by-event to the values of $Mult_{NMA}$ in empty target runs. The $Mult_{NMA}$-dependent portion of the $\langle\eta\rangle$ cut is made on this adjusted value, and the subtraction is performed using the resulting empty target

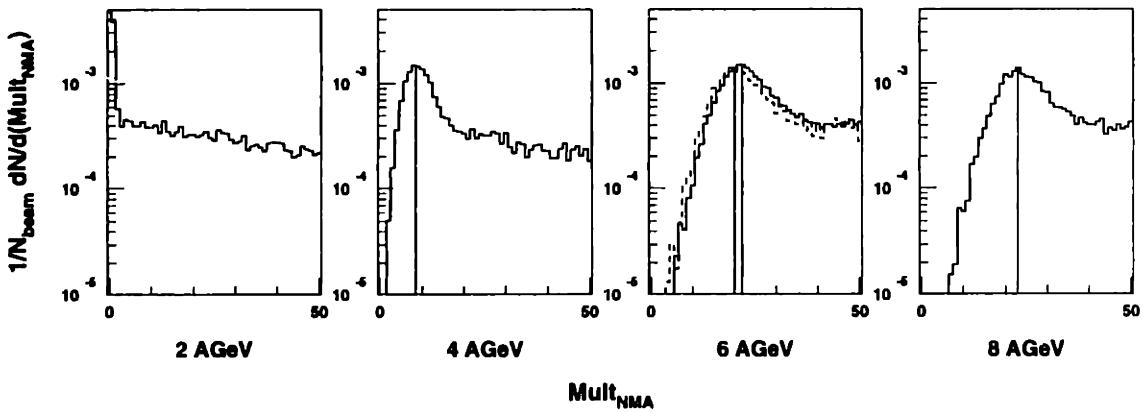

Figure 5-32: A comparison between the location of the low multiplicity peak in $Mult_{NMA}$ for the four beam energies. All beam quality cuts have been applied, and the data are from software INT events, meaning that $BE_{hardsum} < 600$. The lines show the means of the Gaussians applied to the empty target runs. The solid histogram in the 6 $A{\cdot}GeV$ panel is from an early run, while the dashed histogram is from a later run. The data shown are from runs 17911 for the 2 $A{\cdot}GeV$ data, 17555 for the 4 $A{\cdot}GeV$ data, 30175 for the early 6 $A{\cdot}GeV$ data, 30400 for the late 6 $A{\cdot}GeV$ data, and 30800 for the 8 $A{\cdot}GeV$ data.

multiplicity distribution, rather than the raw one.

Figure 5-33 shows the run dependence of the parameters describing the peak. There is a large difference between the 4 and 6 $A{\cdot}GeV$ means and widths, which perists if the Real multiplicity is used rather than the Weighted multiplicity. The distribution at 2 $A{\cdot}GeV$ is too close to the origin for a reliable determination of the parameters, with a mean of approximately 0.6 and width of approximately 2, and so no shift is applied for this beam energy. Figure 5-32 shows typical distributions at low $Mult_{NMA}$ for all four beam energies, which clearly show that the shapes are different at different beam energies. Table 5.7 lists the parameters applied. As in the analysis of the Bull's Eye, there are indications of differences between a set of runs early in the 6$A{\cdot}GeV$ run period and the later set of runs, and so two sets of parameters were applied.

Figure 5-34 shows the raw distributions, along with the corresponding empty target distributions. The effect of the $\langle\eta\rangle$ cut is very pronounced at 6 and 8 $A{\cdot}GeV$. As described in section 5.6.2, the $\langle\eta\rangle$ cut is not applied to the data for $Mult_{NMA}$

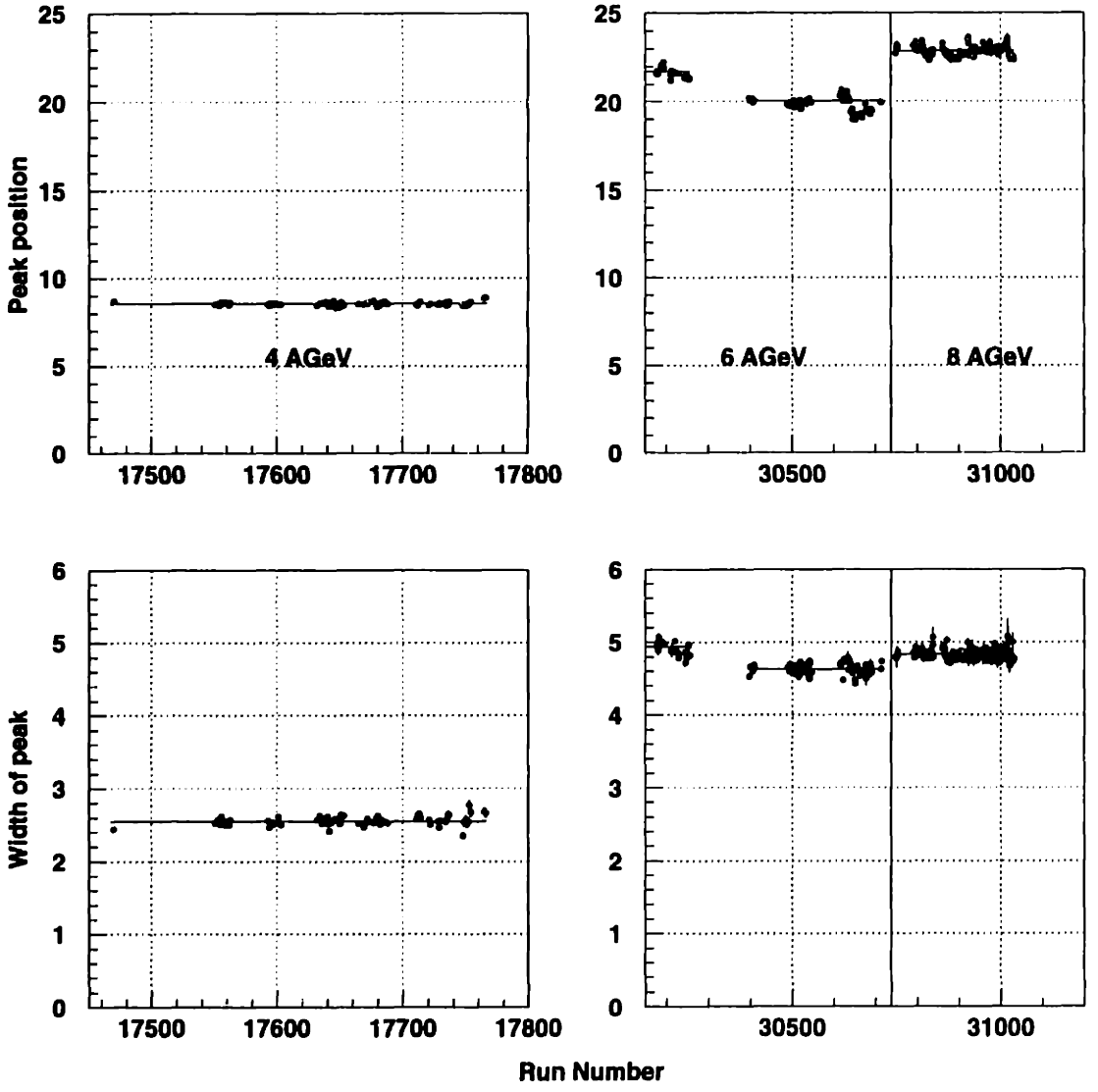

Figure 5-33: The mean and σ of a Gaussian fit to the low multiplicity peak in clean BEAM events, as a function of run. The lines show the parameters of the Gaussian applied to the empty target distributions before subtraction. The 2 $A \cdot GeV$ data are not shown, since the distributions lie too close to the origin for the parameters to be reliably determined.

E_{beam}	Mean	σ
2 $A \cdot GeV$	None	None
4 $A \cdot GeV$	8.5471	2.5484
6 $A \cdot GeV$ (early)	21.7439	4.938
6 $A \cdot GeV$ (late)	20.0319	4.631
8 $A \cdot GeV$	22.907	4.8326

Table 5.7: The parameters of the Gaussian distribution added to the empty target distribution before subtraction. "Early" 6 $A \cdot GeV$ is defined as all run numbers between 30000 and 30300, while "late" is defined as all 6 $A \cdot GeV$ runs after 30300.

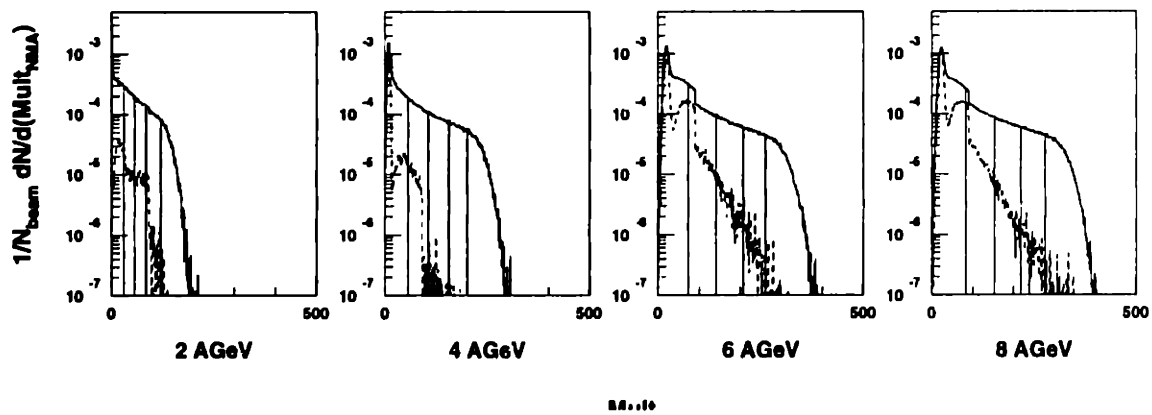

Figure 5-34: The distribution of $Mult_{NMA}$ for all beam energies. All beam quality cuts have been applied. The solid histograms are from target-in runs, and the dashed histograms are from empty target runs. The lines show, schematically, the cuts.

values less than 90. This leads to the sharp discontinuity in the number of counts at this value, before empty target subtraction.

The empty target distibution after adjustment for the peak position matches the data with the target in place, though, even with this sharp falloff. As can be seen in 5-30, there is no sign of a discontinuity in the subtracted quantity. This implies that the $\langle\eta\rangle$ cut is not excluding real events, but is allowing in additional background in the region below the cutoff in $Mult_{NMA}$, which is successfully removed by the empty target subtraction. Note further that the tail of the empty target distribution tails off rather sharply, and does not contribute to the region of the central cuts.

The size of the empty target background at low NMA_{mult} is a potential worry for the more peripheral cuts. Any run-by-run variation in the size of this background, if not correctly determined, can lead to additonal uncertainties in the peripheral normalization. However, as shown in the analysis of the Bull's Eye (section 5.6.6), the total empty target contribution is relatively stable. Despite this stability, for the purposes of this analysis the empty target distribution was separately subtracted by event class and by run group. The boundaries of these run groups were determined either from known changes in the configuration, such as downtime of the beam, or, where no such changes occurred, at the run halfway between the empty target runs.

Run Dependences

Problems in calibration or variations in beam quality not caught by the beam quality cuts can lead to run-by-run variations in the normalization. Correct normalization is crucial for correct yields, since the fractional error in normalization enters directly into the fractional uncertainty in the measured quantities. This is further complicated by the number of different configurations of the spectrometer. If the normalization fluctuates upwards for one set of configurations and downwards for another set, the spectra will show the fluctuations in different regions of phase space. That is to say, not all fluctuations average.

Therefore, the values of $Mult_{NMA}$ necessary to select a given fraction of the cross-section were investigated run-by-run. Figure 5-35 shows the position of this $Mult_{NMA}$

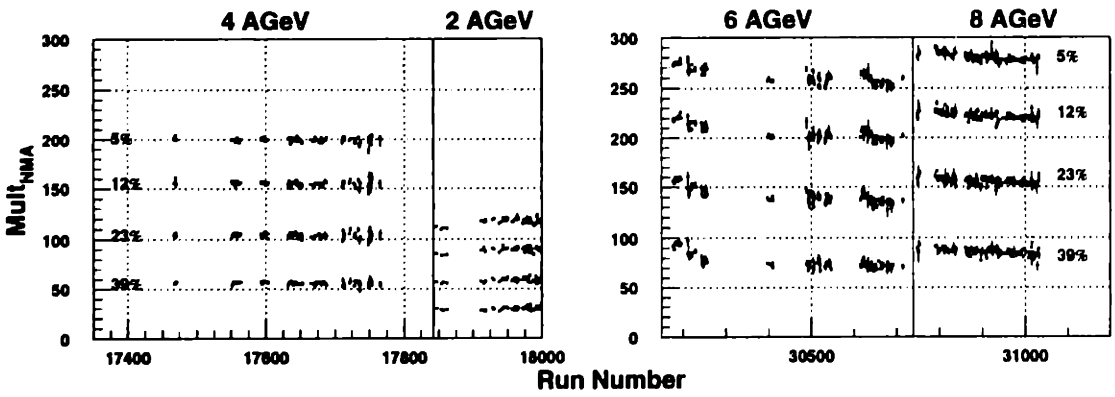

Figure 5-35: The $Mult_{NMA}$ value necessary to contain a given cross-section. The cut is defined as that value of $Mult_{NMA}$ for which the cross-section contained in values greater than or equal to the cut is the given fraction $\times\sigma_{inel}$. σ_{inel} is taken to be 6.78 b, as described in section 6.2.3.

cut value for the fractions used in this thesis. It is shown as a function of run. Unfortunately, there are variations.

The $Mult_{NMA}$ cut values necessary for the 2 and 4 A·GeV run period are relatively stable, although there is one clear shift in the $2A \cdot GeV$ data, between two periods separated by a few days.

The 6 and 8 A·GeV data show some more problems. The 6 A·GeV runs show a set of discrete jumps, which are rather large, while the 8 $A \cdot GeV$ runs show a somewhat steady downward trend. Such variation can cause systematic problems in the data. In order to remove the bulk of these systematics, the $Mult_{NMA}$ cut values used to select the centrality classes were allowed to change as a function of run number. This explicitly ensures that the cross-section for a centrality class is stable across the runs. The cuts placed to select the upper 5% of 6.78 b are plotted in figure 5-36, along with the data on which the cuts were based. All cuts are tabulated in table 5.6.7.

For the 2, 4, and 6 $A \cdot GeV$ running, discrete sets of cuts were placed. For the 8 $A \cdot GeV$ running, a linear fit was made to the cuts necessary as a function of run, and the cut determined run-by-run from the parameters of this fit. Note that, since $Mult_{NMA}$ is an integerized quantity, the cut is rounded from the line to the nearest

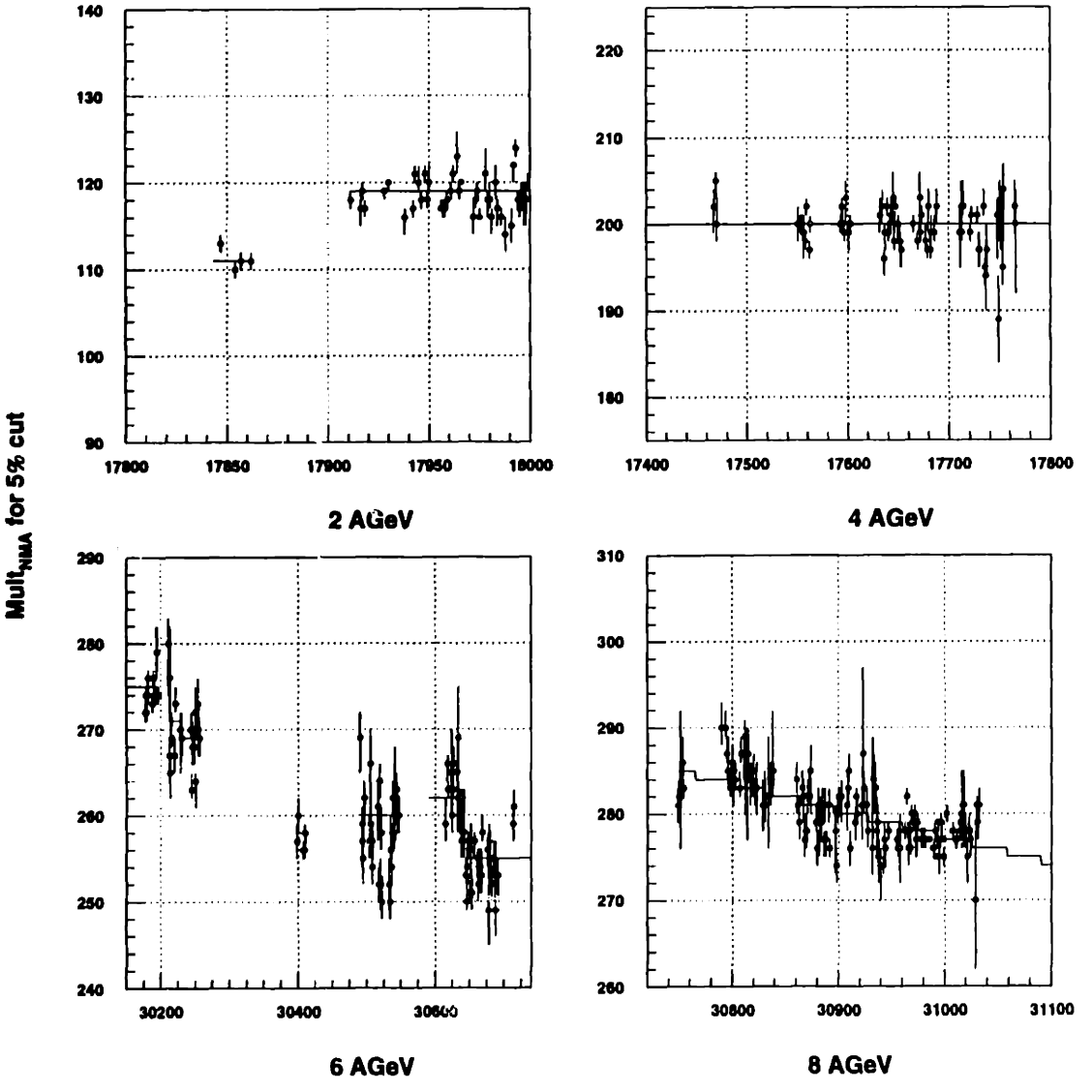

Figure 5-36: The run-by-run 5% cuts placed on $Mult_{NMA}$ to produce a common cross-section within the cuts. σ_{inel} is taken to be 6.78 b, as described in section 6.2.3.

E_{beam}	Run		Cut for fraction of σ_{inel}			
	Low	High	5%	12%	23%	39%
2 A·GeV	17843	17910	111	84	56	29
	17911	18000	119	90	59	30
4 A·GeV	17467	17800	200	155	104	56
6 A·GeV	30150	30196	275	221	158	94
	30211	30231	271	215	151	86
	30232	30260	269	213	146	79
	30395	30412	258	202	140	75
	30490	30547	260	203	140	75
	30590	30644	262	206	140	73
	30645	30740	255	200	136	72

E_{beam}	Fraction of σ_{inel}	Offset	Slope	Run Offset
8 A·GeV	5%	286.5	-3.08×10^{-2}	30700
	12%	228.6	-2.89×10^{-2}	
	23%	160.6	-2.42×10^{-2}	
	39%	90.32	-1.94×10^{-2}	

Table 5.8: The centrality cuts, along with their run dependence, placed on the data. The cuts are defined so that the cross-section in $Mult_{NMA}$ values greater than or equal to the cut is the given fraction of 6780 mb. The $8A$·GeV parameters are from equation 5.15

integer. There is also an offset placed into the run number used, so that the cut becomes:

$$Cut_{mult} = \text{nint}\left(Offset + Slope\left(Run\ Number - Run\ Offset\right)\right) \tag{5.15}$$

The cuts for the 5% centrality bin, on a larger scale for clarity, are shown in figure 5-36.

Figure 5-37 shows the fractional deviation from the mean of $\sigma_{centrality}$ after the cuts in centrality were placed. Deviations in this plot translate directly into systematic uncertainties in the measured cross-sections, although this will be somewhat averaged across runs.

The systematic uncertainty in normalization from this procedure is estimated to be, overall, on the level of a few percent, with a somewhat larger contribution for the 6 A·GeV data. Most of the unbiased SPEC data, which dominates the proton and pion yields but not the kaon yields, occurred during the period of shifts.

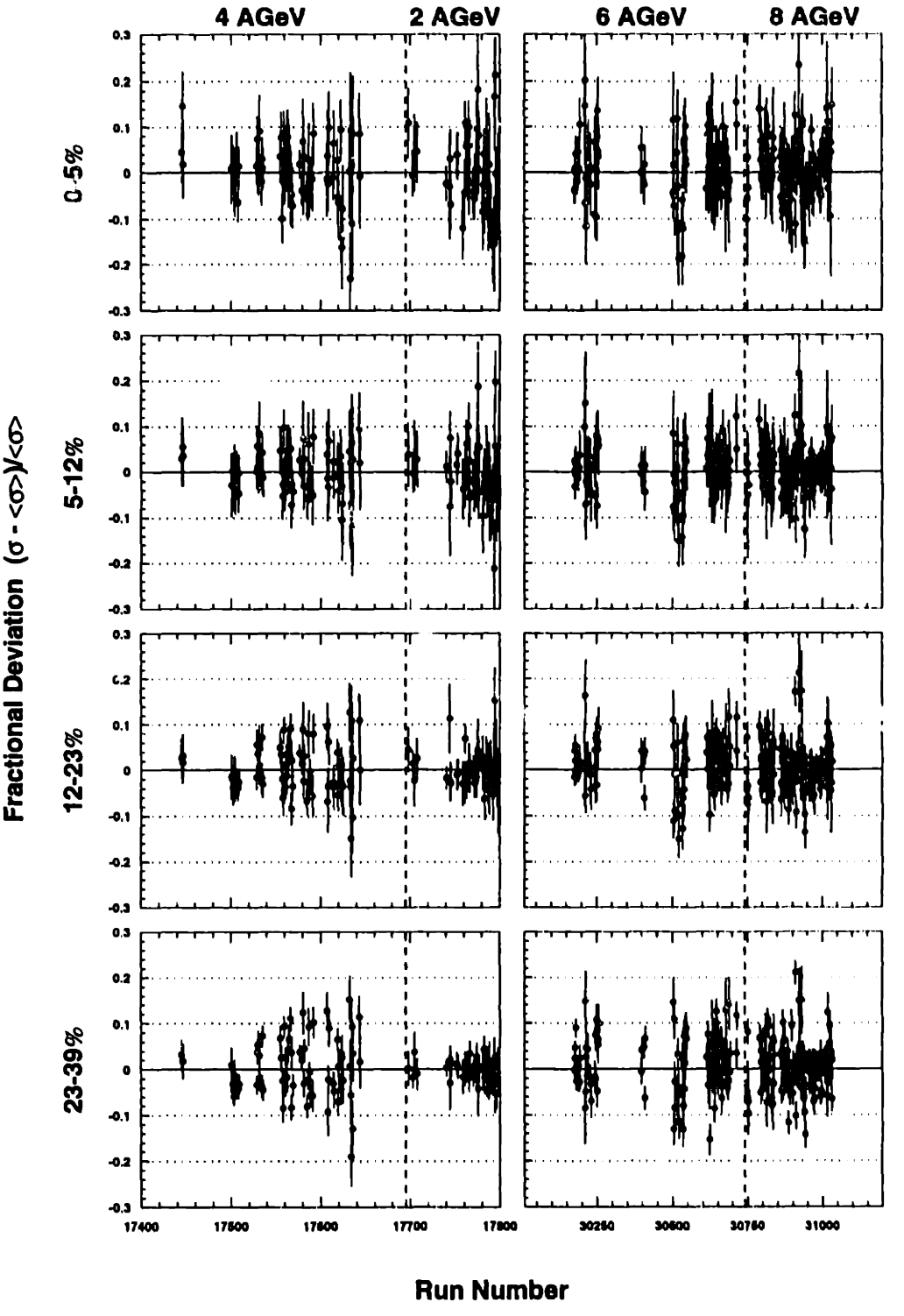

Figure 5-37: The fractional deviation in the cross-section σ_{cut} within the cuts placed on $Mult_{NMA}$. σ_{inel} is taken to be 6.78 b, as described in section 6.2.3.

Energy ($A{\cdot}GeV$)	Calibration Method	Multiplicity Method	Unused Correction	Gap Correction	Method Number
2 & 4	Nonlinear	Real	Y	N	7
6 & 8	Nonlinear	Weighted	Y	N	13

Table 5.9: NMA multiplicity methods used for the data sets of this thesis. The nomenclature follows that in [Ahl97].

Weighting

The Weighted method for $Mult_{NMA}$ (see section 3.2.3) was found to be less stable against run-by-run variation than the Real method for the 2 and 4 $A{\cdot}GeV$ data, and so is not applied for this data set. The opposite is true for the 6 and 8 $A{\cdot}GeV$. I remind the reader that the cuts on $Mult_{NMA}$ are changed to obtain a fixed, stable cross-section, rather than on any predetermined level, or measure, of multiplicity.

Figure 5-38 shows a comparison between $Mult_{NMA}$ from the Real and Weighted methods at the 4 beam energies in this analysis. The two methods give very close results, but one can see the effects of the integerization at the low end and the effects of the weighting at the high end. The cuts are far from the areas in which there is a difference.

Due to these stability issues of $Mult_{NMA}$, this analysis uses the definitions of multiplicity listed in table 5.9.

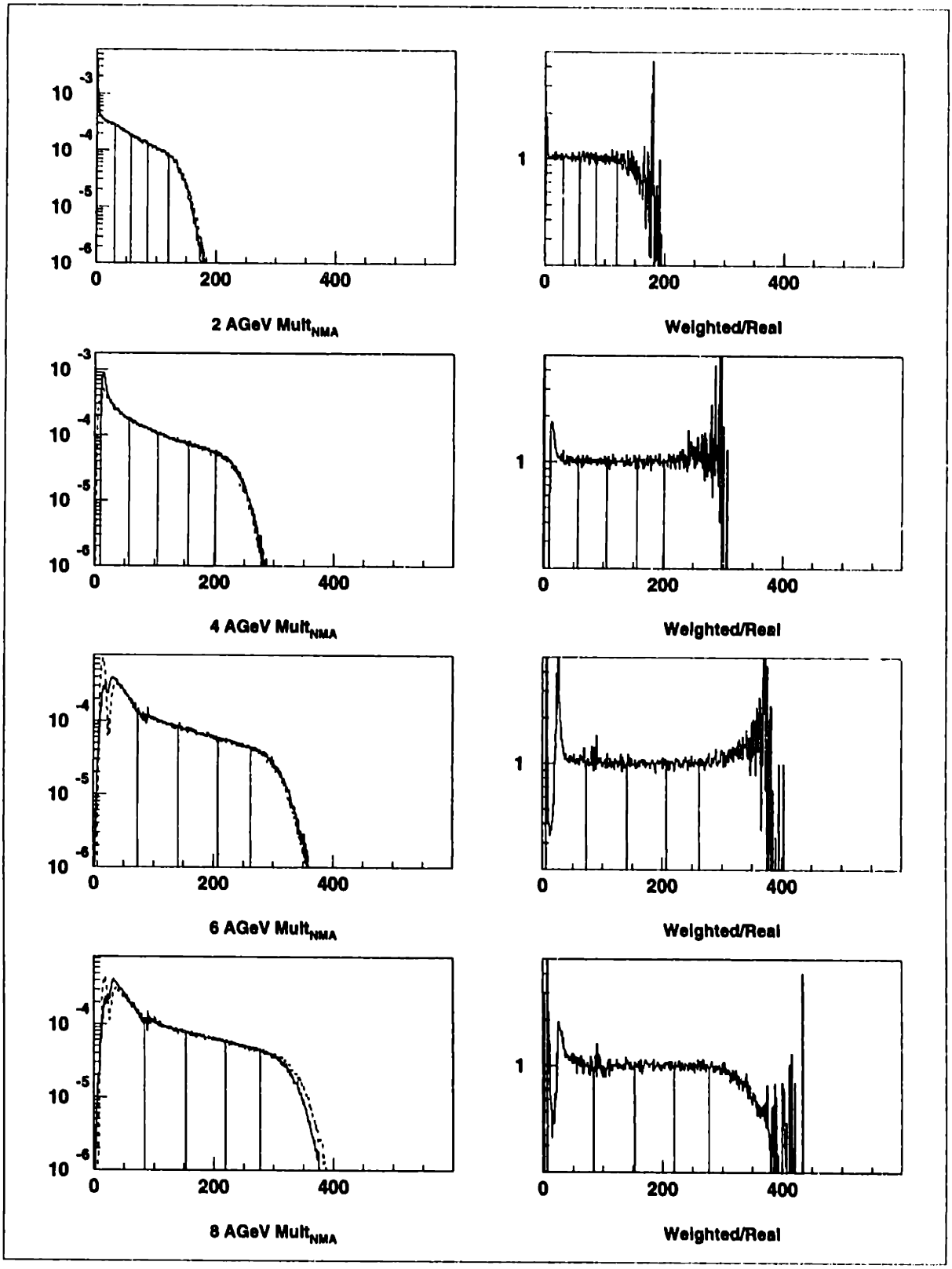

Figure 5-38: Comparison between Real and Weighted $Mult_{NMA}$ at all beam energies. Runs have been combined to increase the statistics, and the empty target contribution has been subtracted. On the right the two methods are superimposed, and on the left the histograms are divided.

Chapter 6

Cross-sections

This thesis presents the differential invariant yield of produced particles from a wide range of conditions. These quantities are obtained from the calibrated and reconstructed data, and corrections are applied. Due to the size of the data set and the large number of different configurations, the corrections and calibrations have a number of dependences, each of which has a potential to affect one portion of the data. This chapter is therefore meant to serve as a summary of these dependences, in order to obtain estimates of the point-to-point systematic errors across the various configurations. It also serves as a repository for the methods used to obtain a yield from the raw data.

6.1 Cross-section definitions

6.1.1 Interaction cross-section

The concept of a production cross-section is a generalization from the basic expression for an interaction cross-section. The interaction cross-section describes the general case of the absorption of a beam of particles in a set of scattering centers. Consider an beam incident on a scatterer. The cross-section for scattering in this process is defined as:

$$\sigma = \frac{Scattered\ flux}{incident\ flux\ per\ unit\ area},$$

where the flux is defined as the number of particles that cross a plane transverse to the direction of motion in unit time, and the area is measured in this plane. Given a number of scatterers with density n, then in a slab of thickness dx in the direction of the incident beam the areal density of scatterers in the plane transverse to the beam is $n\ dx$. Hence the probability of interaction in this slab, dP, is given by

$$dP = \sigma \frac{I_0/S}{I_0} S\ n\ dx = \sigma\ n\ dx,$$

where S is the area covered by the scattering centers. In other words, the cross-section σ gives the constant of proportionality between the probability of scattering and the number of scatterers present.

Continuing with this logic, at a distance x into the collection of scattering centers the number of initial particles that survive, $I(x)$, follows the equation:

$$-dI(x) = dP\ I(x) = I(x)\sigma n dx$$

Therefore it is an exponential function of the distance x into the collection of scattering centers,

$$I(x) = I_0 e^{-\sigma n x} \tag{6.1}$$

where I_0 is the initial flux of beam particles. From this, the total probability for a beam particle to scatter in the distance x is given by

$$P_{scatter}(x) = \left(1 - e^{-\sigma\ n\ x}\right) \tag{6.2}$$

In the limit of a thin target, $\sigma n x \ll 1$, this expression reduces to a simple proportionality relation, $P_{scatter} \approx \sigma n x$, with a relative error $O(\sigma n x)$.

6.1.2 Production Cross-sections

The above description can be generalized to describe the production of particles. If one takes the original expression for the probability of scattering, and, instead of

considering the probability for scattering of the incident particle, one considers the flux of particles produced by an unscattered beam particle in the distance dx, one obtains:

$$dI_{produced} = \sigma_{production}\ n\ I(x)\ dx,$$

where $\sigma_{production}$ is a proportionality factor modeled after that for simple scattering. Continuing with the expression for I(x), one obtains:

$$\begin{aligned} I_{produced} &= I_0 \frac{\sigma_{production}}{\sigma_{tot}} \left(1 - e^{-\sigma_{tot}\ n\ x}\right) \\ &\approx I_0 \sigma_{production}\ nx\ \ (\sigma_{tot} nx \ll 1) \end{aligned}$$

where σ_{tot} denotes the total cross-section for scattering of the incident beam particle, and I_0 still describes the flux of incoming beam particles. In the literature, rather than use the total cross-section in this definition, it is conventional to use the inelastic cross-section σ_{inel}. Therefore the conventional definition for $\sigma_{production}$ treats an elastically scattered beam particle as indistinguishable from an unscattered one.

As in the case of absorption detailed above, in the limit of a thin target this reduces to a simple proportionality. Hence the production cross-section simply parametrizes the proportionality factor between the flux of incoming beam particles and the flux of outgoing particles of a a given type.

The above discussion concerns what is called the "inclusive" cross-section, in which the total number of particles are counted regardless of any other properties of the final state. There are two other types of production cross-sections considered in the literature. The first type, the "exclusive" cross-section, parametrizes a probability, rather than a flux of particles, much as the expression in equation 6.2 above. Given a complete description of the final state, the exclusive cross-section parametrizes the probability for production of that final state. That is to say,

$$\begin{aligned} P_{finalstate} &= \frac{\sigma_{exclusive}}{\sigma_{inel}} (1 - e^{\sigma_{inel} nx}) \\ &\approx \sigma_{exclusive} nx\ \ (\sigma_{inel} nx \ll 1) \end{aligned}$$

The experiment cannot fully measure the final state, so exclusive cross-sections are not presented in this thesis.

There exists a middle ground between the inclusive cross-section, which ignores all portions except one of the final state, and the exclusive cross-section, which parametrizes the entire final state. This is the (somewhat unoriginally named) "semi-inclusive" cross-section. It is related to a conditional probability, but, as in the inclusive case, describes a flux rather than a probability. Given a restricted set of final states, to obtain a semi-inclusive cross-section one simply measures the inclusive cross-section only over that set. In other words, for a set of final states X, the semi-inclusive cross-section is defined by

$$I_{produced|finalstate\in X} = I_0 \frac{\sigma_{semi-inclusive}}{\sigma_{inel}} (1 - e^{\sigma_{inel} n x})$$

6.1.3 Yields

This brings us to the yield. The definition of the semi-inclusive cross-section combines into one number both the probability for producing the final state within the set X and the the number of particles produced within such events. As a trivial consequence, as the requirements on the set X become more restrictive the cross-section decreases accordingly. Perhaps a more telling variable is the "yield", which is defined in the thin target approximation as:

$$Yield = \frac{\sigma_{semi-inclusive}}{\sigma_{trig}}$$

where σ_{trig} is the cross-section for producing an event in the set X. In intuitive terms, the yield measures the mean number of particles produced in an event of a given type.

While it might seem logical to simply measure the cross-section, there is a reason, in terms of accuracy of the data, that this is not done. To obtain the actual value of the cross-section, one must measure both the absolute cross-section for producing an event of the given event class and the number of particles produced in events of that

event class. To obtain a yield, one simply needs to count:

$$yield = \frac{Number\ of\ observed\ particles\ in\ events\ of\ type\ X}{Number\ of\ observed\ events\ of\ type\ X}$$

If there is an uncertainty in the selection criteria for type X, this uncertainty is directly reflected in the measured cross-sections, but not in the yields.

To take an example, assume that the mean number of particles produced in an event of total multiplicity 200 is not very different from that in an event of total multiplicity 201. Assume also that a detector effect causes a multiplicity 201 event to be recorded as a multiplicity 200 event, and assume that events are selected with multiplicities greater than 200, such that the detector effect causes the event to fall outside the cuts. The yield would be affected in that the real event with multiplicity 201 would not be included in the average, while in the case of the cross-section this event would not be counted in the absolute and so the cross-section would decrease. Of course, such a detector effect would affect the quoted event class for which the yield was measured, in that it would decrease the quoted "percent central".

The difference boils down to the effect of systematics in event selection on an average vs an absolute count. An average is almost always less sensitive to selection errors than an absolute. Related to this, neither the target thickness nor the total cross-section for interaction between Au nuclei directly contribute to the measured yield. They do, of course, affect the quoted event class.

6.1.4 Differential Yields

The yields of particles are usually measured differentially, as a function of kinematic variables that describe the particle. This is done both because such a division increases the information available and because the experiment only measures over a restricted kinematic region.

At first glance, the quantity to measure would be simply $d^3\sigma/d^3p$. However this quantity is not invariant under Lorentz transformations, as can be simply seen by the existence of a three-vector rather than a four vector in the denominator.

A number that is an invariant under Lorentz transformations is $E\frac{d^3\sigma}{d^3p}$. This can be be seen by invoking the constraint that a particle must have a fixed mass:

$$\int d^4P\delta\left(E-p^2-m^2\right)=\int\frac{d^3p}{2E}$$

where P is a 4-vector, $(p^0,\vec{p})$. Hence the quantity $\frac{d^3p}{E}$ is a Lorentz scalar. The integrated cross-section, σ, which should be invariant under Lorentz transformations, is

$$\begin{aligned}\sigma &= \int d^3p\frac{d^3\sigma}{d^3p}\\ &= \int\frac{d^3p}{E}\,E\frac{d^3\sigma}{d^3p}\end{aligned}$$

Hence the quantity $E\frac{d^3\sigma}{d^3p}$ is a Lorentz scalar, and is accordingly called the invariant differential cross-section.

Now d^3p needs to be addressed. The simple division into spherical variables, $p^2dp\ d\Omega$, leaves quite a bit to be desired, since these variables are highly dependent on the frame in which they are measured. If one is willing to restrict oneself to boosts along one axis, call it z, then there are two quantities that transform relatively simply. These are the rapidity, Y, along that axis, and the momentum, p_t, transverse to that axis. In terms of spherical variables with respect to the beam axis:

$$\begin{aligned}p_\perp &= p\sin\theta\\ Y &= 0.5\log\left(\frac{E+p\cos(\theta)}{E-p\cos(\theta)}\right)\end{aligned}$$

Under transformations along the z axis, $p_\perp$ remains invariant and Y transforms additively. That is to say: $Y'=Y+Y_{boost}$, where $Y_{boost}=atanh\left(\beta_{boost}\right)$ and β_{boost} is the relative speed of the two frames.

Therefore, with these two quantities, it is very simple to transform frames, at least along the beam direction. In addition, any quantity that is measured differentially in Y and either differentially or absolutely in $p_\perp$ does not change its shape under

boosts. To transform from the laboratory (lab) frame, in which the target is fixed, to the center-of-mass (cms) frame, in which the target and beam move towards one another with equal momentum, one can use:

$$Y_{cms} = Y_{lab} - Y_{lab}^{cms} \tag{6.3}$$

$$= Y_{lab} - \frac{1}{2}Y_{lab}^{beam} \tag{6.4}$$

where the second line applies in the case of a symmetric system such as $Au - Au$. This identity will be applied extensively in the thesis.

Defining the invariant cross-section in terms of these quantities is quite straightforward. The definitions of $p_\perp$ and Y in terms of p and θ can be inverted:

$$\begin{aligned} E &= m_\perp \cosh(Y) \\ p\cos\theta \equiv p_{||} &= m_\perp \sinh(Y) \end{aligned}$$

where $m_\perp = \sqrt{m^2 + p^2}$, and is called the "transverse mass". From this, $dp_{||} = E\, dY$, and so

$$\begin{aligned} E\frac{d^3N}{d^3p} &= E\frac{d^3N}{dp_{||}\, p_\perp dp_\perp d\phi} \\ &= \frac{d^3N}{dY p_\perp dp_\perp d\phi} \end{aligned}$$

expresses the invariant yield in terms of $p_\perp, \phi, Y$. Since $p_\perp dp_\perp = m_\perp dm_\perp$, the expression is the same in $m_\perp$.

Finally, at least for the analysis of this thesis, the orientation of the incoming impact parameter vector is not measured. Hence the measurements are completely rotationally symmetric in ϕ. Therefore ϕ is replaced by its integrated whole, 2π, and the quantity measured is:

$$Differential\ Invariant\ Yield = \frac{1}{2\pi m_\perp}\frac{d^2N}{dY dm_\perp}$$

which has units $1/GeV^2$. To obtain the yield in terms of Y alone, one can integrate:

$$\frac{dN}{dY} = \int_m^\infty \frac{1}{2\pi m_\perp} \frac{d^2N}{dY dm_\perp} 2\pi m_\perp dm_\perp$$

In practice, since the experiment does not measure infinite (or zero) momentum particles, this integration is performed through an extrapolation of a fit to the data, as will be explained later.

6.2 Summary of corrections and cuts

In the preceding section, The expression quoted for the yield in terms of experimental quantities indicated that, in order to obtain an actual yield, all that must be done is to count up the number of particles seen, count up the number of events in the event class, and divide these two quantities. While this is the basic idea, it is not so simple. The problem is that there are numerous corrections to be made.

6.2.1 Experimental Expression

The equation that translates the measured quantities into an invariant differential yield is somewhat complex. To add further complication, the data are divided into classes for combination at various stages of the analysis. These divisions are, in the order of combination, by particle measured, by "run", and by "subbin" in Y and $m_\perp$.

A "run" is defined in 3.1 and basically measures a unit of time. Table 6.1 for a list of the calibrations and that are time-dependent.

Section 6.2.4 details the meaning of "subbin" in Y and $m_\perp$, and the procedure used to combine these bins. Smaller bins are used to obtain the acceptance correction than are used in the final correction.

The value for the yield within a given Y and $m_\perp$ bin is given by:

$$\frac{1}{2\pi m_\perp} \frac{d^2N}{dY dm_\perp} = \sum_{b \in subbins} \sum_{r \in runs} \frac{\sum_{p \in good\ particles \wedge good\ events} weight_{brp} - background_{brp}}{norm_{br}} \tag{6.5}$$

Calibrated dependences

Quantity	Method used	Effect	Section
T1-T4	Discrete	track quality	3.3.1
TRF	Fine	track quality	3.3.2
TOF	Discrete / Fine	track and PID quality	3.4
$BE_{hardsum}$	Fine	normalization	3.2.2
Z_{BTOT}	Fine	beam quality	3.2.1
$NMA_{pulse\ height}$	Fine	normalization and beam quality	3.2.3

Parametrized dependences

Quantity	Method used	Effect	Section
Z_{BTOT}	E_{beam}	beam quality	5.6.2
$HOLE_{ADC}$	Discrete	beam quality	5.6.2
$Mult_{NMA}$	Discrete / Fine	normalization	5.6.7
X_{target}	Fine	acceptance	5.4, 4.7.1

Table 6.1: A list of run-by-run dependences not under direct experimental control, corrections or calibrations of which need to be applied to the data. The "method used" column describes the method applied to correct or calibrate the data. "Fine" means that a run-by-run correction is applied. "Discrete" means that the correction or calibration is applied in distinct run blocks. The "effect" column describes the effect that the dependency has on the data. The final column lists the section in which the dependency is described.

The factors in the numerator and denominator are:

$$weight_{brp} = \frac{1}{m_\perp} \left(\epsilon_{insertion}\ \epsilon_{mc}\right)^{-1}\ \Delta\phi \tag{6.6}$$

$$norm_{br} = acc_{\theta_{xz},tof}\ n_{beam \in good\ events}\ \left(frac_{class}\ p_{int}\right)\ \delta y\ \delta m_\perp \tag{6.7}$$

Not all particles tracked in a given event, not all events in a given run, and not all runs in a given running period are accepted into the sums. The inclusion criteria are carefully chosen, since the cutting of data can potentially bias the results if not done correctly. The cuts on tracks are not based on event quantities, such as the multiplicity within the spectrometer, but on easily applied and understandable cuts in momentum and position within the spectrometer, and are applied across all event classes. The cuts on beam quality are based on global event characteristics that are correlated with the empty target background, as described in section 5.6.2. This set of beam quality cuts are applied both to the normalization events and to the events with tracks, and so are removed from both the numerator and denominator

Cut	Variable by which cut	Run dependency	Section
Basic PID	p		4.8
PID Background	p		5.5
TOF slat	slat to which track points	Slat by slat	5.4
Fiducial acceptance	p, θ_{xz}, $\sin\theta\sin\phi$	X_{target}	5.4

Table 6.2: Reasons for cutting particles from the quoted yields, based on particle-by-particle quantities. The final column lists the section in which the cut is described.

Cut	Cut Description	Type	Section
PRE	Beam particle preceding $\in$ $(300, 500)$ ns	Online	2.11.1
$Follow$	Beam particle following $\in$ $(300, 500)$ ns	Offline	2.11.1
Z_{BTOT}	$Z_{BEAM} \notin 2\sigma$ of Au	Online & Offline	2.5.1, 5.6.2
$HOLE_{ADC}$	Beam halo	Online & Offline	2.5.2, 5.6.2
NMA $\langle\eta\rangle$	Upstream interactions	Offline	5.6.2
$BVER_{BAD}$	Any plane not registering beam	Offline	2.5.3, 5.6.2
Z_{BE}	Signal below threshold	Online & Offline	2.11.1,5.6.6

Table 6.3: Cuts made in order to ensure high quality beam. "Online" means that the cut is required in the trigger decision. "Offline" means that a cut is made in software in the subsequent analysis.

of equation 6.5. Runs are cut based on a large set of monitoring procedures, which attempt to isolate specific problems in detector systems and in their calibration.

Table 6.2 lists the various criteria on a particle-by-particle basis, while table 6.3 lists the beam quality cuts.

6.2.2 Weights

The weights are calculated particle-by-particle, and summed into the average once per particle. They are parametrized as a function of variables that describe either the event in which the particle is measured or properties of the particle itself. A brief summary of the dependences is shown in table 6.4, along with the section in which the correction is defined and described in more detail. For simplicity, the PID background correction is included in this table.

Factor	Particle	Event	Run	Section
$\epsilon_{insertion}$	p, θ_{xz}, $charge$	whs	θ_{HH}, B_{HH}, E_{beam}	5.3
ϵ_{mc}	p, PID	None	year(tracking algorithm)	5.2
$\Delta\phi$	p, θ_{xz}, PID	None	θ_{HH}, B_{HH}, X_{target}	5.5
background	p, PID	$Mult_{NMA}$	θ_{HH}, E_{beam}	5.5

Table 6.4: Dependences of the various corrections applied particle-by-particle to the data. The three middle columns describe the level at which the dependency parameter is calculated: either particle-by-particle, event-by-event, or run-by-run. The final column lists the section in which the correction is described.

6.2.3 Normalization

Consider the denominator of equation 6.5, described in more detail in equation 6.7. Working from the tail to the front, the last two of these terms, δY and $\delta m_{\perp}$, are simply the bin widths. As such, they contain no dependence on run conditions, but reflect that we are approximating a true differential quantity, $\propto d^2N/dYdm_{\perp}$, with a discrete quantity, $\propto (N \in (\delta Y, \delta m_{\perp}))/\delta Y \delta m_{\perp}$.

The next two terms, $Frac_{class}$ and P_{int}, reflect the fact that this measurement is of a semi-inclusive yield. P_{int} is the total interaction probability between the Au beam and the Au target, and $Frac_{class}$ is the fraction of this probability that falls within the cuts that form the event class measured. It is important to note that the experiment does not measure these quantities separately, but instead measures their multiple. This is the reason for the parentheses. As noted in the section on the Bull's Eye (2.6.1), the Bull's Eye, and hence the interaction trigger, is not sensitive to the full inelastic interaction cross-section between Au nuclei. The experiment therefore cannot measure the true P_{int}, but must infer it from the total interaction cross-section measured elsewhere and a knowledge of the target thickness in g/cm^2. I refer the reader to section 5.6.6 for caveats.

For a similar reason, the experiment cannot measure $Frac_{class}$. However, the number of interactions per beam particle is measured, given that the interaction is of a type that satisfies the cuts that define the exclusive portion of the semi-inclusive yield, the "centrality" cuts. This number is exactly the multiple within the parentheses. The required measurement of this number is the reason that both BEAM triggers,

completely unbiased, and INT triggers, unbiased with respect to the centrality cuts, are included into the trigger mix.

Moving back one more step, $N_{good\ beam}$ is a simple count of beam particles that pass the beam quality cuts. The parentheses could have been moved back to include $N_{good\ beam}$, since $N_{good\ beam} Frac_{class} P_{int}$ is just the number of real interactions that satisfy the centrality cuts, if $(Frac_{class} P_{int})$ is measured run-by-run. However, as discussed in section 5.6.7, for this thesis the centrality cuts are determined so as to produce one number for $(Frac_{class} P_{int})$. There is the additional problem that a subtraction of events with no target in place, the empty target runs (2.4.2), must be made in order to obtain a correct measure of this quantity. Since by necessity empty target runs are disjoint from the target-in runs, one cannot avoid the introduction of a number external to the run being analyzed. Hence, rather than making this external number be the empty target quantity, the mean of the $(P_{int} Frac_{class})$ across all runs at a given E_{beam} is used. Therefore one needs to count the beam in order to normalize.

The acceptance is described in section 5.4. There are two things of note here. As detailed in 5.4, the single particle acceptance is divided into two parts. The first, $\Delta\phi$, the ϕ range available to a particle at a given θ_{xz} and momentum p, is applied particle by particle. This is by far the largest correction applied to the data, and it changes sharply with angle, so that it is more accurate to apply this particle-by-particle and allow it to be averaged completely over the actual distribution of particles. This correction is forced to be correct, assuming uniform efficiency along ϕ, by making a fiducial cut directly in the quantity that it measures. The correction for bad TOF slats, which could in principle be applied in the same way, is instead applied bin-by-bin through the normalization. It was decided in the original implementation of the cross-section code [Mor94] that this was more accurate, due to the average nature of the correction, and this decision remains unchanged for this analysis. This is described in more detail in the discussion of the acceptance.

The other thing of note about the acceptance is that there is a run dependence to this quantity, due both to bad TOF slats and to the position of X_{target}.

Factor	Run	Bin	Section
$acc_{\theta_{xz},tof}$	as $\Delta\phi$, + Bad tof slats	p, θ_{xz}	5.4
$N_{beam \in good\ events}$	N_{beam}, good event cuts	None	5.6.2
$(Frac_{class} P_{int})$	target type, event selection, background	None	5.6.7
$\Delta Y \Delta m_\perp$	None	None	

Table 6.5: Dependences of the various normalization quantities applied run-by-run to the data. The two middle columns describe the level at which the dependency parameter is calculated: either run-by-run or bin-by-bin across subbins in Y and $m_\perp$. The final column lists the section in which the correction is described.

Table 6.5 summarizes the various factors that enter into the normalization term, with their dependences.

6.2.4 Averaging Procedure

The data is binned into discrete ranges of Y and $m_\perp$. There are two types of bins, the subbin and the final bin. In addition, each type of bin can be cut based on two criteria, either $acc(TOF, \theta_{xz})$ or the bin acceptance, which does not include bad TOF slats. The binning is checked to ensure that further systematics are not introduced into the final results.

Run-by-run the data is binned into "subbins" of a certain size. In this analysis small subbins of size 0.01×0.01 in $(y, m_\perp)$ were used, mostly to allow for flexibility in deciding the final bins in which to plot the data. These subbins are of smaller size than the final bins chosen, and can be averaged together, with various cuts, to create the final bins. The acceptance is calculated separately for each subbin.

The possibility of changing normalization or acceptance across the different subbins that comprise the final bin complicates the averaging procedure. The quantity measured for a given final bin is a ratio, as shown in equation 6.5. There are two types of averages that can be used for this ratio:

$$a_{ind} \equiv \sum \frac{weight}{norm} \tag{6.8}$$

$$a_{comb} \equiv \frac{\sum weight}{\sum norm} \tag{6.9}$$

where the sums are over subbins. Each has its particular problems.

It's clear that a_{ind} is the correct averaging method. However, when combining angles, a_{ind} is problematic. Different angle and field configurations have different amounts of data in this data set, with some having an extremely low amount. At the edges of the settings, the fluctuations in the low-statistics settings will completely dominate a_{ind}. There is also a bias introduced if any of the subbins have zero counts, since the fluctuations from a bin with zero counts will not affect a_{ind} but those from a bin with a single count will. Therefore for this analysis, as for previous analyses in the $E802$ string of experiments, a_{comb} is used. The effects of changing acceptance across the subbin are corrected to first order by shifting the $\langle m_\perp \rangle$ and $\langle y \rangle$ of the combined bin, weighted by $norm$.

In order to decrease effects of the acceptance on this average, cuts are placed in this analysis. First, to be included into the run-by-run average each subbin must have an acceptance of at least 75% in $acc(\theta_{xz}, TOF)$. This is different from the criteria used in [Ahl97], in which this cut was placed on the final bin acceptance, ignoring bad TOF slats.

Then, when combining subbins, the average $acc(\theta_{xz}, TOF)$ for the final bin must be above 70%, which is trivially satisfied, and the combined bin must have a total average acceptance above 50%. This combined cut is made to decrease problems from changing $\langle y \rangle$ across the bin. The effect of varying these parameters was small on the final points in $m_\perp$, but can affect the results of the fits at the edges of the acceptance, with a total effect of approximately 5% for rapidity bins with a small range in $m_\perp$. When the acceptance in a bin in y has a small range in $m_\perp$, a change in the cut on combined parameters can cause the level of extrapolation to increase.

6.3 Fitting

Fits are separately made to the $m_\perp$ distributions in bins in rapidity in order to extract the dN/dY and parameters related to the transverse shape of the spectra. There are two types of fits used in the analysis, a Gamma fit and an exponential fit. In both

cases the dN/dY is extracted directly in order to remove problems with correlations.

An exponential fit is used for the kaons, and has the form:

$$\frac{1}{2\pi m_\perp}\frac{d^2N}{dm_\perp dY} = \frac{dN/dY}{2\pi\left(Tm_0+T^2\right)}exp\left(-\frac{m_\perp - m_0}{T}\right) \tag{6.10}$$

where the parameters T and dN/dY are the inverse slope of the distribution and the total yield in that bin in rapidity. From the expression, the $\langle m_\perp \rangle$ can be derived:

$$\langle m_\perp \rangle = T\left(2+\frac{(m_0/T)^2}{1+m_0/T}\right) \tag{6.11}$$

Assuming Gaussian errors, the error on $\langle m_\perp \rangle$ can be derived as:

$$\sigma_{\langle m_\perp \rangle} = \sigma_T\left(\frac{m^2+4m_0T+2T^2}{(m_0+T)^2}\right) \tag{6.12}$$

The Gamma distribution is a bit more difficult. It adds in one further parameter, which is constrained by the shape at low $m_\perp$. The distribution is given by:

$$\frac{1}{2\pi m_\perp}\frac{d^2N}{dm_\perp dY} = \frac{dN/dY}{2\pi T^{2-\gamma}G\left(2-\gamma,\frac{m_0}{T}\right)}m_\perp^{-\gamma}\exp\left(-\frac{m_\perp}{T}\right) \tag{6.13}$$

where $G(x,y)$ is the complementary incomplete gamma function,

$$G(x,y) = \int_y^\infty e^{-t}t^{x-1}dt \tag{6.14}$$

and dN/dY, T, and γ are fit parameters. The $\langle mt \rangle$ is obtained by integrating the equation, and the errors by numerical differentiation, taking into account the correlation terms.

There are systematic errors from the fitting procedure. The dN/dY is not completely measured, since the experiment has limited acceptance. Therefore the data is extrapolated into regions where the distributions are not measured. This extrapolation relies on a basic assumption, that the shape of the distributions does not change significantly outside of the range over which the fit is performed. If this assumption is not true, the extrapolation can introduce additional systematics. Since it is an

extrapolation, a small total coverage of the range of the distribution can introduce instabililities into the fit, due to a poor constraint on the parameters.

Because of these problems in extrapolation, in the analysis of this thesis the parameters are not considered to be well-determined if the level of extrapolation is greater than 60%. This is a rather reasonable value at which to place a cut. The level of extrapolation is determined from the $m_\perp$ window over which the measurement has been made and from the parameters from the fit. In addition, there are problems in constraining the shape of the Gamma fit to the protons and pion distributions if the level of extrapolation at the high end of $m_\perp$ is greater than 10%, so the results of Gamma fits will be considered ill-determined in this case.

6.4 Systematic Errors

The overall systematic error on the measurements is estimated to be 15%, due to normalization and efficiency questions. The point-to-point portion of the systematic error is more difficult to obtain, because of the large number of configurations. On the dN/dY, it is estimated to be 5%, due to normalization uncertainties both across energies and across angle settings. These uncertainties can affect the dN/dY because of its rise with centrality. The $\langle m_\perp - m_0 \rangle$ is less sensitive to normalization effects, so for the π and p the point-to-point systematic errors in this quantity are estimated to be 2%. However, it is more sensitive to extrapolation effects, and so for the K^+ the uncertainties in $\langle m_\perp - m_0 \rangle$ can become greater, due to the limited $m_\perp$ range over which the measurement is made. This leads to additional uncertainty, since the extrapolation can be affected by uncertainties in the corrections at the extremes of the phase space measured. This leads to an estimate of 2-5% systematic errors on the $\langle m_\perp - m_0 \rangle$ of the kaons, with a rapidity dependence to the error. Since mid-rapidity moves to higher values as the beam energy increases, this leads to an estimated systematic error of 2, 3, 4, and 5% for the $\langle m_\perp - m_0 \rangle$ of the K^+ and K^-, within $|Y - Y_{nn}| < 0.25 Y_{nn}$ at 2, 4, 6, and 8 $A \cdot GeV$. The systematic errors on the inverse slopes are similarly estimated to be 2, 3, 4, and 5% for rapidity bins 0.6-0.8, 0.8-1.0,

1.0-1.2, and 1.2-1.4, respectively.

Chapter 7

Results and Discussion

7.1 Overview

With the data set collected, one can begin to map out the space of particle production at AGS energies. The data are organized into a grid of beam energy and centrality, which can be explored at varying levels for indications of phenomena related to the degrees of freedom of the system. The following discussion will consist of three parts. In the first section, a search will be made on a broad scale for trends in the data itself, without reference to models of these collisions.

Next, the details of kaon production will be examined, with particular attention paid to possible differences between the two species of kaons measured, the K^+ and K^-. Any differences between the species, or the lack of such differences, serves as a strong constraint on models incorporating effects on kaon masses in-medium. The study of these differences at the beam energies of this analysis, ranging from approximately 140 MeV to 2.4 GeV above threshold, also provides a framework under which to improve the understanding of the effects seen at the subthreshold energies of GSI, approximately 180-360 MeV below threshold.

In the last part of the discussion, some simple comparisons to models will be made.

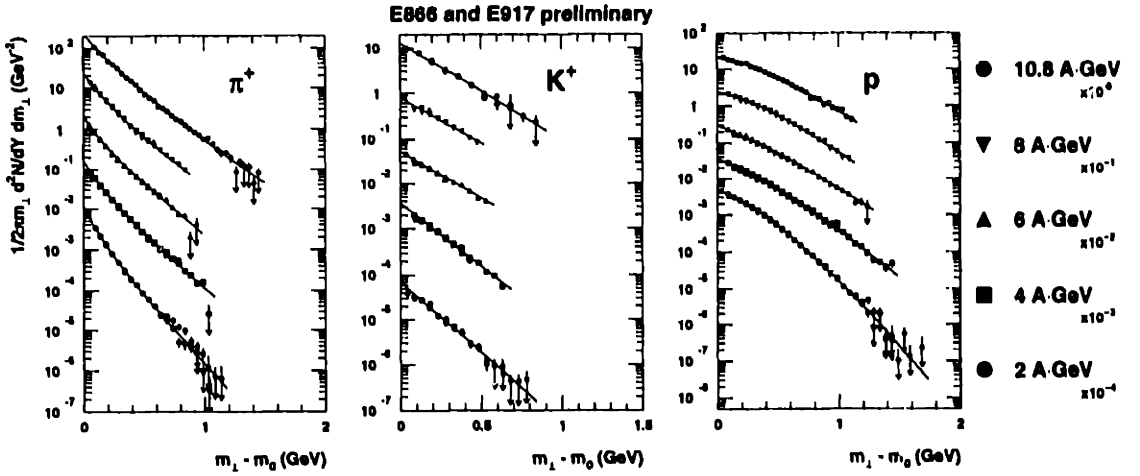

Figure 7-1: The invariant differential yields of π^+, K^+, and p from the 0-5% centrality class, for the 5 beam energies of the AGS. The data are required to lie within a window of $|Y - Y_{NN}| < 0.25 Y_{NN}$ at 2-8 $A{\cdot}GeV$, and $|Y - Y_{NN}| < 0.125 Y_{NN}$ at 10.8 $A{\cdot}GeV$. The open symbols represent data in the range $Y > Y_{NN}$, while the filled symbols that in the range $Y < Y_{NN}$. For clarity in presentation, the yields have been divided by successive factors of 10 at each step in E_{beam}. The arrows indicate relative errors on the points of greater than 30%.

7.2 Global Characteristics

The discussion will begin with one selected portion of the data. The most obvious portion to examine first is that at mid-rapidity, for central collisions, since this is the most extreme situation at a given E_{beam}. The analysis will focus on the produced particles, since the protons are a rather special case, although a few notes will be made about this particle.

7.2.1 $m_\perp$ distributions

Figure 7-1 shows the differential invariant yields of π^+, K^+, and p at mid-rapidity, from the 5% most central collisions, at all E_{beam}. The data are required to lie within a window of a fixed fraction of mid-rapidity, Y_{NN}, and are shown as a function of $m_\perp - m_0$, where m_0 is the mass of the particle. The $m_\perp$ distributions have been binned into two Y bins of equal size on either side of Y_{NN}. The 10.8 $A{\cdot}GeV$ kaon data are from [A+99a], and the 10.8 $A{\cdot}GeV$ pion data are from [A+98a]. Both use

the ZCAL, rather than the NMA, as the centrality selection device, and fall within a smaller range of $|Y - Y_{NN}|$ than the data shown at 2-8 $A{\cdot}GeV$.

There are some regularities in the distributions. As has been shown previously in $Au - Au$ collisions at the beam energies of the AGS [A+98a], the shape of the distributions in $m_\perp$ is not common across particle species. This is in contrast to the situation in $p - p$ collisions [B+74], in which the distributions are exponential in $m_\perp$, with a common slope across species. There is a consistent trend with increasing mass, in that the distributions of the pions show a rise at low $m_\perp$, the kaons are purely exponential, and the protons show a decrease below the exponential. The trend is clear at all beam energies, and the differences are significantly larger at 2 $A{\cdot}GeV$ than at 10.8 $A{\cdot}GeV$.

These differences in shape have been used in the choice of functions with which to extract the dN/dY and $\langle m_\perp \rangle$. The kaons have been fit to an exponential form, while the pions and protons have been fit to a Gamma distribution. The $m_\perp$ distributions have been refit in this analysis to remain consistent with the lower energies. The fits assume that the distributions are uncorrelated across the two Y bins used. The χ^2 of the fits are consistent with 1.

The protons are somewhat problematic. A Boltzmann distribution fits the data marginally well at some beam energies, with a χ^2 per degree of freedom that ranges from a minimum of 1.2 at 6 $A{\cdot}GeV$ to a maximum of 10 at 2 $A{\cdot}GeV$. The χ^2 per degree of freedom resulting from fits to a Gamma distribution is consistently lower across all beam energies, at the proper level of approximately 1. The differences in the parameters resulting from the two fits are not negligible, however, with differences in the extracted yields ranging from 15% at 2 $A{\cdot}GeV$ to 5% at 6 $A{\cdot}GeV$. The $\langle m_\perp \rangle$ is less sensitive to the fit choice. It is difficult to justify the choice of one type of fit over another at every beam energy, so for the purpose of consistency in this analysis the proton data are fit to Gamma distributions across all energies.

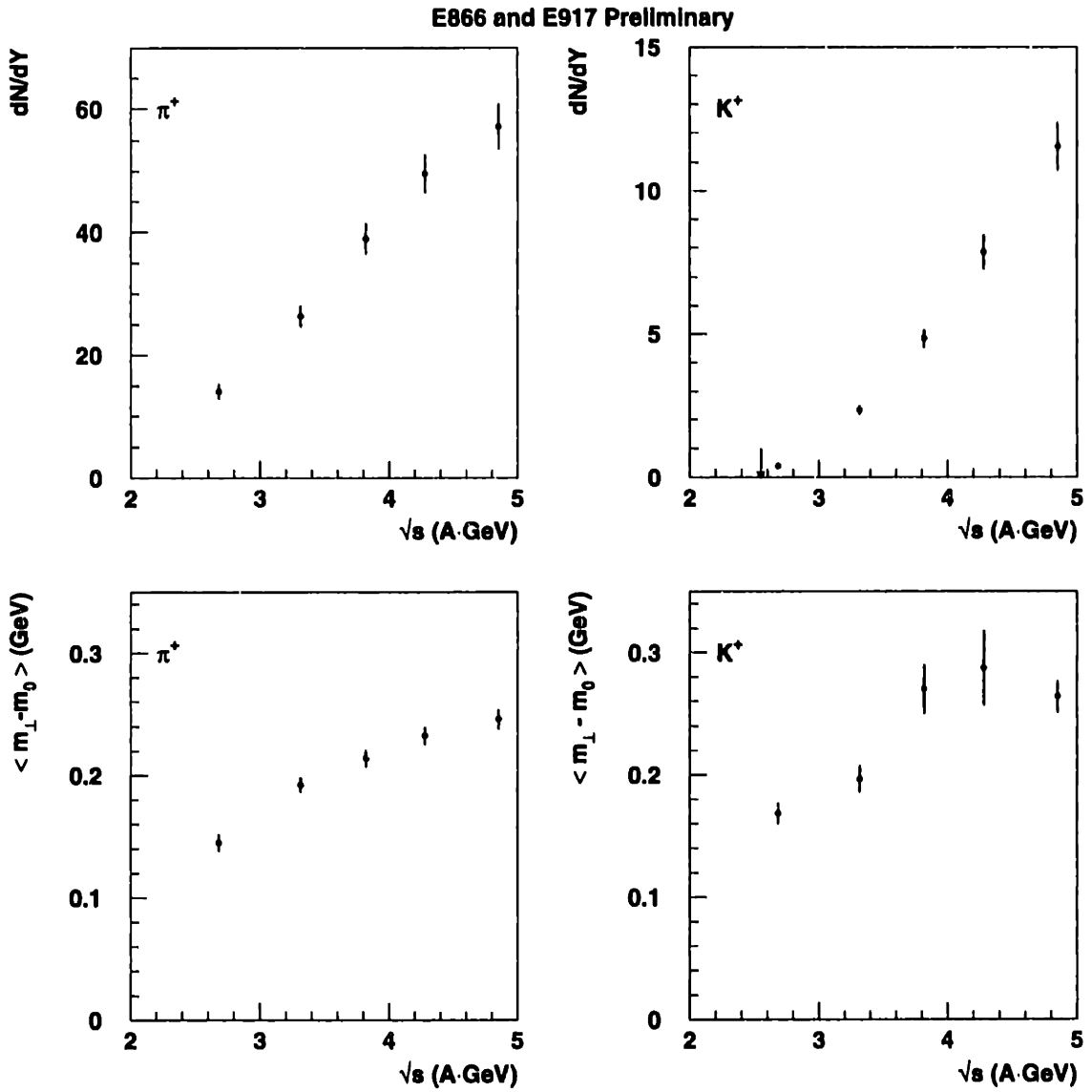

Figure 7-2: The dN/dY and $\langle m_\perp \rangle - m_0$ of π^+ and K^+ at Y_{NN} from the 5% most central collisions, as a function of $\sqrt{s}$ per nucleon. The values are extracted from fits to the differential invariant yields, as described in the text. The arrow on the plot of the K^+ dN/dY indicates the location of the $p-p$ threshold. Point-to-point systematic errors of 5% have been added to the dN/dY values, 2% to the $\langle m_\perp - m_0 \rangle$ of the π, and an E_{beam}-dependent systematic error of 2-5% has been added to the K^+ $\langle m_\perp - m_0 \rangle$, as described in section 6.4.

7.2.2 K^+ and π^+ dN/dY and $\langle m_\perp \rangle$

Figure 7-2 shows the yields and mean $m_\perp - m_0$ as measured for the π^+ and K^+. The $\langle m_\perp \rangle$ is used, rather than an inverse slope, due to the different functional forms. One can see that, over this range of beam energies, the yields of the K^+ change by a factor of 10, while those of the π^+ change by a factor of approximately 5. The $\langle m_\perp \rangle$ also rises with beam energy, but the level of change in this variable is smaller.

These variables provide a gross picture of the distribution of energy from the initial state into the production of particles in the final state. The total available energy in these collisions changes by a large amount over the range of energies of this analysis, as can be seen in the range of $\sqrt{s}$. Taking an extreme model, if one assumes that the incoming nuclei completely stop, so that all of the initial energy is available for production, and neglects effects from Fermi energy, this available energy is given by $\sqrt{s} - 2m_p$. This value ranges from 0.8 GeV at a kinetic energy of the beam of 2 $A GeV$ to 3.0 at 10.8 $A GeV$, changing by a factor of approximately 3. The increased energy can be distributed to the produced particles in the final state either through the production of a greater number of particles, each of which extracts a penalty due to its mass, or through an increase in the momentum imparted to the individual particles. The data indicates that the balance between these two posibilities lies in the direction of increased production.

Both the yields and $\langle m_\perp \rangle$ change smoothly with E_{beam}. There is little indication of a step or a kink, as might be expected at a phase transition boundary.

7.2.3 Protons

The protons have a special place in the understanding of the energetics of these collisions. Proton-antiproton pair production is completely negligible at these beam energies, so any measured protons are, to a high degree of certainty, baryons from the initial state. Baryon number is conserved, so the final distribution of baryons reflects the transfer of energy from the initial state to the final state.

The analysis of the protons is slightly complicated by the fact that baryon number

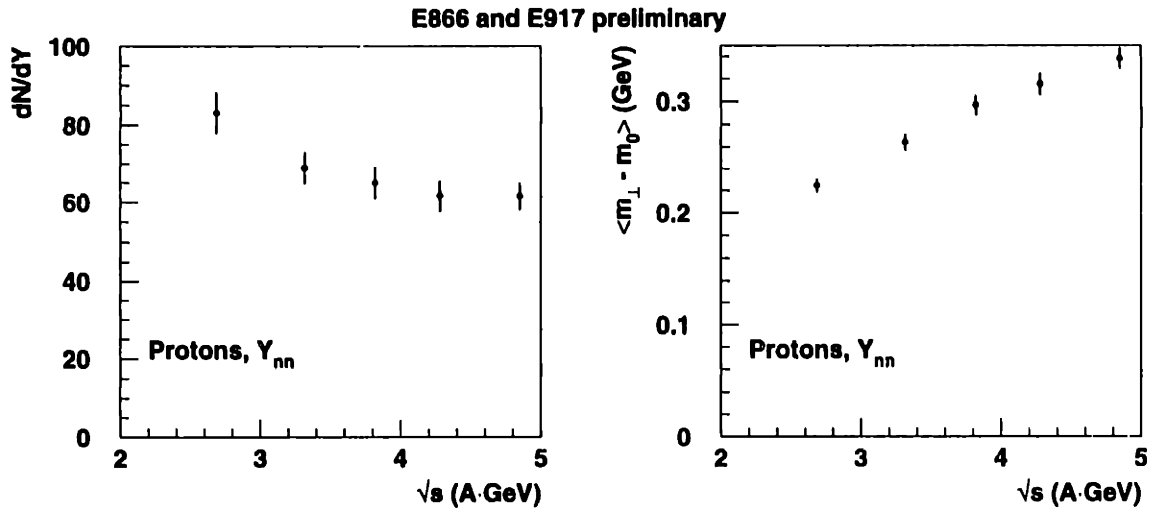

Figure 7-3: The dN/dY and $m_\perp$ of protons, at Y_{NN}, vs E_{beam}. The windows in rapidity for this data are as described in the caption to figure 7-1, and the results are from a Gamma fit. A 5% point-to-point systematic error has been included on the dN/dY, while a 2% systematic error on the $\langle m_\perp - m_0 \rangle$.

is conserved, rather than proton number, so it is not strictly necessary for the total number of protons to sum to twice the charge of Au (158). It is possible for pions produced in the collisions to carry off some of the isospin asymmetry of the initial state, converting neutrons into protons. The initial isospin asymmetry is most easily measured by the Z/A of Au nuclei, approximately 40%, so that in the most extreme case, in which the isospin of the baryons is completely equilibrated, such a conversion can produce a 25% increase in the yield of the protons in the final state. The level of this effect will potentially change with beam energy, since the increase in pion production is rather large. A useful indicator of this effect would be the π^-/π^+ ratio. However, the low-$m_\perp$ rise is larger in the π^- than in the π^+, and leads to significant systematic errors in the π^- due to the level of extrapolation in the fit, so the measured ratio does little to increase the understanding of the rise in the protons.

Despite this extra complication in the analysis, it is clear that the distribution of protons is instructive. Figure 7-3 shows the dN/dY and $\langle m_\perp - m_0 \rangle$ for these particles, at mid-rapidity. The $\langle m_\perp - m_0 \rangle$ rises as the beam energy increases, and

the rise is larger in the protons than in the π^+ by a significant amount. In contrast to the dN/dY of the produced particles, the dN/dY of protons decreases at mid-rapidity as the beam energy increases. The dN/dY at 10.8 $A{\cdot}GeV$ is approximately 25% lower than that at 2 $A{\cdot}GeV$.

There is a simple kinematic effect which will produce such behavior in the dN/dY, to leading order. Over the range of beam energies of this analysis, the difference in rapidity $Y_{beam} - Y_{target}$ rises from 1.8 to 3.2, an increase of approximately 80%. If one assumes that the proton number is conserved, and that the shapes of the dN/dY distributions scale with Y_{beam}, this effect will cause the dN/dY at any given Y value to increase.

More can potentially be learned through the removal of this leading effect. Figure 7-4 shows the variable $dN/d(Y/Y_{beam}^{cms})$ for protons as a function of $\sqrt{s}$. The use of this variable provides a uniform scale with which to compare across energies. There is a steady increase in the proton $dN/d(Y/Y_{beam}^{cms})$ with increasing beam energy, which may indicate that the fraction of energy deposited in the interaction region increases steadily with increasing beam energy. However, many processes do not scale with Y_{beam}, and the dN/dY, as a function of rapidity, do not seem to have a common shape in this variable, so the conclusions from this observation are not quite so clear. The proton distributions do serve as a stringent set of constraints on transport models.

7.2.4 K/π

Turning the focus back to the produced particles, figure 7-5 shows the ratio of K^+ to π^+ as a function of beam energy. This variable has historically been a source of much interest at the AGS. The pions are chosen as a normalization variable for production, since they are the most abundant produced particles. This ratio is therefore meant to measure the relative level of strangeness production in an easily interpreted way. Historically, an enhanced K/π was thought to be a possible signal for QGP formation, [RB82], [Raf82] although soon after its observation it was realized that the effects of hadronic rescattering on this variable are large. Both thermal and cascade models can, with some fine tuning, reproduce the ratio, at least under a single set of

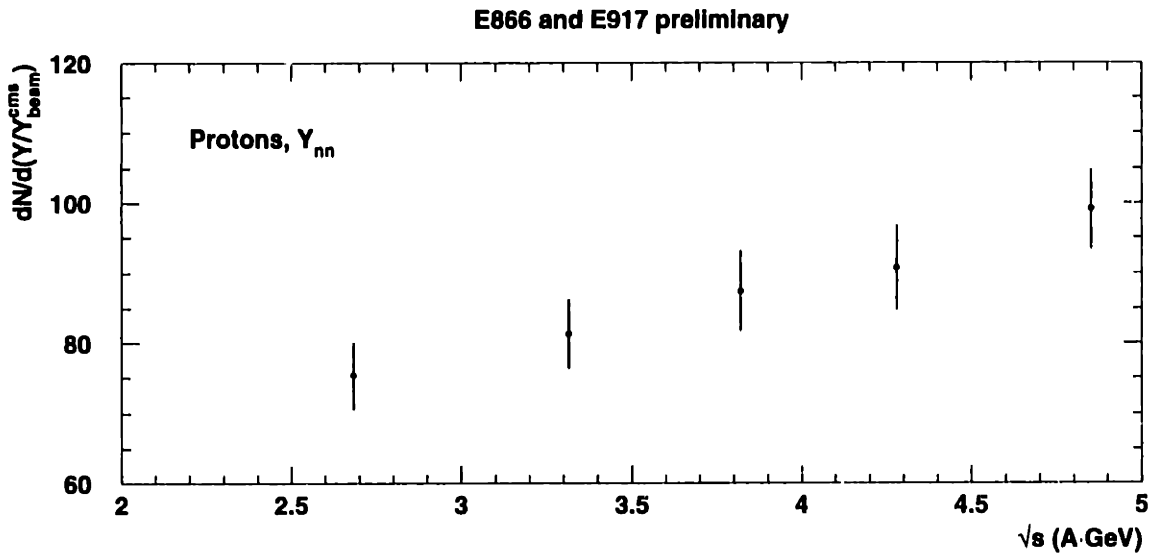

Figure 7-4: $dN/d\,(Y/Y^{cms}_{beam})$ for protons, at Y_{NN}, vs E_{beam}. The windows in rapidity for this data are as described in the caption to figure 7-1, and the results are from a Gamma fit. Point-to-point systematics of 5% have been included.

conditions.

The measured ratio shows a steady increase with the beam energy, and is large at the highest beam energy of the AGS. It is larger at this energy than the measured value at the higher energies of the SPS, measured by NA49 at Y_{NN} to be 0.145+0.02 [A$^+$98c]. Therefore a maximum value must occur at an energy between the AGS and the SPS.

While the existence of a maximum would at first glance seem to be a striking result, indicating a special point in energy, a comparison to the ratio in $p-p$ collisions produces a clear picture of how this can occur, without invoking any special properties for the maximal point.

Figure 7-6 shows a set of data on kaon production as measured in $p-p$ collisions. The data include measuremements by Fesefeldt et al. [F$^+$79] at 12 GeV/c, below 12 GeV/c in the complilation of kaon production in Landolt-Börnstein [lb93] and in recent near-threshold exclusive from COSY [Gro98b], [B$^+$]. The values have not been measured at the exact beam energies of this analysis, so a fit has been made to interpolate the kaon data to the energies of this analysis. The fit has the functional

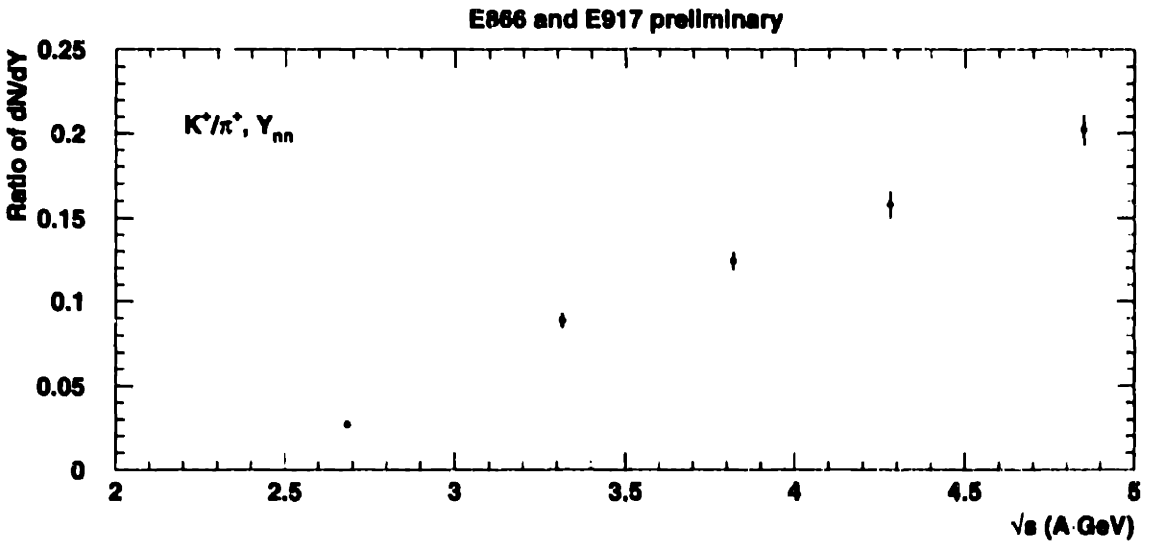

Figure 7-5: The yield ratio of $K^+\pi^+$ as a function of $\sqrt{s}$, at Y_{NN}. The windows in rapidity for this data are as described in the caption to figure 7-1. Point-to-point systematic errors of 2% have been included.

form, suggested by [Sib96]:

$$\text{yield}_{K^+} = A(s/s_{th} - 1)^{\gamma_1}(s/s_{th})^{\gamma_2} \tag{7.1}$$

where s is the center of mass energy squared of the collision, $2m\,(2E_{kin} + m)$, and s_{th} is the threshold in s for the production of the final state $pK^+\Lambda$, $(2.55\,GeV)^2$. The form is constrained to be zero at threshold. The parameters found for A, γ_1, and γ_2 are 0.4323, 1.972, and 2.318×10^-3.

There is no measured pion data from $p - p$ collisions in this region of energies, so the parametrization of the π^+ production cross-sections from [R+75] is used. This parametrization is given by:

$$\text{yield}_{\pi^+} = a + b\ln(s) + c/\sqrt{s} \tag{7.2}$$

where a=-1.85, b=0.82, and c=0.79.

From these parametrizations of the $p - p$ data, the ratio of the total yield of K^+

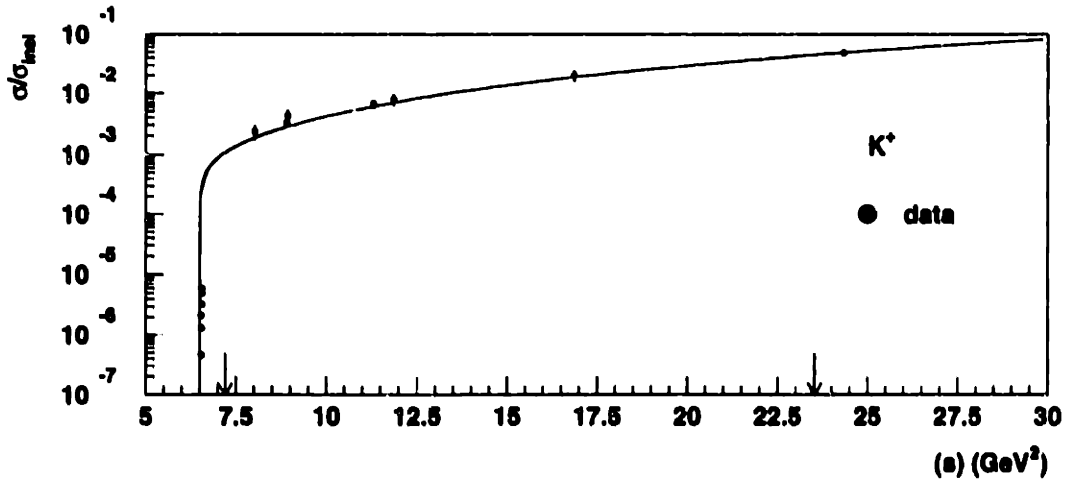

Figure 7-6: The K^+ yield in $p-p$ collisions as a function of $\sqrt{s}$. The data are from [F+79], [lb93], [Gro98b], [B+], and have been refit, with the results shown. The fit is to equation 7.1 of section 7.2.4. The arrows indicate the energy range of the AGS.

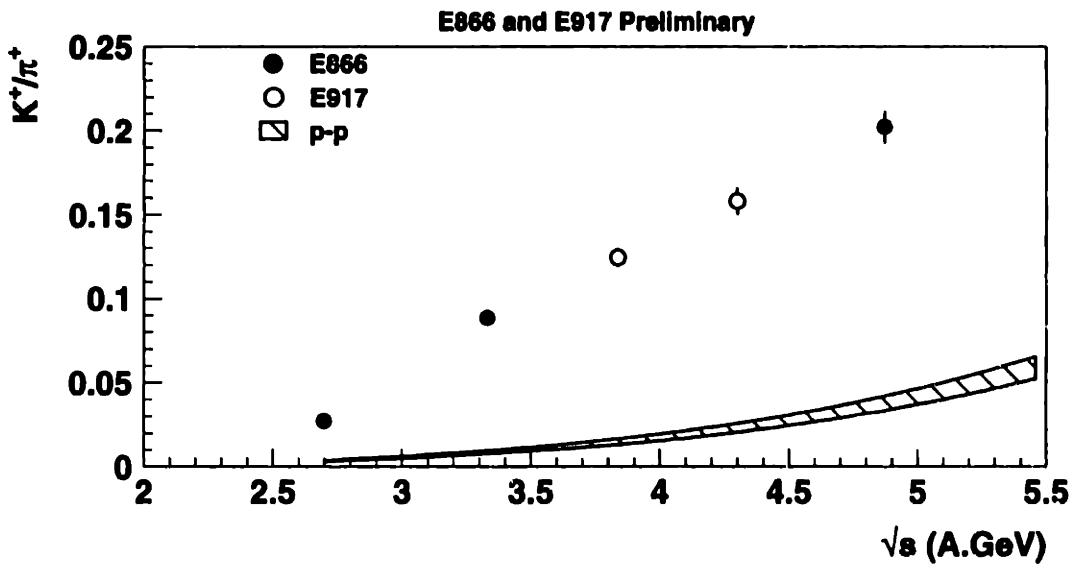

Figure 7-7: The K^+/π^+ ratio as a function of $\sqrt{s}$, along with a parametrization for the ratio in $p-p$ collisions. The $p-p$ data is as described in the text of section 7.2. 2% systematic errors have been added to the ratio in the data. A 5% error has been used for the $p-p$ parametrization for the π^+, a 10% for the K^+, and the two errors have added in quadrature in the $p-p$ K/π ratio.

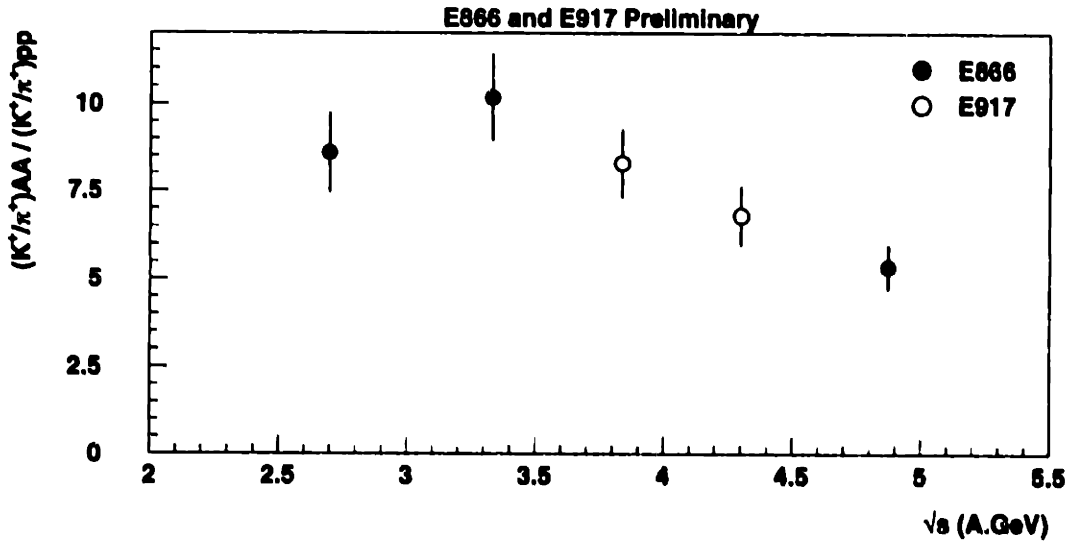

Figure 7-8: The double ratio of the K^+/π^+ in $Au - Au$ collisions, at Y_{NN}, to the K^+/π^+ ratio of total yields in $p-p$ collisions, as a function of $\sqrt{s}$. 2% point-to-point errors have been added to the $Au - Au$ ratio of K^+ and π^+. 5% errors have been used for the K^+, while 10% have been used for the π^+ $p - p$ parametrizations. All errors have been assumed to be uncorrelated in the derivation of the ratio.

to the total yield of π^+ can be formed, as a function of $\sqrt{s}$, for $p - p$ collisions. The ratio that results is significantly lower than that measured in $Au - Au$ collisons, at Y_{NN}, as shown in figure 7-7.

In order to make the interpretation of the data clearer, a double ratio is formed, by dividing the K^+/π^+, ratio, at Y_{NN} in $Au - Au$ collisions, by the ratio of total yields from the parametrization of the $p - p$ data. This double ratio is shown in figure 7-8. The level of this double ratio should be taken cautiously. The division is not strictly valid, since it compares a value measured at one point in rapidity to a value measured over all rapidities. If the relative shapes of the dN/dY distributions of the K^+ and π^+ change across beam energies, this double ratio will be modified, even if the true double ratio of total yields does not change. The leading kinematic effects of changing Y_{beam} (section 7.2.3) across energies are, however, removed in the double ratio.

A comparison between the data at the AGS and that at the SPS is shown in figure 7-9. Unfortunately, the parametrization used for the K^+ $p - p$ cross-sections

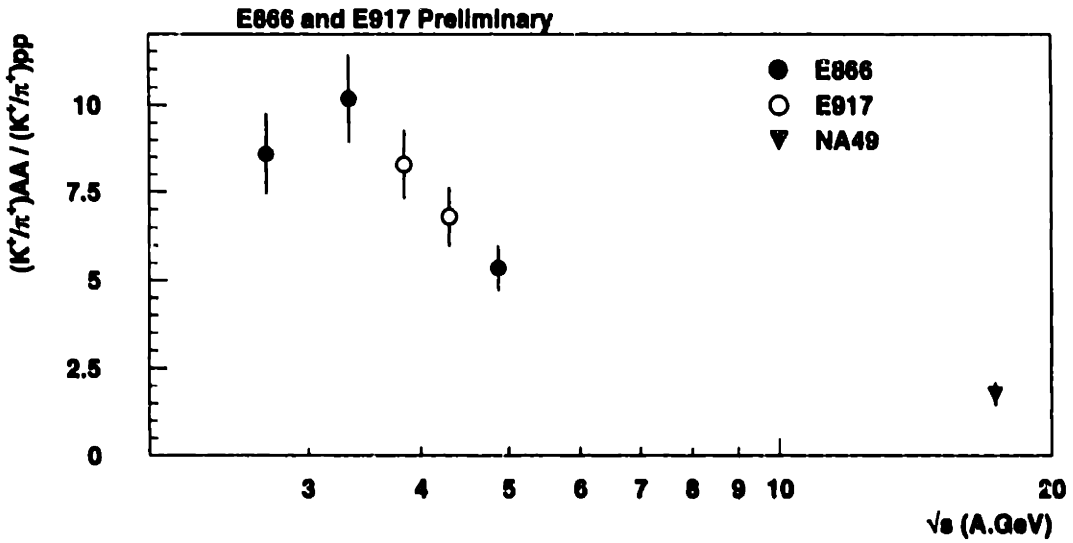

Figure 7-9: The double ratio of the K^+/π^+ in $Au-Au$ collisions, at Y_{NN}, to the K^+/π^+ ratio of total yields in $p-p$ collisions, as a function of $\sqrt{s}$. 2% point-to-point systematic errors have been added to the ratio in the $Au-Au$ data. 5% errors have been used for the K^+ and 10% for the π^+ $p-p$ parametrizations, and all errors have been assumed to be uncorrelated.

at the lower energies of the AGS is inconsistent with measured cross-sections in the energy range of the SPS, and so for the purposes of this plot the parametrization from [F+79] is used at the higher energies. This second parametrization is inconsistent with the data near threshold, but is consistent with the data at the energy at which it is used.

The data in $Pb-Pb$ collisions at the SPS lies on a common curve with the data at the AGS. The comparison of the double ratio shows little indication that there will be anomalous behavior of the K/π in the energy range between SPS and the AGS. This places a limit on the strangeness enhancement signal from the production of a quark-gluon plasma. From the data a prediction can be made, that the K^+/π^+ at Y_{NN} will be enhanced by a factor of approximately 2.5 over that in $p-p$ collisions at the 40 $A{\cdot}GeV$ beam energy of the upcoming SPS run. This beam energy corresponds to a $\sqrt{s}$ of 8.9 $A{\cdot}GeV$. With the parametrization used in this study at AGS energies, this translates to a K^+/π^+ of approximately 0.24, while using the parametrization near SPS energies, this translates to approximately 0.2. It should therefore not be a

surprise if the K^+/π^+ is higher at 40 $A{\cdot}GeV$ than at the AGS.

It is not completely clear what is occurring around 2 $A{\cdot}GeV$, since the double ratio is required to asymptote to infinity at threshold. However, the $p-p$ K^+ production shows a strong dependency on $\sqrt{s}$ in this region, although the data at COSY helps greatly in constraining this dependency. In addition, the extrapolation of the π^+ from the higher energies is at its largest at 2 $A{\cdot}GeV$. From these two effects, perhaps the systematic errors used in the $p-p$ comparison are underestimated at this point. Data from COSY on pion production might help to resolve the question.

It is clear from the double ratio that, at least for a range of energies, the enhancement of the K/π decreases as the beam energy increases. Couple the decrease of the enhancement as the beam energy increases with the overall rise in the level of the $p-p$ K/π, due to threshold effects, and one gets a maximum in the $Au-Au$ K/π. The location of this maximum holds information about the relative balance of enhancement and threshold effects in heavy-ion reactions.

The decrease with increasing beam energy indicates that the relative role of secondary collisions may increase with decreasing beam energy. There may be, however, a significant effect from Fermi motion. If one gives the nucleons of both Au nuclei a kick of 250 MeV in the center of mass frame of the nucleus, and calculates the extreme cases of $\sqrt{s}$ that result, at a beam energy of 2 $A{\cdot}GeV$ the shift to high $\sqrt{s}$ is 0.6 $A{\cdot}GeV$, while it is 1.4 $A{\cdot}GeV$ at a beam energy of 10.8 $A{\cdot}GeV$. These values correspond to the case in which the kick in both nuclei is in the direction towards the collision point, and is given by:

$$E_{Fermi} = \sqrt{p_{Fermi}^2 + m_{Nucleon}^2} \tag{7.3}$$

$$\sqrt{s_{Fermi}^{high}} = 2\left(E_{Fermi}\cosh Y_{beam}^{cms} + p_{Fermi}\sinh Y_{beam}^{cms}\right) \tag{7.4}$$

where the mass of the nucleon within the nucleon has been taken as $m_{nucleon} = m_{Au}/197 = 0.931GeV$, to be consistent with the analysis of $\sqrt{s}$, and where the relation comes from a Lorentz boost of the energy from the rest frame of the nucleus to a frame moving at Y_{beam}^{cms}. Given that the overall level of $\sqrt{s}$ ranges from 2.7 to

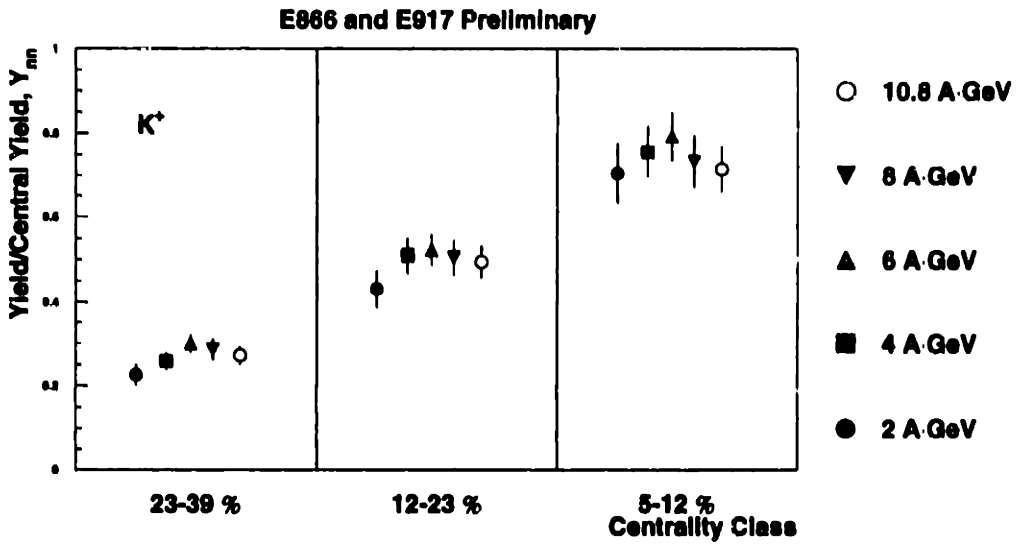

Figure 7-10: The yield ratio of the more peripheral centrality classes to those of the more central centrality clases, as a function of $\sqrt{s}$, at Y_{NN}. The windows in rapidity for this data are as described in the caption to figure 7-1. The errors include a point-to-point systematic of 5%.

4.9 $A \cdot GeV$, and that the kaon production cross-sections are steeply rising with $\sqrt{s}$, the effects of this shift can potentially be large. Further study would require a more sophisticated model than this order-of-magnitude estimate, and would remove the simplicity of the comparison to $p - p$.

The effects of Fermi motion cannot, however, account for the observed centrality dependence of the K^+ yields (section 7.3.3, [A+99a]). Therefore, at any one beam energy, such effects cannot be solely responsible for the enhancement of the K^+. Fermi motion may, however, modify the $\sqrt{s}$ dependence of the double ratio.

7.2.5 Centrality Dependence

To finish the general scan of the mid-rapidity data, figure 7-10 shows the centrality dependence of the mid-rapidity yields of K^+, divided by the central yields. The centrality dependence is strikingly similar at all beam energies, which indicates, on a coarse level, that the same processes that increase kaon production with centrality are at work at each energy.

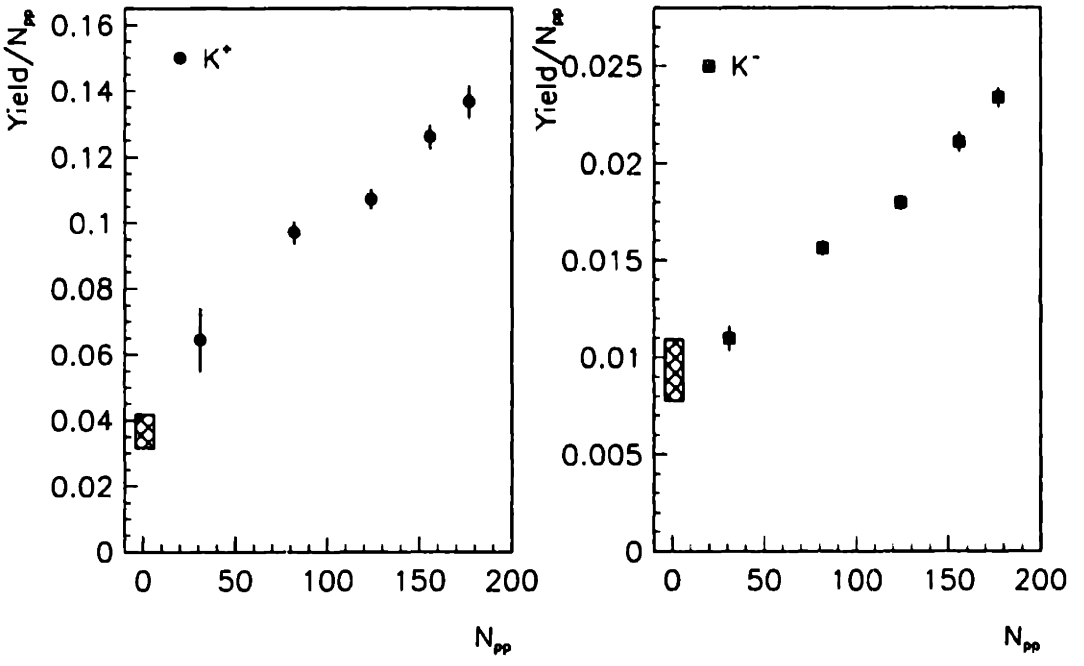

Figure 7-11: The total yield of K^+ per participant, as measured by the ZCAL, at Y_{NN}, at a beam energy of 10.8 $A{\cdot}GeV$. The hatched boxes represent an isospin-corrected value for the $p-p$ yield at the same energy. The plot is from [A+99a].

At 10.8 $A{\cdot}GeV$, the kaons show an increase with N_{pp} that is faster than linear, as can be most easily shown by the ratio of the K^+ yield to N_{pp}, shown in figure 7-11. The figure shows a ratio of total yields to N_{pp}, which is perhaps more clear than the ratio at Y_{NN}, but the same trend is seen in the data at Y_{NN}. At other energies, the number of projectile participants is not directly observable. However, since the centrality cuts at the lower beam energies were chosen to cover the same cross-section as those at 10.8 $A{\cdot}GeV$, and since the centrality dependence is similar, the same statement about kaon enhancement can be made at the lower beam energies. This nonlinear enhancement indicates rather strongly that strangeness production in nuclear collisions is not due simply to the superposition of individual nucleon-nucleon collisions.

7.3 Comparison between K^+ and K^-

There are many differences between the K^+ and K^-, both on the fundamental hadronic level and within models that incorporate medium effects on the kaon masses. Therefore, a search can be made through the data for differences in their production properties, which may indicate the presence of such effects. This search will at the very least produce a large set of constraints on the models that attempt to describe the data.

7.3.1 Mid-Rapidity, Central 5%

Beginning at mid-rapidity, figure 7-12 shows the $m_\perp$ distributions in the same set of rapidity windows used in section 7.2, from the 5% most central collisions. The total sample of K^- at 2 $A{\cdot}GeV$ is small, on the order of 40, and so it does not allow the detailed comparisons made for the other beam energies. For this reason, it will not be used. As shown previously, the K^+ distribution is well described by an exponential in $m_\perp$ at all beam energies. This is also true for the K^- (see figure 7-12). This brings up the first difference between the K^- and K^+: since the K^- contains an s quark while the K^+ contains an $\bar{s}$, the quark-exchange process $K^- + N \rightarrow \Lambda\pi$ is

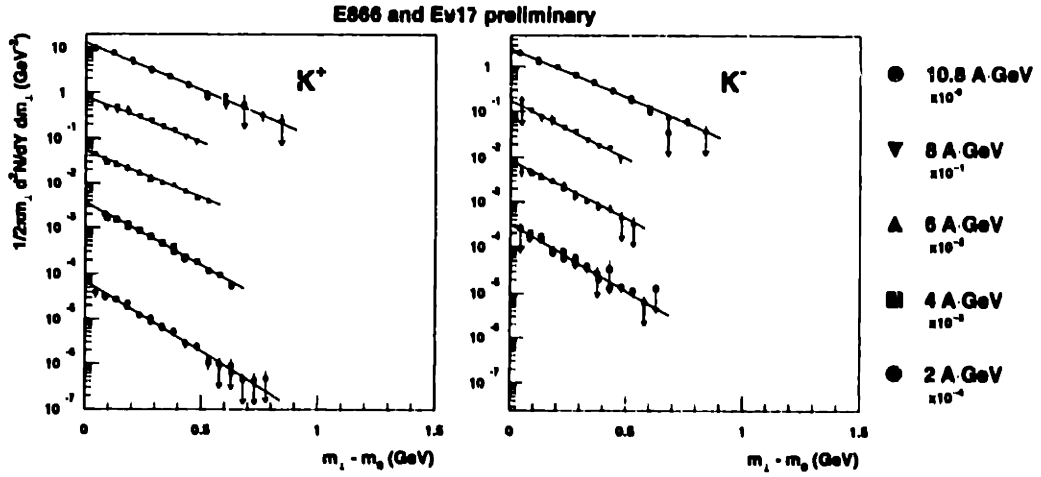

Figure 7-12: The invariant differential yields of K^+ and K^- as a function of $m_\perp$ in a window about Y_{NN}. The data is as described in the caption to figure 7-1.

allowed for the K^- but not for the K^+. This leads to a relatively large absorption cross-section for the K^-, around 20 *mb*. Because this cross-section increases at low momentum, in the most extreme case one might expect to see a change in the shape of the distribution of the K^- at low $m_\perp$. No indication of this is seen in the data. The question of absorption will come up again in section 7.3.4 in the examination of the inverse slopes.

The yields of the K^+ show a different functionality with beam energy than those of the K^-. Figure 7-13 shows the dN/dY at mid-rapidity for K^+ and K^- as a function of the $\sqrt{s}$ of the beam, along with the ratio of the two numbers. The ratio rises with increasing beam energy, changing by a factor greater than 2 over the range of beam energies of this analysis. Figure 7-14 shows this ratio again, along with data measured from $Ni-Ni$ and $C-C$ collisions by the *KaoS* collaboration at the lower energies available at GSI [B+97], [L+99]. The ratio follows a smooth trend with $\sqrt{s}$, and seems to be relatively common across systems.

A rise in the ratio is to be expected from simple threshold arguments, since the threshold for production of K^-, which must be produced pairwise with an associated K^+, is higher than that for K^+, which can be produced along with a Λ. The thresholds in $p-p$ collisions are 2.55 *GeV* for the process $NN \rightarrow N\Lambda K$, and 2.87 *GeV* for the

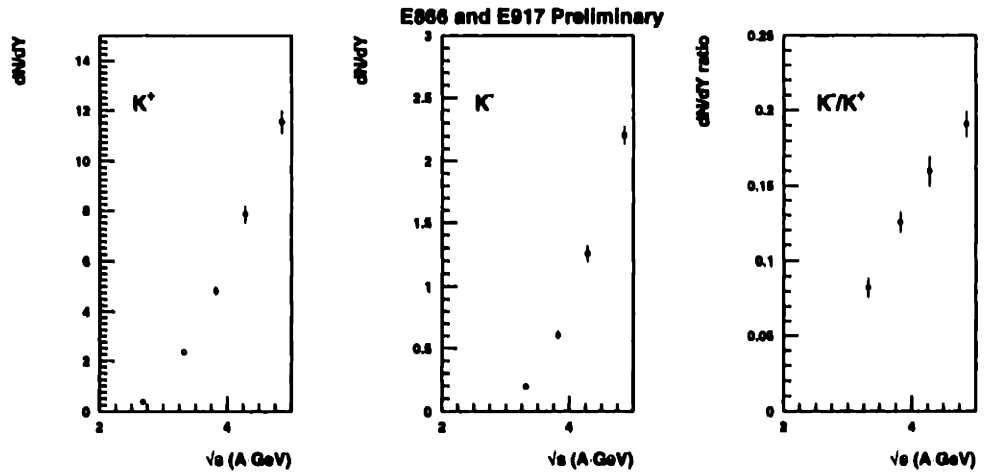

Figure 7-13: The dN/dY of K^+, K^-, and the ratio of the two, at Y_{NN} as a function of $\sqrt{s}$ The window allowed about Y_{NN} is as described in the caption to figure 7-1. Point-to-point systematic errors of 5% have been included in the absolute dN/dY, and of 2% in the ratio.

process $NN \rightarrow NNK^+K^-$. These thresholds are rather significant in the range of $\sqrt{s}$ of this study, from 2.7 GeV at 2 $A{\cdot}GeV$ to 4.9 GeV at 10.8 $A{\cdot}GeV$.

It is clear, however, that the distance from the $p-p$ threshold is not the sole variable determining the yields. This can be most clearly seen by subtracting the threshold energy, s_{th}, from the beam energies, and comparing the yields at Y_{NN} at common values of this subtracted energy. This is done separately for the K^+ and K^-, since the thresholds for these particles are different. Figure 7-15 shows the results of this subtraction, the dN/dY at Y_{NN} as a function of $\sqrt{s} - \sqrt{s_{th}}$. There is an order of magnitude difference between the yields at mid-rapidity of the K^+ and K^- at any given value of this variable.

This result stands in marked contrast to the behavior observed at the subthreshold energies of the SIS at GSI [B+97]. The *KaoS* collaboration measured K^- yields from $Ni-Ni$ collisions at a beam energy of 1.8 $A{\cdot}GeV$, and K^+ yields at 1.0 $A{\cdot}GeV$. These energies translate into a $\sqrt{s} - \sqrt{s_{th}}$ of -0.25 $A{\cdot}GeV$ for the K^+ and -0.24 $A{\cdot}GeV$ for the K^- measurements. The measurements are therefore said to have been made at "equivalent" energies. The ratio of these measurements, K^-/K^+ at equivalent energies, is found to be 1.0±0.4.

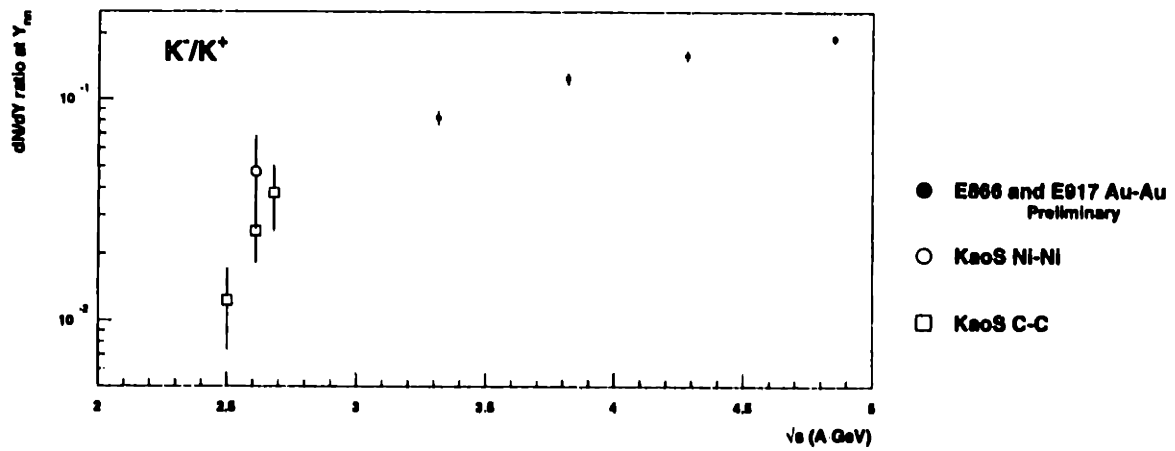

Figure 7-14: The K^-/K^+ ratio as a function of $\sqrt{s}$, along with data from $Ni-Ni$ and $C-C$ collisions at the SIS [L+99], [B+97]. The errors quoted in these articles include a 15% systematic error, which has not been removed in the figure. Point-to-point systematic errors of 2% have been included in the AGS data.

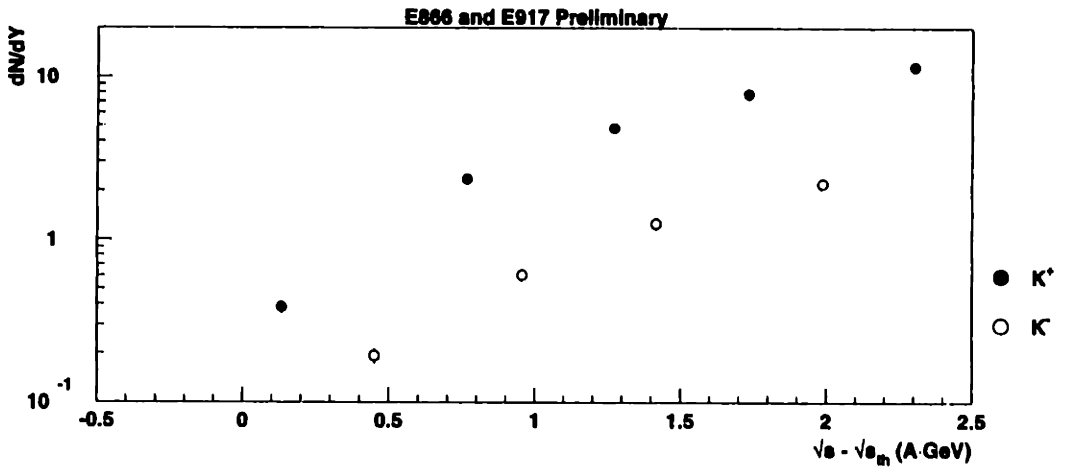

Figure 7-15: The yields at Y_{NN} of K^+ and K^-, as a function of $\sqrt{s}-\sqrt{s_{th}}$, where $\sqrt{s_{th}}$ is the threshold for the lowest production process in $p-p$ collisions. Point-to-point systematic errors of 5% have been included.

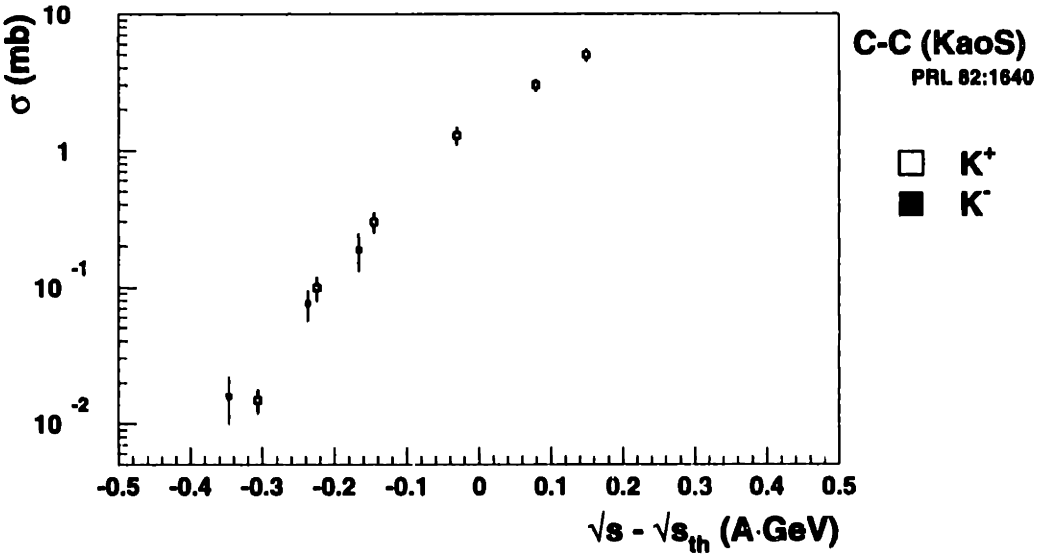

Figure 7-16: The production cross-sections of K^- and K^+ in $C-C$ collisions, as measured by the *KaoS* collaboration, as a function of $\sqrt{s}-\sqrt{s_{th}}$. The data is from [L$^+$99].

The observed equality of the K^- and K^+ yields at the same value of $\sqrt{s}-\sqrt{s_{th}}$ could, of course, be a coincidence. A measurement at one point does not constitute an argument for a functional form. However, the same experiment has recently measured K^- and K^+, from $C-C$ collisions, over a range of values of $\sqrt{s}$, three points of which are rather close in $\sqrt{s}-\sqrt{s_{th}}$ [L$^+$99]. The data are shown in figure 7-16, and show that the scaling is roughly valid, at least for a restricted range of $\sqrt{s}$.

The next logical step is to see how the data of this analysis scales with increasing $\sqrt{s}-\sqrt{s_{th}}$. Unfortunately, none of the beam energies of this thesis were chosen to have equal values of $\sqrt{s}-\sqrt{s_{th}}$ for the K^+ and K^-. It is possible, however, to interpolate between the data measured in order to obtain a ratio at equivalent energies. The interpolation is done extremely simply, using second-order polynomial fits, the χ^2 per degree of freedom of which are consistent with 1. The values obtained are listed in table 7.1. Figure 7-17 shows the ratio of the two interpolations, as a function of $\sqrt{s}-\sqrt{s_{th}}$, along with the data from *KaoS*. The K^-/K^+ is approximately 0.2 at a $\sqrt{s}-\sqrt{s_{th}}$ of 2 $A{\cdot}GeV$, and decreases as $\sqrt{s}-\sqrt{s_{th}}$ approaches 0.

This difference is a striking effect. The ratio needs to rise by a factor of approx-

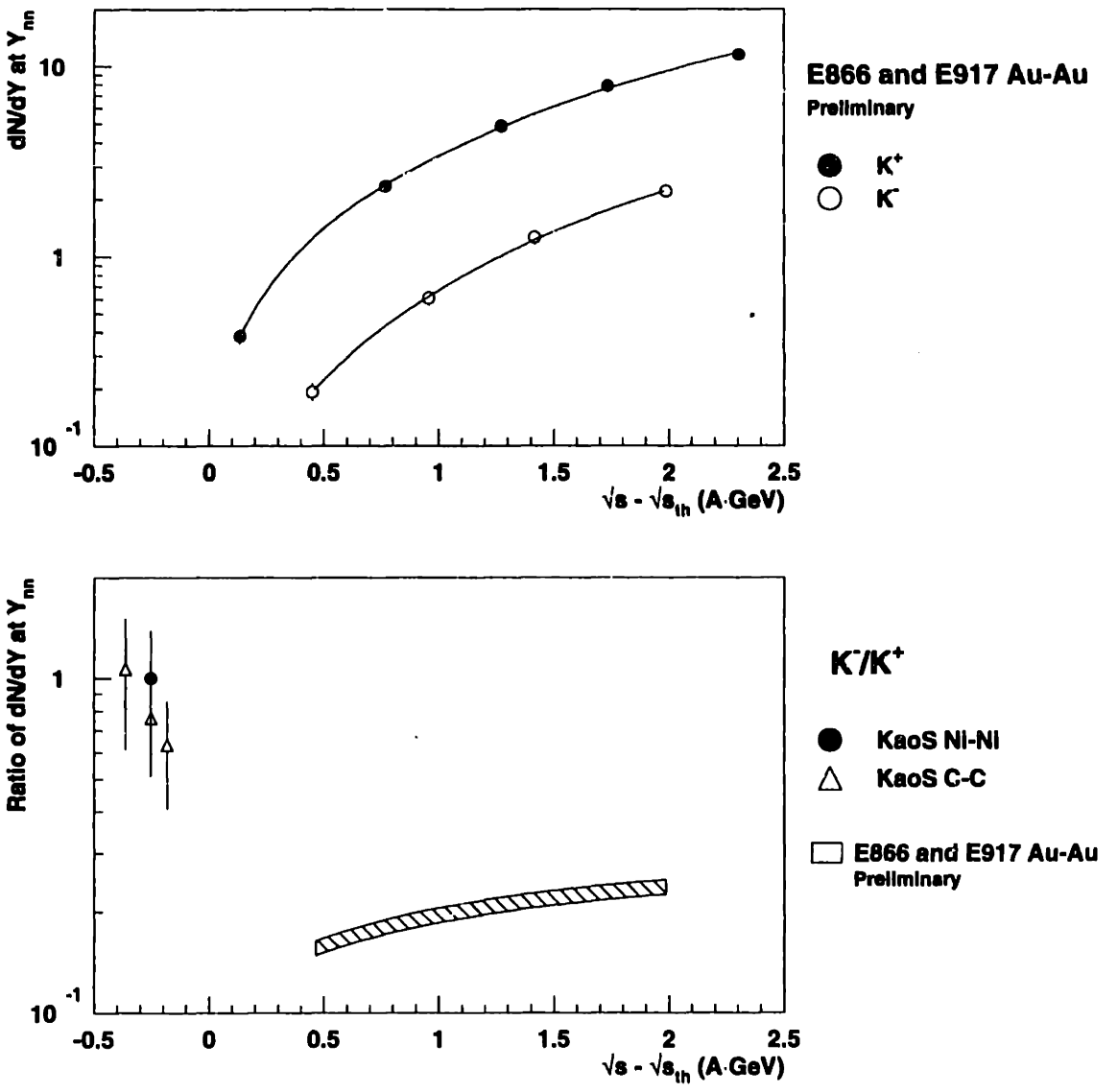

Figure 7-17: The dN/dY at Y_{NN} of K^+ and K^-, as a function of $\sqrt{s} - \sqrt{s_{th}}$, along with fits to the dependence, are shown in the top panel. A division of the results of the fit is shown in the bottom panel, along with data measured by the *KaoS* collaboration in $Ni - Ni$ collisions[B+97]. Point-to-point systematic errors of 5% have been included in the dN/dY for the purposes of the fit. In the bottom panel, point-to-point errors of 5% have been added to the results from the fit, due both to the interpolation and to the comparison across experiments, and the quoted 15% systematic is used for the *KaoS* points. The *KaoS* data is from [B+97],[L+99].

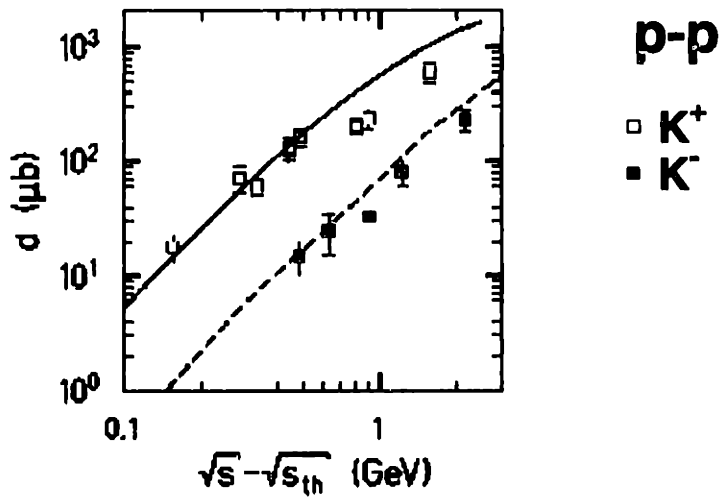

Figure 7-18: Inclusive K^- and K^+ cross-sections in $p-p$ collisions. The figure is from [B+97], and includes data from [FMM84], with parametrizations based on [Mül95].

Particle	P_0	P_1	P_2	χ^2/dof	dof
K^+	0.095	1.92	1.38	0.23	2
K^-	0.015	0.184	0.468	0.22	1

Table 7.1: The fit parameters from a second-order polynomial fit to the K^+ and K^- dN/dY at Y_{NN} vs $\sqrt{s} - \sqrt{s_{th}}$.

imately 5 between a $\sqrt{s} - \sqrt{s_{th}}$ of 0.5 $A \cdot GeV$ and -0.3 $A \cdot GeV$, in order to match both sets of data. In the range from 0.5 $A \cdot GeV$ to 2.0 $A \cdot GeV$ the ratio drops by approximately 50%, so the downward trend needs to reverse. There does seem to be a downward trend towards the AGS data in the GSI $C - C$ data. However, as shown in figure 7-16, the $C - C$ K^+ and K^- measurements were not made at exactly the same value of $\sqrt{s} - \sqrt{s_{th}}$, with the K^- at a lower value throughout. Therefore the division shown in figure 7-17 is not strictly valid.

The difference between the AGS and GSI data is unexpected, given that the K^-/K^+ ratio seems to follow a relatively universal curve with $\sqrt{s}$, as shown in 7-14. The variable $\sqrt{s} - \sqrt{s_{th}}$ is not an obvious variable to use in heavy-ion collisions, especially close to threshold, because of the potentially large role of secondary collisions in the production of K^+ and K^-. For example, the threshold energy of $NN \rightarrow K^+K^-NN$ is approximately 1 GeV, subtracting the mass of the initial state, but that of the secondary process $N\Lambda \rightarrow NpK^-$ is much lower, 0.28 GeV. Since, to a good approximation at these energies, for every K^+ produced a Λ is produced, the ratio K^-/K^+ may be strongly affected by this secondary process. It is therefore not obviously clear that the energy of the $p - p$ threshold is the right energy to use.

The variable $\sqrt{s} - \sqrt{s_{th}}$ also makes little sense in $p - p$ collisions. The inclusive K^+ and K^- cross-sections have been measured from $p - p$ collisions in an energy range close to that of the AGS. and are shown in figure 7-18. These cross-sections show roughly the same level of difference between the K^+ and K^- yields, at a given distance from threshold, that is seen in $Au - Au$ collisions above threshold.

Despite these problems with $\sqrt{s} - \sqrt{s_{th}}$, as a variable, the $C - C$ data does seem to fall on a relatively universal curve, and are consistent with the $Ni - Ni$ results, for the beam energies measured. This regularity in the data argues for the validity of the variable, despite its problems.

The comparison between the AGS data and the GSI data may also suffer from the different systems used in the analysis. A C nucleus has 12 nucleons, while a Au nucleus 197, so the difference in the size of the systems compared is quite large. Absorption effects could be potentially different here, although the lack of a difference

between the Ni ($A = 59$), and the C results suggests that the effects of absorption are not large. Combine this with the observed lack of dependence on centrality of the K^-/K^+ ratio at any given beam energy (see section 7.3.3) and the similar centrality dependence of the K^+ production across energies (see section 7.2.5), and the comparison across systems begins to look more valid.

Models that include in-medium effects on the kaons can reproduce the $Ni - Ni$ results [LLB97],[LB98], at SIS energies, although the effects of hadronic multiple-scattering processes on the results are large within the models. At first glance, the C system seems too small for in-medium effects to be significant. However, calculations of the effects in infinite systems [WW97] predict a significant drop on the order of 20% in the K^- mass at normal nuclear matter density, and so it is possible that the C systems to also display the effect. There is also the possibility of a momentum dependence to the potentials.

The difference between the K^-/K^+ ratio at AGS energies and that at SIS energies constrains strongly the explanations of the SIS data within models. The results of these models therefore need to be consistent with the AGS data in order to be valid.

7.3.2 Rapidity Dependence

The discussion of the previous section focused on measurements at mid-rapidity. It is therefore not strictly valid to compare the results across beam energies, since the shapes of the dN/dY distributions may change as the beam energy changes.

From the $m_\perp$ distributions, binned into windows of rapidity, the dN/dY as a function of Y are obtained. Figure 7-19 shows these distributions for the most central event class. The data have been transformed into the center of mass frame by subtracting Y_{NN} from the measured Y. The arrows indicate the location of beam rapidity, which changes from approximately 0.9 at 2 $A{\cdot}GeV$ to 1.6 at 10.8 $A{\cdot}GeV$.

The shape of the K^+ and K^- dN/dY shows a small level of change as the beam energy decreases, but the precise determination of the level of this change is complicated by the experimental acceptance. The widths of the distributions do not seem to scale with the total range available in Y. Further, given the portion of the shape

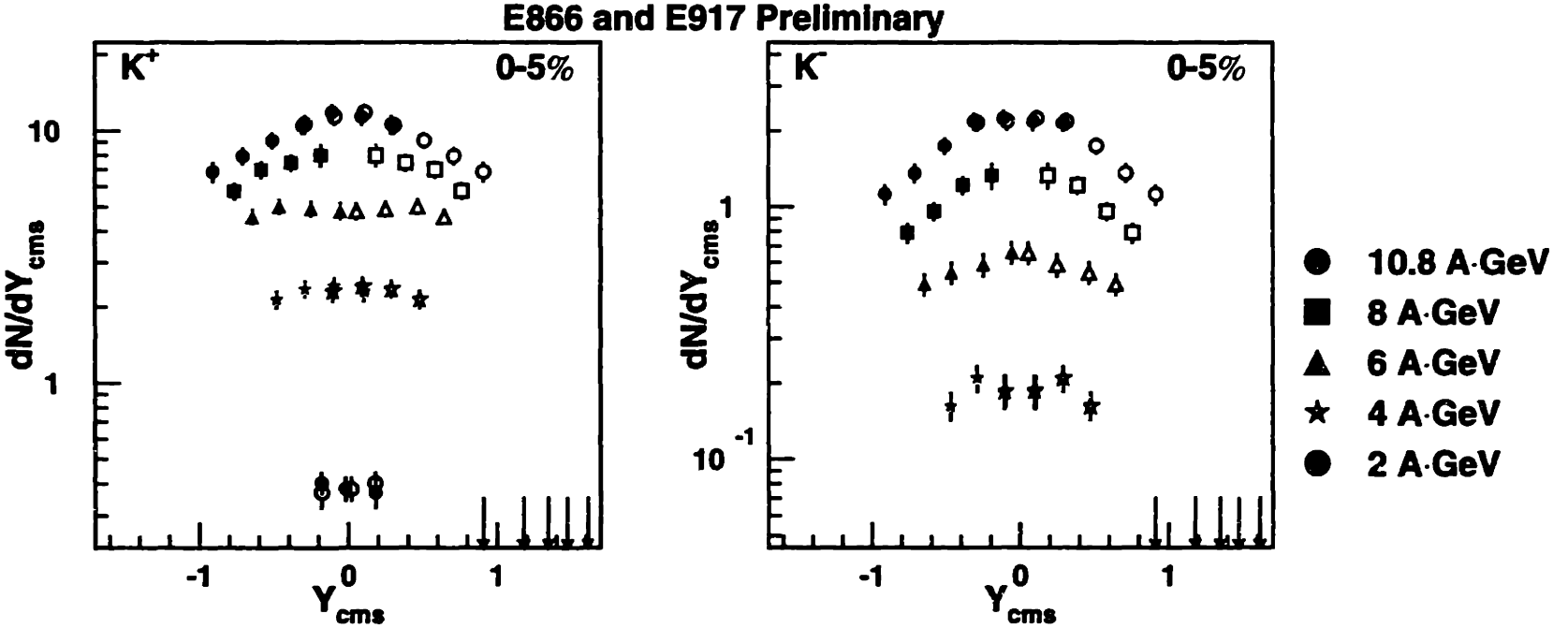

Figure 7-19: The dN/dY, as derived from an exponential fit to the invariant differential yields in $m_\perp$, as a function of Y_{cms}, the rapidity in the center of mass frame, for the 0-5% centrality class, at all beam energies from 4-10.8 $A \cdot GeV$. The errors shown include a 5% point-to-point systematic error. The open symbols denote data that have been reflected about mid-rapidity, and the arrows denote beam rapidity.

that is visible within the acceptance, the distributions do not appear to be Gaussian. This uncertainty in the actual shape of the distributions, combined with the limited acceptance, makes it difficult to extract a total yield of kaons from the distributions. No attempt is made to do so in this analysis.

It is, however, clear that the dN/dY distributions of the K^+ and K^- have different shapes. Figure 7-20 shows the ratio between the dN/dY of K^- and K^+ as a function of Y_{cms}, for the 0-5% most central event class. The K^- distributions are consistently narrower across all beam energies. This observation provides strong constraints on hydrodynamic interpretations of these collisions, since under the simplest hydrodynamic picture the spectral shapes of particles of equal mass, such as the K^+ and K^- , are identical.

At first glance, this difference in shape can be ascribed to the difference in thresholds. For the processes with the lowest thresholds in $p-p$ collisions, the difference in the momentum available in the center of mass is significant, ranging from 0.25 GeV/c at 4 $A{\cdot}GeV$ to 0.15 GeV/c at 10.8 $A{\cdot}GeV$. Therefore the available range for production in Y will be smaller for the K^-, due to the difference in available energy. Such a difference in width is seen in $p-p$ collisions at beam momenta of 12 GeV/c [F+79]. However, as in the case of the ratio at mid-rapidity, a simple interpretation in terms of thresholds can be complicated by a range of effects. The level of difference between the K^+ and K^- shapes is consistent across all beam energies, although due to the limited acceptance it is again difficult to make this statement quantitative. This fact indicates that the energetics alone cannot provide an explanation for the difference in width, since if the difference were solely due to energetics one would expect it to change as the beam energy changes.

7.3.3 Centrality Dependence

The centrality dependence of the K^+/K^- ratio has some potential physical lessons. The nonlinear rise of the K^+ with the number of projectile participants indicates that nuclear effects have an enhanced effect on the kaons, which can in principle affect the K^- differently from the K^+. It is also known that the K^-/K^+ ratio is constant as a

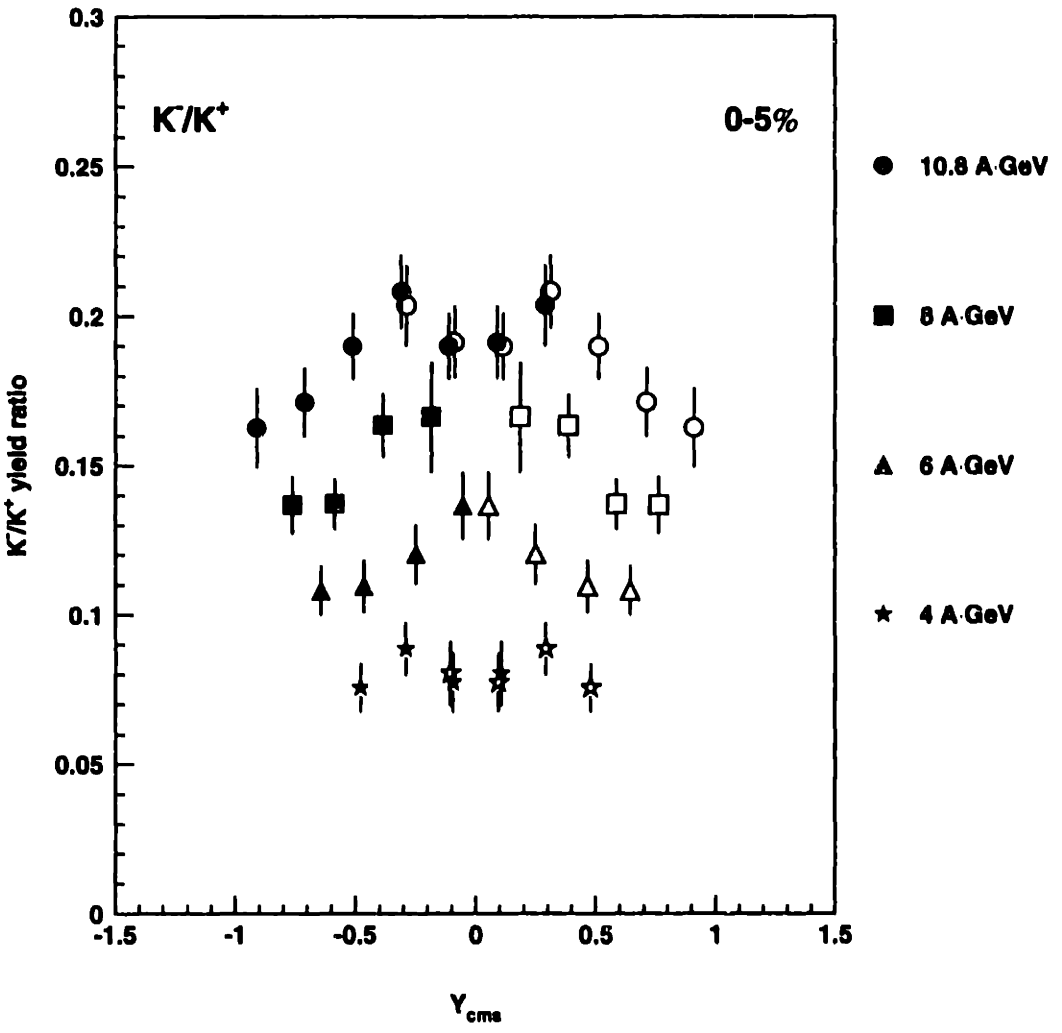

Figure 7-20: The ratio, K^-/K^+, of the dN/dY as a function of Y_{cms}, for the 0-5% centrality class, at all beam energies from 4-10.8 $A{\cdot}GeV$. The errors in the individual dN/dY distributions are assumed to be uncorrelated. 2% systematic errors have been added. The open symbols denote data that have been reflected about mid-rapidity.

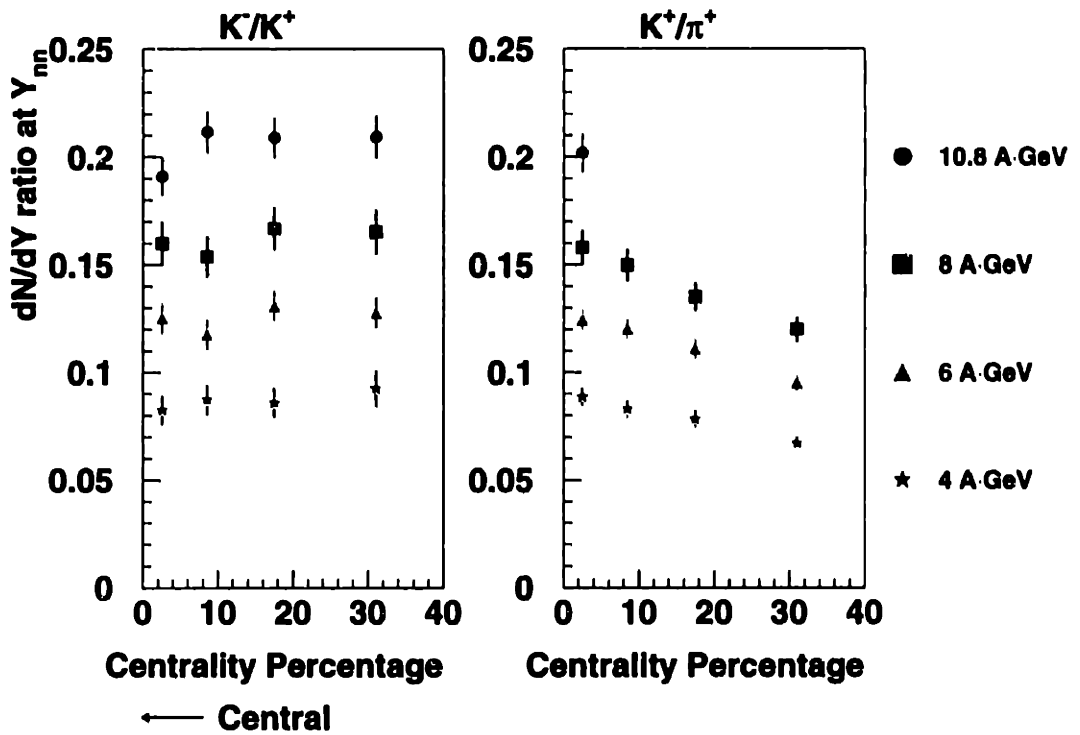

Figure 7-21: The K^-/K^+ and K^+/π^+ ratios, at Y_{NN}, for the four centrality classes and the four beam energies of this analysis. The horizontal axis shows the percent of 6780 *mb* contained within the centrality class. Errors on the ratios include an additional 2% systematic error.

function of centrality in $Au - Au$ collisions at 10.8 $A \cdot GeV$[A+99a], and constant to within the sizeable error bars in $Ni - Ni$ collisions at GSI [B+97].

This lack of dependency is a bit of a puzzle. Within a hadronic framework, the level of rescattering, combined with its effect on the different production thresholds of the K^- and K^+, combined further with the different absorption properties of the K^- and K^+, might lead one to expect that the dependence on centrality would be different between the K^+ and K^-. Within the framework of possible mass shifts of the kaons, a change in baryon density, potentially achieved by changing the centrality of the collision, would also lead to a divergence of the K^+ and K^- yields.

Various models have, however, been able to reproduce the dependence of the K^-/K^+ with centrality. A cascade model, RQMD, described in [SSG89], reproduces the lack of dependency at 10.8 $A \cdot GeV$, although it does get some spectral details wrong at approximately the 25% level[Ahl97]. This model incorporates the full range of hadronic rescatterings, along with some semi-hadronic ideas based on a string picture. It has many parameters within it that are not measured, and it is not clear which of the physical mechanisms is responsible for the lack of a change. At GSI energies, within the framework of shifting masses, models that reproduce the basic trend of the data do so by using absorption to cancel the increase in the yields due to increased baryon density [LB98]. Although this mechanism reproduces the data at the one beam energy studied, it is difficult to believe that such an accidental cancellation will continue as the beam energy increases. Unfortunately, the calculations have not been extended to the study of K^+ and K^- production at higher beam energies.

The current data set therefore provides a testing ground for the ideas of these models. Figure 7-21 shows the centrality dependence of the yield ratios K^-/K^+ and K^+/π^+ at mid-rapidity. The K^-/K^+ is independent of centrality at all beam energies from 2-10.8 $A \cdot GeV$, while the K^+/π^+ shows a significant decrease towards the peripheral region. The change in the K/π shows that, even with the restricted range of centralities made necessary by the performance of the interaction trigger, the experiment is sensitive over the range necessary to see a change in the relative levels of production. No such change in the K^-/K^+ is observed.

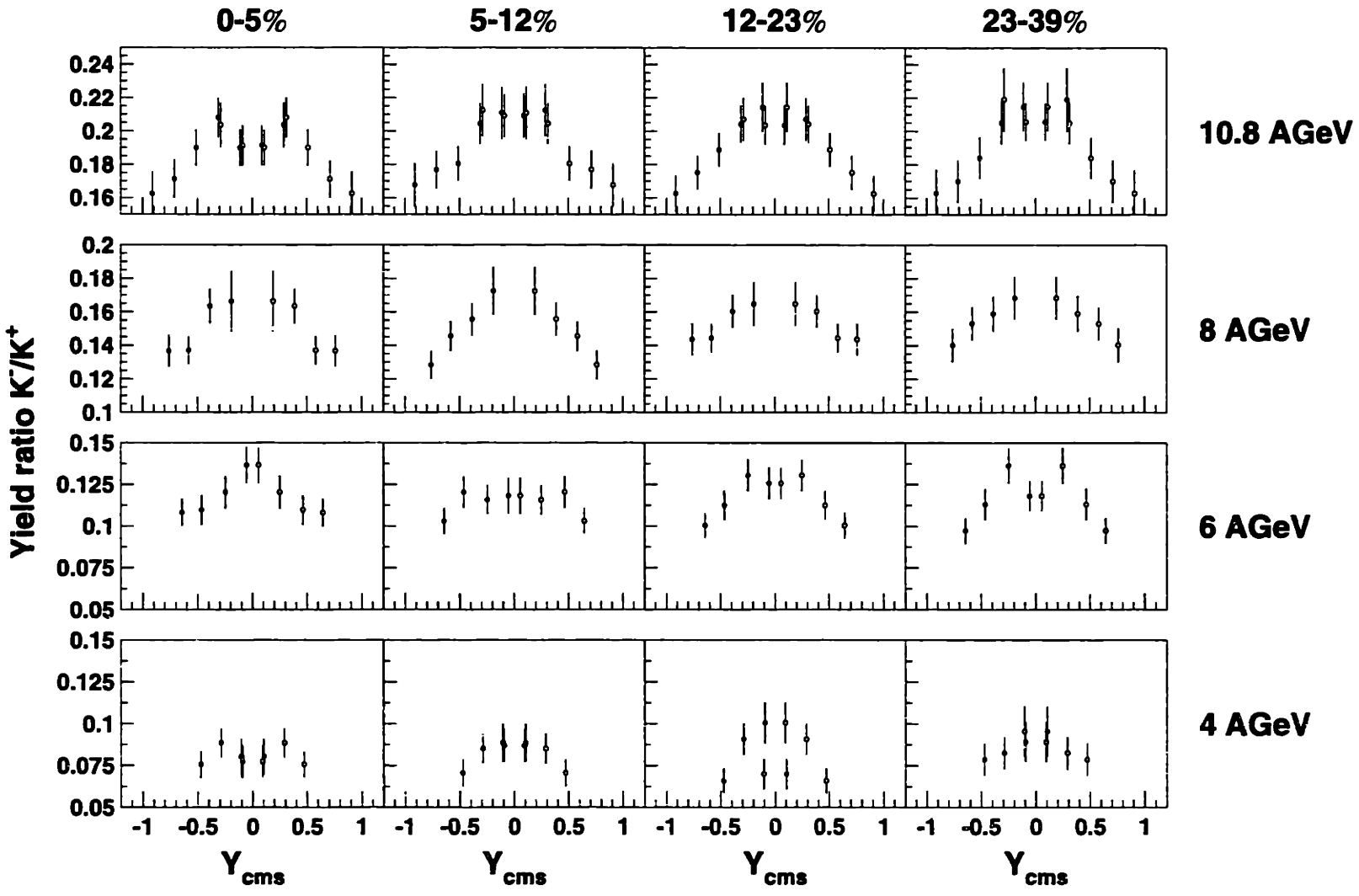

Figure 7-22: The full grid of the dN/dY ratio of K^+/K^-, as a function of Y_{cms}, centrality, and E_{beam}. Point-to-point systematic errors of 2% have been included.

At any given beam energy, the K^- yield at mid-rapidity follows that of the K^+, over an order of magnitude total change in yield with centrality. There is, however, a dependence on rapidity of the ratio between the two yields, so a natural question to ask is whether the ratio remains constant with centrality at all rapidities, for a given beam energy. Figure 7-22 answers this question, over the full range of rapidity that the experiment can measure. The figure shows the data on the ratio in its fullest form, as a grid in beam energy, centrality, and rapidity. Along the horizontal of the figure the events become more peripheral, while along the vertical the beam energy decreases. Each panel of the figure shows the rapidity dependence of the ratio. The data shows a striking similarity. At each beam energy, at each rapidity, the ratio between the yields remains constant, despite the fact that the dN/dY of the K^+ and K^- increase strongly and nonlinearly. It is difficult to believe that this trend in the data is caused by a cancellation of opposing effects. However, it is not clear what mechanism is causing this universal behavior.

7.3.4 Inverse Slopes

The inverse slopes of the K^+ and K^- raise interesting questions. However, as with the low-$m_\perp$ rise of the pions, it is difficult to disentangle the set of explanations to produce a clear answer.

Figure 7-23 shows the inverse slopes of the K^+ as a function of rapidity for central collisions. As noted in the discussion of the mid-rapidity data, the increase with energy of the inverse slopes, or equivalently the mean $m_\perp$, is not as large as that of the yields. The K^- show the same basic behavior as the K^+. Figure 7-24 shows the difference between the two, $T_{K^+} - T_{K^-}$, for the central 5% collisions. The inverse slopes are not completely well-constrained by the data, due to the extrapolation, but a trend can be seen. The inverse slopes of the K^- are systematically lower than those of the K^+, although the level of difference is small, given the errors on the measurements.

Figure 7-25 shows the data for all centralities. The same trend is seen in all data. The inverse slopes are, to the level of the errors, rather consistent between the K^+

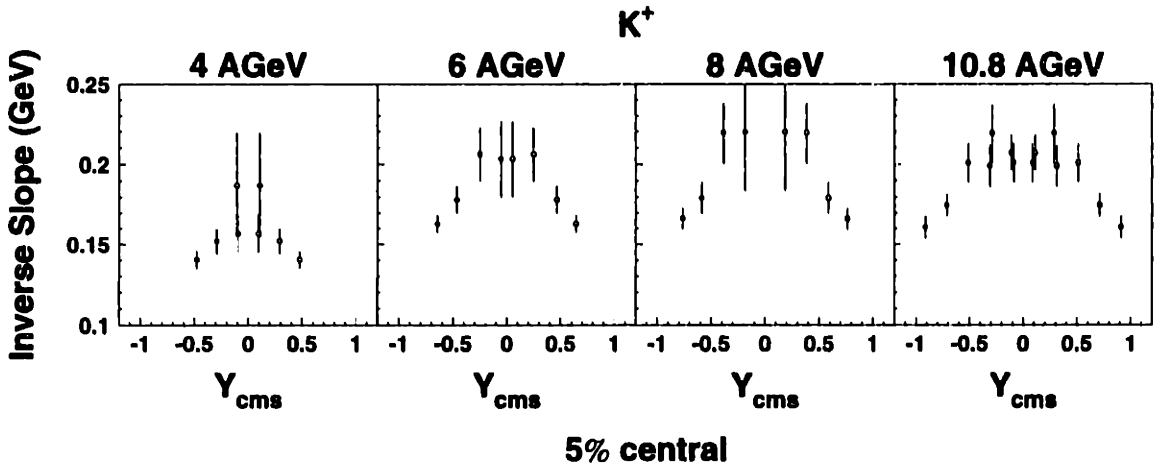

Figure 7-23: The inverse slopes of the K^+ distributions, for all E_{beam}, as a function of Y_{cms}, in central collisions. Point-to-point systematic errors have been included at the lower beam energies, as described in section 6.4, and 2% point-to-point systematic errors have been included at 10.8 $A \cdot GeV$.

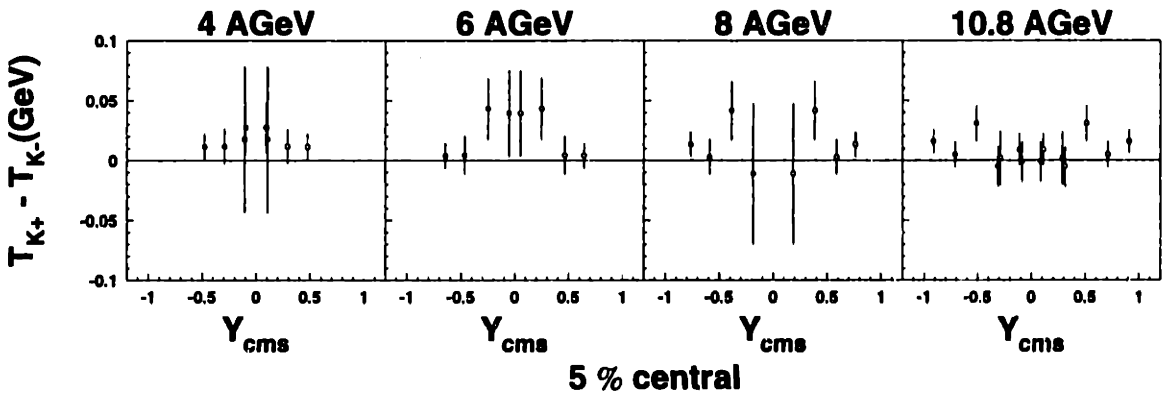

Figure 7-24: The difference in the inverse slopes of the K^+ and K^- distributions, for all E_{beam}, as a function of Y_{cms}, in central collisions. Point-to-point systematic errors have been included at the lower beam energies, as described in section 6.4, and 2% point-to-point systematic errors have been included at 10.8 $A \cdot GeV$. The systematic errors have been applied separately to the K^+ and the K^-, and assumed uncorrelated.

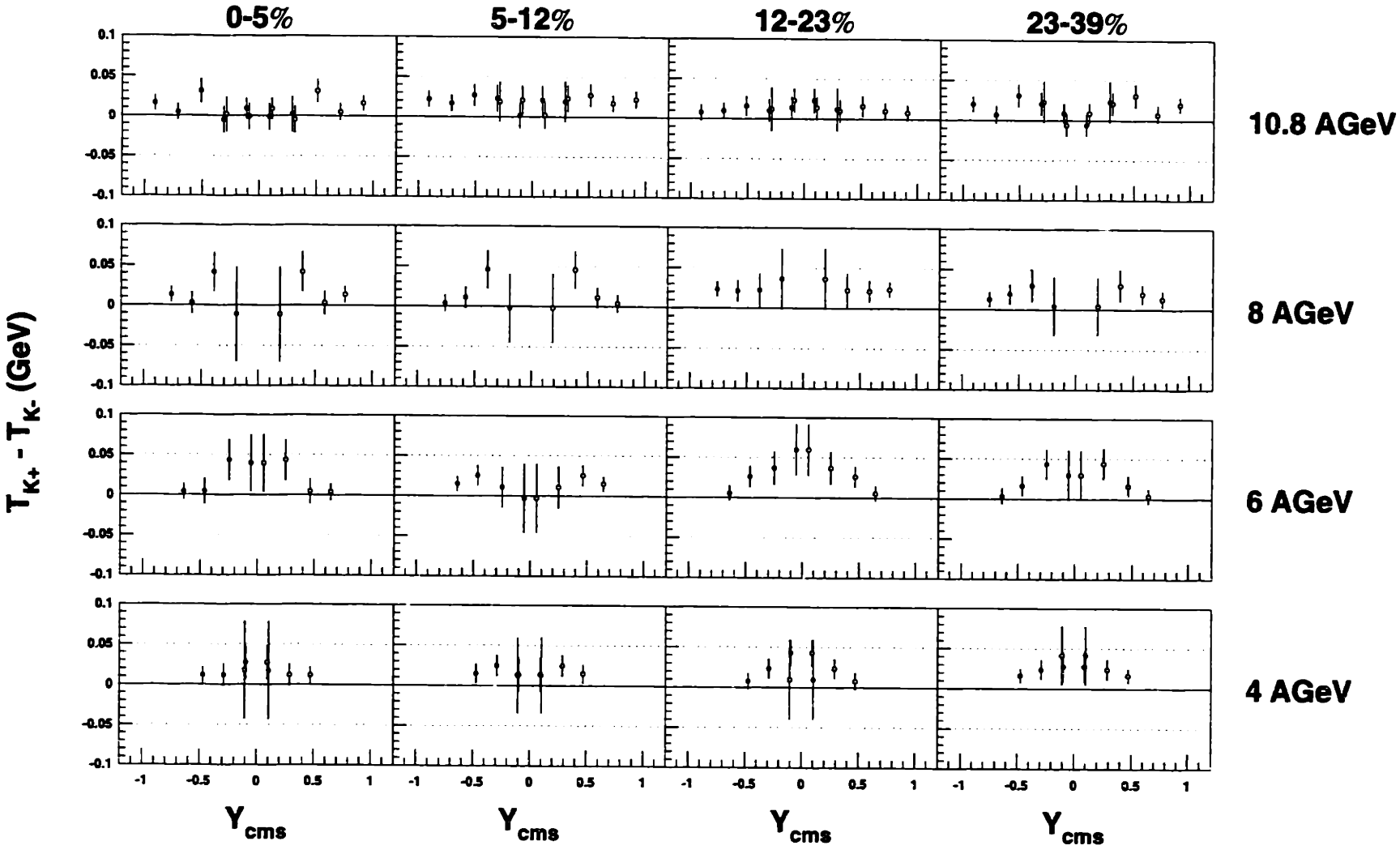

Figure 7-25: The difference of the inverse slopes, $K^+ - K^-$, all E_{beam} and centralities, as a function of Y_{cms}. Point-to-point systematic errors have been included at the lower beam energies, as described in section 6.4, and 2% point-to-point systematic errors have been included at 10.8 $A \cdot GeV$. The systematic errors have been applied separately to the K^+ and the K^-, and assumed uncorrelated.

and K^-, but there is a distinct trend towards smaller inverse slopes for the K^-.

It is difficult at this stage to make claims about the source of this effect, since many explanations are consistent. There is a complicated interplay between absorption, rescattering, and the energetics of the collision, all of which could potentially create a difference. These in principle have different dependencies on rapidity, although the size of these dependences is not clearly known.

An energetic effect, due to thresholds, would lead to a smaller difference in the slopes at mid-rapidity than at back rapidities, since at rapidities away from that of the center-of-mass some energy must be stored in the rapidity itself. However, energetic effects on the transverse spectra are not always as obvious as they may seem in heavy-ion collisions, as the study of processes near the kinematic limit [Col92] shows. The 2 $A \cdot GeV K^+$ data in $m_\perp$ is almost entirely above the kinematic limit from $p - p$ collisions, but the spectra show little effect from this.

Absorption effects, if present, might tend to increase the difference between the inverse slopes at mid-rapidity, and would act in an opposite direction to the trend observed, by absorbing the low-$m_\perp$ K^-, effectively increasing the K^- inverse slopes. This would only be true if the absorbing baryons, the distributions of which are seen to have a maximum at mid-rapidity in the final state, affect particles with rapidities in the final state close to mid-rapidity fractionally more than those particles at other rapidities. One must be very careful about such arguments, though, because they implicitly assume a mapping between the final-state rapidity distributions and the spatial distributions of the particles in the collision zone. It is not *a priori* obvious that such a mapping makes sense at all beam energies, although the mapping does seem to be valid in hadronic models in this energy regime. At lower energies, in cascade models, absorption effects on the yields of the K^- are seen to be strongest at mid-rapidity [LB98].

In-medium potentials would tend to create a difference in the same direction as that observed, since the potentials are expected to be attractive in the K^- channel and repulsive in the K^+ channel. Again making the association between a particle's production point and its final-state value of rapidity, one might expect to see the

largest effect from this at mid-rapidity, since the baryon density seen would be highest for the kaons at mid-rapidity, and the in-medium effect would be highest for regions of highest baryon density. But the level of such an effect is not known. Such effects are constrained by the observation that the differences in the inverse slopes seem to show little or no centrality dependence.

Since the processes which have a potential to influence the inverse slopes have opposing dependences, and the sizes of such effects are not known, it is difficult to make strong conclusions from the observed inverse slopes without solid models with which to compare the results.

7.4 Model Comparisons

The data show some clear trends, but the interpretation of these trends is not completely straightforward. Therefore, models of these collisions were studied briefly.

The models used are of the cascade type. That is to say, they begin with a tablulated set of cross-sections, some measured, some not. Particles are then stepped in time, and at each stage a probabilistic test is made against these tabulated cross-sections to see if a hadron-hadron interaction has occurred. Because of the comprehensive nature of these tables, such models have the advantage that all possible input has been made. However, they also have a disadvantage from their comprehensiveness, in that the link between a physical process and a result is not always clear. Further, not all input to the models has been measured, so that choices must be made.

There is the further problem that the models assume pure two-body interactions. One might expect this assumption to break down as the density increases. There are also frame dependences that arise as the system becomes more relativistic. Different models use different methods to attempt to remove this problem.

Figure 7-26 shows a comparison between two such models and the K^+ data. The first, HSD [GCG98], was developed rather recently, and matches well to data both at the SPS, with a beam energy of 200 $A{\cdot}GeV$, and at the GSI SIS, at a beam energy

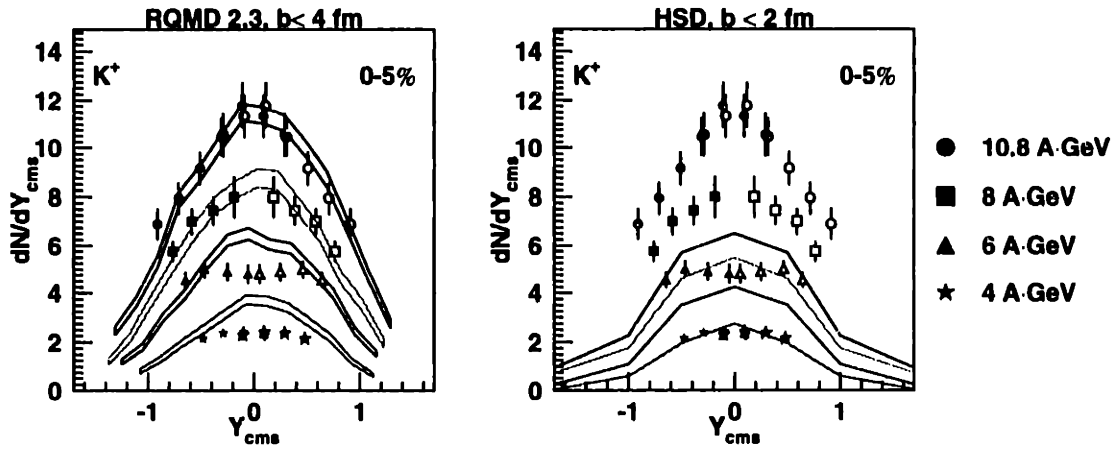

Figure 7-26: A comparison of the production of K^+ to models of the collisions. The left panel shows results from RQMD, and the right from HSD[GCG98], in this range of beam energies. 5% point-to-point systematic errors have been included in the data.

of 1 $A{\cdot}GeV$. The second, RQMD [SHG89], was developed at the AGS, and matches relatively well to the data at 10.8 $A{\cdot}GeV$. The models are very similar, although they do make different choices in the regions in which data has not been measured. Neither model includes in-medium effects on kaon production. The centrality class has been selected in the models in a very simple way, by requiring that the impact parameter of the collision, which is a direct input, be less than a given value.

There are some major problems with the comparison of the results from these models with the data. Discrepancies of factors of 2 are seen, both between the models themselves and between the models and the data. The models seem to match best to the data in the region of energies closest to where they were developed: RQMD matches the data at 10.8 $A{\cdot}GeV$ perfectly, and only begins to show discrepancies as the beam energy decreases. HSD shows the opposite trend, in that it reproduces the data well at low energies and begins to deviate as the energy increases.

Given that the models have nominally the same theoretical ansatz, the factor of two discrepancy provides an estimate of the current theoretical uncertainty in the understanding of these collisions. Any conclusion drawn from the models can be done

only up to the factor of two discrepancy. Therefore, at this stage, the use of these models to search for possible in-medium effects is problematic. The authors of the models are actively working on understanding the discrepancies.

Chapter 8

Conclusion

A study has been made of particle production over the entire range of energies available at the AGS. Two overriding trends are seen in the data. The evolution of particle production in this energy regime is smooth, despite an increase of its level by an order of magnitude. The details of particle production, such as the dependence on centrality and the excitation in the transverse and longitudinal directions, are rather similar, given the size of this increase. Therefore it is difficult not to conclude that, on a gross level, there is little sign of a change in the relevant degrees of freedom of the system.

The details of the K^+ and K^- production yield the same message of similarity, although in this case the lack of dependence is not expected. At all beam energies between 1 and 10.8 $AGeV$, for a given beam energy and rapidity, the yield ratio K^-/K^+ shows no dependence on the centrality of the collision. This lack of dependence can be reproduced by models at either end of the energy range, either through a complicated cancellation of absorption and enhancement of the K^- at the lowest energy or through a mechanism that is not completely clear at the highest energy studied. Cascade models show some problems reproducing the K^+ yields alone in the range of energies between the two, the reasons for which are being actively investigated.

Despite this similarity within the energy range of the AGS, there is a surprising difference between the results on K^- and K^+ production at GSI and those at the AGS. At the energies of the AGS, for which both the K^+ and K^- are above threshold, the yields of these particles in $Au - Au$ collisions do not scale with the distance of

the beam energy from the threshold for production of the particle, $\sqrt{s} - \sqrt{s_{th}}$, over a range from 0.5 to 2 GeV above threshold. The yields of K^- are approximately a factor of 5 below those of the K^+, at equivalent energies from threshold, with a small dependence on $\sqrt{s}$, such that the K^-/K^+ at equivalent energies decreases as the energy approaches threshold. However, it is not clear that the distance from the $p-p$ threshold is a meaningful variable, due to a range of processes that only exist in nuclear collisions. Such a lack of scaling is also seen in the yields from $p-p$ collisions. At GSI energies, at which the K^+ and K^- are subthreshold, the yields of the K^- and K^+ do seem to scale with the distance below threshold, both at one value of $\sqrt{s}-\sqrt{s_{th}}$ of -0.23 GeV, in $Ni-Ni$ collisions, and over a range of equivalent energies from -0.4 to -0.18 GeV, in $C-C$ collisions. The two results, taken together, mean that in the energy range from 0.5 GeV above threshold to 0.3 GeV below threshold the K^-/K^+ ratio at equivalent energies must change by approximately a factor of 5.

The interpretation of the results is made difficult by the complicated nature of heavy-ion reactions. Cascade models show some serious problems reproducing the data over the entire range of energies, which shows that the level of theoretical understanding of these collisions is quite a bit less than had been thought. This underlines a basic point, that a measurement at one set of conditions does very little to constrain the physics of the systems produced in heavy ion reactions. There is therefore an opportunity for a wide range of thermal and transport models, constrained by this data set, to produce a consistent understanding.

There are a few ways around the problem of interpretation in the future. At the low end of the energy, it would be helpful for measurements of K^- production in $A-A$ collisions to be made in the range between GSI and the AGS, in order to map out the details closer to the area of the change. More work must also be done on the models.

At the high end of the energy scale, the first beam will be sent to the experiments at RHIC in a few months, with a greatly increased $\sqrt{s}$ as compared to the beams so far available. The history of the study of $p-p$ collisions shows that, for certain well-selected variables, the interpretation of the data can become clearer as the energy

increases. Perhaps this will happen. Both the choice of variables to measure and the evolution of these variables with changes in the conditions will be key to the success of this program.

The data presented in this thesis shows little clear evidence for a change in the degrees of freedom in the system. This does not, however, preclude such a change, due to the problems in the theoretical interpretation of the data. The data therefore provides a strong set of constraints with which any model that includes such a change must be consistent.

Appendix A

Calibration method for the Time of Flight Wall

A.0.1 Method used in $E859$-$E866$

The method used for calibration of the TOF wall for the 2 and 4 $A{\cdot}GeV$ $E866$ data is unchanged from that detailed in [Cia94] and [Ahl97].

Basic Description

The method consists of the calibration of 13 basic constants, not all of which are adjusted at a given time, as shown in table A.1. Two of these are historical, two more are adjusted separately, and one is a copy, leaving 8 free parameters on which to calibrate. Seven of these are adjusted in blocks of runs, combined to create a necessary level of statistics. One of these is adjusted run-by-run.

These calibration constants are then used in the following set of formulae.

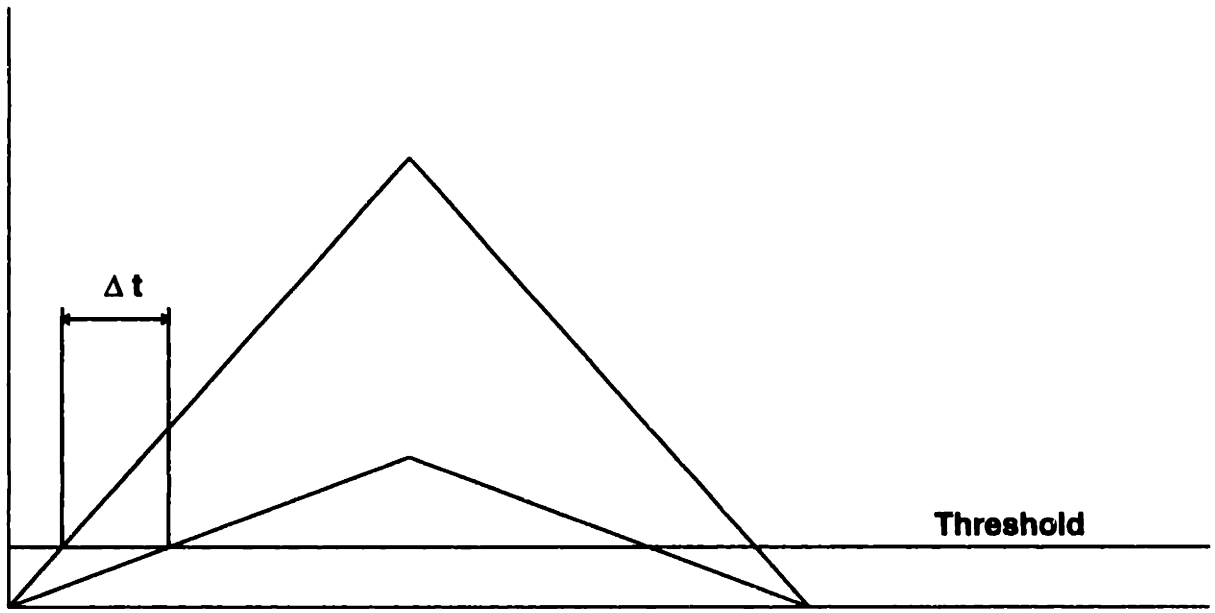

Figure A-1: A schematic drawing of the slew correction. The two pulses are of different height, and are approximated as triangles.

Constant	Meaning	Units	Level of adjustment
$Tped_{up}$	Arbitrary offset (historical)	TDC	Never
$Tped_{down}$	Arbitrary offset (historical)	TDC	Never
Ped_{up}	Pedestal(top)	ADC	Data-taking period
Ped_{down}	Pedestal(bottom)	ADC	Data-taking period
$Gain_{up}$	Gain(top)	$Yasuos/ADC$	Run Block
$Gain_{down}$	Gain(bottom)	$Yasuos/ADC$	Run Block
$Clock$	TDC clock(both)	ns/TDC	Run Block
$Clock_{down}$	TDC clock(both)	ns/TDC	Run Block
T_0	Offset	ns	Run Block
$Slew$	Slew Parameter	$ns \cdot Yasuo^{\frac{1}{2}}$	Run Block
$Speed$	Speed of light along slat	cm/TDC	Run Block
Y_{off}	Offset along slat	cm	Run Block
T_0^{global}	Global offset	ns	Run-by-run

Table A.1: Calibration parameters used in the TOF. This is the set of parameters that convert a raw TOF TDC and ADC value to a time-of-flight, an E_{loss}, and a Y_{TOF}. Not all calibration parameters are adjusted at once. The unit "Yasuo" is a collaboration-specific name. It is defined as the unit of energy that places the energy loss of a minimum-ionizing particle in a TOF slat at 100. TDC and ADC refer to channels in a TDC or ADC, respectively. $Clock_{down}$ and $Clock$ are forced to be equal. All calibration parameters are applied slat-by-slat, with the exception of T_0^{global}, which is a single number applied across the TOF wall.

To obtain the energy loss E_{loss} of a particle in the slat:

$$E_{up} = Gain_{up}\,(ADC_{up} - Ped_{up}) \tag{A.1}$$

$$E_{down} = Gain_{down}\,(ADC_{down} - Ped_{down}) \tag{A.2}$$

$$E_{loss} = \sqrt{E_{up}E_{down}} \tag{A.3}$$

To obtain the Y position along the slat, Y_{TOF}:

$$Y_{TOF} = -Speed\,[(TDC_{up} - Tped_{up}) - (TDC_{dn} - Tped_{down})] + Y_{off} \tag{A.4}$$

For use in obtaining the time of flight:

$$T_{up} = Clock\,(TDC_{up} - Tped_{up}) \tag{A.5}$$

$$T_{down} = Clock\,(TDC_{down} - Tped_{down}) \tag{A.6}$$

$$T_{up}^{slew} = T_{up} - Slew\left(\frac{1}{\sqrt{E_{loss}}} - 0.1\right) \tag{A.7}$$

$$T_{down}^{slew} = T_{down} - Slew\left(\frac{1}{\sqrt{E_{loss}}} - 0.1\right) \tag{A.8}$$

$$T_{BTOT} = \frac{1}{2}\left(Clock_{BTOT}TDC_{BTOT}^{left} + Clock_{BTOT}TDC_{BTOT}^{right}\right) \tag{A.9}$$

Finally, to obtain the time of flight:

$$TOF_{found} = \frac{1}{2}\left(T_{slew}^{up} + T_{slew}^{down}\right) - T_{BTOT} - T_0 - T_0^{global} \tag{A.10}$$

The "slew" in the above equations refers to an effect from discrimination on signals of differing pulse height. The discrimination is made at a fixed level. Therefore, for pulses of different heights, the time at which the pulse crosses the threshold will depend on the total pulse height, as shown schematically in figure A.0.1. The level of the effect can be as large as 20 ns. Empirically, the effect is found to follow a square-root law, with the shift in time being proportional to the square-root of the integrated charge of the pulse. In principle, the slew correction should be applied separately on the two tubes of the TOF wall, especially if the gains of the tubes are

not matched. However, this would be difficult to do in the calibration procedure as it is implemented, so the slew correction is instead made using the calibrated geometric mean of the integrated charge of the pulses, the E_{loss} of equation A.3. The 0.1 places the mean of the slewing correction at 0. Similarly, the TDC clocks for the top and bottom tubes are assumed to be the same.

T_{BTOT} is, as mentioned in 2.5.1, the time of the BTOT tubes as read out through the TOF electronics chain. The calibration proceeds in four stages.

Pedestal Calibration

The first stage is the pedestal determination. Ped_{up} and Ped_{down} are determined from pedestal runs (3.2.1) by separately finding the peak of the ADC distribution, tube-by-tube, in these runs. The pedestal peaks are very narrow, with only a few ADC values recorded. The centers of the peaks are also very stable, both within a running period and across running periods, with drifts on the order of a channel. Therefore the pedestals are determined once per running period (once for the 2 and 4 $A{\cdot}GeV$, and once for the 6 and 8 $A{\cdot}GeV$) and applied uniformly across the running period.

Pre-Reconstruction Calibration

The second stage is done at a low level of granularity before the reconstruction in PASS12. Based on shifts of the center of the Y_{TOF} distribution and of the TOF_{found} at the point of maximum counts, runs are selected at which to calibrate the wall fully. Runs after a shift are reconstructed, and the calibration constants adjusted with the methods detailed below.

The calibrations at this stage require a large level of user intervention, since the shifts in Y_{TOF} can be large on the level of the initial search widths of the reconstruction algorithm (± 10 cm). Therefore, since the reconstruction algorithm uses Y_{TOF} as a seed, tracks will not be found in such a case. Since the procedure needs tracks to calibrate, the Y_{TOF} must be centered by hand in order to proceed.

In addition, the calibration procedure requires TOF_{found} to be roughly correct,

since it uses the initial TOF_{found} of a hit to determine a mass. This initial TOF_{found} can be off by as much as 20 ns, far beyond the level of the windows that determine this mass. This problem was solved by finding the maximum point of the Δ_{TOF} distributions, formed assuming the π mass, and adjusting the slat-by-slat offset, T_0, to place Δ_{TOF} at 0. The accuracy of such a procedure is ~150 ps, although slightly worse for the slats at the edge of the TOF wall, and so is enough to give a starting point to the full procedure.

The correlation between the fitted *Clock* and T_0, noted below, sometimes interfered with the procedure, causing the resulting *Clock* to decrease by a factor of ~2. In such cases, *Clock* was reset to a nominal value, 50 ps. This resetting caused large changes (~20 ns at worst) in TOF_{found}, and so the rough centering of Δ_{TOF} was reperformed and the calibration iterated.

Final Calibration

The third set of calibrations comes at a much finer level of granularity. It occurs after full reconstruction at the PASS12 stage, and is the main reason for a third pass through the data. It is a highly iterative process.

Blocks of data are formed at places of known changes, such as angle shifts. Runs after these shifts are combined in order to gather enough statistics, ~ 100K particles. Then three steps are taken.

A calibration is performed on Y_{TOF} and TOF_{found}. This calibration does not attempt to calibrate the slewing parameter, *Slew*. It instead makes a linear fit of $TOF_{expected}$ vs TOF_{found}, where $TOF_{expected}$ is as in equation 3.8. The mass used for this is that from the full *PICD* algorithm, detailed in 4.8, which depends on the quality of the TOF calibrations themselves. The allowed windows in Δ_{TOF} are adjusted to reflect this. The clock parameter *Clock* and the offset parameter T_0 are determined from the slope and offset of these fits, on a slat-by-slat basis. *Clock* is copied into $Clock_{down}$. Similarly, the parameters *Speed* and Y_{off} are determined from a linear fit of Y_{TOF} vs $Y_{expected}$, where $Y_{expected}$ is formed by projecting a track onto the TOF wall. These fits are done analytically, and the sums that go into the fits are

weighted by the (momentum- and mass-dependent) expected resolution of the TOF.

Using this new set of parameters, the gain parameters $Gain_{up}$ and $Gain_{down}$ are determined. The TOF_{found} for every event in the run block is redetermined, and the $PICD$ algorithm reperformed. The ADC values are collected from TOF hits associated with tracks found to be pions by the $PICD$ algorithm. This algorithm places cuts on the measured charge, which depends on the ADC values themselves, the quality of the gain calibrations, and on the momentum of the track. Based on Y_{TOF}, the quantities:

$$Gain_{up}^{-1} \equiv (ADC_{up} - Ped_{up}) \exp\left(-\frac{Y_{TOF}}{L_{atten}}\right) \quad \text{(A.11)}$$

$$Gain_{down}^{-1} \equiv (ADC_{dow} - Ped_{down}) \exp\left(\frac{Y_{TOF}}{L_{atten}}\right) \quad \text{(A.12)}$$

where L_{atten} is a fixed constant taken to be 72 cm, and reflects the attenuation length of the slats. $Gain_{up}$ and $Gain_{down}$ are then adjusted to place the means of these quantities at 100.

Then, for the final step, the TOF values are again redetermined for all events in the run blocks, using the new gain parameters. This step calibrates three of the parameters: $Slew$, T_0, and $Clock$. Quantities to perform a linear fit of TOF_{found} vs $TOF_{expected}$ are again summed, as are quantities to perform a fit of TOF_{found} vs $1/\sqrt{E_{loss}}$. The quantities actually added together are carefully determined to allow the three parameters to be adjusted independently, without a need to recalculate TOF_{found} for all events. At the end of the summing, a 10-step iterative fit is performed. This fit determines first $Clock$ and T_0 from $TOF_{expected}$ vs TOF_{found}, and then uses these values in fitting TOF_{found} vs $1/\sqrt{E_{loss}}$ to determine the slew parameter $Slew$, along with an associated offset. The results are fed back into the $Clock$ vs T_0 fit, and the process iterated.

Global T0

Finally, run-by-run, a single offset, T_0^{global} is fit from all identified tracks, and is applied across the TOF wall.

A.0.2 Problems with the $E859/E866$ procedure

Each stage of the process depends on the previous stage in a complex way. In addition, there are degeneracies in the fits, in that there is a correlation between the clock parameter and the offset parameter.

There is a region of the TOF wall that is not hit by protons, and therefore has very few particles of late times. The procedure would only be interpolating if the experiment was only interesed in measuring π^- and positives, with the exception of higher-mass nuclei. But the experiment is also interested in the rarer negative particles of higher mass than the π^-, the K^- and $\bar{p}$. For the data of this thesis, all K^- used have a momentum above 450 MeV/c. The range of times for the K^-, of mass $\sim$ 494 MeV, is $\sim$11 ns. This is a significant extrapolation from the $\sim 8ns$ range of the π^-, but is a small range as compared to that of the protons.

If the shift in timing is required to be no more than $\sim \frac{1}{4}\sigma_{TOF}$, 30 ps, over the entire range of the K^-, 11 ns, *Clock* must be determined to within 0.3%. However, there are significant momentum dependencies to the actual quantity of interest, $\sigma_{\Delta_{TOF}}$, which reduce this requirement.

Therefore for the 1995 data (2 and 4 $A{\cdot}GeV$), in this analysis tracks are required to project to a TOF slat in the region covered by the protons.

A.0.3 $E917$ calibration method

Taking a careful look at the correlation between *Clock* and T_0 across multiple calibrations sets, it was noticed that the parameters clustered along parallel lines. This indicates that the variation of *Clock* with run is an artifact of the procedure, and does not reflect true shifts in the TDC clocks. Physically it is more likely that the offsets drift due to variations in temperature and other changes than that the clocks drift. Note that no TDC's were replaced during the run.

Therefore, for the $E917$ data set, one set of *Clock* parameters was determined for the 6 and 8 $A{\cdot}GeV$ data, and the final portion of the procedure revised. The set was determined by combining a high-statistics set of 8 $A{\cdot}GeV$ data from data taken

at both polarities. The parameters were fit separately from those of the high-energy data, due to the differences in timing resolution between the 10.8 $A{\cdot}GeV$ and the 6 and 8 $A{\cdot}GeV$ portions.

Also, the clock parameter for the $BTOT$, used in equation A.9, was refit for this set of runs. The method used was the same. The average timing resolution across the TOF wall decreased by $\sim$5 ps after this change, to $\sim$125 ps from 130 ps.

The revised procedure had minimal changes, although for speed it was implemented somewhat differently. It is done on a run-by-run basis. It starts with the initial set of calibrations, assuming that they are valid for pions and electrons, both of which are required to extrapolate back to the target. First it fits a global offset, T_0^{global}, for electrons and pions. Then, applying this offset to the times of all slats, it fits $Slew$ vs T_0, and injects the new $Clock$ parameters by adjusting the resulting T_0 parameters along the correlation determined above. It then iterates a few times, recalibrating E_{loss} as before, then $Slew$, T_0, and Y_{TOF}. At the end it fits a final T_0^{global}.

In addition, tracks from events which did not pass all of the beam quality cuts (5.6.2) had significantly different timing, ~ 30 ps. Therefore the beam quality cuts were applied to the data on which the TOF wall was calibrated. Note that due to the problems in the NMA calibration (3.2.3) at this point in the analysis, the NMA $\langle\eta\rangle$ cut was not applied.

Appendix B

K^+ spectra

This appendix contains plots of K^+ spectra for each centrality class and beam energy. The double differential yield is plotted vs $m_\perp - m_0$ for rapidity slices of 0.2 units and $m_\perp$ of 0.05 units.

The distributions are fit to an exponential, using a χ^2 minimization. The functional form is:

$$\frac{1}{2\pi m_\perp}\frac{d^2N}{dm_\perp dY} = \frac{dN/dY}{2\pi\left(Tm_0 + T^2\right)} exp\left(-\frac{m_\perp - m_0}{T}\right) \tag{B.1}$$

with T and dN/dY as fit parameters. The results for T and dN/dY are reflected about the appropriate Y_{nn} for the beam energy of the data as it was taken, with the reflected points plotted as open circles. All $m_\perp$ points that satisfied the acceptance cuts are plotted, but no fit is performed if there are fewer than 4 such points within the acceptance. Also, all fits and the results of all fits are plotted. However, results of fits with extrapolation levels greater than 60% are not used in the discussion section. The extrapolation level is determined by the extreme edges of the $m_\perp$ bins measured and the parameters of the fit.

Systematic errors of 2% have been added to the invariant differential yields, but the errors on dN/dY and T are those from the fit.

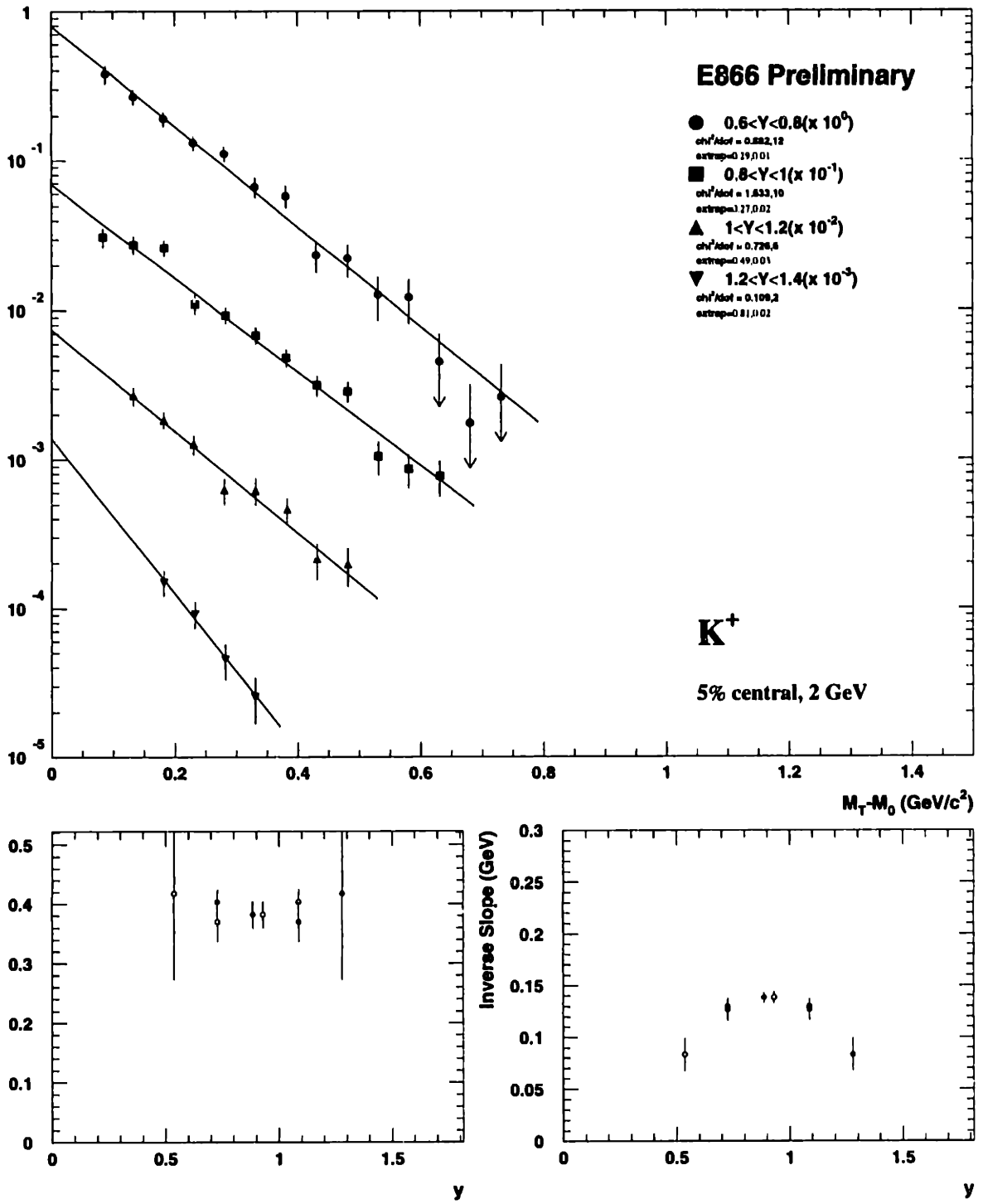
E866 Preliminary
0.6<Y<0.8(x 10^0)
0.8<Y<1(x 10^-1)
1<Y<1.2(x 10^-2)
1.2<Y<1.4(x 10^-3)
K+
5% central, 2 GeV
M_T-M_0 (GeV/c^2)
Inverse Slope (GeV)
y
y

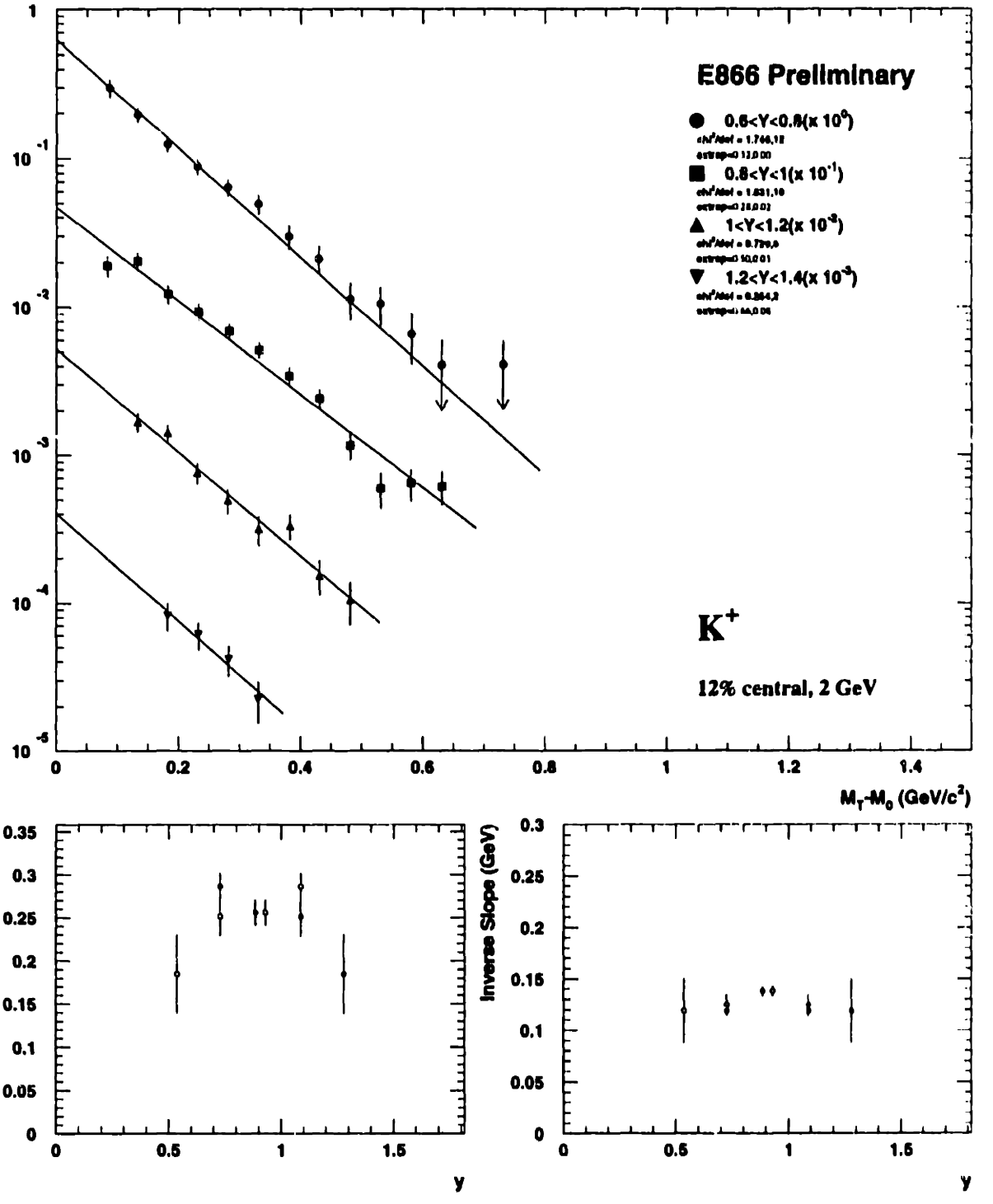
E866 Preliminary
0.6<Y<0.8(x 10^0)
0.8<Y<1(x 10^-1)
1<Y<1.2(x 10^-3)
1.2<Y<1.4(x 10^-5)
K+
12% central, 2 GeV
M_T-M_0 (GeV/c^2)
Inverse Slope (GeV)
y
y

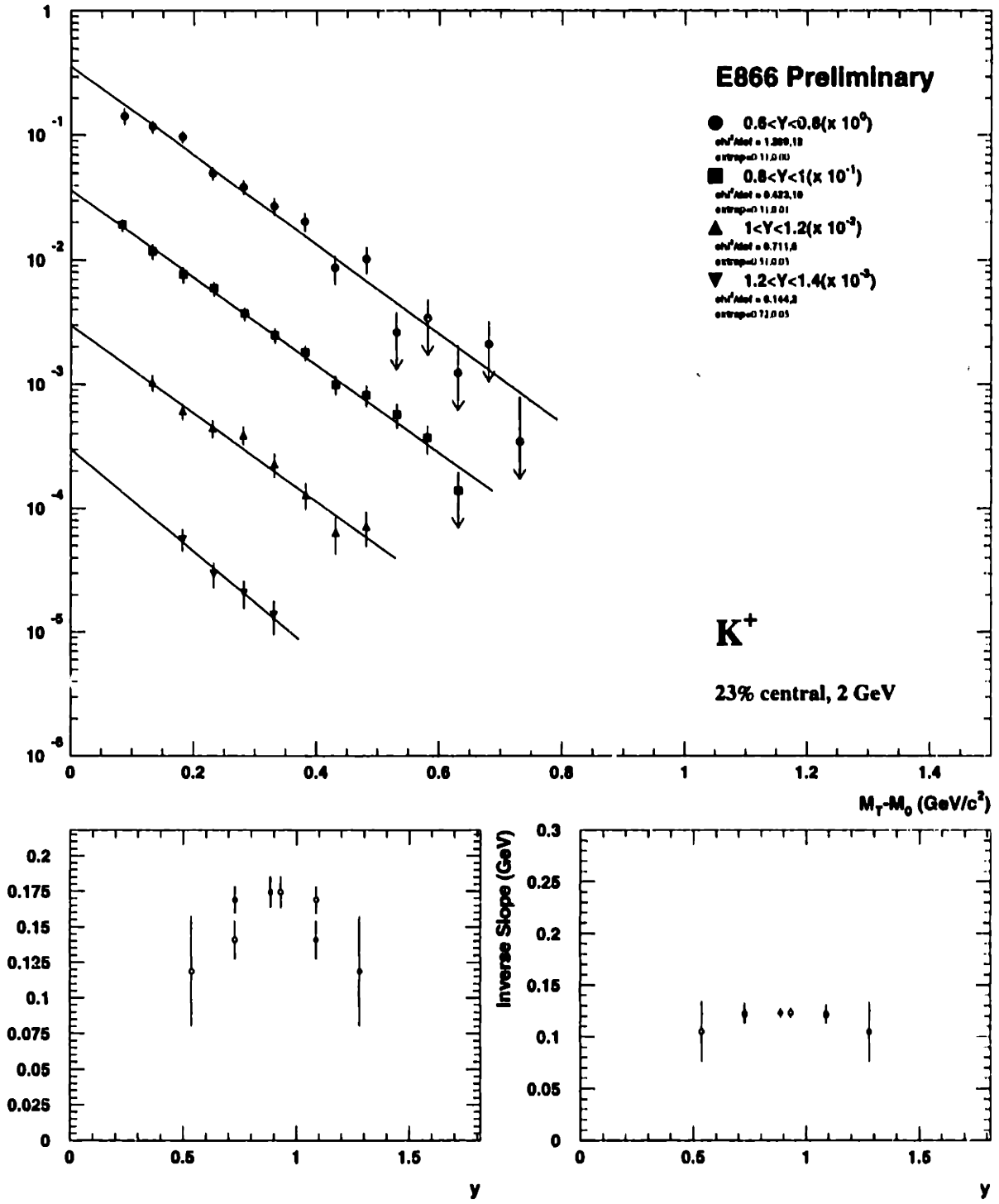
E866 Preliminary
0.6<Y<0.8(x 10^0)
0.8<Y<1(x 10^-1)
1<Y<1.2(x 10^-3)
1.2<Y<1.4(x 10^-5)
K+
23% central, 2 GeV
M_T-M_0 (GeV/c^2)
Inverse Slope (GeV)
y
y

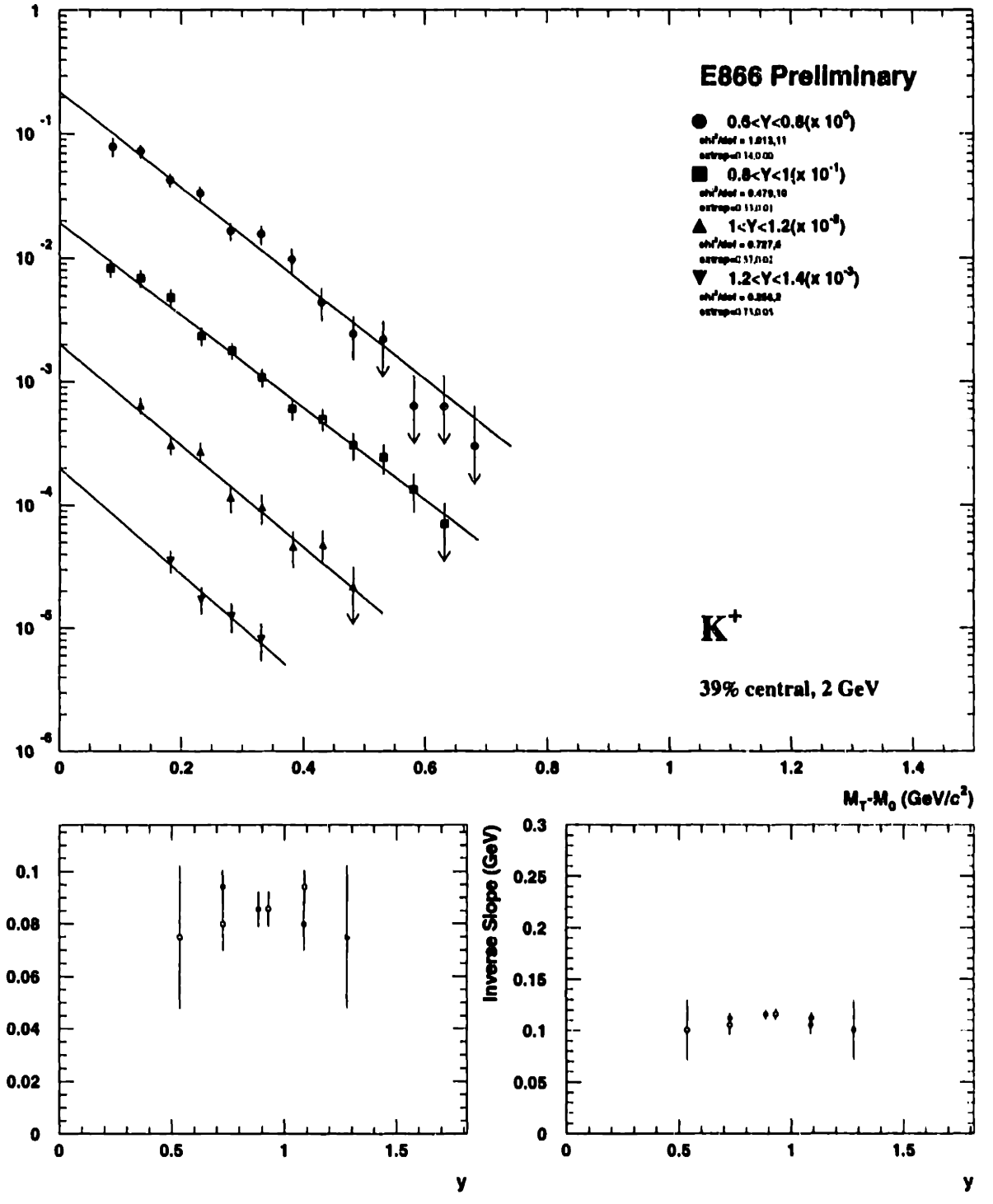
E866 Preliminary
0.6<Y<0.8(x 10^0)
0.8<Y<1(x 10^-1)
1<Y<1.2(x 10^-2)
1.2<Y<1.4(x 10^-3)
K+
39% central, 2 GeV
M_T-M_0 (GeV/c^2)
Inverse Slope (GeV)
y
y

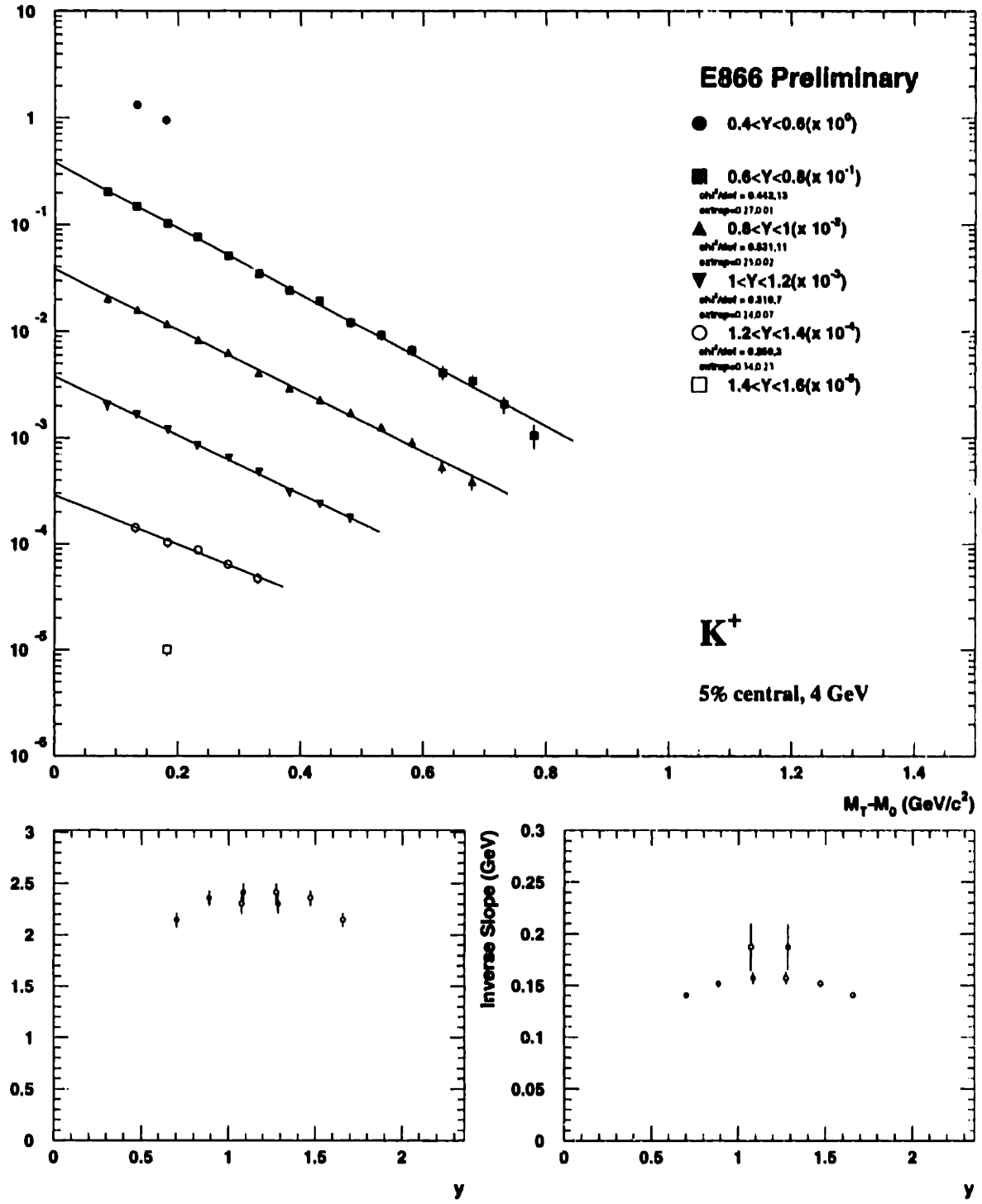
E866 Preliminary
0.4<Y<0.6(x 10^0)
0.6<Y<0.8(x 10^-1)
0.8<Y<1(x 10^-2)
1<Y<1.2(x 10^-3)
1.2<Y<1.4(x 10^-4)
1.4<Y<1.6(x 10^-5)
K+
5% central, 4 GeV
M_T-M_0 (GeV/c^2)
Inverse Slope (GeV)
y
y

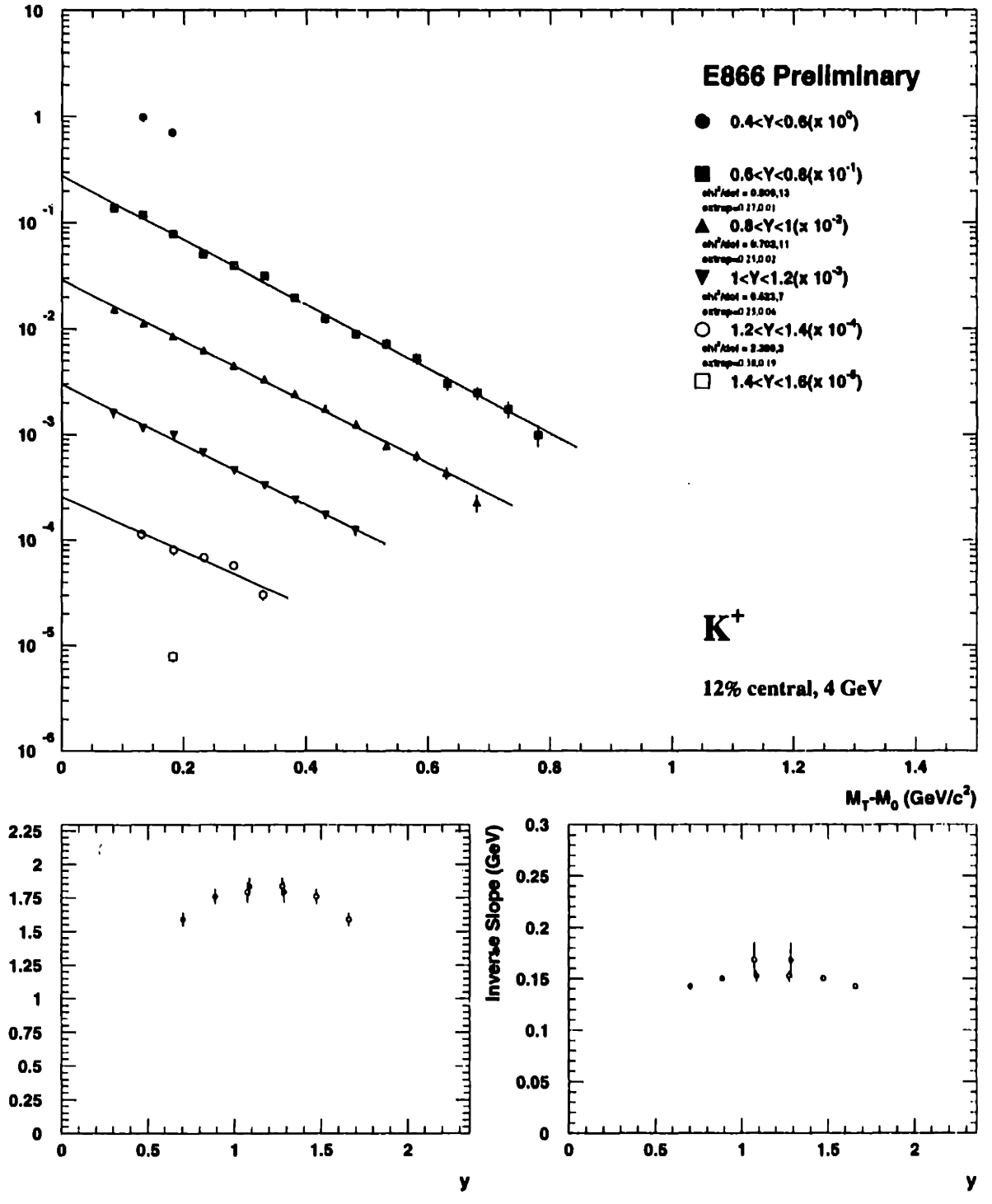
E866 Preliminary
0.4<Y<0.6(x 10^0)
0.6<Y<0.8(x 10^-1)
0.8<Y<1(x 10^-2)
1<Y<1.2(x 10^-3)
1.2<Y<1.4(x 10^-4)
1.4<Y<1.6(x 10^-5)
K+
12% central, 4 GeV
M_T-M_0 (GeV/c^2)
Inverse Slope (GeV)
y
y

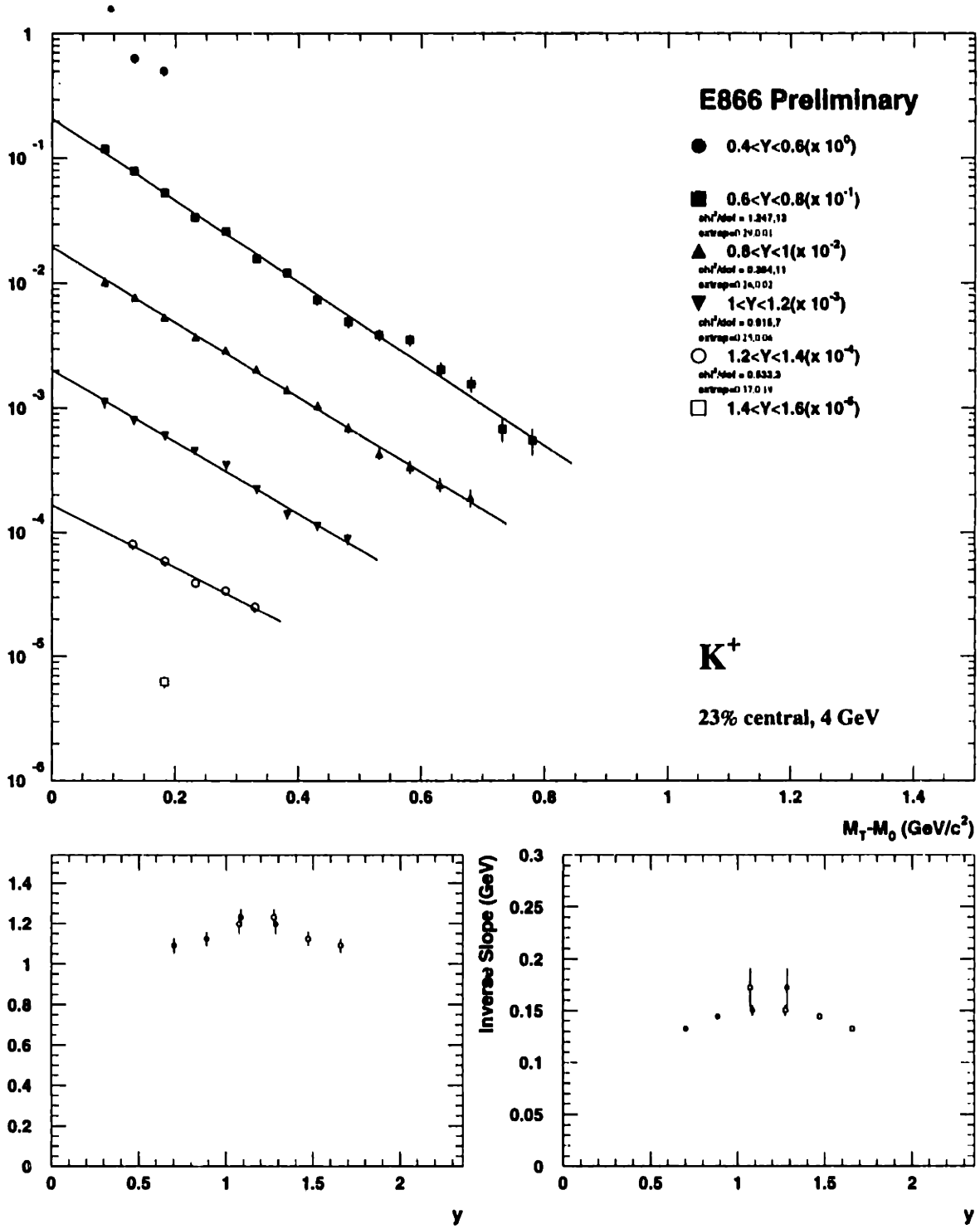
E866 Preliminary
0.4<Y<0.6(x 10^0)
0.6<Y<0.8(x 10^-1)
0.8<Y<1(x 10^-2)
1<Y<1.2(x 10^-3)
1.2<Y<1.4(x 10^-4)
1.4<Y<1.6(x 10^-5)
K+
23% central, 4 GeV
M_T-M_0 (GeV/c^2)
Inverse Slope (GeV)
y
y

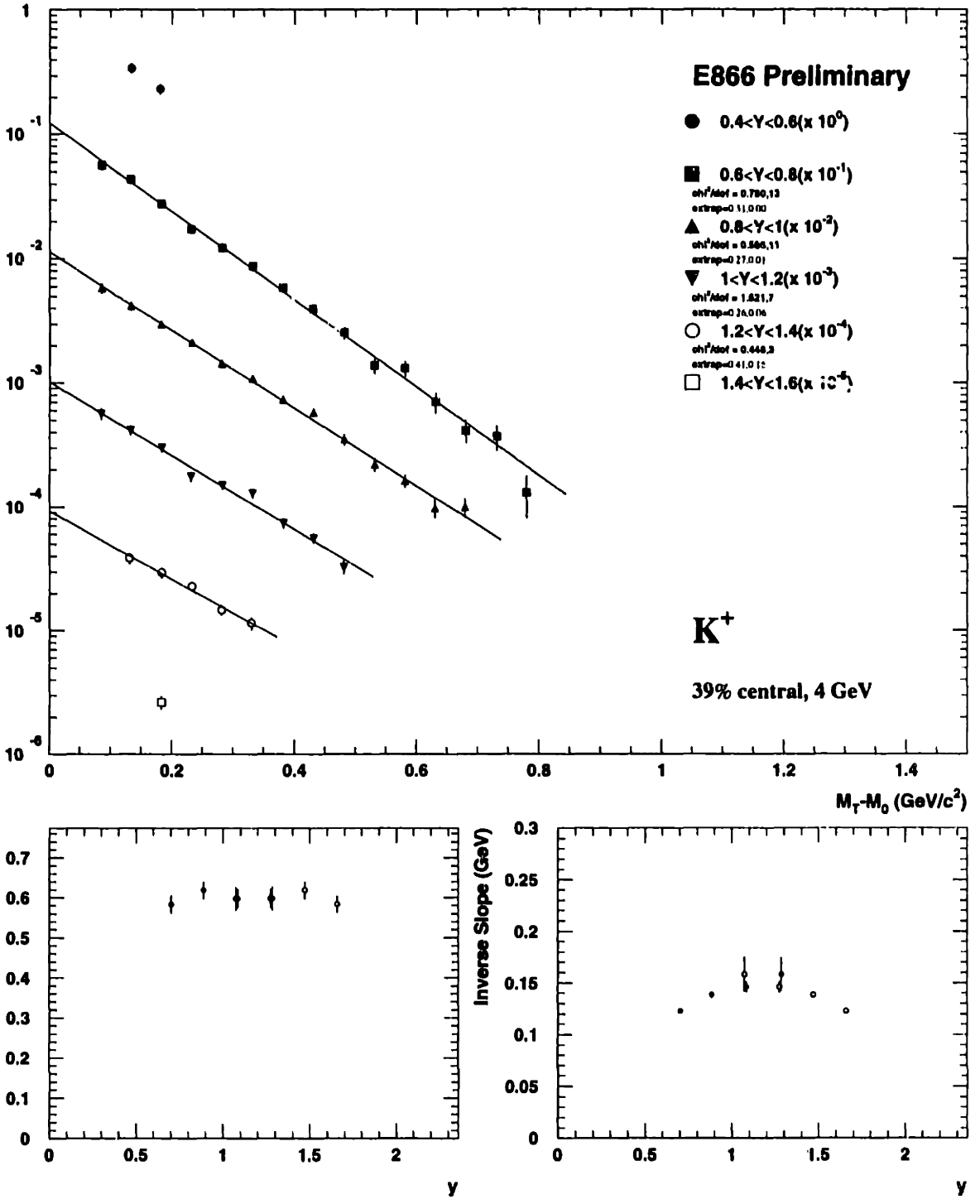
E866 Preliminary
0.4<Y<0.6(x 10^0)
0.6<Y<0.8(x 10^-1)
0.8<Y<1(x 10^-2)
1<Y<1.2(x 10^-3)
1.2<Y<1.4(x 10^-4)
1.4<Y<1.6(x
K+
39% central, 4 GeV
M_T-M_0 (GeV/c^2)
Inverse Slope (GeV)
y
y

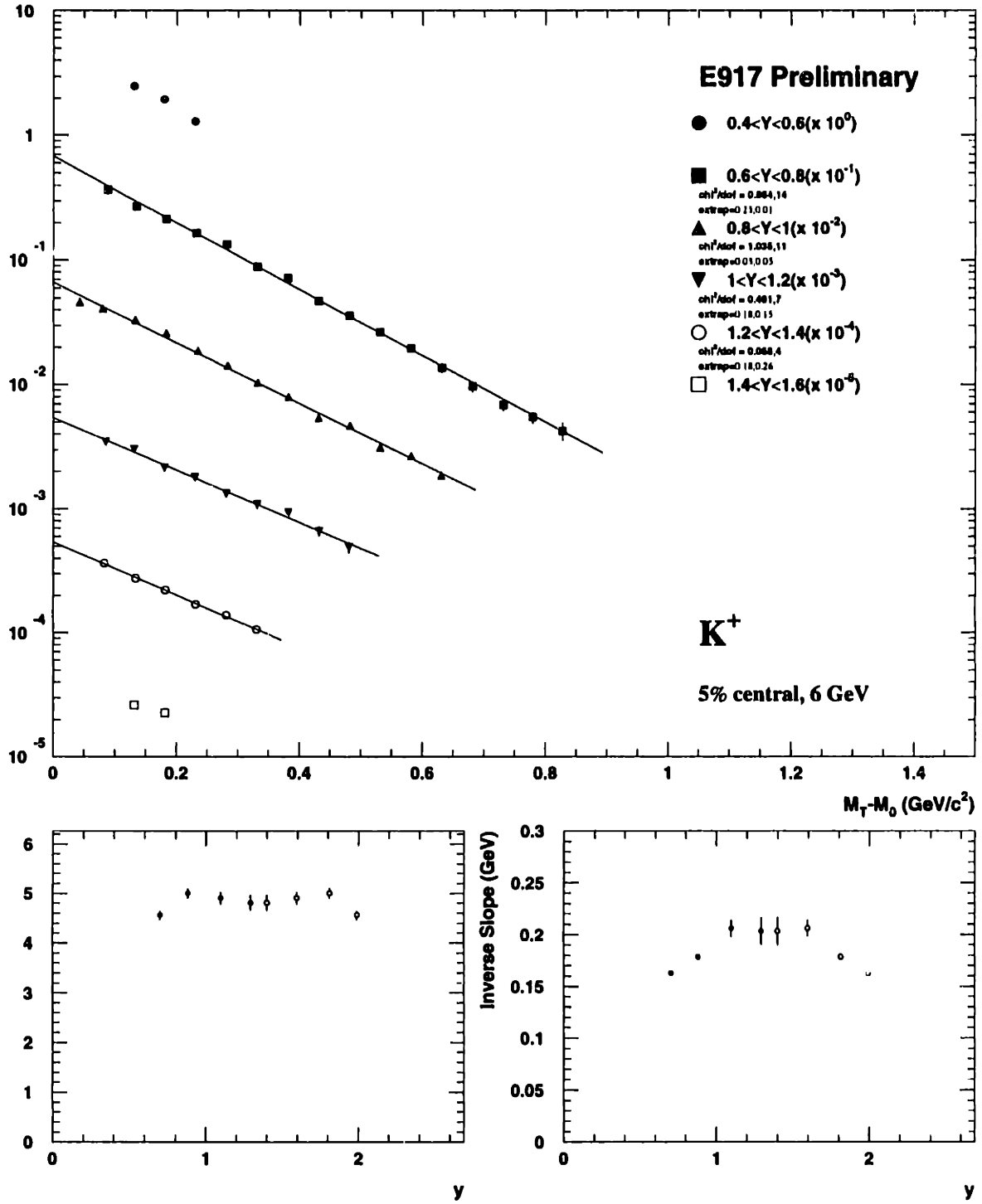
E917 Preliminary
0.4<Y<0.6(x 10^0)
0.6<Y<0.8(x 10^-1)
0.8<Y<1(x 10^-2)
1<Y<1.2(x 10^-3)
1.2<Y<1.4(x 10^-4)
1.4<Y<1.6(x 10^-5)
K+
5% central, 6 GeV
M_T-M_0 (GeV/c^2)
Inverse Slope (GeV)
y
y

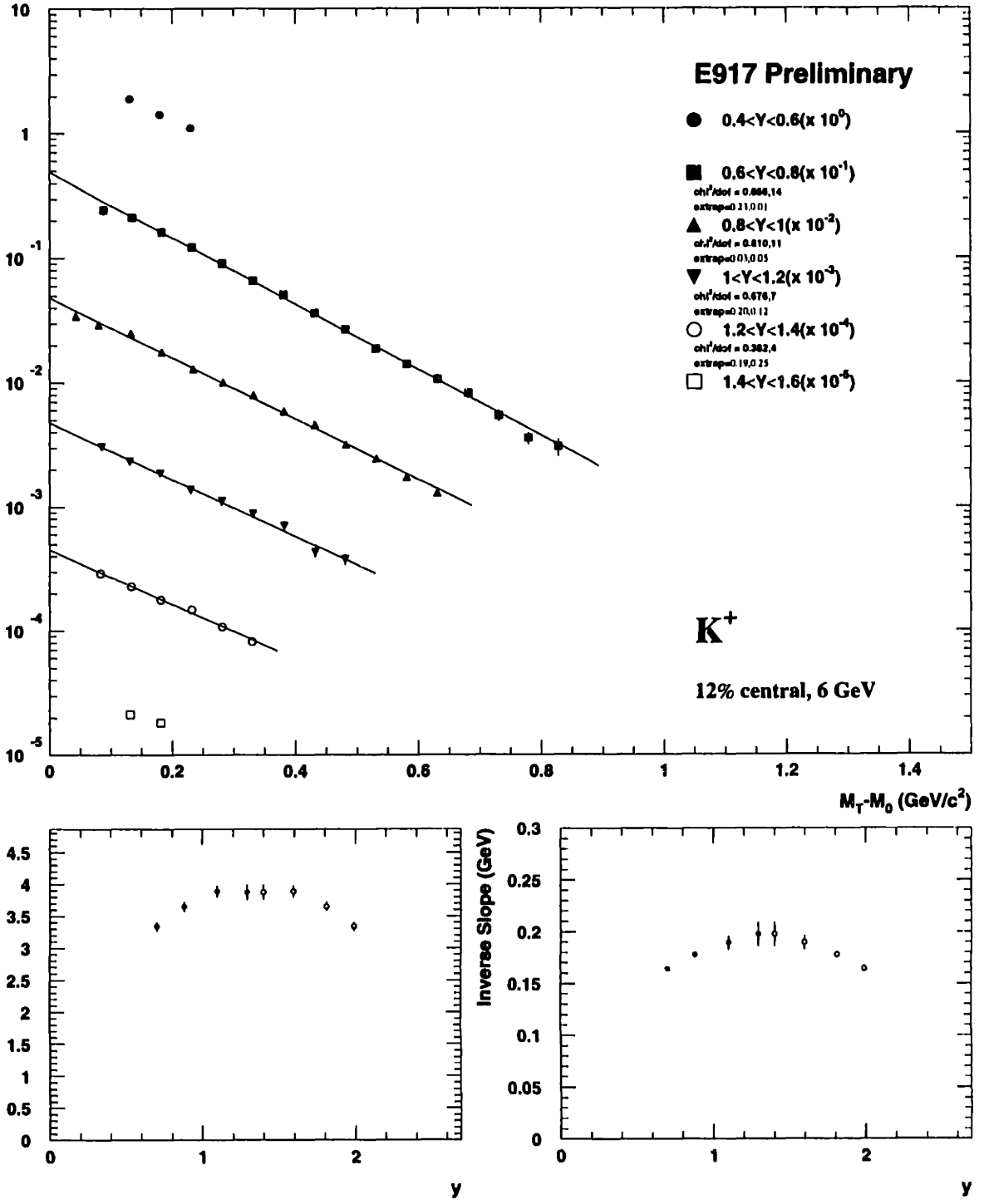
E917 Preliminary
0.4<Y<0.6(x 10^0)
0.6<Y<0.8(x 10^-1)
0.8<Y<1(x 10^-2)
1<Y<1.2(x 10^-3)
1.2<Y<1.4(x 10^-4)
1.4<Y<1.6(x 10^-5)
K+
12% central, 6 GeV
M_T-M_0 (GeV/c^2)
Inverse Slope (GeV)
y
y

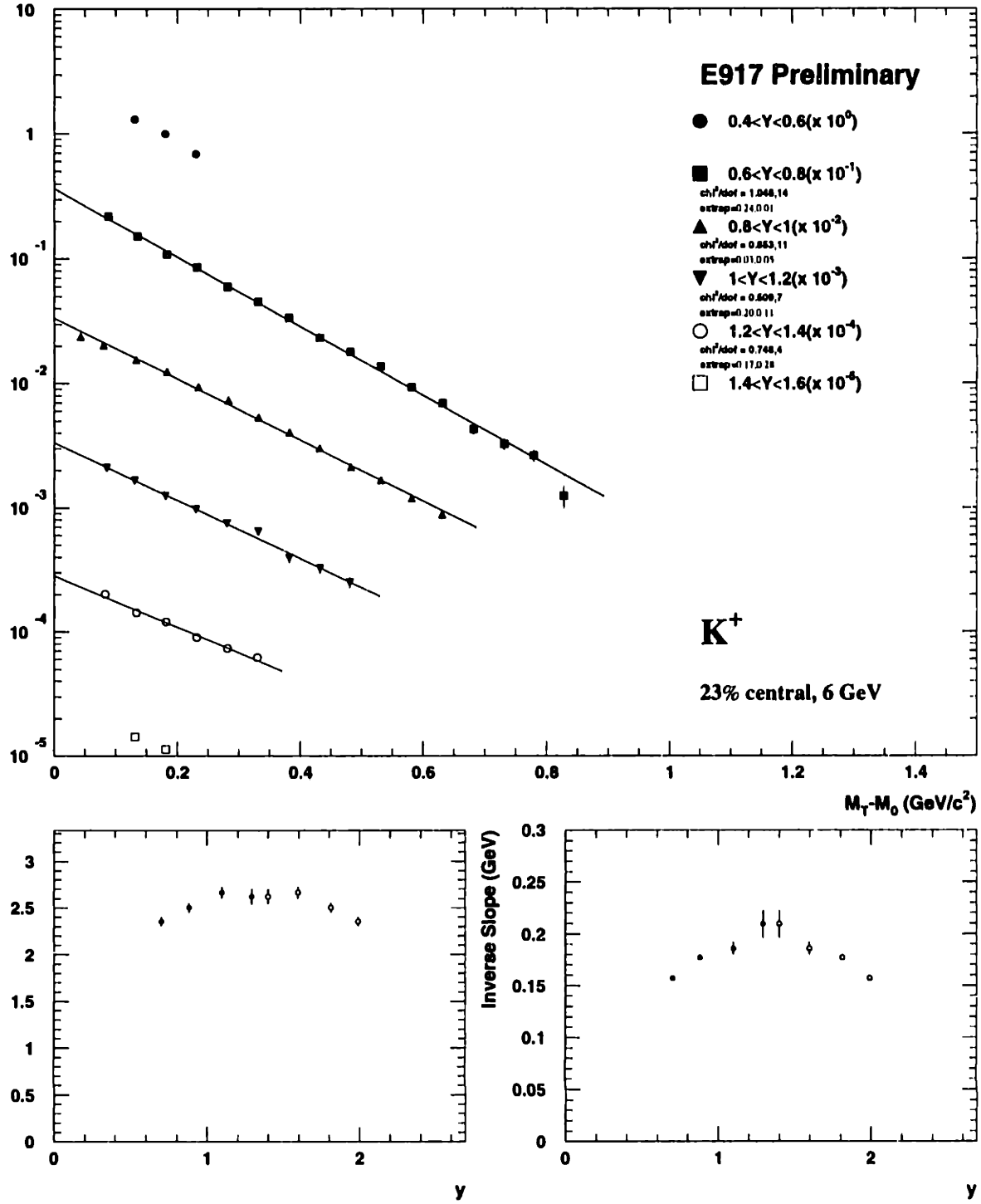
E917 Preliminary
0.4<Y<0.6(x 10^0)
0.6<Y<0.8(x 10^-1)
0.8<Y<1(x 10^-2)
1<Y<1.2(x 10^-3)
1.2<Y<1.4(x 10^-4)
1.4<Y<1.6(x 10^-5)
K+
23% central, 6 GeV
M_T-M_0 (GeV/c^2)
Inverse Slope (GeV)
y
y

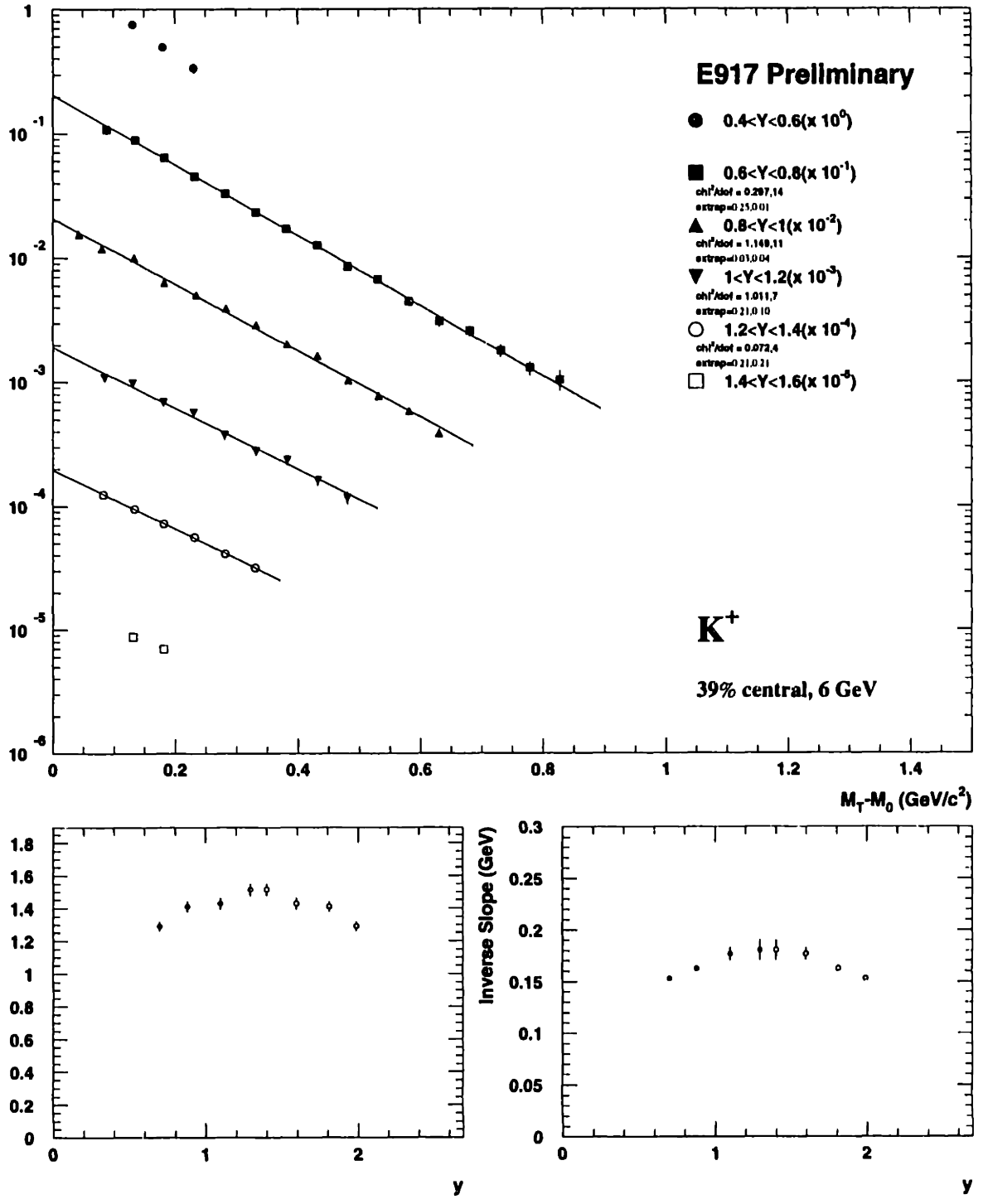
E917 Preliminary
0.4<Y<0.6(x 10^0)
0.6<Y<0.8(x 10^-1)
0.8<Y<1(x 10^-2)
1<Y<1.2(x 10^-3)
1.2<Y<1.4(x 10^-4)
1.4<Y<1.6(x 10^-5)
K+
39% central, 6 GeV
M_T-M_0 (GeV/c^2)
Inverse Slope (GeV)
y
y

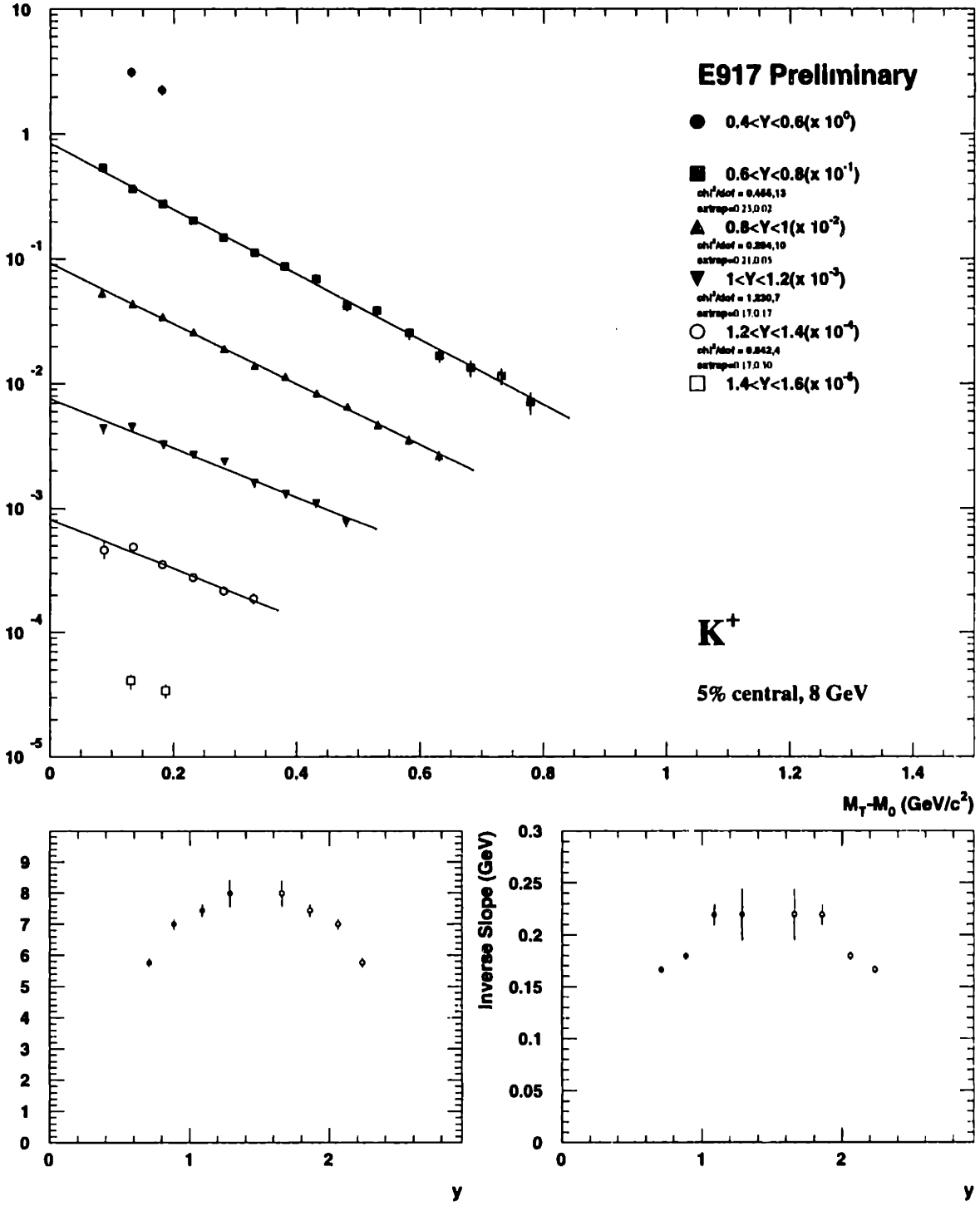
E917 Preliminary
0.4<Y<0.6(x 10^0)
0.6<Y<0.8(x 10^-1)
0.8<Y<1(x 10^-2)
1<Y<1.2(x 10^-3)
1.2<Y<1.4(x 10^-4)
1.4<Y<1.6(x 10^-5)
K+
5% central, 8 GeV
M_T-M_0 (GeV/c^2)
Inverse Slope (GeV)
y
y

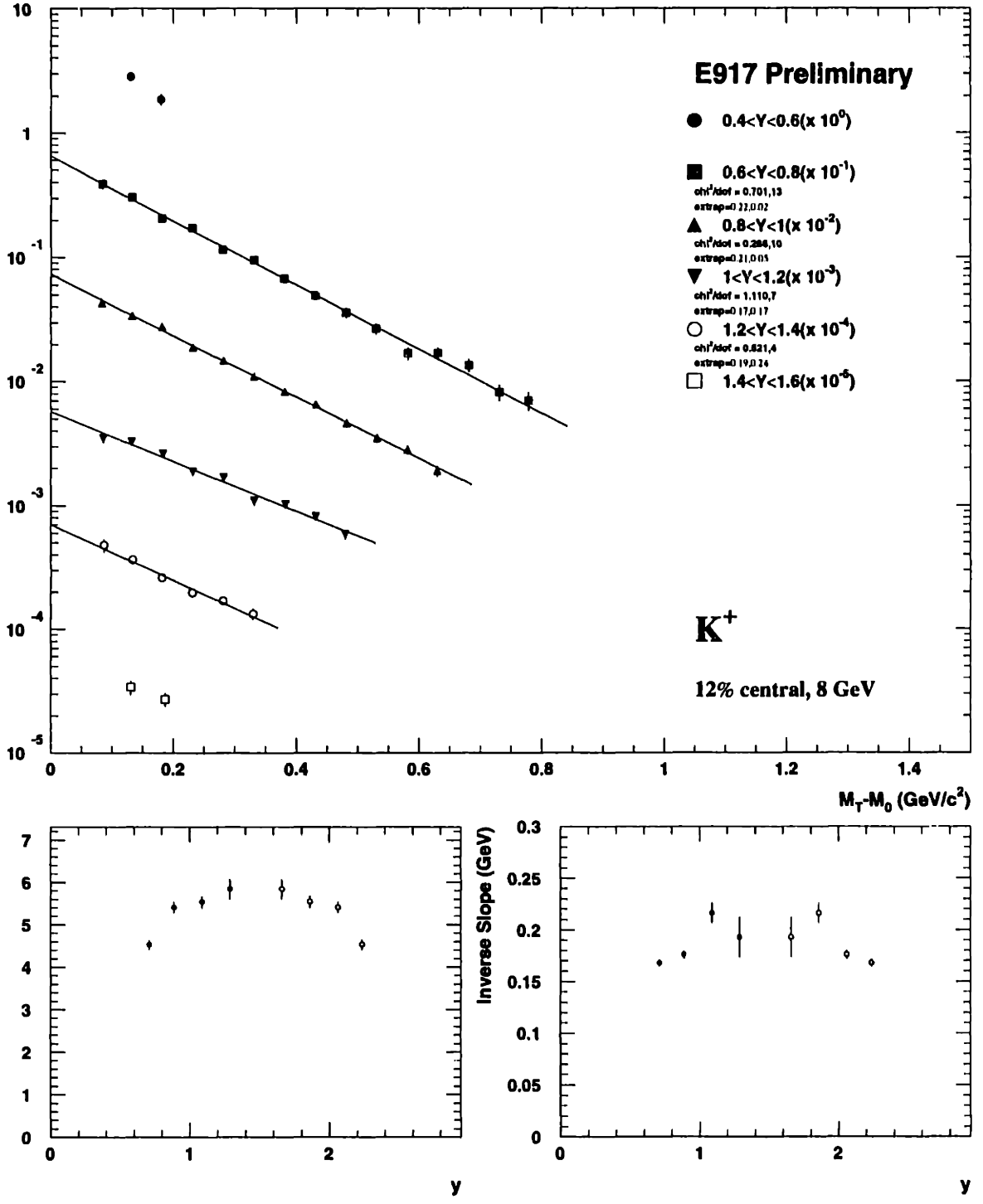
E917 Preliminary
0.4<Y<0.6(x 10^0)
0.6<Y<0.8(x 10^-1)
chi^2/dof = 0.701,13
extrap=0.22,0.02
0.8<Y<1(x 10^-2)
chi^2/dof = 0.286,10
extrap=0.21,0.05
1<Y<1.2(x 10^-3)
chi^2/dof = 1.110,7
extrap=0.17,0.17
1.2<Y<1.4(x 10^-4)
chi^2/dof = 0.821,4
extrap=0.19,0.24
1.4<Y<1.6(x 10^-5)
K+
12% central, 8 GeV
M_T-M_0 (GeV/c^2)
Inverse Slope (GeV)
y
y

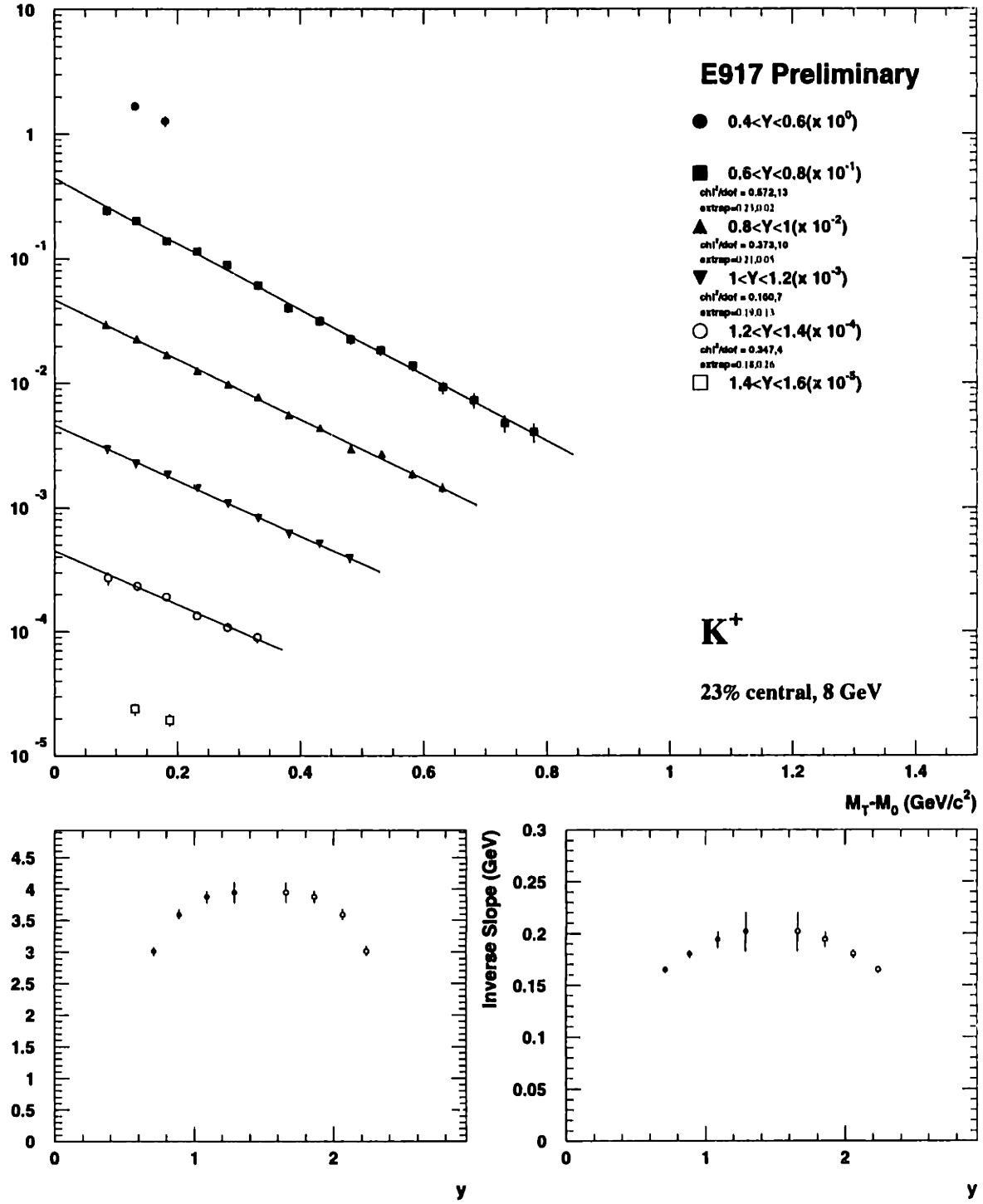
E917 Preliminary
0.4<Y<0.6(x 10^0)
0.6<Y<0.8(x 10^-1)
0.8<Y<1(x 10^-2)
1<Y<1.2(x 10^-3)
1.2<Y<1.4(x 10^-4)
1.4<Y<1.6(x 10^-5)
K+
23% central, 8 GeV
M_T-M_0 (GeV/c^2)
Inverse Slope (GeV)
y
y

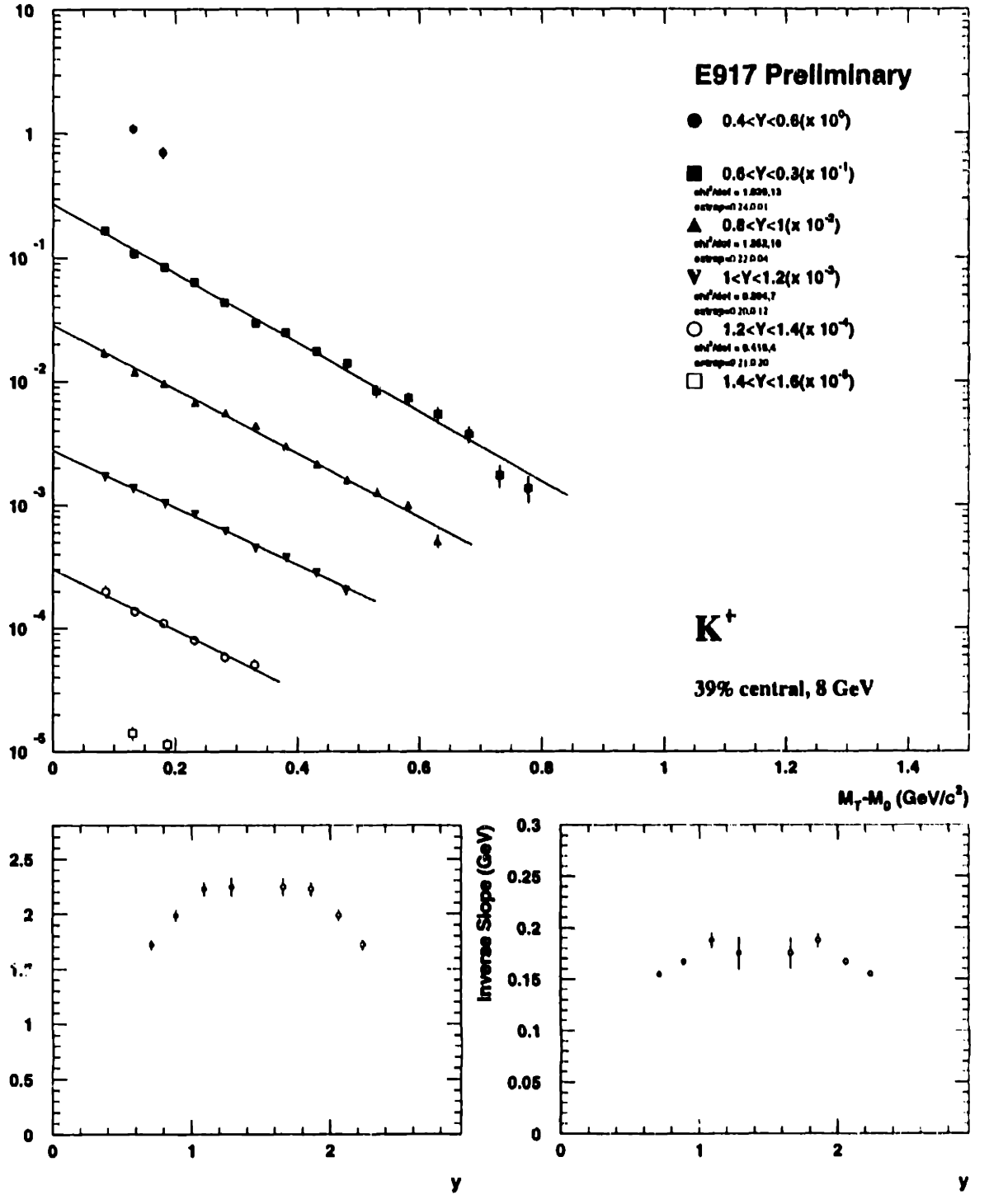
E917 Preliminary
0.4<Y<0.6(x 10^0)
0.6<Y<0.3(x 10^-1)
0.8<Y<1(x 10^-3)
1<Y<1.2(x 10^-3)
1.2<Y<1.4(x 10^-4)
1.4<Y<1.6(x 10^-5)
K+
39% central, 8 GeV
M_T-M_0 (GeV/c^2)
Inverse Slope (GeV)
y
y

Appendix C

K^- spectra

This appendix contains plots of K^- spectra for each centrality class and beam energy. The double differential yield is plotted vs $m_\perp - m_0$ for rapidity slices of 0.2 units and $m_\perp$ of 0.05 units.

The distributions are fit to an exponential, using a χ^2 minimization. The functional form is:

$$\frac{1}{2\pi m_\perp}\frac{d^2N}{dm_\perp dY} = \frac{dN/dY}{2\pi\left(Tm_0 + T^2\right)} exp\left(-\frac{m_\perp - m_0}{T}\right) \qquad (C.1)$$

with T and dN/dY as fit parameters. The results for T and dN/dY are reflected about the appropriate Y_{nn} for the beam energy of the data as it was taken, with the reflected points plotted as open circles. All $m_\perp$ points that satisfied the acceptance cuts are plotted, but no fit is performed if there are fewer than 4 such points within the acceptance. However, results of fits with extrapolation levels greater than 60% are not used in the discussion section. The extrapolation level is determined by the extreme edges of the $m_\perp$ bins measured and the parameters of the fit.

Systematic errors of 2% have been added to the invariant differential yields, but the errors on dN/dY and T are those from the fit.

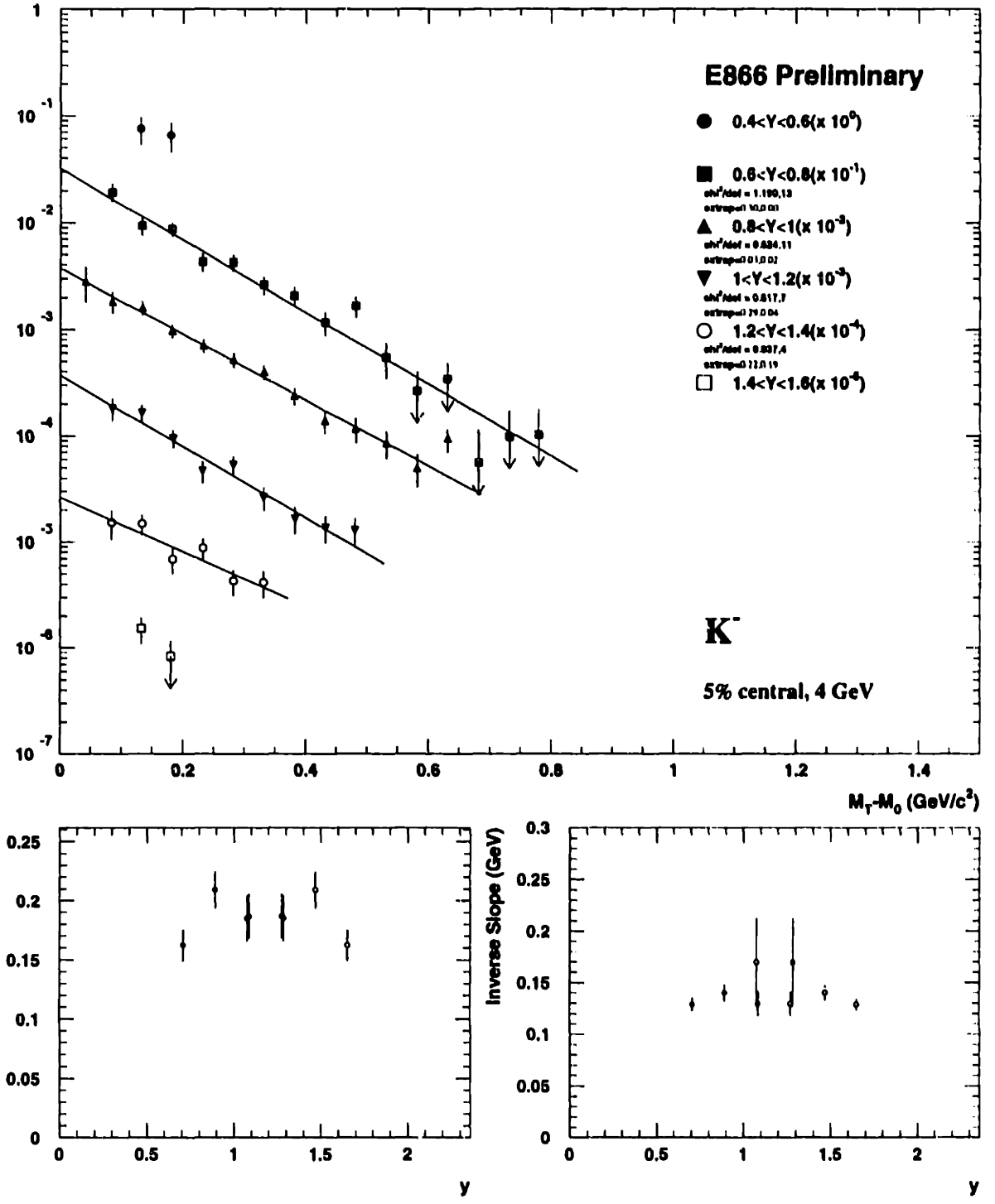
E866 Preliminary
0.4<Y<0.6(x 10^0)
0.6<Y<0.8(x 10^-1)
0.8<Y<1(x 10^-3)
1<Y<1.2(x 10^-3)
1.2<Y<1.4(x 10^-4)
1.4<Y<1.6(x 10^-6)
K^-
5% central, 4 GeV
M_T-M_0 (GeV/c^2)
Inverse Slope (GeV)
y
y

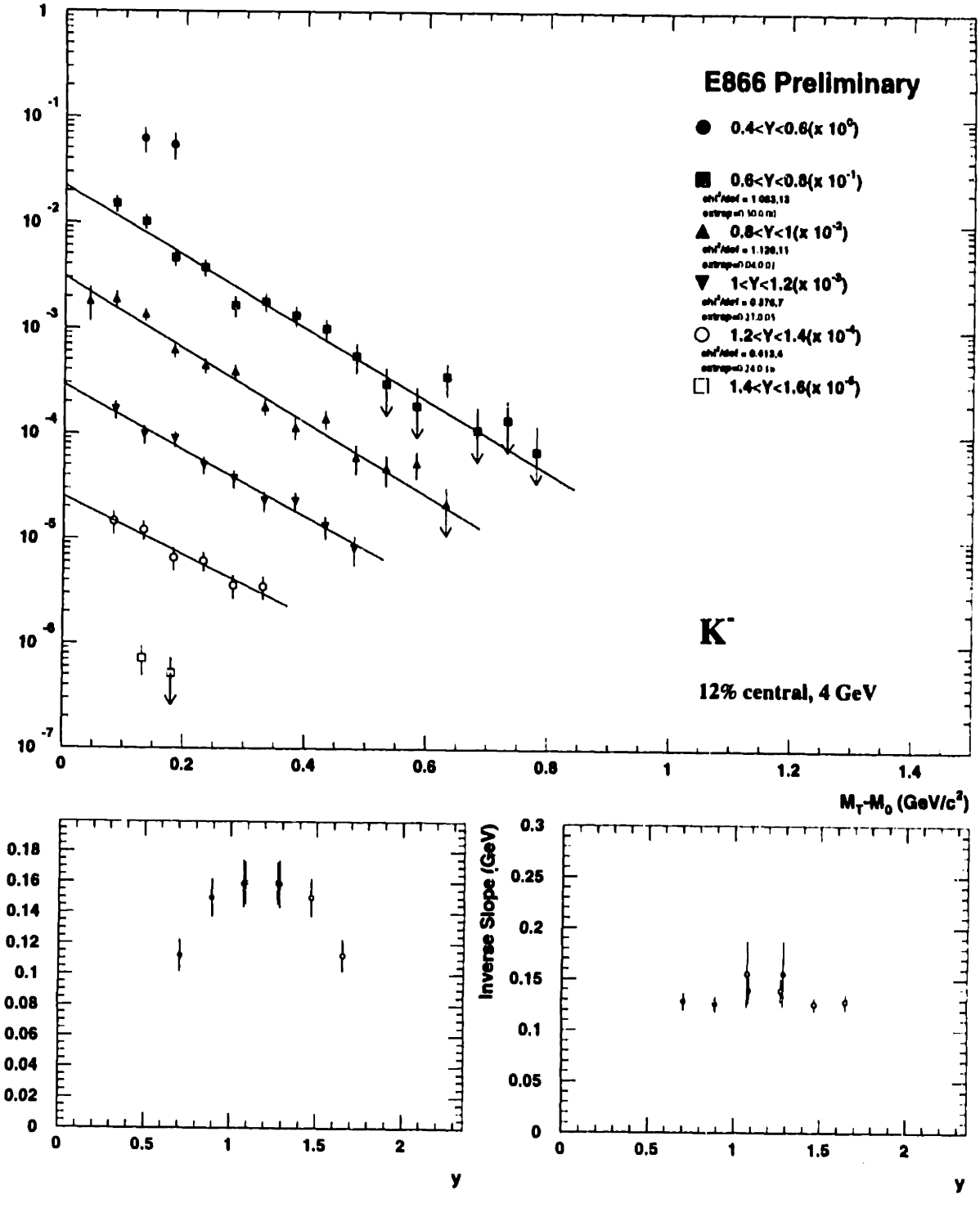
E866 Preliminary
0.4<Y<0.6(x 10^0)
0.6<Y<0.8(x 10^-1)
0.8<Y<1(x 10^-2)
1<Y<1.2(x 10^-3)
1.2<Y<1.4(x 10^-4)
1.4<Y<1.6(x 10^-5)
K-
12% central, 4 GeV
M_T-M_0 (GeV/c^2)
Inverse Slope (GeV)
y
y

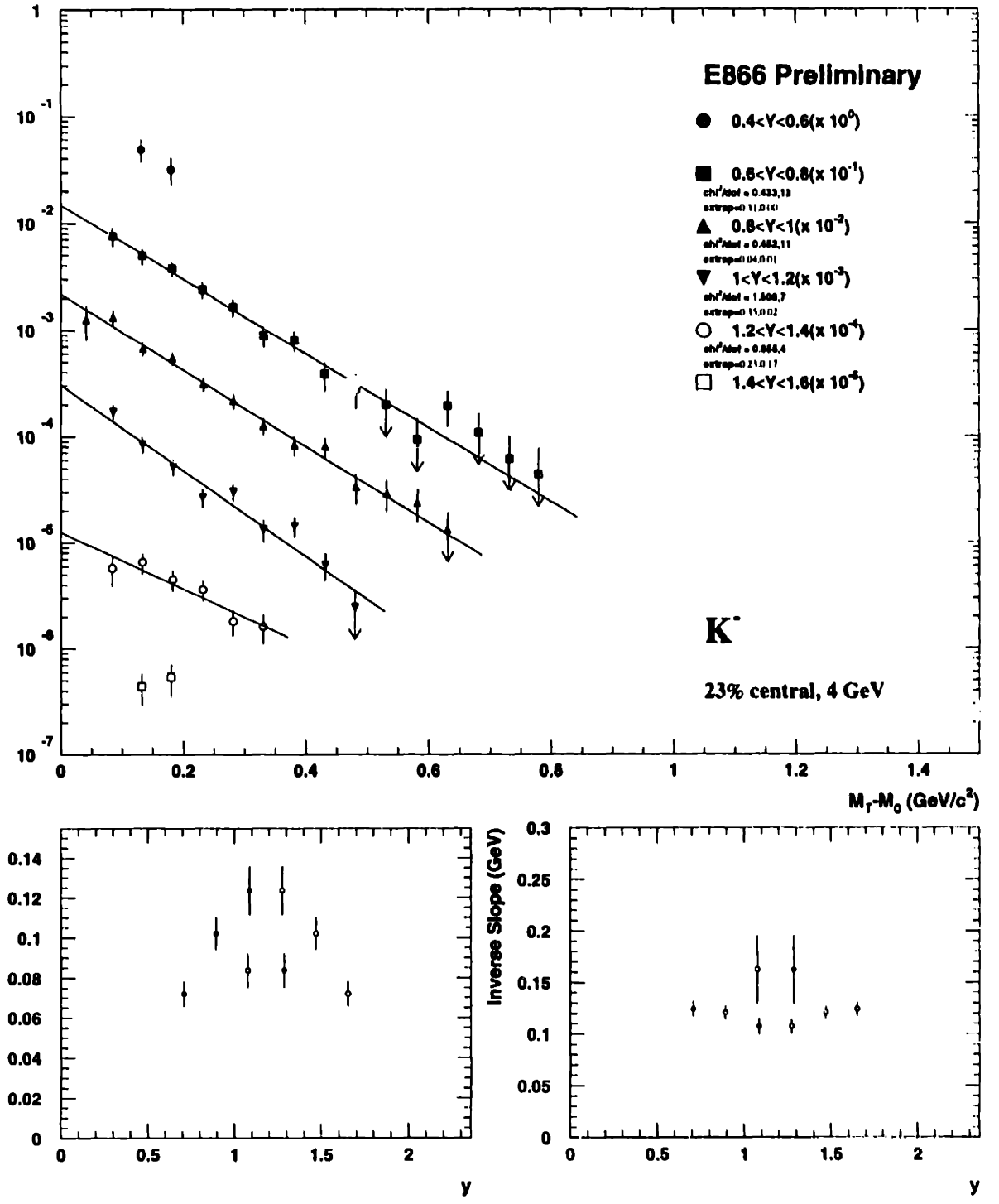
E866 Preliminary
0.4<Y<0.6(x 10^0)
0.6<Y<0.8(x 10^-1)
0.8<Y<1(x 10^-2)
1<Y<1.2(x 10^-3)
1.2<Y<1.4(x 10^-4)
1.4<Y<1.6(x 10^-5)
K-
23% central, 4 GeV
M_T-M_0 (GeV/c^2)
Inverse Slope (GeV)
y
y

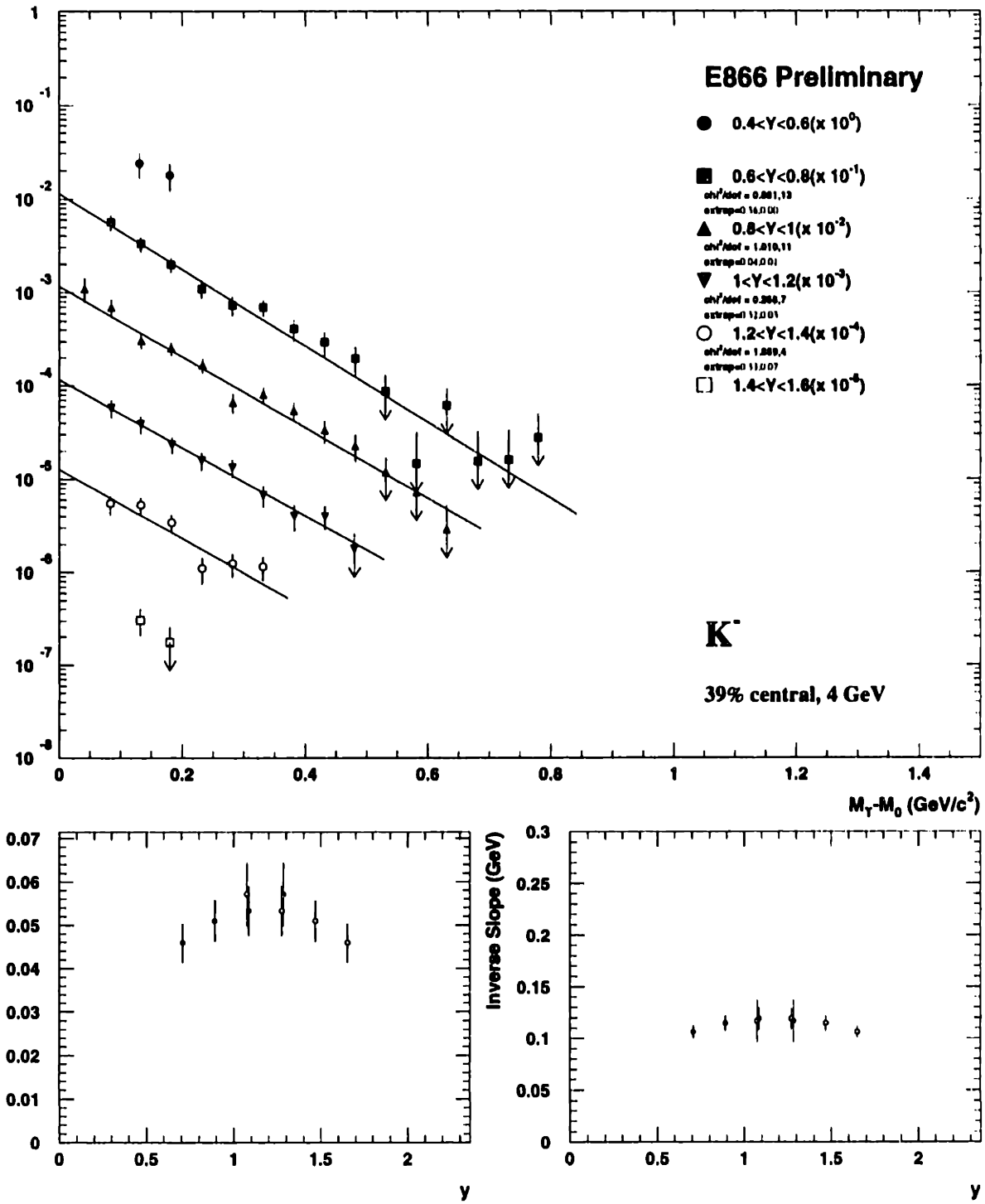
E866 Preliminary
0.4<Y<0.6(x 10^0)
0.6<Y<0.8(x 10^-1)
0.8<Y<1(x 10^-2)
1<Y<1.2(x 10^-3)
1.2<Y<1.4(x 10^-4)
1.4<Y<1.6(x 10^-5)
K-
39% central, 4 GeV
M_T-M_0 (GeV/c^2)
Inverse Slope (GeV)
y
y

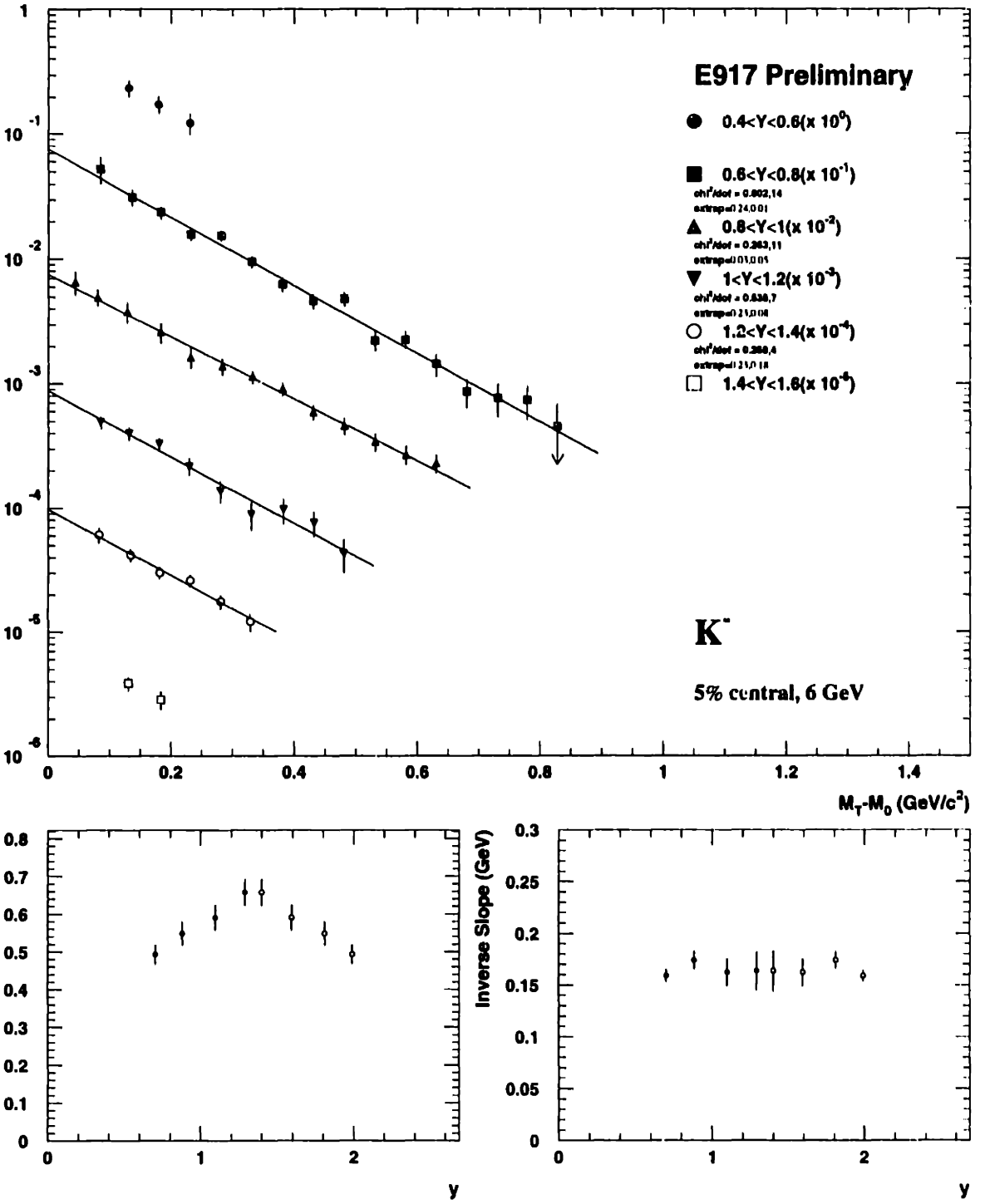
E917 Preliminary
0.4<Y<0.6(x 10^0)
0.6<Y<0.8(x 10^-1)
0.8<Y<1(x 10^-2)
1<Y<1.2(x 10^-3)
1.2<Y<1.4(x 10^-4)
1.4<Y<1.6(x 10^-5)
K-
5% central, 6 GeV
M_T-M_0 (GeV/c^2)
Inverse Slope (GeV)
y
y

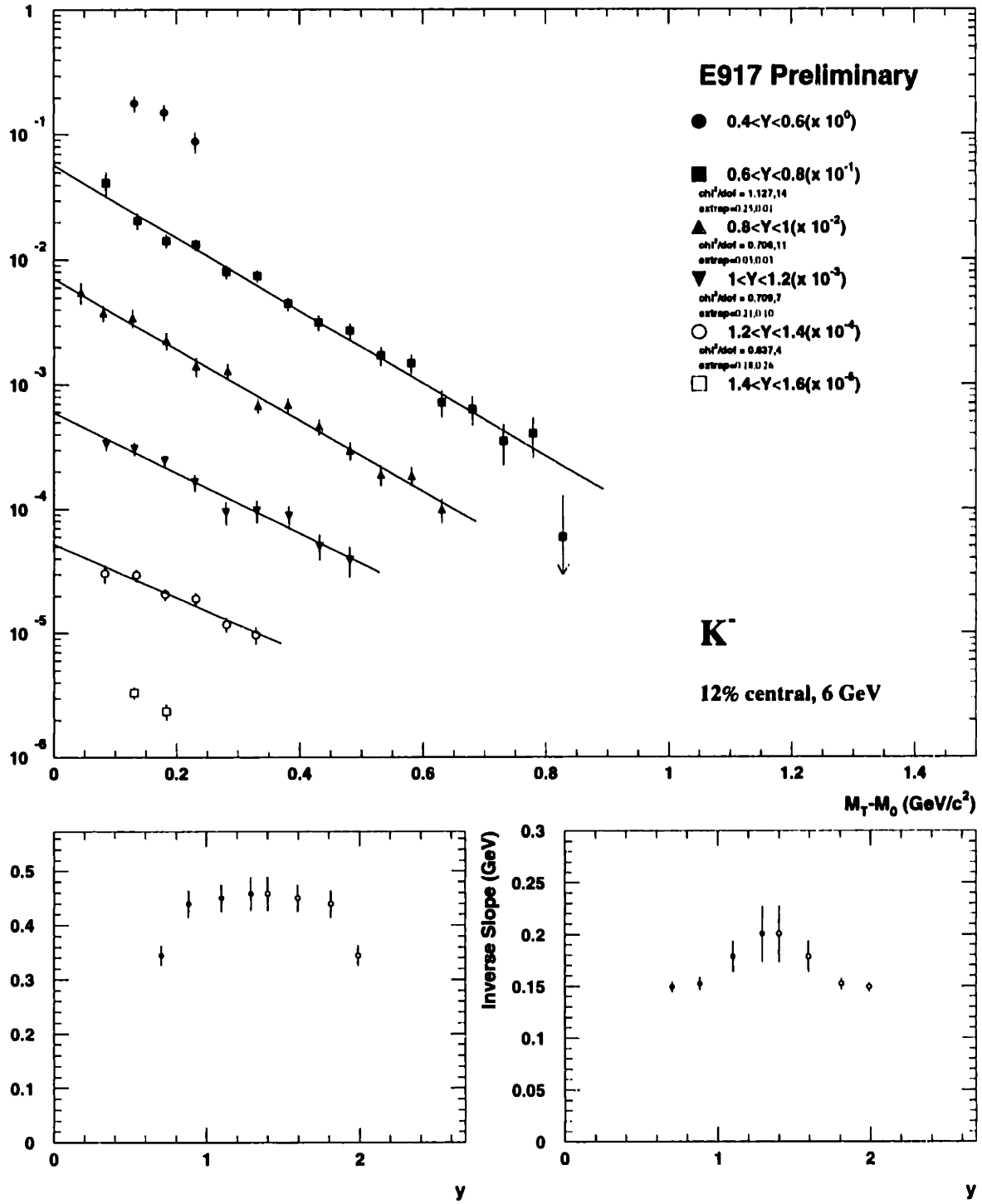
E917 Preliminary
0.4<Y<0.6(x 10^0)
0.6<Y<0.8(x 10^-1)
0.8<Y<1(x 10^-2)
1<Y<1.2(x 10^-3)
1.2<Y<1.4(x 10^-4)
1.4<Y<1.6(x 10^-5)
K-
12% central, 6 GeV
M_T-M_0 (GeV/c^2)
Inverse Slope (GeV)
y
y

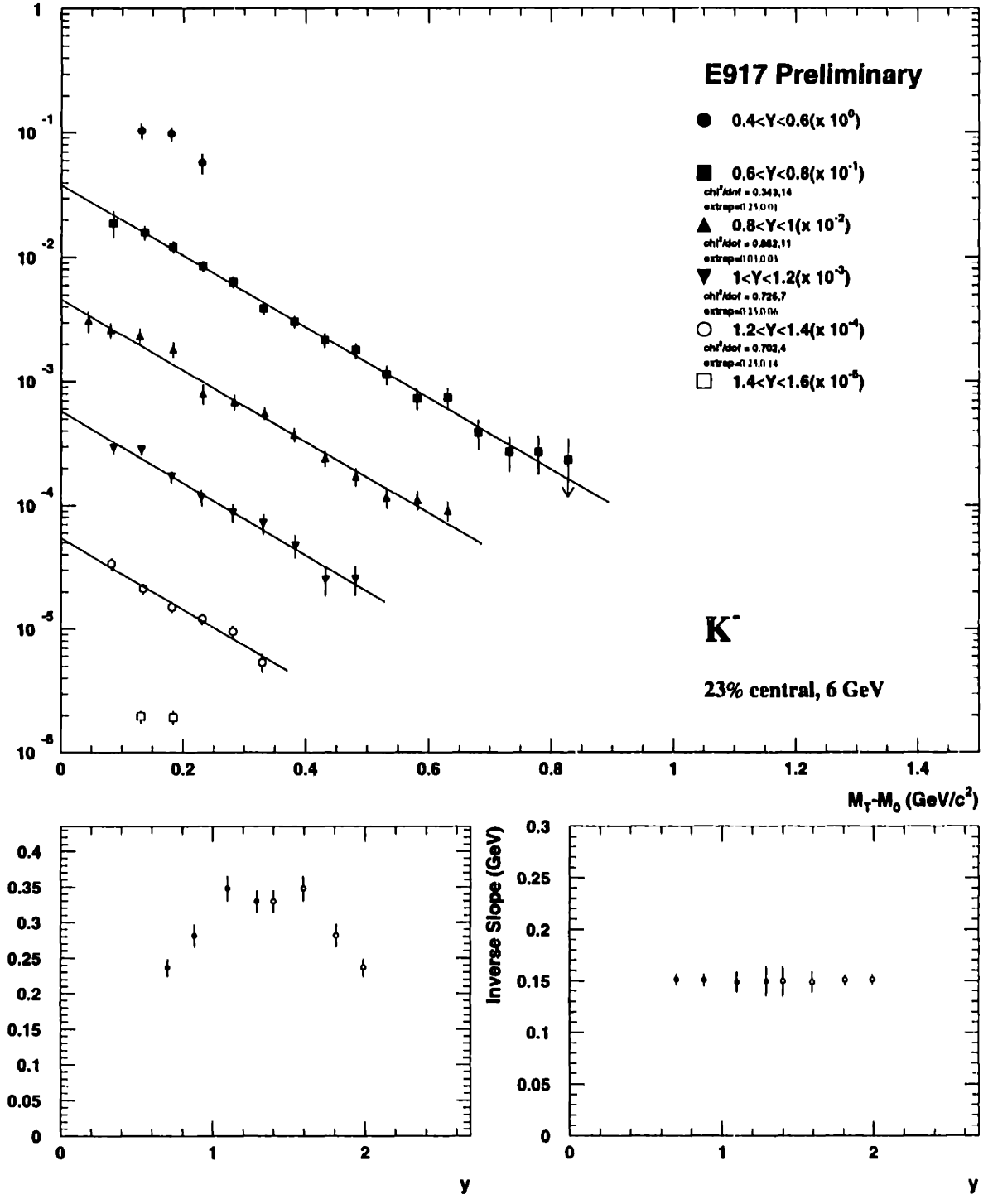
E917 Preliminary
0.4<Y<0.6(x 10^0)
0.6<Y<0.8(x 10^-1)
0.8<Y<1(x 10^-2)
1<Y<1.2(x 10^-3)
1.2<Y<1.4(x 10^-4)
1.4<Y<1.6(x 10^-5)
K-
23% central, 6 GeV
M_T-M_0 (GeV/c^2)
Inverse Slope (GeV)
y
y

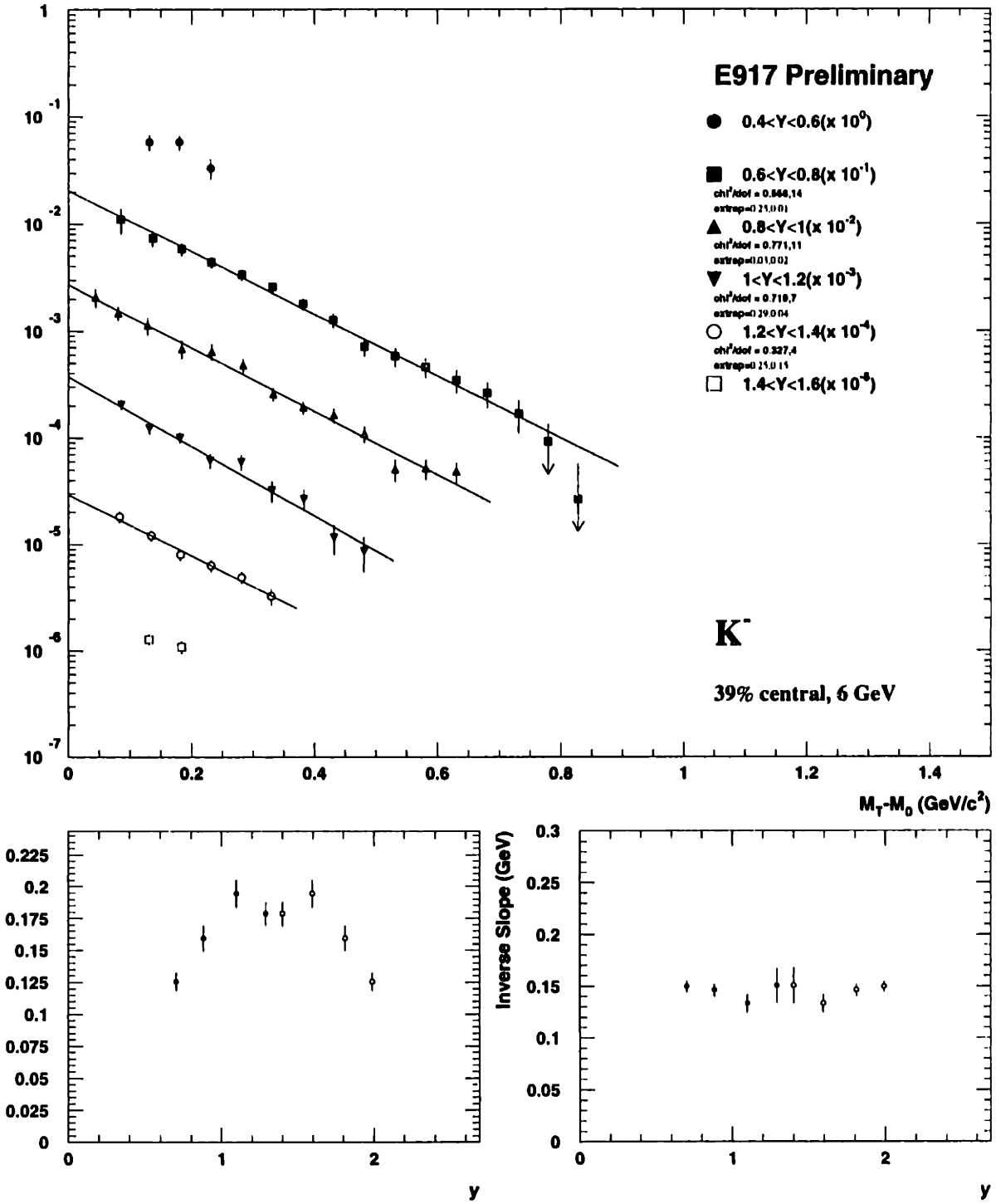
E917 Preliminary
0.4<Y<0.6(x 10^0)
0.6<Y<0.8(x 10^-1)
0.8<Y<1(x 10^-2)
1<Y<1.2(x 10^-3)
1.2<Y<1.4(x 10^-4)
1.4<Y<1.6(x 10^-5)
K^-
39% central, 6 GeV
M_T-M_0 (GeV/c^2)
Inverse Slope (GeV)
y
y

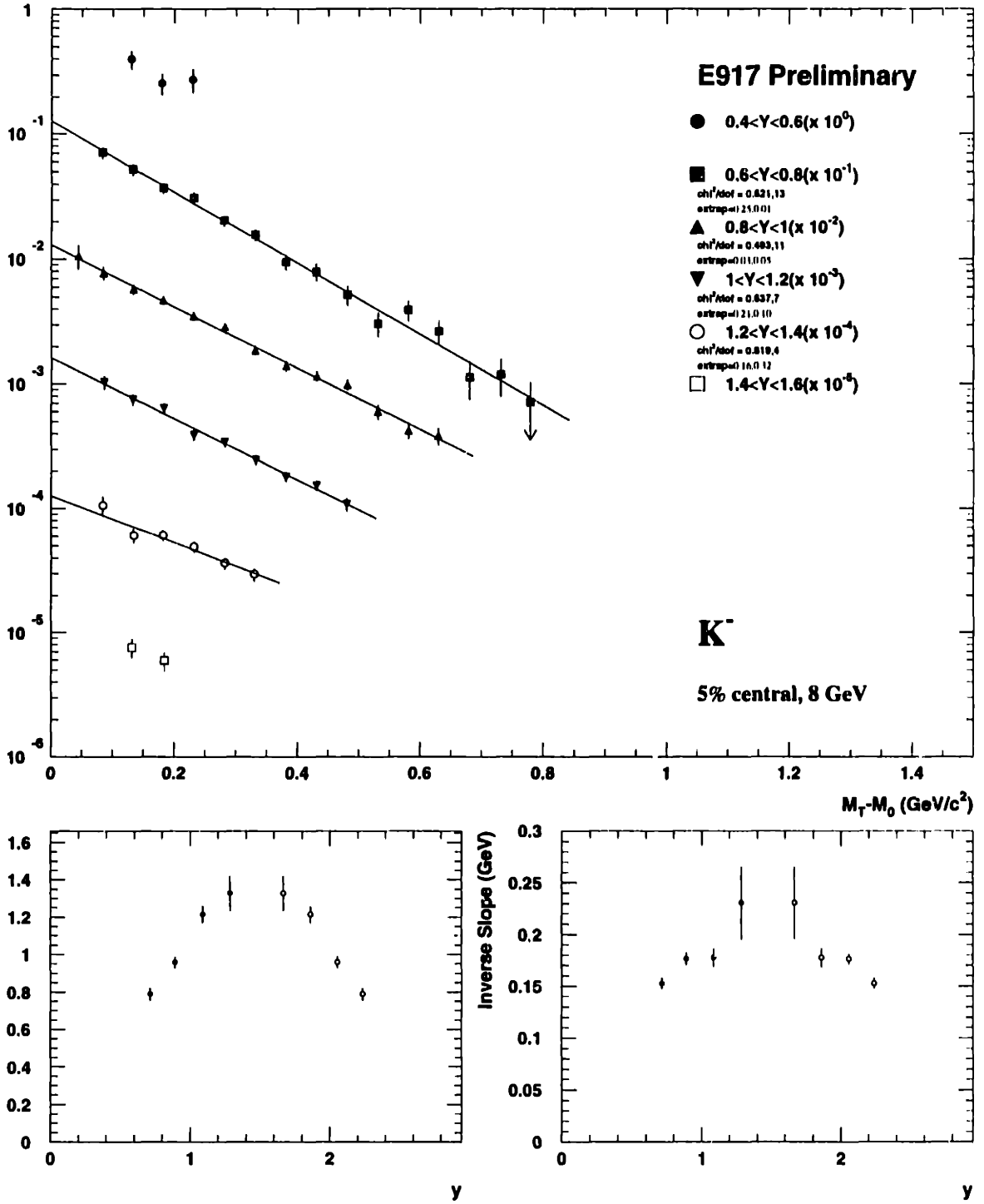
E917 Preliminary
0.4<Y<0.6(x 10^0)
0.6<Y<0.8(x 10^-1)
0.8<Y<1(x 10^-2)
1<Y<1.2(x 10^-3)
1.2<Y<1.4(x 10^-4)
1.4<Y<1.6(x 10^-5)
K-
5% central, 8 GeV
M_T-M_0 (GeV/c^2)
Inverse Slope (GeV)
y
y

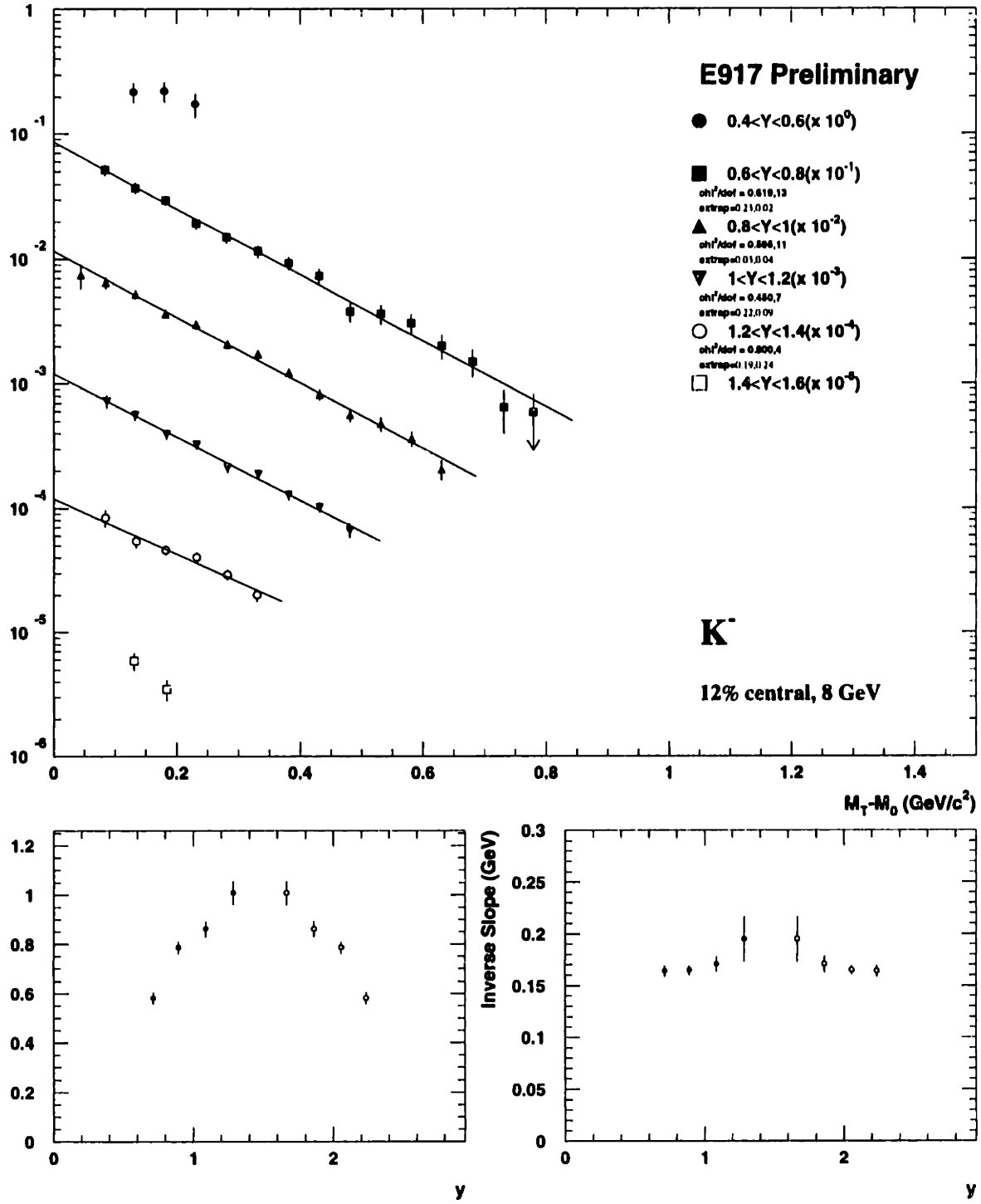
E917 Preliminary
0.4<Y<0.6(x 10^0)
0.6<Y<0.8(x 10^-1)
0.8<Y<1(x 10^-2)
1<Y<1.2(x 10^-3)
1.2<Y<1.4(x 10^-4)
1.4<Y<1.6(x 10^-5)
K-
12% central, 8 GeV
M_T-M_0 (GeV/c^2)
Inverse Slope (GeV)
y
y

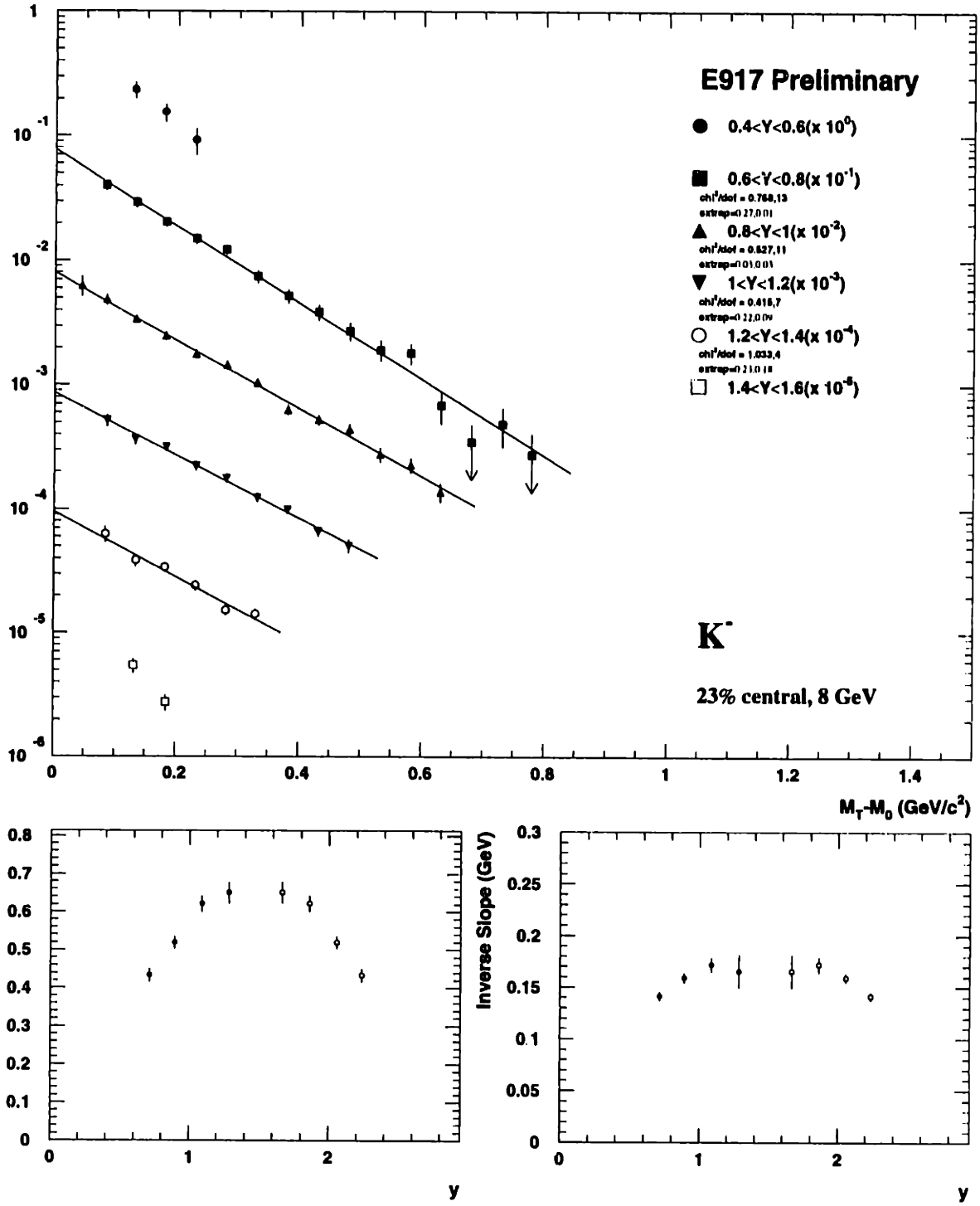
E917 Preliminary
0.4<Y<0.6(x 10^0)
0.6<Y<0.8(x 10^-1)
0.8<Y<1(x 10^-2)
1<Y<1.2(x 10^-3)
1.2<Y<1.4(x 10^-4)
1.4<Y<1.6(x 10^-5)
K^-
23% central, 8 GeV
M_T-M_0 (GeV/c^2)
Inverse Slope (GeV)
y
y

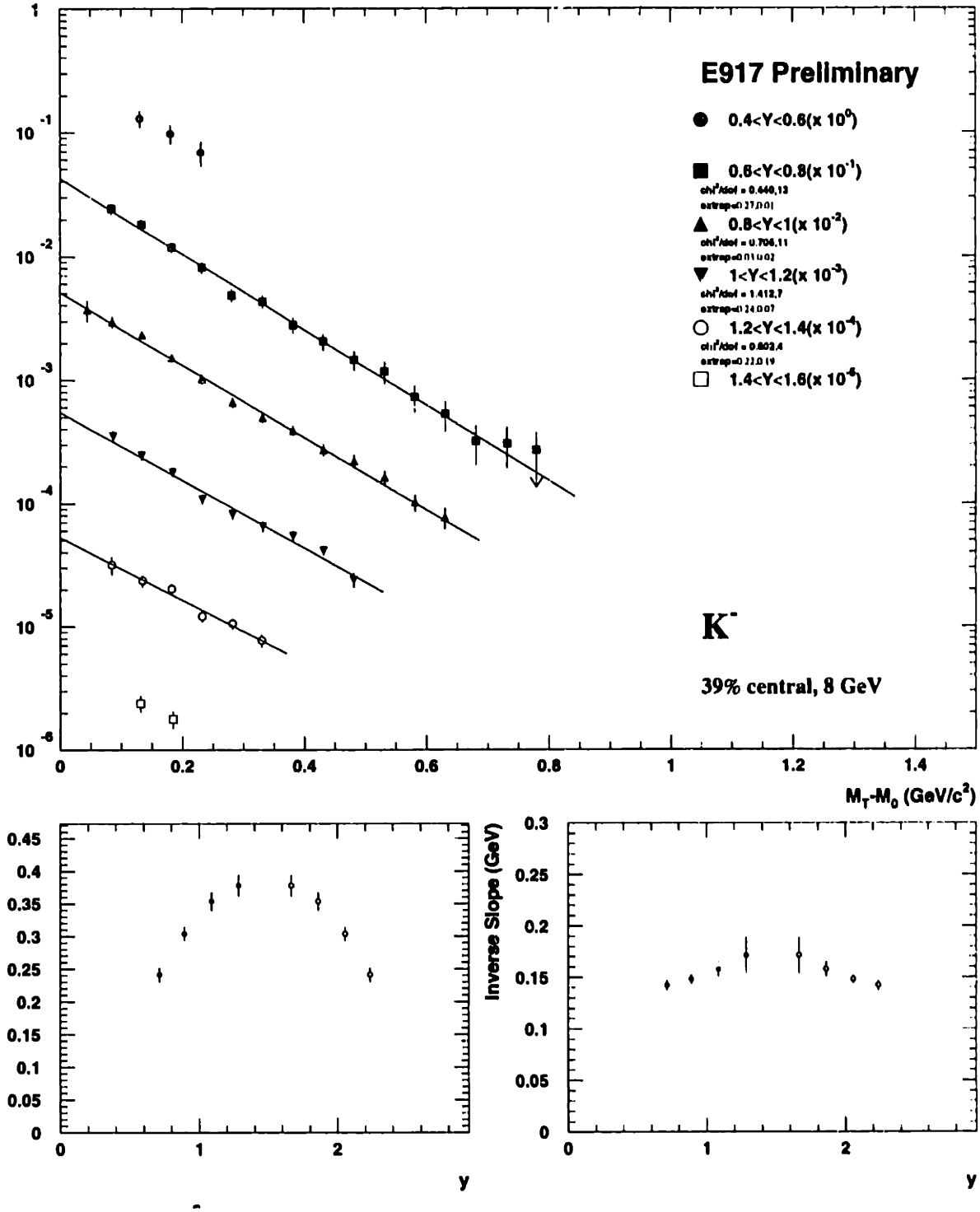
E917 Preliminary
0.4<Y<0.6(x 10^0)
0.6<Y<0.8(x 10^-1)
0.8<Y<1(x 10^-2)
1<Y<1.2(x 10^-3)
1.2<Y<1.4(x 10^-4)
1.4<Y<1.6(x 10^-5)
K-
39% central, 8 GeV
M_T-M_0 (GeV/c^2)
Inverse Slope (GeV)
y
y

Appendix D

Tables of derived quantities, all rapidities

This appendix contains tables of the derived quantities dN/dY, T, the total χ^2, and the number of degrees of freedom of the fits, for K^+, K^-, π^+ and protons. In addition, γ, $\langle m_\perp \rangle$, and $\sigma_{T\gamma}$ are listed for the π^+ and protons. The tables contain information from each centrality class and beam energy, further divided into bins in rapidity. The errors listed are statistical only. The $m_\perp$ distributions to which the fits are made are tabulated in appendix E.

The kaon distributions are fit to an exponential, as described by equation 6.10, with T and dN/dY as fit parameters. The pions and protons are fit to Gamma distributins, as described by equations 6.13 and 6.14, with dN/dY, T, and γ as fit parameters. $\langle m_\perp \rangle$ is derived from T and γ, using the full correlation term, $\sigma_{T\gamma}$.

y	K^+ dN/dy	K^+ T (GeV)	χ^2/d.o.f.
2 $A{\cdot}GeV$, 0-5% Central			
0.7	0.404±0.022	0.130±0.006	10.63/ 12
0.9	0.383±0.023	0.139±0.006	16.38/ 10
1.1	0.371±0.034	0.128±0.011	4.41/ 6
2 $A{\cdot}GeV$, 5-12% Central			
0.7	0.287±0.017	0.119±0.005	21.00/ 12
0.9	0.256±0.016	0.139±0.006	18.36/ 10
1.1	0.252±0.024	0.125±0.011	4.37/ 6
2 $A{\cdot}GeV$, 12-23% Central			
0.7	0.169±0.010	0.122±0.005	15.52/ 12
0.9	0.175±0.012	0.124±0.005	4.28/ 10
1.1	0.141±0.014	0.123±0.011	4.32/ 6
2 $A{\cdot}GeV$, 23-39% Central			
0.7	0.095±0.007	0.113±0.005	11.20/ 11
0.9	0.086±0.007	0.117±0.006	4.75/ 10
1.1	0.080±0.011	0.106±0.010	4.41/ 6

y	K^+ dN/dy	K^+ T (GeV)	χ^2/d.o.f.
4 $A{\cdot}GeV$, 0-5% Central			
0.7	2.147±0.070	0.141±0.003	5.80/ 13
0.9	2.362±0.074	0.153±0.004	5.90/ 11
1.1	2.417±0.085	0.158±0.006	2.22/ 7
1.3	2.305±0.102	0.188±0.023	0.83/ 3
4 $A{\cdot}GeV$, 5-12% Central			
0.7	1.590±0.051	0.143±0.003	11.87/ 13
0.9	1.762±0.054	0.151±0.004	7.78/ 11
1.1	1.836±0.064	0.153±0.006	3.71/ 7
1.3	1.793±0.079	0.169±0.017	7.22/ 3
4 $A{\cdot}GeV$, 12-23% Central			
0.7	1.093±0.037	0.133±0.003	16.26/ 13
0.9	1.126±0.036	0.145±0.004	4.28/ 11
1.1	1.231±0.042	0.151±0.006	6.46/ 7
1.3	1.199±0.051	0.173±0.019	1.65/ 3
4 $A{\cdot}GeV$, 23-39% Central			
0.7	0.584±0.022	0.123±0.003	10.19/ 13
0.9	0.619±0.022	0.139±0.004	6.49/ 11
1.1	0.598±0.024	0.147±0.006	11.40/ 7
1.3	0.598±0.031	0.159±0.017	1.39/ 3

y	K^+ dN/dy	K^+ T (GeV)	χ^2/d.o.f.
6 $A{\cdot}GeV$, 0-5% Central			
0.7	4.562±0.096	0.164±0.003	12.14/ 14
0.9	5.007±0.107	0.179±0.004	11.43/ 11
1.1	4.908±0.123	0.207±0.009	3.49/ 7
1.3	4.815±0.154	0.204±0.014	0.32/ 4
6 $A{\cdot}GeV$, 5-12% Central			
0.7	3.344±0.069	0.165±0.003	9.38/ 14
0.9	3.652±0.077	0.178±0.004	8.95/ 11
1.1	3.890±0.090	0.190±0.007	4.78/ 7
1.3	3.880±0.111	0.198±0.012	1.58/ 4
6 $A{\cdot}GeV$, 12-23% Central			
0.7	2.357±0.048	0.157±0.003	14.72/ 14
0.9	2.506±0.051	0.178±0.003	9.43/ 11
1.1	2.665±0.059	0.187±0.007	3.61/ 7
1.3	2.623±0.082	0.210±0.014	3.04/ 4
6 $A{\cdot}GeV$, 23-39% Central			
0.7	1.292±0.030	0.154±0.003	4.21/ 14
0.9	1.412±0.032	0.163±0.003	12.69/ 11
1.1	1.430±0.035	0.178±0.007	7.13/ 7
1.3	1.516±0.039	0.181±0.010	0.34/ 4

y	K^+ dN/dy	K^+ T (GeV)	χ^2/d.o.f.
8 $A{\cdot}GeV$, 0-5% Central			
0.7	5.765±0.157	0.167±0.004	5.96/ 13
0.9	6.999±0.183	0.180±0.005	2.99/ 10
1.1	7.441±0.196	0.220±0.011	8.66/ 7
1.3	7.989±0.431	0.220±0.025	3.42/ 4
8 $A{\cdot}GeV$, 5-12% Central			
0.7	4.533±0.119	0.169±0.004	9.17/ 13
0.9	5.411±0.139	0.176±0.005	2.91/ 10
1.1	5.540±0.143	0.217±0.010	7.82/ 7
1.3	5.844±0.239	0.193±0.020	2.13/ 4
8 $A{\cdot}GeV$, 12-23% Central			
0.7	3.018±0.078	0.165±0.004	7.48/ 13
0.9	3.596±0.089	0.181±0.005	3.78/ 10
1.1	3.876±0.099	0.195±0.008	1.17/ 7
1.3	3.948±0.166	0.202±0.020	1.44/ 4
8 $A{\cdot}GeV$, 23-39% Central			
0.7	1.720±0.049	0.156±0.004	13.55/ 13
0.9	1.987±0.055	0.168±0.004	12.57/ 10
1.1	2.226±0.061	0.188±0.008	1.48/ 7
1.3	2.243±0.082	0.176±0.016	1.72/ 4

y	K^- dN/dy	K^- T (GeV)	χ^2/d.o.f.
4 $A{\cdot}GeV$, 0-5% Central			
0.7	0.163±0.014	0.129±0.007	15.52/ 13
0.9	0.210±0.016	0.141±0.009	6.92/ 11
1.1	0.187±0.020	0.130±0.013	5.77/ 7
1.3	0.186±0.020	0.170±0.044	3.80/ 4
4 $A{\cdot}GeV$, 5-12% Central			
0.7	0.113±0.011	0.129±0.009	14.13/ 13
0.9	0.150±0.013	0.126±0.008	12.46/ 11
1.1	0.160±0.014	0.139±0.012	2.68/ 7
1.3	0.159±0.016	0.156±0.033	1.70/ 4
4 $A{\cdot}GeV$, 12-23% Central			
0.7	0.073±0.007	0.125±0.008	5.68/ 13
0.9	0.103±0.009	0.122±0.007	5.02/ 11
1.1	0.124±0.013	0.108±0.008	10.61/ 7
1.3	0.084±0.009	0.163±0.034	2.67/ 4
4 $A{\cdot}GeV$, 23-39% Central			
0.7	0.046±0.005	0.107±0.007	11.50/ 13
0.9	0.052±0.005	0.115±0.008	11.16/ 11
1.1	0.054±0.006	0.119±0.011	1.93/ 7
1.3	0.058±0.008	0.117±0.022	7.48/ 4

y	K^- dN/dy	K^- T (GeV)	χ^2/d.o.f.
6 $A{\cdot}GeV$, 0-5% Central			
0.7	0.494±0.027	0.160±0.007	11.28/ 14
0.9	0.549±0.032	0.175±0.009	2.95/ 11
1.1	0.591±0.035	0.163±0.014	3.81/ 7
1.3	0.658±0.036	0.164±0.020	1.12/ 4
6 $A{\cdot}GeV$, 5-12% Central			
0.7	0.345±0.019	0.150±0.006	15.83/ 14
0.9	0.440±0.025	0.153±0.007	7.82/ 11
1.1	0.451±0.026	0.179±0.016	5.01/ 7
1.3	0.459±0.032	0.201±0.028	3.40/ 4
6 $A{\cdot}GeV$, 12-23% Central			
0.7	0.237±0.013	0.152±0.006	4.85/ 14
0.9	0.282±0.017	0.152±0.007	9.53/ 11
1.1	0.348±0.018	0.150±0.010	5.12/ 7
1.3	0.330±0.017	0.150±0.016	2.86/ 4
6 $A{\cdot}GeV$, 23-39% Central			
0.7	0.126±0.008	0.151±0.006	8.00/ 14
0.9	0.160±0.010	0.147±0.007	8.54/ 11
1.1	0.195±0.012	0.134±0.009	5.08/ 7
1.3	0.179±0.010	0.151±0.018	1.36/ 4

y	K^- dN/dy	K^- T (GeV)	χ^2/d.o.f.
8 $A{\cdot}GeV$, 0-5% Central			
0.7	0.789±0.034	0.153±0.006	8.12/ 13
0.9	0.960±0.033	0.177±0.006	5.47/ 11
1.1	1.217±0.044	0.178±0.010	4.51/ 7
1.3	1.329±0.097	0.231±0.036	3.33/ 4
8 $A{\cdot}GeV$, 5-12% Central			
0.7	0.582±0.024	0.165±0.006	8.10/ 13
0.9	0.788±0.026	0.166±0.005	6.59/ 11
1.1	0.862±0.032	0.171±0.009	3.20/ 7
1.3	1.009±0.049	0.196±0.023	3.25/ 4
8 $A{\cdot}GeV$, 12-23% Central			
0.7	0.434±0.018	0.142±0.005	10.03/ 13
0.9	0.520±0.018	0.160±0.005	5.84/ 11
1.1	0.622±0.022	0.172±0.008	2.96/ 7
1.3	0.651±0.029	0.166±0.017	4.18/ 4
8 $A{\cdot}GeV$, 23-39% Central			
0.7	0.242±0.011	0.143±0.006	5.77/ 13
0.9	0.305±0.012	0.149±0.005	7.80/ 11
1.1	0.354±0.015	0.158±0.008	9.93/ 7
1.3	0.378±0.018	0.172±0.019	2.46/ 4

y	π^+ dN/dy	π^+ T (GeV)	γ	$\langle m_\perp \rangle$ (GeV)	$\sigma_{T\gamma}$ $\left(\text{GeV}^2\right)$	χ^2/d.o.f.
2 $A{\cdot}GeV$, 0-5% Central						
0.9	14.142±0.781	0.151±0.012	1.047±0.257	0.288±0.006	0.00334	19.25/ 16
1.1	12.697±0.636	0.133±0.012	0.719±0.302	0.289±0.006	0.00394	12.37/ 14
1.3	10.131±0.552	0.120±0.016	0.442±0.438	0.287±0.006	0.00714	12.15/ 11
2 $A{\cdot}GeV$, 5-12% Central						
0.9	11.534±0.696	0.160±0.014	1.389±0.266	0.275±0.006	0.00391	13.49/ 16
1.1	9.635±0.494	0.131±0.012	0.709±0.305	0.286±0.006	0.00382	9.85/ 14
1.3	9.095±0.578	0.146±0.025	1.215±0.472	0.274±0.006	0.012	4.67/ 11
2 $A{\cdot}GeV$, 12-23% Central						
0.9	8.234±0.531	0.163±0.015	1.650±0.276	0.263±0.006	0.0044	7.57/ 16
1.1	7.348±0.428	0.144±0.015	1.252±0.316	0.269±0.006	0.00485	13.63/ 14
1.3	6.503±0.385	0.155±0.024	1.515±0.400	0.265±0.006	0.00966	6.10/ 11
2 $A{\cdot}GeV$, 23-39% Central						
0.9	4.552±0.358	0.139±0.014	1.237±0.356	0.266±0.007	0.00527	12.05/ 16
1.1	4.313±0.271	0.138±0.016	1.252±0.353	0.265±0.006	0.00569	10.69/ 14
1.3	3.583±0.230	0.104±0.012	0.523±0.454	0.262±0.006	0.00573	10.50/ 11

y	π^+ dN/dy	π^+ T (GeV)	γ	$\langle m_\perp \rangle$ (GeV)	$\sigma_{T\gamma}$ (GeV^2)	χ^2/d.o.f.
4 A·GeV, 0-5% Central						
0.9	24.469±1.268	0.225±0.022	1.332±0.237	0.331±0.008	0.00541	12.21/ 16
1.1	27.707±0.690	0.216±0.015	1.271±0.154	0.329±0.004	0.00272	4.81/ 14
1.3	26.159±0.751	0.209±0.020	1.151±0.202	0.334±0.004	0.00433	8.30/ 11
1.5	22.108±1.070	0.152±0.022	0.355±0.400	0.338±0.007	0.00883	4.85/ 8
4 A·GeV, 5-12% Central						
0.9	20.915±1.209	0.280±0.036	1.889±0.252	0.313±0.008	0.00914	8.69/ 16
1.1	21.910±0.544	0.230±0.016	1.427±0.147	0.325±0.004	0.00277	9.71/ 14
1.3	20.911±0.602	0.204±0.018	1.218±0.194	0.323±0.004	0.00383	1.59/ 11
1.5	19.324±0.962	0.196±0.035	1.120±0.376	0.325±0.006	0.0131	5.25/ 8
4 A·GeV, 12-23% Central						
0.9	14.598±0.762	0.233±0.022	1.672±0.219	0.306±0.007	0.00507	16.05/ 16
1.1	15.617±0.383	0.218±0.014	1.426±0.140	0.317±0.004	0.00235	7.75/ 14
1.3	15.079±0.413	0.213±0.019	1.328±0.181	0.322±0.004	0.00371	5.88/ 11
1.5	13.999±0.623	0.180±0.026	0.981±0.334	0.322±0.006	0.00895	7.81/ 8
4 A·GeV, 23-39% Central						
0.9	8.165±0.435	0.196±0.017	1.307±0.237	0.309±0.007	0.00429	17.65/ 16
1.1	9.251±0.243	0.209±0.014	1.411±0.152	0.311±0.004	0.00251	10.55/ 14
1.3	9.081±0.267	0.217±0.020	1.445±0.187	0.314±0.004	0.00403	7.09/ 11
1.5	8.656±0.513	0.183±0.034	1.161±0.437	0.310±0.006	0.0151	2.61/ 8

y	π^+ dN/dy	π^+ T (GeV)	γ	$\langle m_\perp \rangle$ (GeV)	$\sigma_{T\gamma}$ (GeV^2)	χ^2/d.o.f.
6 A·GeV, 0-5% Central						
0.9	38.510±1.924	0.209±0.020	1.123±0.247	0.337±0.007	0.00524	12.53/ 16
1.1	37.704±1.143	0.188±0.016	0.725±0.212	0.353±0.006	0.00374	16.85/ 14
1.3	39.729±0.804	0.228±0.022	1.056±0.174	0.361±0.005	0.0042	5.93/ 12
1.5	39.289±1.234	0.197±0.027	0.880±0.279	0.349±0.005	0.00772	1.49/ 8
6 A·GeV, 5-12% Central						
0.9	31.957±1.537	0.226±0.021	1.401±0.223	0.325±0.007	0.00498	9.97/ 16
1.1	31.411±0.963	0.224±0.023	1.118±0.216	0.351±0.005	0.00532	6.07/ 14
1.3	31.624±0.621	0.219±0.020	1.074±0.170	0.351±0.005	0.00377	7.61/ 12
1.5	33.329±0.985	0.216±0.029	1.112±0.248	0.344±0.005	0.00741	5.25/ 8
6 A·GeV, 12-23% Central						
0.9	22.250±1.036	0.213±0.019	1.300±0.221	0.324±0.007	0.00443	6.93/ 16
1.1	21.469±0.631	0.208±0.020	1.053±0.207	0.343±0.005	0.00435	15.45/ 14
1.3	23.245±0.436	0.211±0.018	1.115±0.160	0.339±0.004	0.0032	5.33/ 12
1.5	22.968±0.676	0.187±0.023	0.891±0.265	0.336±0.004	0.0064	2.21/ 8
6 A·GeV, 23-39% Central						
0.9	13.922±0.700	0.189±0.017	1.069±0.256	0.323±0.007	0.00472	6.77/ 16
1.1	14.320±0.455	0.202±0.020	1.072±0.225	0.334±0.005	0.00477	3.13/ 14
1.3	15.328±0.295	0.219±0.020	1.225±0.164	0.336±0.004	0.00356	8.45/ 12
1.5	15.967±0.476	0.223±0.030	1.308±0.244	0.331±0.005	0.0076	4.93/ 8

y	π^+ dN/dy	π^+ T (GeV)	γ	$\langle m_\perp \rangle$ (GeV)	$\sigma_{T\gamma}$ $\left(\text{GeV}^2\right)$	χ^2/d.o.f.
8 $A{\cdot}GeV$, 0-5% Central						
0.9	44.749±1.597	0.223±0.017	1.092±0.189	0.352±0.006	0.00361	4.05/ 16
1.1	49.973±1.193	0.227±0.017	1.050±0.161	0.361±0.004	0.00316	8.87/ 14
1.3	51.565±1.177	0.232±0.022	0.964±0.180	0.375±0.005	0.00423	4.34/ 11
1.5	49.294±1.371	0.190±0.022	0.599±0.252	0.369±0.006	0.00594	3.89/ 8
8 $A{\cdot}GeV$, 5-12% Central						
0.9	36.555±1.359	0.215±0.016	1.123±0.186	0.342±0.006	0.0033	12.53/ 16
1.1	38.181±0.876	0.208±0.015	0.868±0.160	0.361±0.004	0.00269	3.55/ 14
1.3	39.273±0.892	0.213±0.019	0.868±0.184	0.366±0.004	0.00382	3.68/ 11
1.5	40.147±1.151	0.235±0.032	0.999±0.237	0.375±0.007	0.00775	1.49/ 8
8 $A{\cdot}GeV$, 12-23% Central						
0.9	26.820±0.965	0.199±0.014	0.977±0.187	0.340±0.006	0.00291	9.01/ 16
1.1	27.705±0.625	0.203±0.014	0.875±0.159	0.355±0.004	0.00259	6.63/ 14
1.3	29.396±0.680	0.232±0.022	1.098±0.181	0.361±0.004	0.00427	1.81/ 11
1.5	29.671±0.821	0.222±0.028	1.057±0.231	0.355±0.005	0.00666	4.05/ 8
8 $A{\cdot}GeV$, 23-39% Central						
0.9	18.229±0.662	0.226±0.017	1.413±0.173	0.324±0.005	0.00323	10.61/ 16
1.1	18.168±0.425	0.212±0.015	1.041±0.156	0.348±0.004	0.00268	4.67/ 14
1.3	18.617±0.424	0.236±0.021	1.179±0.168	0.355±0.004	0.00389	4.12/ 11
1.5	19.393±0.555	0.220±0.028	1.109±0.240	0.348±0.005	0.00705	3.17/ 8

y	proton dN/dy	proton T (GeV)	γ	$\langle m_\perp \rangle$ (GeV)	$\sigma_{T\gamma}$ $\left(\text{GeV}^2\right)$	χ^2/d.o.f.
2 $A{\cdot}GeV$, 0-5% Central						
0.7	85.181±1.133	0.076±0.003	-10.104±0.684	1.159±0.003	0.00246	21.35/ 30
0.9	84.056±1.430	0.080±0.003	-9.653±0.630	1.167±0.003	0.00225	15.30/ 25
2 $A{\cdot}GeV$, 5-12% Central						
0.7	67.401±0.922	0.081±0.004	-8.272±0.668	1.139±0.002	0.00267	24.89/ 27
0.9	65.783±1.186	0.083±0.004	-8.315±0.632	1.147±0.003	0.00241	25.05/ 25
2 $A{\cdot}GeV$, 12-23% Central						
0.7	47.195±0.685	0.075±0.003	-8.696±0.694	1.121±0.002	0.00252	41.65/ 26
0.9	45.691±0.865	0.085±0.004	-7.111±0.645	1.128±0.003	0.00264	15.30/ 25
2 $A{\cdot}GeV$, 23-39% Central						
0.7	29.269±0.526	0.088±0.005	-5.237±0.748	1.098±0.002	0.00371	5.11/ 22
0.9	27.243±0.775	0.092±0.006	-4.899±0.916	1.103±0.003	0.00549	12.55/ 25

y	proton dN/dy	proton T (GeV)	γ	$\langle m_\perp \rangle$ (GeV)	$\sigma_{T\gamma}$ $\left(\text{GeV}^2\right)$	χ^2/d.o.f.
4 $A{\cdot}GeV$, 0-5% Central						
0.7	72.837±0.991	0.099±0.007	-6.457±0.912	1.166±0.003	0.00647	26.29/ 32
0.9	72.701±0.991	0.114±0.005	-5.553±0.464	1.193±0.003	0.0024	21.63/ 26
1.1	68.324±1.190	0.125±0.007	-4.847±0.572	1.206±0.004	0.00397	3.65/ 18
1.3	64.916±1.798	0.125±0.012	-4.939±1.003	1.211±0.005	0.0117	6.65/ 11
4 $A{\cdot}GeV$, 5-12% Central						
0.7	59.323±0.797	0.101±0.007	-5.811±0.875	1.155±0.003	0.00631	19.25/ 30
0.9	58.069±0.817	0.121±0.005	-4.565±0.470	1.181±0.003	0.0027	10.45/ 26
1.1	54.586±0.954	0.129±0.007	-4.131±0.554	1.191±0.003	0.00398	7.43/ 18
1.3	49.612±1.352	0.118±0.010	-5.351±0.969	1.200±0.005	0.00973	3.90/ 11
4 $A{\cdot}GeV$, 12-23% Central						
0.7	45.317±0.618	0.109±0.006	-4.490±0.649	1.142±0.003	0.00414	19.58/ 31
0.9	43.242±0.596	0.129±0.006	-3.227±0.460	1.159±0.003	0.00294	17.47/ 26
1.1	39.950±0.711	0.136±0.007	-3.033±0.535	1.171±0.003	0.00416	6.53/ 18
1.3	36.990±1.021	0.132±0.012	-3.581±0.905	1.181±0.005	0.0107	5.99/ 11
4 $A{\cdot}GeV$, 23-39% Central						
0.7	28.652±0.435	0.116±0.010	-2.780±0.886	1.118±0.003	0.00846	12.52/ 29
0.9	25.948±0.399	0.138±0.008	-1.830±0.570	1.136±0.003	0.00482	0.05/ 1
1.1	23.579±0.481	0.143±0.009	-1.789±0.583	1.145±0.003	0.0053	11.03/ 18
1.3	21.775±0.663	0.121±0.011	-3.696±0.959	1.152±0.004	0.0101	2.91/ 11

y	proton dN/dy	proton T (GeV)	γ	$\langle m_\perp \rangle$ (GeV)	$\sigma_{T\gamma}$ $\left(\text{GeV}^2\right)$	χ^2/d.o.f.
6 $A{\cdot}GeV$, 0-5% Central						
0.7	62.626±0.856	0.113±0.009	-5.363±0.870	1.183±0.003	0.00747	23.48/ 33
0.9	63.775±0.942	0.105±0.005	-7.086±0.553	1.213±0.004	0.00278	57.25/ 26
1.1	65.038±1.266	0.146±0.022	-3.839±1.415	1.232±0.004	0.0308	8.41/ 19
1.3	65.149±1.625	0.150±0.022	-3.719±1.291	1.239±0.006	0.0277	6.89/ 12
6 $A{\cdot}GeV$, 5-12% Central						
0.7	54.023±0.712	0.121±0.009	-4.295±0.814	1.173±0.003	0.00756	24.54/ 31
0.9	54.154±0.805	0.130±0.011	-4.224±0.914	1.199±0.004	0.0104	15.39/ 26
1.1	53.985±0.874	0.143±0.014	-3.585±0.931	1.211±0.004	0.0131	12.97/ 19
1.3	52.568±1.246	0.143±0.019	-3.970±1.228	1.229±0.005	0.0229	4.01/ 12
6 $A{\cdot}GeV$, 12-23% Central						
0.7	41.338±0.531	0.131±0.010	-3.085±0.771	1.159±0.003	0.00786	13.85/ 30
0.9	39.053±0.589	0.138±0.012	-3.231±0.882	1.183±0.004	0.0109	12.27/ 26
1.1	38.674±0.603	0.146±0.014	-3.185±0.880	1.202±0.004	0.0123	12.21/ 19
1.3	38.007±1.120	0.151±0.029	-3.124±1.707	1.213±0.005	0.0487	3.29/ 12
6 $A{\cdot}GeV$, 23-39% Central						
0.7	29.207±0.392	0.132±0.011	-2.211±0.824	1.136±0.003	0.0092	18.34/ 31
0.9	26.247±0.422	0.133±0.013	-2.952±0.955	1.160±0.004	0.012	19.03/ 26
1.1	25.158±0.418	0.151±0.016	-2.216±0.915	1.176±0.003	0.0144	4.80/ 19
1.3	25.709±0.678	0.223±0.044	0.383±1.196	1.186±0.005	0.0523	5.09/ 12

y	proton dN/dy	proton T (GeV)	γ	$\langle m_\perp \rangle$ (GeV)	$\sigma_{T\gamma}$ $\left(\text{GeV}^2\right)$	χ^2/d.o.f.
8 $A{\cdot}GeV$, 0-5% Central						
0.7	60.929±0.796	0.131±0.011	-3.659±0.837	1.178±0.003	0.00907	17.72/ 31
0.9	64.574±0.904	0.126±0.009	-4.825±0.722	1.211±0.004	0.00626	17.21/ 26
1.1	64.521±1.163	0.136±0.018	-4.712±1.335	1.240±0.004	0.0235	8.79/ 19
1.3	59.570±1.295	0.105±0.010	-8.090±1.207	1.257±0.005	0.012	4.25/ 12
8 $A{\cdot}GeV$, 5-12% Central						
0.7	51.502±0.644	0.130±0.010	-3.607±0.791	1.174±0.003	0.00806	23.15/ 33
0.9	52.544±0.727	0.133±0.009	-4.143±0.688	1.205±0.003	0.00627	12.27/ 26
1.1	51.294±0.762	0.141±0.011	-3.972±0.773	1.224±0.004	0.0089	7.65/ 19
1.3	49.409±1.120	0.136±0.016	-4.851±1.142	1.247±0.005	0.0178	8.93/ 12
8 $A{\cdot}GeV$, 12-23% Central						
0.7	41.398±0.546	0.137±0.016	-2.646±1.134	1.159±0.003	0.0179	33.05/ 33
0.9	39.378±0.542	0.135±0.009	-3.635±0.660	1.191±0.003	0.00601	13.05/ 26
1.1	37.692±0.550	0.152±0.012	-3.077±0.730	1.212±0.003	0.00912	6.51/ 19
1.3	37.211±0.883	0.147±0.020	-3.620±1.237	1.226±0.005	0.0246	2.45/ 12
8 $A{\cdot}GeV$, 23-39% Central						
0.7	28.671±0.364	0.143±0.012	-1.655±0.768	1.140±0.003	0.00926	20.85/ 32
0.9	25.903±0.391	0.159±0.013	-1.440±0.687	1.164±0.003	0.00885	16.43/ 26
1.1	24.149±0.380	0.149±0.012	-2.564±0.763	1.183±0.003	0.0096	22.85/ 19
1.3	23.699±0.665	0.197±0.040	-0.628±1.381	1.196±0.005	0.0546	4.13/ 12

Appendix E

Tables of $m_\perp$ distributions, all rapidities

This appendix contains tables of the invariant differential yields of particles, $\frac{1}{2\pi m_\perp}\frac{d^2N}{dYdm_\perp}$, as a function of $m_\perp$. The data have been fully corrected for acceptance and efficiencies, and have been divided by particle type, energy, centrality class, and Y bin.

K^+ 2 $A{\cdot}GeV$, 0-5% Central					
Y: 0.6 - 0.8		Y: 0.8 - 1		Y: 1 - 1.2	
$m_\perp$	Yield	$m_\perp$	Yield	$m_\perp$	Yield
0.58	0.38±0.06	0.58	0.31±0.05	0.626	0.27±0.04
0.63	0.27±0.03	0.63	0.28±0.04	0.675	0.18±0.02
0.67	0.19±0.02	0.68	0.26±0.03	0.725	0.13±0.02
0.72	0.13±0.02	0.73	0.11±0.02	0.774	0.063±0.01
0.77	0.11±0.01	0.78	0.093±0.01	0.825	0.062±0.01
0.82	0.067±0.01	0.83	0.069±0.009	0.876	0.046±0.009
0.87	0.058±0.009	0.87	0.049±0.007	0.925	0.021±0.006
0.92	0.023±0.006	0.93	0.032±0.005	0.975	0.02±0.006
0.97	0.022±0.006	0.98	0.029±0.005		
1.02	0.013±0.004	1.03	0.01±0.003		
1.07	0.012±0.004	1.07	0.0086±0.002		
1.12	0.0045±0.002	1.12	0.0077±0.002		
1.17	0.0018±0.001				

K^+ 2 $A{\cdot}GeV$, 5-12% Central					
Y: 0.6 - 0.8		Y: 0.8 - 1		Y: 1 - 1.2	
$m_\perp$	Yield	$m_\perp$	Yield	$m_\perp$	Yield
0.58	0.3±0.04	0.58	0.19±0.03	0.626	0.17±0.02
0.63	0.2±0.02	0.63	0.2±0.03	0.675	0.14±0.02
0.67	0.12±0.01	0.68	0.12±0.02	0.725	0.077±0.01
0.72	0.089±0.01	0.73	0.094±0.01	0.774	0.05±0.01
0.77	0.064±0.009	0.78	0.069±0.009	0.825	0.032±0.007
0.82	0.05±0.007	0.83	0.051±0.006	0.876	0.033±0.007
0.87	0.03±0.006	0.87	0.034±0.005	0.925	0.015±0.004
0.92	0.021±0.005	0.93	0.024±0.004	0.975	0.011±0.003
0.97	0.011±0.003	0.98	0.012±0.002		
1.02	0.011±0.003	1.03	0.006±0.002		
1.07	0.0066±0.002	1.07	0.0065±0.002		
1.12	0.0041±0.002	1.12	0.0062±0.002		
1.17	00±0.0006				

K^+ 2 $A{\cdot}GeV$, 12-23% Central					
Y: 0.6 - 0.8		Y: 0.8 - 1		Y: 1 - 1.2	
$m_\perp$	Yield	$m_\perp$	Yield	$m_\perp$	Yield
0.58	0.14±0.02	0.58	0.19±0.03	0.626	0.1±0.02
0.63	0.12±0.01	0.63	0.12±0.02	0.675	0.061±0.009
0.67	0.096±0.01	0.68	0.077±0.01	0.725	0.044±0.007
0.72	0.05±0.006	0.73	0.06±0.008	0.774	0.039±0.007
0.77	0.039±0.005	0.78	0.037±0.005	0.825	0.023±0.005
0.82	0.027±0.004	0.83	0.025±0.003	0.876	0.013±0.003
0.87	0.02±0.004	0.87	0.018±0.003	0.925	0.0064±0.002
0.92	0.0087±0.002	0.93	0.0099±0.002	0.975	0.0072±0.002
0.97	0.01±0.002	0.98	0.0082±0.002		
1.02	0.0026±0.001	1.03	0.0057±0.001		
1.07	0.0034±0.001	1.07	0.0037±0.001		
1.12	0.0012±0.0008	1.12	0.0014±0.0006		
1.17	0.0021±0.001				

K^+ 2 $A{\cdot}GeV$, 23-39% Central					
Y: 0.6 - 0.8		Y: 0.8 - 1		Y: 1 - 1.2	
$m_\perp$	Yield	$m_\perp$	Yield	$m_\perp$	Yield
0.58	0.079±0.01	0.58	0.083±0.01	0.626	0.064±0.01
0.63	0.073±0.009	0.63	0.069±0.01	0.675	0.031±0.005
0.67	0.043±0.005	0.68	0.049±0.007	0.725	0.027±0.005
0.72	0.034±0.004	0.73	0.024±0.004	0.774	0.012±0.003
0.77	0.016±0.003	0.78	0.018±0.003	0.825	0.0096±0.003
0.82	0.016±0.003	0.83	0.011±0.002	0.876	0.0046±0.002
0.87	0.0097±0.002	0.87	0.0061±0.001	0.925	0.0048±0.001
0.92	0.0044±0.001	0.93	0.005±0.001	0.975	0.0022±0.001
0.97	0.0024±0.0009	0.98	0.0031±0.0008		
1.02	0.0022±0.0009	1.03	0.0024±0.0007		
1.07	0.00064±0.0005	1.07	0.0013±0.0005		
1.12	0.00063±0.0005	1.12	0.0007±0.0003		

K^+ 4 $A{\cdot}GeV$, 0-5% Central							
Y: 0.6 - 0.8		Y: 0.8 - 1		Y: 1 - 1.2		Y: 1.2 - 1.4	
$m_\perp$	Yield	$m_\perp$	Yield	$m_\perp$	Yield	$m_\perp$	Yield
0.58	2.1±0.2	0.58	02±0.2	0.58	02±0.2	0.625	1.4±0.1
0.63	1.5±0.1	0.63	1.6±0.1	0.63	1.6±0.1	0.677	01±0.1
0.68	01±0.07	0.68	1.2±0.08	0.68	1.2±0.09	0.726	0.88±0.08
0.72	0.76±0.05	0.73	0.83±0.06	0.72	0.85±0.07	0.775	0.65±0.06
0.78	0.51±0.04	0.77	0.63±0.04	0.78	0.65±0.05	0.824	0.48±0.05
0.83	0.35±0.03	0.82	0.41±0.03	0.83	0.48±0.04		
0.88	0.25±0.02	0.87	0.29±0.02	0.88	0.31±0.03		
0.92	0.2±0.02	0.93	0.23±0.02	0.93	0.24±0.02		
0.98	0.12±0.01	0.98	0.17±0.02	0.97	0.18±0.02		
1.02	0.092±0.01	1.03	0.13±0.01				
1.07	0.066±0.008	1.08	0.09±0.009				
1.13	0.041±0.006	1.12	0.053±0.007				
1.17	0.034±0.005	1.17	0.039±0.007				
1.23	0.021±0.004						

K^+ 4 $A{\cdot}GeV$, 5-12% Central							
Y: 0.6 - 0.8		Y: 0.8 - 1		Y: 1 - 1.2		Y: 1.2 - 1.4	
$m_\perp$	Yield	$m_\perp$	Yield	$m_\perp$	Yield	$m_\perp$	Yield
0.58	1.4±0.1	0.58	1.5±0.1	0.58	1.6±0.2	0.625	1.1±0.1
0.63	1.2±0.09	0.63	1.1±0.09	0.63	1.1±0.1	0.677	0.81±0.08
0.68	0.78±0.06	0.68	0.85±0.06	0.68	01±0.07	0.726	0.68±0.06
0.72	0.5±0.04	0.73	0.63±0.04	0.72	0.68±0.05	0.775	0.57±0.05
0.78	0.39±0.03	0.77	0.45±0.03	0.78	0.46±0.04	0.824	0.31±0.03
0.83	0.32±0.02	0.82	0.34±0.02	0.83	0.33±0.03		
0.88	0.2±0.02	0.87	0.24±0.02	0.88	0.24±0.02		
0.92	0.13±0.01	0.93	0.18±0.01	0.93	0.17±0.02		
0.98	0.089±0.009	0.98	0.13±0.01	0.97	0.12±0.01		
1.02	0.072±0.007	1.03	0.079±0.008				
1.07	0.052±0.006	1.08	0.063±0.007				
1.13	0.03±0.004	1.12	0.043±0.005				
1.17	0.025±0.004	1.17	0.023±0.004				
1.23	0.017±0.003						

K^+ 4 $A{\cdot}GeV$, 12-23% Central							
Y: 0.6 - 0.8		Y: 0.8 - 1		Y: 1 - 1.2		Y: 1.2 - 1.4	
$m_\perp$	Yield	$m_\perp$	Yield	$m_\perp$	Yield	$m_\perp$	Yield
0.58	1.2±0.1	0.58	01±0.09	0.58	1.1±0.1	0.625	0.8±0.07
0.63	0.79±0.06	0.63	0.78±0.06	0.63	0.8±0.06	0.677	0.59±0.05
0.68	0.53±0.04	0.68	0.54±0.04	0.68	0.6±0.04	0.726	0.39±0.03
0.72	0.34±0.02	0.73	0.38±0.03	0.72	0.46±0.03	0.775	0.34±0.03
0.78	0.26±0.02	0.77	0.29±0.02	0.78	0.35±0.03	0.824	0.25±0.03
0.83	0.16±0.01	0.82	0.21±0.01	0.83	0.22±0.02		
0.88	0.12±0.01	0.87	0.14±0.01	0.88	0.14±0.01		
0.92	0.074±0.007	0.93	0.1±0.009	0.93	0.11±0.01		
0.98	0.049±0.005	0.98	0.07±0.006	0.97	0.088±0.009		
1.02	0.039±0.004	1.03	0.043±0.005				
1.07	0.035±0.004	1.08	0.034±0.004				
1.13	0.02±0.003	1.12	0.024±0.003				
1.17	0.016±0.002	1.17	0.019±0.003				
1.23	0.0068±0.001						

K^+ 4 $A{\cdot}GeV$, 23-39% Central							
Y: 0.6 - 0.8		Y: 0.8 - 1		Y: 1 - 1.2		Y: 1.2 - 1.4	
$m_\perp$	Yield	$m_\perp$	Yield	$m_\perp$	Yield	$m_\perp$	Yield
0.58	0.57±0.05	0.58	0.58±0.06	0.58	0.57±0.06	0.625	0.39±0.04
0.63	0.44±0.03	0.63	0.42±0.03	0.63	0.42±0.04	0.677	0.3±0.03
0.68	0.28±0.02	0.68	0.3±0.02	0.68	0.3±0.02	0.726	0.23±0.02
0.72	0.17±0.01	0.73	0.21±0.02	0.72	0.18±0.02	0.775	0.15±0.01
0.78	0.12±0.01	0.77	0.14±0.01	0.78	0.15±0.01	0.824	0.11±0.01
0.83	0.087±0.007	0.82	0.11±0.009	0.83	0.13±0.01		
0.88	0.059±0.005	0.87	0.074±0.006	0.88	0.074±0.007		
0.92	0.04±0.004	0.93	0.058±0.005	0.93	0.056±0.005		
0.98	0.026±0.003	0.98	0.035±0.004	0.97	0.033±0.004		
1.02	0.014±0.002	1.03	0.022±0.003				
1.07	0.013±0.002	1.08	0.016±0.002				
1.13	0.007±0.001	1.12	0.0098±0.002				
1.17	0.0041±0.0009	1.17	0.0099±0.002				
1.23	0.0037±0.0008						

K^+ 6 $A{\cdot}GeV$, 0-5% Central							
Y: 0.6 - 0.8		Y: 0.8 - 1		Y: 1 - 1.2		Y: 1.2 - 1.4	
$m_\perp$	Yield	$m_\perp$	Yield	$m_\perp$	Yield	$m_\perp$	Yield
0.58	3.7±0.3	0.54	4.6±0.4	0.58	3.5±0.2	0.576	3.7±0.2
0.63	2.7±0.2	0.57	4.1±0.3	0.62	03±0.2	0.627	2.8±0.2
0.68	2.2±0.1	0.63	3.3±0.2	0.67	2.2±0.1	0.675	2.2±0.1
0.73	1.7±0.08	0.68	2.6±0.2	0.72	1.8±0.1	0.725	1.7±0.1
0.77	1.3±0.06	0.73	1.9±0.1	0.77	1.3±0.1	0.775	1.4±0.08
0.83	0.89±0.05	0.78	1.4±0.08	0.83	1.1±0.1	0.823	1.1±0.08
0.88	0.72±0.04	0.83	01±0.06	0.88	0.93±0.08		
0.93	0.47±0.03	0.88	0.8±0.05	0.93	0.66±0.06		
0.97	0.36±0.02	0.93	0.54±0.03	0.97	0.49±0.05		
1.02	0.26±0.02	0.98	0.47±0.03				
1.08	0.2±0.01	1.03	0.31±0.02				
1.12	0.14±0.01	1.08	0.27±0.02				
1.18	0.097±0.009	1.12	0.19±0.01				
1.23	0.069±0.007						
1.27	0.055±0.007						

K^+ 6 $A{\cdot}GeV$, 5-12% Central							
Y: 0.6 - 0.8		Y: 0.8 - 1		Y: 1 - 1.2		Y: 1.2 - 1.4	
$m_\perp$	Yield	$m_\perp$	Yield	$m_\perp$	Yield	$m_\perp$	Yield
0.58	2.5±0.2	0.54	3.5±0.3	0.58	3.1±0.2	0.576	2.9±0.2
0.63	2.1±0.1	0.57	03±0.2	0.62	2.3±0.1	0.627	2.3±0.1
0.68	1.6±0.08	0.63	2.5±0.2	0.67	1.9±0.1	0.675	1.8±0.09
0.73	1.2±0.06	0.68	1.8±0.1	0.72	1.4±0.09	0.725	1.5±0.08
0.77	0.9±0.04	0.73	1.3±0.09	0.77	1.1±0.08	0.775	1.1±0.06
0.83	0.66±0.03	0.78	01±0.06	0.83	0.89±0.07	0.823	0.82±0.06
0.88	0.51±0.03	0.83	0.8±0.04	0.88	0.71±0.06		
0.93	0.37±0.02	0.88	0.59±0.03	0.93	0.43±0.04		
0.97	0.27±0.02	0.93	0.46±0.03	0.97	0.38±0.04		
1.02	0.19±0.01	0.98	0.32±0.02				
1.08	0.14±0.01	1.03	0.25±0.02				
1.12	0.11±0.009	1.08	0.18±0.01				
1.18	0.082±0.007	1.12	0.13±0.01				
1.23	0.055±0.006						
1.27	0.036±0.004						

K^+ 6 $A{\cdot}GeV$, 12-23% Central							
Y: 0.6 - 0.8		Y: 0.8 - 1		Y: 1 - 1.2		Y: 1.2 - 1.4	
$m_\perp$	Yield	$m_\perp$	Yield	$m_\perp$	Yield	$m_\perp$	Yield
0.58	2.2±0.2	0.54	2.4±0.2	0.58	2.1±0.1	0.576	02±0.1
0.63	1.5±0.08	0.57	02±0.1	0.62	1.7±0.09	0.627	1.4±0.08
0.68	1.1±0.05	0.63	1.6±0.1	0.67	1.3±0.07	0.675	1.2±0.06
0.73	0.85±0.04	0.68	1.3±0.08	0.72	0.98±0.06	0.725	0.9±0.05
0.77	0.6±0.03	0.73	0.94±0.06	0.77	0.75±0.05	0.775	0.74±0.04
0.83	0.46±0.02	0.78	0.73±0.04	0.83	0.64±0.05	0.823	0.62±0.04
0.88	0.34±0.02	0.83	0.53±0.03	0.88	0.4±0.03		
0.93	0.23±0.01	0.88	0.41±0.02	0.93	0.33±0.03		
0.97	0.18±0.01	0.93	0.3±0.02	0.97	0.25±0.02		
1.02	0.14±0.009	0.98	0.21±0.01				
1.08	0.093±0.007	1.03	0.17±0.01				
1.12	0.069±0.005	1.08	0.12±0.008				
1.18	0.043±0.004	1.12	0.088±0.006				
1.23	0.033±0.003						
1.27	0.027±0.003						

K^+ 6 $A{\cdot}GeV$, 23-39% Central							
Y: 0.6 - 0.8		Y: 0.8 - 1		Y: 1 - 1.2		Y: 1.2 - 1.4	
$m_\perp$	Yield	$m_\perp$	Yield	$m_\perp$	Yield	$m_\perp$	Yield
0.58	1.1±0.09	0.54	1.6±0.1	0.58	1.1±0.06	0.576	1.2±0.07
0.63	0.89±0.05	0.57	1.2±0.08	0.62	0.98±0.05	0.627	0.95±0.05
0.68	0.64±0.03	0.63	01±0.07	0.67	0.7±0.04	0.675	0.72±0.04
0.73	0.45±0.02	0.68	0.63±0.05	0.72	0.57±0.04	0.725	0.56±0.03
0.77	0.33±0.02	0.73	0.51±0.03	0.77	0.38±0.03	0.775	0.41±0.02
0.83	0.24±0.01	0.78	0.4±0.02	0.83	0.28±0.03	0.823	0.32±0.02
0.88	0.17±0.01	0.83	0.29±0.02	0.88	0.24±0.02		
0.93	0.13±0.008	0.88	0.2±0.01	0.93	0.16±0.02		
0.97	0.085±0.006	0.93	0.16±0.01	0.97	0.12±0.01		
1.02	0.067±0.005	0.98	0.1±0.007				
1.08	0.045±0.004	1.03	0.078±0.006				
1.12	0.031±0.003	1.08	0.059±0.004				
1.18	0.026±0.003	1.12	0.039±0.003				
1.23	0.018±0.002						
1.27	0.013±0.002						

K^+ 8 $A{\cdot}GeV$, 0-5% Central							
Y: 0.6 - 0.8		Y: 0.8 - 1		Y: 1 - 1.2		Y: 1.2 - 1.4	
$m_\perp$	Yield	$m_\perp$	Yield	$m_\perp$	Yield	$m_\perp$	Yield
0.58	5.3±0.4	0.58	5.3±0.5	0.58	4.4±0.4	0.581	4.6±0.7
0.63	3.7±0.3	0.63	4.4±0.3	0.63	4.5±0.4	0.628	4.9±0.4
0.68	2.8±0.2	0.68	3.5±0.2	0.68	3.3±0.3	0.675	3.5±0.3
0.72	2.1±0.1	0.73	2.6±0.2	0.73	2.7±0.2	0.725	2.8±0.2
0.77	1.5±0.1	0.78	1.9±0.1	0.78	2.4±0.2	0.775	2.2±0.2
0.82	1.1±0.09	0.82	1.4±0.09	0.83	1.6±0.1	0.823	1.9±0.2
0.87	0.87±0.07	0.88	1.1±0.08	0.88	1.3±0.1		
0.92	0.69±0.06	0.93	0.84±0.06	0.93	1.1±0.08		
0.98	0.43±0.04	0.98	0.66±0.05	0.97	0.77±0.07		
1.02	0.39±0.04	1.03	0.47±0.04				
1.08	0.26±0.03	1.07	0.35±0.03				
1.12	0.17±0.02	1.12	0.26±0.03				
1.18	0.13±0.02						
1.23	0.12±0.02						

K^+ 8 $A{\cdot}GeV$, 5-12% Central							
Y: 0.6 - 0.8		Y: 0.8 - 1		Y: 1 - 1.2		Y: 1.2 - 1.4	
$m_\perp$	Yield	$m_\perp$	Yield	$m_\perp$	Yield	$m_\perp$	Yield
0.58	3.9±0.3	0.58	4.3±0.4	0.58	3.5±0.3	0.581	4.8±0.6
0.63	3.1±0.2	0.63	3.4±0.2	0.63	3.3±0.3	0.628	3.6±0.3
0.68	2.1±0.1	0.68	2.8±0.2	0.68	2.6±0.2	0.675	2.6±0.2
0.72	1.7±0.1	0.73	1.9±0.1	0.73	1.9±0.1	0.725	02±0.2
0.77	1.2±0.08	0.78	1.5±0.09	0.78	1.7±0.1	0.775	1.7±0.1
0.82	0.95±0.07	0.82	1.1±0.07	0.83	1.1±0.08	0.823	1.3±0.1
0.87	0.68±0.05	0.88	0.83±0.06	0.88	01±0.07		
0.92	0.49±0.04	0.93	0.66±0.05	0.93	0.82±0.06		
0.98	0.36±0.03	0.98	0.46±0.04	0.97	0.59±0.05		
1.02	0.27±0.03	1.03	0.35±0.03				
1.08	0.17±0.02	1.07	0.28±0.02				
1.12	0.17±0.02	1.12	0.19±0.02				
1.18	0.13±0.02						
1.23	0.082±0.01						

K^+ 8 $A{\cdot}GeV$, 12-23% Central							
Y: 0.6 - 0.8		Y: 0.8 - 1		Y: 1 - 1.2		Y: 1.2 - 1.4	
$m_\perp$	Yield	$m_\perp$	Yield	$m_\perp$	Yield	$m_\perp$	Yield
0.58	2.5±0.2	0.58	03±0.2	0.58	03±0.2	0.581	2.7±0.3
0.63	02±0.1	0.63	2.3±0.2	0.63	2.3±0.2	0.628	2.3±0.2
0.68	1.4±0.09	0.68	1.7±0.1	0.68	1.9±0.1	0.675	1.9±0.1
0.72	1.1±0.07	0.73	1.3±0.08	0.73	1.4±0.1	0.725	1.4±0.1
0.77	0.89±0.06	0.78	0.98±0.06	0.78	1.1±0.08	0.775	1.1±0.09
0.82	0.61±0.04	0.82	0.78±0.05	0.83	0.83±0.06	0.823	0.9±0.09
0.87	0.4±0.03	0.88	0.56±0.04	0.88	0.62±0.04		
0.92	0.32±0.03	0.93	0.44±0.03	0.93	0.51±0.04		
0.98	0.2ɔ±0.02	0.98	0.3±0.02	0.97	0.39±0.04		
1.02	0.19±0.02	1.03	0.27±0.02				
1.08	0.14±0.01	1.07	0.19±0.02				
1.12	0.093±0.01	1.12	0.14±0.01				
1.18	0.073±0.01						
1.23	0.048±0.008						

K^+ 8 $A{\cdot}GeV$, 23-39% Central							
Y: 0.6 - 0.8		Y: 0.8 - 1		Y: 1 - 1.2		Y: 1.2 - 1.4	
$m_\perp$	Yield	$m_\perp$	Yield	$m_\perp$	Yield	$m_\perp$	Yield
0.58	1.6±0.1	0.58	1.7±0.1	0.58	1.7±0.1	0.581	02±0.2
0.63	1.1±0.08	0.63	1.2±0.09	0.63	1.4±0.1	0.628	1.4±0.1
0.68	0.84±0.05	0.68	0.97±0.07	0.68	01±0.08	0.675	1.1±0.08
0.72	0.64±0.04	0.73	0.68±0.05	0.73	0.84±0.06	0.725	0.8±0.06
0.77	0.44±0.03	0.78	0.55±0.04	0.78	0.62±0.05	0.775	0.58±0.05
0.82	0.3±0.02	0.82	0.44±0.03	0.83	0.45±0.03	0.823	0.51±0.05
0.87	0.25±0.02	0.88	0.3±0.02	0.88	0.38±0.03		
0.92	0.18±0.02	0.93	0.22±0.02	0.93	0.28±0.02		
0.98	0.14±0.01	0.98	0.16±0.01	0.97	0.2±0.02		
1.02	0.084±0.01	1.03	0.13±0.01				
1.08	0.073±0.009	1.07	0.099±0.009				
1.12	0.055±0.007	1.12	0.051±0.006				
1.18	0.037±0.006						
1.23	0.017±0.004						

K^- 4 $A{\cdot}GeV$, 0-5% Central							
Y: 0.6 - 0.8		Y: 0.8 - 1		Y: 1 - 1.2		Y: 1.2 - 1.4	
$m_\perp$	Yield	$m_\perp$	Yield	$m_\perp$	Yield	$m_\perp$	Yield
0.58	0.2±0.04	0.53	0.28±0.1	0.58	0.18±0.04	0.577	0.15±0.05
0.63	0.094±0.02	0.58	0.19±0.04	0.63	0.16±0.03	0.627	0.15±0.03
0.68	0.087±0.01	0.63	0.16±0.03	0.68	0.095±0.02	0.676	0.069±0.02
0.73	0.043±0.008	0.68	0.098±0.02	0.73	0.047±0.01	0.725	0.089±0.02
0.77	0.042±0.008	0.73	0.071±0.01	0.78	0.054±0.01	0.775	0.043±0.01
0.83	0.026±0.006	0.78	0.052±0.008	0.83	0.027±0.007	0.824	0.042±0.01
0.87	0.021±0.005	0.83	0.04±0.007	0.88	0.017±0.005		
0.93	0.012±0.003	0.87	0.024±0.005	0.93	0.014±0.004		
0.98	0.017±0.004	0.93	0.014±0.003	0.97	0.013±0.004		
1.02	0.0055±0.002	0.97	0.012±0.003				
1.08	0.0027±0.001	1.02	0.0086±0.002				
1.12	0.0034±0.001	1.07	0.005±0.002				
1.18	0.00056±0.0006	1.12	0.0095±0.003				
1.23	0.00099±0.0007						

K^- 4 $A{\cdot}GeV$, 5-12% Central							
Y: 0.6 - 0.8		Y: 0.8 - 1		Y: 1 - 1.2		Y: 1.2 - 1.4	
$m_\perp$	Yield	$m_\perp$	Yield	$m_\perp$	Yield	$m_\perp$	Yield
0.58	0.15±0.03	0.53	0.18±0.07	0.58	0.17±0.03	0.577	0.15±0.04
0.63	0.1±0.02	0.58	0.19±0.04	0.63	0.099±0.02	0.627	0.12±0.02
0.68	0.046±0.008	0.63	0.14±0.02	0.68	0.089±0.01	0.676	0.066±0.02
0.73	0.037±0.007	0.68	0.062±0.01	0.73	0.051±0.01	0.725	0.061±0.01
0.77	0.017±0.004	0.73	0.045±0.008	0.78	0.038±0.008	0.775	0.036±0.009
0.83	0.018±0.004	0.78	0.039±0.006	0.83	0.023±0.006	0.824	0.035±0.009
0.87	0.013±0.003	0.83	0.018±0.004	0.88	0.023±0.005		
0.93	0.01±0.002	0.87	0.011±0.003	0.93	0.013±0.003		
0.98	0.0055±0.002	0.93	0.014±0.003	0.97	0.0083±0.003		
1.02	0.003±0.001	0.97	0.0061±0.002				
1.08	0.0019±0.001	1.02	0.0048±0.002				
1.12	0.0036±0.001	1.07	0.0053±0.002				
1.18	0.0011±0.0007	1.12	0.0022±0.001				
1.23	0.0014±0.0007						

K^- 4 $A{\cdot}GeV$, 12-23% Central							
Y: 0.6 - 0.8		Y: 0.8 - 1		Y: 1 - 1.2		Y: 1.2 - 1.4	
$m_\perp$	Yield	$m_\perp$	Yield	$m_\perp$	Yield	$m_\perp$	Yield
0.58	0.076±0.02	0.53	0.13±0.05	0.58	0.17±0.03	0.577	0.058±0.02
0.63	0.049±0.009	0.58	0.13±0.02	0.63	0.084±0.02	0.627	0.065±0.01
0.68	0.037±0.006	0.63	0.068±0.01	0.68	0.052±0.009	0.676	0.045±0.01
0.73	0.024±0.004	0.68	0.054±0.008	0.73	0.027±0.005	0.725	0.036±0.008
0.77	0.016±0.003	0.73	0.031±0.005	0.78	0.03±0.005	0.775	0.018±0.005
0.83	0.0089±0.002	0.78	0.022±0.004	0.83	0.013±0.003	0.824	0.016±0.005
0.87	0.0081±0.002	0.83	0.013±0.002	0.88	0.014±0.003		
0.93	0.0039±0.001	0.87	0.0083±0.002	0.93	0.0062±0.002		
0.98	0.0028±0.001	0.93	0.0081±0.002	0.97	0.0025±0.001		
1.02	0.002±0.0008	0.97	0.0034±0.001				
1.08	0.00093±0.0005	1.02	0.0029±0.001				
1.12	0.002±0.0007	1.07	0.0024±0.0008				
1.18	0.0011±0.0005	1.12	0.0013±0.0006				
1.23	0.00062±0.0004						

K^- 4 $A{\cdot}GeV$, 23-39% Central							
Y: 0.6 - 0.8		Y: 0.8 - 1		Y: 1 - 1.2		Y: 1.2 - 1.4	
$m_\perp$	Yield	$m_\perp$	Yield	$m_\perp$	Yield	$m_\perp$	Yield
0.58	0.057±0.01	0.53	0.11±0.03	0.58	0.058±0.01	0.577	0.055±0.01
0.63	0.033±0.006	0.58	0.07±0.01	0.63	0.039±0.008	0.627	0.053±0.01
0.68	0.02±0.004	0.63	0.031±0.006	0.68	0.023±0.005	0.676	0.034±0.007
0.73	0.011±0.002	0.68	0.025±0.004	0.73	0.016±0.003	0.725	0.011±0.004
0.77	0.0073±0.002	0.73	0.017±0.003	0.78	0.013±0.003	0.775	0.012±0.004
0.83	0.0069±0.002	0.78	0.0066±0.002	0.83	0.0068±0.002	0.824	0.011±0.003
0.87	0.0041±0.001	0.83	0.0081±0.002	0.88	0.004±0.001		
0.93	0.003±0.0009	0.87	0.0054±0.001	0.93	0.004±0.001		
0.98	0.002±0.0007	0.93	0.0033±0.0009	0.97	0.0018±0.0008		
1.02	0.00087±0.0004	0.97	0.0023±0.0007				
1.08	0.00015±0.0002	1.02	0.0012±0.0005				
1.12	0.00061±0.0003	1.07	0.00072±0.0004				
1.18	0.00016±0.0002	1.12	0.00029±0.0002				
1.23	0.00016±0.0002						

K^- 6 $A{\cdot}GeV$, 0-5% Central							
Y: 0.6 - 0.8		Y: 0.8 - 1		Y: 1 - 1.2		Y: 1.2 - 1.4	
$m_\perp$	Yield	$m_\perp$	Yield	$m_\perp$	Yield	$m_\perp$	Yield
0.58	0.53±0.1	0.54	0.65±0.1	0.58	0.5±0.06	0.576	0.61±0.09
0.63	0.32±0.05	0.57	0.5±0.08	0.62	0.4±0.05	0.628	0.42±0.05
0.68	0.24±0.03	0.62	0.38±0.08	0.67	0.33±0.04	0.675	0.3±0.04
0.73	0.16±0.02	0.68	0.26±0.05	0.72	0.22±0.04	0.725	0.26±0.03
0.77	0.16±0.02	0.73	0.16±0.03	0.77	0.14±0.03	0.775	0.18±0.02
0.83	0.095±0.01	0.78	0.14±0.02	0.82	0.089±0.02	0.823	0.12±0.02
0.88	0.063±0.008	0.83	0.11±0.02	0.88	0.097±0.02		
0.92	0.047±0.007	0.87	0.091±0.01	0.93	0.076±0.02		
0.98	0.048±0.006	0.93	0.059±0.009	0.97	0.043±0.01		
1.02	0.022±0.004	0.98	0.046±0.007				
1.07	0.023±0.004	1.03	0.034±0.006				
1.12	0.014±0.003	1.08	0.027±0.005				
1.17	0.0087±0.002	1.12	0.023±0.004				
1.23	0.0077±0.002						
1.27	0.0074±0.002						

K^- 6 $A{\cdot}GeV$, 5-12% Central							
Y: 0.6 - 0.8		Y: 0.8 - 1		Y: 1 - 1.2		Y: 1.2 - 1.4	
$m_\perp$	Yield	$m_\perp$	Yield	$m_\perp$	Yield	$m_\perp$	Yield
0.58	0.42±0.09	0.54	0.55±0.1	0.58	0.34±0.04	0.576	0.3±0.05
0.63	0.21±0.03	0.57	0.38±0.05	0.62	0.31±0.04	0.628	0.3±0.03
0.68	0.14±0.02	0.62	0.35±0.06	0.67	0.25±0.03	0.675	0.21±0.02
0.73	0.13±0.01	0.68	0.23±0.04	0.72	0.17±0.03	0.725	0.19±0.02
0.77	0.08±0.009	0.73	0.14±0.03	0.77	0.094±0.02	0.775	0.12±0.02
0.83	0.074±0.009	0.78	0.13±0.02	0.82	0.097±0.02	0.823	0.097±0.02
0.88	0.045±0.006	0.83	0.068±0.01	0.88	0.089±0.02		
0.92	0.032±0.005	0.87	0.069±0.009	0.93	0.051±0.01		
0.98	0.027±0.004	0.93	0.046±0.007	0.97	0.039±0.01		
1.02	0.017±0.003	0.98	0.03±0.005				
1.07	0.015±0.003	1.03	0.019±0.004				
1.12	0.0072±0.002	1.08	0.018±0.003				
1.17	0.0063±0.002	1.12	0.0099±0.002				
1.23	0.0035±0.001						
1.27	0.004±0.001						

K^- 6 $A{\cdot}GeV$, 12-23% Central							
Y: 0.6 - 0.8		Y: 0.8 - 1		Y: 1 - 1.2		Y: 1.2 - 1.4	
$m_\perp$	Yield	$m_\perp$	Yield	$m_\perp$	Yield	$m_\perp$	Yield
0.58	0.19±0.05	0.54	0.31±0.06	0.58	0.29±0.03	0.576	0.34±0.04
0.63	0.16±0.02	0.57	0.26±0.04	0.62	0.28±0.03	0.628	0.21±0.02
0.68	0.12±0.01	0.62	0.24±0.04	0.67	0.17±0.02	0.675	0.15±0.02
0.73	0.085±0.009	0.68	0.18±0.03	0.72	0.12±0.02	0.725	0.12±0.01
0.77	0.064±0.007	0.73	0.08±0.01	0.77	0.088±0.02	0.775	0.096±0.01
0.83	0.039±0.005	0.78	0.069±0.01	0.82	0.072±0.01	0.823	0.054±0.01
0.88	0.031±0.004	0.83	0.056±0.007	0.88	0.048±0.01		
0.92	0.022±0.003	0.87	0.038±0.005	0.93	0.025±0.007		
0.98	0.018±0.003	0.93	0.024±0.004	0.97	0.026±0.007		
1.02	0.011±0.002	0.98	0.017±0.003				
1.07	0.0073±0.001	1.03	0.012±0.002				
1.12	0.0075±0.002	1.08	0.011±0.002				
1.17	0.0039±0.001	1.12	0.0091±0.002				
1.23	0.0027±0.0009						
1.27	0.0027±0.001						

K^- 6 $A{\cdot}GeV$, 23-39% Central							
Y: 0.6 - 0.8		Y: 0.8 - 1		Y: 1 - 1.2		Y: 1.2 - 1.4	
$m_\perp$	Yield	$m_\perp$	Yield	$m_\perp$	Yield	$m_\perp$	Yield
0.58	0.11±0.03	0.54	0.21±0.04	0.58	0.21±0.02	0.576	0.18±0.02
0.63	0.074±0.01	0.57	0.15±0.02	0.62	0.12±0.01	0.628	0.12±0.01
0.68	0.058±0.008	0.62	0.11±0.02	0.67	0.1±0.01	0.675	0.08±0.009
0.73	0.044±0.005	0.68	0.068±0.01	0.72	0.062±0.01	0.725	0.064±0.008
0.77	0.034±0.004	0.73	0.064±0.01	0.77	0.06±0.01	0.775	0.049±0.007
0.83	0.026±0.003	0.78	0.048±0.007	0.82	0.032±0.007	0.823	0.033±0.006
0.88	0.018±0.002	0.83	0.026±0.004	0.88	0.027±0.006		
0.92	0.013±0.002	0.87	0.019±0.003	0.93	0.012±0.004		
0.98	0.0071±0.001	0.93	0.016±0.003	0.97	0.0086±0.003		
1.02	0.0058±0.001	0.98	0.011±0.002				
1.07	0.0046±0.001	1.03	0.0051±0.001				
1.12	0.0035±0.0008	1.08	0.0052±0.001				
1.17	0.0026±0.0007	1.12	0.0049±0.001				
1.23	0.0017±0.0006						
1.27	0.00092±0.0005						

K^- 8 $A{\cdot}GeV$, 0-5% Central							
Y: 0.6 - 0.8		Y: 0.8 - 1		Y: 1 - 1.2		Y: 1.2 - 1.4	
$m_\perp$	Yield	$m_\perp$	Yield	$m_\perp$	Yield	$m_\perp$	Yield
0.58	0.71±0.08	0.54	1.1±0.2	0.58	01±0.1	0.578	1.1±0.2
0.63	0.52±0.05	0.58	0.77±0.09	0.63	0.76±0.08	0.628	0.61±0.08
0.68	0.37±0.04	0.63	0.58±0.05	0.68	0.64±0.05	0.675	0.61±0.06
0.72	0.31±0.03	0.68	0.47±0.04	0.73	0.39±0.04	0.726	0.49±0.05
0.77	0.2±0.02	0.73	0.35±0.03	0.78	0.34±0.03	0.775	0.36±0.04
0.82	0.16±0.02	0.78	0.29±0.02	0.83	0.25±0.02	0.824	0.3±0.03
0.87	0.094±0.01	0.82	0.19±0.02	0.88	0.18±0.02		
0.92	0.079±0.01	0.87	0.14±0.01	0.93	0.15±0.01		
0.97	0.052±0.009	0.93	0.12±0.01	0.97	0.11±0.01		
1.02	0.031±0.007	0.98	0.099±0.01				
1.07	0.039±0.008	1.03	0.06±0.008				
1.12	0.027±0.006	1.07	0.042±0.006				
1.17	0.011±0.004	1.12	0.038±0.006				
1.23	0.012±0.004						

K^- 8 $A{\cdot}GeV$, 5-12% Central							
Y: 0.6 - 0.8		Y: 0.8 - 1		Y: 1 - 1.2		Y: 1.2 - 1.4	
$m_\perp$	Yield	$m_\perp$	Yield	$m_\perp$	Yield	$m_\perp$	Yield
0.58	0.52±0.06	0.54	0.74±0.2	0.58	0.73±0.09	0.578	0.84±0.1
0.63	0.37±0.04	0.58	0.65±0.07	0.63	0.56±0.05	0.628	0.54±0.06
0.68	0.3±0.03	0.63	0.53±0.04	0.68	0.4±0.04	0.675	0.46±0.05
0.72	0.19±0.02	0.68	0.37±0.03	0.73	0.33±0.03	0.726	0.41±0.04
0.77	0.15±0.02	0.73	0.3±0.02	0.78	0.21±0.02	0.775	0.29±0.03
0.82	0.12±0.01	0.78	0.21±0.02	0.83	0.19±0.02	0.824	0.2±0.02
0.87	0.093±0.01	0.82	0.17±0.01	0.88	0.13±0.01		
0.92	0.073±0.01	0.87	0.12±0.01	0.93	0.1±0.01		
0.97	0.038±0.007	0.93	0.083±0.009	0.97	0.067±0.009		
1.02	0.037±0.007	0.98	0.057±0.007				
1.07	0.031±0.006	1.03	0.048±0.006				
1.12	0.02±0.005	1.07	0.036±0.005				
1.17	0.015±0.004	1.12	0.021±0.004				
1.23	0.0065±0.002						

K^- 8 $A{\cdot}GeV$, 12-23% Central							
Y: 0.6 - 0.8		Y: 0.8 - 1		Y: 1 - 1.2		Y: 1.2 - 1.4	
$m_\perp$	Yield	$m_\perp$	Yield	$m_\perp$	Yield	$m_\perp$	Yield
0.58	0.4±0.04	0.54	0.63±0.1	0.58	0.52±0.06	0.578	0.63±0.09
0.63	0.3±0.03	0.58	0.49±0.05	0.63	0.37±0.03	0.628	0.38±0.04
0.68	0.21±0.02	0.63	0.34±0.03	0.68	0.32±0.03	0.675	0.34±0.03
0.72	0.15±0.01	0.68	0.25±0.02	0.73	0.22±0.02	0.726	0.24±0.02
0.77	0.12±0.01	0.73	0.18±0.01	0.78	0.18±0.01	0.775	0.15±0.02
0.82	0.074±0.009	0.78	0.14±0.01	0.83	0.12±0.01	0.824	0.14±0.02
0.87	0.052±0.007	0.82	0.1±0.009	0.88	0.099±0.009		
0.92	0.039±0.006	0.87	0.063±0.006	0.93	0.066±0.006		
0.97	0.027±0.005	0.93	0.053±0.006	0.97	0.051±0.006		
1.02	0.019±0.004	0.98	0.044±0.005				
1.07	0.018±0.004	1.03	0.028±0.004				
1.12	0.0069±0.002	1.07	0.023±0.003				
1.17	0.0035±0.001	1.12	0.014±0.002				
1.23	0.0049±0.002						

K^- 8 $A{\cdot}GeV$, 23-39% Central							
Y: 0.6 - 0.8		Y: 0.8 - 1		Y: 1 - 1.2		Y: 1.2 - 1.4	
$m_\perp$	Yield	$m_\perp$	Yield	$m_\perp$	Yield	$m_\perp$	Yield
0.58	0.25±0.03	0.54	0.37±0.07	0.58	0.35±0.04	0.578	0.32±0.05
0.63	0.18±0.02	0.58	0.3±0.03	0.63	0.25±0.02	0.628	0.24±0.03
0.68	0.12±0.01	0.63	0.24±0.02	0.68	0.18±0.02	0.675	0.2±0.02
0.72	0.081±0.008	0.68	0.15±0.01	0.73	0.11±0.01	0.726	0.12±0.01
0.77	0.048±0.006	0.73	0.1±0.009	0.78	0.082±0.008	0.775	0.11±0.01
0.82	0.043±0.006	0.78	0.066±0.006	0.83	0.065±0.006	0.824	0.077±0.009
0.87	0.028±0.004	0.82	0.05±0.005	0.88	0.055±0.005		
0.92	0.021±0.003	0.87	0.039±0.004	0.93	0.041±0.004		
0.97	0.015±0.003	0.93	0.027±0.003	0.97	0.024±0.003		
1.02	0.012±0.002	0.98	0.022±0.003				
1.07	0.0073±0.002	1.03	0.016±0.002				
1.12	0.0053±0.001	1.07	0.01±0.002				
1.17	0.0032±0.001	1.12	0.0077±0.001				
1.23	0.0031±0.001						

π^+ 2 $A{\cdot}GeV$, 0-5% Central					
Y: 0.8 - 1		Y: 1 - 1.2		Y: 1.2 - 1.4	
$m_\perp$	Yield	$m_\perp$	Yield	$m_\perp$	Yield
0.28	21±1	0.23	31±3	0.227	25±2
0.33	14±0.7	0.28	21±1	0.275	19±1
0.37	8.6±0.5	0.33	13±0.8	0.326	9.9±0.9
0.43	5.1±0.3	0.38	7.8±0.5	0.376	6.6±0.6
0.47	3.3±0.2	0.43	4.8±0.4	0.425	4.1±0.4
0.53	1.9±0.2	0.47	2.8±0.2	0.475	2.4±0.3
0.58	1.4±0.1	0.53	1.8±0.2	0.525	1.4±0.2
0.62	0.83±0.08	0.58	1.3±0.1	0.575	0.77±0.1
0.67	0.59±0.07	0.63	0.81±0.09	0.625	0.78±0.1
0.72	0.4±0.05	0.68	0.57±0.07	0.675	0.37±0.08
0.78	0.31±0.04	0.73	0.38±0.05	0.725	0.26±0.06
0.82	0.2±0.03	0.77	0.18±0.03	0.775	0.17±0.05
0.88	0.14±0.02	0.82	0.22±0.04	0.824	0.12±0.04
0.92	0.092±0.02	0.88	0.11±0.03	0.872	0.12±0.04
0.98	0.088±0.02	0.93	0.057±0.02		
1.03	0.055±0.01	0.97	0.032±0.01		
1.07	0.035±0.01	1.02	0.035±0.01		
1.12	0.021±0.008				

π^+ 2 $A{\cdot}GeV$, 5-12% Central					
Y: 0.8 - 1		Y: 1 - 1.2		Y: 1.2 - 1.4	
$m_\perp$	Yield	$m_\perp$	Yield	$m_\perp$	Yield
0.28	17±0.9	0.23	25±2	0.227	24±2
0.33	10±0.6	0.28	15±0.9	0.275	14±1
0.37	5.9±0.4	0.33	9.7±0.6	0.326	8.3±0.7
0.43	3.6±0.2	0.38	6.1±0.4	0.376	5.2±0.4
0.47	2.4±0.2	0.43	3.4±0.3	0.425	2.9±0.3
0.53	1.4±0.1	0.47	02±0.2	0.475	1.8±0.2
0.58	0.92±0.08	0.53	1.5±0.1	0.525	1.1±0.1
0.62	0.6±0.06	0.58	0.89±0.09	0.575	0.66±0.1
0.67	0.43±0.05	0.63	0.6±0.07	0.625	0.43±0.07
0.72	0.28±0.03	0.68	0.4±0.05	0.675	0.31±0.06
0.78	0.21±0.03	0.73	0.27±0.04	0.725	0.25±0.05
0.82	0.11±0.02	0.77	0.16±0.03	0.775	0.11±0.03
0.88	0.1±0.02	0.82	0.15±0.02	0.824	0.11±0.03
0.92	0.064±0.01	0.88	0.063±0.02	0.872	0.074±0.03
0.98	0.042±0.01	0.93	0.046±0.01		
1.03	0.031±0.009	0.97	0.025±0.009		
1.07	0.022±0.007	1.02	0.01±0.006		
1.12	0.015±0.006				

π^+ 2 $A{\cdot}GeV$, 12-23% Central					
Y: 0.8 - 1		Y: 1 - 1.2		Y: 1.2 - 1.4	
$m_\perp$	Yield	$m_\perp$	Yield	$m_\perp$	Yield
0.28	12±0.6	0.23	20±1	0.227	17±1
0.33	6.9±0.4	0.28	11±0.7	0.275	10±0.7
0.37	3.9±0.2	0.33	6.3±0.4	0.326	5.4±0.4
0.43	2.3±0.1	0.38	3.9±0.3	0.376	3.3±0.3
0.47	1.4±0.1	0.43	2.2±0.2	0.425	02±0.2
0.53	0.89±0.07	0.47	1.4±0.1	0.475	1.1±0.1
0.58	0.54±0.05	0.53	0.85±0.08	0.525	0.6±0.08
0.62	0.35±0.04	0.58	0.55±0.06	0.575	0.5±0.07
0.67	0.25±0.03	0.63	0.36±0.04	0.625	0.31±0.05
0.72	0.2±0.02	0.68	0.25±0.03	0.675	0.23±0.04
0.78	0.099±0.02	0.73	0.16±0.02	0.725	0.11±0.03
0.82	0.079±0.01	0.77	0.1±0.02	0.775	0.094±0.02
0.88	0.042±0.009	0.82	0.084±0.01	0.824	0.044±0.02
0.92	0.038±0.009	0.88	0.022±0.007	0.872	0.04±0.02
0.98	0.022±0.006	0.93	0.035±0.009		
1.03	0.01±0.004	0.97	0.013±0.005		
1.07	0.0072±0.003	1.02	0.019±0.007		
1.12	0.0046±0.002				

π^+ 2 $A{\cdot}GeV$, 23-39% Central					
Y: 0.8 - 1		Y: 1 - 1.2		Y: 1.2 - 1.4	
$m_\perp$	Yield	$m_\perp$	Yield	$m_\perp$	Yield
0.28	7.1±0.4	0.23	11±0.9	0.227	11±0.8
0.33	3.9±0.2	0.28	6.2±0.4	0.275	6.1±0.5
0.37	2.3±0.1	0.33	3.9±0.3	0.326	2.9±0.3
0.43	1.4±0.09	0.38	2.2±0.2	0.376	1.8±0.2
0.47	0.76±0.06	0.43	1.2±0.1	0.425	1.1±0.1
0.53	0.53±0.05	0.47	0.76±0.07	0.475	0.67±0.08
0.58	0.35±0.03	0.53	0.51±0.05	0.525	0.42±0.06
0.62	0.19±0.02	0.58	0.31±0.03	0.575	0.24±0.04
0.67	0.16±0.02	0.63	0.14±0.02	0.625	0.14±0.03
0.72	0.093±0.01	0.68	0.13±0.02	0.675	0.1±0.02
0.78	0.056±0.01	0.73	0.071±0.01	0.725	0.052±0.01
0.82	0.032±0.007	0.77	0.048±0.009	0.775	0.013±0.007
0.88	0.025±0.006	0.82	0.038±0.008	0.824	0.014±0.007
0.92	0.01±0.003	0.88	0.028±0.007	0.872	0.0091±0.007
0.98	0.0055±0.002	0.93	0.012±0.004		
1.03	0.0072±0.003	0.97	0.0058±0.003		
1.07	0.005±0.002	1.02	0.0098±0.004		
1.12	0.0033±0.002				

π^+ 4 $A{\cdot}GeV$, 0-5% Central							
Y: 0.8 - 1		Y: 1 - 1.2		Y: 1.2 - 1.4		Y: 1.4 - 1.6	
$m_\perp$	Yield	$m_\perp$	Yield	$m_\perp$	Yield	$m_\perp$	Yield
0.28	37±2	0.23	61±3	0.23	59±3	0.234	49±4
0.32	22±1	0.28	41±2	0.28	37±2	0.276	34±2
0.37	15±1	0.33	27±1	0.33	26±1	0.327	22±1
0.43	9.8±0.7	0.37	17±0.7	0.38	17±0.8	0.376	16±1
0.48	6.5±0.5	0.43	11±0.5	0.43	12±0.6	0.426	11±0.7
0.53	05±0.4	0.48	8.3±0.4	0.48	7.7±0.4	0.475	7.3±0.5
0.58	3.7±0.3	0.53	5.6±0.3	0.53	5.4±0.3	0.525	5.5±0.4
0.63	2.4±0.2	0.58	3.9±0.2	0.58	04±0.2	0.575	3.5±0.3
0.68	1.9±0.2	0.62	2.8±0.2	0.63	2.6±0.2	0.625	2.9±0.2
0.72	1.3±0.1	0.67	02±0.1	0.67	1.9±0.1	0.675	1.7±0.2
0.78	01±0.1	0.73	1.4±0.1	0.72	1.5±0.1	0.724	1.1±0.1
0.83	0.79±0.09	0.77	1.1±0.08	0.77	01±0.08		
0.88	0.59±0.07	0.82	0.75±0.06	0.82	0.89±0.07		
0.92	0.43±0.06	0.87	0.62±0.05	0.87	0.59±0.06		
0.98	0.32±0.05	0.93	0.46±0.04				
1.03	0.21±0.04	0.97	0.31±0.03				
1.07	0.11±0.03	1.02	0.25±0.04				
1.12	0.14±0.03						

π^+ 4 $A{\cdot}GeV$, 5-12% Central							
Y: 0.8 - 1		Y: 1 - 1.2		Y: 1.2 - 1.4		Y: 1.4 - 1.6	
$m_\perp$	Yield	$m_\perp$	Yield	$m_\perp$	Yield	$m_\perp$	Yield
0.28	31±2	0.23	50±2	0.23	49±2	0.234	43±3
0.32	17±1	0.28	31±1	0.28	31±1	0.276	27±2
0.37	11±0.7	0.33	20±0.8	0.33	19±0.9	0.327	20±1
0.43	7.2±0.5	0.37	13±0.5	0.38	13±0.6	0.376	12±0.7
0.48	5.1±0.4	0.43	8.8±0.4	0.43	8.7±0.4	0.426	8.3±0.5
0.53	3.5±0.3	0.48	6.4±0.3	0.48	5.9±0.3	0.475	5.5±0.4
0.58	2.5±0.2	0.53	4.4±0.2	0.53	4.1±0.2	0.525	3.7±0.3
0.63	1.9±0.2	0.58	3.1±0.2	0.58	2.8±0.2	0.575	2.5±0.2
0.68	1.3±0.1	0.62	2.1±0.1	0.63	2.1±0.1	0.625	1.9±0.2
0.72	01±0.1	0.67	1.5±0.09	0.67	1.5±0.1	0.675	1.4±0.1
0.78	0.68±0.08	0.73	01±0.07	0.72	01±0.07	0.724	1.1±0.1
0.83	0.51±0.06	0.77	0.83±0.06	0.77	0.75±0.06		
0.88	0.43±0.05	0.82	0.65±0.05	0.82	0.51±0.05		
0.92	0.36±0.05	0.87	0.48±0.04	0.87	0.43±0.04		
0.98	0.21±0.03	0.93	0.31±0.03				
1.03	0.16±0.03	0.97	0.27±0.03				
1.07	0.13±0.02	1.02	0.19±0.03				
1.12	0.074±0.02						

π^+ 4 $A{\cdot}GeV$, 12-23% Central							
Y: 0.8 - 1		Y: 1 - 1.2		Y: 1.2 - 1.4		Y: 1.4 - 1.6	
$m_\perp$	Yield	$m_\perp$	Yield	$m_\perp$	Yield	$m_\perp$	Yield
0.28	21±1	0.23	36±1	0.23	34±1	0.234	30±2
0.32	13±0.7	0.28	23±0.8	0.28	23±1	0.276	21±1
0.37	7.6±0.5	0.33	14±0.5	0.33	14±0.6	0.327	13±0.8
0.43	5.3±0.3	0.37	09±0.4	0.38	9.2±0.4	0.376	10±0.6
0.48	3.5±0.2	0.43	6.1±0.3	0.43	6.2±0.3	0.426	5.9±0.3
0.53	2.3±0.2	0.48	4.2±0.2	0.48	4.3±0.2	0.475	3.8±0.2
0.58	1.8±0.1	0.53	03±0.1	0.53	2.8±0.1	0.525	2.7±0.2
0.63	1.2±0.1	0.58	02±0.1	0.58	02±0.1	0.575	1.8±0.1
0.68	0.84±0.08	0.62	1.4±0.08	0.63	1.4±0.08	0.625	1.4±0.1
0.72	0.6±0.06	0.67	0.96±0.06	0.67	01±0.06	0.675	0.98±0.09
0.78	0.53±0.05	0.73	0.74±0.05	0.72	0.71±0.05	0.724	0.72±0.07
0.83	0.27±0.04	0.77	0.54±0.04	0.77	0.56±0.04		
0.88	0.26±0.03	0.82	0.4±0.03	0.82	0.38±0.03		
0.92	0.2±0.03	0.87	0.28±0.02	0.87	0.33±0.03		
0.98	0.15±0.02	0.93	0.23±0.02				
1.03	0.1±0.02	0.97	0.15±0.02				
1.07	0.065±0.01	1.02	0.09±0.01				
1.12	0.035±0.009						

π^+ 4 $A{\cdot}GeV$, 23-39% Central							
Y: 0.8 - 1		Y: 1 - 1.2		Y: 1.2 - 1.4		Y: 1.4 - 1.6	
$m_\perp$	Yield	$m_\perp$	Yield	$m_\perp$	Yield	$m_\perp$	Yield
0.28	12±0.7	0.23	22±0.9	0.23	21±0.9	0.234	21±2
0.32	8.1±0.5	0.28	14±0.5	0.28	14±0.6	0.276	13±0.7
0.37	4.8±0.3	0.33	8.7±0.3	0.33	8.2±0.4	0.327	7.8±0.5
0.43	2.9±0.2	0.37	5.2±0.2	0.38	5.3±0.3	0.376	5.2±0.3
0.48	2.1±0.1	0.43	3.5±0.2	0.43	3.5±0.2	0.426	3.5±0.2
0.53	1.4±0.1	0.48	2.5±0.1	0.48	2.5±0.1	0.475	2.5±0.2
0.58	0.99±0.08	0.53	1.7±0.09	0.53	1.5±0.09	0.525	1.6±0.1
0.63	0.66±0.06	0.58	1.1±0.06	0.58	1.1±0.07	0.575	1.1±0.08
0.68	0.54±0.05	0.62	0.82±0.05	0.63	0.81±0.05	0.625	0.73±0.06
0.72	0.37±0.04	0.67	0.58±0.04	0.67	0.59±0.04	0.675	0.5±0.05
0.78	0.28±0.03	0.73	0.45±0.03	0.72	0.43±0.03	0.724	0.36±0.04
0.83	0.2±0.03	0.77	0.29±0.02	0.77	0.33±0.03		
0.88	0.13±0.02	0.82	0.23±0.02	0.82	0.21±0.02		
0.92	0.081±0.01	0.87	0.13±0.01	0.87	0.14±0.02		
0.98	0.062±0.01	0.93	0.12±0.01				
1.03	0.068±0.01	0.97	0.082±0.01				
1.07	0.027±0.007	1.02	0.05±0.008				
1.12	0.015±0.005						

π^+ 6 $A{\cdot}GeV$, 0-5% Central							
Y: 0.8 - 1		Y: 1 - 1.2		Y: 1.2 - 1.4		Y: 1.4 - 1.6	
$m_\perp$	Yield	$m_\perp$	Yield	$m_\perp$	Yield	$m_\perp$	Yield
0.28	56±3	0.23	82±5	0.19	1.2e+02±7	0.227	86±4
0.33	37±2	0.28	57±3	0.23	86±4	0.276	57±2
0.37	24±1	0.33	39±2	0.28	57±3	0.325	40±2
0.43	19±1	0.38	24±2	0.32	40±2	0.375	26±1
0.48	12±0.8	0.42	19±1	0.38	25±1	0.425	18±0.9
0.53	8.3±0.6	0.47	12±0.9	0.42	19±1	0.475	13±0.7
0.58	5.1±0.4	0.52	09±0.7	0.47	13±0.8	0.525	8.9±0.5
0.63	4.2±0.3	0.58	06±0.6	0.53	8.8±0.6	0.575	6.5±0.4
0.68	3.2±0.3	0.62	5.5±0.5	0.57	6.7±0.5	0.625	4.8±0.3
0.72	2.3±0.2	0.68	3.2±0.3	0.62	4.9±0.4	0.674	3.6±0.3
0.78	1.7±0.2	0.73	2.5±0.3	0.68	3.6±0.3	0.722	2.5±0.2
0.82	1.4±0.1	0.78	1.9±0.2	0.73	2.9±0.3		
0.88	0.92±0.1	0.82	1.6±0.2	0.77	2.2±0.2		
0.92	0.55±0.08	0.88	0.99±0.1	0.82	1.7±0.2		
0.98	0.44±0.07	0.92	0.7±0.1	0.87	1.2±0.2		
1.03	0.31±0.06	0.97	0.72±0.1				
1.08	0.32±0.06	1.02	0.22±0.07				
1.12	0.21±0.04						

π^+ 6 $A{\cdot}GeV$, 5-12% Central							
Y: 0.8 - 1		Y: 1 - 1.2		Y: 1.2 - 1.4		Y: 1.4 - 1.6	
$m_\perp$	Yield	$m_\perp$	Yield	$m_\perp$	Yield	$m_\perp$	Yield
0.28	46±3	0.23	69±4	0.19	1e+02±5	0.227	74±3
0.33	30±2	0.28	45±3	0.23	70±3	0.276	47±2
0.37	19±1	0.33	30±2	0.28	46±2	0.325	33±1
0.43	13±0.8	0.38	21±1	0.32	30±1	0.375	22±1
0.48	8.5±0.5	0.42	14±0.9	0.38	21±1	0.425	15±0.7
0.53	6.5±0.4	0.47	10±0.7	0.42	14±0.8	0.475	10±0.5
0.58	4.2±0.3	0.52	6.8±0.5	0.47	10±0.6	0.525	6.9±0.4
0.63	3.2±0.2	0.58	05±0.4	0.53	07±0.4	0.575	5.2±0.3
0.68	2.2±0.2	0.62	04±0.4	0.57	5.5±0.4	0.625	4.1±0.3
0.72	1.5±0.1	0.68	2.7±0.3	0.62	3.9±0.3	0.674	03±0.2
0.78	1.4±0.1	0.73	1.9±0.2	0.68	2.6±0.2	0.722	02±0.2
0.82	0.85±0.1	0.78	1.3±0.2	0.73	1.7±0.2		
0.88	0.72±0.08	0.82	1.2±0.1	0.77	1.7±0.2		
0.92	0.52±0.07	0.88	0.9±0.1	0.82	1.2±0.1		
0.98	0.31±0.05	0.92	0.67±0.1	0.87	0.95±0.1		
1.03	0.25±0.04	0.97	0.53±0.09				
1.08	0.18±0.03	1.02	0.35±0.08				
1.12	0.19±0.04						

π^+ 6 $A{\cdot}GeV$, 12-23% Central							
Y: 0.8 - 1		Y: 1 - 1.2		Y: 1.2 - 1.4		Y: 1.4 - 1.6	
$m_\perp$	Yield	$m_\perp$	Yield	$m_\perp$	Yield	$m_\perp$	Yield
0.28	32±2	0.23	48±2	0.19	79±4	0.227	52±2
0.33	21±1	0.28	32±2	0.23	54±2	0.276	34±1
0.37	14±0.8	0.33	22±1	0.28	34±1	0.325	23±0.9
0.43	09±0.5	0.38	14±0.8	0.32	22±1	0.375	16±0.7
0.48	06±0.4	0.42	9.4±0.6	0.38	15±0.7	0.425	10±0.5
0.53	4.4±0.3	0.47	7.1±0.5	0.42	10±0.5	0.475	7.2±0.4
0.58	2.9±0.2	0.52	4.6±0.4	0.47	7.2±0.4	0.525	05±0.3
0.63	2.2±0.2	0.58	3.6±0.3	0.53	05±0.3	0.575	3.4±0.2
0.68	1.5±0.1	0.62	2.5±0.2	0.57	3.3±0.2	0.625	2.4±0.2
0.72	1.3±0.1	0.68	1.8±0.2	0.62	2.6±0.2	0.674	1.9±0.1
0.78	0.76±0.08	0.73	1.1±0.1	0.68	1.8±0.1	0.722	1.4±0.1
0.82	0.61±0.07	0.78	0.81±0.1	0.73	1.4±0.1		
0.88	0.47±0.05	0.82	0.74±0.09	0.77	1.1±0.1		
0.92	0.34±0.04	0.88	0.41±0.06	0.82	0.8±0.08		
0.98	0.22±0.03	0.92	0.47±0.06	0.87	0.46±0.07		
1.03	0.18±0.03	0.97	0.4±0.06				
1.08	0.11±0.02	1.02	0.24±0.05				
1.12	0.089±0.02						

π^+ 6 $A{\cdot}GeV$, 23-39% Central							
Y: 0.8 - 1		Y: 1 - 1.2		Y: 1.2 - 1.4		Y: 1.4 - 1.6	
$m_\perp$	Yield	$m_\perp$	Yield	$m_\perp$	Yield	$m_\perp$	Yield
0.28	21±1	0.23	33±2	0.19	53±3	0.227	37±2
0.33	13±0.7	0.28	22±1	0.23	36±1	0.276	23±0.9
0.37	09±0.5	0.33	13±0.8	0.28	23±1	0.325	15±0.6
0.43	5.7±0.3	0.38	09±0.6	0.32	14±0.7	0.375	10±0.5
0.48	3.8±0.2	0.42	6.4±0.4	0.38	9.7±0.5	0.425	6.6±0.3
0.53	2.9±0.2	0.47	4.6±0.3	0.42	6.7±0.4	0.475	4.4±0.2
0.58	02±0.1	0.52	3.1±0.2	0.47	4.5±0.3	0.525	3.4±0.2
0.63	1.4±0.1	0.58	02±0.2	0.53	3.4±0.2	0.575	2.2±0.1
0.68	0.99±0.08	0.62	1.6±0.1	0.57	2.2±0.1	0.625	1.6±0.1
0.72	0.75±0.07	0.68	1.1±0.1	0.62	1.7±0.1	0.674	1.2±0.08
0.78	0.48±0.05	0.73	0.77±0.08	0.68	1.1±0.09	0.722	0.97±0.08
0.82	0.32±0.04	0.78	0.58±0.07	0.73	0.76±0.07		
0.88	0.23±0.03	0.82	0.42±0.05	0.77	0.74±0.07		
0.92	0.18±0.03	0.88	0.32±0.05	0.82	0.53±0.06		
0.98	0.13±0.02	0.92	0.25±0.04	0.87	0.34±0.05		
1.03	0.097±0.02	0.97	0.17±0.03				
1.08	0.097±0.02	1.02	0.11±0.03				
1.12	0.055±0.01						

π^+ 8 $A{\cdot}GeV$, 0-5% Central							
Y: 0.8 - 1		Y: 1 - 1.2		Y: 1.2 - 1.4		Y: 1.4 - 1.6	
$m_\perp$	Yield	$m_\perp$	Yield	$m_\perp$	Yield	$m_\perp$	Yield
0.28	63±3	0.23	1e+02±5	0.23	1.1e+02±4	0.227	98±5
0.33	43±2	0.28	72±3	0.28	71±3	0.276	72±3
0.37	29±1	0.33	46±2	0.33	50±2	0.325	51±2
0.43	20±1	0.37	33±2	0.38	35±2	0.375	35±2
0.48	14±0.7	0.42	24±1	0.42	25±1	0.425	25±1
0.53	10±0.6	0.47	17±0.8	0.48	18±0.9	0.475	18±0.9
0.58	7.7±0.4	0.53	11±0.6	0.52	12±0.6	0.525	12±0.7
0.63	5.1±0.3	0.58	8.7±0.5	0.57	9.4±0.5	0.575	9.3±0.5
0.68	4.1±0.3	0.63	6.6±0.4	0.63	7.2±0.4	0.625	6.5±0.4
0.72	03±0.2	0.68	4.7±0.3	0.68	5.5±0.3	0.674	5.1±0.3
0.77	2.2±0.2	0.73	3.1±0.2	0.73	04±0.3	0.722	4.1±0.3
0.82	1.6±0.1	0.78	2.7±0.2	0.77	03±0.2		
0.88	1.1±0.1	0.82	2.1±0.2	0.82	2.3±0.2		
0.92	0.98±0.1	0.88	1.5±0.1	0.87	1.9±0.2		
0.97	0.7±0.08	0.92	1.3±0.1				
1.03	0.49±0.06	0.97	0.87±0.09				
1.08	0.37±0.05	1.02	0.58±0.08				
1.12	0.33±0.05						

π^+ 8 $A{\cdot}GeV$, 5-12% Central							
Y: 0.8 - 1		Y: 1 - 1.2		Y: 1.2 - 1.4		Y: 1.4 - 1.6	
$m_\perp$	Yield	$m_\perp$	Yield	$m_\perp$	Yield	$m_\perp$	Yield
0.28	53±2	0.23	79±3	0.23	83±3	0.227	82±4
0.33	36±2	0.28	56±2	0.28	56±2	0.276	55±2
0.37	23±1	0.33	38±2	0.33	38±2	0.325	39±2
0.43	16±0.8	0.37	26±1	0.38	27±1	0.375	27±1
0.48	11±0.6	0.42	17±0.8	0.42	20±0.9	0.425	19±0.9
0.53	7.8±0.4	0.47	13±0.6	0.48	13±0.6	0.475	14±0.7
0.58	5.9±0.3	0.53	9.3±0.5	0.52	9.9±0.5	0.525	9.7±0.5
0.63	4.2±0.3	0.58	6.8±0.4	0.57	6.8±0.4	0.575	7.3±0.4
0.68	3.2±0.2	0.63	4.9±0.3	0.63	5.3±0.3	0.625	5.5±0.3
0.72	2.2±0.2	0.68	3.7±0.2	0.68	3.8±0.2	0.674	4.3±0.3
0.77	1.7±0.1	0.73	2.6±0.2	0.73	03±0.2	0.722	3.2±0.2
0.82	1.2±0.1	0.78	02±0.1	0.77	02±0.1		
0.88	01±0.09	0.82	1.5±0.1	0.82	1.7±0.1		
0.92	0.61±0.06	0.88	1.1±0.1	0.87	1.2±0.1		
0.97	0.49±0.06	0.92	0.82±0.08				
1.03	0.35±0.04	0.97	0.68±0.07				
1.08	0.27±0.04	1.02	0.43±0.06				
1.12	0.27±0.04						

π^+ 8 $A{\cdot}GeV$, 12-23% Central							
Y: 0.8 - 1		Y: 1 - 1.2		Y: 1.2 - 1.4		Y: 1.4 - 1.6	
$m_\perp$	Yield	$m_\perp$	Yield	$m_\perp$	Yield	$m_\perp$	Yield
0.28	40±2	0.23	58±2	0.23	64±2	0.227	63±3
0.33	26±1	0.28	40±2	0.28	41±2	0.276	42±2
0.37	18±0.8	0.33	28±1	0.33	28±1	0.325	29±1
0.43	11±0.5	0.37	18±0.8	0.38	19±0.8	0.375	19±0.8
0.48	7.9±0.4	0.42	14±0.6	0.42	14±0.6	0.425	14±0.6
0.53	6.1±0.3	0.47	9.2±0.4	0.48	9.7±0.4	0.475	9.2±0.4
0.58	4.4±0.2	0.53	6.6±0.3	0.52	6.8±0.3	0.525	07±0.3
0.63	3.1±0.2	0.58	4.7±0.3	0.57	05±0.3	0.575	4.9±0.3
0.68	2.2±0.1	0.63	3.5±0.2	0.63	3.8±0.2	0.625	3.6±0.2
0.72	1.6±0.1	0.68	2.6±0.2	0.68	2.8±0.2	0.674	2.9±0.2
0.77	1.1±0.09	0.73	1.9±0.1	0.73	02±0.1	0.722	02±0.1
0.82	0.9±0.07	0.78	1.3±0.09	0.77	1.5±0.1		
0.88	0.66±0.06	0.82	0.93±0.07	0.82	1.2±0.09		
0.92	0.49±0.05	0.88	0.81±0.07	0.87	0.88±0.09		
0.97	0.34±0.04	0.92	0.58±0.05				
1.03	0.23±0.03	0.97	0.44±0.04				
1.08	0.18±0.02	1.02	0.34±0.04				
1.12	0.12±0.02						

π^+ 8 $A{\cdot}GeV$, 23-39% Central							
Y: 0.8 - 1		Y: 1 - 1.2		Y: 1.2 - 1.4		Y: 1.4 - 1.6	
$m_\perp$	Yield	$m_\perp$	Yield	$m_\perp$	Yield	$m_\perp$	Yield
0.28	26±1	0.23	40±2	0.23	41±2	0.227	44±2
0.33	17±0.7	0.28	26±1	0.28	27±1	0.276	27±1
0.37	11±0.5	0.33	17±0.7	0.33	17±0.7	0.325	19±0.7
0.43	7.6±0.4	0.37	12±0.5	0.38	12±0.5	0.375	13±0.5
0.48	5.2±0.3	0.42	8.1±0.4	0.42	8.4±0.4	0.425	09±0.4
0.53	3.3±0.2	0.47	5.9±0.3	0.48	5.8±0.3	0.475	6.1±0.3
0.58	2.5±0.1	0.53	4.1±0.2	0.52	4.2±0.2	0.525	4.2±0.2
0.63	1.7±0.1	0.58	03±0.2	0.57	3.1±0.2	0.575	03±0.2
0.68	1.4±0.09	0.63	2.1±0.1	0.63	2.2±0.1	0.625	2.3±0.1
0.72	0.85±0.06	0.68	1.6±0.1	0.68	1.8±0.1	0.674	1.7±0.1
0.77	0.61±0.05	0.73	1.2±0.08	0.73	1.3±0.08	0.722	1.3±0.1
0.82	0.5±0.04	0.78	0.84±0.06	0.77	0.87±0.06		
0.88	0.4±0.04	0.82	0.63±0.05	0.82	0.75±0.06		
0.92	0.26±0.03	0.88	0.41±0.04	0.87	0.49±0.05		
0.97	0.2±0.02	0.92	0.39±0.04				
1.03	0.14±0.02	0.97	0.25±0.03				
1.08	0.12±0.02	1.02	0.19±0.03				
1.12	0.081±0.01						

proton 2 $A{\cdot}GeV$, 0-5% Central			
Y: 0.6 - 0.8		Y: 0.8 - 1	
$m_\perp$	Yield	$m_\perp$	Yield
1.03	38±1	1.079	31±1
1.08	31±1	1.126	25±1
1.13	26±0.8	1.176	20±0.8
1.18	21±0.7	1.226	16±0.6
1.23	17±0.5	1.275	13±0.5
1.28	13±0.4	1.325	9.7±0.4
1.33	9.9±0.3	1.376	7.6±0.3
1.37	7.3±0.3	1.426	5.6±0.2
1.42	5.4±0.2	1.475	4.1±0.2
1.48	04±0.2	1.525	3.1±0.1
1.52	2.9±0.1	1.575	2.2±0.1
1.57	02±0.1	1.625	1.6±0.09
1.62	1.3±0.08	1.675	1.1±0.06
1.67	0.92±0.06	1.725	0.81±0.05
1.72	0.8±0.06	1.775	0.58±0.04
1.77	0.56±0.05	1.825	0.42±0.03
1.82	0.36±0.04	1.875	0.27±0.03
1.87	0.22±0.03	1.925	0.19±0.02
1.93	0.19±0.02	1.975	0.13±0.02
1.98	0.081±0.02	2.025	0.083±0.01
2.02	0.061±0.01	2.075	0.065±0.01
2.08	0.055±0.01	2.125	0.043±0.008
2.12	0.032±0.01	2.175	0.027±0.006
2.17	0.028±0.009	2.225	0.016±0.005
2.23	0.0079±0.005	2.275	0.026±0.006
2.28	0.0078±0.005	2.325	0.0037±0.002
2.32	0.0051±0.004	2.375	0.0039±0.002
2.37	0.0026±0.003	2.424	0.0015±0.002
2.42	00±0.002		
2.48	0.0026±0.003		
2.53	0.0024±0.002		
2.57	00±0.002		

proton 2 $A{\cdot}GeV$, 5-12% Central			
Y: 0.6 - 0.8		Y: 0.8 - 1	
$m_\perp$	Yield	$m_\perp$	Yield
1.03	32±1	1.079	25±1
1.08	26±0.8	1.126	20±0.7
1.13	20±0.6	1.176	16±0.6
1.18	16±0.5	1.226	12±0.4
1.23	12±0.4	1.275	09±0.3
1.28	9.3±0.3	1.325	07±0.3
1.33	6.9±0.2	1.376	5.1±0.2
1.37	5.1±0.2	1.426	3.7±0.2
1.42	3.6±0.1	1.475	2.7±0.1
1.48	2.6±0.1	1.525	1.9±0.09
1.52	1.8±0.09	1.575	1.3±0.07
1.57	1.2±0.07	1.625	0.97±0.05
1.62	0.86±0.05	1.675	0.72±0.04
1.67	0.62±0.04	1.725	0.48±0.03
1.72	0.38±0.03	1.775	0.37±0.03
1.77	0.25±0.02	1.825	0.24±0.02
1.82	0.22±0.02	1.875	0.15±0.02
1.87	0.15±0.02	1.925	0.12±0.01
1.93	0.11±0.02	1.975	0.073±0.01
1.98	0.087±0.01	2.025	0.049±0.008
2.02	0.037±0.008	2.075	0.037±0.006
2.08	0.039±0.009	2.125	0.031±0.006
2.12	0.015±0.005	2.175	0.013±0.004
2.17	0.0089±0.004	2.225	0.0091±0.003
2.23	0.011±0.005	2.275	0.0082±0.003
2.28	0.016±0.006	2.325	0.0027±0.002
2.32	0.0036±0.003	2.375	00±0.0007
2.37	0.0019±0.002	2.424	0.0044±0.002
2.42	0.004±0.003		

proton 2 $A{\cdot}GeV$, 12-23% Central			
Y: 0.6 - 0.8		Y: 0.8 - 1	
$m_\perp$	Yield	$m_\perp$	Yield
1.03	24±0.8	1.079	18±0.7
1.08	20±0.6	1.126	14±0.5
1.13	14±0.4	1.176	10±0.4
1.18	11±0.3	1.226	7.8±0.3
1.23	7.9±0.2	1.275	5.8±0.2
1.28	5.8±0.2	1.325	4.4±0.2
1.33	4.1±0.1	1.376	03±0.1
1.37	03±0.1	1.426	2.1±0.09
1.42	02±0.08	1.475	1.5±0.07
1.48	1.5±0.07	1.525	1.1±0.05
1.52	0.96±0.05	1.575	0.78±0.04
1.57	0.7±0.04	1.625	0.51±0.03
1.62	0.46±0.03	1.675	0.36±0.02
1.67	0.32±0.02	1.725	0.23±0.02
1.72	0.25±0.02	1.775	0.18±0.01
1.77	0.13±0.01	1.825	0.13±0.01
1.82	0.12±0.01	1.875	0.082±0.009
1.87	0.047±0.008	1.925	0.042±0.006
1.93	0.03±0.006	1.975	0.029±0.005
1.98	0.032±0.006	2.025	0.021±0.004
2.02	0.019±0.005	2.075	0.013±0.003
2.08	0.0082±0.003	2.125	0.0093±0.003
2.12	0.0078±0.003	2.175	0.0079±0.002
2.17	00±0.0009	2.225	0.0042±0.002
2.23	0.0024±0.002	2.275	0.0047±0.002
2.28	0.0035±0.002	2.325	0.0011±0.0008
2.32	0.0023±0.002	2.375	0.0023±0.001
2.37	00±0.001	2.424	0.00069±0.0007

proton 2 $A{\cdot}GeV$, 23-39% Central			
Y: 0.6 - 0.8		Y: 0.8 - 1	
$m_\perp$	Yield	$m_\perp$	Yield
1.03	16±0.5	1.079	11±0.4
1.08	12±0.4	1.126	08±0.3
1.13	8.4±0.3	1.176	5.4±0.2
1.18	06±0.2	1.226	4.1±0.2
1.23	4.3±0.1	1.275	2.9±0.1
1.28	03±0.1	1.325	02±0.08
1.33	2.1±0.08	1.376	1.5±0.07
1.37	1.4±0.06	1.426	0.98±0.05
1.42	0.97±0.04	1.475	0.68±0.04
1.48	0.62±0.03	1.525	0.44±0.03
1.52	0.43±0.02	1.575	0.29±0.02
1.57	0.29±0.02	1.625	0.21±0.02
1.62	0.19±0.01	1.675	0.15±0.01
1.67	0.13±0.01	1.725	0.086±0.008
1.72	0.093±0.01	1.775	0.066±0.007
1.77	0.057±0.007	1.825	0.036±0.005
1.82	0.036±0.006	1.875	0.023±0.004
1.87	0.02±0.004	1.925	0.022±0.004
1.93	0.015±0.004	1.975	0.015±0.003
1.98	0.01±0.003	2.025	0.0077±0.002
2.02	0.0086±0.003	2.075	0.0047±0.001
2.08	0.0044±0.002	2.125	0.0031±0.001
2.12	0.0015±0.001	2.175	0.0023±0.001
2.17	0.0016±0.001	2.225	0.0014±0.0008

proton 4 $A{\cdot}GeV$, 0-5% Central							
Y: 0.6 - 0.8		Y: 0.8 - 1		Y: 1 - 1.2		Y: 1.2 - 1.4	
$m_\perp$	Yield	$m_\perp$	Yield	$m_\perp$	Yield	$m_\perp$	Yield
1.03	32±1	1.03	28±1	1.07	22±1	1.127	17±0.9
1.08	26±0.8	1.08	24±0.8	1.13	19±0.8	1.175	15±0.8
1.13	22±0.6	1.13	21±0.7	1.18	15±0.6	1.225	13±0.7
1.17	17±0.5	1.18	17±0.5	1.23	13±0.5	1.275	10±0.6
1.22	14±0.5	1.23	14±0.4	1.28	11±0.4	1.326	8.3±0.5
1.27	11±0.4	1.27	11±0.4	1.33	8.4±0.3	1.376	6.5±0.4
1.32	08±0.3	1.32	8.8±0.3	1.38	6.8±0.3	1.426	5.3±0.3
1.37	6.2±0.3	1.38	6.9±0.2	1.43	5.3±0.2	1.476	3.8±0.2
1.42	4.8±0.2	1.43	5.4±0.2	1.48	4.2±0.2	1.525	3.1±0.2
1.47	3.6±0.2	1.47	4.2±0.2	1.52	3.3±0.1	1.575	2.5±0.1
1.52	2.6±0.2	1.53	3.3±0.1	1.58	2.5±0.1	1.625	02±0.1
1.57	1.8±0.1	1.57	2.4±0.1	1.63	02±0 09	1.675	1.6±0.1
1.62	1.3±0.1	1.62	1.9±0.09	1.68	1.6±0.08	1.724	1.3±0.09
1.67	1.1±0.09	1.67	1.4±0.07	1.72	1.2±0.06	1.773	0.9±0.08
1.72	0.91±0.08	1.72	1.1±0.06	1.78	0.9±0.05		
1.77	0.53±0.06	1.78	0.83±0.05	1.83	0.72±0.04		
1.82	0.48±0.06	1.83	0.62±0.04	1.87	0.55±0.04		
1.88	0.33±0.05	1.87	0.5±0.04	1.93	0.41±0.03		
1.93	0.24±0.04	1.92	0.36±0.03	1.97	0.33±0.03		
1.98	0.14±0.03	1.97	0.29±0.03	2.02	0.24±0.02		
2.02	0.14±0.03	2.02	0.22±0.02	2.07	0.17±0.02		
2.08	0.065±0.02	2.08	0.14±0.02				
2.12	0.069±0.02	2.12	0.13±0.02				
2.17	0.071±0.02	2.18	0.084±0.01				
2.22	0.034±0.01	2.22	0.042±0.009				
2.28	0.023±0.01	2.27	0.038±0.008				
2.33	00±0.004	2.32	0.028±0.007				
2.37	0.0057±0.006	2.37	0.038±0.01				
2.42	0.0054±0.006	2.42	0.0058±0.004				
2.47	0.011±0.008						
2.52	00±0.005						
2.57	00±0.005						
2.62	00±0.005						
2.67	00±0.006						

proton 4 $A{\cdot}GeV$, 5-12% Central							
Y: 0.6 - 0.8		Y: 0.8 - 1		Y: 1 - 1.2		Y: 1.2 - 1.4	
$m_\perp$	Yield	$m_\perp$	Yield	$m_\perp$	Yield	$m_\perp$	Yield
1.03	26±0.8	1.03	24±1	1.07	18±0.8	1.127	13±0.7
1.08	22±0.6	1.08	20±0.7	1.13	15±0.6	1.175	12±0.6
1.13	18±0.5	1.13	16±0.5	1.18	13±0.5	1.225	10±0.5
1.17	14±0.4	1.18	14±0.4	1.23	9.8±0.4	1.275	7.4±0.4
1.22	11±0.4	1.23	11±0.3	1.28	8.1±0.3	1.326	06±0.3
1.27	8.3±0.3	1.27	8.6±0.3	1.33	6.4±0.2	1.376	4.8±0.3
1.32	6.4±0.2	1.32	6.7±0.2	1.38	5.1±0.2	1.426	3.9±0.2
1.37	4.7±0.2	1.38	5.2±0.2	1.43	3.9±0.2	1.476	2.8±0.1
1.42	3.6±0.2	1.43	3.9±0.1	1.48	3.1±0.1	1.525	2.3±0.1
1.47	2.6±0.1	1.47	3.1±0.1	1.52	2.3±0.1	1.575	1.8±0.1
1.52	1.8±0.1	1.53	2.3±0.09	1.58	1.8±0.08	1.625	1.4±0.08
1.57	1.4±0.1	1.57	1.8±0.08	1.63	1.4±0.07	1.675	1.1±0.07
1.62	1.1±0.08	1.62	1.4±0.06	1.68	1.1±0.05	1.724	0.8±0.06
1.67	0.68±0.06	1.67	1.1±0.05	1.72	0.8±0.04	1.773	0.62±0.05
1.72	0.54±0.05	1.72	0.78±0.04	1.78	0.66±0.04		
1.77	0.46±0.05	1.78	0.58±0.04	1.83	0.5±0.03		
1.82	0.26±0.04	1.83	0.44±0.03	1.87	0.35±0.02		
1.88	0.22±0.03	1.87	0.32±0.02	1.93	0.26±0.02		
1.93	0.15±0.03	1.92	0.25±0.02	1.97	0.22±0.02		
1.98	0.11±0.02	1.97	0.2±0.02	2.02	0.16±0.01		
2.02	0.1±0.02	2.02	0.12±0.01	2.07	0.13±0.01		
2.08	0.05±0.01	2.08	0.091±0.01				
2.12	0.049±0.02	2.12	0.081±0.01				
2.17	0.024±0.01	2.18	0.064±0.009				
2.22	0.027±0.01	2.22	0.047±0.008				
2.28	0.013±0.008	2.27	0.037±0.007				
2.33	0.0039±0.004	2.32	0.017±0.005				
2.37	0.0077±0.006	2.37	0.018±0.006				
2.42	00±0.003	2.42	0.01±0.005				
2.47	0.012±0.007						
2.52	0.012±0.007						
2.57	0.0041±0.004						

proton 4 $A{\cdot}GeV$, 12-23% Central							
Y: 0.6 - 0.8		Y: 0.8 - 1		Y: 1 - 1.2		Y: 1.2 - 1.4	
$m_\perp$	Yield	$m_\perp$	Yield	$m_\perp$	Yield	$m_\perp$	Yield
1.03	21±0.6	1.03	19±0.7	1.07	14±0.6	1.127	10±0.5
1.08	17±0.5	1.08	15±0.5	1.13	11±0.4	1.175	8.6±0.4
1.13	14±0.4	1.13	13±0.4	1.18	9.1±0.3	1.225	6.9±0.3
1.17	10±0.3	1.18	9.8±0.3	1.23	7.1±0.3	1.275	5.3±0.3
1.22	7.9±0.3	1.23	7.6±0.2	1.28	5.5±0.2	1.326	04±0.2
1.27	06±0.2	1.27	5.9±0.2	1.33	4.4±0.2	1.376	03±0.2
1.32	4.4±0.2	1.32	4.5±0.1	1.38	3.3±0.1	1.426	2.6±0.1
1.37	3.3±0.1	1.38	3.4±0.1	1.43	2.6±0.1	1.476	02±0.1
1.42	2.4±0.1	1.43	2.6±0.09	1.48	02±0.08	1.525	1.5±0.08
1.47	1.7±0.09	1.47	1.9±0.07	1.52	1.5±0.06	1.575	1.1±0.06
1.52	1.2±0.07	1.53	1.4±0.06	1.58	1.1±0.05	1.625	0.9±0.05
1.57	0.9±0.06	1.57	1.1±0.05	1.63	0.86±0.04	1.675	0.7±0.04
1.62	0.65±0.05	1.62	0.84±0.04	1.68	0.64±0.03	1.724	0.47±0.03
1.67	0.51±0.04	1.67	0.61±0.03	1.72	0.51±0.03	1.773	0.41±0.03
1.72	0.38±0.04	1.72	0.46±0.03	1.78	0.37±0.02		
1.77	0.25±0.03	1.78	0.36±0.02	1.83	0.29±0.02		
1.82	0.22±0.03	1.83	0.26±0.02	1.87	0.23±0.01		
1.88	0.12±0.02	1.87	0.19±0.01	1.93	0.16±0.01		
1.93	0.11±0.02	1.92	0.13±0.01	1.97	0.12±0.01		
1.98	0.076±0.02	1.97	0.097±0.01	2.02	0.099±0.009		
2.02	0.068±0.01	2.02	0.083±0.009	2.07	0.073±0.009		
2.08	0.036±0.01	2.08	0.042±0.006				
2.12	0.018±0.007	2.12	0.053±0.007				
2.17	0.012±0.006	2.18	0.035±0.006				
2.22	0.015±0.006	2.22	0.026±0.005				
2.28	0.011±0.005	2.27	0.019±0.004				
2.33	0.0076±0.005	2.32	0.011±0.003				
2.37	00±0.002	2.37	0.0076±0.003				
2.42	00±0.002	2.42	0.0063±0.003				
2.47	0.0024±0.002						
2.52	00±0.002						
2.57	00±0.002						
2.62	00±0.002						

proton 4 $A{\cdot}GeV$, 23-39% Central							
Y: 0.6 - 0.8		Y: 0.8 - 1		Y: 1 - 1.2		Y: 1.2 - 1.4	
$m_\perp$	Yield	$m_\perp$	Yield	$m_\perp$	Yield	$m_\perp$	Yield
1.03	15±0.4	1.03	12±0.5	1.07	8.8±0.4	1.127	6.3±0.3
1.08	11±0.3	1.08	9.7±0.3	1.13	6.8±0.3	1.175	4.9±0.2
1.13	8.3±0.2	1.13	7.4±0.2	1.18	05±0.2	1.225	3.7±0.2
1.17	6.1±0.2	1.18	5.6±0.2	1.23	3.8±0.1	1.275	2.8±0.2
1.22	4.5±0.1	1.23	4.3±0.1	1.28	2.9±0.1	1.326	2.2±0.1
1.27	3.3±0.1	1.27	3.1±0.1	1.33	2.2±0.09	1.376	1.7±0.09
1.32	2.4±0.1	1.32	2.3±0.08	1.38	1.7±0.07	1.426	1.2±0.07
1.37	1.7±0.08	1.38	1.7±0.06	1.43	1.3±0.05	1.476	0.92±0.05
1.42	1.2±0.06	1.43	1.3±0.05	1.48	0.93±0.04	1.525	0.69±0.04
1.47	0.84±0.05	1.47	0.96±0.04	1.52	0.7±0.03	1.575	0.5±0.03
1.52	0.59±0.04	1.53	0.69±0.03	1.58	0.51±0.03	1.625	0.4±0.03
1.57	0.41±0.03	1.57	0.5±0.02	1.63	0.38±0.02	1.675	0.3±0.02
1.62	0.3±0.03	1.62	0.39±0.02	1.68	0.29±0.02	1.724	0.19±0.02
1.67	0.21±0.02	1.67	0.28±0.02	1.72	0.23±0.01	1.773	0.16±0.02
1.72	0.17±0.02	1.72	0.2±0.01	1.78	0.16±0.01		
1.77	0.13±0.02	1.78	0.16±0.01	1.83	0.1±0.008		
1.82	0.062±0.01	1.83	0.1±0.009	1.87	0.095±0.007		
1.88	0.049±0.01	1.87	0.084±0.008	1.93	0.056±0.005		
1.93	0.036±0.009	1.92	0.058±0.006	1.97	0.055±0.005		
1.98	0.035±0.008	1.97	0.052±0.006	2.02	0.038±0.004		
2.02	0.019±0.006	2.02	0.027±0.004	2.07	0.025±0.004		
2.08	0.013±0.005	2.08	0.018±0.003				
2.12	0.0074±0.004	2.12	0.014±0.003				
2.17	0.0057±0.003	2.18	0.017±0.003				
2.22	0.0085±0.004	2.22	0.011±0.002				
2.28	0.0053±0.003	2.27	0.0079±0.002				
2.33	0.0034±0.002	2.32	0.0047±0.002				
2.37	0.0017±0.002	2.37	0.0039±0.002				
2.42	0.0018±0.002	2.42	0.0017±0.001				
2.47	00±0.001						
2.52	00±0.001						

proton 6 $A{\cdot}GeV$, 0-5% Central							
Y: 0.6 - 0.8		Y: 0.8 - 1		Y: 1 - 1.2		Y: 1.2 - 1.4	
$m_\perp$	Yield	$m_\perp$	Yield	$m_\perp$	Yield	$m_\perp$	Yield
0.98	31±1	1.03	25±0.9	1.03	24±1	1.076	20±1
1.02	25±1	1.08	21±0.8	1.08	20±0.8	1.128	16±0.8
1.07	22±1	1.12	17±0.7	1.13	17±0.7	1.176	14±0.6
1.13	18±0.8	1.17	15±0.6	1.18	14±0.6	1.226	12±0.5
1.18	15±0.7	1.22	12±0.5	1.22	12±0.5	1.275	10±0.4
1.23	12±0.6	1.27	9.8±0.5	1.28	10±0.4	1.325	8.7±0.4
1.28	8.7±0.4	1.32	8.1±0.4	1.33	08±0.4	1.375	6.7±0.3
1.33	7.9±0.4	1.38	6.3±0.4	1.37	6.9±0.3	1.425	5.2±0.3
1.38	5.4±0.3	1.43	5.1±0.3	1.42	5.3±0.3	1.475	4.5±0.2
1.43	4.6±0.3	1.48	4.1±0.3	1.47	4.2±0.2	1.525	3.7±0.2
1.48	3.2±0.2	1.53	3.3±0.2	1.53	3.7±0.2	1.575	2.9±0.2
1.53	2.6±0.2	1.57	2.8±0.2	1.57	3.1±0.2	1.625	2.2±0.1
1.58	2.1±0.1	1.63	2.1±0.2	1.62	2.3±0.2	1.674	1.9±0.1
1.62	1.4±0.1	1.67	1.6±0.1	1.67	1.6±0.1	1.723	1.7±0.1
1.68	1.2±0.1	1.72	1.2±0.1	1.72	1.5±0.1	1.774	1.2±0.1
1.73	0.87±0.08	1.77	01±0.1	1.77	1.1±0.1		
1.77	0.64±0.06	1.83	0.75±0.09	1.82	0.95±0.09		
1.83	0.49±0.05	1.88	0.52±0.07	1.87	0.68±0.08		
1.88	0.29±0.04	1.93	0.42±0.06	1.93	0.58±0.07		
1.92	0.3±0.04	1.98	0.33±0.05	1.97	0.44±0.06		
1.98	0.2±0.03	2.03	0.25±0.04	2.02	0.35±0.06		
2.02	0.15±0.03	2.08	0.19±0.03	2.07	0.23±0.05		
2.08	0.096±0.02	2.12	0.15±0.03				
2.13	0.095±0.02	2.18	0.079±0.02				
2.17	0.058±0.02	2.23	0.09±0.02				
2.22	0.046±0.01	2.27	0.072±0.02				
2.28	0.023±0.01	2.32	0.045±0.02				
2.32	0.022±0.01	2.37	00±0.004				
2.37	0.0074±0.005	2.42	0.016±0.009				
2.43	0.011±0.007						
2.48	0.0073±0.005						
2.53	0.014±0.007						
2.57	0.01±0.006						
2.62	0.0033±0.003						
2.67	0.0074±0.005						

proton 6 $A{\cdot}GeV$, 5-12% Central							
Y: 0.6 - 0.8		Y: 0.8 - 1		Y: 1 - 1.2		Y: 1.2 - 1.4	
$m_\perp$	Yield	$m_\perp$	Yield	$m_\perp$	Yield	$m_\perp$	Yield
0.98	29±1	1.03	22±0.8	1.03	22±0.9	1.076	17±0.8
1.02	23±0.8	1.08	18±0.7	1.08	17±0.7	1.128	14±0.6
1.07	19±0.8	1.12	15±0.6	1.13	14±0.5	1.176	11±0.5
1.13	16±0.7	1.17	12±0.5	1.18	12±0.5	1.226	9.7±0.4
1.18	12±0.5	1.22	9.7±0.4	1.22	9.9±0.4	1.275	8.1±0.3
1.23	9.6±0.4	1.27	8.4±0.4	1.28	08±0.3	1.325	6.3±0.3
1.28	7.9±0.4	1.32	6.2±0.3	1.33	6.5±0.3	1.375	5.6±0.3
1.33	6.1±0.3	1.38	5.1±0.3	1.37	05±0.2	1.425	4.4±0.2
1.38	4.9±0.2	1.43	3.9±0.2	1.42	4.2±0.2	1.475	3.5±0.2
1.43	3.4±0.2	1.48	3.2±0.2	1.47	3.4±0.2	1.525	2.8±0.2
1.48	2.6±0.2	1.53	2.7±0.2	1.53	2.9±0.2	1.575	2.3±0.1
1.53	2.1±0.1	1.57	1.9±0.1	1.57	2.1±0.1	1.625	1.8±0.1
1.58	1.6±0.1	1.63	1.5±0.1	1.62	1.6±0.1	1.674	1.5±0.1
1.62	1.1±0.08	1.67	1.1±0.1	1.67	1.2±0.1	1.723	1.1±0.09
1.68	0.87±0.07	1.72	0.91±0.08	1.72	0.94±0.08	1.774	0.88±0.09
1.73	0.64±0.06	1.77	0.76±0.07	1.77	0.93±0.08		
1.77	0.47±0.05	1.83	0.57±0.06	1.82	0.65±0.06		
1.83	0.36±0.04	1.88	0.35±0.05	1.87	0.48±0.05		
1.88	0.31±0.04	1.93	0.31±0.04	1.93	0.31±0.04		
1.92	0.22±0.03	1.98	0.22±0.03	1.97	0.24±0.04		
1.98	0.18±0.03	2.03	0.18±0.03	2.02	0.25±0.04		
2.02	0.12±0.02	2.08	0.13±0.02	2.07	0.19±0.04		
2.08	0.094±0.02	2.12	0.11±0.02				
2.13	0.047±0.01	2.18	0.06±0.02				
2.17	0.06±0.01	2.23	0.066±0.02				
2.22	0.02±0.008	2.27	0.05±0.01				
2.28	0.018±0.007	2.32	0.041±0.01				
2.32	0.029±0.009	2.37	0.047±0.01				
2.37	0.024±0.009	2.42	0.0078±0.006				
2.43	0.019±0.008						
2.48	0.011±0.005						
2.53	0.005±0.004						
2.57	0.0025±0.003						

proton 6 $A{\cdot}GeV$, 12-23% Central							
Y: 0.6 - 0.8		Y: 0.8 - 1		Y: 1 - 1.2		Y: 1.2 - 1.4	
$m_\perp$	Yield	$m_\perp$	Yield	$m_\perp$	Yield	$m_\perp$	Yield
0.98	24±0.8	1.03	17±0.6	1.03	16±0.6	1.076	13±0.5
1.02	19±0.6	1.08	14±0.5	1.08	13±0.4	1.128	10±0.4
1.07	15±0.6	1.12	11±0.4	1.13	11±0.4	1.176	8.3±0.3
1.13	12±0.5	1.17	8.8±0.3	1.18	8.7±0.3	1.226	6.9±0.3
1.18	9.5±0.4	1.22	07±0.3	1.22	6.9±0.3	1.275	5.6±0.2
1.23	7.5±0.3	1.27	5.5±0.3	1.28	5.7±0.2	1.325	4.4±0.2
1.28	5.5±0.2	1.32	4.2±0.2	1.33	4.4±0.2	1.375	3.6±0.2
1.33	4.3±0.2	1.38	3.4±0.2	1.37	3.7±0.2	1.425	3.1±0.1
1.38	3.4±0.2	1.43	2.6±0.2	1.42	2.9±0.1	1.475	2.4±0.1
1.43	2.4±0.1	1.48	02±0.1	1.47	2.3±0.1	1.525	1.9±0.1
1.48	1.9±0.1	1.53	1.7±0.1	1.53	1.7±0.1	1.575	1.4±0.08
1.53	1.4±0.08	1.57	1.2±0.09	1.57	1.4±0.09	1.625	1.2±0.07
1.58	01±0.07	1.63	01±0.08	1.62	1.3±0.08	1.674	0.89±0.06
1.62	0.82±0.06	1.67	0.81±0.07	1.67	0.83±0.06	1.723	0.75±0.06
1.68	0.55±0.04	1.72	0.55±0.05	1.72	0.63±0.05	1.774	0.55±0.05
1.73	0.42±0.04	1.77	0.5±0.05	1.77	0.52±0.05		
1.77	0.32±0.03	1.83	0.31±0.04	1.82	0.44±0.04		
1.83	0.26±0.03	1.88	0.23±0.03	1.87	0.26±0.03		
1.88	0.18±0.02	1.93	0.19±0.03	1.93	0.26±0.03		
1.92	0.12±0.02	1.98	0.14±0.02	1.97	0.2±0.03		
1.98	0.1±0.02	2.03	0.09±0.02	2.02	0.16±0.03		
2.02	0.076±0.01	2.08	0.083±0.01	2.07	0.1±0.02		
2.08	0.054±0.01	2.12	0.055±0.01				
2.13	0.058±0.01	2.18	0.056±0.01				
2.17	0.036±0.008	2.23	0.034±0.009				
2.22	0.022±0.007	2.27	0.028±0.008				
2.28	0.017±0.006	2.32	0.018±0.006				
2.32	0.0081±0.004	2.37	0.0083±0.004				
2.37	0.011±0.004	2.42	0.018±0.007				
2.43	0.005±0.003						
2.48	0.0034±0.003						
2.53	0.0031±0.002						

proton 6 $A{\cdot}GeV$, 23-39% Central							
Y: 0.6 - 0.8		Y: 0.8 - 1		Y: 1 - 1.2		Y: 1.2 - 1.4	
$m_\perp$	Yield	$m_\perp$	Yield	$m_\perp$	Yield	$m_\perp$	Yield
0.98	19±0.6	1.03	12±0.4	1.03	11±0.4	1.076	9.1±0.4
1.02	14±0.5	1.08	9.6±0.3	1.08	8.7±0.3	1.128	6.8±0.3
1.07	11±0.4	1.12	7.5±0.3	1.13	6.8±0.2	1.176	5.4±0.2
1.13	8.3±0.3	1.17	5.8±0.2	1.18	5.7±0.2	1.226	4.2±0.2
1.18	6.5±0.3	1.22	4.4±0.2	1.22	4.4±0.2	1.275	3.3±0.1
1.23	4.8±0.2	1.27	3.5±0.2	1.28	3.5±0.1	1.325	2.7±0.1
1.28	3.3±0.2	1.32	2.8±0.1	1.33	2.7±0.1	1.375	2.1±0.1
1.33	2.6±0.1	1.38	02±0.1	1.37	2.1±0.1	1.425	1.7±0.08
1.38	1.9±0.1	1.43	1.6±0.1	1.42	1.6±0.09	1.475	1.3±0.07
1.43	1.5±0.08	1.48	1.3±0.08	1.47	1.2±0.07	1.525	01±0.06
1.48	1.1±0.07	1.53	0.97±0.07	1.53	0.97±0.06	1.575	0.81±0.05
1.53	0.73±0.05	1.57	0.68±0.05	1.57	0.75±0.05	1.625	0.64±0.04
1.58	0.56±0.04	1.63	0.51±0.04	1.62	0.58±0.04	1.674	0.52±0.04
1.62	0.44±0.03	1.67	0.34±0.03	1.67	0.45±0.04	1.723	0.42±0.03
1.68	0.36±0.03	1.72	0.28±0.03	1.72	0.31±0.03	1.774	0.27±0.03
1.73	0.21±0.02	1.77	0.23±0.03	1.77	0.27±0.03		
1.77	0.17±0.02	1.83	0.17±0.02	1.82	0.19±0.02		
1.83	0.12±0.01	1.88	0.13±0.02	1.87	0.16±0.02		
1.88	0.084±0.01	1.93	0.076±0.01	1.93	0.12±0.02		
1.92	0.064±0.01	1.98	0.052±0.01	1.97	0.097±0.02		
1.98	0.047±0.008	2.03	0.065±0.01	2.02	0.069±0.01		
2.02	0.039±0.008	2.08	0.042±0.009	2.07	0.059±0.01		
2.08	0.022±0.005	2.12	0.027±0.007				
2.13	0.016±0.005	2.18	0.03±0.007				
2.17	0.0095±0.004	2.23	0.008±0.003				
2.22	0.0086±0.003	2.27	0.012±0.004				
2.28	0.0093±0.003	2.32	0.011±0.004				
2.32	0.0024±0.002	2.37	0.0044±0.003				
2.37	0.0034±0.002	2.42	0.0017±0.002				
2.43	0.0024±0.002						
2.48	0.0036±0.002						
2.53	0.0032±0.002						
2.57	00±0.0009						

proton 8 $A{\cdot}GeV$, 0-5% Central							
Y: 0.6 - 0.8		Y: 0.8 - 1		Y: 1 - 1.2		Y: 1.2 - 1.4	
$m_\perp$	Yield	$m_\perp$	Yield	$m_\perp$	Yield	$m_\perp$	Yield
0.98	31±1	1.03	24±0.9	1.03	23±1	1.075	17±0.9
1.03	27±1	1.08	21±0.8	1.08	19±0.8	1.129	15±0.7
1.08	22±0.8	1.13	17±0.7	1.13	17±0.6	1.175	14±0.6
1.13	17±0.6	1.18	15±0.6	1.17	15±0.6	1.226	12±0.5
1.18	14±0.5	1.23	12±0.5	1.23	12±0.5	1.275	9.8±0.4
1.23	11±0.4	1.27	9.6±0.4	1.28	10±0.4	1.325	8.3±0.4
1.28	8.8±0.4	1.32	8.2±0.4	1.33	8.1±0.4	1.375	7.1±0.3
1.33	6.9±0.3	1.38	6.5±0.3	1.37	6.6±0.3	1.425	5.6±0.3
1.37	5.3±0.2	1.43	5.2±0.2	1.43	5.8±0.3	1.475	4.9±0.2
1.42	04±0.2	1.48	3.9±0.2	1.48	4.6±0.2	1.525	3.9±0.2
1.47	3.1±0.2	1.53	3.3±0.2	1.53	3.6±0.2	1.575	3.3±0.2
1.52	2.6±0.2	1.58	2.4±0.1	1.57	03±0.2	1.625	2.5±0.2
1.58	1.8±0.1	1.63	02±0.1	1.63	2.3±0.1	1.675	02±0.1
1.62	1.4±0.1	1.67	1.5±0.1	1.68	1.9±0.1	1.723	1.6±0.1
1.67	01±0.08	1.73	1.3±0.09	1.73	1.6±0.1	1.774	1.1±0.1
1.72	0.85±0.07	1.77	0.93±0.07	1.77	1.2±0.09		
1.77	0.63±0.06	1.83	0.71±0.06	1.82	01±0.08		
1.83	0.54±0.06	1.88	0.48±0.05	1.87	0.77±0.06		
1.88	0.35±0.04	1.92	0.43±0.04	1.93	0.53±0.05		
1.92	0.25±0.04	1.98	0.33±0.04	1.97	0.39±0.04		
1.97	0.22±0.03	2.03	0.23±0.03	2.02	0.36±0.04		
2.02	0.16±0.03	2.07	0.16±0.02	2.07	0.28±0.04		
2.08	0.12±0.02	2.13	0.11±0.02				
2.13	0.087±0.02	2.18	0.16±0.02				
2.17	0.079±0.02	2.23	0.079±0.02				
2.22	0.053±0.02	2.27	0.059±0.01				
2.28	0.017±0.009	2.32	0.046±0.01				
2.33	0.016±0.008	2.37	0.031±0.01				
2.37	0.02±0.009	2.42	0.043±0.01				
2.42	0.024±0.01						
2.48	0.016±0.008						
2.53	0.0041±0.004						
2.58	00±0.003						

proton 8 $A{\cdot}GeV$, 5-12% Central							
Y: 0.6 - 0.8		Y: 0.8 - 1		Y: 1 - 1.2		Y: 1.2 - 1.4	
$m_\perp$	Yield	$m_\perp$	Yield	$m_\perp$	Yield	$m_\perp$	Yield
0.98	27±1	1.03	21±0.7	1.03	19±0.8	1.075	15±0.8
1.03	23±0.8	1.08	17±0.6	1.08	16±0.6	1.129	13±0.6
1.08	18±0.6	1.13	15±0.5	1.13	14±0.5	1.175	11±0.4
1.13	15±0.5	1.18	12±0.5	1.17	12±0.4	1.226	9.2±0.4
1.18	12±0.4	1.23	9.7±0.4	1.23	9.5±0.4	1.275	7.6±0.3
1.23	9.5±0.4	1.27	7.7±0.3	1.28	7.6±0.3	1.325	6.1±0.3
1.28	7.3±0.3	1.32	6.4±0.3	1.33	6.3±0.3	1.375	5.5±0.2
1.33	5.3±0.2	1.38	5.1±0.2	1.37	5.1±0.2	1.425	4.5±0.2
1.37	4.5±0.2	1.43	04±0.2	1.43	4.3±0.2	1.475	3.6±0.2
1.42	3.4±0.2	1.48	3.2±0.2	1.48	3.4±0.2	1.525	03±0.2
1.47	2.6±0.1	1.53	2.6±0.1	1.53	2.7±0.1	1.575	2.3±0.1
1.52	02±0.1	1.58	02±0.1	1.57	2.1±0.1	1.625	02±0.1
1.58	1.3±0.09	1.63	1.5±0.09	1.63	1.7±0.1	1.675	1.6±0.1
1.62	1.2±0.08	1.67	1.2±0.07	1.68	1.3±0.08	1.723	1.1±0.09
1.67	0.93±0.07	1.73	0.92±0.06	1.73	1.1±0.07	1.774	0.86±0.09
1.72	0.65±0.06	1.77	0.65±0.05	1.77	0.88±0.06		
1.77	0.55±0.05	1.83	0.58±0.05	1.82	0.62±0.05		
1.83	0.35±0.04	1.88	0.43±0.04	1.87	0.54±0.04		
1.88	0.3±0.04	1.92	0.34±0.03	1.93	0.35±0.03		
1.92	0.21±0.03	1.98	0.23±0.03	1.97	0.29±0.03		
1.97	0.15±0.02	2.03	0.18±0.02	2.02	0.29±0.03		
2.02	0.14±0.02	2.07	0.19±0.02	2.07	0.2±0.03		
2.08	0.1±0.02	2.13	0.1±0.02				
2.13	0.048±0.01	2.18	0.063±0.01				
2.17	0.048±0.01	2.23	0.06±0.01				
2.22	0.049±0.01	2.27	0.051±0.01				
2.28	0.034±0.01	2.32	0.033±0.008				
2.33	0.02±0.008	2.37	0.032±0.009				
2.37	0.014±0.006	2.42	0.023±0.008				
2.42	0.003±0.003						
2.48	0.012±0.006						
2.53	0.0057±0.004						
2.58	0.0026±0.003						
2.62	0.0055±0.004						
2.67	00±0.003						

proton 8 $A{\cdot}GeV$, 12-23% Central							
Y: 0.6 - 0.8		Y: 0.8 - 1		Y: 1 - 1.2		Y: 1.2 - 1.4	
$m_\perp$	Yield	$m_\perp$	Yield	$m_\perp$	Yield	$m_\perp$	Yield
0.98	24±0.8	1.03	17±0.6	1.03	15±0.6	1.075	12±0.5
1.03	19±0.6	1.08	13±0.5	1.08	12±0.4	1.129	9.6±0.4
1.08	15±0.5	1.13	11±0.4	1.13	10±0.4	1.175	8.2±0.3
1.13	12±0.4	1.18	8.8±0.3	1.17	8.5±0.3	1.226	6.9±0.3
1.18	9.1±0.3	1.23	7.1±0.3	1.23	6.8±0.3	1.275	5.6±0.2
1.23	7.2±0.3	1.27	06±0.2	1.28	5.8±0.2	1.325	4.6±0.2
1.28	5.4±0.2	1.32	4.5±0.2	1.33	4.5±0.2	1.375	3.6±0.2
1.33	4.2±0.2	1.38	3.5±0.2	1.37	3.6±0.2	1.425	3.1±0.1
1.37	3.4±0.1	1.43	2.9±0.1	1.43	2.9±0.1	1.475	2.4±0.1
1.42	2.5±0.1	1.48	2.2±0.1	1.48	2.2±0.1	1.525	02±0.1
1.47	1.8±0.09	1.53	1.7±0.08	1.53	1.8±0.09	1.575	1.6±0.09
1.52	1.3±0.08	1.58	1.4±0.07	1.57	1.5±0.08	1.625	1.3±0.07
1.58	1.2±0.07	1.63	01±0.06	1.63	1.2±0.07	1.675	0.95±0.06
1.62	0.83±0.05	1.67	0.82±0.05	1.68	0.93±0.06	1.723	0.77±0.06
1.67	0.59±0.04	1.73	0.58±0.04	1.73	0.69±0.05	1.774	0.63±0.06
1.72	0.42±0.04	1.77	0.46±0.03	1.77	0.57±0.04		
1.77	0.31±0.03	1.83	0.33±0.03	1.82	0.42±0.03		
1.83	0.26±0.03	1.88	0.28±0.03	1.87	0.33±0.03		
1.88	0.2±0.02	1.92	0.21±0.02	1.93	0.26±0.02		
1.92	0.16±0.02	1.98	0.18±0.02	1.97	0.23±0.02		
1.97	0.12±0.02	2.03	0.12±0.01	2.02	0.17±0.02		
2.02	0.096±0.01	2.07	0.093±0.01	2.07	0.12±0.02		
2.08	0.081±0.01	2.13	0.056±0.009				
2.13	0.052±0.01	2.18	0.059±0.009				
2.17	0.033±0.008	2.23	0.044±0.008				
2.22	0.022±0.007	2.27	0.027±0.006				
2.28	0.025±0.007	2.32	0.024±0.006				
2.33	0.0035±0.003	2.37	0.014±0.005				
2.37	0.012±0.005	2.42	0.0064±0.003				
2.42	0.0093±0.004						
2.48	0.0037±0.003						
2.53	0.0017±0.002						
2.58	0.0019±0.002						
2.62	0.0053±0.003						
2.67	00±0.002						

proton 8 $A{\cdot}GeV$, 23-39% Central							
Y: 0.6 - 0.8		Y: 0.8 - 1		Y: 1 - 1.2		Y: 1.2 - 1.4	
$m_\perp$	Yield	$m_\perp$	Yield	$m_\perp$	Yield	$m_\perp$	Yield
0.98	18±0.6	1.03	12±0.4	1.03	11±0.4	1.075	8.2±0.4
1.03	14±0.4	1.08	09±0.3	1.08	08±0.3	1.129	6.2±0.3
1.08	10±0.3	1.13	7.3±0.2	1.13	6.8±0.2	1.175	5.1±0.2
1.13	8.1±0.3	1.18	5.5±0.2	1.17	5.3±0.2	1.226	3.9±0.2
1.18	6.2±0.2	1.23	4.5±0.2	1.23	4.4±0.2	1.275	3.3±0.1
1.23	4.7±0.2	1.27	3.5±0.1	1.28	3.3±0.1	1.325	2.6±0.1
1.28	3.6±0.1	1.32	2.7±0.1	1.33	2.6±0.1	1.375	2.1±0.09
1.33	2.6±0.1	1.38	1.9±0.09	1.37	2.1±0.1	1.425	1.6±0.08
1.37	02±0.09	1.43	1.6±0.07	1.43	1.6±0.08	1.475	1.3±0.07
1.42	1.4±0.07	1.48	1.2±0.06	1.48	1.2±0.06	1.525	01±0.06
1.47	1.1±0.06	1.53	0.95±0.05	1.53	01±0.06	1.575	0.79±0.05
1.52	0.83±0.05	1.58	0.67±0.04	1.57	0.74±0.04	1.625	0.62±0.04
1.58	0.58±0.04	1.63	0.53±0.03	1.63	0.59±0.04	1.675	0.55±0.04
1.62	0.43±0.03	1.67	0.37±0.03	1.68	0.47±0.03	1.723	0.36±0.03
1.67	0.34±0.03	1.73	0.29±0.02	1.73	0.35±0.03	1.774	0.32±0.03
1.72	0.25±0.02	1.77	0.24±0.02	1.77	0.28±0.02		
1.77	0.16±0.02	1.83	0.17±0.02	1.82	0.24±0.02		
1.83	0.15±0.02	1.88	0.14±0.01	1.87	0.16±0.02		
1.88	0.12±0.01	1.92	0.11±0.01	1.93	0.14±0.01		
1.92	0.098±0.01	1.98	0.087±0.01	1.97	0.098±0.01		
1.97	0.059±0.01	2.03	0.064±0.009	2.02	0.044±0.008		
2.02	0.035±0.007	2.07	0.042±0.007	2.07	0.052±0.01		
2.08	0.036±0.007	2.13	0.04±0.006				
2.13	0.026±0.006	2.18	0.025±0.005				
2.17	0.012±0.004	2.23	0.02±0.004				
2.22	0.013±0.004	2.27	0.013±0.003				
2.28	0.0087±0.003	2.32	0.012±0.003				
2.33	0.0024±0.002	2.37	0.0044±0.002				
2.37	0.0025±0.002	2.42	0.0093±0.004				
2.42	0.0027±0.002						
2.48	0.0013±0.001						
2.53	0.0012±0.001						
2.58	0.0012±0.001						
2.62	0.0012±0.001						

π^- 2 $A{\cdot}GeV$, 0-5% Central					
Y: 0.8 - 1		Y: 1 - 1.2		Y: 1.2 - 1.4	
$m_\perp$	Yield	$m_\perp$	Yield	$m_\perp$	Yield
0.28	35±2	0.23	53±4	0.277	25±2
0.33	18±1	0.28	31±2	0.326	15±1
0.38	9.7±0.6	0.33	17±1	0.376	6.9±0.7
0.43	6.6±0.4	0.37	9.5±0.7	0.425	4.6±0.5
0.48	3.7±0.3	0.43	5.9±0.5	0.475	2.5±0.3
0.53	2.2±0.2	0.47	3.3±0.3	0.525	1.5±0.2
0.58	1.4±0.1	0.53	2.3±0.2	0.575	0.94±0.1
0.62	0.96±0.09	0.58	1.5±0.2	0.625	0.57±0.1
0.67	0.66±0.07	0.63	0.96±0.1	0.675	0.45±0.09
0.72	0.47±0.05	0.68	0.51±0.08	0.725	0.42±0.09
0.78	0.29±0.04	0.73	0.4±0.06	0.775	0.14±0.04
0.82	0.21±0.03	0.78	0.35±0.06	0.825	0.074±0.03
0.88	0.11±0.02	0.83	0.17±0.04		
0.92	0.081±0.02	0.87	0.13±0.03		
0.98	0.055±0.01	0.93	0.089±0.02		
1.03	0.068±0.01	0.97	0.067±0.02		
1.07	0.033±0.01	1.02	0.05±0.02		
1.12	0.011±0.006				

π^- 2 $A{\cdot}GeV$, 5-12% Central					
Y: 0.8 - 1		Y: 1 - 1.2		Y: 1.2 - 1.4	
$m_\perp$	Yield	$m_\perp$	Yield	$m_\perp$	Yield
0.28	25±1	0.23	41±3	0.277	19±1
0.33	14±0.7	0.28	22±1	0.326	11±0.9
0.38	7.5±0.4	0.33	14±0.8	0.376	5.8±0.5
0.43	4.2±0.3	0.37	6.6±0.5	0.425	3.1±0.3
0.48	2.5±0.2	0.43	4.3±0.3	0.475	2.1±0.2
0.53	1.6±0.1	0.47	2.7±0.2	0.525	1.3±0.2
0.58	1.1±0.09	0.53	1.5±0.2	0.575	0.63±0.1
0.62	0.68±0.06	0.58	1.1±0.1	0.625	0.57±0.09
0.67	0.41±0.05	0.63	0.74±0.09	0.675	0.48±0.08
0.72	0.32±0.04	0.68	0.36±0.06	0.725	0.21±0.05
0.78	0.19±0.03	0.73	0.26±0.04	0.775	0.13±0.03
0.82	0.12±0.02	0.78	0.13±0.03	0.825	0.11±0.03
0.88	0.094±0.02	0.83	0.12±0.03	0.872	0.078±0.03
0.92	0.076±0.01	0.87	0.097±0.02		
0.98	0.046±0.01	0.93	0.043±0.01		
1.03	0.026±0.008	0.97	0.045±0.01		
1.07	0.016±0.006	1.02	0.02±0.01		
1.12	0.022±0.007				

π^- 2 $A{\cdot}GeV$, 12-23% Central					
Y: 0.8 - 1		Y: 1 - 1.2		Y: 1.2 - 1.4	
$m_\perp$	Yield	$m_\perp$	Yield	$m_\perp$	Yield
0.28	17±0.9	0.23	31±2	0.277	15±1
0.33	8.6±0.5	0.28	16±0.9	0.326	6.4±0.5
0.38	4.7±0.3	0.33	8.2±0.5	0.376	3.9±0.3
0.43	03±0.2	0.37	4.3±0.3	0.425	2.1±0.2
0.48	1.7±0.1	0.43	2.6±0.2	0.475	1.4±0.1
0.53	1.1±0.08	0.47	1.6±0.1	0.525	0.82±0.1
0.58	0.76±0.06	0.53	0.94±0.1	0.575	0.49±0.07
0.62	0.42±0.04	0.58	0.63±0.07	0.625	0.41±0.06
0.67	0.31±0.03	0.63	0.42±0.05	0.675	0.16±0.03
0.72	0.17±0.02	0.68	0.2±0.03	0.725	0.17±0.03
0.78	0.1±0.02	0.73	0.21±0.03	0.775	0.068±0.02
0.82	0.084±0.01	0.78	0.11±0.02	0.825	0.058±0.02
0.88	0.061±0.01	0.83	0.087±0.02	0.872	0.045±0.02
0.92	0.031±0.007	0.87	0.052±0.01		
0.98	0.021±0.006	0.93	0.03±0.009		
1.03	0.013±0.004	0.97	0.023±0.008		
1.07	0.011±0.004	1.02	0.013±0.007		
1.12	0.011±0.004				

π^- 2 $A{\cdot}GeV$, 23-39% Central					
Y: 0.8 - 1		Y: 1 - 1.2		Y: 1.2 - 1.4	
$m_\perp$	Yield	$m_\perp$	Yield	$m_\perp$	Yield
0.28	10±0.6	0.23	18±1	0.277	7.3±0.6
0.33	05±0.3	0.28	9.3±0.5	0.326	3.5±0.3
0.38	2.6±0.2	0.33	4.9±0.3	0.376	2.4±0.2
0.43	1.7±0.1	0.37	2.9±0.2	0.425	1.3±0.1
0.48	0.91±0.07	0.43	1.4±0.1	0.475	0.72±0.08
0.53	0.59±0.05	0.47	0.98±0.09	0.525	0.46±0.06
0.58	0.35±0.03	0.53	0.59±0.06	0.575	0.22±0.04
0.62	0.25±0.02	0.58	0.34±0.04	0.625	0.18±0.03
0.67	0.15±0.02	0.63	0.26±0.03	0.675	0.12±0.03
0.72	0.091±0.01	0.68	0.14±0.02	0.725	0.061±0.02
0.78	0.048±0.009	0.73	0.098±0.02	0.775	0.043±0.01
0.82	0.036±0.007	0.78	0.065±0.01	0.825	0.027±0.01
0.88	0.021±0.005	0.83	0.038±0.009	0.872	0.018±0.01
0.92	0.016±0.004	0.87	0.022±0.007		
0.98	0.015±0.004	0.93	0.021±0.007		
1.03	0.0071±0.003	0.97	0.0086±0.004		
1.07	0.0042±0.002	1.02	0.007±0.004		
1.12	0.0017±0.001				

π^- 4 $A{\cdot}GeV$, 0-5% Central							
Y: 0.8 - 1		Y: 1 - 1.2		Y: 1.2 - 1.4		Y: 1.4 - 1.6	
$m_\perp$	Yield	$m_\perp$	Yield	$m_\perp$	Yield	$m_\perp$	Yield
0.28	51±2	0.23	92±4	0.23	91±5	0.184	1.6e+02±8
0.33	28±1	0.28	50±2	0.28	54±3	0.225	91±5
0.37	19±1	0.33	32±1	0.33	30±2	0.276	50±3
0.43	11±0.6	0.38	19±0.8	0.38	19±1	0.327	29±2
0.48	6.9±0.4	0.43	13±0.6	0.43	13±0.7	0.376	19±1
0.53	5.1±0.3	0.47	8.6±0.4	0.48	8.6±0.5	0.426	12±0.8
0.58	3.7±0.3	0.53	6.3±0.3	0.53	5.6±0.3	0.475	7.6±0.6
0.63	2.8±0.2	0.58	4.4±0.2	0.58	4.4±0.3	0.525	5.5±0.4
0.67	1.7±0.1	0.62	3.1±0.2	0.63	2.9±0.2	0.575	3.8±0.3
0.72	1.3±0.1	0.68	2.1±0.1	0.68	2.1±0.2	0.625	3.1±0.3
0.78	0.96±0.1	0.73	1.6±0.1	0.72	1.7±0.1	0.674	2.1±0.2
0.83	0.6±0.07	0.78	1.1±0.08	0.77	1.2±0.1	0.724	1.6±0.2
0.88	0.57±0.07	0.82	0.86±0.07	0.82	0.83±0.08		
0.92	0.39±0.05	0.88	0.56±0.05	0.87	0.66±0.08		
0.98	0.32±0.04	0.93	0.44±0.04				
1.02	0.25±0.04	0.97	0.33±0.04				
1.07	0.13±0.03	1.02	0.28±0.04				
1.12	0.096±0.02						

π^- 4 $A{\cdot}GeV$, 5-12% Central							
Y: 0.8 - 1		Y: 1 - 1.2		Y: 1.2 - 1.4		Y: 1.4 - 1.6	
$m_\perp$	Yield	$m_\perp$	Yield	$m_\perp$	Yield	$m_\perp$	Yield
0.28	38±2	0.23	73±3	0.23	68±3	0.184	1.1e+02±6
0.33	22±1	0.28	41±2	0.28	40±2	0.225	69±4
0.37	14±0.7	0.33	24±1	0.33	23±1	0.276	42±2
0.43	9.1±0.5	0.38	15±0.6	0.38	15±0.8	0.327	21±1
0.48	5.2±0.3	0.43	9.6±0.4	0.43	9.6±0.5	0.376	15±0.9
0.53	3.8±0.2	0.47	6.6±0.3	0.48	6.3±0.4	0.426	9.7±0.6
0.58	03±0.2	0.53	4.4±0.2	0.53	4.7±0.3	0.475	5.7±0.4
0.63	1.9±0.1	0.58	03±0.2	0.58	3.1±0.2	0.525	4.6±0.3
0.67	1.3±0.1	0.62	2.3±0.1	0.63	2.2±0.2	0.575	2.6±0.2
0.72	01±0.09	0.68	1.6±0.1	0.68	1.6±0.1	0.625	02±0.2
0.78	0.73±0.07	0.73	1.2±0.08	0.72	1.1±0.09	0.674	1.5±0.2
0.83	0.6±0.06	0.78	0.89±0.06	0.77	0.73±0.07	0.724	1.4±0.2
0.88	0.43±0.05	0.82	0.63±0.05	0.82	0.56±0.06		
0.92	0.32±0.04	0.88	0.45±0.04	0.87	0.4±0.05		
0.98	0.19±0.03	0.93	0.34±0.03				
1.02	0.14±0.02	0.97	0.23±0.03				
1.07	0.12±0.02	1.02	0.18±0.03				
1.12	0.073±0.02						

π^- 4 $A{\cdot}GeV$, 12-23% Central							
Y: 0.8 - 1		Y: 1 - 1.2		Y: 1.2 - 1.4		Y: 1.4 - 1.6	
$m_\perp$	Yield	$m_\perp$	Yield	$m_\perp$	Yield	$m_\perp$	Yield
0.28	26±1	0.23	53±2	0.23	51±2	0.184	88±4
0.33	15±0.7	0.28	28±1	0.28	30±1	0.225	52±3
0.37	9.3±0.5	0.33	17±0.7	0.33	18±0.9	0.276	31±2
0.43	5.9±0.3	0.38	10±0.4	0.38	11±0.5	0.327	16±0.9
0.48	3.9±0.2	0.43	6.8±0.3	0.43	6.8±0.4	0.376	11±0.6
0.53	2.7±0.2	0.47	4.5±0.2	0.48	4.7±0.2	0.426	6.7±0.4
0.58	1.9±0.1	0.53	3.3±0.2	0.53	03±0.2	0.475	4.7±0.3
0.63	1.3±0.1	0.58	2.1±0.1	0.58	2.2±0.1	0.525	3.3±0.2
0.67	0.96±0.07	0.62	1.5±0.09	0.63	1.5±0.1	0.575	2.1±0.2
0.72	0.69±0.06	0.68	1.1±0.07	0.68	01±0.08	0.625	1.5±0.1
0.78	0.51±0.05	0.73	0.83±0.05	0.72	0.76±0.06	0.674	1.2±0.1
0.83	0.32±0.04	0.78	0.58±0.04	0.77	0.56±0.05	0.724	0.78±0.09
0.88	0.26±0.03	0.82	0.45±0.03	0.82	0.34±0.04		
0.92	0.21±0.03	0.88	0.34±0.03	0.87	0.29±0.04		
0.98	0.15±0.02	0.93	0.22±0.02				
1.02	0.11±0.02	0.97	0.16±0.02				
1.07	0.088±0.01	1.02	0.11±0.02				
1.12	0.043±0.01						

π^- 4 $A{\cdot}GeV$, 23-39% Central							
Y: 0.8 - 1		Y: 1 - 1.2		Y: 1.2 - 1.4		Y: 1.4 - 1.6	
$m_\perp$	Yield	$m_\perp$	Yield	$m_\perp$	Yield	$m_\perp$	Yield
0.28	16±0.7	0.23	32±1	0.23	30±1	0.184	54±3
0.33	9.1±0.4	0.28	16±0.7	0.28	17±0.8	0.225	30±2
0.37	06±0.3	0.33	9.8±0.4	0.33	11±0.5	0.276	17±1
0.43	3.5±0.2	0.38	6.1±0.3	0.38	6.1±0.3	0.327	11±0.6
0.48	2.5±0.1	0.43	04±0.2	0.43	4.2±0.2	0.376	06±0.4
0.53	1.7±0.1	0.47	2.8±0.1	0.48	2.7±0.2	0.426	3.8±0.2
0.58	1.1±0.08	0.53	1.8±0.1	0.53	1.7±0.1	0.475	2.8±0.2
0.63	0.73±0.06	0.58	1.3±0.07	0.58	1.2±0.08	0.525	1.8±0.1
0.67	0.48±0.04	0.62	0.91±0.05	0.63	0.89±0.06	0.575	1.2±0.1
0.72	0.41±0.04	0.68	0.62±0.04	0.68	0.6±0.05	0.625	0.88±0.08
0.78	0.25±0.03	0.73	0.44±0.03	0.72	0.45±0.04	0.674	0.52±0.06
0.83	0.17±0.02	0.78	0.3±0.02	0.77	0.3±0.03	0.724	0.48±0.06
0.88	0.16±0.02	0.82	0.24±0.02	0.82	0.22±0.02		
0.92	0.12±0.02	0.88	0.15±0.01	0.87	0.18±0.02		
0.98	0.067±0.01	0.93	0.1±0.01				
1.02	0.055±0.01	0.97	0.079±0.01				
1.07	0.04±0.008	1.02	0.048±0.009				
1.12	0.03±0.007						

π^- 6 $A{\cdot}GeV$, 0-5% Central							
Y: 0.8 - 1		Y: 1 - 1.2		Y: 1.2 - 1.4		Y: 1.4 - 1.6	
$m_\perp$	Yield	$m_\perp$	Yield	$m_\perp$	Yield	$m_\perp$	Yield
0.28	73±4	0.23	1.2e+02±5	0.19	2e+02±1e+01	0.227	1.2e+02±5
0.33	42±2	0.27	71±4	0.23	1.2e+02±5	0.277	73±3
0.37	28±2	0.32	45±3	0.28	73±3	0.325	46±2
0.43	19±1	0.37	30±2	0.32	47±2	0.375	30±1
0.48	12±0.8	0.43	21±1	0.37	30±1	0.425	21±1
0.53	09±0.6	0.47	13±1	0.42	21±1	0.475	14±0.8
0.58	5.8±0.4	0.52	9.3±0.8	0.47	14±0.8	0.525	10±0.6
0.63	4.9±0.4	0.58	7.4±0.6	0.52	10±0.6	0.575	7.1±0.4
0.68	3.3±0.3	0.62	5.3±0.5	0.57	7.4±0.5	0.625	4.8±0.3
0.72	2.4±0.2	0.67	3.7±0.4	0.63	5.1±0.4	0.674	3.8±0.3
0.77	1.7±0.2	0.73	2.7±0.3	0.68	3.6±0.3	0.722	2.8±0.3
0.82	1.2±0.1	0.78	1.7±0.2	0.73	2.2±0.2		
0.88	01±0.1	0.82	1.3±0.2	0.77	2.2±0.2		
0.93	0.75±0.1	0.88	0.97±0.1	0.82	1.9±0.2		
0.97	0.49±0.08	0.93	0.96±0.1	0.87	1.1±0.2		
1.03	0.42±0.07	0.97	0.66±0.1				
1.08	0.29±0.05	1.02	0.43±0.1				
1.12	0.24±0.05						

π^- 6 $A{\cdot}GeV$, 5-12% Central							
Y: 0.8 - 1		Y: 1 - 1.2		Y: 1.2 - 1.4		Y: 1.4 - 1.6	
$m_\perp$	Yield	$m_\perp$	Yield	$m_\perp$	Yield	$m_\perp$	Yield
0.28	57±3	0.23	94±4	0.19	1.6e+02±8	0.227	1e+02±4
0.33	34±2	0.27	61±3	0.23	99±4	0.277	59±2
0.37	22±1	0.32	35±2	0.28	61±2	0.325	39±2
0.43	15±0.9	0.37	22±1	0.32	36±2	0.375	24±1
0.48	10±0.6	0.43	16±1	0.37	25±1	0.425	16±0.8
0.53	6.5±0.4	0.47	11±0.8	0.42	17±0.8	0.475	11±0.6
0.58	4.8±0.3	0.52	6.8±0.5	0.47	12±0.7	0.525	7.5±0.4
0.63	3.6±0.3	0.58	5.3±0.4	0.52	8.3±0.5	0.575	5.7±0.3
0.68	2.3±0.2	0.62	3.8±0.3	0.57	5.6±0.4	0.625	3.9±0.2
0.72	1.7±0.2	0.67	3.3±0.3	0.63	04±0.3	0.674	03±0.2
0.77	1.7±0.1	0.73	02±0.2	0.68	3.1±0.2	0.722	2.3±0.2
0.82	01±0.1	0.78	1.3±0.2	0.73	2.3±0.2		
0.88	0.59±0.08	0.82	1.1±0.1	0.77	1.8±0.2		
0.93	0.54±0.07	0.88	0.95±0.1	0.82	1.3±0.1		
0.97	0.37±0.06	0.93	0.7±0.1	0.87	0.86±0.1		
1.03	0.29±0.05	0.97	0.46±0.08				
1.08	0.22±0.04	1.02	0.42±0.09				
1.12	0.15±0.03						

π^- 6 $A{\cdot}GeV$, 12-23% Central							
Y: 0.8 - 1		Y: 1 - 1.2		Y: 1.2 - 1.4		Y: 1.4 - 1.6	
$m_\perp$	Yield	$m_\perp$	Yield	$m_\perp$	Yield	$m_\perp$	Yield
0.28	41±2	0.23	70±3	0.19	1.2e+02±6	0.227	72±3
0.33	25±1	0.27	42±2	0.23	71±3	0.277	43±2
0.37	16±0.9	0.32	27±1	0.28	43±2	0.325	27±1
0.43	11±0.6	0.37	16±0.9	0.32	27±1	0.375	18±0.8
0.48	07±0.4	0.43	11±0.7	0.37	17±0.8	0.425	12±0.5
0.53	4.7±0.3	0.47	7.7±0.5	0.42	12±0.6	0.475	8.2±0.4
0.58	3.1±0.2	0.52	5.9±0.4	0.47	8.3±0.4	0.525	5.8±0.3
0.63	2.3±0.2	0.58	3.7±0.3	0.52	5.8±0.3	0.575	3.9±0.2
0.68	1.7±0.1	0.62	2.5±0.2	0.57	3.8±0.2	0.625	3.1±0.2
0.72	1.2±0.1	0.67	1.9±0.2	0.63	2.9±0.2	0.674	02±0.1
0.77	0.96±0.09	0.73	1.4±0.1	0.68	2.3±0.2	0.722	1.5±0.1
0.82	0.65±0.07	0.78	1.1±0.1	0.73	1.6±0.1		
0.88	0.47±0.06	0.82	0.73±0.09	0.77	0.97±0.09		
0.93	0.31±0.04	0.88	0.54±0.07	0.82	0.78±0.08		
0.97	0.27±0.04	0.93	0.57±0.07	0.87	0.68±0.09		
1.03	0.21±0.03	0.97	0.33±0.05				
1.08	0.15±0.03	1.02	0.25±0.05				
1.12	0.11±0.02						

π^- 6 $A{\cdot}GeV$, 23-39% Central							
Y: 0.8 - 1		Y: 1 - 1.2		Y: 1.2 - 1.4		Y: 1.4 - 1.6	
$m_\perp$	Yield	$m_\perp$	Yield	$m_\perp$	Yield	$m_\perp$	Yield
0.28	26±1	0.23	45±2	0.19	76±4	0.227	48±2
0.33	16±0.9	0.27	27±1	0.23	48±2	0.277	28±1
0.37	9.8±0.6	0.32	18±0.9	0.28	28±1	0.325	18±0.7
0.43	6.6±0.4	0.37	10±0.6	0.32	17±0.7	0.375	11±0.5
0.48	4.6±0.3	0.43	7.4±0.5	0.37	11±0.5	0.425	7.7±0.4
0.53	3.2±0.2	0.47	4.9±0.3	0.42	7.4±0.4	0.475	5.1±0.3
0.58	2.2±0.2	0.52	3.6±0.3	0.47	5.2±0.3	0.525	3.8±0.2
0.63	1.5±0.1	0.58	2.5±0.2	0.52	3.5±0.2	0.575	2.4±0.1
0.68	1.1±0.09	0.62	1.8±0.2	0.57	2.7±0.2	0.625	1.8±0.1
0.72	0.83±0.07	0.67	1.4±0.1	0.63	1.9±0.1	0.674	1.4±0.09
0.77	0.57±0.06	0.73	0.89±0.1	0.68	1.4±0.1	0.722	0.95±0.08
0.82	0.4±0.04	0.78	0.69±0.08	0.73	01±0.08		
0.88	0.3±0.04	0.82	0.43±0.06	0.77	0.77±0.07		
0.93	0.22±0.03	0.88	0.41±0.05	0.82	0.51±0.05		
0.97	0.17±0.03	0.93	0.26±0.04	0.87	0.42±0.06		
1.03	0.13±0.02	0.97	0.22±0.04				
1.08	0.069±0.01	1.02	0.13±0.03				
1.12	0.052±0.01						

π^- 8 $A{\cdot}GeV$, 0-5% Central							
Y: 0.8 - 1		Y: 1 - 1.2		Y: 1.2 - 1.4		Y: 1.4 - 1.6	
$m_\perp$	Yield	$m_\perp$	Yield	$m_\perp$	Yield	$m_\perp$	Yield
0.28	79±3	0.23	1.5e+02±6	0.19	2.3e+02±1e+01	0.228	1.4e+02±6
0.33	50±2	0.28	91±4	0.23	1.5e+02±6	0.276	95±4
0.37	34±2	0.33	57±2	0.28	90±4	0.325	60±2
0.43	22±1	0.38	39±2	0.33	60±2	0.375	41±2
0.48	16±0.8	0.43	28±1	0.38	41±2	0.425	26±1
0.53	11±0.6	0.47	18±0.9	0.42	27±1	0.475	19±0.9
0.58	8.3±0.5	0.53	13±0.7	0.48	20±0.9	0.525	13±0.7
0.62	6.2±0.4	0.58	9.3±0.5	0.53	14±0.7	0.575	11±0.6
0.67	4.3±0.3	0.62	6.6±0.4	0.57	9.7±0.5	0.625	7.8±0.4
0.72	3.2±0.2	0.68	4.9±0.3	0.63	7.4±0.4	0.674	5.8±0.4
0.78	2.4±0.2	0.73	3.9±0.3	0.68	5.5±0.3	0.723	04±0.3
0.82	1.7±0.1	0.78	2.7±0.2	0.73	4.2±0.3		
0.88	1.3±0.1	0.82	2.1±0.2	0.77	03±0.2		
0.92	0.83±0.09	0.88	1.5±0.1	0.82	2.6±0.2		
0.97	0.73±0.08	0.93	01±0.1	0.87	1.9±0.2		
1.03	0.51±0.06	0.97	0.82±0.09				
1.08	0.48±0.06	1.02	0.72±0.1				
1.12	0.28±0.04						

π^- 8 $A{\cdot}GeV$, 5-12% Central							
Y: 0.8 - 1		Y: 1 - 1.2		Y: 1.2 - 1.4		Y: 1.4 - 1.6	
$m_\perp$	Yield	$m_\perp$	Yield	$m_\perp$	Yield	$m_\perp$	Yield
0.28	66±3	0.23	1.2e+02±5	0.19	1.8e+02±8	0.228	1.1e+02±4
0.33	41±2	0.28	71±3	0.23	1.2e+02±4	0.276	72±3
0.37	27±1	0.33	45±2	0.28	73±3	0.325	46±2
0.43	18±0.9	0.38	30±1	0.33	46±2	0.375	33±1
0.48	12±0.6	0.43	20±0.9	0.38	31±1	0.425	21±0.9
0.53	8.4±0.4	0.47	14±0.7	0.42	21±0.9	0.475	15±0.7
0.58	6.2±0.3	0.53	9.6±0.5	0.48	14±0.7	0.525	10±0.5
0.62	4.4±0.3	0.58	7.2±0.4	0.53	10±0.5	0.575	8.1±0.4
0.67	3.6±0.2	0.62	5.1±0.3	0.57	7.4±0.4	0.625	5.7±0.3
0.72	2.5±0.2	0.68	3.8±0.2	0.63	5.6±0.3	0.674	4.1±0.3
0.78	02±0.1	0.73	2.9±0.2	0.68	04±0.3	0.723	3.4±0.2
0.82	1.2±0.1	0.78	02±0.1	0.73	03±0.2		
0.88	01±0.09	0.82	1.6±0.1	0.77	2.3±0.2		
0.92	0.65±0.07	0.88	1.2±0.1	0.82	02±0.2		
0.97	0.5±0.06	0.93	0.92±0.08	0.87	1.4±0.1		
1.03	0.49±0.06	0.97	0.77±0.07				
1.08	0.27±0.04	1.02	0.47±0.06				
1.12	0.21±0.03						

π^- 8 $A{\cdot}GeV$, 12-23% Central							
Y: 0.8 - 1		Y: 1 - 1.2		Y: 1.2 - 1.4		Y: 1.4 - 1.6	
$m_\perp$	Yield	$m_\perp$	Yield	$m_\perp$	Yield	$m_\perp$	Yield
0.28	49±2	0.23	85±3	0.19	1.4e+02±6	0.228	90±3
0.33	28±1	0.28	51±2	0.23	88±3	0.276	55±2
0.37	19±0.8	0.33	33±1	0.28	51±2	0.325	35±1
0.43	13±0.6	0.38	22±0.9	0.33	32±1	0.375	24±1
0.48	8.9±0.4	0.43	14±0.6	0.38	23±0.9	0.425	15±0.6
0.53	5.9±0.3	0.47	10±0.5	0.42	15±0.6	0.475	11±0.5
0.58	4.6±0.2	0.53	7.4±0.4	0.48	11±0.5	0.525	7.6±0.4
0.62	3.2±0.2	0.58	5.1±0.3	0.53	7.7±0.4	0.575	5.8±0.3
0.67	2.5±0.2	0.62	3.7±0.2	0.57	5.7±0.3	0.625	4.3±0.2
0.72	1.7±0.1	0.68	2.8±0.2	0.63	04±0.2	0.674	03±0.2
0.78	1.3±0.09	0.73	2.2±0.1	0.68	2.9±0.2	0.723	2.2±0.2
0.82	0.91±0.07	0.78	1.4±0.1	0.73	2.2±0.1		
0.88	0.61±0.06	0.82	1.1±0.08	0.77	1.6±0.1		
0.92	0.48±0.05	0.88	0.87±0.07	0.82	1.3±0.1		
0.97	0.31±0.04	0.93	0.6±0.05	0.87	0.88±0.09		
1.03	0.28±0.03	0.97	0.43±0.04				
1.08	0.19±0.03	1.02	0.36±0.05				
1.12	0.15±0.02						

π^- 8 $A{\cdot}GeV$, 23-39% Central							
Y: 0.8 - 1		Y: 1 - 1.2		Y: 1.2 - 1.4		Y: 1.4 - 1.6	
$m_\perp$	Yield	$m_\perp$	Yield	$m_\perp$	Yield	$m_\perp$	Yield
0.28	29±1	0.23	53±2	0.19	88±4	0.228	56±2
0.33	19±0.8	0.28	32±1	0.23	55±2	0.276	35±1
0.37	12±0.5	0.33	21±0.9	0.28	34±1	0.325	21±0.8
0.43	8.2±0.4	0.38	14±0.6	0.33	22±0.8	0.375	15±0.6
0.48	5.4±0.3	0.43	09±0.4	0.38	14±0.6	0.425	10±0.4
0.53	3.9±0.2	0.47	6.3±0.3	0.42	9.9±0.4	0.475	7.1±0.3
0.58	2.7±0.1	0.53	4.5±0.2	0.48	6.8±0.3	0.525	4.9±0.2
0.62	1.9±0.1	0.58	3.4±0.2	0.53	4.6±0.2	0.575	3.5±0.2
0.67	1.6±0.1	0.62	2.3±0.1	0.57	3.4±0.2	0.625	2.5±0.1
0.72	1.1±0.07	0.68	1.6±0.1	0.63	2.4±0.1	0.674	1.9±0.1
0.78	0.76±0.06	0.73	1.1±0.08	0.68	1.7±0.1	0.723	1.3±0.09
0.82	0.57±0.05	0.78	0.99±0.07	0.73	1.4±0.09		
0.88	0.39±0.04	0.82	0.63±0.05	0.77	01±0.07		
0.92	0.31±0.03	0.88	0.48±0.04	0.82	0.74±0.06		
0.97	0.21±0.02	0.93	0.36±0.03	0.87	0.48±0.05		
1.03	0.16±0.02	0.97	0.27±0.03				
1.08	0.12±0.02	1.02	0.22±0.03				
1.12	0.088±0.01						

Appendix F

Tables of derived quantities, Y_{NN}

This appendix contains tables of the derived quantities dN/dY, T, the total χ^2, and the number of degrees of freedom of the fits, for K^+, K^-, π^+ and protons. In addition, γ, $\langle m_\perp \rangle$, and $\sigma_{T\gamma}$ are listed for the π^+ and protons. The tables contain information from each centrality class and beam energy, from a combined fit to the $m_\perp$ distributions in rapidity slices of 0.25 $|Y_{NN}|$ on either side of Y_{NN}. The measured points on either side of Y_{NN} are assumed to be uncorrelated in the fits. The errors listed are statistical only. The $m_\perp$ data to which the fits are made are tabulated in appendix G.

The kaon distributions are fit to an exponential, as described by equation 6.10, with T and dN/dY as fit parameters. The pions and protons are fit to Gamma distributins, as described by equations 6.13 and 6.14, with dN/dY, T, and γ as fit parameters. The $\langle m_\perp \rangle$ is derived from T and γ, using the full correlation term, $\sigma_{T\gamma}$.

y	K^+ dN/dy	K^+ T (GeV)	χ^2/d.o.f.
2 A·GeV, 0-5% Central			
0.91	0.382±0.015	0.139±0.004	19.94/ 26
2 A·GcV, 5-12% Central			
0.91	0.269±0.011	0.132±0.004	20.74/ 26
2 A·GeV, 12-23% Central			
0.91	0.165±0.007	0.125±0.004	28.20/ 24
2 A·GeV, 23-39% Central			
0.91	0.087±0.005	0.112±0.004	26.97/ 26

y	K^+ dN/dy	K^+ T (GeV)	χ^2/d.o.f.
4 $A{\cdot}GeV$, 0-5% Central			
1.2	2.343±0.054	0.159±0.004	12.89/ 18
4 $A{\cdot}GeV$, 5-12% Central			
1.2	1.772±0.041	0.156±0.004	18.36/ 18
4 $A{\cdot}GeV$, 12-23% Central			
1.2	1.196±0.028	0.145±0.003	18.05/ 18
4 $A{\cdot}GeV$, 23-39% Central			
1.2	0.605±0.016	0.146±0.004	14.03/ 18

y	K^+ dN/dy	K^+ T (GeV)	χ^2/d.o.f.
6 $A{\cdot}GeV$, 0-5% Central			
1.4	4.844±0.088	0.209±0.007	9.45/ 14
6 $A{\cdot}GeV$, 5-12% Central			
1.4	3.841±0.063	0.195±0.006	6.39/ 14
6 $A{\cdot}GeV$, 12-23% Central			
1.4	2.532±0.040	0.192±0.005	19.25/ 14
6 $A{\cdot}GeV$, 23-39% Central			
1.4	1.454±0.023	0.176±0.005	7.74/ 14

y	K^+ dN/dy	K^+ T (GeV)	χ^2/d.o.f.
8 $A{\cdot}GeV$, 0-5% Central			
1.5	7.849±0.209	0.220±0.011	6.63/ 9
8 $A{\cdot}GeV$, 5-12% Central			
1.5	5.758±0.144	0.205±0.010	3.83/ 9
8 $A{\cdot}GeV$, 12-23% Central			
1.5	3.967±0.095	0.202±0.009	4.53/ 9
8 $A{\cdot}GeV$, 23-39% Central			
1.5	2.246±0.057	0.184±0.008	3.50/ 9

y	K^- dN/dy	K^- T (GeV)	χ^2/d.o.f.
4 $A{\cdot}GeV$, 0-5% Central			
1.2	0.194±0.011	0.149±0.009	17.28/ 19
4 $A{\cdot}GeV$, 5-12% Central			
1.2	0.155±0.009	0.133±0.007	10.77/ 19
4 $A{\cdot}GeV$, 12-23% Central			
1.2	0.103±0.006	0.127±0.006	16.50/ 19
4 $A{\cdot}GeV$, 23-39% Central			
1.2	0.056±0.004	0.116±0.006	8.36/ 19

y	K^- dN/dy	K^- T (GeV)	χ^2/d.o.f.
6 $A{\cdot}GeV$, 0-5% Central			
1.4	0.607±0.023	0.166±0.010	5.47/ 14
6 $A{\cdot}GeV$, 5-12% Central			
1.4	0.453±0.017	0.173±0.011	8.14/ 14
6 $A{\cdot}GeV$, 12-23% Central			
1.4	0.332±0.011	0.153±0.008	8.52/ 14
6 $A{\cdot}GeV$, 23-39% Central			
1.4	0.186±0.007	0.145±0.008	10.01/ 14

y	K^- dN/dy	K^- T (GeV)	χ^2/d.o.f.
8 $A{\cdot}GeV$, 0-5% Central			
1.5	1.256±0.043	0.174±0.010	4.22/ 10
8 $A{\cdot}GeV$, 5-12% Central			
1.5	0.886±0.029	0.192±0.011	16.26/ 10
8 $A{\cdot}GeV$, 12-23% Central			
1.5	0.662±0.021	0.173±0.009	3.74/ 10
8 $A{\cdot}GeV$, 23-39% Central			
1.5	0.372±0.013	0.166±0.009	2.37/ 10

y	π^+ dN/dy	π^+ T (GeV)	γ	$\langle m_\perp \rangle$ (GeV)	$\sigma_{T\gamma}$ (GeV^2)	χ^2/d.o.f.
2 $A{\cdot}GeV$, 0-5% Central						
0.91	14.046±0.514	0.149±0.009	1.061±0.182	0.285±0.004	0.00195	35.01/ 38
2 $A{\cdot}GeV$, 5-12% Central						
0.91	11.048±0.424	0.157±0.010	1.322±0.192	0.277±0.004	0.00233	20.95/ 38
2 $A{\cdot}GeV$, 12-23% Central						
0.91	7.940±0.349	0.147±0.009	1.394±0.204	0.265±0.004	0.00226	35.94/ 37
2 $A{\cdot}GeV$, 23-39% Central						
0.91	4.635±0.221	0.141±0.010	1.338±0.226	0.263±0.004	0.00255	27.41/ 38

y	π^+ dN/dy	π^+ T (GeV)	γ	$\langle m_\perp \rangle$ (GeV)	$\sigma_{T\gamma}$ (GeV^2)	χ^2/d.o.f.
4 $A{\cdot}GeV$, 0-5% Central						
1.2	26.403±0.439	0.206±0.009	1.139±0.102	0.332±0.003	0.00138	33.05/ 33
4 $A{\cdot}GeV$, 5-12% Central						
1.2	21.374±0.368	0.229±0.012	1.434±0.105	0.324±0.003	0.00166	18.86/ 33
4 $A{\cdot}GeV$, 12-23% Central						
1.2	15.236±0.252	0.212±0.009	1.370±0.095	0.317±0.003	0.00132	29.09/ 33
4 $A{\cdot}GeV$, 23-39% Central						
1.2	9.023±0.158	0.206±0.009	1.367±0.100	0.312±0.003	0.00135	27.77/ 33

y	π^+ dN/dy	π^+ T (GeV)	γ	$\langle m_\perp \rangle$ (GeV)	$\sigma_{T\gamma}$ (GeV^2)	χ^2/d.o.f.
6 A·GeV, 0-5% Central						
1.4	38.924±0.524	0.206±0.011	0.911±0.107	0.354±0.003	0.00159	25.86/ 29
6 A·GeV, 5-12% Central						
1.4	31.938±0.420	0.216±0.012	1.066±0.106	0.349±0.003	0.0017	19.48/ 29
6 A·GeV, 12-23% Central						
1.4	22.843±0.294	0.206±0.011	1.067±0.105	0.339±0.003	0.00157	22.38/ 29
6 A·GeV, 23-39% Central						
1.4	15.276±0.199	0.210±0.011	1.173±0.103	0.333±0.003	0.00158	20.06/ 29

y	π^+ dN/dy	π^+ T (GeV)	γ	$\langle m_\perp \rangle$ (GeV)	$\sigma_{T\gamma}$ (GeV^2)	χ^2/d.o.f.
8 A·GeV, 0-5% Central						
1.5	49.657±0.678	0.216±0.012	0.845±0.111	0.373±0.003	0.00175	21.30/ 25
8 A·GeV, 5-12% Central						
1.5	38.445±0.500	0.205±0.010	0.775±0.103	0.367±0.003	0.00147	9.30/ 25
8 A·GeV, 12-23% Central						
1.5	29.349±0.379	0.218±0.011	1.011±0.101	0.356±0.003	0.00156	13.55/ 25
8 A·GeV, 23-39% Central						
1.5	18.725±0.247	0.215±0.011	1.053±0.099	0.349±0.003	0.00151	10.05/ 25

y	proton dN/dy	proton T (GeV)	γ	$\langle m_\perp \rangle$ (GeV)	$\sigma_{T\gamma}$ (GeV^2)	χ^2/d.o.f.
2 A·GeV, 0-5% Central						
0.91	83.077±1.033	0.079±0.002	-9.568±0.440	1.163±0.002	0.00135	63.85/ 58
2 A·GeV, 5-12% Central						
0.91	65.662±0.740	0.085±0.003	-7.824±0.450	1.143±0.002	0.00153	60.55/ 55
2 A·GeV, 12-23% Central						
0.91	46.420±0.557	0.089±0.003	-6.202±0.459	1.122±0.002	0.0017	51.29/ 61
2 A·GeV, 23-39% Central						
0.91	27.670±0.376	0.090±0.004	-5.070±0.521	1.101±0.002	0.0021	51.89/ 54

y	proton dN/dy	proton T (GeV)	γ	$\langle m_\perp \rangle$ (GeV)	$\sigma_{T\gamma}$ (GeV^2)	χ^2/d.o.f.
4 A·GeV, 0-5% Central						
1.2	68.971±0.792	0.126±0.005	-4.703±0.413	1.203±0.003	0.00233	47.35/ 43
4 A·GeV, 5-12% Central						
1.2	54.117±0.620	0.125±0.005	-4.447±0.403	1.191±0.002	0.00223	44.05/ 44
4 A·GeV, 12-23% Central						
1.2	40.173±0.515	0.134±0.005	-3.186±0.381	1.170±0.002	0.00226	34.81/ 44
4 A·GeV, 23-39% Central						
1.2	23.776±0.309	0.142±0.006	-1.834±0.419	1.144±0.002	0.00296	38.77/ 44

y	proton dN/dy	proton T (GeV)	γ	$\langle m_\perp \rangle$ (GeV)	$\sigma_{T\gamma}$ (GeV^2)	χ^2/d.o.f.
6 $A{\cdot}GeV$, 0-5% Central						
1.4	65.030±0.966	0.144±0.013	-4.051±0.829	1.236±0.003	0.0106	14.24/ 33
6 $A{\cdot}GeV$, 5-12% Central						
1.4	53.442±0.881	0.136±0.014	-4.283±1.021	1.220±0.003	0.0142	23.15/ 33
6 $A{\cdot}GeV$, 12-23% Central						
1.4	38.158±0.501	0.142±0.010	-3.531±0.658	1.206±0.003	0.00676	14.90/ 33
6 $A{\cdot}GeV$, 23-39% Central						
1.4	25.115±0.351	0.161±0.013	-1.793±0.659	1.181±0.003	0.00868	7.64/ 33

y	proton dN/dy	proton T (GeV)	γ	$\langle m_\perp \rangle$ (GeV)	$\sigma_{T\gamma}$ (GeV^2)	χ^2/d.o.f.
8 $A{\cdot}GeV$, 0-5% Central						
1.5	61.583±0.933	0.119±0.009	-6.465±0.846	1.254±0.004	0.00763	11.49/ 26
8 $A{\cdot}GeV$, 5-12% Central						
1.5	49.598±0.791	0.126±0.011	-5.450±0.914	1.238±0.004	0.00992	12.27/ 26
8 $A{\cdot}GeV$, 12-23% Central						
1.5	37.263±0.667	0.141±0.016	-3.917±1.071	1.221±0.003	0.0168	13.31/ 26
8 $A{\cdot}GeV$, 23-39% Central						
1.5	23.567±0.362	0.156±0.013	-2.356±0.714	1.192±0.003	0.0094	16.95/ 26

Appendix G

Tables of $m_\perp$ distributions, Y_{NN}

This appendix contains tables of the invariant differential yields of particles, $\frac{1}{2\pi m_\perp}\frac{d^2N}{dYdm_\perp}$, as a function of $m_\perp$. The data have been fully corrected for acceptance and efficiencies, and have been divided by particle type, beam energy, centrality class, and by bins in Y.

2 $A{\cdot}GeV$, 0-5% Central			
Y: 0.68 - 0.91		Y: 0.91 - 1.14	
$m_\perp$ (GeV)	Yield	$m_\perp$ (GeV)	Yield
0.538	0.39±0.097	0.58	0.311 ± 0.0504
0.576	0.331±0.053	0.625	0.273 ± 0.0341
0.629	0.282±0.034	0.674	0.186 ± 0.0247
0.676	0.231±0.022	0.727	0.121 ± 0.0185
0.725	0.124±0.014	0.776	0.0832 ± 0.0127
0.775	0.105±0.011	0.825	0.0629 ± 0.0101
0.825	0.0694±0.0082	0.875	0.0489 ± 0.0081
0.875	0.0532±0.0068	0.925	0.0278 ± 0.00563
0.925	0.0291±0.0046	0.976	0.0236 ± 0.00495
0.975	0.0247±0.004	1.02	0.0103 ± 0.00302
1.03	0.0117±0.0027	1.07	0.0098 ± 0.00338
1.07	0.0094±0.0024	1.12	0.00912 ± 0.00431
1.13	0.00629±0.0018		
1.17	0.00442±0.0015		
1.22	0.0043±0.0018		
1.27	0.00473±0.0027		

K^+ 2 $A{\cdot}GeV$, 5-12% Central			
Y: 0.68 - 0.91		Y: 0.91 - 1.14	
$m_\perp$ (GeV)	Yield	$m_\perp$ (GeV)	Yield
0.538	0.377±0.082	0.58	0.234 ± 0.0365
0.576	0.245±0.039	0.625	0.174 ± 0.0224
0.629	0.208±0.025	0.674	0.131 ± 0.0173
0.676	0.128±0.014	0.727	0.0809 ± 0.0127
0.725	0.0939±0.0099	0.776	0.0605 ± 0.00907
0.775	0.0671±0.0075	0.825	0.045 ± 0.00727
0.825	0.0517±0.006	0.875	0.0368 ± 0.00594
0.875	0.0311±0.0042	0.925	0.0174 ± 0.00366
0.925	0.0234±0.0035	0.976	0.00915 ± 0.00247
0.975	0.0129±0.0024	1.02	0.00852 ± 0.00231
1.03	0.00721±0.0017	1.07	0.00534 ± 0.00207
1.07	0.00703±0.0017	1.12	0.00393 ± 0.00236
1.13	0.00563±0.0014		
1.17	0.00173±0.0008		
1.22	0.00339±0.0014		
1.27	0.000681±0.00083		

K^+ 2 $A{\cdot}GeV$, 12-23% Central			
Y: 0.68 - 0.91		Y: 0.91 - 1.14	
$m_\perp$ (GeV)	Yield	$m_\perp$ (GeV)	Yield
0.538	0.187±0.045	0.58	0.17 ± 0.0251
0.576	0.177±0.026	0.625	0.111 ± 0.0144
0.629	0.129±0.016	0.674	0.0593 ± 0.00913
0.676	0.0911±0.0092	0.727	0.0547 ± 0.00838
0.725	0.0534±0.0059	0.776	0.0356 ± 0.00544
0.775	0.04±0.0047	0.825	0.0294 ± 0.00457
0.825	0.024±0.0032	0.875	0.0137 ± 0.00278
0.875	0.0205±0.0027	0.925	0.00623 ± 0.00171
0.925	0.0101±0.0018	0.976	0.00852 ± 0.00192
0.975	0.0093±0.0016	1.02	0.00446 ± 0.00131
1.03	0.00431±0.0011	1.07	0.00436 ± 0.00148
1.07	0.00349±0.00094		
1.13	0.00165±0.0006		
1.17	0.00187±0.00066		
1.22	0.000422±0.00038		

K^+ 2 $A{\cdot}GeV$, 23-39% Central			
Y: 0.68 - 0.91		Y: 0.91 - 1.14	
$m_\perp$ (GeV)	Yield	$m_\perp$ (GeV)	Yield
0.538	0.122±0.03	0.58	0.0746 ± 0.0134
0.576	0.0905±0.015	0.625	0.0551 ± 0.00809
0.629	0.0745±0.0095	0.674	0.0343 ± 0.00581
0.676	0.0461±0.0053	0.727	0.0259 ± 0.00464
0.725	0.0307±0.0037	0.776	0.0157 ± 0.00294
0.775	0.0162±0.0024	0.825	0.00828 ± 0.00188
0.825	0.0136±0.002	0.875	0.00612 ± 0.0015
0.875	0.0078±0.0014	0.925	0.00518 ± 0.00128
0.925	0.00483±0.00098	0.976	0.00178 ± 0.000688
0.975	0.00346±0.00078	1.02	0.00129 ± 0.000559
1.03	0.0028±0.0007	1.07	0.000628 ± 0.000453
1.07	0.00125±0.00045	1.12	0.00113 ± 0.000817
1.13	0.000451±0.00025		
1.17	0.000196±0.00017		
1.22	0.000149±0.00018		
1.27	0.000335±0.00038		

K^+ 4 $A{\cdot}GeV$, 0-5% Central			
Y: 0.88 - 1.17		Y: 1.17 - 1.46	
$m_\perp$ (GeV)	Yield	$m_\perp$ (GeV)	Yield
0.578	1.98±0.18	0.588	1.66 ± 0.268
0.628	1.56±0.11	0.627	1.47 ± 0.135
0.677	1.22±0.08	0.677	1.04 ± 0.0885
0.726	0.853±0.055	0.725	0.882 ± 0.0707
0.775	0.666±0.042	0.776	0.617 ± 0.0546
0.826	0.453±0.03	0.824	0.465 ± 0.0467
0.875	0.302±0.022	0.874	0.384 ± 0.0471
0.925	0.235±0.018	0.921	0.212 ± 0.0432
0.975	0.181±0.015		
1.02	0.117±0.012		
1.07	0.0953±0.011		
1.12	0.0554±0.01		

K^+ 4 $A{\cdot}GeV$, 5-12% Central			
Y: 0.88 - 1.17		Y: 1.17 - 1.46	
$m_\perp$ (GeV)	Yield	$m_\perp$ (GeV)	Yield
0.578	1.52±0.13	0.588	1.43 ± 0.206
0.628	1.1±0.078	0.627	1.12 ± 0.0991
0.677	0.902±0.058	0.677	0.858 ± 0.069
0.726	0.652±0.041	0.725	0.67 ± 0.052
0.775	0.469±0.03	0.776	0.56 ± 0.0447
0.826	0.341±0.022	0.824	0.301 ± 0.0313
0.875	0.234±0.016	0.874	0.295 ± 0.0345
0.925	0.165±0.012	0.921	0.232 ± 0.0386
0.975	0.117±0.0098		
1.02	0.0837±0.0084		
1.07	0.0701±0.0082		
1.12	0.0566±0.0089		

K^+ 4 $A{\cdot}GeV$, 12-23% Central			
Y: 0.88 - 1.17		Y: 1.17 - 1.46	
$m_\perp$ (GeV)	Yield	$m_\perp$ (GeV)	Yield
0.578	1.11±0.09	0.588	0.909 ± 0.131
0.628	0.821±0.055	0.627	0.842 ± 0.0691
0.677	0.556±0.036	0.677	0.58 ± 0.0447
0.726	0.416±0.026	0.725	0.386 ± 0.0307
0.775	0.317±0.019	0.776	0.324 ± 0.0266
0.826	0.217±0.014	0.824	0.241 ± 0.0225
0.875	0.143±0.01	0.874	0.138 ± 0.0182
0.925	0.103±0.0077	0.921	0.15 ± 0.0243
0.975	0.083±0.0066		
1.02	0.0464±0.0048		
1.07	0.0308±0.0042		
1.12	0.0246±0.0045		

K^+ 4 $A{\cdot}GeV$, 23-39% Central			
Y: 0.88 - 1.17		Y: 1.17 - 1.46	
$m_\perp$ (GeV)	Yield	$m_\perp$ (GeV)	Yield
0.578	0.618±0.054	0.588	0.401 ± 0.0679
0.628	0.435±0.032	0.627	0.374 ± 0.0358
0.677	0.296±0.021	0.677	0.29 ± 0.0251
0.726	0.201±0.014	0.725	0.221 ± 0.0186
0.775	0.151±0.011	0.776	0.141 ± 0.0136
0.826	0.118±0.0083	0.824	0.116 ± 0.0123
0.875	0.0764±0.0059	0.874	0.0746 ± 0.0106
0.925	0.0577±0.0047	0.921	0.0506 ± 0.0112
0.975	0.036±0.0034		
1.02	0.026±0.0029		
1.07	0.0188±0.0027		
1.12	0.0104±0.0024		

K^+ 6 $A{\cdot}GeV$, 0-5% Central			
Y: 1.01 - 1.35		Y: 1.35 - 1.69	
$m_\perp$ (GeV)	Yield	$m_\perp$ (GeV)	Yield
0.538	4.61±0.43	0.585	3.01 ± 0.239
0.577	3.59±0.19	0.626	2.69 ± 0.156
0.625	2.89±0.14	0.675	2.29 ± 0.136
0.675	2.18±0.11	0.725	1.77 ± 0.112
0.724	1.77±0.094	0.77	1.25 ± 0.11
0.775	1.39±0.08		
0.824	1.07±0.068		
0.874	0.935±0.069		
0.925	0.682±0.061		
0.975	0.481±0.052		
1.02	0.404±0.046		

K^+ 6 $A{\cdot}GeV$, 5-12% Central			
Y: 1.01 - 1.35		Y: 1.35 - 1.69	
$m_\perp$ (GeV)	Yield	$m_\perp$ (GeV)	Yield
0.538	3.46±0.31	0.585	2.65 ± 0.189
0.577	3.06±0.15	0.626	2.17 ± 0.119
0.625	2.32±0.11	0.675	1.81 ± 0.101
0.675	1.85±0.087	0.725	1.42 ± 0.0848
0.724	1.47±0.074	0.77	1.12 ± 0.0887
0.775	1.09±0.06		
0.824	0.851±0.052		
0.874	0.664±0.049		
0.925	0.458±0.041		
0.975	0.369±0.039		
1.02	0.281±0.033		

K^+ 6 $A{\cdot}GeV$, 12-23% Central			
Y: 1.01 - 1.35		Y: 1.35 - 1.69	
$m_\perp$ (GeV)	Yield	$m_\perp$ (GeV)	Yield
0.538	2.6±0.21	0.585	1.7 ± 0.118
0.577	2.1±0.098	0.626	1.46 ± 0.0756
0.625	1.56±0.069	0.675	1.16 ± 0.063
0.675	1.23±0.056	0.725	0.85 ± 0.0505
0.724	0.937±0.046	0.77	0.677 ± 0.0533
0.775	0.759±0.04		
0.824	0.63±0.036		
0.874	0.428±0.031		
0.925	0.306±0.027		
0.975	0.253±0.025		
1.02	0.165±0.019		

K^+ 6 $A{\cdot}GeV$, 23-39% Central			
Y: 1.01 - 1.35		Y: 1.35 - 1.69	
$m_\perp$ (GeV)	Yield	$m_\perp$ (GeV)	Yield
0.538	1.58±0.13	0.585	1.12 ± 0.0771
0.577	1.15±0.057	0.626	0.882 ± 0.0472
0.625	0.967±0.044	0.675	0.721 ± 0.04
0.675	0.708±0.034	0.725	0.535 ± 0.0324
0.724	0.566±0.029	0.77	0.41 ± 0.0336
0.775	0.406±0.023		
0.824	0.301±0.019		
0.874	0.23±0.018		
0.925	0.167±0.016		
0.975	0.114±0.014		
1.02	0.085±0.011		

K^+ 8 $A{\cdot}GeV$, 0-5% Central			
Y: 1.1 - 1.48		Y: 1.48 - 1.84	
$m_\perp$ (GeV)	Yield	$m_\perp$ (GeV)	Yield
0.582	4.47±0.46	0.627	4.19 ± 0.683
0.627	4.69±0.32	0.674	4.07 ± 0.907
0.676	3.52±0.23		
0.725	2.83±0.18		
0.775	2.32±0.16		
0.825	1.76±0.13		
0.875	1.45±0.12		
0.924	1.05±0.097		
0.969	0.844±0.12		

K^+ 8 $A{\cdot}GeV$, 5-12% Central			
Y: 1.1 - 1.48		Y: 1.48 - 1.84	
$m_\perp$ (GeV)	Yield	$m_\perp$ (GeV)	Yield
0.582	4.05±0.36	0.627	3.72 ± 0.527
0.627	3.49±0.23	0.674	2.23 ± 0.541
0.676	2.62±0.16		
0.725	2.06±0.13		
0.775	1.6±0.11		
0.825	1.17±0.089		
0.875	1.04±0.083		
0.924	0.845±0.074		
0.969	0.618±0.087		

K^+ 8 $A{\cdot}GeV$, 12-23% Central			
Y: 1.1 - 1.48		Y: 1.48 - 1.84	
$m_\perp$ (GeV)	Yield	$m_\perp$ (GeV)	Yield
0.582	2.8±0.24	0.627	2.35 ± 0.314
0.627	2.3±0.15	0.674	2.56 ± 0.461
0.676	1.87±0.11		
0.725	1.43±0.086		
0.775	1.07±0.072		
0.825	0.919±0.065		
0.875	0.683±0.053		
0.924	0.5±0.045		
0.969	0.453±0.06		

K^+ 8 $A{\cdot}GeV$, 23-39% Central			
Y: 1.1 - 1.48		Y: 1.48 - 1.84	
$m_\perp$ (GeV)	Yield	$m_\perp$ (GeV)	Yield
0.582	1.8±0.15	0.627	1.3 ± 0.184
0.627	1.41±0.094	0.674	1.16 ± 0.241
0.676	1.05±0.065		
0.725	0.826±0.052		
0.775	0.596±0.043		
0.825	0.471±0.036		
0.875	0.4±0.033		
0.924	0.282±0.027		
0.969	0.184±0.03		

K^+ 4 $A{\cdot}GeV$, 0-5% Central			
Y: 0.88 - 1.17		Y: 1.17 - 1.46	
$m_\perp$ (GeV)	Yield	$m_\perp$ (GeV)	Yield
0.539	0.257±0.091	0.58	0.206 ± 0.0473
0.578	0.156±0.033	0.626	0.15 ± 0.0303
0.627	0.171±0.025	0.677	0.0788 ± 0.0171
0.676	0.0886±0.014	0.726	0.0793 ± 0.0151
0.726	0.0574±0.0097	0.774	0.045 ± 0.0111
0.775	0.0601±0.0088	0.825	0.0389 ± 0.011
0.825	0.0373±0.0063	0.871	0.0278 ± 0.0116
0.875	0.021±0.0043	0.924	0.0343 ± 0.02
0.925	0.0132±0.0031		
0.974	0.0137±0.003		
1.02	0.0114±0.0028		
1.07	0.00632±0.0023		
1.12	0.0128±0.004		

K^- 4 $A{\cdot}GeV$, 5-12% Central			
Y: 0.88 - 1.17		Y: 1.17 - 1.46	
$m_\perp$ (GeV)	Yield	$m_\perp$ (GeV)	Yield
0.539	0.195±0.065	0.58	0.142 ± 0.0318
0.578	0.183±0.031	0.626	0.115 ± 0.0221
0.627	0.119±0.018	0.677	0.056 ± 0.0128
0.676	0.0766±0.011	0.726	0.0536 ± 0.0101
0.726	0.0461±0.0072	0.774	0.0371 ± 0.00848
0.775	0.0411±0.0062	0.825	0.0311 ± 0.00803
0.825	0.0231±0.0041	0.871	0.012 ± 0.00632
0.875	0.0163±0.0031	0.924	0.0325 ± 0.0156
0.925	0.0121±0.0025		
0.974	0.00642±0.0017		
1.02	0.00632±0.0017		
1.07	0.00569±0.0018		
1.12	0.0018±0.0012		

K^- 4 $A{\cdot}GeV$, 12-23% Central			
Y: 0.88 - 1.17		Y: 1.17 - 1.46	
$m_\perp$ (GeV)	Yield	$m_\perp$ (GeV)	Yield
0.539	0.145±0.044	0.58	0.0956 ± 0.021
0.578	0.14±0.021	0.626	0.0659 ± 0.0134
0.627	0.0772±0.011	0.677	0.0445 ± 0.00873
0.676	0.046±0.0068	0.726	0.0376 ± 0.00678
0.726	0.0287±0.0046	0.774	0.0191 ± 0.00481
0.775	0.0288±0.0041	0.825	0.0151 ± 0.00448
0.825	0.0149±0.0026	0.871	0.00853 ± 0.00435
0.875	0.0133±0.0023	0.924	0.0175 ± 0.00911
0.925	0.00722±0.0015		
0.974	0.00292±0.00092		
1.02	0.00394±0.0011		
1.07	0.00306±0.0011		
1.12	0.00194±0.001		

K^- 4 $A{\cdot}GeV$, 23-39% Central			
Y: 0.88 - 1.17		Y: 1.17 - 1.46	
$m_\perp$ (GeV)	Yield	$m_\perp$ (GeV)	Yield
0.539	0.112±0.033	0.58	0.0483 ± 0.0115
0.578	0.0588±0.011	0.626	0.0476 ± 0.00911
0.627	0.042±0.0067	0.677	0.0282 ± 0.00559
0.676	0.0262±0.0042	0.726	0.0137 ± 0.00327
0.726	0.0161±0.0028	0.774	0.0106 ± 0.00294
0.775	0.0114±0.002	0.825	0.0121 ± 0.00333
0.825	0.00713±0.0014	0.871	0.0067 ± 0.00314
0.875	0.00451±0.0011	0.924	0.00489 ± 0.00418
0.925	0.0034±0.00084		
0.974	0.00236±0.0007		
1.02	0.00141±0.00055		
1.07	0.000621±0.0004		
1.12	0.000254±0.00031		

K^- 6 $A{\cdot}GeV$, 0-5% Central			
Y: 1.01 - 1.35		Y: 1.35 - 1.69	
$m_\perp$ (GeV)	Yield	$m_\perp$ (GeV)	Yield
0.541	0.509±0.14	0.587	0.473 ± 0.0917
0.578	0.528±0.057	0.626	0.375 ± 0.0486
0.626	0.414±0.039	0.677	0.315 ± 0.0404
0.675	0.313±0.032	0.723	0.21 ± 0.0304
0.725	0.254±0.028	0.772	0.139 ± 0.0395
0.775	0.164±0.021		
0.824	0.108±0.017		
0.874	0.0825±0.018		
0.925	0.0734±0.018		
0.974	0.0466±0.015		
1.02	0.0339±0.012		

K^- 6 $A{\cdot}GeV$, 5-12% Central			
Y: 1.01 - 1.35		Y: 1.35 - 1.69	
$m_\perp$ (GeV)	Yield	$m_\perp$ (GeV)	Yield
0.541	0.513±0.11	0.587	0.359 ± 0.064
0.578	0.328±0.037	0.626	0.323 ± 0.0378
0.626	0.3±0.028	0.677	0.213 ± 0.0272
0.675	0.229±0.023	0.723	0.167 ± 0.0225
0.725	0.189±0.02	0.772	0.146 ± 0.0336
0.775	0.107±0.014		
0.824	0.0945±0.013		
0.874	0.0693±0.014		
0.925	0.0402±0.011		
0.974	0.0406±0.012		
1.02	0.033±0.011		

K^- 6 $A{\cdot}GeV$, 12-23% Central			
Y: 1.01 - 1.35		Y: 1.35 - 1.69	
$m_\perp$ (GeV)	Yield	$m_\perp$ (GeV)	Yield
0.541	0.379±0.078	0.587	0.263 ± 0.0433
0.578	0.305±0.028	0.626	0.189 ± 0.0219
0.626	0.249±0.02	0.677	0.189 ± 0.0201
0.675	0.157±0.015	0.723	0.12 ± 0.0148
0.725	0.123±0.013	0.772	0.0899 ± 0.0202
0.775	0.0914±0.01		
0.824	0.0615±0.0085		
0.874	0.0431±0.0084		
0.925	0.0283±0.0073		
0.974	0.0238±0.0069		
1.02	0.0118±0.0048		

K^- 6 $A{\cdot}GeV$, 23-39% Central			
Y: 1.01 - 1.35		Y: 1.35 - 1.69	
$m_\perp$ (GeV)	Yield	$m_\perp$ (GeV)	Yield
0.541	0.18±0.042	0.587	0.149 ± 0.0257
0.578	0.205±0.019	0.626	0.135 ± 0.0152
0.626	0.12±0.011	0.677	0.0902 ± 0.011
0.675	0.0949±0.0094	0.723	0.0594 ± 0.00833
0.725	0.0639±0.0074	0.772	0.0465 ± 0.012
0.775	0.0548±0.0066		
0.824	0.0336±0.0051		
0.874	0.0277±0.0056		
0.925	0.0118±0.0038		
0.974	0.00906±0.0034		
1.02	0.0103±0.0038		

K^- 8 $A{\cdot}GeV$, 0-5% Central			
Y: 1.1 - 1.48		Y: 1.48 - 1.84	
$m_\perp$ (GeV)	Yield	$m_\perp$ (GeV)	Yield
0.541	1.69±0.51	0.627	0.748 ± 0.149
0.581	1.05±0.13	0.669	0.682 ± 0.178
0.627	0.746±0.072		
0.676	0.632±0.051		
0.725	0.448±0.037		
0.775	0.365±0.031		
0.825	0.244±0.023		
0.874	0.182±0.02		
0.924	0.163±0.019		
0.969	0.0964±0.021		

K^- 8 $A{\cdot}GeV$, 5-12% Central			
Y: 1.1 - 1.48		Y: 1.48 - 1.84	
$m_\perp$ (GeV)	Yield	$m_\perp$ (GeV)	Yield
0.541	0.296±0.16	0.627	0.539 ± 0.101
0.581	0.726±0.085	0.669	0.417 ± 0.112
0.627	0.548±0.051		
0.676	0.411±0.034		
0.725	0.358±0.028		
0.775	0.262±0.022		
0.825	0.2±0.018		
0.874	0.136±0.014		
0.924	0.107±0.013		
0.969	0.0735±0.016		

K^- 8 $A{\cdot}GeV$, 12-23% Central			
Y: 1.1 - 1.48		Y: 1.48 - 1.84	
$m_\perp$ (GeV)	Yield	$m_\perp$ (GeV)	Yield
0.541	0.588±0.18	0.627	0.506 ± 0.0777
0.581	0.555±0.06	0.669	0.314 ± 0.0713
0.627	0.411±0.035		
0.676	0.314±0.024		
0.725	0.242±0.018		
0.775	0.179±0.014		
0.825	0.14±0.012		
0.874	0.106±0.01		
0.924	0.0662±0.0081		
0.969	0.0605±0.011		

K^- 8 $A{\cdot}GeV$, 23-39% Central			
Y: 1.1 - 1.48		Y: 1.48 - 1.84	
$m_\perp$ (GeV)	Yield	$m_\perp$ (GeV)	Yield
0.541	0.461±0.13	0.627	0.214 ± 0.0377
0.581	0.316±0.035	0.669	0.174 ± 0.0422
0.627	0.246±0.022		
0.676	0.193±0.015		
0.725	0.13±0.01		
0.775	0.0975±0.0084		
0.825	0.0704±0.0066		
0.874	0.0535±0.0058		
0.924	0.0433±0.0053		
0.969	0.0309±0.0065		

K^- 2 $A{\cdot}GeV$, 0-5% Central			
Y: 0.68 - 0.91		Y: 0.91 - 1.14	
$m_\perp$ (GeV)	Yield	$m_\perp$ (GeV)	Yield
0.276	20.7±1.4	0.235	33.7 ± 2.25
0.325	013±0.88	0.278	21.7 ± 1.16
0.375	8.13±0.56	0.325	13.7 ± 0.726
0.425	4.98±0.38	0.375	8.11 ± 0.472
0.475	3.29±0.26	0.426	5.06 ± 0.314
0.525	1.86±0.18	0.475	2.94 ± 0.203
0.575	1.38±0.14	0.525	1.96 ± 0.155
0.625	0.886±0.1	0.575	1.39 ± 0.116
0.675	0.605±0.078	0.625	0.869 ± 0.0842
0.725	0.405±0.058	0.675	0.58 ± 0.0658
0.775	0.231±0.04	0.725	0.397 ± 0.0488
0.825	0.177±0.035	0.775	0.252 ± 0.0361
0.875	0.173±0.032	0.825	0.226 ± 0.0323
0.925	0.121±0.025	0.875	0.11 ± 0.0216
0.975	0.0981±0.022	0.925	0.0497 ± 0.0131
1.03	0.0525±0.016	0.975	0.0449 ± 0.0122
1.08	0.0391±0.013	1.02	0.0379 ± 0.0109
1.13	0.0099±0.0059	1.07	0.028 ± 0.0105
1.17	0.00325±0.0033	1.12	0.0259 ± 0.0121
1.22	0.007±0.0051	1.17	0.0118 ± 0.012
1.27	0.00644±0.0066		

π^+ 2 $A{\cdot}GeV$, 5-12% Central			
Y: 0.68 - 0.91		Y: 0.91 - 1.14	
$m_\perp$ (GeV)	Yield	$m_\perp$ (GeV)	Yield
0.276	16.2±1.1	0.235	25.1 ± 1.65
0.325	10.3±0.67	0.278	16.6 ± 0.867
0.375	5.69±0.39	0.325	10.3 ± 0.534
0.425	3.61±0.27	0.375	6.29 ± 0.354
0.475	2.36±0.19	0.426	3.46 ± 0.216
0.525	1.46±0.13	0.475	2.22 ± 0.149
0.575	0.771±0.084	0.525	1.41 ± 0.11
0.625	0.562±0.067	0.575	0.978 ± 0.0818
0.675	0.419±0.055	0.625	0.635 ± 0.0605
0.725	0.226±0.035	0.675	0.419 ± 0.0464
0.775	0.191±0.031	0.725	0.301 ± 0.0359
0.825	0.113±0.023	0.775	0.177 ± 0.0253
0.875	0.0987±0.02	0.825	0.136 ± 0.0208
0.925	0.0637±0.015	0.875	0.0727 ± 0.0148
0.975	0.0408±0.012	0.925	0.0591 ± 0.0124
1.03	0.0261±0.0092	0.975	0.037 ± 0.00925
1.08	0.0217±0.0077	1.02	0.0192 ± 0.00645
1.13	0.0142±0.0061	1.07	0.0123 ± 0.00573
1.17	0.00441±0.0032	1.12	0.0109 ± 0.00652
1.22	0.0125±0.0059		
1.27	0.00438±0.0045		
1.32	0.00896±0.0091		

π^+ 2 $A{\cdot}GeV$, 12-23% Central			
Y: 0.68 - 0.91		Y: 0.91 - 1.14	
$m_\perp$ (GeV)	Yield	$m_\perp$ (GeV)	Yield
0.276	11.3±0.72	0.235	020 ± 1.23
0.325	6.71±0.43	0.278	012 ± 0.604
0.375	3.81±0.26	0.325	6.86 ± 0.352
0.425	2.22±0.17	0.375	3.95 ± 0.226
0.475	1.43±0.12	0.426	2.22 ± 0.139
0.525	0.814±0.079	0.475	1.47 ± 0.0983
0.575	0.567±0.059	0.525	0.936 ± 0.0729
0.625	0.328±0.041	0.575	0.519 ± 0.0467
0.675	0.223±0.031	0.625	0.354 ± 0.0358
0.725	0.188±0.026	0.675	0.256 ± 0.029
0.775	0.0895±0.017	0.725	0.158 ± 0.0205
0.825	0.0504±0.012	0.775	0.104 ± 0.0154
0.875	0.0428±0.01	0.825	0.0956 ± 0.0142
0.925	0.0353±0.009	0.875	0.0345 ± 0.00805
0.975	0.0295±0.008	0.925	0.0412 ± 0.00884
1.03	0.00919±0.0043	0.975	0.00994 ± 0.00372
1.08	0.00811±0.0038	1.02	0.016 ± 0.00476
1.13	0.00148±0.0015	1.07	0.00628 ± 0.00327
1.17	0.00281±0.002	1.12	0.00704 ± 0.00421
1.22	0.00157±0.0016	1.17	0.0104 ± 0.00758

π^+ 2 $A{\cdot}GeV$, 23-39% Central			
Y: 0.68 - 0.91		Y: 0.91 - 1.14	
$m_\perp$ (GeV)	Yield	$m_\perp$ (GeV)	Yield
0.276	7.15±0.47	0.235	11.3 ± 0.739
0.325	3.89±0.27	0.278	6.89 ± 0.368
0.375	2.12±0.15	0.325	3.95 ± 0.215
0.425	1.42±0.11	0.375	2.37 ± 0.141
0.475	0.803±0.071	0.426	1.29 ± 0.0864
0.525	0.522±0.052	0.475	0.729 ± 0.0547
0.575	0.36±0.039	0.525	0.511 ± 0.0432
0.625	0.196±0.026	0.575	0.325 ± 0.0305
0.675	0.158±0.022	0.625	0.162 ± 0.0195
0.725	0.0903±0.015	0.675	0.14 ± 0.0174
0.775	0.0657±0.012	0.725	0.0765 ± 0.0116
0.825	0.027±0.0073	0.775	0.0459 ± 0.00828
0.875	0.0205±0.0059	0.825	0.0374 ± 0.00709
0.925	0.0137±0.0046	0.875	0.0289 ± 0.00615
0.975	0.00399±0.0024	0.925	0.0121 ± 0.00361
1.03	0.00761±0.0033	0.975	0.00617 ± 0.00246
1.08	0.0057±0.0027	1.02	0.00764 ± 0.0027
1.13	0.00207±0.0015	1.07	0.00554 ± 0.00259
1.17	0.000957±0.00098	1.12	0.00327 ± 0.00238
1.22	0.0011±0.0011	1.17	0.00355 ± 0.00362
1.27	0.00199±0.002		

π^+ 4 $A{\cdot}GeV$, 0-5% Central			
Y: 0.88 - 1.17		Y: 1.17 - 1.46	
$m_\perp$ (GeV)	Yield	$m_\perp$ (GeV)	Yield
0.232	59.4±2.5	0.193	83.8 ± 7.81
0.276	40.2±1.5	0.227	58.3 ± 2.55
0.325	26.1±01	0.276	37.1 ± 1.58
0.375	017±0.71	0.326	25.3 ± 1.06
0.425	10.9±0.49	0.376	16.6 ± 0.705
0.475	7.85±0.36	0.425	11.6 ± 0.505
0.525	5.43±0.27	0.475	7.8 ± 0.36
0.575	3.83±0.2	0.525	5.54 ± 0.275
0.625	2.71±0.15	0.575	4.03 ± 0.209
0.675	1.93±0.12	0.625	2.69 ± 0.151
0.725	1.46±0.094	0.675	1.83 ± 0.113
0.775	1.08±0.075	0.725	1.44 ± 0.0944
0.825	0.744±0.058	0.775	1.02 ± 0.0733
0.875	0.609±0.05	0.825	0.878 ± 0.0695
0.925	0.458±0.041	0.873	0.614 ± 0.0601
0.975	0.306±0.031	0.921	0.554 ± 0.0739
1.02	0.239±0.029		
1.07	0.154±0.026		
1.12	0.16±0.034		
1.17	0.0261±0.019		

π^+ 4 $A{\cdot}GeV$, 5-12% Central			
Y: 0.88 - 1.17		Y: 1.17 - 1.46	
$m_\perp$ (GeV)	Yield	$m_\perp$ (GeV)	Yield
0.232	48.5±02	0.193	68.5 ± 5.99
0.276	30.9±1.2	0.227	49.7 ± 2.06
0.325	19.8±0.77	0.276	30.8 ± 1.26
0.375	12.5±0.52	0.326	19.7 ± 0.802
0.425	8.3±0.36	0.376	12.7 ± 0.528
0.475	6.06±0.27	0.425	8.83 ± 0.376
0.525	4.24±0.2	0.475	5.91 ± 0.267
0.575	2.95±0.15	0.525	4.17 ± 0.203
0.625	2.04±0.11	0.575	2.84 ± 0.148
0.675	1.44±0.087	0.625	2.07 ± 0.112
0.725	0.981±0.065	0.675	1.42 ± 0.0853
0.775	0.781±0.054	0.725	1.04 ± 0.0677
0.825	0.609±0.045	0.775	0.786 ± 0.055
0.875	0.48±0.038	0.825	0.553 ± 0.0459
0.925	0.309±0.028	0.873	0.426 ± 0.0419
0.975	0.248±0.024	0.921	0.466 ± 0.0579
1.02	0.179±0.021		
1.07	0.111±0.019		
1.12	0.101±0.023		
1.17	0.112±0.035		

π^+ 4 $A{\cdot}GeV$, 12-23% Central			
Y: 0.88 - 1.17		Y: 1.17 - 1.46	
$m_\perp$ (GeV)	Yield	$m_\perp$ (GeV)	Yield
0.232	35.8±1.4	0.193	56.7 ± 4.48
0.276	23.2±0.83	0.227	34.2 ± 1.39
0.325	13.9±0.53	0.276	22.6 ± 0.886
0.375	8.66±0.35	0.326	14.1 ± 0.556
0.425	5.86±0.25	0.376	9.2 ± 0.367
0.475	4.01±0.18	0.425	6.24 ± 0.258
0.525	2.82±0.13	0.475	4.26 ± 0.185
0.575	1.98±0.099	0.525	2.76 ± 0.132
0.625	1.38±0.075	0.575	2.01 ± 0.101
0.675	0.927±0.056	0.625	1.45 ± 0.0762
0 725	0.702±0.044	0.675	001 ± 0.0576
0.775	0.55±0.036	0.725	0.713 ± 0.0449
0.825	0.358±0.027	0.775	0.542 ± 0.0366
0.875	0.268±0.022	0.825	0.385 ± 0.0306
0.925	0.223±0.019	0.873	0.332 ± 0.0299
0.975	0.149±0.015	0.921	0.239 ± 0.0322
1.02	0.0918±0.012		
1.07	0.0688±0.012		
1.12	0.0375±0.011		
1.17	0.0408±0.016		

π^+ 4 $A{\cdot}GeV$, 23-39% Central			
Y: 0.88 - 1.17		Y: 1.17 - 1.46	
$m_\perp$ (GeV)	Yield	$m_\perp$ (GeV)	Yield
0.232	21.7±0.87	0.193	29.7 ± 2.57
0.276	13.3±0.49	0.227	21.7 ± 0.895
0.325	8.48±0.33	0.276	13.6 ± 0.55
0.375	5.15±0.22	0.326	8.27 ± 0.339
0.425	3.29±0.15	0.376	5.27 ± 0.22
0.475	2.31±0.11	0.425	3.54 ± 0.153
0.525	1.61±0.08	0.475	2.58 ± 0.116
0.575	1.14±0.06	0.525	1.58 ± 0.0795
0.625	0.765±0.044	0.575	1.09 ± 0.0586
0.675	0.576±0.036	0.625	0.797 ± 0.0448
0.725	0.441±0.029	0.675	0.577 ± 0.0352
0.775	0.281±0.021	0.725	0.412 ± 0.0274
0.825	0.211±0.017	0.775	0.317 ± 0.0226
0.875	0.128±0.012	0.825	0.22 ± 0.0187
0.925	0.109±0.011	0.873	0.145 ± 0.0157
0.975	0.0787±0.0085	0.921	0.136 ± 0.0198
1.02	0.0579±0.0077		
1.07	0.0325±0.0066		
1.12	0.02±0.0064		
1.17	0.0198±0.0093		

π^+ 6 $A{\cdot}GeV$, 0-5% Central			
Y: 1.01 - 1.35		Y: 1.35 - 1.69	
$m_\perp$ (GeV)	Yield	$m_\perp$ (GeV)	Yield
0.189	113±6.7	0.186	126 ± 6.89
0.225	84.8±3.7	0.227	86.6 ± 3.51
0.275	56.1±2.5	0.276	57.2 ± 2.26
0.325	40.1±1.9	0.325	38.9 ± 1.55
0.375	24.5±1.2	0.375	25.3 ± 1.07
0.425	19.3±01	0.425	17.6 ± 0.783
0.475	12.9±0.73	0.475	12.8 ± 0.598
0.525	8.83±0.54	0.525	9.04 ± 0.456
0.575	6.45±0.42	0.575	6.55 ± 0.356
0.625	5.18±0.36	0.624	4.85 ± 0.286
0.675	3.32±0.26	0.674	3.64 ± 0.249
0.725	2.74±0.22	0.723	2.6 ± 0.224
0.775	1.99±0.17	0.771	2.2 ± 0.258
0.825	1.71±0.16		
0.874	1.09±0.12		
0.924	0.738±0.11		
0.974	0.687±0.12		
1.02	0.208±0.078		
1.07	0.434±0.16		

π^+ 6 $A{\cdot}GeV$, 5-12% Central			
Y: 1.01 - 1.35		Y: 1.35 - 1.69	
$m_\perp$ (GeV)	Yield	$m_\perp$ (GeV)	Yield
0.189	96.1±5.3	0.186	107 ± 5.46
0.225	69.2±2.9	0.227	73.2 ± 2.82
0.275	44.8±1.9	0.276	47.7 ± 1.8
0.325	30.2±1.4	0.325	31.9 ± 1.22
0.375	21.1±01	0.375	21.5 ± 0.86
0.425	13.9±0.73	0.425	14.6 ± 0.616
0.475	10.2±0.56	0.475	10.1 ± 0.453
0.525	6.91±0.41	0.525	6.81 ± 0.335
0.575	5.42±0.34	0.575	5.03 ± 0.265
0.625	3.9±0.26	0.624	3.97 ± 0.222
0.675	2.61±0.2	0.674	003 ± 0.194
0.725	1.82±0.15	0.723	1.93 ± 0.161
0.775	1.61±0.13	0.771	1.4 ± 0.17
0.825	1.19±0.11		
0.874	0.88±0.094		
0.924	0.682±0.094		
0.974	0.514±0.088		
1.02	0.298±0.08		
1.07	0.345±0.12		

π^+ 6 $A{\cdot}GeV$, 12-23% Central			
Y: 1.01 - 1.35		Y: 1.35 - 1.69	
$m_\perp$ (GeV)	Yield	$m_\perp$ (GeV)	Yield
0.189	74.3±3.8	0.186	78.7 ± 3.75
0.225	51.3±02	0.227	52.8 ± 1.94
0.275	33.1±1.4	0.276	034 ± 1.23
0.325	21.8±0.95	0.325	22.6 ± 0.832
0.375	14.3±0.67	0.375	15.4 ± 0.592
0.425	10.1±0.5	0.425	9.92 ± 0.407
0.475	7.08±0.37	0.475	7.05 ± 0.305
0.525	4.88±0.28	0.525	4.8 ± 0.226
0.575	3.48±0.21	0.575	3.48 ± 0.175
0.625	2.51±0.16	0.624	2.53 ± 0.139
0.675	1.89±0.13	0.674	1.78 ± 0.115
0.725	1.32±0.1	0.723	1.4 ± 0.11
0.775	0.932±0.079	0.771	1.22 ± 0.128
0.825	0.779±0.069		
0.874	0.442±0.052		
0.924	0.495±0.064		
0.974	0.382±0.06		
1.02	0.215±0.054		
1.07	0.072±0.043		

π^+ 6 $A{\cdot}GeV$, 23-39% Central			
Y: 1.01 - 1.35		Y: 1.35 - 1.69	
$m_\perp$ (GeV)	Yield	$m_\perp$ (GeV)	Yield
0.189	50.1±2.6	0.186	54.4 ± 2.57
0.225	34.4±1.4	0.227	36.8 ± 1.35
0.275	22.4±0.92	0.276	023 ± 0.837
0.325	13.8±0.61	0.325	15.1 ± 0.558
0.375	9.32±0.44	0.375	010 ± 0.39
0.425	6.7±0.34	0.425	6.52 ± 0.27
0.475	4.44±0.24	0.475	4.43 ± 0.196
0.525	3.25±0.19	0.525	3.34 ± 0.156
0.575	2.06±0.13	0.575	2.16 ± 0.112
0.625	1.65±0.11	0.624	1.65 ± 0.0919
0.675	1.09±0.082	0.674	1.2 ± 0.0779
0.725	0.754±0.063	0.723	0.918 ± 0.0731
0.775	0.674±0.056	0.771	0.722 ± 0.0804
0.825	0.465±0.044		
0.874	0.327±0.037		
0.924	0.258±0.039		
0.974	0.172±0.033		
1.02	0.127±0.034		
1.07	0.1±0.043		

π^+ 8 $A{\cdot}GeV$, 0-5% Central			
Y: 1.1 - 1.48		Y: 1.48 - 1.84	
$m_\perp$ (GeV)	Yield	$m_\perp$ (GeV)	Yield
0.192	133±07	0.229	94.2 ± 4.34
0.227	105±3.7	0.277	67.9 ± 2.68
0.275	72.1±2.6	0.325	48.3 ± 1.88
0.325	49.6±1.8	0.375	33.8 ± 1.38
0.375	35.2±1.3	0.425	23.5 ± 0.999
0.425	24.8±0.98	0.475	17.4 ± 0.762
0.475	018±0.74	0.525	012 ± 0.557
0.525	11.8±0.52	0.574	8.7 ± 0.441
0.575	9.34±0.43	0.623	6.34 ± 0.386
0.625	7.17±0.35	0.673	5.05 ± 0.376
0.675	5.26±0.27	0.72	4.57 ± 0.466
0.725	3.68±0.21		
0.774	2.92±0.18		
0.824	2.22±0.15		
0.874	1.74±0.14		
0.924	1.3±0.14		
0.973	0.933±0.13		

π^+ 8 $A{\cdot}GeV$, 5-12% Central			
Y: 1.1 - 1.48		Y: 1.48 - 1.84	
$m_\perp$ (GeV)	Yield	$m_\perp$ (GeV)	Yield
0.192	104±5.3	0.229	078 ± 3.39
0.227	81.8±2.8	0.277	54.5 ± 2.06
0.275	55.9±1.9	0.325	37.7 ± 1.42
0.325	37.6±1.4	0.375	26.1 ± 1.03
0.375	26.9±0.99	0.425	18.1 ± 0.745
0.425	19.3±0.74	0.475	12.8 ± 0.546
0.475	13.4±0.54	0.525	9.35 ± 0.418
0.525	9.82±0.42	0.574	7.07 ± 0.339
0.575	6.91±0.31	0.623	5.56 ± 0.311
0.625	5.24±0.25	0.673	4.13 ± 0.288
0.675	3.91±0.2	0.72	3.11 ± 0.319
0.725	2.96±0.16		
0.774	2.07±0.13		
0.824	1.58±0.11		
0.874	1.22±0.099		
0.924	0.818±0.089		
0.973	0.658±0.091		

π^+ 8 $A{\cdot}GeV$, 12-23% Central			
Y: 1.1 - 1.48		Y: 1.48 - 1.84	
$m_\perp$ (GeV)	Yield	$m_\perp$ (GeV)	Yield
0.192	86.2±04	0.229	64.2 ± 2.57
0.227	062±2.1	0.277	43.4 ± 1.54
0.275	41.3±1.4	0.325	28.9 ± 1.03
0.325	28.3±0.98	0.375	19.8 ± 0.743
0.375	18.8±0.67	0.425	13.6 ± 0.53
0.425	13.7±0.51	0.475	9.63 ± 0.389
0.475	9.43±0.37	0.525	6.9 ± 0.291
0.525	6.71±0.28	0.574	4.95 ± 0.228
0.575	4.8±0.21	0.623	3.91 ± 0.209
0.625	3.58±0.17	0.673	003 ± 0.197
0.675	2.73±0.13	0.72	1.9 ± 0.194
0.725	1.96±0.1		
0.774	1.44±0.084		
0.824	1.12±0.073		
0.874	0.916±0.069		
0.924	0.64±0.064		
0.973	0.432±0.058		

π^+ 8 $A{\cdot}GeV$, 23-39% Central			
Y: 1.1 - 1.48		Y: 1.48 - 1.84	
$m_\perp$ (GeV)	Yield	$m_\perp$ (GeV)	Yield
0.192	56.6±2.6	0.229	42.7 ± 1.7
0.227	40.8±1.4	0.277	27.1 ± 0.971
0.275	26.8±0.9	0.325	18.4 ± 0.661
0.325	17.6±0.62	0.375	12.4 ± 0.468
0.375	12.1±0.44	0.425	8.56 ± 0.336
0.425	8.39±0.32	0.475	5.99 ± 0.244
0.475	5.91±0.24	0.525	4.22 ± 0.181
0.525	4.14±0.18	0.574	3.13 ± 0.145
0.575	3.06±0.14	0.623	2.24 ± 0.125
0.625	2.18±0.1	0.673	1.66 ± 0.116
0.675	1.68±0.085	0.72	1.26 ± 0.128
0.725	1.27±0.068		
0.774	0.85±0.052		
0.824	0.725±0.048		
0.874	0.453±0.038		
0.924	0.358±0.039		
0.973	0.26±0.037		

π^+ 2 $A{\cdot}GeV$, 0-5% Central			
Y: 0.68 - 0.91		Y: 0.91 - 1.14	
$m_\perp$ (GeV)	Yield	$m_\perp$ (GeV)	Yield
0.278	32.8±1.9	0.234	55.2 ± 3.62
0.327	16.4±0.95	0.277	33.2 ± 1.86
0.376	9.76±0.58	0.325	19.1 ± 1.09
0.425	6.36±0.41	0.375	9.72 ± 0.652
0.475	3.63±0.27	0.427	5.93 ± 0.418
0.525	2.15±0.18	0.476	3.48 ± 0.258
0.575	1.46±0.14	0.525	2.35 ± 0.191
0.625	0.896±0.098	0.576	1.36 ± 0.124
0.675	0.717±0.081	0.625	001 ± 0.0978
0.725	0.501±0.061	0.675	0.569 ± 0.0687
0.775	0.323±0.047	0.725	0.431 ± 0.0552
0.825	0.199±0.034	0.775	0.303 ± 0.0432
0.876	0.0989±0.023	0.825	0.199 ± 0.0331
0.925	0.0883±0.02	0.875	0.141 ± 0.0268
0.975	0.0527±0.015	0.925	0.0756 ± 0.018
1.03	0.0556±0.015	0.975	0.0733 ± 0.0171
1.08	0.0217±0.0087	1.02	0.0606 ± 0.0155
1.12	0.0178±0.0076	1.07	0.0443 ± 0.0142
1.18	0.011±0.0057	1.12	0.00613 ± 0.00625

π^- 2 $A{\cdot}GeV$, 5-12% Central			
Y: 0.68 - 0.91		Y: 0.91 - 1.14	
$m_\perp$ (GeV)	Yield	$m_\perp$ (GeV)	Yield
0.278	23.8±1.4	0.234	41.9 ± 2.67
0.327	13.1±0.73	0.277	22.7 ± 1.29
0.376	6.98±0.42	0.325	14.1 ± 0.791
0.425	4.23±0.28	0.375	7.32 ± 0.48
0.475	2.4±0.18	0.427	4.32 ± 0.3
0.525	1.64±0.14	0.476	2.66 ± 0.19
0.575	1.09±0.1	0.525	1.54 ± 0.128
0.625	0.725±0.075	0.576	1.07 ± 0.0935
0.675	0.483±0.057	0.625	0.699 ± 0.0681
0.725	0.297±0.039	0.675	0.385 ± 0.0475
0.775	0.194±0.03	0.725	0.307 ± 0.0391
0.825	0.113±0.021	0.775	0.157 ± 0.0256
0.876	0.0598±0.015	0.825	0.104 ± 0.0198
0.925	0.0669±0.015	0.875	0.118 ± 0.0206
0.975	0.0442±0.012	0.925	0.0598 ± 0.0137
1.03	0.0311±0.0092	0.975	0.0465 ± 0.0113
1.08	0.0187±0.0066	1.02	0.0185 ± 0.0069
1.12	0.0124±0.0053	1.07	0.014 ± 0.00656
1.18	0.0117±0.005	1.12	0.0365 ± 0.0136
1.22	0.00462±0.0034	1.17	0.024 ± 0.0174
1.27	0.00407±0.0041		

π^- 2 $A{\cdot}GeV$, 12-23% Central			
Y: 0.68 - 0.91		Y: 0.91 - 1.14	
$m_\perp$ (GeV)	Yield	$m_\perp$ (GeV)	Yield
0.278	15.7±0.89	0.234	29.4 ± 1.81
0.327	8.72±0.48	0.277	16.5 ± 0.898
0.376	4.65±0.27	0.325	8.35 ± 0.48
0.425	2.97±0.19	0.375	4.64 ± 0.306
0.475	1.62±0.12	0.427	2.74 ± 0.193
0.525	0.991±0.085	0.476	1.69 ± 0.122
0.575	0.751±0.068	0.525	1.08 ± 0.087
0.625	0.44±0.046	0.576	0.7 ± 0.0608
0.675	0.259±0.032	0.625	0.444 ± 0.0436
0.725	0.173±0.024	0.675	0.279 ± 0.0327
0.775	0.101±0.017	0.725	0.19 ± 0.0246
0.825	0.0992±0.016	0.775	0.117 ± 0.0178
0.876	0.0609±0.012	0.825	0.067 ± 0.0127
0.925	0.04±0.0092	0.875	0.0605 ± 0.0118
0.975	0.019±0.0061	0.925	0.0275 ± 0.00722
1.03	0.012±0.0045	0.975	0.0243 ± 0.00657
1.08	0.00972±0.0039	1.02	0.0105 ± 0.00416
1.12	0.00797±0.0034	1.07	0.00913 ± 0.00427
1.18	0.00632±0.003	1.12	0.0148 ± 0.00691

π^- 2 $A{\cdot}GeV$, 23-39% Central			
Y: 0.68 - 0.91		Y: 0.91 - 1.14	
$m_\perp$ (GeV)	Yield	$m_\perp$ (GeV)	Yield
0.278	9.54±0.57	0.234	18.1 ± 1.16
0.327	4.78±0.28	0.277	9.82 ± 0.562
0.376	2.54±0.16	0.325	5.14 ± 0.307
0.425	1.75±0.12	0.375	2.71 ± 0.189
0.475	0.914±0.074	0.427	1.5 ± 0.114
0.525	0.604±0.054	0.476	0.956 ± 0.0741
0.575	0.37±0.038	0.525	0.506 ± 0.0474
0.625	0.231±0.027	0.576	0.327 ± 0.0332
0.675	0.149±0.02	0.625	0.243 ± 0.0263
0.725	0.103±0.015	0.675	0.158 ± 0.0201
0.775	0.0473±0.0096	0.725	0.0908 ± 0.0139
0.825	0.0382±0.0083	0.775	0.0655 ± 0.011
0.876	0.0192±0.0055	0.825	0.0383 ± 0.00789
0.925	0.0129±0.0042	0.875	0.0267 ± 0.00636
0.975	0.0162±0.0047	0.925	0.0195 ± 0.00513
1.03	0.011±0.0037	0.975	0.0106 ± 0.00356
1.08	0.00388±0.002	1.02	0.00422 ± 0.0022
1.12	0.00179±0.0013	1.07	0.0039 ± 0.00233
1.18	0.00256±0.0015		
1.22	0.000953±0.00097		

π^- 4 $A{\cdot}GeV$, 0-5% Central			
Y: 0.88 - 1.17		Y: 1.17 - 1.46	
$m_\perp$ (GeV)	Yield	$m_\perp$ (GeV)	Yield
0.233	87.7±04	0.183	169 ± 9.5
0.278	48.9±1.9	0.227	92.9 ± 4.18
0.325	30.9±1.2	0.276	53.5 ± 2.39
0.375	19.3±0.8	0.326	29.7 ± 1.4
0.426	12.6±0.55	0.376	19.2 ± 0.902
0.475	8.17±0.38	0.425	013 ± 0.626
0.525	5.89±0.28	0.475	8.47 ± 0.438
0.575	4.2±0.21	0.525	5.66 ± 0.322
0.625	003±0.16	0.575	4.19 ± 0.25
0.675	1.95±0.12	0.625	2.82 ± 0.181
0.725	1.54±0.097	0.675	2.07 ± 0.144
0.775	1.05±0.073	0.725	1.62 ± 0.12
0.825	0.828±0.062	0.774	1.15 ± 0.095
0.875	0.567±0.048	0.825	0.789 ± 0.0762
0.925	0.437±0.04	0.873	0.67 ± 0.075
0.975	0.34±0.033	0.922	0.477 ± 0.0777
1.02	0.277±0.032		
1.07	0.157±0.026		
1.12	0.119±0.028		
1.17	0.125±0.044		

π^- 4 $A{\cdot}GeV$, 5-12% Central			
Y: 0.88 - 1.17		Y: 1.17 - 1.46	
$m_\perp$ (GeV)	Yield	$m_\perp$ (GeV)	Yield
0.233	67.4±03	0.183	118 ± 6.65
0.278	39.2±1.5	0.227	71.3 ± 3.14
0.325	23.6±0.91	0.276	041 ± 1.79
0.375	14.7±0.6	0.326	23.1 ± 1.07
0.426	9.24±0.4	0.376	14.9 ± 0.681
0.475	6.16±0.28	0.425	9.94 ± 0.469
0.525	4.28±0.21	0.475	6.3 ± 0.322
0.575	3.06±0.15	0.525	4.68 ± 0.254
0.625	2.26±0.12	0.575	3.07 ± 0.181
0.675	1.49±0.089	0.625	2.17 ± 0.135
0.725	1.15±0.071	0.675	1.66 ± 0.11
0.775	0.854±0.057	0.725	1.14 ± 0.0844
0.825	0.606±0.045	0.774	0.788 ± 0.0656
0.875	0.452±0.037	0.825	0.57 ± 0.0551
0.925	0.325±0.029	0.873	0.407 ± 0.0486
0.975	0.227±0.023	0.922	0.369 ± 0.058
1.02	0.177±0.021		
1.07	0.124±0.02		
1.12	0.0731±0.019		
1.17	0.041±0.021		

π^- 4 $A{\cdot}GeV$, 12-23% Central			
Y: 0.88 - 1.17		Y: 1.17 - 1.46	
$m_\perp$ (GeV)	Yield	$m_\perp$ (GeV)	Yield
0.233	48.7±2.1	0.183	96.4 ± 4.96
0.278	27.1±01	0.227	51.1 ± 2.17
0.325	16.4±0.62	0.276	30.1 ± 1.26
0.375	10.2±0.41	0.326	17.1 ± 0.75
0.426	6.65±0.28	0.376	10.4 ± 0.462
0.475	4.33±0.19	0.425	6.62 ± 0.306
0.525	3.11±0.14	0.475	4.76 ± 0.229
0.575	2.12±0.1	0.525	3.18 ± 0.168
0.625	1.49±0.079	0.575	2.18 ± 0.123
0.675	1.09±0.062	0.625	1.48 ± 0.0899
0.725	0.799±0.048	0.675	1.07 ± 0.0705
0.775	0.573±0.037	0.725	0.732 ± 0.0539
0.825	0.422±0.03	0.774	0.562 ± 0.0444
0.875	0.307±0.024	0.825	0.354 ± 0.0341
0.925	0.221±0.019	0.873	0.314 ± 0.0342
0.975	0.157±0.015	0.922	0.216 ± 0.0349
1.02	0.111±0.013		
1.07	0.0766±0.012		
1.12	0.0576±0.014		
1.17	0.0248±0.013		

π^- 4 $A{\cdot}GeV$, 23-39% Central			
Y: 0.88 - 1.17		Y: 1.17 - 1.46	
$m_\perp$ (GeV)	Yield	$m_\perp$ (GeV)	Yield
0.233	29.3±1.3	0.183	56.1 ± 3.02
0.278	15.9±0.62	0.227	30.8 ± 1.35
0.325	9.78±0.38	0.276	17.3 ± 0.757
0.375	6.14±0.25	0.326	10.4 ± 0.471
0.426	3.82±0.17	0.376	6.07 ± 0.281
0.475	2.72±0.12	0.425	4.1 ± 0.195
0.525	1.7±0.084	0.475	2.68 ± 0.136
0.575	1.26±0.064	0.525	1.7 ± 0.0969
0.625	0.876±0.049	0.575	1.2 ± 0.0726
0.675	0.581±0.036	0.625	0.897 ± 0.0568
0.725	0.443±0.028	0.675	0.594 ± 0.0421
0.775	0.295±0.021	0.725	0.43 ± 0.0335
0.825	0.215±0.017	0.774	0.285 ± 0.0253
0.875	0.156±0.014	0.825	0.229 ± 0.0225
0.925	0.113±0.011	0.873	0.167 ± 0.02
0.975	0.0738±0.0083	0.922	0.0963 ± 0.0187
1.02	0.0499±0.0072		
1.07	0.0451±0.0079		
1.12	0.0316±0.0079		
1.17	0.0212±0.0099		

π^- 6 $A{\cdot}GeV$, 0-5% Central			
Y: 1.01 - 1.35		Y: 1.35 - 1.69	
$m_\perp$ (GeV)	Yield	$m_\perp$ (GeV)	Yield
0.19	191±10	0.188	193 ± 011
0.226	121±4.5	0.228	122 ± 4.73
0.275	71.8±2.8	0.276	73.4 ± 2.77
0.325	45.5±02	0.326	46.6 ± 1.78
0.375	30.8±1.4	0.375	29.3 ± 1.18
0.425	021±1.1	0.425	20.8 ± 0.877
0.475	13.8±0.76	0.475	13.5 ± 0.621
0.525	9.76±0.57	0.525	9.82 ± 0.485
0.575	7.41±0.46	0.575	7.08 ± 0.377
0.625	5.2±0.35	0.624	4.73 ± 0.284
0.675	3.88±0.29	0.674	3.59 ± 0.248
0.725	2.49±0.21	0.723	2.57 ± 0.222
0.775	2.06±0.18	0.771	2.03 ± 0.25
0.825	1.64±0.15		
0.874	1.08±0.12		
0.924	1.02±0.14		
0.974	0.702±0.12		
1.02	0.454±0.12		
1.07	0.154±0.092		

π^- 6 $A{\cdot}GeV$, 5-12% Central			
Y: 1.01 - 1.35		Y: 1.35 - 1.69	
$m_\perp$ (GeV)	Yield	$m_\perp$ (GeV)	Yield
0.19	153±7.9	0.188	149 ± 8.17
0.226	97.3±3.5	0.228	99.5 ± 3.7
0.275	60.4±2.3	0.276	59.5 ± 2.16
0.325	35.7±1.5	0.326	038 ± 1.4
0.375	024±1.1	0.375	23.7 ± 0.922
0.425	16.1±0.79	0.425	16.4 ± 0.668
0.475	11.3±0.59	0.475	10.8 ± 0.477
0.525	7.42±0.42	0.525	7.82 ± 0.37
0.575	5.45±0.33	0.575	5.44 ± 0.28
0.625	3.89±0.26	0.624	004 ± 0.224
0.675	3.14±0.22	0.674	2.95 ± 0.191
0.725	2.17±0.17	0.723	2.32 ± 0.182
0.775	1.58±0.13	0.771	1.81 ± 0.2
0.825	1.24±0.11		
0.874	0.916±0.097		
0.924	0.629±0.092		
0.974	0.462±0.082		
1.02	0.456±0.099		
1.07	0.399±0.13		

π^- 6 $A{\cdot}GeV$, 12-23% Central			
Y: 1.01 - 1.35		Y: 1.35 - 1.69	
$m_\perp$ (GeV)	Yield	$m_\perp$ (GeV)	Yield
0.19	108±5.3	0.188	117 ± 5.85
0.226	71.4±2.4	0.228	69.9 ± 2.5
0.275	42.1±1.5	0.276	043 ± 1.5
0.325	27.4±1.1	0.326	26.6 ± 0.945
0.375	16.6±0.72	0.375	17.2 ± 0.638
0.425	11.2±0.53	0.425	11.1 ± 0.44
0.475	8.07±0.4	0.475	8.13 ± 0.337
0.525	5.85±0.31	0.525	5.56 ± 0.251
0.575	3.76±0.22	0.575	3.91 ± 0.19
0.625	2.69±0.17	0.624	3.02 ± 0.158
0.675	2.15±0.15	0.674	2.03 ± 0.126
0.725	1.48±0.11	0.723	1.57 ± 0.118
0.775	1.02±0.084	0.771	1.13 ± 0.124
0.825	0.769±0.069		
0.874	0.616±0.063		
0.924	0.537±0.067		
0.974	0.335±0.056		
1.02	0.26±0.058		
1.07	0.125±0.06		

π^- 6 $A{\cdot}GeV$, 23-39% Central			
Y: 1.01 - 1.35		Y: 1.35 - 1.69	
$m_\perp$ (GeV)	Yield	$m_\perp$ (GeV)	Yield
0.19	71.3±3.5	0.188	78.6 ± 3.94
0.226	46.8±1.6	0.228	47.3 ± 1.69
0.275	27.3±01	0.276	028 ± 0.984
0.325	17.5±0.71	0.326	17.2 ± 0.617
0.375	10.7±0.48	0.375	10.8 ± 0.408
0.425	7.53±0.36	0.425	7.45 ± 0.295
0.475	5.01±0.26	0.475	5.13 ± 0.217
0.525	3.62±0.2	0.525	3.71 ± 0.168
0.575	2.67±0.16	0.575	2.39 ± 0.12
0.625	1.79±0.12	0.624	1.81 ± 0.0988
0.675	1.32±0.094	0.674	1.4 ± 0.0869
0.725	0.98±0.074	0.723	0.942 ± 0.0744
0.775	0.71±0.058	0.771	0.872 ± 0.0912
0.825	0.462±0.044		
0.874	0.419±0.043		
0.924	0.263±0.038		
0.974	0.211±0.037		
1.02	0.123±0.033		
1.07	0.0462±0.028		

π^- 8 $A{\cdot}GeV$, 0-5% Central			
Y: 1.1 - 1.48		Y: 1.48 - 1.84	
$m_\perp$ (GeV)	Yield	$m_\perp$ (GeV)	Yield
0.187	225±9.1	0.189	213 ± 12.2
0.226	148±4.9	0.228	140 ± 5.51
0.275	91.9±3.2	0.276	91.6 ± 3.43
0.325	59.4±2.1	0.325	57.8 ± 2.21
0.375	40.7±1.5	0.375	38.4 ± 1.55
0.425	27.2±1.1	0.426	25.1 ± 1.07
0.475	19.1±0.78	0.475	18.7 ± 0.815
0.525	13.7±0.59	0.525	13.1 ± 0.606
0.575	9.51±0.44	0.575	10.1 ± 0.5
0.625	7.15±0.35	0.624	8.32 ± 0.466
0.675	5.4±0.28	0.673	5.6 ± 0.404
0.725	4.02±0.22	0.72	3.86 ± 0.419
0.774	2.92±0.18		
0.824	2.48±0.17		
0.874	1.76±0.14		
0.924	0.97±0.11		
0.973	0.835±0.12		

π^- 8 $A{\cdot}GeV$, 5-12% Central			
Y: 1.1 - 1.48		Y: 1.48 - 1.84	
$m_\perp$ (GeV)	Yield	$m_\perp$ (GeV)	Yield
0.187	183±7.1	0.189	167 ± 9.07
0.226	118±3.8	0.228	111 ± 4.2
0.275	72.1±2.4	0.276	69.8 ± 2.54
0.325	45.2±1.6	0.325	45.7 ± 1.69
0.375	31.1±1.1	0.375	30.7 ± 1.19
0.425	20.7±0.79	0.426	20.2 ± 0.82
0.475	14.5±0.58	0.475	14.5 ± 0.61
0.525	10.3±0.44	0.525	010 ± 0.449
0.575	7.35±0.33	0.575	7.8 ± 0.371
0.625	5.44±0.26	0.624	5.76 ± 0.32
0.675	4.03±0.2	0.673	4.22 ± 0.293
0.725	3.04±0.16	0.72	3.57 ± 0.342
0.774	2.24±0.13		
0.824	1.91±0.12		
0.874	1.38±0.11		
0.924	1.07±0.1		
0.973	0.831±0.1		

π^- 8 $A{\cdot}GeV$, 12-23% Central			
Y: 1.1 - 1.48		Y: 1.48 - 1.84	
$m_\perp$ (GeV)	Yield	$m_\perp$ (GeV)	Yield
0.187	137±5.1	0.189	135 ± 6.65
0.226	87.9±2.7	0.228	89.7 ± 3.17
0.275	51.6±1.7	0.276	55.6 ± 1.91
0.325	33.1±1.1	0.325	34.2 ± 1.2
0.375	22.5±0.79	0.375	24.2 ± 0.88
0.425	14.9±0.55	0.426	14.8 ± 0.573
0.475	10.8±0.42	0.475	10.4 ± 0.417
0.525	7.54±0.31	0.525	7.53 ± 0.318
0.575	5.77±0.24	0.575	5.34 ± 0.245
0.625	3.96±0.18	0.624	4.32 ± 0.225
0.675	2.86±0.14	0.673	2.96 ± 0.196
0.725	2.22±0.11	0.72	2.22 ± 0.211
0.774	1.57±0.089		
0.824	1.19±0.077		
0.874	0.898±0.068		
0.924	0.643±0.064		
0.973	0.468±0.06		

π^- 8 $A{\cdot}GeV$, 23-39% Central			
Y: 1.1 - 1.48		Y: 1.48 - 1.84	
$m_\perp$ (GeV)	Yield	$m_\perp$ (GeV)	Yield
0.187	84.8±3.2	0.189	86.8 ± 4.27
0.226	54.9±1.7	0.228	56.4 ± 2.01
0.275	33.9±1.1	0.276	34.7 ± 1.2
0.325	21.5±0.74	0.325	22.3 ± 0.784
0.375	14.3±0.5	0.375	14.5 ± 0.539
0.425	9.86±0.37	0.426	9.57 ± 0.372
0.475	6.66±0.26	0.475	6.79 ± 0.272
0.525	4.71±0.19	0.525	4.8 ± 0.204
0.575	3.36±0.15	0.575	3.49 ± 0.159
0.625	2.43±0.11	0.624	2.53 ± 0.135
0.675	1.73±0.087	0.673	1.94 ± 0.128
0.725	1.27±0.068	0.72	1.27 ± 0.128
0.774	1.02±0.059		
0.824	0.719±0.048		
0.874	0.486±0.04		
0.924	0.369±0.039		
0.973	0.268±0.037		

π^- 2 $A{\cdot}GeV$, 0-5% Central			
Y: 0.68 - 0.91		Y: 0.91 - 1.14	
$m_\perp$ (GeV)	Yield	$m_\perp$ (GeV)	Yield
1.03	37.4±1.5	1.03	32.9 ± 2.34
1.08	031±1.1	1.08	030 ± 1.44
1.13	25.6±0.86	1.13	24.2 ± 1.05
1.18	20.8±0.68	1.18	19.5 ± 0.787
1.23	16.6±0.54	1.23	15.3 ± 0.617
1.28	13.4±0.44	1.27	012 ± 0.501
1.33	9.84±0.33	1.33	9.04 ± 0.391
1.37	7.68±0.27	1.38	6.66 ± 0.3
1.43	5.66±0.21	1.43	5.23 ± 0.24
1.48	4.13±0.16	1.48	3.81 ± 0.187
1.52	3.05±0.13	1.53	2.76 ± 0.143
1.58	2.09±0.097	1.57	2.1 ± 0.116
1.62	1.52±0.077	1.63	1.48 ± 0.0891
1.68	001±0.057	1.68	1.03 ± 0.0689
1.72	0.807±0.049	1.73	0.801 ± 0.0578
1.77	0.559±0.038	1.78	0.514 ± 0.0438
1.82	0.38±0.03	1.83	0.411 ± 0.0377
1.88	0.263±0.023	1.88	0.248 ± 0.0268
1.93	0.191±0.019	1.93	0.182 ± 0.0219
1.98	0.11±0.014	1.98	0.109 ± 0.0159
2.03	0.0719±0.011	2.02	0.0749 ± 0.0127
2.07	0.0636±0.0098	2.07	0.0578 ± 0.0109
2.13	0.037±0.0074	2.12	0.0416 ± 0.00933
2.18	0.0205±0.0052	2.17	0.0478 ± 0.0103
2.22	0.00796±0.0032	2.22	0.0222 ± 0.00748
2.27	0.0193±0.0051	2.27	0.0211 ± 0.00788
2.33	0.00445±0.0023	2.32	0.00381 ± 0.00388
2.37	0.00334±0.002	2.37	0.00459 ± 0.00468
2.42	0.00101±0.001		
2.47	0.00548±0.0026		
2.52	0.00132±0.0013		
2.57	000±0.0014		
2.62	0.00221±0.0023		

proton 2 $A{\cdot}GeV$, 5-12% Central			
Y: 0.68 - 0.91		Y: 0.91 - 1.14	
$m_\perp$ (GeV)	Yield	$m_\perp$ (GeV)	Yield
1.03	31.3±1.2	1.03	27.1 ± 1.82
1.08	25.8±0.88	1.08	24.5 ± 1.12
1.13	20.2±0.66	1.13	19.3 ± 0.806
1.18	15.9±0.51	1.18	015 ± 0.589
1.23	12.1±0.39	1.23	11.7 ± 0.46
1.28	9.41±0.31	1.27	8.25 ± 0.345
1.33	7.16±0.24	1.33	6.28 ± 0.272
1.37	5.21±0.18	1.38	4.73 ± 0.212
1.43	3.75±0.14	1.43	3.43 ± 0.161
1.48	2.64±0.11	1.48	2.55 ± 0.127
1.52	1.9±0.083	1.53	1.83 ± 0.0962
1.58	1.31±0.063	1.57	1.21 ± 0.0709
1.62	0.912±0.049	1.63	0.896 ± 0.0571
1.68	0.672±0.039	1.68	0.641 ± 0.0447
1.72	0.438±0.029	1.73	0.469 ± 0.036
1.77	0.311±0.023	1.78	0.334 ± 0.0291
1.82	0.21±0.018	1.83	0.268 ± 0.0251
1.88	0.145±0.014	1.88	0.148 ± 0.0171
1.93	0.121±0.013	1.93	0.0968 ± 0.013
1.98	0.0689±0.009	1.98	0.0706 ± 0.0107
2.03	0.051±0.0075	2.02	0.0338 ± 0.00686
2.07	0.0437±0.0068	2.07	0.0264 ± 0.00603
2.13	0.0238±0.0049	2.12	0.029 ± 0.00651
2.18	0.0127±0.0034	2.17	0.0116 ± 0.0041
2.22	0.012±0.0033	2.22	0.00463 ± 0.00277
2.27	0.0122±0.0034	2.27	0.00746 ± 0.00388
2.33	0.00324±0.0017	2.32	0.00264 ± 0.00269
2.37	0.000793±0.00081		
2.42	0.00452±0.0019		
2.47	0.000811±0.00083		
2.52	0.00091±0.00093		

proton 2 $A{\cdot}GeV$, 12-23% Central			
Y: 0.68 - 0.91		Y: 0.91 - 1.14	
$m_\perp$ (GeV)	Yield	$m_\perp$ (GeV)	Yield
1.03	23.8±0.88	1.03	22.6 ± 1.38
1.08	18.6±0.62	1.08	17.6 ± 0.781
1.13	14.1±0.45	1.13	014 ± 0.565
1.18	10.4±0.34	1.18	10.1 ± 0.392
1.23	7.8±0.25	1.23	7.7 ± 0.301
1.28	5.82±0.19	1.27	5.11 ± 0.215
1.33	4.28±0.15	1.33	3.76 ± 0.166
1.37	003±0.11	1.38	2.67 ± 0.124
1.43	2.12±0.083	1.43	1.98 ± 0.0958
1.48	1.51±0.063	1.48	1.34 ± 0.0711
1.52	1.04±0.048	1.53	0.993 ± 0.0553
1.58	0.751±0.037	1.57	0.697 ± 0.0424
1.62	0.497±0.028	1.63	0.472 ± 0.032
1.68	0.331±0.021	1.68	0.326 ± 0.0248
1.72	0.243±0.017	1.73	0.218 ± 0.0191
1.77	0.146±0.012	1.78	0.177 ± 0.0166
1.82	0.128±0.011	1.83	0.127 ± 0.0134
1.88	0.0648±0.0073	1.88	0.0808 ± 0.01
1.93	0.037±0.0052	1.93	0.0475 ± 0.00714
1.98	0.0325±0.0048	1.98	0.0347 ± 0.00587
2.03	0.0195±0.0037	2.02	0.0253 ± 0.00486
2.07	0.0131±0.0028	2.07	0.0155 ± 0.0037
2.13	0.00965±0.0025	2.12	0.00786 ± 0.00265
2.18	0.00558±0.0018	2.17	0.00506 ± 0.00217
2.22	0.00407±0.0015	2.22	0.00197 ± 0.00144
2.27	0.00412±0.0015	2.27	0.00474 ± 0.00247
2.33	0.00154±0.00092	2.32	0.00168 ± 0.00172
2.37	0.000931±0.00068	2.37	0.00426 ± 0.0031
2.42	0.00199±0.001		
2.47	000±0.00041		
2.52	000±0.0005		
2.57	000±0.00062		
2.62	000±0.00081		
2.67	000±0.0012		
2.72	000±0.0017		
2.77	0.00374±0.0038		

proton 2 $A{\cdot}GeV$, 23-39% Central			
Y: 0.68 - 0.91		Y: 0.91 - 1.14	
$m_\perp$ (GeV)	Yield	$m_\perp$ (GeV)	Yield
1.03	15.6±0.58	1.03	14.3 ± 0.898
1.08	11.3±0.39	1.08	10.8 ± 0.494
1.13	8.18±0.27	1.13	7.73 ± 0.33
1.18	5.89±0.2	1.18	5.35 ± 0.222
1.23	4.26±0.14	1.23	3.91 ± 0.165
1.28	2.99±0.11	1.27	2.71 ± 0.123
1.33	2.03±0.075	1.33	1.94 ± 0.0927
1.37	1.41±0.056	1.38	1.33 ± 0.0681
1.43	0.992±0.043	1.43	0.882 ± 0.0487
1.48	0.659±0.031	1.48	0.605 ± 0.0367
1.52	0.467±0.024	1.53	0.399 ± 0.0265
1.58	0.3±0.018	1.57	0.253 ± 0.0193
1.62	0.2±0.013	1.63	0.204 ± 0.0165
1.68	0.136±0.01	1.68	0.142 ± 0.0129
1.72	0.0877±0.0078	1.73	0.0929 ± 0.00977
1.77	0.0605±0.0062	1.78	0.0649 ± 0.00789
1.82	0.0346±0.0044	1.83	0.0379 ± 0.0057
1.88	0.0225±0.0035	1.88	0.0247 ± 0.00435
1.93	0.0158±0.0028	1.93	0.0247 ± 0.00422
1.98	0.0132±0.0025	1.98	0.0104 ± 0.0026
2.03	0.00822±0.0019	2.02	0.00364 ± 0.00145
2.07	0.00529±0.0015	2.07	0.00299 ± 0.00128
2.13	0.00254±0.001	2.12	0.00481 ± 0.0017
2.18	0.00249±0.00099	2.17	0.00173 ± 0.00103
2.22	0.0021±0.0009	2.22	000 ± 0.000554
2.27	0.000347±0.00035	2.27	0.000827 ± 0.000844
2.33	0.000659±0.00048	2.32	0.00115 ± 0.00117
2.37	0.000346±0.00035		
2.42	0.000654±0.00048		
2.47	0.000321±0.00033		

proton 4 $A{\cdot}GeV$, 0-5% Central			
Y: 0.88 - 1.17		Y: 1.17 - 1.46	
$m_\perp$ (GeV)	Yield	$m_\perp$ (GeV)	Yield
1.03	28.2±1.3	1.08	20.3 ± 1.25
1.08	22.8±0.86	1.13	017 ± 0.827
1.13	19.9±0.69	1.18	14.4 ± 0.687
1.18	16.4±0.53	1.23	12.5 ± 0.611
1.23	13.2±0.42	1.28	9.66 ± 0.482
1.28	10.9±0.35	1.33	8.13 ± 0.388
1.33	8.68±0.28	1.38	6.43 ± 0.303
1.38	6.92±0.23	1.43	5.26 ± 0.246
1.43	5.38±0.19	1.48	3.88 ± 0.191
1.48	4.22±0.15	1.53	3.08 ± 0.155
1.52	3.37±0.13	1.57	2.42 ± 0.129
1.58	2.49±0.098	1.62	1.97 ± 0.111
1.63	1.91±0.08	1.68	1.56 ± 0.0946
1.68	1.53±0.067	1.72	1.26 ± 0.0813
1.72	1.14±0.054	1.77	0.918 ± 0.0691
1.77	0.898±0.045	1.82	0.653 ± 0.0621
1.83	0.711±0.038	1.87	0.509 ± 0.0602
1.87	0.549±0.032	1.93	0.56 ± 0.0717
1.93	0.391±0.025		
1.98	0.322±0.022		
2.02	0.238±0.018		
2.07	0.16±0.015		
2.12	0.137±0.015		
2.17	0.0917±0.012		
2.22	0.0596±0.01		
2.27	0.0527±0.011		
2.32	0.0372±0.01		
2.37	0.0492±0.014		

proton 4 $A{\cdot}GeV$, 5-12% Central			
Y: 0.88 - 1.17		Y: 1.17 - 1.46	
$m_\perp$ (GeV)	Yield	$m_\perp$ (GeV)	Yield
1.03	22.6±0.97	1.08	16.3 ± 0.954
1.08	18.8±0.68	1.13	13.3 ± 0.623
1.13	15.7±0.53	1.18	11.3 ± 0.52
1.18	13.2±0.41	1.23	9.75 ± 0.459
1.23	10.4±0.32	1.28	7.3 ± 0.355
1.28	8.32±0.26	1.33	5.99 ± 0.282
1.33	6.52±0.21	1.38	4.9 ± 0.225
1.38	5.21±0.17	1.43	3.85 ± 0.178
1.43	3.94±0.14	1.48	2.87 ± 0.139
1.48	3.07±0.11	1.53	2.28 ± 0.113
1.52	2.35±0.088	1.57	1.86 ± 0.096
1.58	1.82±0.071	1.62	1.38 ± 0.0776
1.63	1.42±0.059	1.68	1.08 ± 0.0655
1.68	1.08±0.047	1.72	0.819 ± 0.0543
1.72	0.801±0.038	1.77	0.625 ± 0.0476
1.77	0.624±0.032	1.82	0.504 ± 0.0463
1.83	0.479±0.026	1.87	0.341 ± 0.0409
1.87	0.343±0.021	1.93	0.3 ± 0.0433
1.93	0.264±0.017		
1.98	0.219±0.015		
2.02	0.145±0.012		
2.07	0.112±0.01		
2.12	0.0866±0.0095		
2.17	0.0721±0.009		
2.22	0.0515±0.008		
2.27	0.0386±0.0077		
2.32	0.0177±0.006		
2.37	0.0174±0.0069		
2.42	0.00911±0.0066		

proton 4 $A \cdot GeV$, 12-23% Central			
Y: 0.88 - 1.17		Y: 1.17 - 1.46	
$m_\perp$ (GeV)	Yield	$m_\perp$ (GeV)	Yield
1.03	17.7±0.71	1.08	13.1 ± 0.705
1.08	14.4±0.5	1.13	10.4 ± 0.451
1.13	11.9±0.38	1.18	8.62 ± 0.371
1.18	9.38±0.29	1.23	6.89 ± 0.311
1.23	7.34±0.22	1.28	5.1 ± 0.238
1.28	5.67±0.18	1.33	4.17 ± 0.189
1.33	4.41±0.14	1.38	3.11 ± 0.142
1.38	3.34±0.11	1.43	2.62 ± 0.117
1.43	2.55±0.087	1.48	1.95 ± 0.0916
1.48	1.97±0.07	1.53	1.51 ± 0.0732
1.52	1.48±0.055	1.57	1.11 ± 0.0578
1.58	1.14±0.045	1.62	0.895 ± 0.0497
1.63	0.854±0.036	1.68	0.684 ± 0.0414
1.68	0.635±0.028	1.72	0.471 ± 0.0322
1.72	0.498±0.024	1.77	0.401 ± 0.0301
1.77	0.374±0.019	1.82	0.276 ± 0.0268
1.83	0.279±0.016	1.87	0.229 ± 0.027
1.87	0.21±0.013	1.93	0.202 ± 0.0286
1.93	0.144±0.0098		
1.98	0.11±0.0082		
2.02	0.0963±0.0076		
2.07	0.0629±0.0061		
2.12	0.0535±0.0059		
2.17	0.0402±0.0053		
2.22	0.0276±0.0046		
2.27	0.018±0.0041		
2.32	0.0101±0.0036		
2.37	0.00777±0.0036		
2.42	0.00849±0.0051		

proton 4 $A{\cdot}GeV$, 23-39% Central			
Y: 0.88 - 1.17		Y: 1.17 - 1.46	
$m_\perp$ (GeV)	Yield	$m_\perp$ (GeV)	Yield
1.03	11.5±0.47	1.08	7.74 ± 0.43
1.08	9.03±0.32	1.13	6.27 ± 0.28
1.13	7.08±0.24	1.18	4.93 ± 0.221
1.18	5.29±0.17	1.23	3.7 ± 0.178
1.23	4.03±0.13	1.28	2.79 ± 0.138
1.28	3.03±0.098	1.33	2.15 ± 0.105
1.33	2.26±0.076	1.38	1.68 ± 0.0814
1.38	1.7±0.059	1.43	1.23 ± 0.0611
1.43	1.29±0.047	1.48	0.926 ± 0.0483
1.48	0.941±0.036	1.53	0.694 ± 0.0376
1.52	0.709±0.029	1.57	0.507 ± 0.0299
1.58	0.504±0.022	1.62	0.411 ± 0.0259
1.63	0.39±0.018	1.68	0.3 ± 0.021
1.68	0.291±0.015	1.72	0.208 ± 0.0166
1.72	0.215±0.012	1.77	0.15 ± 0.0141
1.77	0.165±0.0097	1.82	0.132 ± 0.0147
1.83	0.103±0.007	1.87	0.0858 ± 0.0129
1.87	0.0923±0.0065	1.93	0.0592 ± 0.0121
1.93	0.0576±0.0047		
1.98	0.0539±0.0046		
2.02	0.0345±0.0035		
2.07	0.0214±0.0028		
2.12	0.0178±0.0027		
2.17	0.0193±0.0029		
2.22	0.0111±0.0023		
2.27	0.00809±0.0023		
2.32	0.00535±0.0021		
2.37	0.00652±0.0028		
2.42	0.00395±0.0029		

proton 6 $A{\cdot}GeV$, 0-5% Central			
Y: 1.01 - 1.35		Y: 1.35 - 1.69	
$m_\perp$ (GeV)	Yield	$m_\perp$ (GeV)	Yield
1.03	23.9±1.1	1.09	17.6 ± 1.4
1.08	20.3±0.75	1.13	16.9 ± 0.921
1.13	16.6±0.6	1.18	15.3 ± 0.759
1.18	014±0.51	1.23	12.3 ± 0.599
1.23	11.8±0.43	1.28	9.75 ± 0.46
1.27	10.3±0.39	1.33	8.38 ± 0.404
1.33	8.36±0.33	1.38	6.52 ± 0.334
1.37	6.89±0.28	1.42	5.41 ± 0.293
1.42	5.28±0.23	1.47	4.63 ± 0.261
1.47	4.32±0.2	1.52	3.65 ± 0.237
1.52	3.73±0.18	1.57	2.9 ± 0.224
1.57	3.01±0.16	1.62	2.24 ± 0.229
1.63	2.24±0.13		
1.67	1.77±0.11		
1.72	1.58±0.1		
1.77	1.17±0.087		
1.82	0.96±0.08		
1.87	0.693±0.069		
1.92	0.57±0.067		
1.97	0.454±0.066		
2.02	0.365±0.062		
2.07	0.223±0.053		
2.12	0.227±0.058		
2.17	0.18±0.064		

proton 6 $A{\cdot}GeV$, 5-12% Central			
Y: 1.01 - 1.35		Y: 1.35 - 1.69	
$m_\perp$ (GeV)	Yield	$m_\perp$ (GeV)	Yield
1.03	21.2±0.87	1.09	16.7 ± 1.17
1.08	17.3±0.61	1.13	13.6 ± 0.697
1.13	14.2±0.49	1.18	11.6 ± 0.552
1.18	11.8±0.41	1.23	9.64 ± 0.446
1.23	9.82±0.35	1.28	8.25 ± 0.364
1.27	8.04±0.3	1.33	6.75 ± 0.308
1.33	6.39±0.25	1.38	5.65 ± 0.268
1.37	5.28±0.21	1.42	4.52 ± 0.228
1.42	4.31±0.18	1.47	3.7 ± 0.198
1.47	3.44±0.15	1.52	2.96 ± 0.18
1.52	2.83±0.13	1.57	2.33 ± 0.169
1.57	2.17±0.11	1.62	2.04 ± 0.187
1.63	1.64±0.091		
1.67	1.36±0.08		
1.72	1.02±0.067		
1.77	0.912±0.065		
1.82	0.672±0.056		
1.87	0.495±0.05		
1.92	0.326±0.041		
1.97	0.243±0.04		
2.02	0.252±0.043		
2.07	0.195±0.042		
2.12	0.163±0.041		
2.17	0.165±0.051		

proton 6 $A{\cdot}GeV$, 12-23% Central			
Y: 1.01 - 1.35		Y: 1.35 - 1.69	
$m_\perp$ (GeV)	Yield	$m_\perp$ (GeV)	Yield
1.03	15.5±0.6	1.09	12.6 ± 0.797
1.08	12.5±0.42	1.13	9.79 ± 0.47
1.13	10.5±0.35	1.18	8.54 ± 0.379
1.18	8.54±0.28	1.23	6.73 ± 0.295
1.23	6.94±0.24	1.28	5.52 ± 0.233
1.27	5.67±0.2	1.33	4.45 ± 0.195
1.33	4.41±0.16	1.38	3.61 ± 0.166
1.37	3.65±0.14	1.42	2.9 ± 0.142
1.42	3.02±0.12	1.47	2.26 ± 0.119
1.47	2.32±0.1	1.52	1.9 ± 0.113
1.52	1.78±0.084	1.57	1.45 ± 0.102
1.57	1.39±0.07	1.62	1.14 ± 0.106
1.63	1.24±0.065		
1.67	0.859±0.05		
1.72	0.703±0.044		
1.77	0.536±0.039		
1.82	0.415±0.034		
1.87	0.268±0.028		
1.92	0.253±0.029		
1.97	0.198±0.029		
2.02	0.163±0.028		
2.07	0.104±0.024		
2.12	0.0878±0.024		
2.17	0.0429±0.02		

proton 6 $A{\cdot}GeV$, 23-39% Central			
Y: 1.01 - 1.35		Y: 1.35 - 1.69	
$m_\perp$ (GeV)	Yield	$m_\perp$ (GeV)	Yield
1.03	10.9±0.42	1.09	8.53 ± 0.535
1.08	8.75±0.29	1.13	6.94 ± 0.325
1.13	6.8±0.23	1.18	5.55 ± 0.247
1.18	5.59±0.19	1.23	4.32 ± 0.19
1.23	4.31±0.15	1.28	3.39 ± 0.146
1.27	3.38±0.12	1.33	2.67 ± 0.12
1.33	2.7±0.1	1.38	2.14 ± 0.102
1.37	2.14±0.086	1.42	1.68 ± 0.0858
1.42	1.65±0.071	1.47	1.26 ± 0.0703
1.47	1.25±0.058	1.52	1.04 ± 0.0659
1.52	1.01±0.05	1.57	0.856 ± 0.0634
1.57	0.777±0.042	1.62	0.635 ± 0.0634
1.63	0.608±0.035		
1.67	0.497±0.031		
1.72	0.37±0.025		
1.77	0.272±0.022		
1.82	0.195±0.019		
1.87	0.171±0.018		
1.92	0.118±0.016		
1.97	0.0966±0.016		
2.02	0.0726±0.015		
2.07	0.0638±0.016		
2.12	0.0375±0.013		
2.17	0.046±0.017		

proton 8 $A{\cdot}GeV$, 0-5% Central			
Y: 1.1 - 1.48		Y: 1.48 - 1.84	
$m_\perp$ (GeV)	Yield	$m_\perp$ (GeV)	Yield
1.03	20.4±1.1	1.13	14.2 ± 1.15
1.08	17.6±0.75	1.18	13.6 ± 0.852
1.13	16.1±0.62	1.23	11.8 ± 0.722
1.18	14.1±0.53	1.27	9.77 ± 0.622
1.23	11.9±0.44	1.33	8.79 ± 0.628
1.28	9.91±0.37	1.38	6.95 ± 0.505
1.33	8.31±0.32	1.43	6.38 ± 0.456
1.38	7.07±0.28	1.47	4.61 ± 0.383
1.42	5.54±0.23		
1.48	4.77±0.21		
1.53	3.82±0.17		
1.57	3.14±0.15		
1.62	2.43±0.13		
1.67	2.05±0.12		
1.72	1.64±0.1		
1.77	1.21±0.089		
1.82	1.1±0.087		
1.87	0.714±0.07		
1.92	0.572±0.065		
1.97	0.396±0.062		
2.02	0.366±0.074		

proton 8 $A{\cdot}GeV$, 5-12% Central			
Y: 1.1 - 1.48		Y: 1.48 - 1.84	
$m_\perp$ (GeV)	Yield	$m_\perp$ (GeV)	Yield
1.03	17.9±0.89	1.13	12.7 ± 0.902
1.08	15.1±0.6	1.18	10.5 ± 0.61
1.13	13.3±0.48	1.23	10.1 ± 0.551
1.18	10.9±0.39	1.27	8.26 ± 0.462
1.23	9.26±0.33	1.33	6.2 ± 0.425
1.28	7.59±0.28	1.38	5.14 ± 0.35
1.33	6.3±0.24	1.43	4.38 ± 0.309
1.38	5.4±0.21	1.47	3.67 ± 0.285
1.42	4.5±0.18		
1.48	3.49±0.15		
1.53	2.89±0.13		
1.57	2.3±0.11		
1.62	1.91±0.096		
1.67	1.55±0.085		
1.72	1.11±0.07		
1.77	0.874±0.063		
1.82	0.668±0.056		
1.87	0.557±0.052		
1.92	0.39±0.045		
1.97	0.312±0.046		
2.02	0.237±0.05		

proton 8 $A{\cdot}GeV$, 12-23% Central			
Y: 1.1 - 1.48		Y: 1.48 - 1.84	
$m_\perp$ (GeV)	Yield	$m_\perp$ (GeV)	Yield
1.03	14.1±0.64	1.13	8.85 ± 0.58
1.08	11.9±0.44	1.18	8.58 ± 0.439
1.13	9.84±0.34	1.23	7.26 ± 0.366
1.18	8.17±0.28	1.27	006 ± 0.309
1.23	6.79±0.23	1.33	4.65 ± 0.28
1.28	5.65±0.2	1.38	3.84 ± 0.237
1.33	4.64±0.17	1.43	2.95 ± 0.195
1.38	3.62±0.14	1.47	2.43 ± 0.177
1.42	2.97±0.12		
1.48	2.33±0.096		
1.53	1.92±0.082		
1.57	1.61±0.072		
1.62	1.25±0.062		
1.67	0.916±0.051		
1.72	0.747±0.046		
1.77	0.613±0.042		
1.82	0.484±0.038		
1.87	0.331±0.031		
1.92	0.272±0.03		
1.97	0.257±0.034		
2.02	0.156±0.032		

proton 8 $A{\cdot}GeV$, 23-39% Central			
Y: 1.1 - 1.48		Y: 1.48 - 1.84	
$m_\perp$ (GeV)	Yield	$m_\perp$ (GeV)	Yield
1.03	10.1±0.44	1.13	6.01 ± 0.381
1.08	7.74±0.28	1.18	5.37 ± 0.273
1.13	6.5±0.22	1.23	4.3 ± 0.217
1.18	5.16±0.18	1.27	3.52 ± 0.183
1.23	4.11±0.14	1.33	2.61 ± 0.161
1.28	3.29±0.12	1.38	2.38 ± 0.146
1.33	2.58±0.096	1.43	1.6 ± 0.11
1.38	2.11±0.081	1.47	1.27 ± 0.0983
1.42	1.6±0.066		
1.48	1.29±0.056		
1.53	1.03±0.046		
1.57	0.771±0.038		
1.62	0.619±0.033		
1.67	0.51±0.03		
1.72	0.366±0.025		
1.77	0.31±0.023		
1.82	0.227±0.02		
1.87	0.167±0.018		
1.92	0.153±0.018		
1.97	0.11±0.018		
2.02	0.0503±0.014		

Bibliography

[A+90] T. Abbott et al. A single arm spectrometer detector system for high energy heavy ion experiments. *Nuclear Instruments and Methods in Physics Research*, A290:41–60, 1990.

[A+98a] L. Ahle et al. Particle production at high baryon density in central Au + Au reactions at 11.6A GeV/c. *Physical Review*, C57:R466–R470, 1998.

[A+98b] L. Ahle et al. Proton, deuteron, and triton emission at target rapidity in Au + Au collisions at 10.20A GeV: Spectra and directed flow. *Physical Review*, C57:1416–1427, 1998.

[A+98c] H. Appelshauser et al. Recent results on central pb + pb collisions from experiment na49. *Nucl. Phys.*, A638:91, 1998.

[A+99a] L. Ahle et al. Kaon production in Au+Au collisions at 11.6 A GeV/c. *Physical Review*, C58:3523–3538, 1999.

[A+99b] L. Ahle et al. Simultaneous multiplicity and forward energy characterization of particle spectra in Au+Au collisions at 11.6 $A\cdot$ GeV/c. *Physical Review*, C59, 1999. in press.

[Ahl97] Larry Ahle. *Kaon Production in Au-Au Collisions at 11.6 GeV/c per Nucleon.* PhD thesis, Massachusetts Institute of Technology, 1997.

[ARW98] Mark Alford, Krishna Rajagopal, and Frank Wilczek. QCD at finite baryon density: nucleon droplets and color superconductivity. *Physics Letters*, B422:247–256, 1998.

[B+] J.T. Balewski et al. *Physics Letters.*

[B+74] V. Blobel et al. Multiplicities, topological cross sections, and single particle inclusive distributions from pp interactions at 12 and 24 GeV/c. *Nuclear Physics*, B69:454–492, 1974.

[B+89] D. Beavis et al. A calorimeter for relativistic heavy ion experiments. *Nuclear Instruments and Methods in Physics Research*, A281:367–372, 1989.

[B+97] R. Barth et al. Subthreshold production of kaons and antikaons in nucleus-nucleus collisions at equivalent beam energies. *Physical Review Letters*, 78:4007–4010, 1997.

[B+98] B.B. Back et al. A beam vertex detector using scintillating fibers. *Nuclear Instruments and Methods in Physics Research*, A412:191–199, 1998.

[BG88] G.F. Bertsch and S. Das Gupta. *Physics Reports*, 160, 1988.

[C+90] W. Cassing et al. *Physics Reports*, 188, 1990.

[Cia94] Vincent Cianciolo. *Bose-Einstein Correlations in 14.6 A·GeV/c Si + Au → 2K+ + X Central Collisions.* PhD thesis, Massachusetts Institute of Technology, 1994.

[Col92] Brian A. Cole. *Particle Production at High Transverse Momentum in Nucleus-Nucleus Collisions at the AGS.* PhD thesis, Massachusetts Institute of Technology, 1992.

[DeT96] C. DeTar. Quark gluon plasma in numerical simulations of lattice QCD. In *Quark-Gluon Plasma 2.* World Scientific, 1996.

[DMC98] R. Debbe, C. Müntz, and J. B. Cumming. A high-resolution quartz čerenkov detector for relativistic heavy ion beams. *Nuclear Instruments and Methods in Physics Research*, A403:256–262, 1998.

[E+83] S. Eiseman et al. The MPS II drift chamber system. *Nuclear Instruments and Methods in Physics Research*, 215:140–148, 1983.

[EK80] A. Etkin and M. A. Kramer. The Brookhaven National Laboratory's multiparticle spectrometer drift chamber system. *IEEE Transactions on Nuclear Science*, NS-27:139–144, 1980.

[Etk79] A. Etkin. A drift chamber system for use in high rate environment. *IEEE Transactions on Nuclear Science*, NS-26:54–58, 1979.

[F+79] H. Fesefeldt et al. Strangeness-transfer distributions in proton-proton collisions at 12 and 24 GeV/c. *Nuclear Physics*, B147:317–335, 1979.

[FMM84] V. Flaminio, W.G. Moorhead, and D.R.O. Morrison. Compilation of cross-sections; 3, p and $\overline{p}$ induced reactions. Report 84-01, CERN HERA, 1984.

[G+95a] L. Geer et al. Charge-changing fragmentation of 10.6 GeV/nucleon ^{197}Au nuclei. *Physical Review*, C52:334–345, 1995.

[G+95b] M. Gonin et al. Comparison of experimental data to the Relativistic Quantum Molecular Dynamics model for Si+Al collisons at 14.6 GeV/c. *Physical Review*, C51:310–317, 1995.

[GCG98] J. Geiss, W. Cassing, and C. Greiner. Strangeness production in the hsd transport approach from sis to sps energies. *Nuclear Physics*, A644:107–138, 1998.

[Gro98a] Particle Data Group. Review of particle physics. *European Physical Journal*, C3, 1998.

[Gro98b] D. Groznka. *Nuclear Physics*, A631:262–275c, 1998.

[Hei99] George Heintzelman. *Antibaryon Production in Au+Au Collisions at 11.7 A· GeV/c.* PhD thesis, Massachusetts Institute of Technology, 1999.

[Jac75] J. D. Jackson. *Classical Electrodynamics.* John Wiley & Sons, second edition, 1975.

[L+99] F. Laue et al. Medium effects in kaon and antikaon production in nuclear collisions at subthreshold beam energies. *Physical Review Letters*, 82:1640–1643, 1999.

[lb93] *Numerical Data and Functional Relationships in Science and Technology*, volume I/12B of *Landolt-Börnstein New Series*. Springer-Verlag, Berlin, 1993.

[LB98] G.Q. Li and G.E. Brown. K^-/K^+ ratios in relativistic heavy-ion collisons. *Physical Review*, C58:1698–1705, 1998.

[LK95] B-A. Li and C.M. Ko. *Physical Review*, C52:2037, 1995.

[LLB97] G.Q. Li, C.-H. Lee, and G.E. Brown. Kaon production in heavy ion collisions and maximum mass of neutron stars. *Physical Review Letters*, 79:5214–1643, 1997.

[Mor94] David P. Morrison. *Rapidity Dependence of Kaon Production in Si+Au and Si+Al at 14.6 A GeV/c*. PhD thesis, Massachusetts Institute of Technology, 1994.

[Mou98] Matt Moulson. Private communication, 1998.

[Mül95] H. Müller. Hadron production in proton-proton interactions at medium energies. *Zeitschrift für Physik*, A353:103–111, 1995.

[O+98] C. A. Ogilvie et al. Kaon production in au + au collisions at the ags. *Nucl. Phys.*, A630:571C, 1998.

[Par92] Charles G. Parsons. *Strange Particle Production in 14.6 GeV/A Nucleus-Nucleus Collisions*. PhD thesis, Massachusetts Institute of Technology, 1992.

[R+75] A.M. Rossi et al. Experimental study of the energy dependence in proton-proton inclusive reactions. *Nuclear Physics*, B84:269–305, 1975.

[Raf82] J. Rafelski. *Physics Reports*, page 331, 1982.

[RB82] J. Rafelski and Berndt Müller. Strangeness production in the quark-gluon plasma. *Physical Review Letters*, 48:1066–1069, 1982.

[Rot94] Peter J. Rothschild. *Rapidity Dependence of Antiproton Production in Relativisitic Heavy Ion Collisions at 14.6 GeV/c per Nucleon.* PhD thesis, Massachusetts Institute of Technology, 1994.

[Sak97] Hiroyuki Sako. *Antiproton Production in Au+Au Collisions at 11.7 A·GeV/c.* PhD thesis, University of Tokyo, 1997.

[SG86] H. Stöcker and W. Greiner. *Physics Reports*, 137:277, 1986.

[SHG89] H. Sorge, H. Stöcker, and W. Griener. Poincaré invariant Hamiltonian dynamics: Modelling multi-hadronic interactions in a phase space approach. *Annals of Physics*, 102:266–306, 1989.

[Shi94] Kenta Shigaki. *Study of Hadron Production in Au+Au Collisions at 10.9 A GeV/c with a new Forward-Angle Spectrometer.* PhD thesis, University of Tokyo, 1994.

[Sib96] A.A. Sibirtsev. *Nuclear Physics*, A604:455, 1996.

[SJWR] W. Bauer S.-J. Wang, B.-A. Li and J. Randrup.

[SSG89] H. Sorge, H. Stöcker, and W. Greiner. Poincaré invariant hamiltonian dynamics: Modeling multi-hadronic interactions in a phase space approach. *Annals of Physics*, 102:266–306, 1989.

[Ste90] G. S. F. Stephans. Tracking chamber geometry arrays and data. E802 Internal Memo 54, Brookhaven National Laboratory, 1990.

[Wan96] Fuqiang Wang. *Kaon Production and K/π Ratios in Au+Au Collisions at 11.09 A·GeV/c at the AGS.* PhD thesis, Columbia University, 1996.

[WW97] T. Waas and W. Weise. S-wave interactions of anti-k and eta mesons in nuclear matter. *Nuclear Physics*, A625:287–306, 1997.

[Yao97] Hongbin Yao. Implementation of UNIX workstation and BIT3 VME BUS adaptor in real time DAQ system. Master's thesis, Massachusetts Institute of Technology, 1997.